

Pertanika Journal of  
**SCIENCE &  
TECHNOLOGY**

**JST**

**VOL. 31 (6) OCT. 2023**



PERTANIKA  
JOURNALS

A scientific journal published by Universiti Putra Malaysia Press

# PERTANIKA JOURNAL OF SCIENCE & TECHNOLOGY

## About the Journal

### Overview

Pertanika Journal of Science & Technology is an official journal of Universiti Putra Malaysia. It is an open-access online scientific journal. It publishes original scientific outputs. It neither accepts nor commissions third party content.

Recognised internationally as the leading peer-reviewed interdisciplinary journal devoted to the publication of original papers, it serves as a forum for practical approaches to improve quality on issues pertaining to science and engineering and its related fields.

Pertanika Journal of Science & Technology currently publishes 6 issues a year (*January, March, April, July, August, and October*). It is considered for publication of original articles as per its scope. The journal publishes in **English** and it is open for submission by authors from all over the world.

The journal is available world-wide.

### Aims and scope

Pertanika Journal of Science & Technology aims to provide a forum for high quality research related to science and engineering research. Areas relevant to the scope of the journal include: bioinformatics, bioscience, biotechnology and bio-molecular sciences, chemistry, computer science, ecology, engineering, engineering design, environmental control and management, mathematics and statistics, medicine and health sciences, nanotechnology, physics, safety and emergency management, and related fields of study.

### History

Pertanika Journal of Science & Technology was founded in 1993 and focuses on research in science and engineering and its related fields.

### Vision

To publish a journal of international repute.

### Mission

Our goal is to bring the highest quality research to the widest possible audience.

### Quality

We aim for excellence, sustained by a responsible and professional approach to journal publishing. Submissions can expect to receive a decision within 90 days. The elapsed time from submission to publication for the articles averages 180 days. We are working towards decreasing the processing time with the help of our editors and the reviewers.

### Abstracting and indexing of Pertanika

Pertanika Journal of Science & Technology is now over 27 years old; this accumulated knowledge and experience has resulted the journal being abstracted and indexed in SCOPUS (Elsevier), Clarivate Web of Science (ESCI), EBSCO, ASEAN CITATION INDEX, Microsoft Academic, Google Scholar, and MyCite.

### Citing journal articles

The abbreviation for Pertanika Journal of Science & Technology is *Pertanika J. Sci. & Technol.*

### Publication policy

*Pertanika* policy prohibits an author from submitting the same manuscript for concurrent consideration by two or more publications. It prohibits as well publication of any manuscript that has already been published either in whole or substantial part elsewhere. It also does not permit publication of manuscript that has been published in full in proceedings.

### Code of Ethics

The *Pertanika* journals and Universiti Putra Malaysia take seriously the responsibility of all of its journal publications to reflect the highest in publication ethics. Thus, all journals and journal editors are expected to abide by the journal's codes of ethics. Refer to *Pertanika's Code of Ethics* for full details, or visit the journal's web link at [http://www.pertanika.upm.edu.my/code\\_of\\_ethics.php](http://www.pertanika.upm.edu.my/code_of_ethics.php)

### Originality

The author must ensure that when a manuscript is submitted to *Pertanika*, the manuscript must be an original work. The author should check the manuscript for any possible plagiarism using any program such as Turn-It-In or any other software before submitting the manuscripts to the *Pertanika* Editorial Office, Journal Division.

All submitted manuscripts must be in the journal's acceptable similarity index range:  
**≤ 20% – PASS; > 20% – REJECT.**

### International Standard Serial Number (ISSN)

An ISSN is an 8-digit code used to identify periodicals such as journals of all kinds and on all media—print and electronic.

Pertanika Journal of Science & Technology: e-ISSN 2231-8526 (Online).

### Lag time

A decision on acceptance or rejection of a manuscript is reached in 90 days (average). The elapsed time from submission to publication for the articles averages 180 days.

### Authorship

Authors are not permitted to add or remove any names from the authorship provided at the time of initial submission without the consent of the journal's Chief Executive Editor.

### Manuscript preparation

For manuscript preparation, authors may refer to *Pertanika*'s **INSTRUCTION TO AUTHORS**, available on the official website of *Pertanika*.

### Editorial process

Authors who complete any submission are notified with an acknowledgement containing a manuscript ID on receipt of a manuscript, and upon the editorial decision regarding publication.

*Pertanika* follows a **double-blind peer-review** process. Manuscripts deemed suitable for publication are sent to reviewers. Authors are encouraged to suggest names of at least 3 potential reviewers at the time of submission of their manuscripts to *Pertanika*, but the editors will make the final selection and are not, however, bound by these suggestions.

Notification of the editorial decision is usually provided within 90 days from the receipt of manuscript. Publication of solicited manuscripts is not guaranteed. In most cases, manuscripts are accepted conditionally, pending an author's revision of the material.

### The journal's peer review

In the peer-review process, 2 to 3 referees independently evaluate the scientific quality of the submitted manuscripts. At least 2 referee reports are required to help make a decision.

Peer reviewers are experts chosen by journal editors to provide written assessment of the **strengths** and **weaknesses** of written research, with the aim of improving the reporting of research and identifying the most appropriate and highest quality material for the journal.

### Operating and review process

What happens to a manuscript once it is submitted to *Pertanika*? Typically, there are 7 steps to the editorial review process:

1. The journal's Chief Executive Editor and the Editor-in-Chief examine the paper to determine whether it is relevance to journal needs in terms of novelty, impact, design, procedure, language as well as presentation and allow it to proceed to the reviewing process. If not appropriate, the manuscript is rejected outright and the author is informed.
2. The Chief Executive Editor sends the article-identifying information having been removed, to 2 to 3 reviewers. They are specialists in the subject matter of the article. The Chief Executive Editor requests that they complete the review within 3 weeks.

Comments to authors are about the appropriateness and adequacy of the theoretical or conceptual framework, literature review, method, results and discussion, and conclusions. Reviewers often include suggestions for strengthening of the manuscript. Comments to the editor are in the nature of the significance of the work and its potential contribution to the research field.

3. The Editor-in-Chief examines the review reports and decides whether to accept or reject the manuscript, invite the authors to revise and resubmit the manuscript, or seek additional review reports. In rare instances, the manuscript is accepted with almost no revision. Almost without exception, reviewers' comments (to the authors) are forwarded to the authors. If a revision is indicated, the editor provides guidelines for attending to the reviewers' suggestions and perhaps additional advice about revising the manuscript.
4. The authors decide whether and how to address the reviewers' comments and criticisms and the editor's concerns. The authors return a revised version of the paper to the Chief Executive Editor along with specific information describing how they have addressed the concerns of the reviewers and the editor, usually in a tabular form. The authors may also submit a rebuttal if there is a need especially when the authors disagree with certain comments provided by reviewers.
5. The Chief Executive Editor sends the revised manuscript out for re-review. Typically, at least 1 of the original reviewers will be asked to examine the article.
6. When the reviewers have completed their work, the Editor-in-Chief examines their comments and decides whether the manuscript is ready to be published, needs another round of revisions, or should be rejected. If the decision is to accept, the Chief Executive Editor is notified.
7. The Chief Executive Editor reserves the final right to accept or reject any material for publication, if the processing of a particular manuscript is deemed not to be in compliance with the S.O.P. of *Pertanika*. An acceptance letter is sent to all the authors.

The editorial office ensures that the manuscript adheres to the correct style (in-text citations, the reference list, and tables are typical areas of concern, clarity, and grammar). The authors are asked to respond to any minor queries by the editorial office. Following these corrections, page proofs are mailed to the corresponding authors for their final approval. At this point, **only essential changes are accepted**. Finally, the manuscript appears in the pages of the journal and is posted on-line.

Pertanika Journal of

**SCIENCE  
& TECHNOLOGY**

Vol. 31 (6) Oct. 2023



A scientific journal published by Universiti Putra Malaysia Press



## EDITOR-IN-CHIEF

**Luqman Chuah Abdullah**  
*Chemical Engineering*

## CHIEF EXECUTIVE EDITOR

**Mohd Sapuan Salit**

## UNIVERSITY PUBLICATIONS

### COMMITTEE

#### CHAIRMAN

#### EDITORIAL STAFF

##### Journal Officers:

Ellyianur Puteri Zainal  
Kanagamalar Silvarajoo  
Siti Zuhaila Abd Wahid  
Tee Syin Ying

##### Editorial Assistants:

Ku Ida Mastura Ku Baharom  
Siti Juridah Mat Arip  
Zulinaardawati Kamarudin

##### English Editor:

Norhanizah Ismail

#### PRODUCTION STAFF

##### Pre-press Officers:

Nur Farrah Dila Ismail  
Wong Lih Jiu

#### WEBMASTER

##### IT Officer:

Illi Najwa Mohamad Sakri

#### EDITORIAL OFFICE

##### JOURNAL DIVISION

Putra Science Park  
1<sup>st</sup> Floor, IDEA Tower II  
UPM-MTDC Technology Centre  
Universiti Putra Malaysia  
43400 Serdang, Selangor Malaysia.

##### General Enquiry

Tel. No: +603 9769 1622 | 1616

##### E-mail:

[executive\\_editor.pertanika@upm.edu.my](mailto:executive_editor.pertanika@upm.edu.my)

URL: [www.journals-jd.upm.edu.my](http://www.journals-jd.upm.edu.my)

#### PUBLISHER

##### UPM Press

Universiti Putra Malaysia  
43400 UPM, Serdang, Selangor, Malaysia.

Tel: +603 9769 8851

E-mail: [penerbit@putra.upm.edu.my](mailto:penerbit@putra.upm.edu.my)

URL: <http://penerbit.upm.edu.my>



#### ASSOCIATE EDITOR

##### 2021-2023

**Adem Kilicman**  
*Mathematical Sciences*  
Universiti Putra Malaysia, Malaysia

**Miss Laiha Mat Kiah**  
*Security Services Sn: Digital Forensic, Steganography, Network Security, Information Security, Communication Protocols, Security Protocols*  
Universiti Malaya, Malaysia

**Saidur Rahman**  
*Renewable Energy, Nanofluids, Energy Efficiency, Heat Transfer, Energy Policy*  
Sunway University, Malaysia

#### EDITORIAL BOARD

##### 2022-2024

**Abdul Latif Ahmad**  
*Chemical Engineering*  
Universiti Sains Malaysia, Malaysia

**Ho Yuh-Shan**  
*Water research, Chemical Engineering and Environmental Studies*  
Asia University, Taiwan

**Mohd Zulkifly Abdullah**  
*Fluid Mechanics, Heat Transfer, Computational Fluid Dynamics (CFD)*  
Universiti Sains Malaysia, Malaysia

**Ahmad Zaharin Aris**  
*Hydrochemistry, Environmental Chemistry, Environmental Forensics, Heavy Metals*  
Universiti Putra Malaysia, Malaysia

**Hsiu-Po Kuo**  
*Chemical Engineering*  
National Taiwan University, Taiwan

**Mohd. Ali Hassan**  
*Bioprocess Engineering, Environmental Biotechnology*  
Universiti Putra Malaysia, Malaysia

**Azlina Harun@Kamaruddin**  
*Enzyme Technology, Fermentation Technology*  
Universiti Sains Malaysia, Malaysia

**Ivan D. Rukhlenko**  
*Nonlinear Optics, Silicon Photonics, Plasmonics and Nanotechnology*  
The University of Sydney, Australia

**Nor Azah Yusof**  
*Biosensors, Chemical Sensor, Functional Material*  
Universiti Putra Malaysia, Malaysia

**Bassim H. Hameed**  
*Chemical Engineering: Reaction Engineering, Environmental Catalysis & Adsorption*  
Qatar University, Qatar

**Lee Keat Teong**  
*Energy Environment, Reaction Engineering, Waste Utilization, Renewable Energy*  
Universiti Sains Malaysia, Malaysia

**Norbahiah Misran**  
*Communication Engineering*  
Universiti Kebangsaan Malaysia, Malaysia

**Biswajeet Pradhan**  
*Digital image processing, Geographical Information System (GIS), Remote Sensing*  
University of Technology Sydney, Australia

**Mohamed Othman**  
*Communication Technology and Network, Scientific Computing*  
Universiti Putra Malaysia, Malaysia

**Roslan Abd-Shukur**  
*Physics & Materials Physics, Superconducting Materials*  
Universiti Kebangsaan Malaysia, Malaysia

**Daud Ahmad Israf Ali**  
*Cell Biology, Biochemical, Pharmacology*  
Universiti Putra Malaysia, Malaysia

**Mohd Shukry Abdul Majid**  
*Polymer Composites, Composite Pipes, Natural Fibre Composites, Biodegradable Composites, Bio-Composites*  
Universiti Malaysia Perlis, Malaysia

**Wing Keong Ng**  
*Aquaculture, Aquatic Animal Nutrition, Aqua Feed Technology*  
Universiti Sains Malaysia, Malaysia

**Hari M. Srivastava**  
*Mathematics and Statistics*  
University of Victoria, Canada

#### INTERNATIONAL ADVISORY BOARD

##### 2021-2024

**CHUNG, Neal Tai-Shung**  
*Polymer Science, Composite and Materials Science*  
National University of Singapore, Singapore

**Mohamed Pourkashanian**  
*Mechanical Engineering, Energy, CFD and Combustion Processes*  
Sheffield University, United Kingdom

**Yulong Ding**  
*Particle Science & Thermal Engineering*  
University of Birmingham, United Kingdom

**Hiroshi Uyama**  
*Polymer Chemistry, Organic Compounds, Coating, Chemical Engineering*  
Osaka University, Japan

**Mohini Sain**  
*Material Science, Biocomposites, Biomaterials*  
University of Toronto, Canada

#### ABSTRACTING AND INDEXING OF PERTANIKA JOURNALS

The journal is indexed in SCOPUS (Elsevier), Clarivate-Emerging Sources Citation Index (ESCI), BIOSIS, National Agricultural Science (NAL), Google Scholar, MyCite, ISC. In addition, Pertanika JSSH is recipient of "CREAM" Award conferred by Ministry of Higher Education (MoHE), Malaysia.





**Pertanika Journal of Science & Technology**  
**Vol. 31 (6) Oct. 2023**

**Contents**

Foreword	i
<i>Mohd Sapuan Salit</i>	
 <i>Review Article</i>	
Poultry Manure and its Contribution to Inflammation and Cancer Progression	2645
<i>Ana Masara Ahmad Mokhtar, Brennan Tang Yet Shen, Azam Muzafar Ahmad Mokhtar, Nor Hawani Salikin, Muaz Mohd Zaini Makhtar, Fatin Nur Izzati Mohd Fadzil, Nur Azzalia Kamaruzaman and Muggunna Balasubramaniam</i>	
 <i>Review Article</i>	
Integrating Ice Protection and Noise Abatement Systems for Aircraft Application: A Review	2667
<i>Fathima Rehana Munas, Yu Kok Hwa, Norwahida Yusoff, Abdul Majeed Muzathik and Mohd Azmi Ismail</i>	
Magnetic Susceptibility and Hydrogen Cyanide Levels as Proxy Indicator for Gold Mining Pollution in River Sediment	2689
<i>Siti Zulaikah, Arif Juliansyah, Muhammad Fathur Rouf Hasan, Bambang Heru Iswanto, Mariyanto Mariyanto, Ardyanto Tanjung, Satria Bijaksana and Ann Marie Hirt</i>	
Recognition of Fruit Types from Striking and Flicking Sounds	2703
<i>Rong Phoophuangpairoj</i>	
Development of Artificial Neural Network Model for Medical Specialty Recommendation	2723
<i>Winda Hasuki, David Agustriawan, Arli Aditya Parikesit, Muammar Sadrawi, Moch Firmansyah, Andreas Whisnu, Jacquelin Natasya, Ryan Mathew, Florensia Irena Napitupulu and Nanda Rizqia Pradana Ratnasari</i>	
Effect of Scaling the Electrostatic Interactions on the Free Energy of Transfer of Azurin from Water to Lipid Membrane Determined by Coarse-grained Simulations	2735
<i>Dian Fitrasari, Acep Purqon and Suprijadi</i>	

- Effect of Lysine and Poultry Slaughterhouse by Product Meal on Growth Performance, Feed Efficiency, and Blood Profile of Sangkuriang Catfish (*Clarias gariepinus* var. Sangkuriang) 2751  
*Diana Rachmawati, Tita Elfitasari, Istiyanto Samidjan, Putut Har Riyadi and Dewi Nurhayati*
- Polynomial Regression Calibration Method of Total Dissolved Solids Sensor for Hydroponic Systems 2769  
*Ansar Jamil, Teo Sheng Ting, Zuhairiah Zainal Abidin, Maisara Othman, Mohd Helmy Abdul Wahab, Mohammad Faiz Liew Abdullah, Mariyam Jamilah Homam, Lukman Hanif Muhammad Audah and Shaharil Mohd Shah*
- Intelligence System via Machine Learning Algorithms in Detecting the Moisture Content Removal Parameters of Seaweed Big Data 2783  
*Olayemi Joshua Ibidoja, Fam Pei Shan, Mukhtar Eri Suheri, Jumat Sulaiman and Majid Khan Majahar Ali*
- Response Surface Methodology: A Versatile Tool for the Optimization of Particle Sizes of Cellulose Beads 2805  
*Kimberly Wei Wei Tay, Suk Fun Chin, Mohd Effendi Wasli and Zaki Musa*
- Review Article*
- A Review on Analysis Method of Proximal Hyperspectral Imaging for Studying Plant Traits 2823  
*Jian Wen Lin, Mohd Shahrimie Mohd Asaari, Haidi Ibrahim, Mohamad Khairi Ishak dan Abdul Sattar Din*
- Influence of Heat Treatment on the Mechanical Properties and Precipitation Kinetic of Sugar Palm Fiber Ash Reinforced LM26 Al Matrix Composites 2851  
*Isah Aliyu, Mohd Sapuan Salit, Edi Syams Zainudin, Mohd Zuhri Mohamed Yusoff and Ridwan Yahaya*
- Development of a Web-based Application by Employing a Convolutional Neural Network (CNN) to Identify Pests and Diseases on Pakcoy (*Brassica rapa* subsp. *chinensis*) 2873  
*Achmad Zein Feroza, Nelly Oktavia Adiwijaya and Bayu Taruna Widjaja Putra*
- Review Article*
- Renewable Energy Impact on Distance Relay Power Swing Blocking and Fault Discrimination: A Review 2887  
*Chidiebere Okeke, Othman Mohammad Lutfi, Hizam Hashim, Mohd Zainal Abdin Ab Kadir, Noor Izzri Abdul Wahab, Osaji Emmanuel, Samuel Nwagbara and Collins Chimeleze*

The Influence of Cavity Size and Location Within Insulation Paper on the Partial Discharge Activities <i>Muhammad Hakirin Roslan, Norhafiz Azis, Mohd Zainal Abidin Ab Kadir, Jasronita Jasni and Mohd Fairouz Mohd Yousof</i>	2915
Short-term Ageing Study on the Palm Oil and Mineral Oil in the Presence of Insulation Paper, Moisture, Low Molecular Weight Acid, and Oxygen <i>Muhammad Muzamil Mustam, Norhafiz Azis, Jasronita Jasni, Rasmina Halis, Mohd Aizam Talib, Robiah Yunus, Nurliyana Abdul Raof and Zaini Yaakub</i>	2931
Development of Sago-based Analog Rice Using Kansei and Value Engineering <i>Violetta Putri Rizky Septiani, Mirwan Ushada and Suharno</i>	2947
Utilizing Rainwater Harvesting System for Water Scarcity at a Double-story Residential House <i>Muhammad Izzuddin Rosli, Sharifah Abdullah and Nur Asmaliza Mohd Noor</i>	2961
Measuring Vulnerability Assessment Tools' Performance on the University Web Application <i>Pita Jarupunphol, Suppachochai Seatun and Wipawan Buathong</i>	2973
Nitrogen Dynamics in Soil Treated with Plant-growth Promoting Bacteria and Urea Fertilizer <i>Amaily Akter, Ali Tan Kee Zuan, Susilawati Kasim, Adibah Mohd Amin, Zakry Fitri Ab Aziz, Noor Md Rahmatullah, Buraq Musa Sadeq, Sayma Serine Chompa and Md Ekhlatur Rahman</i>	2995
Chitosan Dissolution in [BMIM]Cl Ionic Liquid: An Optimisation and Bacterial Ecotoxicity Study <i>Mok Shue Yee, Magaret Sivapragasam and Maisara Shahrom Raja Shahrom</i>	3013
Novel Pre-treatment for Lignocellulosic Biomass Delignification Using Alkaline-assisted Ohmic Heating <i>Izzah Farhana Ab Aziz, Hasfalina Che Man, Muhammad Hazwan Hamzah, Nur Syakina Jamali and Rozita Omar</i>	3039
Numerical Analysis and Validation of Characterization of Polydimethylsiloxane Using Hyper-elastic Constitutive Models <i>Sana Zulfiqar, Abdullah Aziz Saad, Zulkifli Ahmad, Feizal Yusof and Zuraihana Bachok</i>	3059

The Design of an Efficient Low-cost FPGA-based Unit for Generation Ultrasound Beamforming <i>Soufiane Dangoury, Mouncef El marghichi, Mohamed Sadik and Abderrahim Fail</i>	3077
Sound Sensor Placement Strategy for Condition Monitoring of Induction Motor Bearing <i>Iradiratu Diah Prahmana Karyatanti, Istiyo Winarno, Ardik Wijayanto, Dwisetiono, Nuddin Harahab, Ratno Bagus Edy Wibowo and Agus Budiarto</i>	3093
Adaptive Threshold-based Fault Detection for Systems Exposed to Model Uncertainty and Deterministic Disturbance <i>Masood Ahmad and Rosmiwati Mohd-Mokhtar</i>	3107
Dibenzofuran Degradation by Bacterial Community in Landfill Leachate <i>Farah Najwa Ahmad, Noor Faizul Hadry Nordin, Muhamad Shirwan Abdullah Sani and Wan Syibrah Hanisah Wan Sulaiman</i>	3125
Numerical Investigation on the Distribution of Pressure Coefficients of Modified Building Shapes <i>Siti Rohani Mohd Isdris, Shaharudin Shah Zaini, Mohammad Hafifi Hafiz Ishaik, Mohammad Sharizal Abdul Aziz and Noorhazlinda Abd Rahman</i>	3139
<i>Review Article</i>	
A Systematic Review of Ergonomics Risk Assessment Methods for Pushing and Pulling Activities at Workplace <i>Hari Krishnan Tamil Selvan and Mohd Nasrull Abdol Rahman</i>	3157
An Extreme Learning Machine Approach for Forecasting the Wholesale Price Index of Food Products in India <i>Dipankar Das and Satyajit Chakrabarti</i>	3179

# Foreword

Welcome to the sixth issue of 2023 for the *Pertanika Journal of Science and Technology (PJST)*!

PJST is an open-access journal for studies in Science and Technology published by Universiti Putra Malaysia Press. It is independently owned and managed by the university for the benefit of the world-wide science community.

This issue contains 30 articles; five review articles and the rest are regular articles. The authors of these articles come from different countries namely Bangladesh, India, Indonesia, Malaysia, Morocco, Nigeria, Pakistan, Sri Lanka, Switzerland and Thailand.

A review on poultry manure and its contribution to inflammation and cancer progression was conducted by Ana Masara Ahmad Mokhtar and colleagues from Malaysia. Indiscriminate manure disposal has been highlighted as a significant cause of environmental contamination due to various biological and chemical irritants that harm the environment and human health. Several incidents have been reported, most notably among farmers and those living near the farms, because of air and water pollution caused by manure losses, which result in various health issues, including infection, inflammation, and even cancer. This review discusses the potential health risks or diseases linked to poultry manure and recommends future measures to minimize the hazards to health and the environment. Details of this study are available on page 2645.

A regular article titled “Effect of Scaling the Electrostatic Interactions on the Free Energy of Transfer of Azurin from Water to Lipid Membrane Determined by Coarse-Grained Simulations” was presented by Dian Fitrasari and co-researchers from Bandung Institute of Technology, Indonesia. Azurin protein potentially plays an important role as an anti-cancer therapeutic agent, particularly in treating breast cancer without having a negative effect on normal cells. Although the interaction mechanism between protein and lipid membrane is complicated, it can be modeled as protein-lipid interaction. Since the all-atom (AA) model simulation is cost computing, the researchers applied a coarse-grained (CG-MARTINI) model to calculate the protein-lipid interaction. They investigated the binding free energy value dependency by varying the windows separation and electrostatic scale parameters. After scaling the electrostatic interactions by a factor of 0.04, the best result in terms of free energy is -140.831 kcal/mol, while after window-separation optimization, it reaches -71.859 kcal/mol. The detailed information of this study is available on page 2735.

A numerical investigation on the distribution of pressure coefficients of modified building shapes was conducted by Siti Rohani Mohd Isdris et al. from Universiti Sains Malaysia. This study evaluates the impact of shape mitigation on tall buildings by applying corner modifications, such as chamfered, corner cut, plan changes with height, tapered, and setback, and combining a single modification model. The numerical simulations were carried out using Computational Fluid

Dynamic (CFD) simulation with the RNG k- $\epsilon$  type of turbulence model. All single modifications reduced the maximum +C<sub>p</sub> and -C<sub>p</sub> better than the basic model. The setback model is more effective in reducing suction than the basic and tapered model. Choosing an efficient geometry modification for high-rise structures can help mitigate aerodynamic concerns, particularly in pressure distribution on the building surfaces. Further details of the investigation can be found on page 3139.

In the last 12 months, of all the manuscripts peer-reviewed, 16% were accepted. This seems to be the trend in PJST.

We anticipate that you will find the evidence presented in this issue to be intriguing, thought-provoking and useful in reaching new milestones in your own research. Please recommend the journal to your colleagues and students to make this endeavour meaningful.

All the papers published in this edition underwent Pertanika's stringent peer-review process involving a minimum of two reviewers comprising internal as well as external referees. This was to ensure that the quality of the papers justified the high ranking of the journal, which is renowned as a heavily-cited journal not only by authors and researchers in Malaysia but by those in other countries around the world as well.

We would also like to express our gratitude to all the contributors, namely the authors, reviewers, Editor-in-Chief and Editorial Board Members of PJST, who have made this issue possible.

PJST is currently accepting manuscripts for upcoming issues based on original qualitative or quantitative research that opens new areas of inquiry and investigation.

**Chief Executive Editor**

**Mohd Sapuan Salit**

[executive\\_editor.pertanika@upm.edu.my](mailto:executive_editor.pertanika@upm.edu.my)

Review Article

## Poultry Manure and its Contribution to Inflammation and Cancer Progression

Ana Masara Ahmad Mokhtar<sup>1,2\*</sup>, Brennan Tang Yet Shen<sup>3</sup>, Azam Muzafar Ahmad Mokhtar<sup>4</sup>, Nor Hawani Salikin<sup>1</sup>, Muaz Mohd Zaini Makhtar<sup>1</sup>, Fatin Nur Izzati Mohd Fadzil<sup>1</sup>, Nur Azzalia Kamaruzaman<sup>5</sup> and Muggunna Balasubramaniam<sup>1</sup>

<sup>1</sup>Bioprocess Technology Division, School of Industrial Technology, Universiti Sains Malaysia, Gelugor 11800 USM, Penang, Malaysia

<sup>2</sup>Green Biopolymer Coating and Packaging Centre, School of Industrial Technology, Universiti Sains Malaysia, 11800 USM, Penang, Malaysia

<sup>3</sup>Department of Molecular Biology, Faculty of Resource Science and Technology, Universiti Malaysia Sarawak, 94300 UNIMAS, Kota Samarahan, Sarawak, Malaysia

<sup>4</sup>Department of Biology, Faculty of Science and Mathematics, Universiti Pendidikan Sultan Idris, Tanjong Malim, Perak, 35900 UPSI, Malaysia

<sup>5</sup>National Poison Centre, Universiti Sains Malaysia, 11800 USM, Penang, Malaysia

### ABSTRACT

Indiscriminate manure disposal has been highlighted as a significant cause of environmental contamination due to the presence of various biological and chemical irritants. It includes pathogens, antibiotics, and organic pollutants, all of which have the potential to harm not only the environment but also human health. Several incidents have been reported, most notably among farmers and those living near the farms, as a result of air and water pollution caused by manure losses. Acute and chronic exposure to these hazards may result in a variety of health issues, including infection, inflammation, and even cancer. Despite this, humans are

constantly exposed to these risk agents due to a lack of awareness of proper disposal methods and knowledge of the risk agents' associations with diseases. Thus, the review discusses the potential health risk or diseases linked to poultry manure and recommends future measures to minimise the hazards to farmers' health and the environment posed by their existing practices.

**Keywords:** Cancer, infection, inflammation, pathogenic bacteria, poultry manure

#### ARTICLE INFO

*Article history:*

Received: 03 August 2022

Accepted: 06 March 2023

Published: 08 September 2023

DOI: <https://doi.org/10.47836/pjst.31.6.01>

*E-mail addresses:*

anamasara@usm.my (Ana Masara Ahmad Mokhtar)

brennantang8@gmail.com (Brennan Tang Yet Shen)

azam.muzafar20@gmail.com (Azam Muzafar Ahmad Mokhtar)

norhawani@usm.my (Nor Hawani Salikin)

muazzaini@usm.my (Muaz Mohd Zaini Makhtar)

fatinfadzil20@yahoo.com (Fatin Nur Izzati Mohd Fadzil)

azzalia@usm.my (Nur Azzalia Kamaruzaman)

muggunabala99@gmail.com (Muggunna Balasubramaniam)

\* Corresponding author

## INTRODUCTION

The growing demand for food products, whether proteins, carbohydrates, or fibre, has rapidly increased over the last decade, in lockstep with the world's population growth. The global population was 7.9 billion in 2022 (Population Matters, 2023), expected to reach 9.7 billion by 2050. On the other hand, population growth will undoubtedly increase the demand for poultry production for human consumption. According to the United Nations Food and Agriculture Organization (2021), poultry meat production increased from 9 to 132 million tonnes worldwide between 1961 and 2019, accounting for nearly 39% of global meat production. Additionally, global broiler meat production reached approximately 83.2 million metric tonnes in 2012 and is expected to reach approximately 102 million in 2021 (<https://www.statista.com/aboutus/our-research-commitment/1239/m-shahbandeh>). In Malaysia, the yearly per capita consumption of poultry meat increased from 41.9 kg in 2012 to 53.1 kg in 2022 (Organisation for Economic Co-operation and Development, 2022).

While modern agricultural technology has increased production efficiency and safety, the risks to the human population posed by these industries have remained relatively constant. It is because as poultry farming becomes more popular, the production of poultry waste will increase, endangering humans and contributing to environmental contamination. It has been established that poultry excrement contains a variety of contaminants, including veterinary antimicrobials, heavy metals, and pathogens. These contaminants can enter surface water, groundwater, and agricultural soil during storage and disposal, posing direct or indirect threats to public health (Gbotosho & Burt, 2013).

Poultry manure is the faeces of poultry (chicken, turkey, duck, and geese), which is frequently used as an organic fertiliser to increase the soil's nitrogen, phosphate, and potassium levels. However, it is a major source of pathogens that can harm humans. For example, *Listeria*, *Salmonella*, *Staphylococcus*, *Actinobacillus* and *Campylobacter* are just a few pathogens that have been prevalent in poultry wastes and have been linked to adverse effects on human health and the human food chain (Kyakuwaire et al., 2019). These pathogens may be spread from poultry wastes to water sources through run-off, which humans may consume or ingest as a source of water or marine-based food (Kyakuwaire et al., 2019).

Additionally, due to easier market access, most poultry industries are massive and concentrated in urban areas. However, this location is frequently near critical areas such as rivers and drainage systems that provide water to nearby residents (Taiwo & Arowolo, 2017). Inadequate waste management increases their risk of contracting infections, which can cause life-threatening conditions (Food and Agriculture Organization of the United Nations, 2013). Exposure to these zoonotic pathogens, which are pathogens that have spread from animals to humans, has been shown to cause a variety of infectious diseases in humans, including Listeriosis, Salmonellosis, and Campylobacteriosis (Kyakuwaire et



al., 2019). Thus, appropriate and preventive strategies must be implemented at all levels of agriculture to mitigate health risks (Food and Agriculture Organization of the United Nations, 2013). Additionally, this approach would contribute to sustainable agriculture without the risk or concern of zoonotic pathogen contamination (Garcia et al., 2020).

## **CURRENT MANAGEMENT OF POULTRY MANURE AND ITS DISADVANTAGES TO HUMANS**

Poultry manure contains thirteen essential nutrients required for plant growth and development, including Nitrogen (N), calcium (Ca), phosphorous (P), sulphur (S), copper (Cu), chlorine (Cl), iron (Fe), molybdenum (Mo), potassium (K), magnesium (Mg), manganese (Mn), zinc (Zn), and Boron (B) (Singh et al., 2018). These nutrients are frequently derived from poultry feed, medications, supplements, and drinking water. The abundance of nutrients in poultry manure can be regarded as one of the best fertilisers as it fulfils the main plant growth requirements (Singh et al., 2018).

### **Reused Poultry Manure as Bedding Material**

Poultry litter usually consists of bedding material mixed with manure, feathers, spilt water and waste feed accumulated during the production cycle. Although poultry litter is often used as an excellent fertiliser for enhancing the growth of vegetable crops, it also has been extensively re-used as bedding materials for subsequent batches of broilers due to the high cost and demand for high-quality wood shaving bedding, the primary component of litter (Redding, 2011). This re-used practice is prevalent in several countries, including the United States of America (Macklin et al., 2006) and Australia (Runge, 2007).

Unfortunately, this practice will promote certain food-borne pathogens such as *Salmonella* and *Campylobacter*, which are commensals in poultry, increasing the risk of human contamination via direct contact with food crops or spray irrigation (Kyakuwaire et al., 2019). Despite concerns about the spread of harmful pathogens into the environment, this practice of reusing bedding material is expected to grow in the future due to limited supplies of suitable bedding material. Nevertheless, Bucher et al. (2020) found the benefit of using reused poultry litter to deter the growth of *Salmonella*. It contradicts ideas probably due to the environmental stressors or alteration of physiochemical parameters disrupting the normal mechanism that regulates the complex interplay between bacterial members of the community, driving the lower abundance of *Salmonella* in reused bedding.

### **Source of Energy Production**

Additionally, as poultry manure is a complex source of organic components, these wastes could be utilised for energy production. Among the common methods for converting poultry litter to energy is fluidised bed combustion (FBC) technology. The heat produced from this

method can then be used to produce energy or to provide heating for buildings or poultry houses (Choudhury et al., 2020). Nevertheless, the main concern with this technique is the number of gases produced, such as carbon dioxide (CO<sub>2</sub>), methane (CH<sub>4</sub>) and nitrous oxide (N<sub>2</sub>O), all of which is known as greenhouse gases (GHG) contributor, and particulates that are being released and polluting the air. Exposure to these particles may promote several cardiovascular and respiratory consequences for humans, including cardiac arrhythmias, asthma attacks, and bronchitis (Manisalidis et al., 2020).

### **Stockpiled of Poultry Manure**

In some countries, surplus poultry litter is also openly stockpiled in the environment. Normally, poultry stacking generates heat, which kills any pathogens present in the litter (Wilkinson et al., 2011). However, it may cause pathogen run-off into adjacent rivers and creeks, particularly during heavy rain or flooding (Kyakuwaire et al., 2019). Although certain measures were implemented to ensure the effective use of poultry manure while minimising its negative impacts, there is still a risk to the environment and human health if it is not correctly managed.

## **ROUTE OF HUMAN EXPOSURE TO POULTRY MANURE**

### **Inhalation**

It is common knowledge that poultry farms generate excessive dust from bedding materials, feed, dried faeces, and feather particles. Dust may contain microorganisms, including endotoxins, fungi, and bacteria, affecting living things when inhaled. Dust-containing living organisms are referred to as bioaerosol, and they can spread throughout the environment and food chain, causing numerous diseases such as pulmonary disease, infection, and skin irritation (Jerez et al., 2014).

*Salmonella*, *Listeria*, and *Campylobacter* are among the pathogens known to be released from the internal environment of poultry facilities (Hakeem & Lu, 2021) (Figure 1). After poultry have been transported or eliminated, the broiler house is contaminated to varying degrees, increasing the likelihood of their release into the environment. In order to prevent infections in large-scale poultry farms, it is required to disinfect the housing. Disinfection can minimise or eliminate potential pathogenic bacteria in the home and prevent their spread across batches. Infectious diseases in poultry houses can be effectively controlled by selecting the most appropriate disinfectants, disinfection procedures, and strategies (Jiang et al., 2018). Some pathogens released into the environment can adapt to harsh environmental circumstances, allowing them to grow, breed, infect other hosts, and produce toxic compounds that may damage human health (Mokhtar et al., 2022). Among the potentially produced toxic compounds are listeriolysin O (LLO), a pore-forming toxin

encoded by the *hly* gene of *Listeria monocytogenes* (Churchill et al., 2006) and *Salmonella* cytolethal distending toxin (S-CDT), a toxin that can cause DNA damage in eukaryotic cells, produced by *Salmonella enterica* serotype Typhi (Miller et al., 2018).

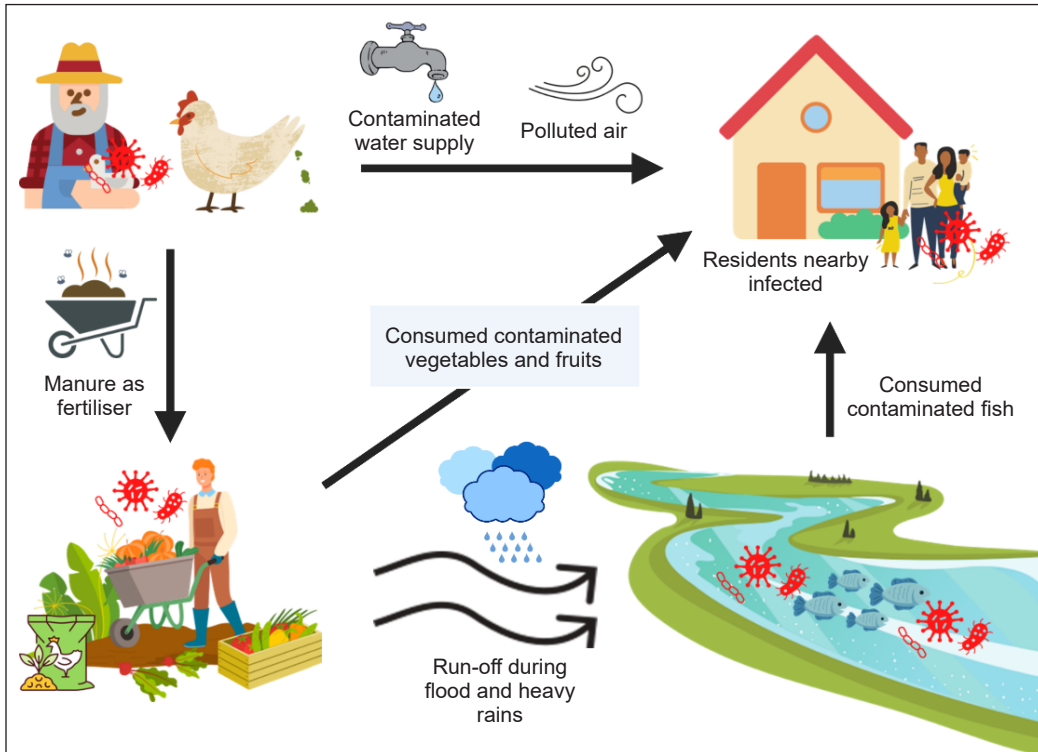


Figure 1. Possible pathogen transmission routes from poultry manure to humans. Improper waste management will spread pathogens to poultry farmers, adjacent inhabitants, and farmers who use contaminated manure as fertiliser via air pollution, water contamination, and the ingestion of contaminated vegetables and fruits. In addition, infections may spread from poultry wastes to water sources via run-off, which occurs during floods or heavy rains, resulting in humans consuming or ingesting water or marine-based food. Created with BioRender.com

Farmers are also typically exposed to the poultry manure-associated hazard, ranging from mild conditions, such as loss of olfactory recognition, to severe chronic pulmonary diseases, such as asthma and chronic obstructive pulmonary disease (COPD), that require special attention (Kitjakrancharoensin et al., 2020). For instance, the amounts of respirable dust and bioaerosol on exposed farmers were more significant than those measured with stationary indoor samplers. Although the respirable dust is still below the Occupational Safety and Health Administration's permissible exposure level, it surpasses the limit for animal buildings suggested by other studies (Jerez et al., 2014).

Some nearby inhabitants were also exposed to harmful odour compounds such as ammonium, dimethylamine, trimethylamine, butyric acid, phenol, and indole that may

irritate the human respiratory tract (Fan et al., 2020). Additionally, since poultry manures may also spread some bioaerosol-containing harmful pathogens, excessive and sustained intake of these pathogens might result in the fatal illnesses listed in Table 1. Meningitis and encephalitis are common disorders associated with pathogen infections caused by excessive inflammation. Chronic or sustained exposure to these inflammatory processes may also contribute to the advancement of cancer as inflammation and cancer cross-talked (Grivennikov et al., 2010).

Table 1  
List of pathogens commonly found in poultry waste

Pathogen	Host	Route	Disease
<i>Listeria monocytogenes</i>	Cattle, sheep, pigs	Food, water	Listeriosis, febrile gastroenteritis, Perinatal infection
<i>Brucella</i> spp.	Cattle	Direct food, inhalation	Brucellosis
Enterohemorrhagic <i>E. coli</i>	Cattle, sheep, pigs	Food, water	Haemorrhagic colitis
<i>Campylobacter jejuni</i>	Poultry, pig, Cattle	Food, water, direct	A neurological disorder in very young, elderly or immunocompromised human patients. Guillain-Barre syndrome in human Campylobacteriosis
Hepatitis E virus	Pigs, poultry, rats	Faecal-oral, food, water	Hepatitis
<i>Yersinia enterocolitica</i>	Pigs	Food, direct water	Yersiniosis
<i>Mycobacterium bovis</i> & <i>M. tuberculosis</i>	Pigs, cattle	Inhalation	Tuberculosis
<i>Salmonella</i> spp.	Pigs, cattle	Faecal-oral, food, water, direct	Diarrhoea, nausea, chills, fever, headache, abdominal pain
<i>Escherichia coli</i>	Cattle, pigs and sheep	Food, water	Diarrhoea

### Drainage and Surface Water System

Pathogen transport from poultry manure can also occur via tilled drained land or drainage and surface water systems such as spray irrigation for agricultural activities. The reused of agricultural wastewater, including manure and other wastes from farms, poultry houses and slaughterhouses, is common, especially in some European and Mediterranean countries that suffer from water scarcity (Al-Gheethi et al., 2018). Some Italian regions have been adversely affected by drought, and the lack of water resources has primarily hampered agricultural activity, which consumes more than half of the total available water. For these reasons, other water sources are required, and usually, the most readily available source of water to meet the rising need for crop irrigation is treated municipal wastewater. Besides, agriculture wastewater recycling has gained importance because it provides a significant

amount of irrigation water, helps conserve potable resources, and reduces the environmental impact of effluents discharged into water systems (Mokhtar et al., 2022). However, vigilance must be exercised while reusing these wastewaters to minimise the hazards to agricultural goods, soil, and groundwater from toxic and pathogenic pollutants, which pose possible health risks to consumers when they reach the food chain (Mokhtar et al., 2022).

## IMPLICATIONS TO HUMANS: HEALTH-RELATED RISKS

### Infection-Induced Inflammation

Although sewage sludge contains several nutrients and organic matter useful for improving soil structural, chemical and biological properties (Gubišová et al., 2020), it also contains several pathogens that may affect human health (Table 1). It is because of the favourable conditions of poultry manure, including high moisture, nutrients, and optimal pH and temperature, which are suitable for pathogens to thrive and grow in abundance (Black et al., 2021). As a result, pathogens have a high proclivity for spreading from poultry to humans via a variety of routes, such as via food, water, inhalation or direct contact. All these pathogens are the source of infection and may elicit an immune response, causing inflammation.

**Listeria Infection.** *Listeria* species are Gram-positive bacteria that belong to the *Listeriaceae* family. There are 17 *Listeria* species in the phylogeny, with 9 recently described in 2009 (Orsi & Wiedmann, 2016). It favours cool, damp environments and can be found throughout the environment (Zhu et al., 2017). Apart from their reputation as food-borne diseases, numerous *Listeria* species, the most common of which are *Listeria monocytogenes*, *L. innocua*, and *L. ivanovii*, have been found plentiful in poultry manure. Exposure to these bacteria can cause listeriosis in humans. Some species have also developed resistance to more than three types of antibiotics (multidrug resistance), including ciprofloxacin, penicillin, and fluoroquinolone (Cokal et al., 2022). Hence, to reduce cross-contamination and the zoonotic potential of listeriosis, food safety management systems and interventions were required at all phases of the broiler-rearing cycle (Zhu et al., 2017). It is due to its adaptability to hostile environments. For instance, *Listeria* was found to survive for three months in animal slurries and unclean water and one month in manure heaps with temperatures exceeding 55 °C. Even after manure was spread to agricultural land, *Listeria* survived for over a month in clay loam grassland soils up until 270 days (Chen & Jiang, 2014).

Furthermore, *Listeria* may persist in severe environments and build biofilms on a range of environmental surfaces (Beresford et al., 2001). Because of the possibility of contamination, this clearly poses a substantial risk to human safety and hence signifies the need to eradicate *Listeria*, such as through disinfection with disinfectants or antibiotics. Nevertheless, the persistence used of antibiotics in animals as a growth stimulant and

infection control measure may result in the evolution or development of antibiotic-resistant *Listeria* (Chattopadhyay, 2014), especially those resistant to chloramphenicol and ampicillin (Odjadjare et al., 2010). It could eventually become a global issue as present antibiotics may be insufficient in addressing its pathogenicity.

*Listeria* is primarily spread to people by consuming infected food or drink. Depending on the host's health, listeriosis infection causes various clinical symptoms ranging from invasive to non-invasive. During invasive manifestation, *L. monocytogenes* can infect its host's body by penetrating the blood-brain barrier or the placenta, resulting in a brain or foetal infection. In most cases, the invasive type of Listeriosis affects mainly high-risk people, such as immunocompromised people, the elderly, and newborns. This population typically gets meningitis and septicaemia at the start of listeriosis (Silk et al., 2012). Non-invasive Listerial gastroenteritis, also known as febrile Listerial gastroenteritis, is a milder infection commonly accompanied by fever, diarrhoea, headache, and muscle discomfort (Sim et al., 2002).

*L. monocytogenes* was found in 20 to 50 % of retail beef and poultry meat items sold in Malaysian wet markets and supermarkets. Despite this, no instances of food-borne listeriosis have been documented, which could be attributable to a lack of recognition of the disease or a lack of a national registry (Goh et al., 2012). The presence of *L. monocytogenes* in raw chicken meat is undesirable yet unavoidable. As a result, additional research on the processing procedure to minimise and eliminate this type of bacteria in chicken meat before eating is required.

**Salmonella Infection.** *Salmonella* is the next most frequently encountered pathogen in poultry waste. It is abundant and is thought to be associated with reptiles, rodents, and mammals' intestinal tracts. *Salmonella* is a motile bacterium that is a member of the Enterobacteriaceae family. According to Voetsch et al. (2004), *Salmonella* causes 1.4 million cases yearly, with 15,000 requiring hospitalisation and 400 resulting in death. Additionally, it is widely accepted that humans' primary Salmonellosis sources are poultry and poultry products (Moultotou et al., 2017). According to Djefal et al. (2018), approximately 34.37% of poultry farms were found to be contaminated with *Salmonella*. *Salmonella* is classified into two distinct species: *S. enterica* and *S. bongori*, and six distinct subspecies: *enterica*, *houtenae*, *arizonae*, *diarizonae*, *salamae*, and *indica* (Lamas et al., 2018). Only *S. enterica* serovar Gallinarum and *S. enterica* serovar Pullorum, however, are primarily associated with poultry (Xiong et al., 2018), whereas *S. enterica* serovar Typhi is primarily associated with humans (Garai et al., 2012).

Humans may become infected with *Salmonella* because of improper poultry farming management (Moultotou et al., 2017). Besides, since it can survive months in soil (Jechalke et al., 2019), the risk of human infection, particularly among poultry farmers, is high. You

et al. (2006) discovered that *S. enterica* serovar Newport can survive for 184, 332, and 405 days in manure, manure-amended unsterilised soil, and manure-amended sterilised soil, respectively (You et al., 2006). Additionally, *S. enterica* serovar Enteritidis persisted for approximately a year in the dust of an empty broiler breeder, despite disinfection and cleaning (van Immerseel et al., 2009). Therefore, it is vital to explore viable methods for reducing the risk of Salmonellosis, such as employing composting techniques that have effectively prevented pathogen growth (Chen & Jiang, 2014). Although high-temperature composting helps reduce *Salmonella*, the pathogen persists in manure and litter by adapting to thrive in dry environments (Avidov et al., 2021), contributing to *Salmonella*'s dispersion throughout the food chain (Waldner et al., 2012).

***Campylobacter* Infection.** *Campylobacter* is also thought to be a source of human infections from poultry waste. While it colonises the intestines of poultry without generating symptoms, it is known to induce food-borne enteritis in humans (Facciola et al., 2017). *Campylobacter jejuni* is the most common *Campylobacter* species linked with poultry and the most common *Campylobacter* species involved with human disease (Sibanda et al., 2018). Infected laying hens regularly excrete large amounts of *C. jejuni* with their faeces, representing a reservoir of infection within the flock and animals in the region. Culturable *C. jejuni* can survive up to 96 hours in artificially infected faeces and 120 to 144 hours in spontaneously colonised flocks to make matters worse (Ahmed et al., 2013), making it highly transmissible to humans.

Pigeon manure piles may also contribute to *Campylobacter* infection in humans via vectors like flies (Nichols, 2005). The flies will then contaminate human food with *Campylobacter*, resulting in food poisoning. Arsenault et al. (2007) consistently discovered that when manure is located approximately 200 meters from a poultry farm, the prevalence of *Campylobacter* in poultry is 5.2 times higher.

Although the number of infection cases in Malaysia is not documented, there is an increased number of Listeriosis, Salmonellosis and Campylobacteriosis cases in Australia from 67, 6151 and 13595 cases in 2000 (Lin et al., 2010) to 84, 18088 and 24164 cases in 2016 (Hood, 2021), respectively. A similar pattern has been observed for Campylobacteriosis in England and Wales, between 2013 and 2020, with 3099 cases in 2013 (Public Health England, 2013) and 3378 cases in 2020 (UK Health Security Agency, 2020). It proves that the infection can occur in any nation but critically depend on the farmers' existing practices. Nevertheless, although significant measures and awareness have been taken, the number of cases continues to rise, highlighting the need for a more robust global response.

Numerous studies have also demonstrated that persistent infections may promote inflammation and that chronic or protracted inflammation may lead to cancer development.

It is because aberrant inflammatory responses have a role in numerous phases of tumour growth, including initiation, promotion, malignant conversion, invasion, and metastasis (Grivennikov et al., 2010). Germline mutations cause only 10% of all malignancies, while somatic mutations and environmental factors cause most (90%). According to Aggarwal et al. (2009), these environmental factors are highly related to bacterial or viral infections that induce chronic inflammation.

## Cancer

**Viral Infection-induced Cancer.** Exposure to poultry manure is also linked to cancer development in humans, particularly among poultry workers. It could be due to recurrent or extended contact with oncogenic viruses in poultry faeces. According to Johnson et al. (2010), workers are more prone to get these oncogenic viruses due to daily contact with a high number of fowl and wound or skin injury that often occurs among workers. Oncogenic viruses discovered in poultry manure include reticuloendotheliosis virus (REV), avian leucosis sarcoma viruses (ALSV), papillomaviruses, and Marek's disease virus (MDV), all of which have been linked to haematological and lymphatic malignancies in both poultry and humans (Gopal et al., 2012).

Viral infection induces an inflammatory response necessary for virus elimination and tissue homeostasis, including tissue repair, regeneration, and remodelling (Medzhitov, 2008). Nonetheless, mounting evidence shows that tumour-associated viruses might avoid host protection, boosting cancer growth. It is owing to similarities between the innate immune system and tumour suppressor signalling, as both processes initiate cell cycle arrest and trigger apoptotic pathways. For instance, the main players of these signalling networks, p21 cyclin-dependent kinase inhibitor and p53, are present in both tumour suppressor and innate immune surveillance signalling networks. It suggests that the virus's capacity to target tumour suppressor pathways may be an immune evasion response that inhibits antiviral pathways and promotes the malignant transformation of the infected cell (Moore & Chang, 2010).

Interestingly, almost 20% of cancer cases begin with infection and chronic inflammation at the same site of inflammation (Grivennikov et al., 2010). Usually, chronic inflammation caused by infections may promote oncogenic mutations, early tumour promotion, genomic instability, and angiogenesis (Grivennikov et al., 2010). Nonetheless, tumour-associated inflammation often co-occurs with tumour formation, with upregulation of responses to tumour development, inflammation, neoangiogenesis, metastatic dissemination, tumour progression, local immunosuppression, and genomic instability (Grivennikov et al., 2010).

Aside from cancer, viral infection can cause various illnesses ranging from mild upper respiratory tract infection to severe pneumonia, acute respiratory distress syndrome, and even death. The fact that most human cases of influenza A (H5N1) and A (H7N9) virus



infection have been attributed to direct or indirect contact with infected live or dead poultry poses a public health risk. Hence, to reduce the risk to humans, it is necessary to establish an effective and safer poultry waste disposal system for all poultry, regardless of their health status. It is because the infection can only be discovered after it has affected individuals, making the treatments more challenging (Christin et al., 2016).

**Heavy Metals-induced Cancer.** Furthermore, it was revealed that poultry manure has a high concentration of heavy metals such as Cu, Mn, Zn, Fe, Mo, cobalt (Co), nickel (Ni), and selenium (Se), which are all beneficial to plant growth and development (Singh et al., 2018). Poultry manure also contains arsenic (As) and chromium (Cr) (Wang et al., 2021), both of which are known to generate epigenetic alterations and genetic defects when exposed to them for an extended period (Abdul et al., 2015).

Heavy metal poisoning may accelerate cancer growth by creating reactive oxygen and nitrogen species, which may result in oxidative stress and DNA damage. Consequently, this genetic instability will result in protein misfolding and the inactivation of enzymes essential for cells' proper functioning. Lead (Pb), nickel (Ni), and arsenic (As) are heavy metals that have been linked to an increased risk of cancer, with excessive exposure or ingestion promoting the growth of skin, bladder, lung, liver, colon, and kidney cancers (Mokhtar et al., 2022) (Figure 2).

Despite these risks, heavy metals such as As, Cu, Co, Fe, Se, Mn, and Zn are continuously added to poultry feed at levels greater than those permitted by regulatory authorities such as the National Research Council (NRC) and the European Union (EU), primarily for disease prevention and to increase weight gain and egg production in poultry (Adekanmi, 2021). According to Bolan et al. (2010), approximately

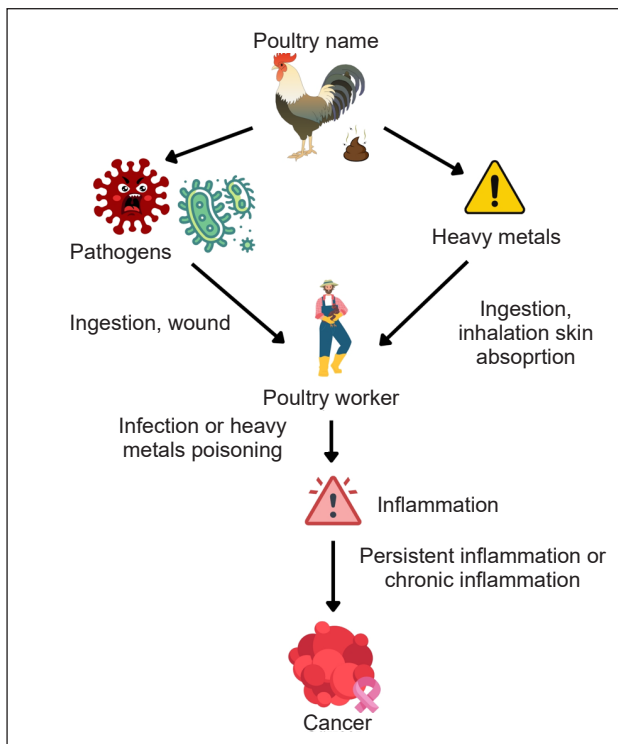


Figure 2. Human health-related risks associated with exposure to poultry manure. Poultry manure is known to contain pathogens and heavy metals. Exposure to these contaminants through ingestion, inhalation, wound or skin absorption may promote inflammation in humans, especially among poultry workers. Persistence or chronic inflammation will later promote cancer progression. Created with Canva.com

5 to 15% of heavy metals are absorbed, while the rest are excreted in faeces and urine into the poultry litter, which is then used as manure (Bolan et al., 2010). As a result, safe levels of heavy metals in poultry manure must be established for land application to avoid these negative consequences. Besides, using these supplements raises the daily discharge of anthropogenic wastes into the environment, particularly the aquatic environment, posing a severe health danger to humans and marine life (Adekanmi, 2021).

With these risks and implications, there is a need for suggestions to ease this issue and to ensure that the use of poultry manure is beneficial rather than detrimental. As mentioned previously, poultry manure is an excellent fertiliser due to its high concentration of nutrients necessary for plant growth and development, but it can also generate electricity via microbial fuel cell (MFC) technology due to high carbon sources, which could eventually serve as another source of renewable energy (Oyiwona et al., 2018).

## **SUGGESTIONS TO ALLEVIATE THE HEALTH-RELATED RISKS**

Intense farming, livestock and poultry can excrete bacteria and viruses, including opportunistic pathogens, through their faeces, which may harm humans and the environment (Jiang et al., 2018). Treatment practices that aid in pathogen reduction in poultry waste are necessary to prevent the spread of these pathogenic microorganisms to humans. However, it is also critical to consider their implications in agricultural settings to ensure that agricultural production is not affected and that agricultural products are safe for consumption (Manyi-Loh et al., 2018).

### **Disinfection**

Disinfection of poultry houses is a crucial step in preventing the transmission of pathogenic germs between batches in large-scale poultry farms. Infectious diseases can be prevented in poultry houses by selecting the appropriate disinfectants, disinfection procedures, and technologies. These techniques consist primarily of washing, soaking, fumigating, spraying, and UV irradiation (Jiang et al., 2018). Furthermore, aerosolised disinfectants have been utilised for more than half a century, as it is known to preserve resources while providing a disinfecting aerosol-vapour gas system. Besides, aerosolised disinfectant also improves the disinfectant's ability to penetrate the bacterial cell wall, increases the disinfection impact, and shortens the disinfection time (Jiang et al., 2018).

### **Composting**

Composting, where poultry wastes are processed to be utilised as organic fertiliser, is one of the most used treatment procedures (Glatz et al., 2011). It is a microbe-driven process that is beneficial for eradicating pathogens such as *Campylobacter* and *Listeria*. *Bacillus* and *Lentibacillus* are two effective microorganisms (EMs) commonly used in composting

due to their high amino acid metabolism. These EMs secrete diverse proteases and can stimulate the dominant microbiota in poultry manure's carbohydrate metabolism (Zhang et al., 2018). Several co-composting options combine various kinds of waste to obtain 'tailored' products with designed properties (Giagnoni et al., 2020).

Although composting has been used for an extended period, the accumulation of waste at the producer level underscored the importance of proposing an environmentally safe composting system. According to Lemunier et al. (2005), *L. monocytogenes* was detected in 4-week-old seeded in-vessel biowaste composts, showing the need for a more thorough and prolonged composting process that can inhibit the pathogen's survival. Thus, by extending the composting process, it is possible to reduce the pathogens' survivability and thus prevent their spread and manifestations in humans. However, composting does not guarantee that the composted product is pathogen free, as some pathogens, such as thermolabile *Salmonella*, are heat resistant. In addition, some cells may become stress-adapted throughout the build-up or composting process, which protects them from future treatments (Lemunier et al., 2005).

### Deep Stacking

The storage of poultry litter serves two primary functions: (1) it serves as a holding area between cleaning and feeding, and (2) it serves to eradicate any pathogens found in the litter (Waziri, 2017). Deep stacking is the most widely used and cost-effective storage method for four to six weeks. The litter is said to undergo a combined composting-ensiling process, where EMs are used as an initiator due to their metabolic processes, which heat the litter stacks from 140 °F to 160 °F. With this elevated temperature, any pathogens found in raw litter, such as *Salmonella*, can be eradicated (Bush et al., 2007; Wilkinson et al., 2011). However, caution should avoid overheating the litter, which can deplete the nutrients.

The litter should contain between 20%–30% moisture and be stacked at approximately 6–8 feet to ensure proper heating during deep stacking. It is because humidity below this point can obstruct heating to the 130-degree threshold, interfering with the margin of safety against pathogens. Additionally, it has been discovered that deeper stacking promotes better heating due to its critical mass and can inhibit mould growth. Before use, it is recommended that the litter be deep stacked for four to six weeks to allow for sufficient heat generation to kill pathogens, including some thermolabile pathogens such as *Salmonella* (Bush et al., 2007).

### Microbial Fuel Cell (MFC) Technology

Interestingly, due to the large number of carbon sources in poultry waste, it has also been used as a substrate for producing renewable energy. It is accomplished through a process known as microbial fuel cell (MFC) technology, which utilises electrogenic bacteria (EB)

such as *Bacillus subtilis* as a catalyst to oxidise the organic and inorganic matter in poultry waste to generate electricity (Muaz et al., 2019) (Figure 3). Not only can this technology be used to generate electricity, but it can also initiate and promote the biodegradation of organic wastes (Muaz et al., 2019).

Although no study has been conducted to date on the benefits of MFC in reducing health-related risks, it may aid in the removal of harmful substances found in poultry manure (Mokhtar et al., 2022). It is because MFC utilised some EB that may secrete metabolites, bacteriocin or macromolecules with anti-inflammatory or anti-cancer properties. Interestingly, *Bacillus subtilis* has been shown to possess an anti-inflammatory property due to its ability to secrete Exopolysaccharide (EPS), which promotes the development of M2 macrophages, inhibiting T cell activation (Paynich et al., 2017). Additionally, bioflocculant, a metabolite composed of polysaccharides, proteins, glycoproteins, and proteoglycans from *Bacillus subtilis* F9, was shown to have a high capacity for scavenging DPPH, hydroxyl, and superoxide radicals, making it a promising antioxidant or anti-cancer agent (Giri et al., 2019). The MFC also produces carbon dioxide and water, which are essential vegetation components, demonstrating the MFC's utility in an agricultural setting.

Aside from that, several studies have discovered the benefits of MFC technology in promoting bacteria found in WWTPs to be susceptible to antibiotics. It is due to MFC's ability to break down antibiotics and Antibiotic resistance genes (ARGs), which is a major contributor to AMR development, increasing the likelihood that it will help prevent AMR transmission in the environment. It is proven by Ondon et al. (2020) and Xue et al. (2019), who found MFC technology to be able to remove 85.1% and 65.5% of sulfamethoxazole (SMX) and norfloxacin (NFLX), respectively (Ondon et al., 2020; Xue et al., 2019).

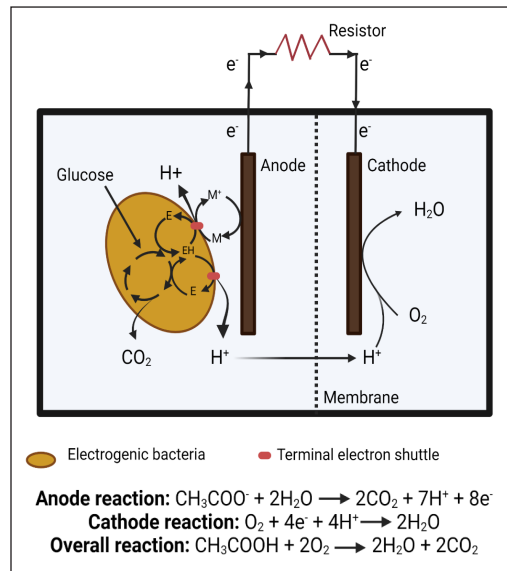


Figure 3. The principal operation of the microbial Fuel cell. Biodegradable substrates varying from pure chemicals to complex mixtures of organic compounds are metabolised by electrogenic bacteria (EB). EB near the anode would decompose the organic materials, transporting the electrons directly through cell components such as proteases or nanowires on the membrane surface or indirectly via the electron shuttle. The cathode accepts electrons and protons from the anode and initiates a reduction process. The MFC, also known as mediator-less MFC, should no mediators be added or utilised. M: redox mediator; E and EH represent the enzyme in reduced and oxidised form, respectively. Adapted from (Zhu et al., 2019). Created with BioRender.com

Additionally, the number of ARGs and integrons after MFC treatment was significantly less than that discovered in WWTPs. For example, the relative abundance of the *int11* is between 63.11 and 652.00 copies/mL(g) in the MFC product compared to 109 to 1011 copies/mL in WWTPs (Chen et al., 2021).

Nevertheless, it is critical to remember that each treatment process must be appropriately managed. Even composting, which is exceptionally effective at pathogen reduction, may cause *Salmonella* regrowth if the composting process and composed litter are adequately handled (Sidhu, 2001). The most effective way to prevent disease outbreaks among poultry farmers is to dress appropriately and avoid confined or poorly ventilated areas, which is more practical and applicable to everyone. Additionally, the awareness of farmers and authorities needs to be raised regarding poultry manure management. There should be stricter enforcement of existing environmental regulations and the enactment of new legislation to minimise the threats that the farmers' current practices pose to their health and the environment.

## CONCLUSION AND FUTURE DIRECTIONS

Even though poultry manure has been routinely applied to land as organic fertiliser or soil improvement, it will surely influence the survival and spread of pathogens such as *Listeria*, *Salmonella*, and *Campylobacter* to the environment. Improper handling and treatment of poultry manure contribute to spreading these pathogens to the environment and humans, promoting inflammation and cancer progression in the long run. Thus, before land application, it is vital to improve current approaches for preventing these pathogens from colonising. Nonetheless, current therapies are ineffective and require additional refinements, such as developing new technologies or procedures capable of fully utilising poultry manure while eradicating pathogenic microflora and pathogens. Furthermore, it would be advantageous to implement new technologies or techniques that expedite manure processing while minimising capital expenditures.

Physical, chemical, and biological treatments are all viable options for eliminating and inactivating heavy metals and quantifying reductions in various bacterial pathogens and indigenous microorganisms in poultry manure. However, these treatments may not eradicate heavy metals or food-borne microorganisms permanently. It is due to the possibility of pathogens, such as faecal coliforms, which are resistant to treatment and undiscovered by existing laboratory detection methods. However, not all faecal coliforms or detected pathogens originate from animal faeces, making it more challenging to study the fate of pathogens in animal wastes after various treatments. Nevertheless, the priority should be inactivating the most resistant and tenacious varieties of infections one could encounter. Therefore, future research should focus on analysing the survivability of selected pathogens in response to various treatments under specific conditions often encountered

when treating poultry manure. It will enable the identification of a comprehensive profile of the various types and concentrations of each pathogen following various treatment approaches, facilitating an accurate evaluation of their risk to humans. These data would aid the poultry business, the healthcare sector, and allied agricultural industries, allowing them to manage waste effectively and reap its benefits without endangering human life.

In addition, each type of treatment can be employed in conjunction with other disinfection or treatment procedures to increase pathogen lethality. This approach may completely eradicate pathogens from poultry manure if the appropriate control mechanisms are implemented. However, owing to the many treatments involved, it will undoubtedly increase the capital costs associated with poultry management.

## ACKNOWLEDGEMENT

This work was supported by the Universiti Sains Malaysia (Apex ERA) (Grant numbers No. 1001.PTEKIND.881006) granted to AMAM.

## REFERENCES

- Abdul, K. S. M., Jayasinghe, S. S., Chandana, E. P. S., Jayasumana, C., & De Silva, P. M. C. S. (2015). Arsenic and human health effects: A review. *Environmental Toxicology and Pharmacology*, 40(3), 828-846. <https://doi.org/10.1016/j.etap.2015.09.016>
- Adekanmi, A. T. (2021). Health hazards of toxic and essential heavy metals from the poultry waste on human and aquatic organisms. In A. K. Patra (Ed.), *Animal Feed Science and Nutrition* (pp. 1-23). IntechOpen. <https://doi.org/10.5772/intechopen.99549>
- Aggarwal, B. B., Vijayalekshmi, R. V., & Sung, B. (2009). Targeting inflammatory pathways for prevention and therapy of cancer: short-term friend, long-term foe. *Clinical Cancer Research*, 15(2), 425-430. <https://doi.org/10.1158/1078-0432.CCR-08-0149>
- Ahmed, M. F. M., Schulz, J., & Hartung, J. (2013). Survival of *Campylobacter jejuni* in naturally and artificially contaminated laying hen feces. *Poultry Science*, 92(2), 364-369. <https://doi.org/10.3382/ps.2012-02496>
- Al-Gheethi, A. A., Efaq, A. N., Bala, J. D., Norli, I., Abdel-Monem, M. O., & Kadir, M. O. A. (2018). Removal of pathogenic bacteria from sewage-treated effluent and biosolids for agricultural purposes. *Applied Water Science*, 8(2), Article 74. <https://doi.org/10.1007/s13201-018-0698-6>
- Arsenault, J., Letellier, A., Quessy, S., Normand, V., & Boulianne, M. (2007). Prevalence and risk factors for *Salmonella* spp. and *Campylobacter* spp. caecal colonization in broiler chicken and turkey flocks slaughtered in Quebec, Canada. *Preventive Veterinary Medicine*, 81(4), 250-264. <https://doi.org/10.1016/j.prevetmed.2007.04.016>
- Avidov, R., Varma, V. S., Saadi, I., Hanan, A., Lublin, A., Saldinger, S. S., Chen, Y., & Laor, Y. (2021). Factors influencing the persistence of *Salmonella infantis* in broiler litter during composting and stabilization processes and following soil incorporation. *Frontiers in Sustainable Food Systems*, 5, Article 645721. <https://doi.org/10.3389/fsufs.2021.645721>

- Beresford, M. R., Andrew, P. W., & Shama, G. (2001). *Listeria monocytogenes* adheres to many materials found in food-processing environments. *Journal of Applied Microbiology*, *90*(6), 1000-1005. <https://doi.org/10.1046/j.1365-2672.2001.01330.x>
- Black, Z., Balta, I., Black, L., Naughton, P. J., Dooley, J. S. G., & Corcionivoschi, N. (2021). The fate of foodborne pathogens in manure treated soil. *Frontiers in Microbiology*, *12*, Article 781357. <https://doi.org/10.3389/fmicb.2021.781357>
- Bolan, N. S., Szogi, A. A., Chuasavathi, T., Seshadri, B., Rothrock, M. J., Jr., & Panneerselvam, P. (2010). Uses and management of poultry litter. *World's Poultry Science Journal*, *66*(4), 673-698. <https://doi.org/10.1017/S0043933910000656>
- Bucher, M. G., Zwirzitz, B., Oladeinde, A., Cook, K., Plymel, C., Zock, G., Lakin, S., Aggrey, S. E., Ritz, C., Looft, T., Lipp, E., Agga, G. E., Abdo, Z., & Sistani, K. R. (2020). Reused poultry litter microbiome with competitive exclusion potential against *Salmonella* Heidelberg. *Journal of Environmental Quality*, *49*(4), 869-881. <https://doi.org/10.1002/jeq2.20081>
- Bush, D. J., Poore, M. H., Rogers, G. M., & Altier, C. (2007). Effect of stacking method on *Salmonella* elimination from recycled poultry bedding. *Bioresource Technology*, *98*(3), 571-578. <https://doi.org/10.1016/j.biortech.2006.02.017>
- Chattopadhyay, M. K. (2014). Use of antibiotics as feed additives: a burning question. *Frontiers in Microbiology*, *5*, Article 334. <https://doi.org/10.3389/fmicb.2014.00334>
- Chen, P., Guo, X., Li, S., & Li, F. (2021). A review of the bioelectrochemical system as an emerging versatile technology for reduction of antibiotic resistance genes. *Environment International*, *156*, Article 106689. <https://doi.org/https://doi.org/10.1016/j.envint.2021.106689>
- Chen, Z., & Jiang, X. (2014). Microbiological safety of chicken litter or chicken litter-based organic fertilizers: A review. *Agriculture*, *4*(1), 1-29. <https://doi.org/10.3390/agriculture4010001>
- Choudhury, A., Felton, G., Moyle, J., & Lansing, S. (2020). Fluidized bed combustion of poultry litter at farm-scale: Environmental impacts using a life cycle approach. *Journal of Cleaner Production*, *276*, Article 124231. <https://doi.org/10.1016/j.jclepro.2020.124231>
- Christin, P., Susanne, H., & Carole, S. (2016). Human influenza virus infections. *Seminars in Respiratory and Critical Care Medicine*, *37*(04), 487-500. <https://doi.org/10.1055/s-0036-1584801>
- Churchill, R. L. T., Lee, H., & Hall, J. C. (2006). Detection of *Listeria monocytogenes* and the toxin listeriolysin O in food. *Journal of Microbiological Methods*, *64*(2), 141-170. <https://doi.org/10.1016/j.mimet.2005.10.007>
- Cokal, Y., Gunaydin, E., & Goncagul, G. (2022). The investigation of the presence of *Listeria* species in poultry farms and antimicrobial resistance profiles of *Listeria monocytogenes* strains. *Journal of Istanbul Veterinary Sciences*, *6*(1), 26-34. <https://doi.org/10.30704/http-www-jivs-net.1075016>
- Djeffal, S., Mamache, B., Elgroud, R., Hireche, S., & Bouaziz, O. (2018). Prevalence and risk factors for *Salmonella* spp. contamination in broiler chicken farms and slaughterhouses in the northeast of Algeria. *Veterinary World*, *11*(8), 1102-1108. <https://doi.org/10.14202/vetworld.2018.1102-1108>

- Facciola, A., Riso, R., Avventuroso, E., Visalli, G., Delia, S. A., & Laganà, P. (2017). *Campylobacter*: From microbiology to prevention. *Journal of Preventive Medicine and Hygiene*, 58(2), E79-E92. <http://www.ncbi.nlm.nih.gov/pubmed/28900347>
- Fan, D., Mao, Y., Xu, L., & Wang, W. (2020). Effects of livestock and poultry breeding pollution on health risks: Evidence from a hog breeding case in rural China. *Chinese Journal of Population, Resources and Environment*, 18(4), 342-349. <https://doi.org/10.1016/j.cjpre.2021.04.008>
- Food and Agriculture Organization of the United Nations. (2013). *Poultry Development Review*. <https://www.fao.org/3/i3531e/i3531e.pdf>
- Runge, G. A., Blackall, P. J., & Casey, K. D. (2007). *Chicken litter: Issues associated with sourcing and use*. Rural Industries Research and Development Corporation. <https://www.agrifutures.com.au/wp-content/uploads/publications/07-035.pdf>
- Garai, P., Gnanadhas, D. P., & Chakravorty, D. (2012). *Salmonella enterica* serovars Typhimurium and Typhi as model organisms: Revealing paradigm of host-pathogen interactions. *Virulence*, 3(4), 377-388. <https://doi.org/10.4161/viru.21087>
- Garcia, S. N., Osburn, B. I., & Jay-Russell, M. T. (2020). One health for food safety, food security, and sustainable food production. *Frontiers in Sustainable Food Systems*, 4, Article 1. <https://doi.org/10.3389/fsufs.2020.00001>
- Gbotosho, O., & Burt, P. J. A. (2013). Environmental and health impacts of poultry manure disposal methods: A case study of Lagelu and Egbeda local government areas in Oyo State, Nigeria. *International Journal of Agricultural Sustainability*, 11(1), 38-51. <https://doi.org/10.1080/14735903.2012.700100>
- Giagnoni, L., Martellini, T., Scodellini, R., Cincinelli, A., & Renella, G. (2020). Co-composting: an opportunity to produce compost with designated tailor-made properties. In H. Hettiarachchi, S. Caucci & K. Schwärzel (Eds.), *Organic Waste Composting through Nexus Thinking: Practices, Policies, and Trends* (pp. 185-211). Springer. [https://doi.org/10.1007/978-3-030-36283-6\\_9](https://doi.org/10.1007/978-3-030-36283-6_9)
- Giri, S. S., Ryu, E., & Park, S. C. (2019). Characterization of the antioxidant and anti-inflammatory properties of a polysaccharide-based bioflocculant from *Bacillus subtilis* F9. *Microbial Pathogenesis*, 136, Article 103642. <https://doi.org/10.1016/j.micpath.2019.103642>
- Glatz, P., Miao, Z., & Rodda, B. (2011). Handling and treatment of poultry hatchery waste: A review. *Sustainability*, 3(1), 216-237. <https://doi.org/10.3390/su3010216>
- Goh, S. G., Kuan, C. H., Loo, Y. Y., Chang, W. S., Lye, Y. L., Soopna, P., Tang, J. Y. H., Nakaguchi, Y., Nishibuchi, M., Afsah-Hejri, L., & Son, R. (2012). *Listeria monocytogenes* in retailed raw chicken meat in Malaysia. *Poultry Science*, 91(10), 2686-2690. <https://doi.org/10.3382/ps.2012-02349>
- Gopal, S., Manoharan, P., Kathaperumal, K., Chidambaram, B., & Divya, K. C. (2012). Differential detection of avian oncogenic viruses in poultry layer farms and Turkeys by use of multiplex PCR. *Journal of Clinical Microbiology*, 50(8), 2668-2673. <https://doi.org/10.1128/JCM.00457-12>
- Grivennikov, S. I., Greten, F. R., & Karin, M. (2010). Immunity, inflammation, and cancer. *Cell*, 140(6), 883-899. <https://doi.org/10.1016/j.cell.2010.01.025>



- Gubišová, M., Horník, M., Hřčková, K., Gubiš, J., Jakubcová, A., Hudcovicová, M., & Ondreičková, K. (2020). Sewage sludge as a soil amendment for growing biomass plant *Arundo donax* L. *Agronomy*, *10*(5), Article 678. <https://doi.org/10.3390/agronomy10050678>
- Hakeem, M. J., & Lu, X. (2021). Survival and control of *campylobacter* in poultry production environment. *Frontiers in Cellular and Infection Microbiology*, *10*, Article 615049. <https://doi.org/10.3389/fcimb.2020.615049>
- Jechalke, S., Schierstaedt, J., Becker, M., Flemer, B., Grosch, R., Smalla, K., & Schikora, A. (2019). *Salmonella* establishment in agricultural soil and colonization of crop plants depend on soil type and plant species. *Frontiers in Microbiology*, *10*, Article 967. <https://doi.org/10.3389/fmicb.2019.00967>
- Jerez, S. B., Cheng, Y., & Bray, J. (2014). Exposure of workers to dust and bioaerosol on a poultry farm. *Journal of Applied Poultry Research*, *23*(1), 7-14. <https://doi.org/10.3382/japr.2012-00710>
- Jiang, L., Li, M., Tang, J., Zhao, X., Zhang, J., Zhu, H., Yu, X., Li, Y., Feng, T., & Zhang, X. (2018). Effect of different disinfectants on bacterial aerosol diversity in poultry houses. *Frontiers in Microbiology*, *9*, Article 2113. <https://doi.org/10.3389/fmicb.2018.02113>
- Johnson, E. S., Ndetan, H., & Lo, K. M. (2010). Cancer mortality in poultry slaughtering/processing plant workers belonging to a union pension fund. *Environmental Research*, *110*(6), 588-594. <https://doi.org/10.1016/j.envres.2010.05.010>
- Kitjakrancharoensin, P., Yasan, K., Hongyantarachai, K., Ratanachokthorani, K., Thammasarn, J., Kuwuttiwai, D., Ekanaprach, T., Jittakarm, R., Nuntapravechpun, R., Hotarapavanon, S., Kulrattanak, S., Tongkaew, S., Deemeechai, S., Mungthin, M., Rangsin, R., Wongsrichanalai, V., & Sakboonyarat, B. (2020). Prevalence and risk factors of chronic obstructive pulmonary disease among agriculturists in a rural community, central Thailand. *International Journal of Chronic Obstructive Pulmonary Disease*, *15*, 2189-2198. <https://doi.org/10.2147/COPD.S262050>
- Kyakuwaire, M., Olupot, G., Amoding, A., Nkedi-Kizza, P., & Basamba, T. A. (2019). How safe is chicken litter for land application as an organic fertilizer? A review. *International Journal of Environmental Research and Public Health*, *16*(19), Article 3521. <https://doi.org/10.3390/ijerph16193521>
- Lamas, A., Miranda, J. M., Regal, P., Vázquez, B., Franco, C. M., & Cepeda, A. (2018). A comprehensive review of non-enterica subspecies of *Salmonella enterica*. *Microbiological Research*, *206*, 60-73. <https://doi.org/10.1016/j.micres.2017.09.010>
- Lemunier, M., Francou, C., Rousseaux, S., Houot, S., Dantigny, P., Piveteau, P., & Guzzo, J. (2005). Long-term survival of pathogenic and sanitation indicator bacteria in experimental biowaste composts. *Applied and Environmental Microbiology*, *71*(10), 5779-5786. <https://doi.org/10.1128/AEM.71.10.5779-5786.2005>
- Lin, M., Roche, P., Spencer, J., Milton, A., Wright, P., Witteveen, D., Leader, R., Merianos, A., Bunn, C., Gidding, H., Kaldor, J., Kirk, M., Hall, R., & Della-Porta, T. (2010). *Australia's notifiable diseases status, 2000: Annual report of the National Notifiable Diseases Surveillance System*. National Notifiable Diseases Surveillance System. [https://www1.health.gov.au/internet/main/publishing.nsf/Content/cda-2002-cdi2602-pdf-cnt.htm/\\$FILE/cdi2602b.pdf](https://www1.health.gov.au/internet/main/publishing.nsf/Content/cda-2002-cdi2602-pdf-cnt.htm/$FILE/cdi2602b.pdf)
- Macklin, K. S., Hess, J. B., Bilgili, S. F., & Norton, R. A. (2006). Effects of in-house composting of litter on bacterial levels. *Journal of Applied Poultry Research*, *15*(4), 531-537. <https://doi.org/10.1093/japr/15.4.531>

- Manisalidis, I., Stavropoulou, E., Stavropoulos, A., & Bezirtzoglou, E. (2020). Environmental and health impacts of air pollution: A review. *Frontiers in Public Health*, 8, Article 14. <https://doi.org/10.3389/fpubh.2020.00014>
- Manyi-Loh, C., Mamphweli, S., Meyer, E., & Okoh, A. (2018). Antibiotic use in agriculture and its consequential resistance in environmental sources: Potential public health implications. *Molecules*, 23(4), Article 795. <https://doi.org/10.3390/molecules23040795>
- Medzhitov, R. (2008). Origin and physiological roles of inflammation. *Nature*, 454, 428-435. <https://doi.org/10.1038/nature07201>
- Miller, R. A., Betteken, M. I., Guo, X., Altier, C., Duhamel, G. E., & Wiedmann, M. (2018). The typhoid toxin produced by the nontyphoidal *Salmonella enterica* serotype Javiana is required for induction of a DNA damage response *in vitro* and systemic spread *in vivo*. *mBio*, 9(2), Article e00467-18. <https://doi.org/10.1128/mBio.00467-18>
- Mokhtar, A. M. B. A., Makhtar, M. M. Z., & Mokhtar, A. M. A. (2022). Waste and health: sewage sludge and its hazard to human. In A. Z. Yaser, H. A. Tajarudin & A. Embrandiri (Eds.), *Waste Management, Processing and Valorisation* (pp. 135-158). Springer. [https://doi.org/10.1007/978-981-16-7653-6\\_8](https://doi.org/10.1007/978-981-16-7653-6_8)
- Moore, P. S., & Chang, Y. (2010). Why do viruses cause cancer? Highlights of the first century of human tumour virology. *Nature Reviews Cancer*, 10(12), 878-889. <https://doi.org/10.1038/nrc2961>
- Mouttotou, N., Ahmad, S., Kamran, Z., & Koutoulis, K. C. (2017). Prevalence, risks and antibiotic resistance of *Salmonella* in poultry production chain. In M. Mares (Ed.), *Current Topics in Salmonella and Salmonellosis* (pp. 215-234). IntechOpen. <https://doi.org/10.5772/67438>
- Muaz, M. Z. M., Abdul, R., & Vadivelu, V. M. (2019). Recovery of energy and simultaneous treatment of dewatered sludge using membrane-less microbial fuel cell. *Environmental Progress and Sustainable Energy*, 38(1), 208-219. <https://doi.org/10.1002/ep.12919>
- Nichols, G. L. (2005). Fly transmission of *Campylobacter*. *Emerging Infectious Diseases*, 11(3), 361-364. <https://doi.org/10.3201/eid1103.040460>
- Odadjare, E. E. O., Obi, L. C., & Okoh, A. I. (2010). Municipal wastewater effluents as a source of listerial pathogens in the aquatic milieu of the Eastern Cape Province of South Africa: A concern of public health importance. *International Journal of Environmental Research and Public Health*, 7(5), 2376-2394. <https://doi.org/10.3390/ijerph7052376>
- Hood, J. (2021). Australia's notifiable disease status, 2016: Annual report of the National Notifiable Diseases Surveillance System. *Communicable Diseases Intelligence*, 45, 1-92. <https://doi.org/10.33321/cdi.2021.45.28>
- Ondon, B. S., Li, S., Zhou, Q., & Li, F. (2020). Simultaneous removal and high tolerance of norfloxacin with electricity generation in microbial fuel cell and its antibiotic resistance genes quantification. *Bioresource Technology*, 304, Article 122984. <https://doi.org/https://doi.org/10.1016/j.biortech.2020.122984>
- Organisation for Economic Co-operation and Development. (2022). *Meat Consumption*. OECD. <https://doi.org/10.1787/fa290fd0-en>

- Orsi, R. H., & Wiedmann, M. (2016). Characteristics and distribution of *Listeria* spp., including *Listeria* species newly described since 2009. *Applied Microbiology and Biotechnology*, *100*(12), 5273-5287. <https://doi.org/10.1007/s00253-016-7552-2>
- Oyiwona, G. E., Ogbonna, J. C., Anyanwu, C. U., & Okabe, S. (2018). Electricity generation potential of poultry droppings wastewater in microbial fuel cell using rice husk charcoal electrodes. *Bioresources and Bioprocessing*, *5*, Article 13. <https://doi.org/10.1186/s40643-018-0201-0>
- Paynich, M. L., Jones-Burrage, S. E., & Knight, K. L. (2017). Exopolysaccharide from *Bacillus subtilis* induces anti-inflammatory M2 macrophages that prevent T cell-mediated disease. *Journal of Immunology*, *198*(7), 2689-2698. <https://doi.org/10.4049/jimmunol.1601641>
- Population Matters. (2023). *Population: The Numbers*. <https://populationmatters.org/the-facts-numbers/>
- Public Health England. (2013). *Notified Diseases: 2013 Annual Figures*. <https://webarchive.nationalarchives.gov.uk/ukgwa/20211105220847/https://www.gov.uk/government/publications/notifiable-diseases-annual-report>
- Redding, M. R. (2011). Bentonites and layered double hydroxides can decrease nutrient losses from spent poultry litter. *Applied Clay Science*, *52*(1-2), 20-26. <https://doi.org/10.1016/j.clay.2011.01.016>
- Singh, G., Shamsuddin, M. R., Aqsha, & Lim, S. W. (2018). Characterization of chicken manure from Manjung region. *IOP Conference Series: Materials Science and Engineering*, *458*, Article 012084. <https://doi.org/10.1088/1757-899X/458/1/012084>
- Sibanda, N., McKenna, A., Richmond, A., Ricke, S. C., Callaway, T., Stratakos, A. C., Gundogdu, O., & Corcionivoschi, N. (2018). A review of the effect of management practices on *Campylobacter* prevalence in poultry farms. *Frontiers in Microbiology*, *9*, Article 2002. <https://doi.org/10.3389/fmicb.2018.02002>
- Sidhu, J., Gibbs, R. A., Ho, G. E., & Unkovich (2001). The role of indigenous microorganisms in suppression of *salmonella* regrowth in composted biosolids. *Water Research*, *35*(4), 913-920. [https://doi.org/10.1016/S0043-1354\(00\)00352-3](https://doi.org/10.1016/S0043-1354(00)00352-3)
- Silk, B. J., Date, K. A., Jackson, K. A., Pouillot, R., Holt, K. G., Graves, L. M., Ong, K. L., Hurd, S., Meyer, R., Marcus, R., Shiferaw, B., Norton, D. M., Medus, C., Zansky, S. M., Cronquist, A. B., Henao, O. L., Jones, T. F., Vugia, D. J., Farley, M. M., & Mahon, B. E. (2012). Invasive listeriosis in the foodborne diseases active surveillance network (FoodNet), 2004-2009: Further targeted prevention needed for higher-risk groups. *Clinical Infectious Diseases*, *54*(suppl\_5), S396-S404. <https://doi.org/10.1093/cid/cis268>
- Sim, J., Hood, D., Finnie, L., Wilson, M., Graham, C., Brett, M., & Hudson, J. A. (2002). Series of incidents of *Listeria monocytogenes* non-invasive febrile gastroenteritis involving ready-to-eat meats. *Letters in Applied Microbiology*, *35*(5), 409-413. <https://doi.org/10.1046/j.1472-765X.2002.01207.x>
- Taiwo, A. M., & Arowolo, T. A. (2017). Impacts of agricultural poultry farming on water and sediment qualities. In *Proceedings of the 2nd World Congress on Civil, Structural, and Environmental Engineering (CSEE'17)* (pp 1-9). ICESDP Publishing. <https://doi.org/10.11159/icesdp17.159>
- UK Health Security Agency. (2020). *Notified Diseases: 2020 Annual Figures*. <https://www.gov.uk/government/publications/notifiable-diseases-annual-report>

- van Immerseel, F., de Zutter, L., Houf, K., Pasmans, F., Haesebrouck, F., & Ducatelle, R. (2009). Strategies to control *Salmonella* in the broiler production chain. *World's Poultry Science Journal*, 65(3), 367-392. <https://doi.org/10.1017/S0043933909000270>
- Voetsch, A. C., van Gilder, T. J., Angulo, F. J., Farley, M. M., Shallow, S., Marcus, R., Cieslak, P. R., Deneen, V. C., Tauxe, R. V., & Group, for the E. I. P. F. W. (2004). FoodNet estimate of the burden of illness caused by nontyphoidal *Salmonella* infections in the United States. *Clinical Infectious Diseases*, 38(Supplement\_3), S127-S134. <https://doi.org/10.1086/381578>
- Waldner, L. L., MacKenzie, K. D., Köster, W., & White, A. P. (2012). From exit to entry: Long-term survival and transmission of *Salmonella*. *Pathogens*, 1(2), 128-155. <https://doi.org/10.3390/pathogens1020128>
- Wang, A., Zou, D., Zeng, X., Chen, B., Zheng, X., Li, L., Zhang, L., Xiao, Z., & Wang, H. (2021). Speciation and environmental risk of heavy metals in biochars produced by pyrolysis of chicken manure and water-washed swine manure. *Scientific Reports*, 11(1), Article 11994. <https://doi.org/10.1038/s41598-021-91440-8>
- Wilkinson, K. G., Tee, E., Tomkins, R. B., Hepworth, G., & Premier, R. (2011). Effect of heating and aging of poultry litter on the persistence of enteric bacteria. *Poultry Science*, 90(1), 10-18. <https://doi.org/10.3382/ps.2010-01023>
- Xiong, D., Song, L., Pan, Z., & Jiao, X. (2018). Identification and discrimination of *Salmonella enterica* serovar Gallinarum biovars Pullorum and Gallinarum based on a one-step multiplex PCR Assay. *Frontiers in Microbiology*, 9, Article 1718. <https://doi.org/10.3389/fmicb.2018.01718>
- Xue, W., Li, F., & Zhou, Q. (2019). Degradation mechanisms of sulfamethoxazole and its induction of bacterial community changes and antibiotic resistance genes in a microbial fuel cell. *Bioresource Technology*, 289, Article 121632. <https://doi.org/https://doi.org/10.1016/j.biortech.2019.121632>
- You, Y., Rankin, S. C., Aceto, H. W., Benson, C. E., Toth, J. D., & Dou, Z. (2006). Survival of *Salmonella enterica* serovar Newport in manure and manure-amended soils. *Applied and Environmental Microbiology*, 72(9), 5777-5783. <https://doi.org/10.1128/AEM.00791-06>
- Zhang, L., Li, L., Pan, X., Shi, Z., Feng, X., Gong, B., Li, J., & Wang, L. (2018). Enhanced growth and activities of the dominant functional microbiota of chicken manure composts in the presence of maize straw. *Frontiers in Microbiology*, 9, Article 1131. <https://doi.org/10.3389/fmicb.2018.01131>
- Zhu, Q., Gooneratne, R., & Hussain, M. A. (2017). *Listeria monocytogenes* in fresh produce: outbreaks, prevalence and contamination levels. *Foods*, 6(3), Article 21. <https://doi.org/10.3390/foods6030021>
- Zhu, Y., Goh, F. W. T., & Wang, Q. (2019). Redox catalysts for aprotic Li-O<sub>2</sub> batteries: Toward a redox flow system. *Nano Materials Science*, 1(3), 173-183. <https://doi.org/10.1016/j.nanoms.2019.02.008>

*Review Article*

## **Integrating Ice Protection and Noise Abatement Systems for Aircraft Application: A Review**

**Fathima Rehana Munas<sup>1,2</sup>, Yu Kok Hwa<sup>1</sup>, Norwahida Yusoff<sup>1</sup>, Abdul Majeed Muzathik<sup>2</sup> and Mohd Azmi Ismail<sup>1\*</sup>**

<sup>1</sup>*School of Mechanical Engineering, Universiti Sains Malaysia, Engineering Campus, 14300 USM, Nibong Tebal, Penang, Malaysia*

<sup>2</sup>*Department of Mechanical Engineering, Faculty of Engineering, South Eastern University of Sri Lanka, 32360 Oluvil, Eastern Province, Sri Lanka*

### **ABSTRACT**

Aircraft icing remains a key aviation hazard as the global fleet of aircraft in various sectors continues to expand, posing a serious threat to flight safety. As previously stated, the growth of this type of aircraft has been accompanied by an increase in noise levels, and aircraft is reportedly the second most bothersome noise source after traffic. However, integrating an acoustic liner with anti-icing techniques on the leading edge of a nacelle would not efficiently eliminate forward radiated noise and improve the thermal performance of the anti-icing system. Hence, it is of the utmost importance to research the integration of ice protection and noise abatement systems for aircraft applications. This review discusses the integration of ice accretion and noise abatement systems in aircraft applications. The prominence of this review is to explain significant features such as ice protection systems, Computational Fluid Dynamics in ice protection, noise abatement systems, and the integration of ice protection systems and noise abatement systems wherever they are described.

#### ARTICLE INFO

*Article history:*

Received: 06 September 2022

Accepted: 12 April 2023

Published: 08 September 2023

DOI: <https://doi.org/10.47836/pjst.31.6.02>

*E-mail addresses:*

rehana@seu.ac.lk (Fathima Rehana Munas)

yukokhwa@usm.my (Yu Kok Hwa)

menorwahida@usm.my (Norwahida Yusoff)

muzathik64@seu.ac.lk (Abdul Majeed Muzathik)

azmi\_meche@usm.my (Mohd Azmi Ismail)

\* Corresponding author

*Keywords:* Acoustic liner, bias acoustic liner, ice protection, noise abatement

### **INTRODUCTION**

As the global fleet of aircraft in many sectors continues to expand, aircraft icing remains a major aviation hazard that significantly impacts flight safety. Aircraft icing is

characterized by the accretion of ice on aircraft surfaces. Icing occurs frequently on the leading edges of an aircraft's wing, tails, engine inlet, windshield, and helicopter blade (Sreedharan et al., 2014). Moreover, ice accumulation on the rotating spinner positioned at the engine's front surface would impair the uniformity of the inlet flow field, resulting in airflow separation and compressor surge (Zheng et al., 2019). Additionally, ice of the inlet lip would affect the vanes, resulting in mechanical damage and a drop in downstream performance (Shen et al., 2013). The icing on the other surface, i.e., the windshield, would affect output performance and result in energy loss (Yang et al., 2022).

Also, the accumulation of ice on the aircraft tail would impair the stability and control of the aircraft. This phenomenon is most noticeable during landing, cruising, and rising (Ronaudo et al., 1991). Ice buildup on the aircraft wing surface would exacerbate the aircraft's control and stability. Furthermore, the lift force is reduced due to ice on the wing, thus increasing drag and altering moment characteristics (Ronaudo et al., 1991). As a result, the aircraft's fuel consumption increases, thus raising operational costs. Overall, aircraft icing would hinder aircraft performance, increase aircraft weight and drag force, reduce lift forces, and degrade thrust handling, thus creating significant safety concerns (Hassaani et al., 2020).

Therefore, it is necessary to remove ice from aircraft to ensure its safe performance and operation (Shen et al., 2013). As a consequence, several techniques to eliminate ice accretion have been developed. Anti-icing and de-icing are the two primary methods of an ice protection system. The de-icing method removes ice periodically when it has accumulated to a significant thickness (Nagappan, 2013). Electro Magnetic Expulsion and the Pneumatic Inflatable Boot are ice protection devices that use de-icing. On the other hand, the anti-icing method is a prompting system that is activated prior to the onset of icing conditions (Nagappan, 2013). Thermal and chemical fluids are examples of ice protection systems that employ anti-icing methods. Thermal anti-icing is the more prevalent of the two and is classified as either an electric heater or hot bleed air. As previously discussed, an increase in the number of flights is frequently accompanied by a rise in noise levels. It is considered that aircraft noise is the second most infuriating source of noise after traffic noise (Ives, 2009). Researchers have proposed several solutions for reducing engine and turbine noise, including installing an acoustic liner (AL) in a noise cowl zone. However, combining an acoustic liner and anti-icing on the leading edge of a nacelle lip skin would not be adequate to boost thermal performance (Ismail, 2013). Therefore, it is of the utmost importance to research the integration of ice protection and noise abatement systems for aviation applications.

This review discusses the integration of ice protection and noise abatement systems in aircraft applications, particularly focusing on ice protection systems, CFD in ice protection, and noise abatement systems.

## ICE PROTECTION SYSTEMS

Ice protection has been an important component of all aviation for a long time. The United States National Transportation Safety Board (2007) reported that icing problems caused many aircraft crashes. Chemical fluid, mechanical, thermal, hybrid, and other ice protection methods are widely used in commercial aircraft. The chemical fluid ice protection method removes ice deposits and forms a protective film on airplane surfaces (Grishaev et al., 2021). This method protects aircraft surfaces from icing by lowering the freezing temperature of supercooled water below the ambient temperature by mixing a chemical fluid with supercooled water that has been impinged. The mechanical ice protection method, i.e., pneumatic inflatable boot, on the other hand, breaks the ice's bond from the aircraft's surface, and the ice fragments are blown away into the atmosphere. Also, the thermal ice protection method uses hot bleed air or electricity to the protected aircraft surface. Lastly, a hybrid ice protection system comprises a running wet electro-thermal anti-icing system and an Electro-Mechanical Expulsion De-icing System (EMEDS). While the former system maintains temperatures above freezing point, the actuators of the latter system periodically eradicate ice.

Two systems in aircraft ice protection are widely used in commercial aircraft: the anti-icing system (AI) and the de-icing system (DI). The DI system removes or breaks ice accumulation periodically, while the AI system prevents ice from always forming on aircraft components. Therefore, it is understood that the fundamentals of ice protection tools can guide researchers in recommending the most appropriate ice protection device for a given icing condition. The types of ice protection tools are described, and their strengths and weaknesses are listed in Table 1.

Table 1  
*Types of ice protection devices*

Examples of Ice Protection Devices	AI/DI	Strengths	Weaknesses
Mechanical Deformation Ice Protection	DI	These are light and have low operational costs. Useful for small aircraft. Less energy consumption and maintenance and the cost and weight are comparably small and reliable (Li, 2012).	Special compound material and stretchable fabric-reinforced elastomer are needed for PIB to avoid weathering and erosion.
Electro-Mechanical Expulsion Ice Protection System	DI	Mostly used to lift aircraft surfaces, such as wings. Low power consumption. The cycling time would be controlled and varied. Efficient and automatic ice protection	Conductive strips should be fabricated on the flexible dielectric sheet.
The Pulse Electro-Thermal Ice Protection Systems (PETD)	DI	Low energy consumption is required. Very useful on the windshields of many modes of transportation, including airplanes, bridges, and automobiles. (Petrenko, 2005).	Difficult to manage ice formation outside the ice protection area (Ma, 2011)

Table 1 (continue)

Examples of Ice Protection Devices	AI/DI	Strengths	Weaknesses
Thermo-Mechanical Expulsion Ice Protection System	AI	This system provides excellent anti-icing performance while consuming less energy (June 2020).	This system is too expensive (Jun et al., 2020).
Thermal Ice Protection System	AI	The optimum heat transfer from the jet to the impinging surface occurs at a distance from the hole to the impinging surface of 5-7 times that of the jet diameter (Raghunathan et al., 2006).	Weight and manufacturing costs are comparatively high (Syed et al., 2018). Higher energy costs are required.
Hybrid Ice Protection System	DI and AI	It is a more cost-effective method instead of using hot air.	Warm and high liquid water content condition is required.
Double-walled Ice Protection System	AI	Provides a more uniform temperature. Avoids hotspots occurring on the nacelle lip skin.	Disrupts installation of noise abatement material. Complex construction is required, resulting in higher installation and maintenance costs (Birbragher, 1988).
Chemical Liquids Ice Protection System	DI and AI	Useful in small aircraft	The required glycol solution must be carried on board. Limited duration of ice protection (Ramamurthy et al., 1991).
Swirl Ice Protection System	AI	Construction is very simple in comparison to other ice protection systems. Provide uniform temperature distribution on the nacelle lip-skin, preventing the runback ice accretion on the downstream area.	A huge amount of hot air is required.

### Mechanical Deformation Ice Protection

The pneumatic inflatable boot (PIB) is a mechanical deformation ice protection device commonly used in light airplanes. The development of the inflatable boot began in 1928, and this has been used in more than 30,000 small aircraft worldwide (Ramamurthy et al., 1991). This device has inflatable rubber strips on the wings' outer surface and control surfaces where ice is accreted (Ronaudo et al., 1991). The ducts inside the rubber strips function as an air conduit and become inflated when they receive pumped air from the engine. Due to the combination of shear, bending, and peel forces, the surface distorts and breaks the ice down. Then the broken ice is carried away from the surface by aerodynamic force (Ramamurthy et al., 1991). The working principle of the pneumatic inflatable boot is shown in Figure 1.



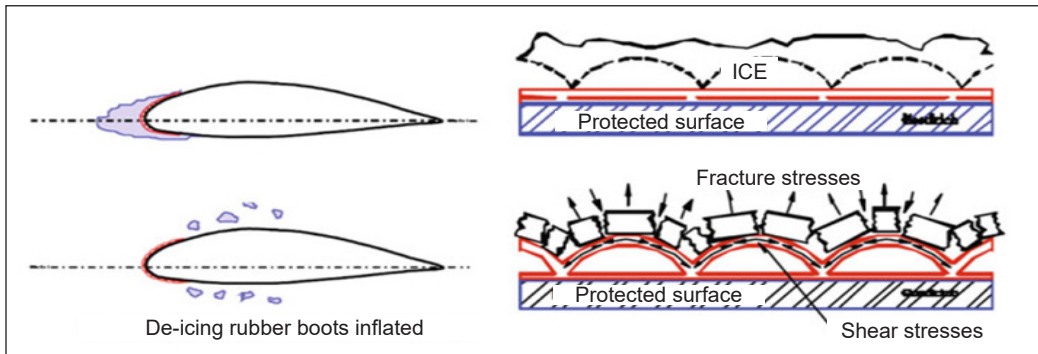


Figure 1. Working principle of Pneumatic Inflatable Boot (PIB) (Battisti, 2015)

### Electro Impulse Ice Protection System

This system ensures the aircraft's safety during icing conditions. The capacitors are discharged through an electric coil. This system produces a huge magnetic field and, thus, large amplitude and impulse, which act on a nearby electrically conductive plate. The impulse force exerted on the nacelle's surface slightly expands, then contracts, generating mechanical vibrations on the leading edge. As a result, ice on the surface is shed due to mechanical vibration caused by the Electro Impulse Ice Protection System's impulse forces (Li, 2012). Figure 2 shows the elementary circuit of this ice protection system. In this system, the pulse coils are connected to a high voltage capacitor by low resistance, low inductance cables. When the switch is turned on, the discharge of the capacitor through the impulse coils creates a rapidly forming and collapsing electromagnetic field. According to Maxwell's law, it is known that the time-dependent magnetic field induces eddy currents in the metal skin. Therefore, the Lorentz force formula obtains the instantaneous impulse force of several hundred pounds in magnitude. However, the duration is only a few hundred microseconds. A small amplitude, high acceleration movement of the skin acts to shatter, de-bond, and expel the ice (Jiang & Wang, 2019).

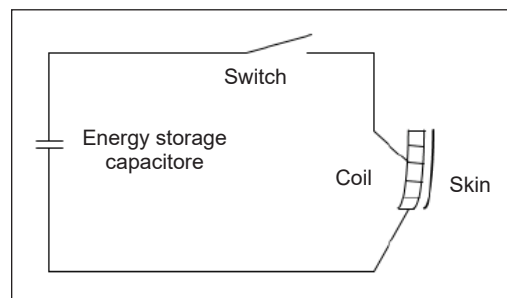


Figure 2. Working principle of Electro Impulse Ice Protection (Jiang & Wang, 2019)

Therefore, the Lorentz force formula obtains the instantaneous impulse force of several hundred pounds in magnitude. However, the duration is only a few hundred microseconds. A small amplitude, high acceleration movement of the skin acts to shatter, de-bond, and expel the ice (Jiang & Wang, 2019).

### Electro-mechanical Expulsion Ice Protection System

This system is a modern ice protection technique used in aircraft. In this case, opposing electromagnetic fields are generated in actuators by a high-current electric pulse, which causes the actuators to deflect. This deflection is then transmitted to the erosion shield, which bends and vibrates at a very high frequency. As a result, the accumulated ice on

the erosion shield is released (Goraj, 2004). The working principle of this type of ice protection system is shown in Figure 3.

### The Pulse Electro-thermal Ice Protection Systems (PETD)

It is an improvement of the Electro-Thermal Ice protection system that uses an electro-thermal pulse approach. This system encompasses strips and shedding zones as heating components. While the partition strips maintain the surface temperature above freezing, the shedding zones melt the ice contact on the leading-edge surface (Ma, 2011). In addition, the thin ice layer is melted by high-density power, which reduces the amount of melted runback water. Figure 4 displays the working principle of this type of system. In this system, the airflow cools the skin temperature below freezing very quickly when the power is cut off. Thus, the impinged water freezes quickly, resulting in minimal runback ice formation.

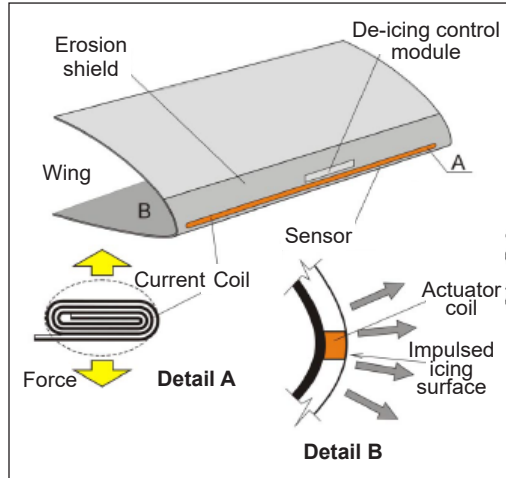


Figure 3. Working principle of Electro-Mechanical Expulsion Ice Protection System (Goraj, 2004)

### Thermo-mechanical Expulsion Ice Protection System

It is a hybrid system designed to provide ice protection on icing surfaces using less power. This system employs a resistive heater connected to the leading edge, with special attention paid to the impingement zone where the incoming air stream divides between upper and lower surfaces and engineering applications require additional time (Al-Khalid, 2007). Figure 5 shows a schematic representation of the system.

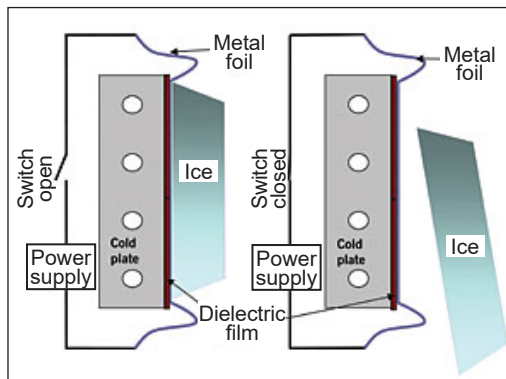


Figure 4. Working principle of PETDS (Pulse Electro Thermal De-icing, 2005)

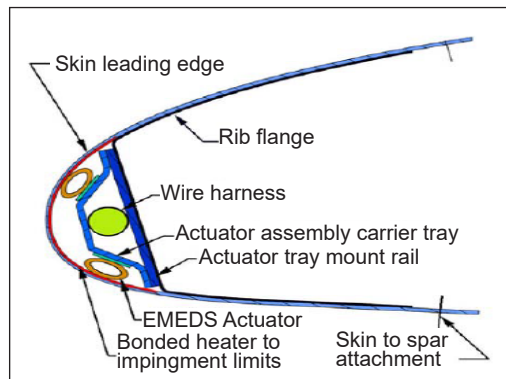


Figure 5. Thermo Mechanical Expulsion Ice protection system (Al-Khalid, 2007)

### Thermal Ice Protection System

In this technique, thermal energy is transferred to the nacelle lip skin as well as a wing in modern commercial aviation (Khai et al., 2020). This energy evaporates the impinging water, a consequence of keeping the surface temperature above freezing. Particularly, Piccolo Tube Anti Icing (PTAI) is one of the most popular thermal anti-icing systems for aircraft, and it has staggered holes around the tube. The engine compressors supply hot air at high temperatures and pressure. This hot, high-pressure air is then introduced to PTAI, where the supply pipe is directed toward the internal surface through discrete holes in the perforated piccolo tube. After impinging on the internal surface, the exhaust air circulates the D-chamber and exits through the exhaust grill, as shown in Figure 6 (Ismail, 2013). In this case, the pneumatically operated valves control the PTAI system. The hot air is distributed via a piccolo tube that runs the length of an aircraft slat within the D-chamber (Raghunathan et al., 2006).

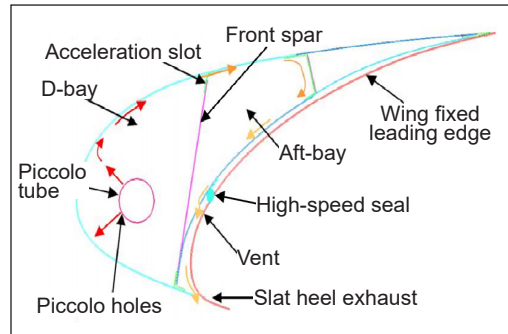


Figure 6. Thermal Ice Protection System (Ismail, 2013)

### Hybrid Ice Protection System

The fundamental concept of this system is similar to that of the Thermomechanical Expulsion Ice protection system. Electric heaters and a low-power ice protection system are combined to reduce energy consumption, which is therefore known as a hybrid anti-icing system (Al-Khalil et al., 1997).

### Double-walled Ice Protection System

It is another alternative ice protection system, as shown in Figure 7. This system forces hot air from the D-chamber into a channel between two walls. Consequently, the heat from the hot air is transferred to the walls by convection (Rosenthal & Nelepovitz, 1985). This method provides a more uniform temperature distribution and prevents the occurrence of hotspots on the nacelle lip skin.

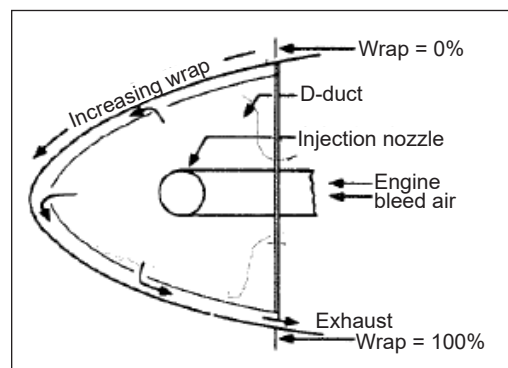


Figure 7. Doubled-walled Ice Protection System (Rosenthal & Nelepovitz, 1985)

### Chemical Liquids Ice Protection System

The chemical ice protection system works by lowering the freezing point of an ethylene glycol-based fluid through laser-drilled titanium panels on the leading edges of the wings, horizontal and vertical stabilizers, and a slinger ring that protects the propeller. The fluid is dispersed as air flows over the wing and empennage, coating the surfaces and preventing the formation and adhesion of ice (Whitfeld, 2021).

### Swirl Ice Protection System

This system transfers high-pressure and high-temperature air from the jet engine to the D-chamber by a supply pipe (Ismail & Wang, 2018). The nozzle is located at the end of the supply pipe and bent 90° to direct the high-pressure, hot air into the D-chamber. The air with a high temperature and velocity exits the nozzle and comes into contact with the cooler air in the D-chamber, causing a relatively large amount of cold air to be entrained by hot air. Thus, the air is entrained in a circular motion around the annular D-chamber. As a result, this system transfers heat from hot air to the nacelle lip skin more uniformly than other ice protection systems (Ismail, 2013).

This technique has a variety of nozzle designs and arrangements which enhance heat transfer and temperature distribution in stationary air due to turbulent enhancement, thus increasing the mixing process between hot air and stationary air. As a result, the duration of heat and momentum transfers from hot air to the nacelle lip skin has been reduced significantly (Syed et al., 2018). Figure 8 illustrates a schematic representation of this type of system.

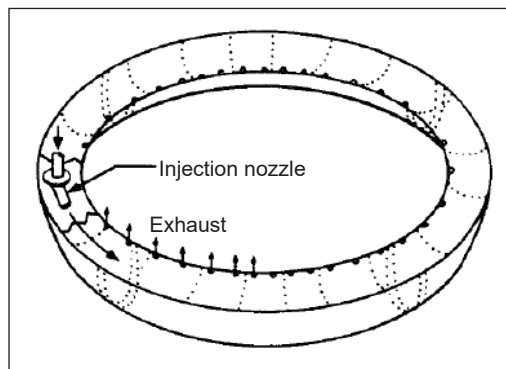


Figure 8. Swirl Ice Protection system (Rosenthal & Nelepovitz, 1985)

### CFD APPLICATION IN ICE PROTECTION SYSTEM

Many researchers use CFD applications in anti-icing due to the difficulty and cost constrain in experiments and validation tests. Previous researchers applied CFD techniques to optimize the performance of hot-air anti-icing systems, particularly Piccolo Tube Anti Icing (PTAI). Al-Khalil et al. (1997) investigated the performance of hot-air anti-icing using engine inlet ice protection. Here, the authors utilized trajectory code to estimate local water-impingement rates on the nacelle inlet surface. The temperature distribution on the nacelle lip skin was determined by solving the energy balance on surface runback water and nacelle lip skin. According to the results, the authors recommended that a large amount of heat be concentrated on the stagnation point of water droplet impingement

to evaporate these water droplets. The results also showed that the runback water might reach freezing temperature downstream of the nacelle lip-skin. Therefore, the authors also suggested protecting this area with moderate thermal anti-icing systems, such as Electro Thermal Heaters (ETH).

Subsequently, Morency et al. (1997) introduced a simple mathematical model to analyze the heat transfer phenomenon on the aerofoil surface. This mathematical model was used to simulate the temperature changes of the runback water film and the conduction in the airfoil's skin. The results demonstrated that evaporation heat loss increases with temperature more rapidly than convection heat loss.

Later, Smith and Taylor. (1997) examined the simulation of a 2D anti-icing system in dry and wet conditions using the PHEONICS code. This code solved the energy equation to determine the cooling effects of water impingement. The simulation result was congruent with the flight test. Afterward, Croce et al. (1998) obtained the predicted results from the FENSAPICE code they had developed. The code utilized a finite element method to determine ice accretion, droplet impingement, and conjugate heat transfer by solving the Navier-Stokes equation. They used a standard k-epsilon model to resolve turbulent flows inside the wing's leading edge. Their results were claimed to be satisfactory. However, there was no validation against experimental results. In addition, de Mattos and Olivera (2000) studied conjugate heat transfer on an anti-icing system wing slat using the FLUENT CFD code. The results showed that the heat transfer characteristics were proportional to the mass flow rate of hot air.

Morency et al. (2000) once again developed a numerical code and implemented it into a CANICE CFD code to design an ice protection system on wing-leading edges. The boundary layer equations were solved by the finite difference method and integral method. The results showed that the finite difference method was able to give results that were in good agreement with experimental results obtained by the integral method. Hua and Liu (2005) used the FLUENT CFD code to predict the temperature distribution along the wing's leading edge. They focused on two-dimensional bay slice approximations to obtain predicted results. This method needed a low number of meshes and the shortest time for the convergent. Further, the authors compared the results from the flow field of the two-dimensional bay slice with those from the flow field of the three-dimensional simulation. The comparison concluded that the results of the two-dimensional bay slice had overestimated the vortex area inside the wing leading edge and the wing leading edge temperature, confirmed by experimental results.

Subsequently, Planquart et al. (2005) employed the FLUENT CFD code to map heat transfer coefficients in a multi-impinging jet anti-icing system. The authors observed that their simulation results were relatively close to the experimental data for the surface heat transfer coefficients measured by infrared thermography. Rigby (2006) later conducted a

numerical analysis of the diamond hole arrangement of PTAI. He utilized a GLENNHT code, which employed a standard k-epsilon model to fix the turbulent flow of jet impingement, to forecast anti-icing performance. The author presented that a significant improvement occurred even if a small amount of total heat was supplied to PTAI in the design.

Papadakis and Wong (2006) then applied the FLUENT CFD code to examine the effect of piccolo tube configuration on the temperature distribution of the wing leading edge. They reported that the predicted results closely matched the experimental results they obtained in the same study. According to their investigation, the best configuration of the piccolo tube occurred when the piccolo pipe center was 0.75 inches and 0.193 inches behind and under the wing highlight, respectively.

Hua et al. (2007) developed 3D unsteady thermodynamic models to characterize the dynamic response of an aircraft wing anti-icing operation. The results obtained by the authors demonstrated that the three-dimensional CFD unsteady simulation yielded an outstanding correlation with the flight test. However, the 2D unsteady simulation underestimated the increment of skin temperature at the initial period and suddenly overestimated the increment of skin surface when the flow was well set up.

Wang et al. (2007) used the FENSAPICE CFD code to investigate PTAI performance on the wing slat under wet conditions. Based on the findings, they recommended double-wall anti-icing on the lower slat surface to prevent icing on the wing leading edge surface. In the same year, Elangovan and Hung (2007) formulated a new C++ code to predict the temperature distribution on the wing leading edge, the minimum heat required for PTAI, and skin temperature. A comprehensive experimental and numerical study of PTAI was conducted by Wong et al. (2009). The authors predicted the temperature distribution on the leading edge of a wing in wet and dry conditions using the FLUENT CFD code. In this method, the authors could determine the minimum heat requirement of PTAI to protect the wing from icing. The skin temperature prediction has been achieved by using alternating direction implicit methods. The proposed heat transfer correlations and their applications have been published in heat transfer literature to estimate heat transfer of impinging jets on the inside skin. They also utilized thermodynamic energy transfer rate to resolve thermodynamic energy and boundary conditions on the external wing skin. The simulation showed that the wing skin temperature under dry conditions was higher than that under wet conditions.

Domingos et al. (2010) then developed a 2D computational method to analyze hot-air anti-icing systems. Using this method, they could predict the temperature of the wing leading edge in both dry and wet situations, as well as the runback ice phenomenon. Reid et al. (2012) conducted a numerical simulation of in-flight electro-thermal anti-icing using a conjugate heat transfer technique, which had been implemented in FENSAPICE for solving complex heat transfer phenomena. Here, the external and internal flow was

decoupled before being used to provide boundary conditions to the steady-state thermal dynamic model. They used a 2D RANS equation with SST  $k-\omega$  turbulent model to compute gaseous phase flow for external flow. A Nusselt number correlation was also used to solve the heat transfer problem in the internal flow module. It is claimed that the simulation results showed good agreement with experimental data for both dry and wet conditions.

Following that, Bu et al. (2012) proposed mathematical models and a numerical code for the simulation of thermal ice protection. In their study, heat transfer coefficient distributions were determined using the boundary layer integral method, and the external flow field and local water collecting efficiency statistics were predicted with the Eulerian method. This numerical code also calculates airfoil equilibrium surface temperature, the mass flux of runback water, and runback ice mass flux. In addition, a user interface is developed to integrate the computation fluid dynamic code to achieve a method for analyzing a thermal anti-icing system.

A fully three-dimensional ice accretion model was developed by Shen et al. (2013) to characterize ice shapes at the engine inlet. They determined the film flow direction and the mass flux distribution of the runback water using the shear stress on the inlet surface. Hannat and Morency (2014) introduced an anti-icing conjugate heat transfer method based on the ANSYS-CFX flow solver and FENSAP-ICE software. Later, Bu et al. (2013) analyzed the performance of the hot air ice protection system to calculate the external heat transfer coefficient and thermal conductivity. Sreedharan et al. (2014) generated a CAD model of the wing-piccolo tube using CATIA software. The discretization of the flow domain and the steady-state CFD analysis of the internal and external flow field were performed using ANSYS ICEM CFD and the ANSYS FLUENT, respectively. It was observed that a piccolo tube-wing surface spacing of 9 mm provides desired temperature distribution. Ismail and Abdullah (2015) then investigated the factor influencing the temperature distribution on the nacelle lip. They demonstrated that the temperature deviation coefficient increases as the nozzle diameter increases while the nacelle lip skin average temperature drops as the average air velocity inside the nacelle lip decreases. However, the authors have not studied the temperature distribution on the nacelle lip with bias flow.

Cao et al. (2016) presented a numerical simulation of three-dimensional ice accretion on an aircraft wing. In this study, they derived the governing equations for supercooled droplets in three-dimensional applications using the conservation of mass and momentum laws. The droplet phase was regarded as pseudo-fluid. Furthermore, some meteorological parameters involved in ice accumulation were also investigated in this study. In a separate study, a 2D simulation of thermal Pitot tube de-icing was conducted by Asante et al. (2016). By applying heat to the walls of the pitot probe, they determined the time taken to melt the ice surrounding the pitot probe. Azam et al. (2016) subsequently investigated the effect of

bias flow on the lift and drag forces. With a bias acoustic liner, the drag coefficient of the nacelle lip is reduced by 90.5% compared to without a bias acoustic liner.

Zhou et al. (2017) published an article on temperature and runback ice prediction methods for three-dimensional hot-air anti-icing systems. According to their findings, two parameters, such as liquid water content and Mach number, significantly affect runback ice accretion. Syed et al. (2018) used one-way fluid-structure interaction (FSI) to investigate the influence of the Reynolds number based on the effective impingement surface of the piccolo tube anti-icing system on the maximum thermal stress and strain of the nacelle lip skin for different aluminum series. According to their simulation, the maximum strain increases with the Reynolds number. The maximum stress, on the other hand, rises to a peak and then quickly decays with the Reynolds number.

Liu et al. (2019) proposed a three-dimensional ice accretion model to simulate a stratospheric airship icing performance in an ascending process. Rohini et al. (2019) conducted additional research to compare the performance of a rotating piccolo tube with a piccolo tube using CFD. Based on the results, the piccolo tube model performed better in temperature distribution and had a higher surface temperature than the rotational piccolo tube model. However, a higher and more concentrated temperature zone was obtained for the fixed piccolo tube model.

The effect of ice accretion on an aircraft's longitudinal aerodynamic properties was then investigated by Cao et al. (2020). An engineering prediction of the longitudinal aerodynamic derivatives was established based on the individual component CFD calculation and narrow strip theory. Based on the flight test data, the longitudinal aerodynamic parameters of clean aircraft and icing aircraft were calculated. Based on their findings, the icing makes an aircraft's lift and elevator less effective, and increases drag. Barzanouni et al. (2020) numerically investigated the blowing-out impact on the NACA0012 airfoil surface to prevent ice accretion. The shear-stress transport  $k-\omega$  model was selected to simulate the turbulence closure model and make better predictions. The results demonstrated that the diameter and pitch of the holes are important parameters for reducing ice accretion and ice weight, respectively.

Khalil et al. (2020) examined the effects of hot air arrangement from a piccolo tube using ANSYS software. In their studies, three distinct jet configurations were used: an inclined shape with one jet row, a staggered shape with two jet rows, and a shape with three jet rows. Based on the results, the third shape covers a larger surface area on the leading edge as compared to the other two shapes.

Following this, Bu et al. (2020) carried out a numerical simulation of an aircraft thermal anti-icing system based on a tight coupling method. The authors have established the heat and mass transfer model of runback water. According to the results, this approach produces downstream surfaces with a greater temperature and a lower drop rate. It contributes to



a higher convective heat transfer coefficient. In another study, Hassaani et al. (2020) performed a numerical investigation of the thermal anti-icing system of the aircraft wing. Three-dimensional Navier-Stokes codes were used to simulate jet flow impinging on aircraft leading edge surfaces, and the numerical results were claimed to be in excellent agreement with the experimental data. In the same year, Huanyu et al. (2020) investigated the optimisation of a simulated icing environment by altering the arrangement of nozzles in atomization equipment for aircraft anti-icing and de-icing. According to the authors, the study's findings will contribute to creating a better-simulated icing environment.

Wang et al. (2022) investigated the numerical simulation of aircraft icing under a local thermal protection state. The authors demonstrated the method for icing by considering the water film flow. They designed different protection ranges and powers and simulated them under different conditions. They found that when the protection range is large, and the protection power is low, the ice will accumulate in the protection range. Further, ice will accumulate outside the protected area when the protection range is small. They also claimed that the ice ridges degrade the aerodynamic characteristics. Bennani et al. (2023) presented the numerical simulation of an electro-thermal ice protection system in AI and DI mode. The authors presented the models to describe the behavior of the thermal protection system and unsteady ice accretion. They used many methods to solve the boundary layer flow, and the solvers were used to compute the heat transfer coefficient. They also claimed that this approach is easier to prolong to a three-dimensional solver than the Prandtl boundary layer solver.

## **NOISE ABATEMENT SYSTEMS**

The concept of noise abatement has been around since the Greek civilization. The ancient Greeks used this concept to absorb and amplify sound, and their acoustic absorption coefficient was at its highest value when fluid trapped inside resonated (Hoffman, 2007). On the other hand, noise abatement tools are installed on commercial aircraft to reduce excessive engine noise that may cause noise pollution in the surrounding environment (Azam & Ismail, 2018). In this sense, porous material has been introduced and incorporated to enhance the acoustic resistance of the acoustic liner. In contrast to the air cavity of the Helmholtz type, as depicted in Figure 9, porous materials are effective acoustic energy absorbers throughout a broad frequency range. Despite being commonly used in air-conditioning and motorcycle exhausts, this material is unsuitable for aircraft applications due to a tendency to migrate, fracture, and blind due to ash, dust, or liquid (Amin & Garris, 1996). As a result, modified acoustic liners for aircraft applications have been introduced, and these types of acoustic liners comprise porous plates, honeycomb channels, composite woven materials for acoustic absorbent, and the backplate sheet, as displayed in Figure 10 (Azam et al., 2017). Bias acoustic liners (BAL) have also been developed to advance this technique.

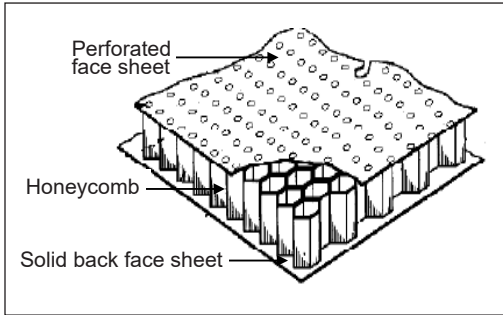


Figure 9. Perforated face system (Moe et al., 2009)

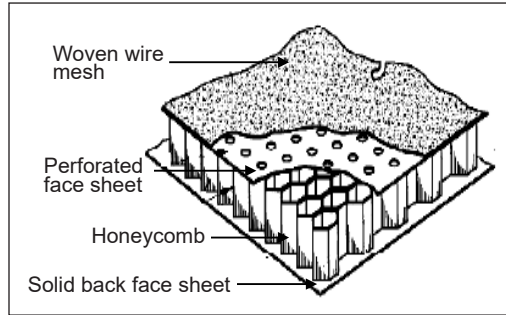


Figure 10. Modified acoustic liners (Amin and Garris, 1996)

### Bias Acoustic Liner (BAL)

With technological advancements, the Boeing Company patented an improved version of an acoustic liner known as the BAL, which uses hot air from the compressor (Ives, 2009). The benefit of using BAL is that it produces bias flow, which has a greater impact on acoustic absorption (Sun et al., 2002). The bias acoustic liner and bias flow within the bias acoustic liner are represented in Figures 11 and 12, respectively.

The performance of BAL for noise reduction is also important. BAL behaves similarly to Helmholtz resonators that allow noise reduction within an optimized frequency range. As a result, BAL is suitable for fan noise, which is essentially atonal noise. Superimposed layers of BAL, known as 2 degrees of freedom or 3 degrees of freedom acoustic liner, are typically used to broaden the absorption range (Leylekian et al., 2014).

Research has been carried out to analyze the noise abatement effect of BAL, although there were just a few. Legendre et al. (2014) investigated sound absorption using an acoustic liner with bias flow. Based on their results, BAL with bias flow at a small Mach number changes the acoustic pressure in the boundary layer, thus improving its acoustic properties. Azam et al. (2017) presented a state-of-the-art noise abatement system in commercial

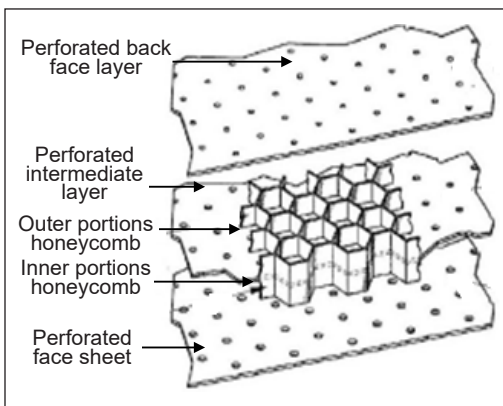


Figure 11. Bias acoustic liner (Breer et al., 2021)

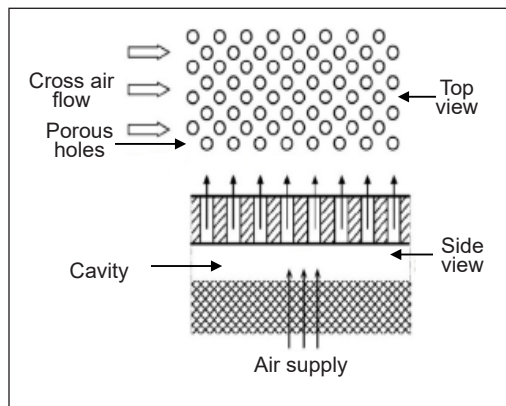


Figure 12. Bias flow diagram (Azam et al., 2016)

aircraft using BAL. According to their article, the BAL has an excellent noise-absorbing capacity and is best used with the nacelle anti-icing system liner on the nacelle lip skin. Azam and Ismail (2018) researched the effect of BAL on the lip skin of the nacelle on civil aircraft and claimed that BAL significantly improves the aerodynamic performance of the nacelle lip skin.

Thanapal et al. (2019) investigated the effect of perforated liners' porosity in the presence of grazing flow. According to their findings, acoustic amplification will occur instead of damping when the perforated liner has very low porosity. Increasing porosity will increase the acoustic damping capability of the perforated liner until optimal porosity is attained. Further increase in porosity will affect the performance of liners. Khai (2021) conducted additional CFD research to study the thermal characteristics of the AL and BAL in real flight conditions. The study concluded that the thermal performance of hot air anti-icing systems with BAL is improved over those with AL and without any noise abatement tools and is directly proportional to the number of BAL.

## **INTEGRATING ICE PROTECTION SYSTEM AND NOISE ABATEMENT SYSTEM**

Integrating ice protection systems with noise abatement systems is vital in aircraft applications to eliminate thermal hotspots as well as noise pollution. In most aircraft anti-icing systems that use hot bleed air, ice can be melted, which can cause the nacelle surface to overheat due to non-uniform temperature distribution. Acoustic liners have been developed to reduce noise while cooling the combustion chamber. However, acoustic liners have desirable acoustic properties for absorbing excessive engine noise. Due to their poor heat transfer characteristics, which lower the overall temperature of the lip skin surface, these have an adverse effect when combined with hot air anti-icing. Consequently, a higher anti-icing temperature must be supplied to hot air in the nacelle D-chamber, thus increasing engine power, consumption, and expense (Khai, 2021).

Several studies have examined the aerothermal properties and noise abatement effect of BAL. Ives (2009) reviewed the current state of the art of aerothermal properties of acoustic liners. Based on their review, the author concluded that the heat transfer rate may be insufficient due to the flow and thermal properties of the acoustic liner. Further studies have been conducted on the noise abatement system in a nacelle lip skin application.

Khai et al. (2020) investigated hot air anti-icing adjoining with a noise abatement system using a bias acoustic liner. The study concluded that the BAL has tunable sound absorption characteristics due to various bias flow velocities through the perforated faceplate. This sound absorption property gives BAL a higher heat transfer rate and a longer lifespan than AL (Ma & Su, 2020).

Researching the integration of the ice protection system with the noise abatement system is crucial. However, only a few studies have been initiated to date. According to

the research by Ives et al. (2011), the heat transfer coefficient of BAL is higher than that of AL as fluid can pass through two porous plates in BAL, whereas only one porous plate exists in AL. As a result, the active area for heat transfer between a fluid and a solid surface in BAL is approximately double that of AL (Ives, 2009).

Studies were performed by Ibrahim et al. (2018) to examine the effect of the perforation shape of a perforated fin during heat transfer. They revealed that the perforation on the fin facilitates heat transfer with higher turbulence intensity. Additionally, the turbulence intensity depends on the shape or geometry of perforations. Since the higher turbulence intensity causes rapid heat dissipation, BAL with a perforated back-face sheet has a higher heat transfer rate than AL.

Therefore, scientists and researchers have proposed incorporating BAL into aircraft anti-icing systems to diminish hotspots and maintain uniform temperatures (Khai, 2021). In addition, flight manufacturers also intend to integrate an ice protection system with this noise abatement tool due to its adverse heat transfer characteristics as well as minimizing environmental noise pollution. However, employing this concept in real flight scenarios is challenging due to the cost constraint in experiment and validation. In this sense, CFD analysis gives the great opportunity of studying the comprehensive factors of integrating the ice protection system with noise abatement technique. Surface temperature distribution, bias flow velocity, uniformity of lip skin temperature, and air velocity and temperature profiles inside bias acoustic liner are the important characteristics that are difficult to measure during real flight conditions. However, these characteristics can be predicted by using CFD. Hence, designing and analyzing these systems using CFD before implementation is essential. Furthermore, this system would be designed by extending the noise abatement tool from the nacelle nose cowl zone to the nacelle lip skin. Then, the hot air would be sent to the nacelle lip skin via the PTAI system. Hence, this would be the most effective technique for absorbing excessive engine noise and preventing noise pollution.

## CONCLUSION

The article has reviewed the recent findings regarding integrating ice protection and noise abatement systems. This review emphasizes various factors pertaining to integrating the ice protection system with the noise abatement system. In the present review, various ice protection systems are discussed in detail. Also discussed are the advantages and disadvantages of each ice protection system. Anti-icing studies utilizing CFD have been the subject of a limited number of studies. These are explained properly; the information is very important for future research. In addition, noise abatement tools are crucial, particularly in aircraft, to minimize excessive engine noise that might cause noise pollution to the surroundings; these tools are therefore described in length. As it is essentially important to integrate the ice protection system with the noise abatement system, this

is also explored, along with prior research findings. Thus, this review will be valuable for researchers interested in anti-icing and noise abatement techniques. Recently, many researchers proposed substituting electric motors for jet engines in aircraft thrust systems. The designer of aircraft thermal systems, therefore, faces a new challenge in overcoming icing and noise problems.

## ACKNOWLEDGMENT

The authors acknowledge funding of Universiti Sains Malaysia, Organization for Women in Science for the Developing World (OWSD), and the Swedish International Development Cooperation Agency (SIDA).

## REFERENCES

- Al-Khalil, K., Ferguson, T., & Phillips, D. (1997). A hybrid anti-icing ice protection system. In *35th Aerospace Sciences Meeting and Exhibit* (p. 302). American Institute of Aeronautics and Astronautics. <https://doi.org/10.2514/6.1997-302>
- Al-Khalil, K. (2007, January). Thermo-mechanical expulsive deicing system-TMEDS. In *45th AIAA Aerospace Sciences Meeting and Exhibit* (p. 692). American Institute of Aeronautics and Astronautics. <https://doi.org/10.2514/6.2007-692>
- Asante, C. J., Pokhrel, M., & Cho, J. (2016). CFD simulation study of de-icing on a pitot tube. *International Journal of Applied Engineering Research*, *11*(5), 2986-2989.
- Azam, Q., Ismail, M. A., Mazlan, N. M., & Bashir, M. (2016). Numerical comparison of drag coefficient between nacelle lip-skin with and without bias acoustic liner. *International Review of Mechanical Engineering*, *10*(6), 390-394. <https://doi.org/10.15866/ireme.v10i6.9427>
- Azam, Q., & Ismail, M. A. (2017, August 2). Noise abatement system in commercial aircraft by using Bias Acoustic Liner on nacelle lip-skin. In *International Conference on Vibration, Sound and System Dynamics (ICVSSD)* (p. 49-54). Universiti Sains Malaysia. <https://www.researchgate.net/publication/320584447>
- Azam, Q., & Ismail, M. A. (2018). Experimental study of bias acoustic liner on nacelle lip-skin. *Journal of Mechanical Engineering*, *5*(2), 67-77.
- Barzanouni, Y., Gorji-Bandpy, M., & Tabrizi, H. B. (2020). Simulation of different shapes and arrangements of holes over the leading edge of airfoil by blowing to prevent ice accretion. *Journal of the Brazilian Society of Mechanical Sciences and Engineering*, *42*(9), Article 448. <https://doi.org/10.1007/s40430-020-02524-x>
- Battisti, L. (2015). *Wind turbines in cold climates: Icing impacts and mitigation systems*. Springer.
- Bennani, L., Trontin, P., & Radenac, E. (2023). Numerical simulation of an electrothermal ice protection system in anti-icing and deicing mode. *Aerospace*, *10*(1), Article 75. <https://doi.org/10.3390/aerospace10010075>
- Birbragher, F. (1988). *Nacelle anti-icing system* (U.S. Patent No. 4,738,416). U.S. Patent and Trademark Office. <https://image-ppubs.uspto.gov/dirsearch-public/print/downloadPdf/4738416>

- Bu, X., Lin, G., Yu, J., Yang, S., & Song, X. (2012). Numerical simulation of an airfoil electrothermal anti-icing system. *Proceedings of the Institution of Mechanical Engineers, Part G: Journal of Aerospace Engineering*, 227(10), 1608-1622. <https://doi.org/10.1177/0954410012463525>
- Bu, X., Lin, G., Yu, J., Shen, X., & Hou, P. (2013). Numerical analysis of a swept wing hot air ice protection system. *Proceedings of the Institution of Mechanical Engineers, Part G: Journal of Aerospace Engineering*, 228(9), 1507-1518. <https://doi.org/10.1177/0954410013494515>
- Bu, X., Lin, G., Shen, X., Hu, Z., & Wen, D. (2020). Numerical simulation of aircraft thermal anti-icing system based on a tight-coupling method. *International Journal of Heat and Mass Transfer*, 148, Article 119061. <https://doi.org/10.1016/j.ijheatmasstransfer.2019.119061>
- Cao, Y., Huang, J., & Yin, J. (2016). Numerical simulation of three-dimensional ice accretion on an aircraft wing. *International Journal of Heat and Mass Transfer*, 92, 34-54. <https://doi.org/10.1016/j.ijheatmasstransfer.2015.08.027>
- Cao, Y., Tan, W., Su, Y., Xu, Z., & Zhong, G. (2020). The effects of icing on aircraft longitudinal aerodynamic characteristics. *Mathematics*, 8(7), Article 1171. <https://doi.org/10.3390/math8071171>
- Croce, G., Habashi, W. G., Guevremont, G., & Tezok, F. (1998). *3D thermal analysis of an anti-icing device using FENSAP-ICE*. In *36th AIAA Aerospace Sciences Meeting and Exhibit* (p. 193). American Institute of Aeronautics and Astronautics. <https://doi.org/10.2514/6.1998-193>
- de Mattos, B. S., & Oliveira, G. L. (2000). Three-dimensional thermal coupled analysis of a wing slice slat with a piccolo tube. In *18th Applied Aerodynamics Conference* (p. 3921). American Institute of Aeronautics and Astronautics. <https://doi.org/10.2514/6.2000-3921>
- Domingos, R. H., Papadakis, M., & Zamora, A. O. (2010). *Computational methodology for bleed air ice protection system parametric analysis*. In *AIAA Atmospheric and Space Environments Conference* (p. 7834). American Institute of Aeronautics and Astronautics. <https://doi.org/10.2514/6.2010-7834>
- Elangovan, R., & Hung, K. E. (2007). Minimum heating energy requirements of piccolo tube jet impingement thermal anti-icing system. In *ASME/JSME 2007 Thermal Engineering Heat Transfer Summer Conference (Vol. 1, pp. 959-967)*. The American Society of Mechanical Engineers. <https://doi.org/10.1115/ht2007-32080>
- Goraj, Z. (2004). *An overview of the de-icing and anti-icing technologies with prospects for the future*. In *24th International Congress of the Aeronautical Sciences* (Vol. 29). International Council of the Aeronautical Sciences.
- Grishaev, V. G., Borodulin, I. S., Usachev, I. A., Amirfazli, A., Drachev, V. P., Rudenko, N. I., Gattarov, R. K., Bakulin, I. K., Makarov, M. V., & Akhatov, I. S. (2021). Anti-icing fluids interaction with surfaces: Ice protection and wettability change. *International Communications in Heat and Mass Transfer*, 129, Article 105698. <https://doi.org/10.1016/j.icheatmasstransfer.2021.105698>
- Hannat, R., & Morency, F. (2014). Numerical validation of conjugate heat transfer method for anti-/de-icing piccolo system. *Journal of Aircraft*, 51(1), 104-116. <https://doi.org/10.2514/1.c032078>
- Hassaani, A., Elsayed, A. F., & Khalil, E. E. (2020). Numerical investigation of thermal anti-icing system of aircraft wing. *International Robotics & Automation Journal*, 6(2), 60-65. <https://doi.org/10.15406/iratj.2020.06.00202>

- Huanyu, D., Chang, S., & Mengjie, S. (2020). The optimization of simulated icing environment by adjusting the arrangement of nozzles in an atomization equipment for the anti-icing and deicing of aircrafts. *International Journal of Heat and Mass Transfer*, 155, Article 119720. <https://doi.org/10.1016/j.ijheatmasstransfer.2020.119720>
- Hoffman, D. A. (2007). *Experimental investigation of turbojet thrust augmentation using an ejector* [Doctoral dissertation]. Air Force Institute of Technology, USA. <https://scholar.afit.edu/cgi/viewcontent.cgi?article=3966&context=etd>
- Hua, J., Kong, F., & Liu, H. H. T. (2007). Unsteady thermodynamic computational fluid dynamics simulations of aircraft wing anti-icing operation. *Journal of Aircraft*, 44(4), 1113-1117. <https://doi.org/10.2514/1.24122>
- Hua, J., & Liu, H. H. (2005). Fluid flow and thermodynamic analysis of a wing anti-icing system. *Canadian Aeronautics and Space Journal*, 51(1), 35-40. <https://doi.org/10.5589/q05-004>
- Ismail, M. A. (2013). *Enhancement of heat transfer performance on nacelle lip-skin for swirl anti-icing* [Unpublished Doctoral dissertation]. Kingston University, England.
- Ismail, M. A., & Abdullah, M. Z. (2015). Applying computational fluid dynamic to predict the thermal performance of the nacelle anti-icing system in real flight scenarios. *Indian Journal of Science and Technology*, 8(30), Article 66. <https://doi.org/10.17485/ijst/2015/v8i30/86058>
- Ismail, M. A., & Wang, J. (2018). Effect of nozzle rotation angles and sizes on thermal characteristic of swirl anti-icing. *Journal of Mechanical Science and Technology*, 32(9), 4485-4493. <https://doi.org/10.1007/s12206-018-0845-x>
- Ives, A. O. (2009). *Perforated honeycomb acoustic liner heat transfer* [Unpublished Doctoral dissertation]. Queen University Belfast, UK.
- Ives, A. O., Wang, J., Raghunathan, S., & Sloan, P. (2011). Heat transfer through single hole bias flow acoustic liner. *Journal of Thermophysics and Heat Transfer*, 25(3), 409-423. <https://doi.org/10.2514/1.T3637>
- Jiang, X., & Wang, Y. (2019). Studies on the electro-impulse de-icing system of aircraft. *Aerospace*, 6(6), Article 67. <https://doi.org/10.3390/aerospace6060067>
- Jun, S., Dongguang, X., Lin, Y., & Dongyu, Z. (2020). *Experimental study of hybrid deicing system*. *IOP Conference Series: Materials Science and Engineering*, 751, Article 012042. <https://doi.org/10.1088/1757-899X/751/1/012042>
- Khai, L. C. (2021). *CFD study on thermal characteristics of acoustic liner and bias acoustic liner in real flight conditions* [Unpublished Master's thesis]. University Sains Malaysia, Malaysia.
- Khai, L. C., Ismail, M. A., Azam, Q., & Mazlan, N. M. (2020). Experimental study on aerodynamic performance of nacelle lip-skin bias flow. *Journal of Mechanical Science and Technology*, 34(4), 1613-1621. <https://doi.org/10.1007/s12206-020-0323-0>
- Khalil, E. E., Said, E., AlSaleh, A., & ElHariry, G. (2020). *Effect of hot air jet arrangement from a piccolo tube in aircraft wing anti-icing system*. In *AIAA Propulsion and Energy 2020 Forum* (p. 3952). American Institute of Aeronautics and Astronautics. <https://doi.org/10.2514/6.2020-3952>
- Liu, Q., Yang, Y., Wang, Q., Cui, Y., & Cai, J. (2019). Icing performance of stratospheric airship in ascending process. *Advances in Space Research*, 64(11), 2405-2416. <https://doi.org/10.1016/j.asr.2019.09.013>

- Ma, Q. (2011). *Aircraft icing and thermo-mechanical expulsion de-icing technology* [Master's thesis]. Cranfield University, UK. [https://dspace.lib.cranfield.ac.uk/bitstream/handle/1826/12478/Ma\\_Q\\_2010.pdf?sequence=1&isAllowed=y](https://dspace.lib.cranfield.ac.uk/bitstream/handle/1826/12478/Ma_Q_2010.pdf?sequence=1&isAllowed=y)
- Moe, J. W., Wunsch, J. J., & Sperling, M. S. (2009). *Method and apparatus for noise abatement and ice protection of an aircraft engine nacelle inlet lip*. (U.S. Patent No. 7,588,212). U.S. Patent and Trademark Office. <https://image-ppubs.uspto.gov/dirsearch-public/print/downloadPdf/7588212>
- Morency, F., Brahimi, M., Tezok, F., & Paraschivoiu, I. (1997). Hot air anti-icing system modelization in the ice prediction code CANICE. In *36th AIAA Aerospace Sciences Meeting and Exhibit* (p. 192). American Institute of Aeronautics and Astronautics. <https://doi.org/10.2514/6.1998-192>
- Morency, F., Tezok, F., & Paraschivoiu, I. (2000). Heat and mass transfer in the case of anti-icing system simulation. *Journal of Aircraft*, 37(2), 245-252. <https://doi.org/10.2514/2.2613>
- Nagappan, N. M. (2013). *Numerical modeling of anti-icing using an array of heated synthetic jets* [Doctoral dissertation]. Embry-Riddle Aeronautical University, Florida. <https://commons.erau.edu/cgi/viewcontent.cgi?article=1108&context=edt>
- Papadakis, M., & Wong, S. H. J. (2006). Parametric investigation of a bleed air ice protection system. In *44th AIAA Aerospace Sciences Meeting and Exhibit* (p. 1013). American Institute of Aeronautics and Astronautics. <https://doi.org/10.2514/6.2006-1013>
- Petrenko, V. F. (2005). *System and method for modifying ice-to-object interface* (U.S. Patent No. 6,870,139). U.S. Patent and Trademark Office. <https://image-ppubs.uspto.gov/dirsearch-public/print/downloadPdf/6870139>
- Raghunathan, S., Benard, E., Watterson, J. K., Cooper, R. K., Curran, R., Price, M., Yao, H., Devine, R., Crawford, B., Riordan, D., Linton, A., Richardson, J., & Tweedie, J. (2006). Key aerodynamic technologies for aircraft engine nacelles. *The Aeronautical Journal*, 110(1107), 265-288. <https://doi.org/10.1017/s0001924000013154>
- Ramamurthy, S., Keith, T. G., Jr., De Witt, K. J., Putt, J. C., Martin, C. A., & Leffel, K. L., (1991). Numerical modelling of an advanced pneumatic impulse ice protection system (PIIP) for aircraft. In *AIAA 29th Aerospace and Science Meeting* (p. 555). American Institute of Aeronautics and Astronautics. <https://doi.org/10.2514/6.1991-555>
- Reid, T., Baruzzi, G. S., & Habashi, W. G. (2012). FENSAP-ICE: Unsteady conjugate heat transfer simulation of electrothermal de-icing. *Journal of Aircraft*, 49(4), 1101-1109. <https://doi.org/10.2514/1.c031607>
- Rigby, D. (2006). *Numerical investigation of hole pattern effect on piccolo tube anti-icing*. In *44th AIAA Aerospace Sciences Meeting and Exhibit* (p. 1012). American Institute of Aeronautics and Astronautics. <https://doi.org/10.2514/6.2006-1012>
- Rohini, D., Lokesgarun, D., Naveen, R., & Samiyappan, P. (2019). Comparison of rotating piccolo tube with fixed piccolo tube by using CFD. *International Journal of Engineering and Technology*, 11(1), 26-34. <https://doi.org/10.21817/ijet/2019/v11i1/191101017>
- Ronauo, R. J., Batterson, J. G., Reehors, A. L., Bonds, T. H., & O'Mara, T. M. (1991). Effect of tail ice on longitudinal aerodynamic derivatives. *Journal of Aircraft*, 28(3), 193-199. <https://doi.org/10.2514/3.46012>



- Rosenthal, H. A., & Nelepovitz, D. O. (1985). *AIAA/SAE/ASME/ASEE 21st Joint Propulsion Conference, Monterey California*. American Institute of Aeronautics and Astronautics
- Shen, X., Lin, G., Yu, J., Bu, X., & Du, C. (2013). Three-dimensional numerical simulation of ice accretion at the engine inlet. *Journal of Aircraft*, 50(2), 635-642. <https://doi.org/10.2514/1.c031992>
- Smith, A. G., & Taylor, K. (1997). The simulation of an aircraft engine intake anti-icing system. *The PHOENICS Journal of Computational Fluid Dynamics and its Applications*, 10(2), 150-166.
- Sreedharan, C., Nagpurwala, Q. H., Subbaramu, S. (2014). Effect of hot air jets from a piccolo tube in aircraft wing anti-icing unit. *SASTech - Technical Journal of RUAS*, 13(2), 2-5.
- Syed, M. H. Y., Ismail, M. A., Azam, Q., Rajendran, P., & Mazlan, N. M. (2018). Simulation study of the effect of anti-icing on the nacelle lip-skin material. In *IOP Conf. Series: Materials Science and Engineering* (Vol. 370, p. 012011). IOP Publishing. <https://doi.org/10.1088/1757-899X/370/1/012011>
- United States National Transportation Safety Board. (2007). *Aircraft accident report: Crash during approach to landing, circuit city stores, Inc., Cessna citation 560, N500AT, Pueblo, Colorado, February 16, 2005*. [https://reports.aviation-safety.net/2007/20070317-1\\_C500\\_N511AT.pdf](https://reports.aviation-safety.net/2007/20070317-1_C500_N511AT.pdf)
- Wang, H., Tran, P., Habashi, W. G., Chen, Y., Zhang, M., & Feng, L. (2007). *Anti-icing simulation in wet air of a piccolo system using FENSAP-ICE*. SAE Technical Paper 2007-01-3357. SAE International. <https://doi.org/10.4271/2007-01-3357>
- Wang, Z., Zhao, H., & Liu, S. (2022). Numerical Simulation of Aircraft Icing under Local Thermal Protection State. *MDPI Aerospace*, 9(2), Article 84. <https://doi.org/10.3390/aerospace9020084>
- Wong, S. H., Papadakis, M., & Zamora, A. (2009). *Computational Investigation of Bleed Air Ice Protection System*. In *1st AIAA Atmospheric and Space Environments Conference* (p. 3966). American Institute of Aeronautics and Astronautics. <https://doi.org/10.2514/6.2009-3966>
- Yang, K., Liu, Q., Lin, Z., Liang, Y., & Liu, C. (2022). Investigations of interfacial heat transfer and droplet nucleation on bioinspired superhydrophobic surface for anti-icing/de-icing. *SSRN Electronic Journal*, 1-22. <https://doi.org/10.2139/ssrn.4002238>
- Zhou, Y., Lin, G., Bu, X., Mu, Z., Pan, R., Ge, Q., & Qiao, X. (2017, March). Temperature and Runback Ice Prediction Method for Three-Dimensional Hot Air Anti-Icing System. In *IOP Conference Series: Materials Science and Engineering* (Vol. 187, No. 1, p. 012017). IOP Publishing. <https://doi.org/10.1088/1757-899x/187/1/012017>
- Zheng, M., Guo, Z., Dong, W., & Guo, X. (2019). Experimental investigation on ice accretion on a rotating aero-engine spinner with hydrophobic coating. *International Journal of Heat and Mass Transfer*, 136, 404-414. <https://doi.org/10.1016/j.ijheatmasstransfer.2019.02.104>



## Magnetic Susceptibility and Hydrogen Cyanide Levels as Proxy Indicator for Gold Mining Pollution in River Sediment

Siti Zulaikah<sup>1\*</sup>, Arif Juliansyah<sup>1</sup>, Muhammad Fathur Rouf Hasan<sup>2,3</sup>, Bambang Heru Iswanto<sup>4</sup>, Mariyanto Mariyanto<sup>5</sup>, Ardyanto Tanjung<sup>6</sup>, Satria Bijaksana<sup>7</sup> and Ann Marie Hirt<sup>8</sup>

<sup>1</sup>Department of Physics, Faculty of Mathematic and Natural Sciences, Universitas Negeri Malang, 65145 Malang, Indonesia

<sup>2</sup>Department of Civil Engineering, Politeknik Negeri Jakarta, 16425 Jakarta, Indonesia

<sup>3</sup>Department of Physics, Universitas Brawijaya, 65145 Malang, Indonesia

<sup>4</sup>Department of Physics, Faculty of Mathematic and Natural Sciences, Universitas Negeri Jakarta, 13220 Jakarta, Indonesia

<sup>5</sup>Department of Geophysical Engineering, Faculty of Civil, Environmental Planning and GeoEngineering, Institut Teknologi Sepuluh Nopember, 60111 Surabaya, Indonesia

<sup>6</sup>Department of Geography, Faculty of Social Science, Universitas Negeri Malang, 65145 Malang, Indonesia

<sup>7</sup>Faculty of Mining and Petroleum Engineering, Institut Teknologi Bandung, Jalan Ganesha 10, 40132 Bandung, Indonesia

<sup>8</sup>Institute of Geophysics, Sonneggstrasse 5 ETH, Zurich, CH-8092 Zurich, Switzerland

### ABSTRACT

Sumbawa's Kuris River is one of the rivers contaminated by the island's traditional gold mine. In order to detect contaminant levels, we examine the magnetic susceptibility, HCN levels, and the heavy metal contents on the river's surface sediment. Environmental pollution has been widely assessed using a combination of magnetic properties and geochemical analysis. The goals of this research are to discover how magnetic susceptibility ( $\chi$ ) can be used as a first-order proxy for pollution. The relation between susceptibility

and HCN is of particular interest, as this is a major contaminant associated with gold mining. The surface sediment samples were collected at ten different locations along the rivers. The magnetic susceptibility was determined using the Bartington MS2B, and the hydrogen cyanide (HCN) concentration was determined using Argentometric titration. The element content was determined by an Atomic Absorption Spectrometer (AAS). The low-frequency

#### ARTICLE INFO

##### Article history:

Received: 11 September 2022

Accepted: 06 March 2023

Published: 08 September 2023

DOI: <https://doi.org/10.47836/pjst.31.6.03>

##### E-mail addresses:

siti.zulaikah.fmipa@um.ac.id (Siti Zulaikah)

arifjuliansyah95@gmail.com (Arif Juliansyah)

rouf@sipil.pnj.ac.id (Muhammad Fathur Rouf Hasan)

bhi@unj.ac.id (Bambang Heru Iswanto)

mariyantof27@gmail.com (Mariyanto Mariyanto)

ardyanto.tanjung.fs@um.ac.id (Ardyanto Tanjung)

satria.fi@itb.ac.id (Satria Bijaksana)

ann.hirt@erdw.ethz.ch (Ann Marie Hirt)

\* Corresponding author

magnetic susceptibility ( $\chi_{lf}$ ) ranges from 71 to  $115 \times 10^{-8}$  m<sup>3</sup>/kg, with an average of  $97 \times 10^{-8}$  m<sup>3</sup>/kg, and the  $\chi_{fd}(\%)$  analysis ranges from 2% to 4%. The presence of spherical iron oxides, which are indicative of combustion byproducts, was also confirmed by SEM. The samples have low magnetic susceptibility but high levels of Hg and HCN. AAS results showed high Fe, Zn, and Cu concentrations in river sediments, with more variable concentrations of Hg, Mn, As, Cr, and Au. Because Fe, Cu, As, Hg, and HCN have a significant Pearson's correlation with  $\chi_{fd}(\%)$ , this parameter can be a useful indicator for contamination caused by gold mining waste.

*Keywords:* Geochemistry, hydrogen cyanide (HCN), magnetic susceptibility, river sediments, tailings

---

## INTRODUCTION

Tailings from traditional gold mines in Sumbawa, Indonesia, are allegedly the source of serious pollution in this region's environment, including rivers and lakes, residential and agricultural areas, and, eventually, the sea. This type of pollution can be caused by the direct disposal of gold mining processing waste or the runoff from waste collection areas, typically located near rivers during rainy seasons (Bruno et al., 2020). Lake Lebo in Taliwang is an example of river pollution because the Suning and Seran Rivers feed it, and it overflows into the Brang Rea River. The Hg levels in the lake's fish are above the hazard level (Junaidi et al., 2019). Humans, particularly their hair and livestock, are affected (Anderson, 2010; Donato et al., 2007; Junaidi et al., 2019). Human consumption of contaminated fish or livestock meat can have short- and long-term negative consequences. Anthropogenic contamination has also been observed to affect bacterial communities in China's Jiaolai River, increasing the Ni content in its sediment (Li et al., 2016).

Geochemical data, such as anomalous levels of heavy metals in an area, are frequently used to assess the degree of contamination of soils or sediment (Salomão et al., 2021). The study used elemental analysis obtained from atomic mass spectrometry (AMS) at the Tembi River in Iran was discovered an increase in Cd, Cr, Cu, Fe, Pb, Ni, and Zn concentrations in sewage both upstream and downstream of the entry point (Shanbehzadeh et al., 2014). Similar studies in rivers showed heavy metal contamination was conducted in India's Beas River (Kumar et al., 2018), rivers in Kabul, Pakistan (Ali & Khan, 2018), the urban river in the Philippines (Decena et al., 2018), rivers in Ukraine (Alokhina, 2021), and Vistula River in Poland (Szczepaniak-Wnuk et al., 2020). Heavy metal pollution in sediment was also assessed in Ghana's Pre Basin using the geo-accumulation index (Igeo), which tracked As, Pb, Zn, Mn, Cr, Ni, and Fe using atomic absorption spectroscopy (AAS) (Duncan et al., 2018). Heavy metal tracking can also be used in the case of leather factory tanning waste that has polluted the river. Cr tracking is used in this case to determine pollutant waste (Świetlik & Trojanowska, 2016). Geochemistry methods for monitoring pollution

can be combined with magnetic methods; magnetoresponse for arsenic pollution tracking is one example (Ouyang et al., 2020). There are numerous examples in the literature, such as research into coastal sediments (Ravisankar et al., 2018; Suresh et al., 2011), topsoil (Ouyang et al., 2020); snow deposits (Alfonsi et al., 2021), and sediments in a reservoir (Chaparro et al., 2020). In Indonesia, a combination of geochemical and magnetic methods has been used to study lacustrine sediment at Lake Limboto in Sulawesi (Yunginger et al., 2018), sediment of Citarum River in West Java (Sudarningsih et al., 2017), and sediment in Brantas River in East Java (Mariyanto et al., 2019a; Mariyanto et al., 2019b).

Few studies have used magnetic properties in conjunction with geochemistry analysis to track contamination associated with gold mining. Jordanova et al. (2013) demonstrated that sediment from the floodplain of the Ogosta River in Bulgaria exhibits enhanced magnetization, which can be linked to high concentrations of As, Pb, Zn, and Cu. This study compared the magnetic susceptibility of river sediments from the Labuan Kuris River in Sumbawa, Indonesia, to geochemical elemental data and hydrogen cyanide (HCN) concentration. Artisanal gold mining occurs along the river, and mine waste frequently enters the river. For comparison, samples also were taken from processing wastes at mining sites.

## METHODS

Hijrah and Labuan Kuris areas of Sumbawa, Indonesia, were chosen for sampling because of the high artisanal gold mining activities. Labuan Kuris River receives input from mining processing waste, particularly waste associated with the first processing stage, known as Gelondong, labeled GL. Tong (labeled as TG) is a secondary processing stage. Here gold-containing rocks are ground in the first stage, and the gold is bonded with Hg. The left-over material from the first stage is processed again in the second stage using HCN and Pb. After the GL and TG treatment, surface river sediment (SP) and ground rock samples were collected. Figure 1 depicts the location of the sampling sites. SP1 was obtained from the upstream trial of Kuris River, while SP10 was acquired from the downstream trial near an estuary mangrove forest at an inlet leading to the sea.

Surface sediments were taken 1 kg and placed in a plastic bag for transport to the laboratory. Three samples were collected from each site: one from the left bank facing downstream, one from the center of the river, and one from the right bank. The sediment was then washed and filtered with distilled water and a 325-mesh sieve. After drying at room temperature, the sample was ground into powder and placed in a standard cylindrical plastic holder for magnetic measurement. A digital weight balance was used to weigh the samples. The magnetic susceptibility of all samples was measured using Bartington Magnetic Susceptibility Meter MS2B in two frequencies, 470 Hz,  $\chi_{lf}$  and 4700Hz,  $\chi_{hf}$ . Frequency-dependent magnetic susceptibility,  $\chi_{fd}(\%)$ , was defined using Equation 1 (Dearing, 1999):

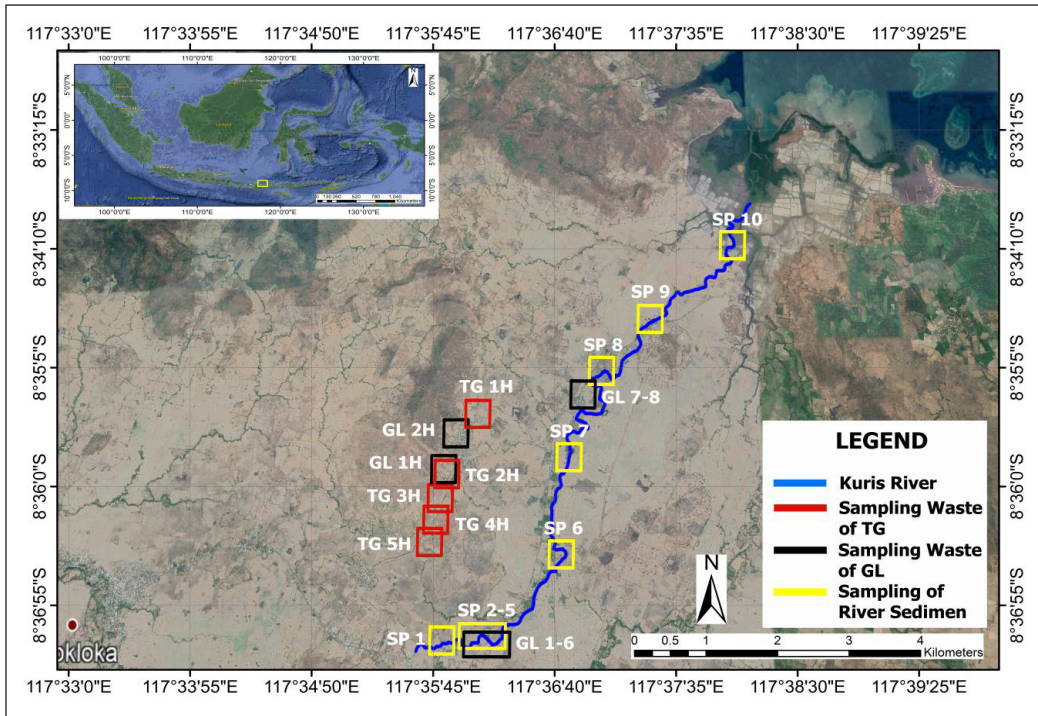


Figure 1. Geographic location of Sumbawa sampling points in the Kuris River

$$\chi_{fd} (\%) = \left[ \frac{\chi_{470} - \chi_{4700}}{\chi_{470}} \right] \times 100\% \quad [1]$$

Several representative samples were prepared from the remaining powder for chemical elements analysis using Atomic Absorption Spectrometer (AAS) and HCN concentration measurement using argentometric titration. The magnetic minerals extracted from several samples were morphologically tested for tailing using scanning electron microscope (SEM) analysis.

## RESULTS

AAS was used to determine the elemental concentration in all river surface sediment samples and the three tailing samples. Table 1 shows the results of the AAS magnetic susceptibility and HCN analysis. The Fe concentrations in the river and the tailing samples are significantly higher than other elements. Earlier reported XRF results also confirmed it. In sediment rivers, the elements with the highest concentrations are Si and Fe, followed by Mn, Al, Ca, and K. Meanwhile, Ba, Cu, Cr, Zn, and Ti have relatively low concentrations (Juliansyah et al., 2020). The concentration of heavy metals varies. On average, the tailing samples have the highest concentrations of Au, As, and Hg, while the river sediments have higher concentrations of Mn, Zn, Cu, and Cr.

Table 1

Magnetic susceptibility, elemental analysis obtained from AAS, and argentometric titration for HCN detection

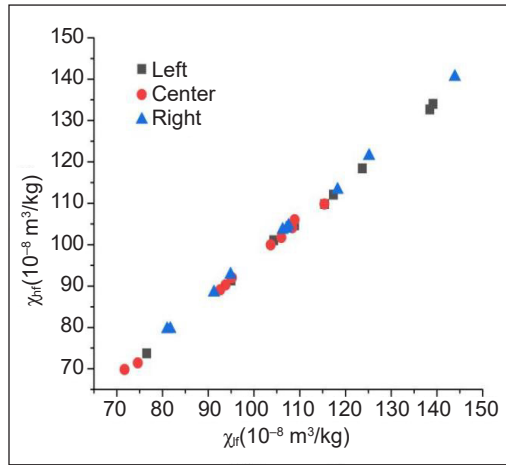
Sample ID	$\chi_{ir}$ ( $10^{-8} \text{m}^3/\text{kg}$ )	$\chi_{fd}$ (%)	(ppm)												
			Au	Cu	Pb	Zn	Ni	Cd	Fe	Cr	Mn	V	As	Hg	HCN
SP 1.2	95.17	3.31	<0.06	52	12	110		1	52200	36	4925		116	3.923	70.17
SP 2.2	103.67	3.57	<0.06	49	<12	108		<1	52300	30	3535		128	5.061	75.10
SP 3.2	105.97	4.01	-	-	-	-	-	-	-	-	-	-	-	-	-
SP 4.2	71.72	2.64	0.13	46	82	93		<1	45000	34	1819		121	2.692	50.12
SP 5.2	74.63	4.29	0.74	51	<12	74		<1	46700	31	1426		107	9.639	59.52
SP 6.2	108.39	3.97	1.61	50	<12	65	7		50600	105	987	145	212	31.53	67.74
SP 7.2	92.63	3.85	1.36	57	<12	85		<1	49000	33	1426		98	33.42	52.71
SP 8.2	115.38	4.83	<0.06	63	<12	101		<1	51900	40	1484		115	2.200	44.95
SP 9.2	108.90	2.65	0.21	62	<12	103		<1	50100	72	1204		113	6.204	63.33
SP 10.2	93.80	3.76	0.12	59	<12	129		<1	46000	43	716		122	3.923	72.59
GL 1 K	20.39	2.29	6.19	34	<12	17	<5		30300	28	110	47	248	68.57	99.29
TG 1 H	140.46	0.52	0.3	15	186	<15	<5		20600	18	154	30	265	28.16	109.80
GL 1 H	231.49	0.70	9.33	321	17	23		<1	50500	45	218		191	126.1	-

The concentration of HCN in river sediments ranges from 45 (SP 8.2) to 75 (SP 2.2) ppm, with an average of 62 ppm. The concentration of HCN in the river is still smaller than the two samples from Gelondong and Tong, which are about 100 ppm, smaller than the concentration of HCN in the gold mine soil in China, which is about 70.55 ppm (Shehong et al., 2005), and higher than that reported result from Brazil, which is around 0.83 - 1.44 ppm (Prereira & Neto, 2007).

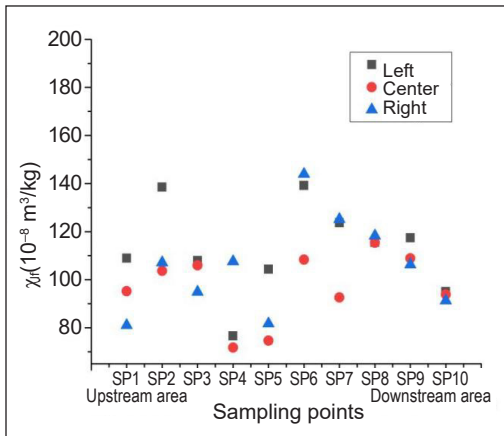
The TG sample has the highest concentration of HCN as weighed by argentometric titration. It is expectable because HCN is used in the Au extraction processes. Although it should not be used in GL processing, the high HCN concentration indicates that the substance is being used to some extent. There is a considerable concentration in the river sediment, especially at SP 6.2 and SP7.2, indicating that HCN is entering the river ecosystem. It may be coming from the GL waste tailing that enters the river. It also holds for sites SP1.2 and SP2.2, which are upstream from the present mining and processing sites used by the local population. It suggests that the local runoff from GL processing is broader than the immediate processing area.

Magnetic susceptibility varies in river sediment samples; the  $\chi_{ir}$  ranges from 71 to  $115 \times 10^{-8} \text{m}^3/\text{kg}$ . The susceptibility, measured in low and high frequencies, is consistent (Figure 2a). It varies according to its location at a site, but no consistent difference exists (Figure 2b).  $\chi_{fd}$ (%) is low in samples from the river and is between 2.6% to 4.8% (Figure 2c). It suggests that the grains are larger than 17 nm (Hrouda, 2011). These low values suggest that the ferromagnetic particles are blocked and do not exhibit superparamagnetic

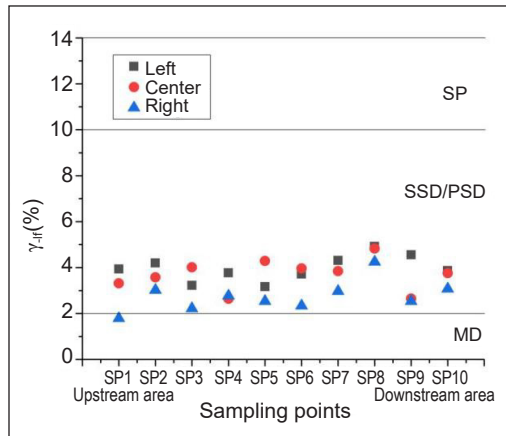
behavior (Dearing, 1999). Eight GL samples were taken from different mine processing locations, and the  $\chi_{lf}$  is between 20.39 and  $112.8 \times 10^{-8} \text{ m}^3/\text{kg}$  with the average  $\chi_{lf}$  of  $(60.64 \pm 35.08) \times 10^{-8} \text{ m}^3/\text{kg}$ . The TG samples have a slightly higher  $\chi_{lf}$  compared to the GL samples, with values between 32.16 and  $140.4 \times 10^{-8} \text{ m}^3/\text{kg}$  and an average of  $(90.43 \pm 35.08) \times 10^{-8} \text{ m}^3/\text{kg}$ . The samples from the tailing wastes have the  $\chi_{fd}(\%)$  of between 0.5% and 2.3%, which is lower than in the river sediment.



(a)



(b)

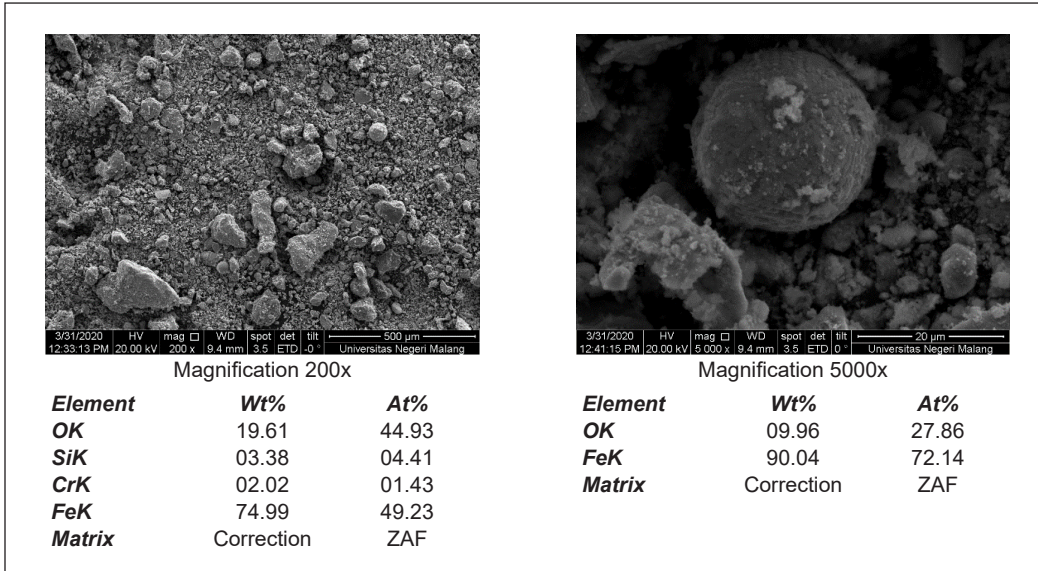


(c)

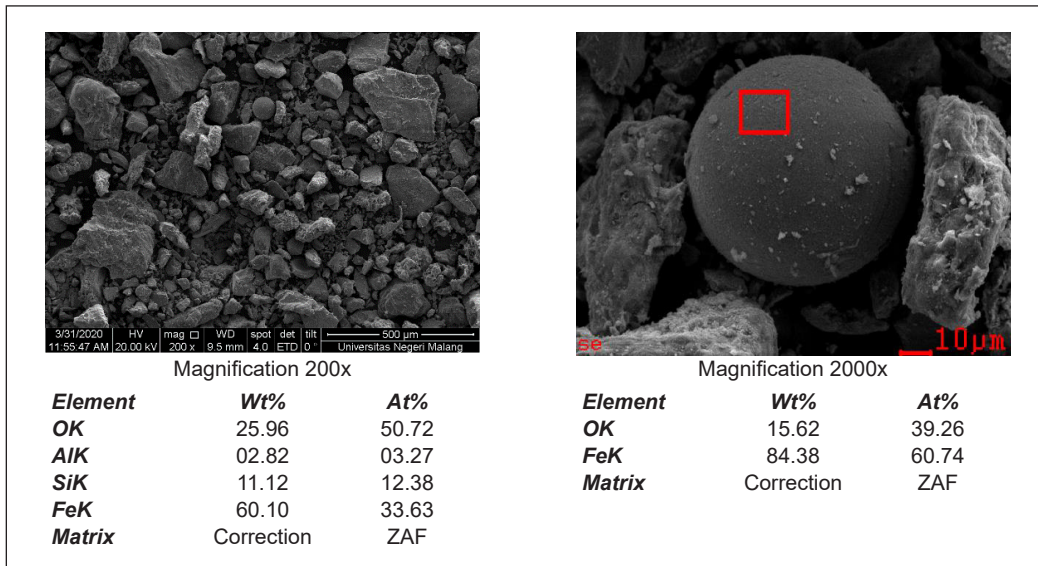
Figure 2. Distribution of: (a) relations between  $\chi_{lf}$  and  $\chi_{hf}$ ; (b) sampling point and  $\chi_{lf}$ ; and (c) sampling point and  $\chi_{fd}(\%)$  showing their variation along the course of the Kuris River

The magnetic minerals were extracted from Gelondong and Tong tailings samples with a hand-permanent magnet and analyzed using SEM (Figure 3) to aid in identifying ferromagnetic minerals in the tailings. Many magnetic phases were irregular in shape and size, but there were also spherules (Figure 3a and 3b, right). Some irregularly shaped grains are iron oxide, but they may also contain Si and, to a lesser extent, Al or Cr (Figures 3a and 3b, left). Magnetic minerals with spherules have a 30–50 m diameter and are pure iron oxides that could be magnetite (see the EDAX data in the bottom right of Figures 3a and 3b). The surface may be smooth or have an orange skin texture (Figures 3a & 3b, right). These spherules are commonly found in combustion processes in, for example, factories and automobiles (Kelepertzis et al., 2019; Wang et al., 2017; Zajzon et al., 2013).





(a)



(b)

Figure 3. The SEM capture of magnetic minerals and composition of extraction results using EDAX show that magnetic minerals are dominated by Fe content in a representative: (a) Gelondong sample; and (b) Tong sample

## DISCUSSION

The magnetic susceptibility of low frequency,  $\chi_{lf}$  in the surface sediment of Kuris River is influenced by lithogenic and anthropogenic input. The average magnetic susceptibility of this area is  $104.8 \times 10^{-8} \text{ m}^3/\text{kg}$ , which is lower than other areas in Indonesia, such as Brantas

River with  $3022.9 \times 10^{-8} \text{ m}^3/\text{kg}$  (Mariyanto et al., 2019a) and Cikapundung River with  $734.7 \times 10^{-8} \text{ m}^3/\text{kg}$  (Sudarningsih et al., 2017) in Java, where the contribution of volcanic sources is larger. Its magnetic susceptibility dependence frequency,  $\chi_{fd}(\%)$ , is about 3.1%. This value is larger than that of the Brantas River (1.03%) and is similar to the reported value from the Cikapundung River. The values of more than 2% mean that the grain size of the magnetic minerals is smaller and that it is the contribution by anthropogenic input as reported in Cikapundung River. Other areas, such as Lake Limboto, have magnetic susceptibility in the same order as this study (Yunginger et al., 2018). Therefore, the magnetic susceptibility of the samples from Kuris River is not largely affected by volcanic but by anthropogenic input, as found in the tailing samples.

The high Fe content is related to the high lithogenic contribution to the sediment in the river. The lower Fe concentration in the TG sample suggests that some of the Fe contents were removed during the second step of the Au extraction process. Here the residue sample of Gelondong inserted into the vertical spinning Tong will make heavy metals, including Fe, seep into the bottom of the disposal pond, which reduces the ingress of Fe into river sediments. It would also explain the lower Mn, Zn, and Cu concentration in the tailing samples. It should be noted that the GL samples have a higher concentration of Au compared to TG samples and river sediment. It indicates that the GL processing does not bind all the Au in the first processing step; Au is removed after the second step. Au is also relatively low in the river samples but slightly higher at SP6.2 and SP7.2. These two sites also have high Hg concentration, on the same level as in the TG samples.

HCN levels in tailing waste and river samples are both high. It is important to note that the values in the river sediments exceed the government's 0.02 ppm threshold (Government Regulation of the Republic of Indonesia, 2001). The negative correlation between  $\chi_{fd}(\%)$  and HCN, Cu, Fe, As dan Hg suggests that  $\chi_{fd}(\%)$  can become a quick first-order proxy to monitor HCN levels in river sediments. The correlation indicates an increase in the magnetic domain and the formation of possible strong compounds, i.e., Fe - CN and/or Au - CN, and weak compounds, such as Ag - CN and/or Cu - CN. The formation of these compounds may occur in the environment, as described in previous studies (Jaszczak et al., 2017). Further research should be conducted along other rivers that flow through areas of artisanal gold mining to determine how robust this correlation is. It has been established that the Tong waster area or tailing ponds have a relatively high frog fatality rate, which may be linked to the high HCN concentration (Donato et al., 2007). A method that allows for rapid first-order monitoring of a large area would be beneficial, allowing more time-consuming or expensive methods to focus on areas where the environment may be threatened. Figure 4 shows the correlation between  $\chi_{fd}$  or  $\chi_{fd}(\%)$  with different major elements as determined from AAS. Pearson's correlation list is available in Table 2. There is a good correlation between  $\chi_{fd}$  and Fe content in the river sediments, but this does not hold for the tailing

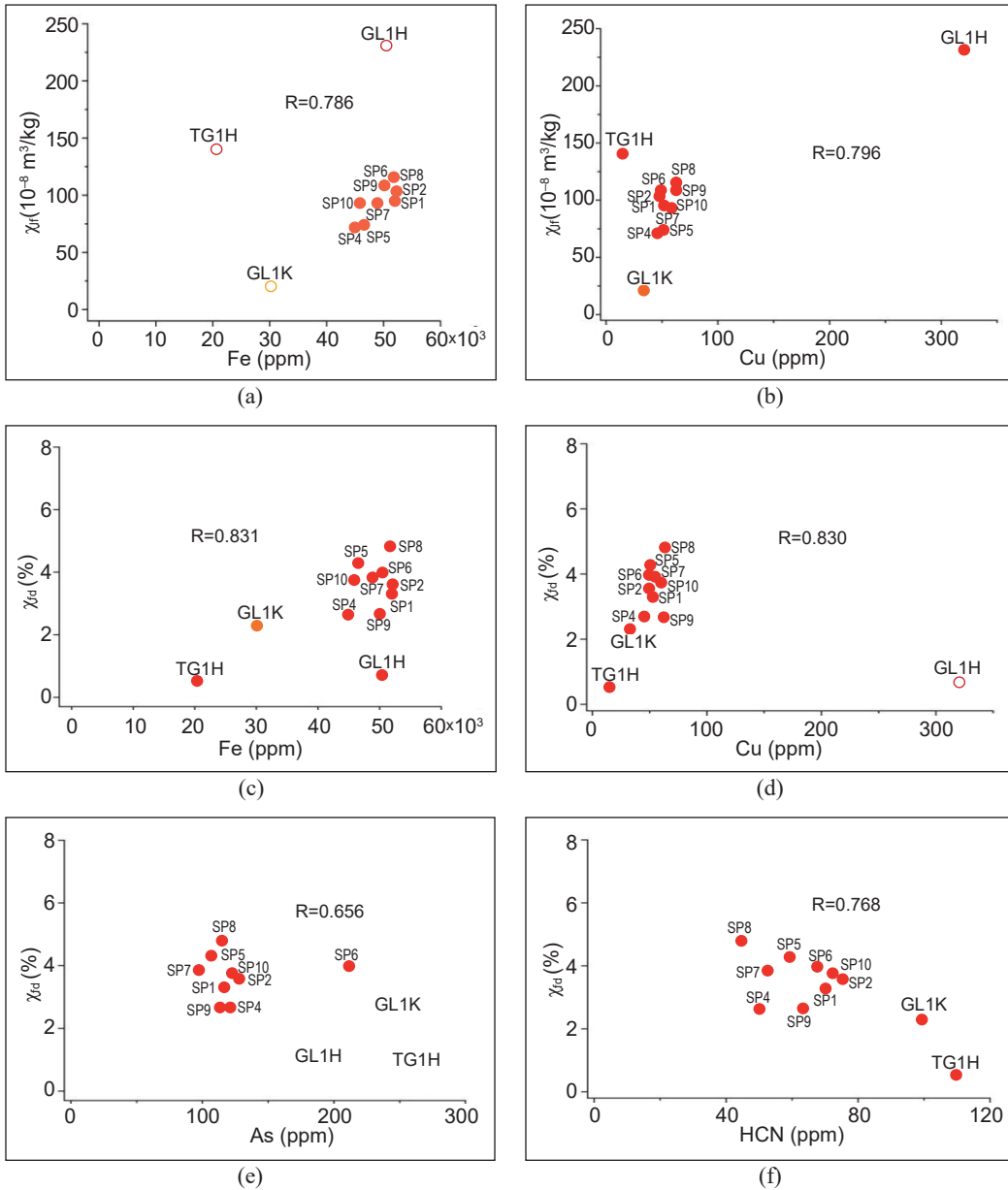


Figure 4. Linear correlations that are statistically significant for: (a) Fe versus  $\chi_{if}$ ; (b) Cu versus  $\chi_{if}$ ; (c) Fe versus  $\chi_{fd}$  (%); (d) Cu versus  $\chi_{fd}$  (%); (e) As versus  $\chi_{fd}$  (%); and (f) HCN versus  $\chi_{fd}$  (%)

Note. Open symbols are not considered in the respective correlation

sample (Figure 4a), and a particularly good correlation with Cu when all samples are considered. It suggests that the lithogenic component of river sediments controls  $\chi_{if}$ . A significant correlation between magnetic susceptibility of low frequency and Fe element was also reported from the surface sediment of the Brantas River (Mariyanto et al., 2019a).

Table 2

Pearson Correlations (R) between magnetic susceptibility and elements <sup>1</sup>using only river sediments; <sup>2</sup>including GLIH

	Xhf	Xlf	Xfd	Cu	Fe	Cr	Mn	As	Hg
Xlf	0.999								
Xfd	-0.240	-0.70							
Cu	0.012	0.796**	0.830**						
Fe	0.157	(0.786 <sup>1</sup> )	0.831**	0.906**					
Cr	0.279	0.200	0.301	0.401	0.437				
Mn	0.101	0.107	0.292	0.316	0.596	-0.105			
As	-0.071	-0.052	-0.656* <sup>2</sup>	-0.837**	-0.812**	0.828** <sup>1</sup>	-0.518		
Hg	-0.448	-0.505	-0.620* <sup>2</sup>	-0.786** <sup>2</sup>	-0.587	-0.023	-0.522	0.718*	
HCN	-0.125	-0.042	-0.768**	-0.834**	-0.822**	-0.262	-0.300	0.840**	0.567

\* p < 0.05, \*\* p < .005

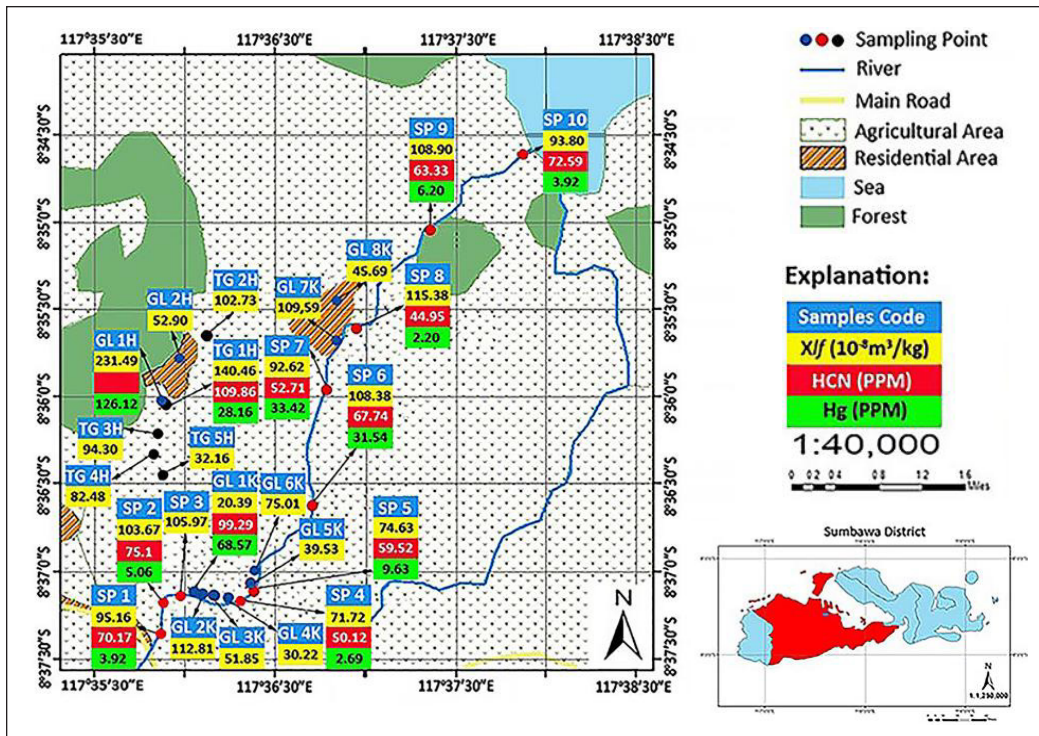


Figure 5. The mapping of low-frequency magnetic susceptibility and Hg and HCN content along Kuris River and some point of tailing area

Furthermore, strong significant correlations are seen between  $\chi_{fd}(\%)$  and Cu and HCN and between  $\chi_{fd}(\%)$  and Fe and As. (Figure 4). Usually, high correlations are shown by  $\chi_{lf}$  and some heavy metals as well as in other polluted sediment, but in this case, a good correlation is present between  $\chi_{fd}(\%)$  and some pollution inputs like HCN. In this case,

where an anthropogenic input is not strong enough,  $\chi_{fd}(\%)$  may serve as a good proxy indicator of pollution. It is different from the fact that the wastes of mining activities are heavy metals (Morales et al., 2016). The high correlation between Hg and HCN suggests that those elements and compounds are used in high concentrations in the second step of gold binding. Figure 5 illustrates magnetic susceptibility as well as Hg and HCN content of all surface sediment samples collected along Kuris River, including the gold mining waste.

Figure 5 depicts the mapping for the levels of magnetic susceptibility, HCN, and Hg content in each sampling point as a result of Kuris River's dominant pollutant input, which represents how much pollutant enters the river where agriculture and residential areas are irrigated by the river. Based on this evidence, we can estimate how much HCN and Hg will pollute agricultural soils over time if traditional mining cannot be stopped or improved with immediate waste management. As previously stated, cyanide weakens the human body and causes various diseases, such as hypothyroidism, renal damage, and miscarriages (Jaszczak et al., 2017).

## CONCLUSION

Kuris River sediments have an average  $\chi_{lf}$  of  $97 \times 10^{-8} \text{m}^3/\text{kg}$ , which is relatively low compared to other rivers in Indonesia, generally contributed by volcanic materials. The correlation between  $\chi_{lf}$  and lithogenic elements suggests the dominant influence of the component. There is no trend in  $\chi_{lf}$  along the river flow, which supports the notion that, in this case, the contribution of anthropogenic  $\chi_{lf}$  is minor.  $X_{fd}(\%)$  indicates that the magnetic minerals are larger than SP. The correlation between  $\chi_{fd}(\%)$  and HCN and other elements such as Cu, Fe, As, and Hg suggests that  $\chi_{fd}(\%)$  may be used as the first-order proxy for HCN, As, and Hg content in sediment for nonmagnetic pollutant input, particularly in the case of gold mine tailing.

## ACKNOWLEDGEMENT

The authors express their gratitude to Universitas Negeri Malang, Indonesia, for the financial support through Hibah Unggulan Perguruan Tinggi–PNBP 2020 with the grant number of: 4.3.487/UN32.14.1/LT/2020, in which the first author serves as the principal researcher.

## REFERENCES

- Alfonsi, L., Nazzari, M., & Macri, P. (2021). Rock magnetic and micro-morphological analysis on snow deposits: Recognition of anthropogenic origin of particulate matter in urban and wilderness areas (central Italy). *Annals of Geophysics*, 64(2), Article GM215. <https://doi.org/10.4401/ag-8515>
- Ali, H., & Khan, E. (2018). Assessment of potentially toxic heavy metals and health risk in water, sediments, and different fish species of River Kabul, Pakistan. *Human and Ecological Risk Assessment: An International Journal*, 24(8), 2101-2118. <https://doi.org/10.1080/10807039.2018.1438175>

- Alokhina, T. (2021). Magnetic particles in the sediments of the south Ukraine rivers as the marker of the technogenic impact on the hydroecosystems. *E3S Web of Conferences*, 234, Article 00048. <https://doi.org/10.1051/e3sconf/202123400048>
- Anderson, C. (2010). *Assessment of biogeochemical mercury cycling: Sekotong artisanal mining area, Lombok, West Nusa Tenggara (WNT) Province, Indonesia* [IDRF Final Report No. GRA/347/7]. New Zealand Ministry of Foreign Affairs and Trade. <https://www.mfat.govt.nz/assets/Aid-Prog-docs/Assessment-of-biogeochemical-mercury-cycling-research-report.pdf>
- Bruno, D. E., Ruban, D. A., Tiess, G., Pirrone, N., Perrotta, P., Mikhailenko, A. V., Ermolaev, V. A., & Yashalova, N. N. (2020). Artisanal and small-scale gold mining, meandering tropical rivers, and geological heritage: Evidence from Brazil and Indonesia. *Science of The Total Environment*, 715, Article 136907. <https://doi.org/10.1016/j.scitotenv.2020.136907>
- Chaparro, M. A. E., Ramírez-Ramírez, M., Chaparro, M. A. E., Miranda-Avilés, R., Puy-Alquiza, M. J., Böhnelt, H. N., & Zanor, G. A. (2020). Magnetic parameters as proxies for anthropogenic pollution in water reservoir sediments from Mexico: An interdisciplinary approach. *Science of The Total Environment*, 700, Article 134343. <https://doi.org/10.1016/j.scitotenv.2019.134343>
- Dearing, J. (1999). *Environmental magnetic susceptibility using the Bartington MS2 system*. (2nd ed.). Bartington Instruments. <https://gmw.com/wp-content/uploads/2019/03/JDearing-Handbook-OM0409.pdf>
- Decena, S. C. P., Arguelles, M. S., & Robel, L. L. (2018). Assessing heavy metal contamination in surface sediments in an urban river in the Philippines. *Polish Journal of Environmental Studies*, 27(5), 1983-1995. <https://doi.org/10.15244/pjoes/75204>
- Donato, D. B., Nichols, O., Possingham, H., Moore, M., Ricci, P. F., & Noller, B. N. (2007). A critical review of the effects of gold cyanide-bearing tailings solutions on wildlife. *Environment International*, 33(7), 974-984. <https://doi.org/10.1016/j.envint.2007.04.007>
- Duncan, A. E., de Vries, N., & Nyarko, K. B. (2018). Assessment of heavy metal pollution in the sediments of the River Pra and its tributaries. *Water, Air, & Soil Pollution*, 229(8), Article 272. <https://doi.org/10.1007/s11270-018-3899-6>
- Government Regulation of the Republic Indonesia (2001). *Peraturan pemerintah (PP) No. 82 tahun 2001: Pengelolaan kualitas air dan pengendalian pencemaran air* [Number 82 of 2001: Concerning Water Quality Management and Water Pollution Control]. Badan Pemeriksa Keuangan Republik Indonesia. <https://peraturan.bpk.go.id/Home/Details/53103/pp-no-82-tahun-2001>
- Hrouda, F. (2011). Models of frequency-dependent susceptibility of rocks and soils revisited and broadened. *Geophysical Journal International*, 187(3), 1259-1269. <https://doi.org/10.1111/j.1365-246X.2011.05227.x>
- Jaszczak, E., Polkowska, Ż., Narkowicz, S., & Namieśnik, J. (2017). Cyanides in the environment-analysis-problems and challenges. *Environmental Science and Pollution Research*, 24(19), 15929-15948. <https://doi.org/10.1007/s11356-017-9081-7>
- Jordanova, D., Goddu, S. R., Kotsev, T., & Jordanova, N. (2013). Industrial contamination of alluvial soils near Fe-Pb mining site revealed by magnetic and geochemical studies. *Geoderma*, 192, 237-248. <https://doi.org/10.1016/j.geoderma.2012.07.004>

- Juliansyah, A., Zulaikah, S., Mufti, N., Agustin, E. Y., Pujiastuti, R., & Iswanto, B. H. (2020). Magnetic susceptibility of river sediment in polluted area of traditional gold mining in Kuris Sumbawa Indonesia. In *AIP Conference Proceedings*, 2251(1), Article 040020. <https://doi.org/10.1063/5.0016519>
- Junaidi, M., Krisnayanti, B. D., Juharfa, J., & Anderson, C. (2019). Risk of mercury exposure from fish consumption at artisanal small-scale gold mining areas in West Nusa Tenggara, Indonesia. *Journal of Health and Pollution*, 9(21), Article 190302. <https://doi.org/10.5696/2156-9614-9.21.190302>
- Kelepertzis, E., Argyraki, A., Botsou, F., Aidona, E., Szabó, Á., & Szabó, C. (2019). Tracking the occurrence of anthropogenic magnetic particles and potentially toxic elements (PTEs) in house dust using magnetic and geochemical analyses. *Environmental Pollution*, 245, 909-920. <https://doi.org/10.1016/j.envpol.2018.11.072>
- Kumar, V., Sharma, A., Minakshi, Bhardwaj, R., & Thukral, A. K. (2018). Temporal distribution, source apportionment, and pollution assessment of metals in the sediments of Beas river, India. *Human and Ecological Risk Assessment: An International Journal*, 24(8), 2162-2181. <https://doi.org/10.1080/10807039.2018.1440529>
- Li, J., Lin, S., & Qin, S. (2016). Characteristics of sediment bacterial community in response to environmental impacts in a sewage polluted river. *Journal of Coastal Research*, 74, 196-206. <https://doi.org/10.2112/SI74-017.1>
- Mariyanto, M., Amir, M. F., Utama, W., Hamdan, A. M., Bijaksana, S., Pratama, A., Yunginger, R., & Sudarningsih, S. (2019a). Environmental magnetism data of Brantas River bulk surface sediments, Jawa Timur, Indonesia. *Data in Brief*, 25, Article 104092. <https://doi.org/10.1016/j.dib.2019.104092>
- Mariyanto, M., Amir, M. F., Utama, W., Hamdan, A. M., Bijaksana, S., Pratama, A., Yunginger, R., & Sudarningsih, S. (2019b). Heavy metal contents and magnetic properties of surface sediments in volcanic and tropical environment from Brantas River, Jawa Timur Province, Indonesia. *Science of The Total Environment*, 675, 632-641. <https://doi.org/10.1016/j.scitotenv.2019.04.244>
- Morales, J., Hernández-Bernal, M. D. S., Corona-Chávez, P., Gogichaishvili, A., & Bautista, F. (2016). Further evidence for magnetic susceptibility as a proxy for the evaluation of heavy metals in mining wastes: Case study of Tlalpujahua and El Oro mining districts. *Environmental Earth Sciences*, 75(4), Article 309. <https://doi.org/10.1007/s12665-015-5187-8>
- Ouyang, T., Li, M., Appel, E., Tang, Z., Peng, S., Li, S., & Zhu, Z. (2020). Magnetic response of Arsenic pollution in a slag covered soil profile close to an abandoned tungsten mine, southern China. *Scientific Reports*, 10, Article 4357. <https://doi.org/10.1038/s41598-020-61411-6>
- Prereira, L. B. F., & Neto, J. A. S. (2007). Cyanide distribution in the stream sediments and tailings at the bonfim (W-AU-BI-TE) mine northeastern Brazil. *Geochimica Brasiliensis*, 21, 261-273. <https://www.geobrasiliensis.org.br/geobrasiliensis/article/view/271/pdf>
- Ravisankar, R., Harikrishnan, N., Chandrasekaran, A., Gandhi, M. S., & Alagarsamy, R. (2018). Data on heavy metal and magnetic relationships in coastal sediments from South East Coast of Tamilnadu, India. *Data in Brief*, 16, 392-400. <https://doi.org/10.1016/j.dib.2017.11.056>
- Salomão, G. N., Farias, D. D. L., Sahoo, P. K., Dall'Agnol, R., & Sarkar, D. (2021). Integrated geochemical assessment of soils and stream sediments to evaluate source-sink relationships and background variations

- in the Parauapebas River Basin, Eastern Amazon. *Soil Systems*, 5(1), Article 21. <https://doi.org/10.3390/soilsystems5010021>
- Shanbehzadeh, S., Dastjerdi, M. V., Hassanzadeh, A., & Kiyanzadeh, T. (2014). Heavy metals in water and sediment: A case study of Tembi River. *Journal of Environmental and Public Health*, 2014, Article 858720. <https://doi.org/10.1155/2014/858720>
- Shehong, L., Baoshan, Z., Jianming, Z., & Xiaoying, Y. (2005). The distribution and natural degradation of cyanide in goldmine tailings and polluted soil in arid and semiarid areas. *Environmental Geology*, 47(8), 1150-1154. <https://doi.org/10.1007/s00254-005-1253-y>
- Sudarningsih, S., Bijaksana, S., Ramdani, R., Hafidz, A., Pratama, A., Widodo, W., Iskandar, I., Dahrin, D., Fajar, S. J., & Santoso, N. A. (2017). Variations in the concentration of magnetic minerals and heavy metals in suspended sediments from Citarum river and its tributaries, West Java, Indonesia. *Geosciences*, 7(3), Article 66. <https://doi.org/10.3390/geosciences7030066>
- Suresh, G., Ramasamy, V., Meenakshisundaram, V., Venkatachalapathy, R., & Ponnusamy, V. (2011). Influence of mineralogical and heavy metal composition on natural radionuclide concentrations in the river sediments. *Applied Radiation and Isotopes*, 69(10), 1466-1474. <https://doi.org/10.1016/j.apradiso.2011.05.020>
- Świetlik, R., & Trojanowska, M. (2016). Mobility of chromium and its chemical fractions in river sediment polluted by tannery effluents (Poland). *Soil and Sediment Contamination: An International Journal*, 25(3), 266-278. <https://doi.org/10.1080/15320383.2016.1130686>
- Szczepaniak-Wnuk, I., Górka-Kostrubiec, B., Dytłow, S., Szwarczewski, P., Kwapuliński, P., & Karasiński, J. (2020). Assessment of heavy metal pollution in Vistula river (Poland) sediments by using magnetic methods. *Environmental Science and Pollution Research*, 27(19), 24129-24144. <https://doi.org/10.1007/s11356-020-08608-4>
- Wang, J., Li, S., Li, H., Qian, X., Li, X., Liu, X., Lu, H., Wang, C., & Sun, Y. (2017). Trace metals and magnetic particles in PM<sub>2.5</sub>: Magnetic identification and its implications. *Scientific Reports*, 7(1), 1-11. <https://doi.org/10.1038/s41598-017-08628-0>
- Yunginger, R., Bijaksana, S., Dahrin, D., Zulaikah, S., Hafidz, A., Kirana, K. H., Sudarningsih, S., Mariyanto, M., & Fajar, S. J. (2018). Lithogenic and anthropogenic components in surface sediments from Lake Limboto as shown by magnetic mineral characteristics, trace metals, and REE Geochemistry. *Geosciences*, 8(4), Article 116. <https://doi.org/10.3390/geosciences8040116>
- Zajzon, N., Marton, E., Sipos, P., Kristaly, F., Nemeth, T., Kis-Kovacs, V., & Weiszburg, T. G. (2013). Integrated mineralogical and magnetic study of magnetic airborne particles from potential pollution sources in industrial-urban environment. *Carpathian Journal of Earth and Environmental Sciences*, 8(1), 179-186



## Recognition of Fruit Types from Striking and Flicking Sounds

**Rong Phoophuangpairoj**

*Department of Computer Engineering, College of Engineering, Rangsit University, Pathumthani 12000, Thailand*

### ABSTRACT

This paper proposes a method to recognize fruits whose quality, including their ripeness, grades, brix values, and flesh characteristics, cannot be determined visually from their skin but from striking and flicking sounds. Four fruit types consisting of durians, watermelons, guavas, and pineapples were studied in this research. In recognition of fruit types, preprocessing removes the non-striking/non-flicking parts from the striking and flicking sounds. Then the sequences of frequency domain acoustic features containing 13 Mel Frequency Cepstral Coefficients (MFCCs) and their 13 first- and 13 second-order derivatives were extracted from striking and flicking sounds. The sequences were used to create the Hidden Markov Models (HMMs). The HMM acoustic models, dictionary, and grammar were incorporated to recognize striking and flicking sounds. When testing the striking and flicking sounds obtained from the fruits used to create the training set but were collected at different times, the recognition accuracy using 1 through 5 strikes/flicks was 98.48%, 98.91%, 99.13%, 98.91%, and 99.57%, respectively. For an unknown test set, of which the sounds obtained from the fruits that were not used to create the training set, the recognition accuracy using 1 through 5 strikes/flicks were 95.23%, 96.82%, 96.82%, 97.05%, and 96.59%, respectively. The results also revealed that the proposed method could accurately distinguish the striking sounds of durians from the flicking sounds of watermelons, guavas, and pineapples.

*Keywords:* Flicking sounds, fruit grading, fruit recognition, Hidden Markov Models, striking

### ARTICLE INFO

*Article history:*

Received: 15 September 2022

Accepted: 06 March 2023

Published: 08 September 2023

DOI: <https://doi.org/10.47836/pjst.31.6.04>

*E-mail address:*

[rong.p@rsu.ac.th](mailto:rong.p@rsu.ac.th)

ISSN: 0128-7680

e-ISSN: 2231-8526

### INTRODUCTION

Fruits are vital for health which supply necessary nutrition supplements to life. When buying fruits, customers anticipate getting their desired fruit quality, including ripeness, sweetness, and characteristics of the flesh inside. However, when cutting or

peeling them, many customers were unsatisfied with the quality of the fruits they bought. For certain kinds of fruits, for example, durians, watermelons, guavas, and pineapples (Figure 1), the characteristics of fruit pulp and physiochemical properties were generally unknown by observing from their outer skins.



Figure 1. Four types of fruits in the recognition: (a) durians; (b) watermelons; (c) guavas; and (d) pineapples

Experienced fruit merchants usually determine the fruit quality by striking or flicking them and listening to the generated sounds. When flicking, the index or middle finger is released from the thumb against an object (Figure 2). Flicking can assess the quality of fruits, e.g., watermelon, guava, and pineapple. However, flickering a durian- the thorny king of fruit- is not practical as it can injure the finger. Striking or tapping the durian with a tapping stick and listening to the sounds to determine the ripeness of durians are shown in Figure 3.



Figure 2. Flicking a guava



Figure 3. Tapping a durian

Figure 4 shows the characteristics of the striking/flicking sounds of durians, watermelons, guavas, and pineapples. They are quite similar and difficult to be visually distinguished. They consist of non-striking/non-flicking parts and striking/flicking parts. Each striking/flicking sound normally begins with a non-striking/non-flicking part, followed by a striking/flicking part, and ends with a non-striking/non-flicking part. The flicking/

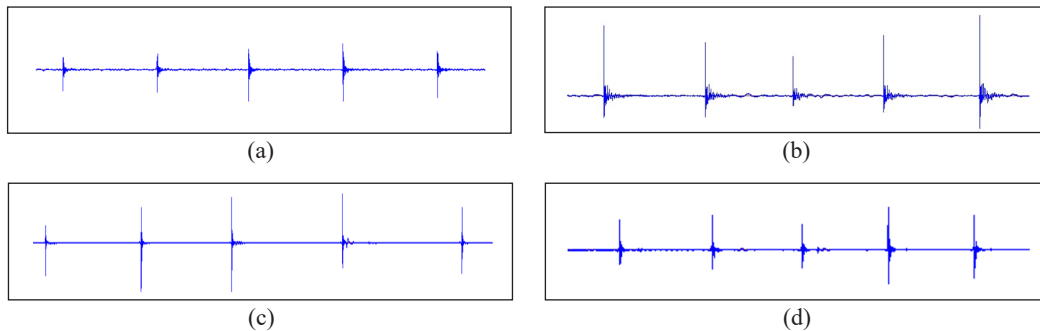


Figure 4. Striking and flicking sounds of fruits five times: (a) durian; (b) watermelon; (c) guava; and (d) pineapple

striking parts have higher amplitude than the non-flicking/non-striking parts. The striking/flicking parts, usually much shorter than the non-striking/non-flicking parts, contain more information about the types of fruits and fruit characteristics. In addition, the duration and the amplitude of flicking/striking signals derived from the same or different fruits fluctuate, resulting in difficulties in recognition. The pace of flicking/striking the fruits can affect the results, especially if the duration of non-flicking/non-striking parts is long. In order to overcome these differences, the preprocessing method of reducing the flickering parts based on the amplitude of the signals was proposed (Phoophuangpairaj, 2014a). The duration of striking/flicking parts depends on when the finger or the tapping stick hits the fruits. The hardness or impact of flicking and striking affects the amplitude of signals.

Therefore, it is not practical to determine the quality of fruits from the amplitude but from the frequency-based features extracted from signals and models that can efficiently capture acoustic phenomena. It can be seen from how some merchants recognize short flicking and striking sounds, which have some frequency differences to predict the internal fruit flesh. Based on the results, using HMMs with frequency-based features could efficiently handle the different impacts of watermelon flicking and durian tapping (Phoophuangpairaj, 2014a; Phoophuangpairaj, 2014b). For guavas, repeatedly flicking the same area can affect the recognition results. The flicking should be applied to the different areas of the guavas to classify the freshness of the guavas.

There was research applying speech recognition technologies to recognize the quality of watermelons and guavas using flicking sounds (Phoophuangpairaj, 2014a; Phoophuangpairaj, 2013). For the recognition of firm flesh and flesh with cracks, the average watermelon quality recognition rates of 95.0%, 97.0%, 98.0%, 98.0%, and 98.0% were achieved by using 1 through 5 flicks, respectively. For guavas stored in a normal refrigerator, the average correct freshness recognition rates of 92.0%, 88.0%, and 94.0% were obtained from fresh, 3-day-kept, and 6-day-kept guavas, respectively. The striking sounds were also used to recognize ripe and unripe durians using a dictionary and grammar (Phoophuangpairaj, 2014b) and an N-gram language model (Phoophuangpairaj, 2014c).

The recognition system using MFCC-based features and HMMs efficiently recognized the quality of watermelons and durians. When using grammar, the durian ripeness recognition rates of 91.0%, 92.0%, 90.0%, 92.0%, and 92.0% were achieved using 1 through 5 strikes, respectively. Using an N-gram language model, the durian ripeness recognition rates of 88.0%, 91.0%, 91.0%, 92.0%, 92.0%, and 90.0% were achieved using 1 through 5 strikes, respectively. The flicking sounds were also studied to classify pineapples and their physicochemical properties. Even though predicting pineapple grades using flicking sounds cannot be done efficiently, the results showed that pineapples classified as grade 1 and grade 3 differed significantly in terms of total soluble solid (TSS), pH value, and water content (Phoophuangpairoj & Srikun, 2014).

When recognizing some fruit types whose internal characteristics cannot be visually determined from their skin, flicking and striking sounds can also be applied. Studying the feasibility of recognizing the types of fruits from the flicking and striking sounds without using image processing is beneficial. The image processing requires another different source of data, while the proposed method merely utilizes a source of data, which is more efficient. Hence, this work proposed a novel method to recognize the fruit types without using image processing but did not stress the quality of fruits because this issue had already been researched.

## LITERATURE SURVEY

Automation in food processing plays a crucial role in increasing the productivity, quality, and profitable growth of countries. Fruit grading is a process for producers which affects fruit quality evaluation and export markets (Raja et al., 2018). Automatic fruit classification is an interesting issue in the retailing and fruit-growing industry because it can help farmers and supermarkets identify the status of fruits from stock or containers (Shahi et al., 2022). Computer vision and machine learning methods have been applied for fruit detection, ripeness, and categorization in the past decade (Fan et al., 2020; Hossain et al., 2018). The problem of classifying fruits and vegetables in computer vision remains a challenge because some fruits look alike and have similar colors, shapes, and textures. CNNs (Convolutional Neural Networks) and transfer learning have obtained impressive results in image classification (Albarrak et al., 2022). Based on the previous work, CNN recognized 26 categories of fruits and vegetable images (Zeng, 2017) and orange grades (Asriny et al., 2020). A system has to extract image features and use them as a source to recognize the fruits to recognize the fruit quality from a video. Meanwhile, the system has to use striking or flicking sounds as the other source to recognize their qualities. Such a system requires two different sources, and this may not be as practical, resulting in creating a more complex heterogeneous system when compared to the system using only one source of flicking or striking sounds.

The success of MFCC acoustic features combined with their cost-effective and robust computation turned them into a standard choice in speech recognition applications. In speech recognition systems such as an Arabic speech recognition system, 39 MFCC-based acoustic features were extracted by partitioning the speech signals into frames (Elharati et al., 2020). HMM is a model used to represent the acoustic phenomenon and acoustic changes according to time. HMMs provide a highly reliable method of recognizing spoken signals (Chavan & Sable, 2013; Naithani et al., 2018; Najkar et al., 2010). HMMs were also applied to recognize inhaling and exhaling signals (Phoophuangpairaj, 2020) and sleep spindles (Stevner et al., 2019). For HMM, Gaussian Mixture Models (GMMs), which are the components within each HMM state, were primarily utilized to compute the probabilistic distribution of each phone or phoneme (or any speech signal atom), and the fusion of GMMs-HMMs has led to many successful automatic speech recognition (ASR) applications (Kiranyaz et al., 2021). Phonemes or syllables were combined into words and sentences using a dictionary and language model. The main reasons for this success are this model's analytic ability in the speech phenomenon and its accuracy in practical speech recognition systems (Najkar et al., 2010).

Viterbi is an algorithm that searches HMM states to find the most probable phone, phoneme, word, and sentence from the acoustic models of phones or phonemes connected based on a dictionary and grammar. Viterbi algorithm was applied to recognize or search the possible phones in a speech recognition system (Hatala & Puturu, 2019).

## MATERIALS AND METHODS

### Data

Data were collected from four different types of fruits: 100 durians, 100 watermelons, 150 guavas, and 110 pineapples. The striking/flicking sounds were recorded at 11,025 Hz. The data were collected from fruits of different quality, grades, and ripeness. Nonetheless, the work studied the differentiation of the fruit types. Striking sounds were derived from 100 durians struck five times each to train the HMM acoustic models. The flicking sounds were obtained from 100 watermelons and 150 guavas, all flicked five times each, while the pineapple flicking sounds were obtained from 110 pineapples, ten times each. For testing, untrained and unknown sets were used. The untrained set was collected from the same set of fruits used in the training but at different times, whereas the unknown set was collected from different fruits not included in the training. The untrained set consisted of 1 through 5 striking/flicking sounds, each collected from 100 durians, 100 watermelons, 150 guavas, and 110 pineapples. The unknown set consisted of 1 through 5 striking/flicking sounds, each collected from 100 durians, 100 watermelons, 150 guavas, and 90 pineapples.

## Preprocessing

As a rule, the striking/flicking parts contain information about fruit quality and types. Preprocessing was performed to reduce the non-striking/non-flicking parts. The digitized signals contain positive, negative, and zero values. As a result, it is easier to set a removing threshold by computing their absolute values. Additionally, a clipping or cut-off threshold was applied to handle the high difference in the signal amplitude. The threshold ( $Th$ ) to reduce non-flicking/striking parts was computed from all frames using Equation 1:

$$framesize = \frac{frame\_duration}{1000} \times sampling\_rate \quad (1)$$

where:  $framesize$  is the number of points or values in each frame;  $frame\_duration$  is the frame duration or size in milliseconds;  $sampling\_rate$  is the recording sampling rate (11,025 Hz).

The frame duration ( $frame\_duration$ ) was set to 2 milliseconds. The number of samples ( $num\_smp\_file$ ) was obtained from each wav file. Then the  $nFrame$ , which is the number of frames in a striking/flicking file, was computed using Equation 2.

$$nFrame = \frac{num\_smp\_file}{framesize} \quad (2)$$

$Clip()$  was a function used to clip the signals. If any value of  $|s_i|$  was higher than a clipping threshold ( $Th_{clip}$ ) (e.g., 10,000), the value was set to the threshold (Equations 3-5).

$$Frame_{abs_n} = \sum_{i=(n-1) \times framesize + 1}^{n \times framesize} clip(|s_i|), \quad 1 \leq n \leq nFrame \quad (3)$$

$$AvgFrame_{abs} = \frac{\sum_{i=1}^{nFrame} Frame_{abs_i}}{nFrame} \quad (4)$$

$$Th = C * AvgFrame_{abs} \quad (5)$$

where:  $Frame_{abs_n}$  is the sum of clipped absolute values computed from the  $n^{\text{th}}$  frame;  $AVGFrame_{abs}$  is the average of  $Frame_{abs_n}$  computed from all frames;  $C$  is a constant (e.g., 3);  $Th$  is the threshold to reduce non-striking/non-flicking parts.

Then the following method was applied to remove non-striking/non-flicking parts (frames) from the signals.

```
for(n=1;n<=nFrame;n++)
  KeepFrame[n] = 0
  if((vFrameabsn >= Th) OR (n equals to 1, 2, nFrame-1 or nFrame))
    KeepFrame[n] = 1; // The nth frame is flagged to be kept.
```

The method scanned all frames. If it was the first or last two frames or the sum of clipped absolute values computed from the  $n^{\text{th}}$  frame ( $Frame_{abs_n}$ ) was greater than or equal to the threshold to reduce non-striking/non-flicking parts, the  $KeepFrame[n]$  was set to 1. When the  $KeepFrame[n]$  was equal to 1, the  $n^{\text{th}}$  frame was kept. When the  $KeepFrame[n]$  was equal to 0, the  $n^{\text{th}}$  frame was removed. Removing all non-striking/non-flicking parts without losing some precious short striking/flicking parts is difficult. According to the algorithm below, some parts before and after each striking/flicking were kept to ensure that the precious data in striking/flicking parts were not removed and to obtain longer signals for recognizing HMMs, which contained a higher number of states. The algorithm kept the frames before and after each striking/flicking part, as described below.

```

for( $n=2;n<nFrame;n=n+1$ )
    if( $KeepFrame[n]$  equals to 1 AND  $KeepFrame[n-1]$  equals to 0)
         $KeepFrame[n-1] = 1$ ;

for( $n=nFrame-1;n>1;n=n-1$ )
    if( $KeepFrame[n]$  equals to 1 AND  $KeepFrame[n+1]$  equals to 0)
         $KeepFrame[n+1] = 1$ ;

```

The data in the  $n^{\text{th}}$  frame of which  $KeepFrame[n]$  equals 1 were written in the preprocessed file. Thereafter, the Hidden Markov Model Toolkit (HTK) (<http://htk.eng.cam.ac.uk/>) was used to extract acoustic features from the preprocessed signals, train HMM acoustic models and detect the types of fruits. As for the evaluation, HResult, a tool in HTK, was used to find the fruit type recognition accuracy.

### Extracting Acoustic Features

The time-domain or the visual characteristics of the durian striking, watermelon, guava, and pineapple flicking were similar. Therefore, the frequency-domain features of the signals were computed and used instead. Acoustic features consisting of 13 MFCCs and their 13 first- and 13 second-order derivatives were extracted from each particular time or window. The feature extraction used a window size of 4 milliseconds and a window shift rate of 1 millisecond. Left-to-right HMMs were used to model striking/flicking parts of each fruit type and a shared model of non-striking/non-flicking parts.

### Creating Acoustic Models

The sounds were transcribed without providing the position of each part. For each fruit type, the non-flicking and non-striking parts which remained after the preprocessing were represented using sil (silence). Each striking/flicking part was represented based on the types of fruits, drstrike for each striking signal of a durian, wmflick, gvfflick, and pafflick for

each flicking signal of watermelon, guava, and pineapple, respectively. The transcriptions of each 5-striking/5-flicking signal used in the training are shown in Table 1.

The transcriptions without the positions of striking/flicking parts were used in the training. HTK tried to find acoustic features of striking/flicking and non-striking/non-flicking parts to create the acoustic models according to the transcriptions. In training, the number of HMM states varied from 4 to 7, and the number of Gaussian mixtures in each state was from 2 to 6.

Table 1  
*Transcriptions of each 5-striking/5-flicking signal used in the training*

Types of fruits	Transcriptions for each 5-striking/5-flicking sound
durian	sil drstrike sil drstrike sil drstrike sil drstrike sil drstrike sil
watermelon	sil wmflick sil wmflick sil wmflick sil wmflick sil wmflick sil
guava	sil gvfflick sil gvfflick sil gvfflick sil gvfflick sil gvfflick sil
pineapple	sil pafflick sil pafflick sil pafflick sil pafflick sil pafflick sil

### Creating a Dictionary to Recognize Fruit Types

Words representing 1 through 5 strikes/flicks were defined according to the characteristics of the striking and flicking sounds. For example, the one-flick word consists of a non-flicking/non-striking model followed by each fruit type’s striking or flicking model and the sil model. In the Thai language, words can be pronounced in different ways. The words in the dictionary consisting of durian, watermelon, guava, and pineapple were created from different numbers of phones. The words in the dictionary to represent the sounds of 1 through 5 strikes/flicks are shown below.

durian [durian]	sil drstrike sil
watermelon [watermelon]	sil wmflick sil
guava [guava]	sil gvfflick sil
pineapple [pineapple]	sil pafflick sil
durian [durian]	sil drstrike sil drstrike sil
watermelon [watermelon]	sil wmflick sil wmflick sil
guava [guava]	sil gvfflick sil gvfflick sil
pineapple [pineapple]	sil pafflick sil pafflick sil
durian [durian]	sil drstrike sil drstrike sil drstrike sil
watermelon [watermelon]	sil wmflick sil wmflick sil wmflick sil
guava [guava]	sil gvfflick sil gvfflick sil gvfflick sil
pineapple [pineapple]	sil pafflick sil pafflick sil pafflick sil
durian [durian]	sil drstrike sil drstrike sil drstrike sil drstrike sil
watermelon [watermelon]	sil wmflick sil wmflick sil wmflick sil wmflick sil
guava [guava]	sil gvfflick sil gvfflick sil gvfflick sil gvfflick sil



```

pineapple [pineapple] sil paflick sil paflick sil paflick sil paflick sil
durian [durian] sil drstrike sil drstrike sil drstrike sil drstrike sil drstrike sil
watermelon [watermelon] sil wmflick sil wmflick sil wmflick sil wmflick sil wmflick sil
guava [guava] sil gvfflick sil gvfflick sil gvfflick sil gvfflick sil gvfflick sil
pineapple [pineapple] sil paflick sil paflick sil paflick sil paflick sil paflick sil

```

### Creating Grammar to Recognize Fruit Types

Grammar was applied to constrain the recognition results. The following grammar was created to recognize the fruit types.

```

$fruittype = durian | watermelon | guava | pineapple;
($fruittype)

```

The | means “or” while the () means no repetition. The first line of recognition grammar states that \$fruittype can be durian, watermelon, guava, or pineapple, while the second line states that only the \$fruittype without repetition can be derived.

### Recognizing Types of Fruits

The acoustic models, dictionary, and grammar were integrated to recognize the extracted acoustic features. The dictionary and grammar make the recognition more flexible and easy to handle the arbitrary numbers of strikes and flicks. The Viterbi algorithm decided which hypotheses or word-connected paths comprising phones were most likely to be the correct textual interpretation of the signals.

## RESULTS

To investigate the results, the number of strikes/flicks, the number of HMM states, and the number of Gaussian mixtures per state were varied. Table 2 shows the accuracy obtained from the untrained set. The results reported that of N testing times in which each time used F strikes or flicks, H times were recognized correctly. There were S substitution errors. When using 1 strike/flick, the accuracy of 98.48% was obtained by using 6 states and 5 Gaussian mixtures per state (6S5M). For 2 through 5 strikes/flicks, 98.91%, 99.13%, 98.91%, and 99.57% accuracy rates were obtained using 6 states and 4 Gaussian mixtures per state (6S4M), respectively. However, when using one strike or flick with HMMs containing 7 states, there were six striking/flicking sounds that the system was not provided the recognition results because the number of the feature vectors extracted from very short signals was not adequate to be recognized using the HMMs.

Table 3 shows the fruit type recognition accuracy obtained from the unknown set.

Table 2

*Accuracy of fruit type recognition obtained from the untrained set based on the number of strikes/flicks, states, and Gaussian mixtures*

Number of strike(s)/flick(s) (T)	Number of states	Number of Gaussian mixtures	Accuracy (%)	H	S	N
<b>1</b>	4	2	93.48	430	30	460
	4	3	93.70	431	29	460
	4	4	93.04	428	32	460
	4	5	93.70	431	29	460
	4	6	96.74	445	15	460
	5	2	95.65	440	20	460
	5	3	95.65	440	20	460
	5	4	95.00	437	23	460
	5	5	95.87	441	19	460
	5	6	96.09	442	18	460
	6	2	95.87	441	19	460
	6	3	97.39	448	12	460
	6	4	98.04	451	9	460
	6	5	98.48	453	7	460
	6	6	98.26	452	8	460
	7	2	94.93	431	23	460
	7	3	96.04	436	18	454
	7	4	96.70	439	15	454
	7	5	97.14	441	13	454
	7	6	97.58	443	11	454
<b>2</b>	4	2	94.13	433	27	460
	4	3	95.43	439	21	460
	4	4	95.22	438	22	460
	4	5	95.43	439	21	460
	4	6	96.52	444	16	460
	5	2	95.87	441	19	460
	5	3	96.74	445	15	460
	5	4	95.87	441	19	460
	5	5	95.43	439	21	460
	5	6	97.17	447	13	460
	6	2	98.04	451	9	460
	6	3	98.70	454	6	460
	6	4	98.91	455	5	460
	6	5	98.70	454	6	460
	6	6	98.26	452	8	460
	7	2	96.30	443	17	460
	7	3	98.04	451	9	460
7	4	98.04	451	9	460	

Table 2 (continue)

Number of strike(s)/flick(s) (T)	Number of states	Number of Gaussian mixtures	Accuracy (%)	H	S	N
	7	5	97.61	449	11	460
	7	6	98.04	451	9	460
<b>3</b>	4	2	93.48	430	30	460
	4	3	94.35	434	26	460
	4	4	95.22	438	22	460
	4	5	95.22	438	22	460
	4	6	96.96	446	14	460
	5	2	96.74	445	15	460
	5	3	96.74	445	15	460
	5	4	96.09	442	18	460
	5	5	95.87	441	19	460
	5	6	97.39	448	12	460
	6	2	97.83	450	10	460
	6	3	98.91	455	5	460
	6	4	99.13	456	4	460
	6	5	98.70	454	6	460
	6	6	98.70	454	6	460
	7	2	97.17	447	13	460
	7	3	99.13	456	4	460
	7	4	98.91	455	5	460
	7	5	98.70	454	6	460
	7	6	99.13	456	4	460
<b>4</b>	4	2	94.78	436	24	460
	4	3	94.57	435	25	460
	4	4	94.78	436	24	460
	4	5	95.22	438	22	460
	4	6	96.74	445	15	460
	5	2	96.52	444	16	460
	5	3	97.17	447	13	460
	5	4	95.43	439	21	460
	5	5	96.30	443	17	460
	5	6	97.83	450	10	460
	6	2	97.83	450	10	460
	6	3	98.70	454	6	460
	6	4	98.91	455	5	460
	6	5	98.48	453	7	460
	6	6	98.70	454	6	460
	7	2	97.61	449	11	460
	7	3	98.26	452	8	460

Table 2 (continue)

Number of strike(s)/flick(s) (T)	Number of states	Number of Gaussian mixtures	Accuracy (%)	H	S	N
	7	4	98.48	453	7	460
	7	5	98.48	453	7	460
	7	6	98.70	454	6	460
<b>5</b>	4	2	94.35	434	26	460
	4	3	95.00	437	23	460
	4	4	95.00	437	23	460
	4	5	95.43	439	21	460
	4	6	96.52	444	16	460
	5	2	97.17	447	13	460
	5	3	97.39	448	12	460
	5	4	96.30	443	17	460
	5	5	96.52	444	16	460
	5	6	98.26	452	8	460
	6	2	98.04	451	9	460
	6	3	98.91	455	5	460
	6	4	99.57	458	2	460
	6	5	98.70	454	6	460
	6	6	98.70	454	6	460
	7	2	97.39	448	12	460
	7	3	98.91	455	5	460
	7	4	99.13	456	4	460
	7	5	98.70	454	6	460
	7	6	99.13	456	4	460

Table 3

*Accuracy of fruit type recognition obtained from the unknown set based on the number of strikes/flicks, states, and Gaussian mixtures*

Number of strike(s)/flick(s) (T)	Number of states	Number of Gaussian mixtures	Accuracy (%)	H	S	N
<b>1</b>	4	2	92.50	407	33	440
	4	3	92.27	406	34	440
	4	4	92.73	408	32	440
	4	5	92.73	408	32	440
	4	6	93.41	411	29	440
	5	2	92.73	408	32	440
	5	3	92.73	408	32	440
	5	4	94.09	414	26	440
	5	5	95.23	419	21	440
	5	6	93.86	413	27	440

Table 3 (continue)

Number of strike(s)/flick(s) (T)	Number of states	Number of Gaussian mixtures	Accuracy (%)	H	S	N
	6	2	94.55	416	24	440
	6	3	94.09	414	26	440
	6	4	94.55	416	24	440
	6	5	95.23	419	21	440
	6	6	95.00	418	22	440
	7	2	93.74	404	27	431
	7	3	94.66	408	23	431
	7	4	94.20	406	25	431
	7	5	93.27	402	29	431
	7	6	93.50	403	28	431
<b>2</b>	4	2	92.27	406	34	431
	4	3	94.55	416	24	440
	4	4	94.55	416	24	440
	4	5	94.32	415	25	440
	4	6	94.77	417	23	440
	5	2	94.32	415	25	440
	5	3	95.23	419	21	440
	5	4	94.55	416	24	440
	5	5	95.68	421	19	440
	5	6	95.45	420	20	440
	6	2	95.23	419	21	440
	6	3	96.36	424	16	440
	6	4	95.91	422	18	440
	6	5	96.82	426	14	440
	6	6	96.36	424	16	440
	7	2	94.32	415	25	440
	7	3	94.77	417	23	440
	7	4	95.45	420	20	440
	7	5	95.68	19	19	440
	7	6	95.91	422	18	440
<b>3</b>	4	2	92.05	405	35	440
	4	3	93.64	412	28	440
	4	4	93.64	412	28	440
	4	5	94.09	414	26	440
	4	6	94.77	417	23	440
	5	2	94.09	414	26	440
	5	3	95.23	419	21	440
	5	4	95.23	419	21	440
	5	5	94.77	417	23	440

Table 3 (continue)

Number of strike(s)/flick(s) (T)	Number of states	Number of Gaussian mixtures	Accuracy (%)	H	S	N
	5	6	95.68	421	19	440
	6	2	95.23	419	21	440
	6	3	97.05	427	13	440
	6	4	96.82	426	14	440
	6	5	96.82	426	14	440
	6	6	96.59	425	15	440
	7	2	94.55	416	24	440
	7	3	95.00	418	22	440
	7	4	95.23	419	21	440
	7	5	96.14	423	17	440
	7	6	96.59	425	15	440
<b>4</b>	4	2	92.73	408	32	440
	4	3	93.18	410	30	440
	4	4	94.09	414	26	440
	4	5	94.77	417	23	440
	4	6	94.55	416	24	440
	5	2	94.32	415	25	440
	5	3	95.00	418	22	440
	5	4	95.23	419	21	440
	5	5	95.45	420	20	440
	5	6	94.55	416	24	440
	6	2	95.00	418	22	440
	6	3	96.14	423	17	440
	6	4	95.91	422	18	440
	6	5	97.05	427	13	440
	6	6	96.36	424	16	440
	7	2	95.00	418	22	440
	7	3	95.00	418	22	440
	7	4	96.14	423	17	440
	7	5	95.68	421	19	440
	7	6	96.14	423	17	440
<b>5</b>	4	2	92.27	406	34	440
	4	3	93.41	411	29	440
	4	4	93.64	412	28	440
	4	5	95.00	418	22	440
	4	6	95.00	418	22	440
	5	2	94.09	414	26	440
	5	3	94.77	417	23	440
	5	4	95.23	419	21	440

Table 3 (continue)

Number of strike(s)/flick(s) (T)	Number of states	Number of Gaussian mixtures	Accuracy (%)	H	S	N
	5	5	95.00	418	22	440
	5	6	95.00	418	22	440
	6	2	94.55	416	24	440
	6	3	96.14	423	17	440
	6	4	96.14	423	17	440
	6	5	96.14	423	17	440
	6	6	95.91	422	18	440
	7	2	95.45	420	20	440
	7	3	95.91	422	18	440
	7	4	96.59	425	15	440
	7	5	96.59	425	15	440
	7	6	96.36	424	16	440

When using 1 through 4 strikes/flicks, the highest accuracy of 95.23%, 96.82%, 96.82%, and 97.05% were respectively obtained by using 6 states and 5 Gaussian mixtures per state (6S5M). For 5 strikes/flicks, the highest accuracy of 96.59% was yielded when using 7 states and 5 Gaussian mixtures per state (7S5M). However, when using one strike or flick with HMMs containing 7 states, there were nine striking/flicking sounds that the system was not provided the recognition results because the number of the feature vectors extracted from very short signals was not adequate to be recognized using the HMMs. Next, the results were further investigated, and the confusion matrix derived from recognizing the untrained set was shown in Table 4.

For the untrained set, the highest accuracy was derived when using 5 strikes/flicks. The results showed high watermelon, guava, and durian recognition rates. The errors occurred when recognizing pineapple flicking sounds. The errors occurred when recognizing pineapple flicking sounds. There were 1.89% pineapples incorrectly recognized as watermelons.

Table 5 shows the confusion matrix of fruit-type recognition obtained from the unknown set.

The results revealed that although the striking and flicking sounds look similar, the proposed method could correctly distinguish durian striking sounds from those of watermelons, guavas, and pineapples. Although there were some errors when recognizing the flicking sounds of the different types of fruits, the overall accuracy was higher than 90%. When using 4 flicks, the highest recognition accuracy rates of 91%, 99.33%, 97.27%, and 100% were achieved for watermelons, guavas, pineapples, and durians, respectively.

Table 4  
Confusion matrix (untrained set)

Number of strike(s)/flick(s)	Actual type of fruit	Recognized as			
		Durian	Watermelon	Guava	Pineapple
<b>1 strike/flick (6S5M)</b>	Durian	100% (100)	0% (0)	0% (0)	0% (0)
	Watermelon	0% (0)	98% (98)	0% (0)	2% (2)
	Guava	0% (0)	0.67% (1)	99.33% (149)	0% (0)
	Pineapple	0% (0)	3.64% (4)	0% (0)	96.36% (106)
<b>2 strikes/flicks (6S4M)</b>	Durian	100% (100)	0% (0)	0% (0)	0% (0)
	Watermelon	0% (0)	98% (98)	0% (0)	2% (2)
	Guava	0% (0)	0% (0)	98.67% (148)	1.33% (2)
	Pineapple	0% (0)	0.91% (1)	0% (0)	99.09% (109)
<b>3 strikes/flicks (6S4M)</b>	Durian	100% (100)	0% (0)	0% (0)	0% (0)
	Watermelon	0% (0)	99% (99)	0% (0)	1% (1)
	Guava	0% (0)	0% (0)	98.67% (148)	1.33% (2)
	Pineapple	0% (0)	0.91% (1)	0% (0)	99.09% (109)
<b>4 strikes/flicks (6S4M)</b>	Durian	100% (100)	0% (0)	0% (0)	0% (0)
	Watermelon	0% (0)	99% (99)	0% (0)	1% (1)
	Guava	0% (0)	0% (0)	100% (150)	0% (0)
	Pineapple	0% (0)	3.64% (4)	0% (0)	96.36% (106)
<b>5 strikes/flicks (6S4M)</b>	Durian	100% (100)	0% (0)	0% (0)	0% (0)
	Watermelon	0% (0)	100% (100)	0% (0)	0% (0)
	Guava	0% (0)	0% (0)	100% (150)	0% (0)
	Pineapple	0% (0)	1.89% (2)	0% (0)	98.18% (108)



Table 5  
Confusion matrix (unknown set)

Number of strike(s)/flick(s)	Actual type of fruit	Recognized as			
		Durian	Watermelon	Guava	Pineapple
<b>1 strike/flick (6S5M)</b>	Durian	100% (100)	0% (0)	0% (0)	0% (0)
	Watermelon	0% (0)	93% (93)	0% (0)	7% (7)
	Guava	0% (0)	0% (0)	98.67% (148)	1.33% (2)
	Pineapple	0% (0)	7.27% (8)	3.64% (4)	89.10% (98)
<b>2 strikes/flicks (6S5M)</b>	Durian	100% (100)	0% (0)	0% (0)	0% (0)
	Watermelon	0% (0)	94% (94)	0% (0)	96% (6)
	Guava	0% (0)	0% (0)	98.67% (148)	1.33% (2)
	Pineapple	0% (0)	3.64% (4)	1.82% (2)	94.55% (104)
<b>3 strikes/flicks (6S5M)</b>	Durian	100% (100)	0% (0)	0% (0)	0% (0)
	Watermelon	0% (0)	93% (93)	0% (0)	7% (7)
	Guava	0% (0)	0% (0)	98.67% (148)	1.33% (2)
	Pineapple	0% (0)	2% (3)	1.33% (2)	96.67% (145)
<b>4 strikes/flicks (6S5M)</b>	Durian	100% (100)	0% (0)	0% (0)	0% (0)
	Watermelon	0% (0)	91% (91)	0% (0)	99% (9)
	Guava	0% (0)	0% (0)	99.33% (149)	0.67% (1)
	Pineapple	0% (0)	0.91% (1)	1.82% (2)	97.27% (107)
<b>5 strikes/flicks (6S5M)</b>	Durian	100% (100)	0% (0)	0% (0)	0% (0)
	Watermelon	0% (0)	90% (90)	0% (0)	10% (10)
	Guava	0% (0)	0% (0)	99.33% (149)	0.67% (1)
	Pineapple	0% (0)	1.82% (2)	1.82% (2)	96.36% (106)

## DISCUSSION

Even though the types of fruits can be manually provided for recognizing the fruit quality, it will be better if we can simultaneously recognize the types of fruits and their quality from the striking and flicking signals. The duration of the flicking and striking sounds of the fruits is very short, and the sounds resemble. Therefore, the method to recognize the different types of fruits should be studied. HMMs can model striking and flicking signals for recognizing the quality of fruits and fruit types. Nowadays, the prices of fruits are much higher when compared with those in the past decade, which makes non-destructive fruit grading more important. According to the derived results and previous studies (Phoophuangpairoj, 2014a, 2014b), it revealed some possibility of creating an application that can recognize the quality of durians and watermelons from the striking and flicking sounds without recognizing the types of fruits from images or manually giving the type of fruits in advance.

When using HMMs, if the number of feature vectors extracted from the signals is insufficient for HMM states, the HMM decoder will not give the result. Therefore, it is suggested that the large number of HMM states is inappropriate for recognizing short signals such as 1 striking or flicking sound.

In the future, CNN, which has been used in several computer vision applications and will be more widely used in processing sequential data, including natural language processing and speech recognition (Kiranyaz et al., 2021), long short-term memory networks (LSTM), and deep learning techniques should be explored along with frequency domain features such as MFCCs for the recognition of the fruits from striking and flicking sounds.

## CONCLUSION

This paper proposes using preprocessing, acoustic models, a dictionary, and grammar to recognize the fruit types from flicking/striking sounds. The dictionary and grammar provide flexibility to design the recognition system and can be used to recognize arbitrary duration of flicking/striking sounds. The parameters to extract acoustic features, including the window size, have to be adjusted to fit the problem. The preprocessing acoustic models, dictionaries, and grammar have to be designed based on the characteristic of the striking and flicking sounds. The results when using the different number of flicking and striking sounds, number of states, and number of Gaussian mixtures were compared. The method could correctly differentiate durian striking sounds from watermelon, guava, and pineapple flicking sounds. Averagely, more than 95% of recognition accuracy was obtained from recognizing striking and flicking sounds. The findings shed light on the feasibility of recognizing the durian ripeness of fruits and watermelon flesh from the flicking and striking sounds without image processing.

## ACKNOWLEDGEMENT

The author thanks everyone who had helped and supported completing the study and publication. The author also thanks the reviewers for their dedication, timing, and fruitful comments in improving and increasing the quality of the manuscript. Sincerely, the author expresses gratitude to Rangsit University, Thailand, for supporting the publication fee.

## REFERENCES

- Albarrak, K., Gulzar, Y., Hamid, Y., Mehmood, A., & Soomro, A. B. (2022). A deep learning-based model for date fruit classification. *Sustainability*, *14*(10), Article 6339. <https://doi.org/10.3390/su14106339>
- Asriny, D. M., Rani, S., & Hidayatullah, A. F. (2020). Orange fruit images classification using convolutional neural networks. *IOP Conference Series: Materials Science and Engineering*, *803*(1), Article 012020. <https://doi.org/10.1088/1757-899X/803/1/012020>
- Chavan, R. S., & Sable, G. S. (2013). An overview of speech recognition using HMM. *International Journal of Computer Science and Mobile Computing*, *2*(6), 233-238.
- Elharati, H. A., Alshaari, M., & Kępuska, V. Z. (2020) Arabic speech recognition system based on MFCC and HMMs. *Journal of Computer and Communications*, *8*(3), 28-34. <https://doi.org/10.4236/jcc.2020.83003>
- Fan, S., Li, J., Zhang, Y., Tian, X., Wang, Q., He, X., Zhang, C., & Huang, W. (2020). On line detection of defective apples using computer vision system combined with deep learning methods. *Journal of Food Engineering*. *286*, Article 110102. <https://doi.org/10.1016/j.jfoodeng.2020.110102>
- Hatala, Z., & Puturuhi, F. (2021). Viterbi algorithm and its application to Indonesian speech recognition. *Journal of Physics: Conference Series*, *1752*(1), Article 012085. <https://doi.org/10.1088/1742-6596/1752/1/012085>
- Hossain, M. S., Al-Hammadi, M., & Muhammad, G. (2018). Automatic fruit classification using deep learning for industrial applications. *IEEE Transactions on Industrial Informatics*, *15*(2), 1027-1034. <https://doi.org/10.1109/TII.2018.2875149>
- Kiranyaz, S., Avci, O., Abdeljaber, O., Ince, T., Gabbouj, M., & Inman, D. J. (2021). 1D convolutional neural networks and applications: A survey. *Mechanical Systems and Signal Processing*, *151*, Article 107398. <https://doi.org/10.1016/j.ymsp.2020.107398>
- Naithani, K., Thakkar, V. M., & Semwal, A. (2018, August 22-24). *English language speech recognition using MFCC and HMM*. [Paper presentation]. International Conference on Research in Intelligent and Computing in Engineering (RICE), Salvador, El Salvador. <https://doi.org/10.1109/RICE.2018.8509046>
- Najkar, N., Razzazi, F., & Sameti, H. (2010). A novel approach to HMM-based speech recognition systems using particle swarm optimization. *Mathematical and Computer Modelling*, *52*(11-12), 1910-1920. <https://doi.org/10.1016/j.mcm.2010.03.041>
- Phoophuangpairroj, R. (2013). Determining guava freshness by flicking signal recognition using HMM acoustic models. *International Journal of Computer Theory and Engineering*, *5*(6), 877-884. <https://doi.org/10.7763/IJCTE.2013.V5.815>

- Phoophuangpairoj, R. (2014a). Automated classification of watermelon quality using non-flicking reduction and HMM sequences derived from flicking sound characteristics. *Journal of Information Science and Engineering*, 30(4), 1015-1033.
- Phoophuangpairoj, R. (2014b). Computerized unripe and ripe durian striking sound recognition using syllable-based HMMs. *Applied Mechanics and Materials*, 446-447, 927-935. <https://doi.org/10.4028/www.scientific.net/amm.446-447.927>
- Phoophuangpairoj, R. (2014c). Durian ripeness striking sound recognition using N-gram models with N-best lists and majority voting. In S. Boonkrong, H. Unger & P. Meesad (Eds), *Recent Advances in Information and Communication Technology: Proceedings of the 10th International Conference on Computing and Information Technology (IC2IT2014)* (pp. 167-176). Springer
- Phoophuangpairoj, R., & Srikun, N. (2014). Computerized recognition of pineapple grades using physicochemical properties and flicking sounds. *International Journal of Agricultural and Biological Engineering*, 7(3), 93-101.
- Phoophuangpairoj, R. (2020, October 21-22). *Recognizing breathing sounds using HMMs and grammar*. [Paper presentation]. Proceedings of the 5<sup>th</sup> International Conference on Information Technology (InCIT2020), ChonBuri, Thailand. <https://doi.org/10.1109/InCIT50588.2020.9310966>
- Raja S. L., Ambika, N, Divya, V., & Kowsalya, T, (2018). Fruit classification system using computer vision: A review. *International Journal of Trend in Research and Development*, 5(1), 22-26.
- Shahi, T. B., Sitaula, C., Neupane, A., & Guo, W. (2022). Fruit classification using attention-based MobileNetV2 for industrial applications. *Plos One* 17(2), Article e0264586. <https://doi.org/10.1371/journal.pone.0264586>
- Stevner, A. B. A., Vidaurre, D., Cabral, J., Rapuano, K., Nielsen, S. F. V., Tagliazucchi, E., Laufs, H., Vuust, P., Deco, G., Woolrich, M. W., Someren, E. V. & Kringelbach (2019). Discovery of key whole-brain transitions and dynamics during human wakefulness and non-REM sleep. *Nature Communications*, 10(1), Article 1035. <https://doi.org/10.1038/s41467-019-08934-3>
- Zeng, G. (2017, October 3-5). *Fruit and vegetables classification system using image saliency and convolutional neural network*. [Paper presentation]. *IEEE 3rd Information Technology and Mechatronics Engineering Conference (ITOEC)*, Chongqing, China. <https://doi.org/10.1109/ITOEC.2017.8122370>

## Development of Artificial Neural Network Model for Medical Specialty Recommendation

Winda Hasuki<sup>1</sup>, David Agustriawan<sup>1</sup>, Arli Aditya Parikesit<sup>1\*</sup>, Muammar Sadrawi<sup>1</sup>, Moch Firmansyah<sup>2</sup>, Andreas Whisnu<sup>3</sup>, Jacquelin Natasya<sup>1</sup>, Ryan Mathew<sup>4</sup>, Florensia Irena Napitupulu<sup>5</sup> and Nanda Rizqia Pradana Ratnasari<sup>1</sup>

<sup>1</sup>Department of Bioinformatics, School of Life Sciences, Indonesia International Institute for Life Sciences, Jakarta 13210, Indonesia

<sup>2</sup>Information Technology Department, Lira Medika Hospital, Jawa Barat 41314, Indonesia

<sup>3</sup>Information Technology Department, Indonesia International Institute for Life Sciences, Jakarta 13210, Indonesia

<sup>4</sup>Department of Biotechnology, School of Life Sciences, Indonesia International Institute for Life Sciences, Jakarta 13210, Indonesia

<sup>5</sup>Department of Food Science, School of Life Sciences, Indonesia International Institute for Life Sciences, Jakarta 13210, Indonesia

### ABSTRACT

Timely diagnosis is crucial for a patient's future care and treatment. However, inadequate medical service or a global pandemic can limit physical contact between patients and healthcare providers. Combining the available healthcare data and artificial intelligence methods might offer solutions that can support both patients and healthcare providers. This study developed one of the artificial intelligence methods, artificial neural network (ANN),

the multilayer perceptron (MLP), for medical specialist recommendation systems. The input of the system is symptoms and comorbidities. Meanwhile, the output is the medical specialist. Leave one out cross-validation technique was used. As a result, this study's F1 score of the model was about 0.84. In conclusion, the ANN system can be an alternative to the medical specialist recommendation system.

**Keywords:** Machine learning, medical specialty, multilayer perceptron, neural network, recommendation

#### ARTICLE INFO

##### Article history:

Received: 19 September 2022

Accepted: 25 January 2023

Published: 08 September 2023

DOI: <https://doi.org/10.47836/pjst.31.6.05>

##### E-mail addresses:

winda.hasuki@student.i3l.ac.id (Winda Hasuki)

david.agustrawan@i3l.ac.id (David Agustriawan)

arli@daad-alumni.de (Arli Aditya Parikesit)

muammar.sadrawi@i3l.ac.id (Muammar Sadrawi)

moch.firmansyah@pundiraya.co.id (Moch Firmansyah)

johnkecops@yahoo.co.uk (Andreas Whisnu)

jacquelin.natasya@student.i3l.ac.id (Jacquelin Natasya)

ryan.mathew@student.i3l.ac.id (Ryan Mathew)

florensia.napitupulu@i3l.ac.id (Florensia Irena Napitupulu)

nanda.ratnasari@i3l.ac.id (Nanda Rizqia Pradana Ratnasari)

\* Corresponding author

## INTRODUCTION

Digitalization of healthcare provides new possibilities to improve healthcare services. One problem that can arise in health care is limited physical contact between patients and healthcare providers, which can prolong the diagnosis process. Patients must rely on healthcare providers, such as primary care physicians, to determine the most suitable medical specialty for treating their condition. The delayed diagnosis can result in missed opportunities for intervention. Contact between patients and healthcare providers can be hindered due to various situations. For example, during the COVID-19 pandemic, it was harder for patients to meet healthcare providers (Lee et al., 2021). Such situations can also happen to patients who live in remote or impoverished areas.

With the increasing number of healthcare data, incorporating artificial intelligence (AI) methods can offer useful insights to help decision-making. One of the most popular methods in medical applications is the artificial neural network (ANN) (Jiang et al., 2017). The architecture of ANN consists of three types of layers: input, hidden, and output. Information or features from the external environment would be received by the input layer and passed to the hidden layers. In the hidden layers, the pattern of data would be extracted. After that, the output layer would present the network output (da Silva et al., 2017). In the simplest form, ANN can have no hidden layer, making it a single-layer neural network that consists of only input and output layers. Models with one or more hidden layers are usually referred to as multilayer neural networks. ANN can have a feed-forward or feedback architecture.

ANN has been applied in various studies, including classification, prediction, and diagnosis (Shahid et al., 2019). This method is chosen for many studies as it can process a large amount of data. It is also found to be less likely to overlook important information, and it can reduce diagnosis time (Amato et al., 2013). Although ANN is often applied for large datasets, some studies suggested that this method can also work for small datasets. Feng et al. (2019) created a model to predict material defects with 487 data. Their deep neural network model showed high accuracy. The ANN-based dengue predictive model also reached high accuracy, sensitivity, and specificity and was trained with a small dataset (Silitonga et al., 2021). In another study, a model trained with 116 data achieved an accuracy of 82% without signs of overfitting (Olson et al., 2018).

This study developed a classification model using ANN, focusing on one type of feed-forward neural network, which is the multilayer perceptron (MLP). MLP is fully connected, and it uses backpropagation during training. Some common machine-learning Python libraries were used to build, train, and test the MLP model, including Keras, TensorFlow, and scikit-learn. This study trained the model with a small dataset containing 111 data points. This dataset consisted of common symptoms, comorbidities, and medical specialties. Leave-one-out cross-validation (LOOCV) was also conducted to estimate the performance of the model. This study aimed to create a model that can recommend suitable medical specialties for patients based on their symptoms and comorbidities.

## RELATED WORK

### ANN in Healthcare

ANN has been implemented in many diagnostics models. Yao et al. (2019) applied ANN with a backpropagation procedure to diagnose diabetic retinopathy. This model was developed based on the results of multivariable logistic regression (MLR) using data from 530 residents. The AUC of the ANN model reached 0.84, which was higher than the AUC of MLR. Aguiar et al. (2016) developed two ANN models to support the diagnosis of pulmonary tuberculosis. The first was an MLP model for classification, while the second was for risk assignment. Both models showed good performance. In another study, an MLP model was developed to classify hypertension (Chai et al., 2021). The model achieved an accuracy of 0.76 and an AUC of 0.75. They noted that although their model cannot be used as a clinical decision-making tool, it can still be used as an early warning mechanism.

Besides diagnosis, ANN has also been used to help decision-making management. The ANN model was applied for syncope risk stratification in the Casagrande et al. (2016) study. This study also compared the ANN model to a multivariate logistic regression model. The ANN model showed better performance. Ippoliti et al. (2021) proposed ANN models to predict the outcome of hospital admission. The results showed that applying their models could reduce the average length of stay. The result of these studies can be useful for hospital managers. On a global scale, a forecasting model for the COVID-19 time series was created with ANN (Borghetti et al., 2021). Their study included data from 30 countries. The model they developed could predict time series behavior related to the number of COVID-19 infections and deaths. ANN has also been applied to analyze corruption in healthcare (Buscema et al., 2017). The result of this study suggested that countries with similar Human Development Index would perceive corruption in the same way.

### AI Methods for Medical Specialty Recommendation

Various algorithms have been applied to create a model for disease prediction or doctor recommendations for different purposes. Rémy et al. (2018) created a logistic regression model to predict which healthcare practitioner is the most appropriate for a patient. Some diseases may require multiple specialists to provide an accurate diagnosis, and their study aimed to see if it is possible to form a group of physicians using a probabilistic model. Their proposed model also assumed that 4 symptoms were enough to describe a disease and that patients have no comorbidities. A study by Kumar et al. (2021) also tested four machine learning approaches—Naive Bayes, random forest, logistic regression, and KNN. They created a website where users enter their symptoms and get medical specialty recommendations (pro-prediction). They also provide an option for specific predictions, such as prediction for heart disease and diabetes. The dataset that they used for pro-

prediction was coded into binary classification. The four models showed good accuracy for pro-prediction, with random forest showing the best performance (90.2%). In another study, Lee et al. (2021) applied deep learning-based NLP. They developed an AI chatbot that can give medical specialty recommendations. Their dataset consisted of 51,134 sentences and included data for 26 medical specialties. Implementing MLP in medical specialty recommendations has not been found in any literature but has been used for other applications such as diagnosis models.

### **Cross-validation Methods for Small Dataset**

In the development of machine learning models, cross-validation is often applied to evaluate the performance of the models. There are many cross-validation methods. The simplest and most common method is the hold-out cross-validation, in which the dataset is divided into training and testing sets, and the model would usually be trained only once. Usually, 80% of the dataset is used as the training set, while the remaining 20% is used for the testing set. However, this method is more suitable for large datasets. Another common method is k-fold cross-validation. For this method, there would be k iterations of training and validation; for each iteration, different segments would be used for validation (Refaeilzadeh et al., 2009). There is also the leave-one-out cross-validation (LOOCV), where the number of segments would be equal to the number of instances in the dataset (Webb et al., 2011). This method shows a lower bias compared to k-fold. However, it also shows higher variability in test error. In larger datasets, LOOCV is considered computationally expensive, but in small datasets, it can maximize the extension of the training set (Pasini, 2015).

### **Problem Statement**

Some situations can lead to patients being unable to see primary care providers for a diagnosis and referral to medical specialists. Models proposed in other studies often ignored comorbidities, even though it is important in deciding which medical specialty suits a patient's condition. This study addressed this problem by developing a model to give medical specialty recommendations based on the symptoms and comorbidities.

## **METHODOLOGY**

This study proposed an MLP model for a medical specialty recommendation system. The workflow consisted of four steps: data collection and cleaning, model building, model training and testing, and performance evaluation. All steps in this study were done in Python 3.6.13, with some libraries including Pandas, Numpy, TensorFlow, Keras, and scikit-learn. For the first step, Pandas and Numpy were used. Data on common symptoms and comorbidities, as well as the suitable medical specialties, were collected, creating a dataset for a multi-class classification problem. The categorical variables were coded into



binary classifications (0 or 1). There were some missing and ambiguous values found. These data were removed from the dataset. After that, the dataset was separated into input and output data. The output data was then converted into an array.

The MLP model was created by using Keras and Tensorflow. MLP was chosen as it is suitable for our dataset, which has labeled input. Due to the size of the dataset, it is not necessary to apply a more advanced model as well. For the MLP model, the sequential model API was chosen, while dense was chosen for the layers. The initial weight for the model was set with HeUniform. Different combinations of hyperparameters, such as the number of hidden layers, number of nodes, and activation function, were tried for the model. The performance of the model stopped improving significantly after the addition of the fifth hidden layer. As for the number of nodes, there were 26 nodes in the input layer. The number of nodes for each hidden layer was 200, 150, 100, 50, and 9 for the last layer. Softmax was chosen as the activation function for the output layer, while the performance of ReLU and tanh were compared for the hidden layers of the model. The former showed an overall better result. The model was then compiled; the loss function was set to categorical hinge loss, Adam was chosen as the optimizer, and the learning rate was set to 0.001. The model was built using the Keras Classifier class. For the training process, LOOCV was conducted to estimate the performance of the model. Because the dataset used in this study was small, LOOCV was chosen to avoid overfitting (Pasini, 2015). This way, we could assess whether the model could generalize patterns in the training set despite the limited amount of data points. LOOCV was done using the function from the scikit-learn library. The epoch and batch size were set to 40 and 32, respectively.

The average score from LOOCV was used to evaluate the performance of the model. The prediction results from LOOCV were compared with the actual data. The accuracy was computed. A confusion matrix was created to see the classification performance of the model. The visualization was made using the Matplotlib library. The metrics used in this study were precision, recall, and F1 score. These metrics were calculated from rates of true positive, true negative, false positive, and false negative (Equations 1-3).

$$\text{Precision} = \frac{\text{true positives}}{\text{true positives} + \text{false positives}} \quad (1)$$

$$\text{Recall} = \frac{\text{true positives}}{\text{true positives} + \text{false negatives}} \quad (2)$$

$$\text{F1 score} = 2 \times \frac{\text{precision} \times \text{recall}}{\text{precision} + \text{recall}} \quad (3)$$

The F1 score was computed for each class. From this score, the macro average and weighted average F1 score can be calculated.

## RESULTS AND DISCUSSION

This study utilized the ANN method for generating a chatbot system using the symptom and comorbidities as the input and the medical specialist as the output. In total, 129 data of common symptoms, comorbidities, and the corresponding medical specialist were collected. After removing missing and ambiguous values, the final dataset consisted of 111 instances. In order to handle the missing and ambiguous values, we checked and manually filtered the data by eye. It is time-consuming, but having a good data portion in the training session will likely positively affect the testing results.

For the inputs, there were 18 symptoms and 8 comorbidities included in the dataset: chest discomfort, fainting, discomfort in the shoulder, neck, back, and jaw, shortness of breath, fractured bone, persistent headache, cuts, foreign material stuck, skin infection, the problem with vision, fever, diarrhea, cold sweat, back pain, weakness, trouble in speaking seeing and walking, vomit, and stomachache for common symptoms; hypertension, diabetes, heart disease, liver disease, stroke, tumor/cancer, respiration disease, and gastric for common comorbidities.

Meanwhile, there are nine types of medical specialties in the dataset. These medical specialties are internists, neurologists, cardiologists, ophthalmologists, pulmonologists, orthopedists, general surgeons, dermatologists, and Ear, Nose, and Throat/ENT specialists.

The percentage of data for each medical specialty can be seen in Table 1. Compared to other medical specialties, internists had the highest amount of data, while ENT had the lowest. Three medical specialties—internist, neurologist, and cardiologist—made up more than 70% of the dataset. On the other hand, each of the rest of the medical specialties made up less than 10%. Some solutions are suggested for the class imbalance problem in multi-class classification. These solutions include data resampling (oversampling or undersampling) and changing learning algorithms (Agrawal et al., 2015; Koziarski et al., 2020; So & Valdez, 2021; Tanha et al., 2020). Another important suggestion is choosing the most suitable performance evaluation method (Alejo et al., 2013; Luque et al., 2019).

The architecture of the best model in this study can be seen in Figure 1. It is an MLP model with five hidden layers, with the Rectified linear unit (ReLU) as the activation function for these layers. ReLU is considered the most popular activation function in deep learning (Cao et al., 2018). On the output layer, the chosen activation

Table 1  
*Percentage of data for each medical specialty*

Medical Specialty	Percentage of Data (%)
SpPD / Internist	28.8
SpS / Neurologist	25.2
SpJP / Cardiologist	21.6
SpM / Ophthalmologist	8.1
Paru / Pulmonologist	5.4
SpOT / Orthopedist	4.5
SpKK / Dermatologist	2.7
SpB / General Surgeon	2.7
THT / ENT	0.9

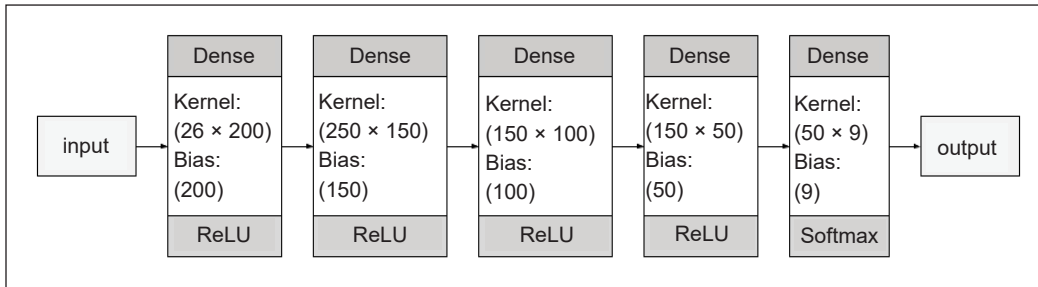


Figure 1. Architecture of the model

function was softmax. This activation function was also chosen because only one correct (medical specialty) answer is needed. After the model was compiled, the predictions made by the model during the LOOCV iterations with the actual data were compared. The result showed that the model has about 85.6% accuracy.

Because of the class imbalance, accuracy might not be the best metric to evaluate the model performance. Accuracy is the result of dividing the number of correct predictions by the total number of predictions without considering the number of correct classifications for each class. Accuracy with an imbalanced dataset can be misleading, as the score would not show how well the model performs at classifying the underrepresented classes. Kulkarni et al. (2021) suggested that metrics based on a confusion matrix can be more useful for evaluating the performance of models trained with an imbalanced dataset. These metrics include precision, recall, and F1 score.

Although the accuracy score was good, the model only seemed to classify some medical specialties correctly. It can be observed in the visualization of the confusion matrix (Figure 2). The model can classify data of internists, neurologists, and cardiologists really well; it can classify all of the cardiologist data correctly. However, the model showed poorer performance for classes with fewer data. The model seemed to misclassify all data for the two most underrepresented classes, ENT and surgeon. The macro average and weighted average F1 scores were computed to evaluate the performance of the model. Due to the class imbalance, the weighted average F1 score was higher than the macro average. The values for these metrics were about 0.59 for the macro average and about 0.84 for the weighted average.

The precision, recall, and F1 score were obtained from the confusion matrix. The scores for each class can be seen in Table 2. High precision, recall, and F1 scores were shown for the three classes with the highest amount of data. Neurologist, the class with the most data, achieved an F1 score of 0.91. Another class, internist, also achieved the same score. A perfect score on all three metrics was observed for the cardiologist class. The model also seemed able to classify all orthopedist data correctly, but classify some data of other classes as an orthopedist, resulting in perfect recall but a lower precision score. The pulmonologist

class can see the opposite, as the precision is higher than recall. Most data classified as pulmonologists were correct, but the model misclassified 40% of pulmonologist data. For ophthalmologist and dermatologist classes, the model showed poor performance, with an F1 score of 0.53 and 0.40, respectively.

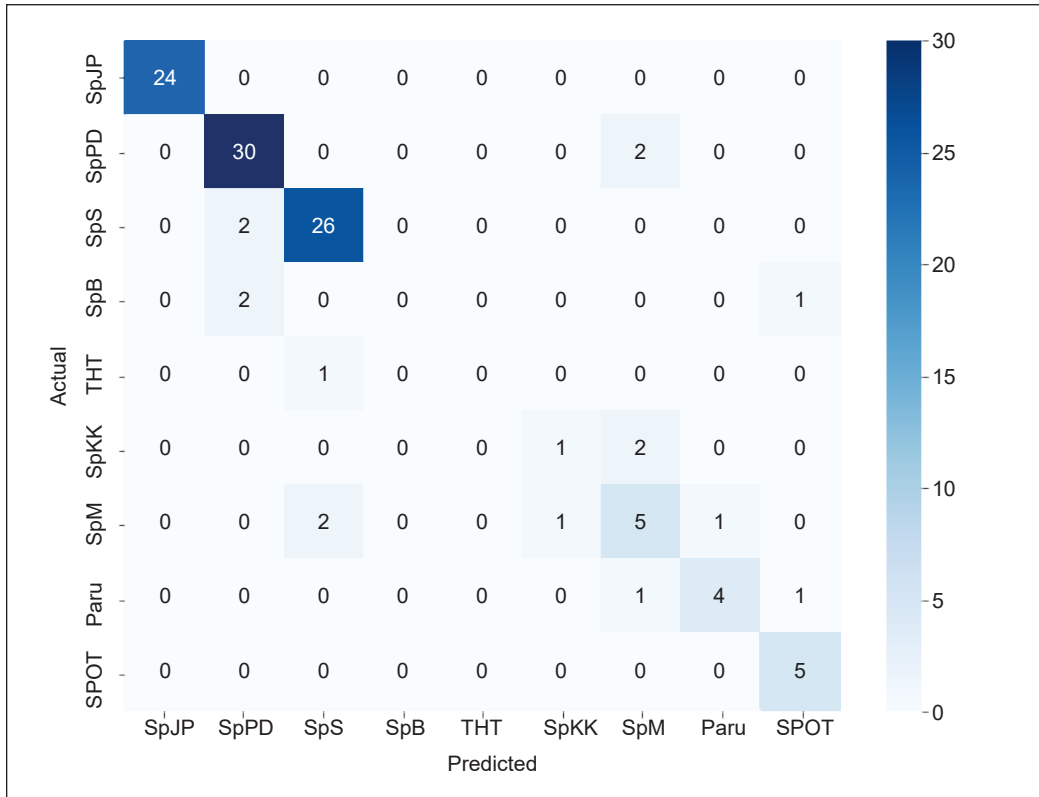


Figure 2. Heat map of the confusion matrix

Table 2  
Precision, recall, and F1 score for each medical specialty

Medical Specialty	Precision	Recall	F1 score
SpPD	0.88	0.94	0.91
SpS	0.90	0.93	0.91
SpJP	1.00	1.00	1.00
SpM	0.50	0.56	0.53
Paru	0.80	0.60	0.73
SpOT	0.71	1.00	0.83
SpKK	0.50	0.33	0.40
SpB	0.00	0.00	0.00
THT	0.00	0.00	0.00

The class imbalance in the dataset affected the performance of the model. Lee et al. (2021) also used an imbalanced dataset in their study in which they developed a deep learning-based NLP for medical specialty recommendations. Two models in their study achieved a macro average F1 score of 0.74 and 0.77. Compared to this study, the dataset they used had more instances; their dataset contained 51,134 data points. The better classification performance despite the class imbalance can be due to the dataset size and the use of a pre-trained model.

Besides the small and imbalanced dataset, this study also has other limitations. Firstly, it would be difficult for the model to recommend patients with more complicated conditions: who have several symptoms and at the same time also have multiple comorbidities. The next limitation is that we did not consider the sub-specialist. For future works, we will consider using more advanced AI techniques, such as convolutional neural networks (CNN).

## CONCLUSION

In this study, an ANN model was developed for medical specialty recommendations. ANN can be a useful method for classification, even for smaller datasets. The model proposed in this study can correctly classify classes of medical specialties with 24 to 32 data points, which shows that ANN can be suitable for small datasets. However, the class imbalance in the dataset caused the model to perform well at predicting only 5 out of 9 medical specialties. More data is needed, especially for classes such as ENT, Surgeon, Ophthalmologist, and Dermatologist.

## ACKNOWLEDGMENT

The project is funded under Hibah Keilmuan Dirjen Dikti 2022, Indonesia. The authors thank the Department of Research and Community Service of Indonesia International Institute for Life Sciences for supporting this research.

## REFERENCES

- Agrawal, A., Viktor, H. L., & Paquet, E. (2015, November 12-14). SCUT: Multi-class imbalanced data classification using SMOTE and cluster-based undersampling. [Paper presentation]. *International Joint Conference on Knowledge Discovery, Knowledge Engineering and Knowledge Management (IC3K)*, Lisbon, Portugal. <https://doi.org/10.5220/0005595502260234>
- Aguiar, F. S., Torres, R. C., Pinto, J. V. F., Kritski, A. L., Seixas, J. M., & Mello, F. C. Q. (2016). Development of two artificial neural network models to support the diagnosis of pulmonary tuberculosis in hospitalized patients in Rio de Janeiro, Brazil. *Medical & Biological Engineering & Computing*, 54(11), 1751-1759. <https://doi.org/10.1007/s11517-016-1465-1>
- Alejo, R., Antonio, J. A., Valdovinos, R. M., & Pacheco-Sánchez, J. H. (2013). Assessments Metrics for Multi-class Imbalance Learning: A Preliminary Study. In J. A. Carrasco-Ochoa, J. F. Martinex-Trinidad, J. S.

- Rodriuez & G. S. D. Baja (Eds.), *Pattern Recognition: 5th Mexican Conference, MCPR 2013, Querétaro, Mexico Proceedings 5* (pp. 335-343). Springer. [https://doi.org/10.1007/978-3-642-38989-4\\_34](https://doi.org/10.1007/978-3-642-38989-4_34)
- Amato, F., López, A., Peña-Méndez, E. M., Vañhara, P., Hampl, A., & Havel, J. (2013). Artificial neural networks in medical diagnosis. *Journal of Applied Biomedicine*, *11*(2), 47-58. <https://doi.org/10.2478/v10136-012-0031-x>
- Borgi, P. H., Zakordonets, O., & Teixeira, J. P. (2021). A COVID-19 time series forecasting model based on MLP ANN. *Procedia Computer Science*, *181*, 940-947. <https://doi.org/10.1016/j.procs.2021.01.250>
- Buscema, P. M., Gitto, L., Russo, S., Marcellusi, A., Fiori, F., Maurelli, G., Massini, G., & Mennini, F. S. (2017). The perception of corruption in health: AutoCM methods for an international comparison. *Quality & Quantity*, *51*(1), 459-477. <https://doi.org/10.1007/s11135-016-0315-4>
- Cao, C., Liu, F., Tan, H., Song, D., Shu, W., Li, W., Zhou, Y., Bo, X., & Xie, Z. (2018). Deep learning and its applications in biomedicine. *Genomics, Proteomics & Bioinformatics*, *16*(1), 17-32. <https://doi.org/10.1016/j.gpb.2017.07.003>
- Casagrande, I., Costantino, G., Falavigna, G., Furlan, R., & Ippoliti, R. (2016). Artificial neural networks and risk stratification models in emergency departments: The policy maker's perspective. *Health Policy*, *120*(1), 111-119. <https://doi.org/10.1016/j.healthpol.2015.12.003>
- Chai, S. S., Cheah, W. L., Goh, K. L., Chang, Y. H. R., Sim, K. Y., & Chin, K. O. (2021). A multilayer perceptron neural network model to classify hypertension in adolescents using anthropometric measurements: A cross-sectional study in Sarawak, Malaysia. *Computational and Mathematical Methods in Medicine*, *2021*, Article 2794888. <https://doi.org/10.1155/2021/2794888>
- da Silva, I. N., Spatti, D. H., Flauzino, R. A., Liboni, L. H. B., & Alves, S. F. D. R. (2017). Artificial neural network architectures and training processes. In *Artificial Neural Networks: A Practical Course* (pp. 21-28). Springer International Publishing. [https://doi.org/10.1007/978-3-319-43162-8\\_2](https://doi.org/10.1007/978-3-319-43162-8_2)
- Feng, S., Zhou, H., & Dong, H. (2019). Using deep neural network with small dataset to predict material defects. *Materials & Design*, *162*, 300-310. <https://doi.org/10.1016/j.matdes.2018.11.060>
- Ippoliti, R., Falavigna, G., Zanelli, C., Bellini, R., & Numico, G. (2021). Neural networks and hospital length of stay: An application to support healthcare management with national benchmarks and thresholds. *Cost Effectiveness and Resource Allocation*, *19*(1), Article 67. <https://doi.org/10.1186/s12962-021-00322-3>
- Jiang, F., Jiang, Y., Zhi, H., Dong, Y., Li, H., Ma, S., Wang, Y., Dong, Q., Shen, H., & Wang, Y. (2017). Artificial intelligence in healthcare: Past, present and future. *Stroke and Vascular Neurology*, *2*(4), 230-243. <https://doi.org/10.1136/svn-2017-000101>
- Koziarski, M., Woźniak, M., & Krawczyk, B. (2020). Combined cleaning and resampling algorithm for multi-class imbalanced data with label noise. *Knowledge-Based Systems*, *204*, Article 106223. <https://doi.org/10.1016/j.knosys.2020.106223>
- Kulkarni, A., Chong, D., & Batarseh, F. A. (2021). Foundations of data imbalance and solutions for a data democracy. In F. A. Batarseh & R. Yang (Eds.), *Data Democracy* (pp. 83-106). Academic Press. <https://doi.org/10.1016/B978-0-12-818366-3.00005-8>

- Kumar, A., Prakash, U. M., & Sharma, G. K. (2021). Disease prediction and doctor recommendation system using machine learning approaches. *International Journal for Research in Applied Science and Engineering Technology*, 9(VII), 34-44. <https://doi.org/10.22214/ijraset.2021.36234>
- Lee, H., Kang, J., & Yeo, J. (2021). Medical specialty recommendations by an artificial intelligence chatbot on a smartphone: Development and deployment. *Journal of Medical Internet Research*, 23(5), Article e27460. <https://doi.org/10.2196/27460>
- Luque, A., Carrasco, A., Martín, A., & de las Heras, A. (2019). The impact of class imbalance in classification performance metrics based on the binary confusion matrix. *Pattern Recognition*, 91, 216-231. <https://doi.org/10.1016/j.patcog.2019.02.023>
- Olson, M., Wyner, A., & Berk, R. (2018, December 2-8). *Modern neural networks generalize on small data sets*. [Paper presentation]. Conference on Neural Information Processing Systems (NeurIPS), Montreal, Canada.
- Pasini, A. (2015). Artificial neural networks for small dataset analysis. *Journal of Thoracic Disease*, 7(5), 953-960. <https://doi.org/10.3978/j.issn.2072-1439.2015.04.61>
- Refaeilzadeh, P., Tang, L., & Liu, H. (2009). Cross-validation. In L. Liu & M. T. Oszu (Eds.), *Encyclopedia of Database Systems* (pp. 532-538). Springer. [https://doi.org/10.1007/978-0-387-39940-9\\_565](https://doi.org/10.1007/978-0-387-39940-9_565)
- Rémy, N. M., Martial, T. T., & Clémentin, T. D. (2018). The prediction of good physicians for prospective diagnosis using data mining. *Informatics in Medicine Unlocked*, 12, 120-127. <https://doi.org/10.1016/j.imu.2018.07.005>
- Shahid, N., Rappon, T., & Berta, W. (2019). Applications of artificial neural networks in health care organizational decision-making: A scoping review. *PloS One*, 14(2), Article e0212356. <https://doi.org/10.1371/journal.pone.0212356>
- Silitonga, P., Bustamam, A., Muradi, H., Mangunwardoyo, W., & Dewi, B. E. (2021). Comparison of dengue predictive models developed using artificial neural network and discriminant analysis with small dataset. *Applied Sciences*, 11(3), Article 943. <https://doi.org/10.3390/app11030943>
- So, B., & Valdez, E. A. (2021). *The SAMME.C2 algorithm for severely imbalanced multi-class classification*. ArXiv. <https://doi.org/10.48550/arXiv.2112.14868>
- Tanha, J., Abdi, Y., Samadi, N., Razzaghi, N., & Asadpour, M. (2020). Boosting methods for multi-class imbalanced data classification: an experimental review. *Journal of Big Data*, 7(1), Article 70. <https://doi.org/10.1186/s40537-020-00349-y>
- Webb, G. I., Sammut, C., Perlich, C., Horváth, T., Wrobel, S., Korb, K. B., Noble, W. S., Leslie, C., Lagoudakis, M. G., Quadrianto, N., Buntine, W. L., Quadrianto, N., Buntine, W. L., Getoor, L., Namata, G., Getoor, L., Han, X. J. J., Ting, J. A., Vijayakumar, S., ... & Raedt, L. D. (2011). Leave-One-Out Cross-Validation. In C. Sammut & G. I. Webb (Eds.), *Encyclopedia of Machine Learning* (pp. 600-601). Springer. [https://doi.org/10.1007/978-0-387-30164-8\\_469](https://doi.org/10.1007/978-0-387-30164-8_469)
- Yao, L., Zhong, Y., Wu, J., Zhang, G., Chen, L., Guan, P., Huang, D., & Liu, L. (2019). Multivariable logistic regression and back propagation artificial neural network to predict diabetic retinopathy. *Diabetes, Metabolic Syndrome and Obesity*, 12, 1943-1951. <https://doi.org/10.2147/DMSO.S219842>





## Effect of Scaling the Electrostatic Interactions on the Free Energy of Transfer of Azurin from Water to Lipid Membrane Determined by Coarse-grained Simulations

Dian Fitrasari<sup>1</sup>, Acep Purqon<sup>1</sup> and Suprijadi<sup>1,2\*</sup>

<sup>1</sup>Department of Physics, Bandung Institute of Technology, Bandung, Jawa Barat 40132, Indonesia

<sup>2</sup>Research Centre of Nanoscience and Nanotechnology, Bandung Institute of Technology, Bandung, Jawa Barat 40132, Indonesia

### ABSTRACT

Azurin protein potentially plays an important role as an anti-cancer therapeutic agent, particularly in treating breast cancer in experiments and showing without having a negative effect on normal cells. Although the interaction mechanism between protein and lipid membrane is complicated, it can be modeled as protein-lipid interaction. Since the all-atom (AA) model simulation is cost computing, we apply a coarse-grained (CG-MARTINI) model to calculate the protein-lipid interaction. We investigate the binding free energy value dependency by varying the windows separation and electrostatic scale parameters. After scaling the electrostatic interactions by a factor of 0.04, the best result in terms of free energy is -140.831 kcal/mol, while after window-separation optimization, it reaches -71.859 kcal/mol. This scaling was necessary because the structures from the CG MARTINI model have a higher density than the corresponding all-atom structures. We thus postulate that electrostatic interactions should be scaled down in this case of CG-MARTINI simulations.

*Keywords:* Coarse-Grained MARTINI method, electrostatic scaling, free energy analysis, protein-lipid membrane model, windows separation

### ARTICLE INFO

*Article history:*

Received: 20 September 2022

Accepted: 06 March 2023

Published: 08 September 2023

DOI: <https://doi.org/10.47836/pjst.31.6.06>

*E-mail addresses:*

dianfitrasari30@gmail.com (Dian Fitrasari)

acep.purqon@itb.ac.id (Acep Purqon)

suprijadi@itb.ac.id (Suprijadi)

\* Corresponding author

### INTRODUCTION

Azurin is one of the blue copper proteins known as an anti-cancer agent (Frauenfelder et al., 2009), and it is produced by the gram-negative bacteria *Pseudomonas aeruginosa*. Azurin is widely known as a donor in the electron transfer process (Pozdnyakova & Wittung-Stafshede, 2001). Moreover, the

blue copper ions in the Azurin active site contribute to this protein's stability (Pozdnyakova & Wittung-Stafshede, 2001; Pozdnyakova et al., 2002). Furthermore, the protein is also an anti-cancer agent that causes apoptosis without much negative effect in cancer patients when it enters the human breast cancer cells (Frauenfelder et al., 2009). The less negative effect in Azurin interaction relates to the interaction with the normal cell under treatment. It represents the relation between Azurin as the protein and membrane lipids. The interaction between protein and membrane accommodates such essential processes, i.e., membrane trafficking, membrane protrusions, cytokinesis, signaling, and cell communication (Arumugam et al., 2011).

The interaction between protein and membrane has been modeled by membrane insertion. The challenge of this model is to identify the folded structure of the protein membrane. The sequence statistic succeeded in the comprehensive understanding of energy, which enforces the importance of membrane insertion to acknowledge this challenge. Numerous work approach has been made to define the free energy of amino-acid insertion. There are disagreements between experiment and theory. On the other hand, molecular dynamic simulation has been developed through various applications of membrane insertion and reproducing experimental free energy. However, the differences in microscopic processes make usable free energy of membrane insertion difficult (Gumbart & Roux, 2012).

Free energy transfer has been determined for arginine and leucine amino acids using Free Energy Perturbation (FEP) method. There is a significant result regarding the insertion penalty. The result is reduced and has the same compression observed in the experiment-based scale (Gumbart et al., 2011). On the other hand, simulation time challenges and precision dynamics to study the fluctuation of this interaction establish researchers to develop various models and methods. One type of model which narrates the complex simulation with efficient time is the CG-MARTINI model by Marrink et al. (2007).

The CG models typically provide the mapping of four heavy atoms of Carbon (C), Nitrogen (N), Oxygen (O), and Phosphor (P) in one bead. The mapping definition builds the complex system, such as protein-lipid interaction, which is less computationally than the AA model. There are some coarse-grained (CG) models, and CG-MARTINI models provide a good model of the protein-lipid environment. However, calculating the precise models from CG-MARTINI is quite challenging because of the different degrees of freedom from the beads mapping.

Since current CG-MARTINI lacks copper information, we use the active site binding from other work's definition (Kurniawan et al., 2019). The copper also describes the electron transfer related to this protein's stabilization. Then, we analyze the dynamics, interaction, and free energy values to understand whether Azurin is favorable in the lipid system. Meanwhile, even with a CG model, free energy calculation still needs a longer

simulation to reach the expected values. This study uses FEP as one widely known method to calculate precise energy values. In general, the FEP application is used for calculating small molecules or mutations. The challenge of a complex system with FEP analysis relates to the magnification of perturbation.

For this reason, we optimize the two parameters we expect to impact to reach a shorter simulation and accurate result. The electrostatic scaling parameter was previously studied by Jiang et al. (2009), increasing the acceptance ratio and decreasing free energy values (Li & Nam, 2020). The second parameter which we optimize is an electrostatic scaling parameter. Previous research by Beveridge and DiCapua (1989) also states that the precision of the electrostatic scaling parameter is higher than the Van Der Waals (VDW) parameter.

This work investigates the relation between area per lipid (APL) and density of the CG-MARTINI model with free energy value. To investigate the relationship or scaling between electrostatic parameters and free energy value. We investigate the possibility of finding a scaling factor between CG and all-atom (AA) simulation. The potential candidate parameter could be in tuning the electrostatic parameter so that the electrostatic scaling dependency is interesting to be discussed.

## METHODOLOGY

### Coarse-grained Method

In this study, the CG-MARTINI model is used to build the protein and membrane lipid structure, and it is a CG model type describing four heavy atoms in one bead. The definition of beads makes the complex system simulation achievable with less computational cost. Although the CG-MARTINI has less resolution and diverges from the AA model, the physical properties can maintain for the whole system. This model widely uses in a complex system to understand the dynamic trend.

### Free Energy Perturbation (FEP)

Alchemical FEP can analyze the physical properties in this research. In this method, the Hamiltonian system is defined by the general extent parameter,  $\lambda$ , and the initial state,  $a$ , and the final state,  $b$ , can be connected by this parameter. It is described and achieved by the Hamiltonian linear combination by Beveridge and Mark (Beveridge & DiCapua, 1989; Mark, 1998). Equation 1 is as follows:

$$H(x, p_x; \lambda) = H_0(x, p_x) + \lambda H_b(x, p_x) + (1 - \lambda) H_a(x, p_x) \quad (1)$$

$H_a(x, p_x)$  describes the Hamiltonian for the group of atoms, representing the initial state  $a$ . Meanwhile,  $\lambda H_b(x, p_x)$  is the interaction of the final state,  $b$ . Hamiltonian  $H_0(x, p_x)$  describes atoms that are not transforming during simulation. Furthermore,  $\lambda$  and  $1 - \lambda$

are the initial and final Hamiltonian parameters. Those parameters describe the function of energy and forces.

In this equation, the coupling parameter is shown as  $\lambda_{LJ}$ . It is a scale of the Lennard-Jones interactions. Electrostatic interactions describe as  $\lambda_{elec}$ . The actual value of  $\lambda$  is as stated in Equation 2:

$$V_{NB}(r_{ij}) = \lambda_{LJ} \epsilon_{ij} \left[ \left( \frac{R_{ij}^{min\ 2}}{r_{ij}^2 + \delta(1 - \lambda_{LJ})} \right)^6 - \left( \frac{R_{ij}^{min\ 2}}{r_{ij}^2 + \delta(1 - \lambda_{LJ})} \right)^3 \right] + \lambda_{elec} \frac{q_i q_j}{\epsilon_1 r_{ij}} \quad (2)$$

The free energy calculation will not change the intermolecular bonded potentials in this method. The perturbed atom which interacts in a vacuum is scale. However, in hydration conditions, the interaction is scale is only non-bonded interactions. The free energy difference, which is defined between the initial and final state, is as stated in Equation 3:

$$\Delta A_{a \rightarrow b} = -\frac{1}{\beta} \ln(\exp\{-\beta[H_b(x, p_x) - H_a(x, p_x)]\}) \quad (3)$$

Here,  $\beta^{-1} \equiv k_B T$ . The Boltzmann constant and temperature describe by  $k_B$  and  $T$ , respectively. The Hamiltonian for states  $a$  and  $b$  describes by  $H_a(x, p_x)$  and  $\lambda H_b(x, p_x)$ , respectively. The ensemble average over configuration denotes by  $\langle \dots \rangle_a$ . It is representative of the initial reference state,  $a$ . The  $a$  series of transformations between non-physical, intermediate states along a well-delineated pathway that connects  $a$  to  $b$  is replacing the transformation between two thermodynamic states. Here we assume the Helmholtz free energy ( $A$ ) is under the constant volume. Meanwhile, the constant-pressure system thermodynamics should be described by Gibbs free energy ( $G$ ), with  $G=A+PV$ , where  $P$  is pressure, and  $V$  is volume. However, the  $PV$  term is typically small for biomolecule systems (Zhu et al., 2022). In conclusion, we consider the  $\Delta A_{a \rightarrow b} = \Delta G_{a \rightarrow b}$ .

The pathway is characterized by the general extent parameter  $\lambda$  causing the Hamiltonian and the free energy as a continuous function between  $a$  and  $b$  (Equation 4):

$$\Delta G_{a \rightarrow b} = -\frac{1}{\beta} \ln(\exp\{-\beta[H(x, p_x; \lambda_{i+1}) - H(x, p_x; \lambda_i)]\}) \quad (4)$$

$N$  describes the number of intermediate stages. Meanwhile, Gibbs's free energy, which we use in this work, is absolute free energy symbolized by  $\Delta G$ .

### Model and Software Package

We perform the molecular dynamic simulation in this study using the NAMD 2.12-multicore program package (Phillips et al., 2020). Visualizing Azurin and lipid membrane use VMD 1.9.3 (Humphrey et al., 1996). The initial configuration of Azurin obtains from a protein data bank with PDB ID: 1AZU (Adman & Jensen, 1981), while The VMD 1.9.3 is used to

prepare the initial structure coordinates for the MARTINI CG model through the coarse-grained builder menu. Moreover, the Azurin structure has 128 residues and comprises two layers of sheet- $\beta$  with eight  $\beta$ -strands. This initial state uses a 2.7 Å resolution X-ray structure. The initial configuration of Azurin contains 930 atoms with one copper.

The AA structure is then modeled in CG structure. This process maps 930 atoms to 269 beads. The hydration state is defined by adding water molecules in the form of BP<sub>4</sub> (Marrink et al., 2007) to prevent the water from freezing at room temperature. This anti-freeze (AF) water model contains around 10% of total water molecules. The salt concentration of this model is 0.1 mol/L, and the coulomb potential defines by cut-offs 9 Å and 15 Å. The minimization and equilibration time step is 10 fs with an NPT ensemble. The final state contains the water molecules and POPC lipid membrane and is neutralized by adding 3 Na<sup>+</sup> ions. In this state, the molecules of POPC are assigned as atoms that appear during the simulation. The parameter that shows atoms appearing during a simulation is flag characterization. The flag characterization is shown as a +1.00 value if the atoms appear in the final state. This model represents a system with a salt concentration of 0.1 mol/L.

## RESULTS AND DISCUSSION

In this study, we have two models of Azurin. The first model describes Azurin hydration, and the second describes Azurin with POPC membrane lipids. In the first model, we analyze free energy hydration. We analyze free energy values in the second model by optimizing the separation of the windows ( $\delta\lambda$ ) and electrostatic parameters  $\lambda_{elec}$  using various parameters.

### Azurin Hydration

The first model describes the free energy of hydration Azurin. In this model, we define two states, the Azurin appearing in the final state by flag characterization +1.00. The environment described by the water molecule remains still, defined by 0.00 flag characterization. The free energy value is defined by the change of exnihilated to annihilation Azurin in water. The scheme of the perturbation by this system is shown in Figure 1.

The free energy values of Azurin hydration relate to the  $\lambda$  state condition, shown in Figure 1. Figure 2(a) shows the free

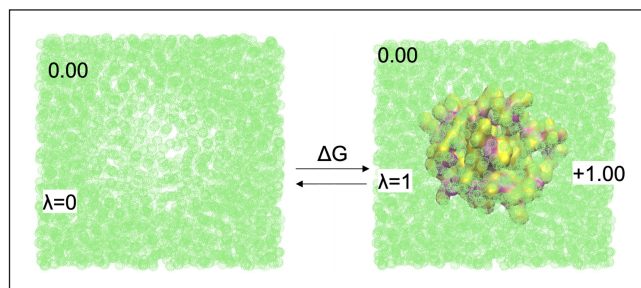


Figure 1. Scheme for free energy calculation in the model I,  $\lambda=0$  represents the water system as the initial state, and  $\lambda=1$  represents the Azurin in water as the final state. The Azurin is shown in the purple and yellow surfaces. The water is shown in the green box. The flag characterization for the water box is 0.00, which means water is unchanged during the simulation. The Azurin system uses flag characterization +1.00, which means appearing in the final state.

energy values as a function of the  $\lambda$  state, and Figure 2(b) shows the average electrostatic energy difference. The dotted line in Figure 2(a) shows the annihilated Azurin free energy. The dotted line in Figure 2(b) shows the annihilated Azurin. The simulation was done for 100000 steps with an electrostatic parameter  $\lambda_{elec} = 0.5$ , Lennard-jones parameter  $\lambda_{LJ} = 1.0$ , and  $21(\delta\lambda = 0.05)$  windows separation. The change of free energy hydration is  $-174.636$  kcal/mol. Meanwhile, the average electrostatic energy difference changes are  $-101.298$  kcal/mol.

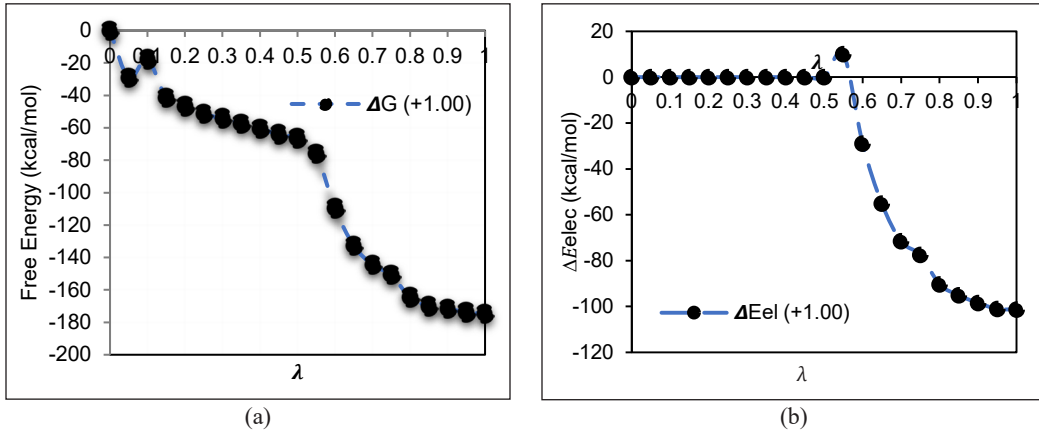


Figure 2. The analysis of free energy and average electrostatic energy difference in model I: (a) The free energy of annihilated Azurin during simulation with  $\Delta G = -174.636$  kcal/mol; and (b) The average electrostatic energy difference of annihilated Azurin:  $\Delta E_{el} = -101.298$  kcal/mol.

### The Effect of Azurin Insertion in Membrane Lipids POPC

The second model describes the free energy of Azurin in POPC. In this model, we define two states, the Azurin appearing in the final state by flag characterization +1.00. The environment described by the POPC-water remains still, defined by 0.00 flag characterization. It appears Azurin defines the free energy value in POPC. The scheme of the perturbation by this system is shown in Figure 3.

The free energy values of Azurin in POPC relate to the state condition, shown in Figure 4. Figure 4(a) shows the free energy values as a function of the  $\lambda$  state, and Figure 4(b) shows the average electrostatic

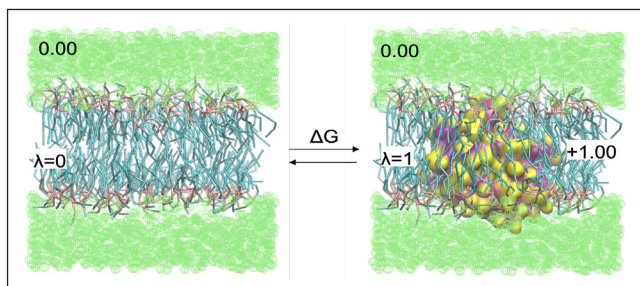


Figure 3. Scheme for free energy calculation in model II.  $\lambda=0$  represent the POPC system as the initial state, and  $\lambda=1$  represents the Azurin in POPC as the final state. The Azurin is shown in purple and yellow surface, and the water box is shown in the green box. Moreover, the POPC membrane is shown by lines blue and pink. The flag characterization for the water box is 0.00, which means water is unchanged during the simulation. The Azurin system uses flag characterization +1.0,0, which means appearing in the final state.

energy difference. The dotted line in Figure 4(a) shows the annihilated Azurin free energy. The dotted line in Figure 4(b) shows the annihilated Azurin and the straight line shows the changes in average electrostatic energy differences. The simulation was done for 100000 steps with electrostatic parameter  $\lambda_{elec} = 0.5$ , Lennard-jones parameter  $\lambda_{LJ} = 1.0$  and 21 ( $\delta\lambda = 0.05$ ) windows separation. The changes in free energy hydration are  $-200.340$  kcal/mol. Meanwhile, the average electrostatic energy difference changes are  $-130.02$  kcal/mol.

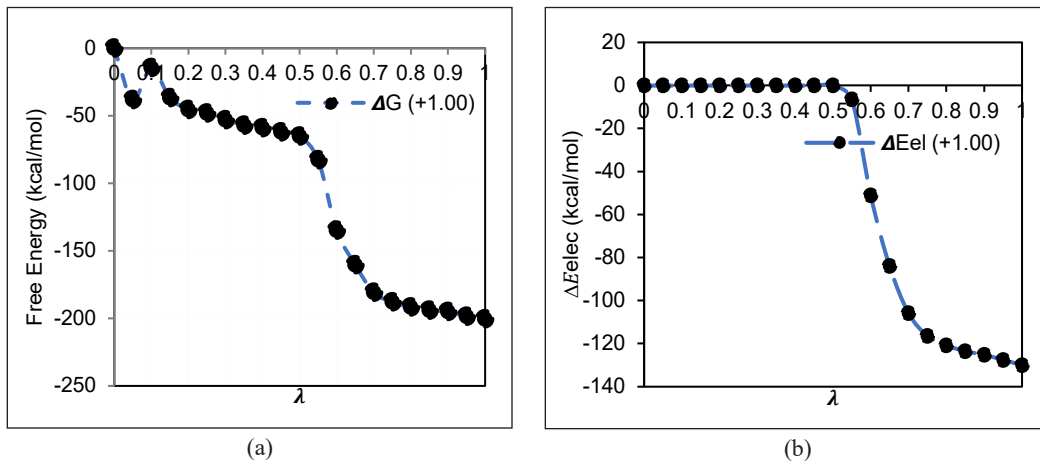


Figure 4. The analysis of free energy and average electrostatic energy difference in model II. (a) The free energy of annihilated Azurin during simulation with  $\Delta G = -200.340$  kcal/mol; (b) The average electrostatic energy difference of annihilated Azurin:  $\Delta E_{el} = -130.02$  kcal/mol

### The Difference Between Azurin Hydration Free Energy and Azurin Insertion in Membrane Lipids

Figure 5(a) shows the free energy difference between Azurin in water and the POPC lipid membrane. Figure 5(a) shows a dotted line showing Azurin hydration, and the bold line shows Azurin in POPC. Figure 5(b) shows the changes in the average electrostatic energy difference between Azurin hydration and Azurin in POPC. The dotted line shows Azurin hydration, and the bold line shows Azurin on POPC. Both figures show in the POPC lipid membrane that the free energy and electrostatic energy tend to decrease, as shown by the more negative energy. We compare the free energy of Azurin in a different state, shown in Table 1. This table shows that even in the POPC environment, the free energy tends to be more negative. Still, the experimental value shows a larger value indicating some difference in perturbation type for the CG-MARTINI model. However, we can reach efficient ways in terms of simulation time. The effective ways to find the exact value in CG-MARTINI seem related to the non-bonded interaction described in the next part.

The free energy value shows tendencies to make Azurin have like-able tendencies inside the POPC membrane. It is also shown in Table 1, which indicates that Azurin is more favorable in the POPC environment, shown by more negative free energy values.

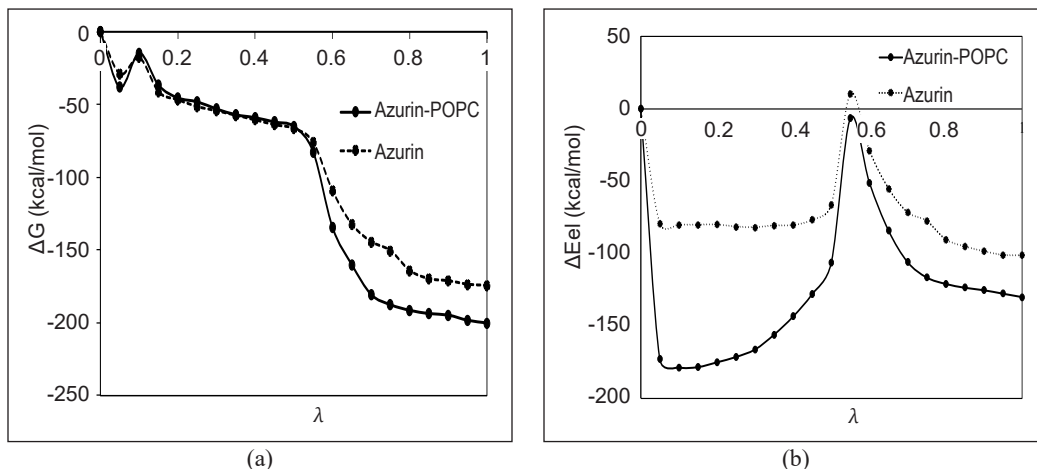


Figure 5. The analysis of free energy and average electrostatic energy difference for Azurin hydration and Azurin-POPC system. (a) The free energy of annihilated Azurin during simulation with, Azurin-POPC:  $\Delta G = -200.34$  kcal/mol, Azurin:  $\Delta G = -174.636$  kcal/mol; (b) The average electrostatic energy difference of annihilated Azurin, in POPC:  $\Delta E_{el} = -130.021$  kcal/mol, water:  $\Delta E_{el} = -101.298$  kcal/mol.

Table 1

The differences in free energy analysis of Azurin in water and POPC, respectively

The System of Azurin	$\Delta G$ Experiment Hydration (Pappalardo et al., 2003)	$\Delta G$ (Azurin)	$\Delta G$ (Azurin-POPC)
Free Energy (kcal/mol)	-32.7438	-174.636	-200.340

### The Windows Separation Changes

Table 2 shows the difference in free energy values related to the changes in the windows separation number. In Figure 6(a), we can see that the fewer separation windows value decreases the free energy value. Figure 6(b) also shows the same trend, which changes average electrostatic energy differences. In previous research by Li and Nam (2020), this separation tends to decrease the free energy values in thermodynamic integration (TI) methods. We choose windows separation randomly.

The free energy values tend to increase with window separation addition. The higher acceptance ratio relates to increasing the number of windows, although its cost is computational (Jiang et al., 2009). The separation windows describe the replica of the system.

The free energy relation with windows separation is shown in Figure 7. Figure 7(a) specifically shows the relation between free energy values and the change of windows separation, and Figure 7(b) is about the average electrostatic difference. Although it has polynomial fourth-order tendencies, some average electrostatic difference value looks to decrease in higher separation windows. It also means the trendline is nonlinear between the separation windows and energy changes.



Table 2  
The absolute binding free energy ( $\Delta G$ ) of Azurin in POPC membrane ( $\lambda_{elec} = 0.5$ ,  $\lambda_{ij} = 1.0$ ,  $numsteps = 100000$  steps) with windows ( $\delta\lambda$ ) variations

$N(\delta\lambda)$	3	5	9	11	13	15	17	21	31	41	45	47	48	51	60
$\Delta G$ (kcal/mol)			-INF		-337.779	-286.619	-252.335	-200.340	-132.227	-104.211	-85.450	-91.329	-87.566	-84.201	-71.859
$\Delta Eel$ (kcal/mol)					-219.110	-186.900	-163.480	-130.020	-83.616	-68.930	-53.580	-59.49	-57.51	-55.80	-47.827

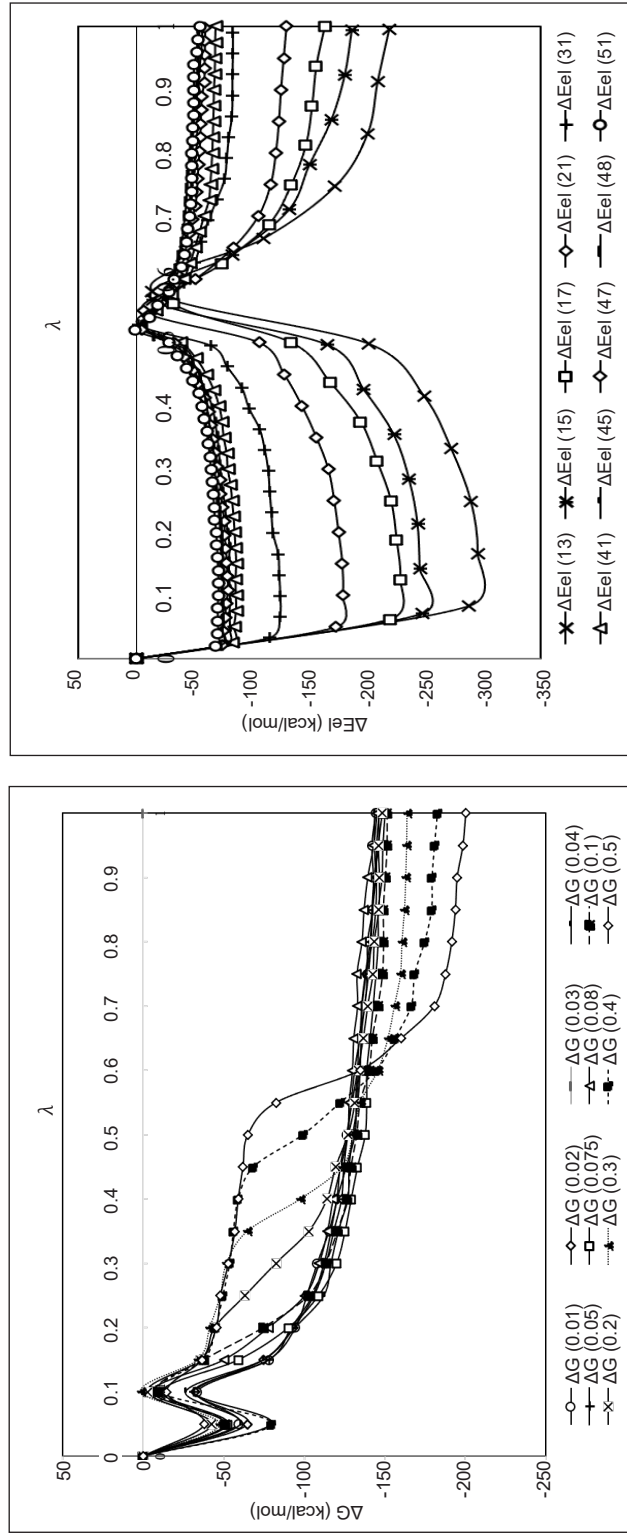


Figure 6. The analysis of free energy and average electrostatic difference with various windows separation. (a) The relation of free energy and lambda state; (b) The relation of the average electrostatic difference and lambda state

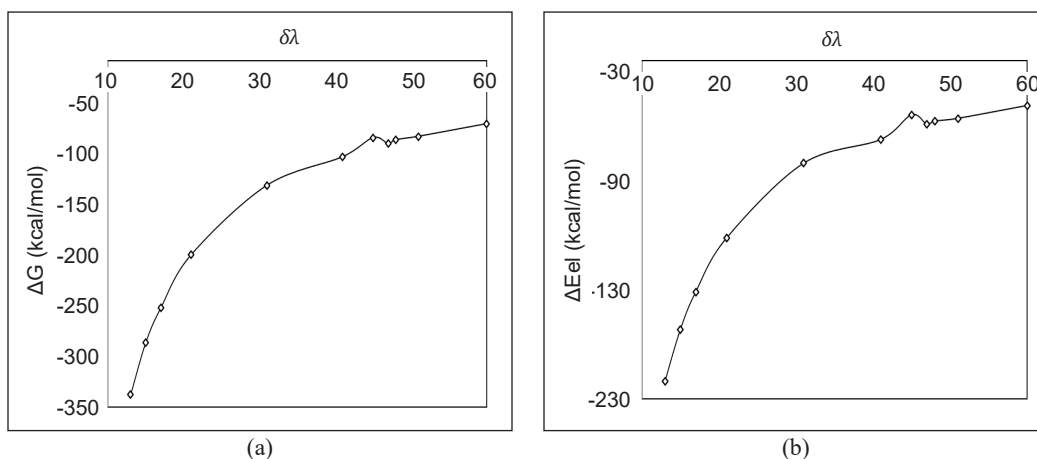


Figure 7. The relation between free energy, average electrostatic difference, and windows separation. (a) The analysis of free energy and windows separation; (b) The analysis of average electrostatic difference and windows separation

### The Electrostatic Parameter Changes

The electrostatic scale parameter affects the changes in the free energy of Azurin shown in Table 3. To find the effect of the electrostatic scale parameter, we introduce the value and relation of this parameter with interatomic distance. In NAMD, which uses free energy perturbation,  $\lambda_{elec}$  A value less than or equal to the user-defined ( $=0.5$ ).

In FEP calculated by NAMD, the electrostatic parameter is used to avoid “end-point catastrophe,” which avoids growing particles overlapping with existing particles with an unbounded interaction potential that will approach infinity as the interaction distance approaches zero.

We can see the additional effect of  $\lambda_{elec}$ . It tends to decrease the free energy values. In this part, we calculate the effect of this parameter in Azurin-POPC systems. We find the free energy differences shown in Table 3.

Table 3

The absolute binding free energy and average electrostatic analysis differentiate by electrostatic parameter values ( $\lambda_{ij} = 10$ ,  $numstep = 100000$ ,  $\delta\lambda = 0.05$ )

$\lambda_{elec}$	0.04	0.05	0.075	0.08	0.1	0.2	0.3	0.4	0.5
$\Delta G$ (kcal/mol)	-143.859	-146.367	-150.173	-145.040	-151.485	-148.474	-163.879	-182.797	-200.340
$\Delta E_{el}$ (kcal/mol)	-81.34	-78.16	-79.92	-76.98	-85.21	-80.21	-95.67	-114.49	-130.02

Figure 8(a) shows the free energy differences related to the electrostatic parameter changes. This figure shows difference curvature, which describes how the energy change when the electrostatic parameter change. It has a higher value in 0.5 values of the electrostatic parameter. Meanwhile, we can assume that lowering this value can get the free energy as expected. Figure 8(b) shows free energy and interatomic distance. We can see that as the free energy reach  $\lambda_{elec} = 0.1$ , the free energy has been saturated, which means the scaling makes the maximal interaction. The free energy tends to saturate after  $\lambda_{elec} = 0.1$  until the  $\lambda_{elec}$  reaches 0.04. We can see in Figure 8(b) that the curve changes slightly as the interatomic distance becomes larger. We suppose this situation could be because the atom's interaction has reached the peak of interaction.

Figure 9 shows the differences of average electrostatic differences from different electrostatic parameters. The free energy value tends to increase in the lower electrostatic parameter and fade away at the 0.01 value of the electrostatic parameter. We assume this relates to the model which we use. Figure 9(b) shows the average electrostatic difference with interatomic distance. This relation is quite the same with free energy, as we mentioned in Figure 9(b); however, after  $\lambda_{elec} = 0.1$ , it also has some tendencies with free energy values, which have slightly different values.

In CG-MARTINI, the densities become higher than AA, which we can assume may be why there are different free energy values when the electrostatic parameter varies. In a higher electrostatic parameter value, the free energy considers higher, which tends to be close to the Azurin hydration experimental value. We assume the difference in density of the AA model and CG-MARTINI model makes this free energy differs. Table 4 shows the APL from the experiment and our result. It shows that CG-MARTINI has a larger APL.

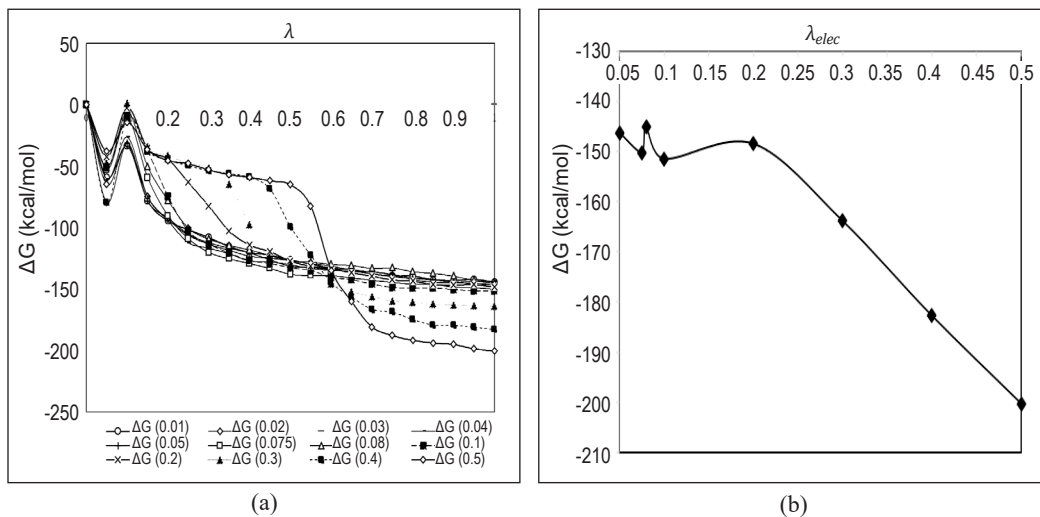


Figure 8. The free energy analysis relates to different electrostatic parameter values. (a) Free energy as a function of  $\lambda$  state; (b) Free energy as a function of the electrostatic scale parameter

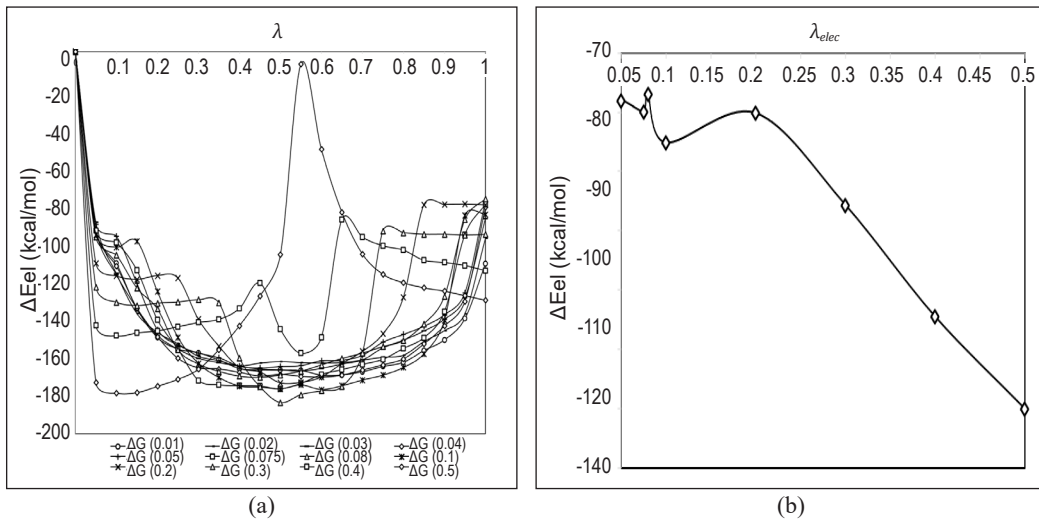


Figure 9. The average electrostatic difference analysis relates to different electrostatic parameter values. (a) Average electrostatic difference as a function of  $\lambda$  state; (b) Average electrostatic difference as the function of the electrostatic scale parameter

Table 4

The area per lipid (APL) of CG-MARTINI compared to the experiment

	Experiment (Kucerka et al., 2006)	Our result
Area Per Lipid ( $\text{\AA}^2$ )	68.3 at 303.15 K	89.4 at 310 K

The CG-MARTINI has a difference in resolution, which impacts density in the same APL. That also explains that this model creates a value gap for free energy. The AA model is closer to free energy in the experiment. However, CG has advantages in terms of cost computing to look for trends, not accuracy. Because of this reason, it might be possible to approach the experiment by varying some of the scaling parameters as the candidates, as we mentioned before.

We illustrate the density change in Figure 10 to understand the magnification of the electrostatic scale parameter in the CG-MARTINI model. From this figure, there are different densities between these two models. Figure 10 shows the AA model mapping to the CG-MARTINI model and the density differences. The changes in the electrostatic scale parameter lead to a different approach through free energy calculation. This work assumes that electrostatic scaling influences the free energy calculation. Since the density in the CG-MARTINI model is larger than an AA model, the rescaling on electrostatic needs to reach the free energy accurately. Based on Beveridge and Dicapua's (1989) work, the change of electrostatic parameters is more precise than van der Waals's parameters related to free energy values. Previous research has shown that the energy and forces dominate by previous interaction before the latter repulsive component becomes larger to prevent

counterfeit collisions from atoms of a constituent during the scaling of Coulomb and Van Der Waals interaction (Pohorille et al., 2010).

The electrostatic scaling is the constant that affects the non-bonded potential related to the distance among atom units. The distance among atoms changes in the CG-MARTINI model, which makes the mass density larger.

The electrostatic scaling in FEP shows how it changes the interatomic distance. However, as shown in Figure 11, we can see that the density values of CG-MARTINI are larger than the AA model by Gurtovenko and Anwar (2009). It explains why the free energy values can change each time the electrostatic parameter has been rescaled. We assume the larger density in CG-MARTINI needs the scaling with a value of 0.05-0.2 because the atoms are tightly bound to one another, which needs some spacing value to make the free energy as expected.

The density of CG-MARTINI is higher than all-atom, so it needs scaling of electrostatic scale parameter to reach the free energy values as expected. Figure 11 shows the density

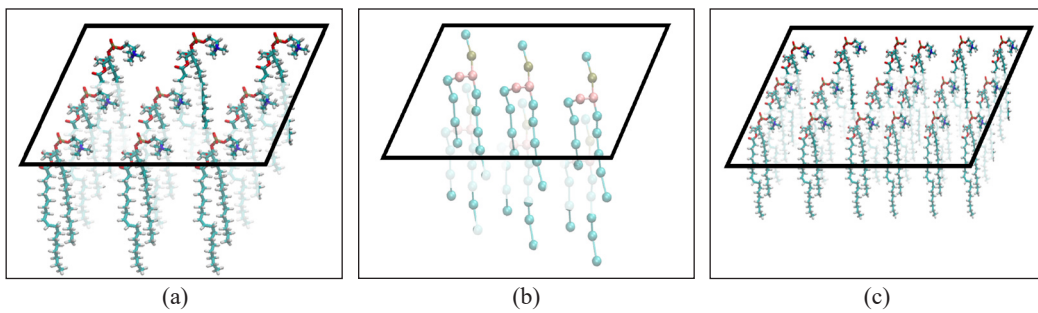


Figure 10. The comparison of CG-MARTINI Model with All-Atom Model: (a) AA Model; (b) CG-MARTINI Model; and (c) CG-MARTINI Model comparison in AA Model

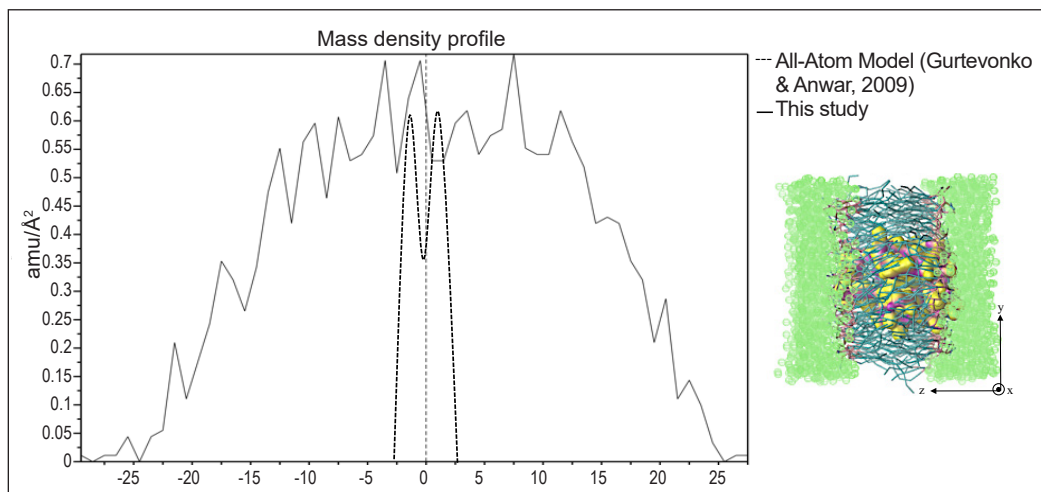


Figure 11. The mass density profile of the CG-MARTINI model compared to the All-Atom Model

change for CG-MARTINI compared to the AA Model. It could be why free energy in CG-MARTINI Model with electrostatic scale parameter optimized and reached -140.831 kcal/mol and -32.74 kcal/mol in the experiment. Although this makes free energy has no barriers, it cannot describe the binding or unfolded protein process, which is somehow described in free energy analysis in higher electrostatic parameters.

## CONCLUSION

Our study concludes that the CG-MARTINI method with windows separation and electrostatic scaling is one alternative method that can reduce the simulation time for the complex system. The free energy values fairly approach the experimental value. The CG-MARTINI describes how it reduces the definition of the atom into beads. CG-MARTINI methods with a MARTINI force field build a protein's structure in an equilibration state. The effects of the addition of lipid membrane, the conformation, and the stabilities have been analyzed from the free energy of the conformation system to find the favorable structure using free energy perturbation (FEP) calculation. FEP calculation results show that a few factors affect free energy values with the CG-MARTINI method: windows separation, electrostatic parameter, and flag characterization parameter.

Interestingly, this work has relationships or scaling between the electrostatic parameter and free energy value. For this reason, we try to rescale for the possibility of running coarse-grained and comparable to all-atom simulation. Our results show that the potential candidate is in tuning the electrostatic parameter, so the electrostatic scaling effect is an interesting parameter.

Our results suggest a kind of scaling to bring CG-MARTINI closer to all-atom by finding a hidden parameter scaling. One of the candidates that we propose is to use electrostatic scaling. With this kind of scale, it is possible to produce free energy values closer to the experimental results. This step could be useful for approaching experimental results. Furthermore, this scale factor can be used by CG-MARTINI for similar cases.

## ACKNOWLEDGEMENT

The authors thank the support from the Faculty of Mathematics and Natural Sciences, Institute of Technology Bandung (ITB), Indonesia, through Program Penelitian, Pengabdian Masyarakat, dan Inovasi (PPMI), and partly supported by the Indonesian Endowment Fund for Education (LPDP) Indonesia.

## REFERENCES

Adman, E. T., & Jensen, L. H. (1981). Structural features of Azurin at 2.7 angstroms resolution. *Israel Journal of Chemistry*, 21(1), 8-12. <https://doi.org/10.1002/ijch.198100003>

- Arumugam, S., Chwastek, G., & Schwille, P. (2011). Protein–membrane interactions: The virtue of minimal systems in systems biology. *Wiley Interdisciplinary Reviews: Systems Biology and Medicine*, 3(3), 269-280. <https://doi.org/10.1002/wsbm.119>
- Beveridge, D. L., & DiCapua, F. M. (1989). Free energy via molecular simulation: Applications to chemical and biomolecular systems. *Annual Review of Biophysics and Biophysical Chemistry*, 18(1), 431-492. <https://doi.org/10.1146/annurev.bb.18.060189.002243>
- Frauenfelder, H., Chena, G., Berendzena, J., Fenimore, P. W., Janssonb, H., McMahon, B. H., Stroec, I. R., Swensond, J., & Younge, R. D. (2009). A unified model of protein dynamics. *Proceedings of the National Academy of Sciences*, 106(13), 5129-5134. <https://doi.org/10.1073/pnas.0900336106>
- Gumbart, J., & Roux B. (2012). Determination of membrane-insertion free energies by molecular dynamics simulations. *Biophysical Journal*, 102(4), 795-801. <https://doi.org/10.1016/j.bpj.2012.01.021>
- Gumbart J., Chipot C., & Schultena K. (2011). Free-energy cost for translocon-assisted insertion of membrane proteins. *Proceedings of the National Academy of Sciences*, 108(9), 3596-3601. <https://doi.org/10.1073/pnas.1012758108>
- Gurtovenko, A. A., & Anwar, J. (2009). Interaction of ethanol with biological membranes: The formation of non-bilayer structures within the membrane interior and their significance. *Journal of Physical Chemistry B*, 2009, 113(7), 1983-1992. <https://doi.org/10.1021/jp808041z>
- Humphrey, W., Dalke, A., & Schulten, K. (1996). VMD-visual molecular dynamics. *Journal of Molecular Graphics*, 14(1), 33-38. [https://doi.org/10.1016/0263-7855\(96\)00018-5](https://doi.org/10.1016/0263-7855(96)00018-5)
- Jiang, W., Hodoseck, M., & Roux, B. (2009). Computation of absolute hydration and binding free energy with free energy perturbation distributed replica-exchange molecular dynamics (FEP/REMD). *Journal of Chemical Theory and Computation*, 5(10), 2583-2588. <https://doi.org/10.1021/ct900223z>
- Kucerka, N., Tristram-Nagle, S., & Nagle, J. F. (2006). Structure of fully hydrated fluid phase lipid bilayers with monounsaturated chains. *Journal of Membrane Biology*, 208(3), 193-202. <https://doi:10.1007/s00232-005-7006-8>
- Kurniawan, I., Kawaguchi, K., Sugimori, K., Sakurai, T., & Nagao, H. (2019). Theoretical studies on electronic structure and proteins of type I copper center in copper proteins. *Science Report Kanazawa University*, 63, 1-13.
- Li, Y., & Nam, K. (2020). Repulsive soft-core potentials for efficient alchemical free energy calculations. *Journal of Chemical Theory and Computation*, 16(8), 4776-4789. <https://doi:10.1021/acs.jctc.0c00163>
- Marrink, S. J., Risselada, H. J., Yefimov, S., Tieleman, D. P., & De Vries, A. H. (2007). The MARTINI force field: Coarse-grained model for biomolecular simulations. *Journal of Physical Chemistry B*, 111(27), 7812-7824. <https://doi.org/10.1021/jp071097f>
- Mark, A. E. (1998). Free energy perturbation calculations. In P. V. R. Schleyer, N. L. Allinger, T. Clark, J. Gasteiger, P. A. Kollman, H. F. Schaefer & P. R. Schreiner (Eds.), *Encyclopedia of Computational Chemistry* (pp.1070-1083). Wiley and Sons.

- Pappalardo, M., Milardi, D., Grasso, D. M., & La Rosa, C. (2003). Free energy perturbation and molecular dynamics calculations of copper binding to Azurin. *Journal of Computational Chemistry*, 24(6), 779-785. <https://doi.org/10.1002/jcc.10213>
- Phillips, J. C., Hardy, D. J., Maia, J. D. C., Stone, J. E., Ribeiro, J. V., Bernardi, R. C., Buch, R., Fiorin, G., Henin, J., Jiang, W., McGreevy, R., Melo, M. C. R., Radak, B. K., Skeel, R. D., Singharoy, A., Wang, Y., Roux, B., Aksimentiev, A. Luthey-Schulten, Z., ... & Tajkhorshid, E. (2020). Scalable molecular dynamics on CPU and GPU architectures with NAMD. *Journal of Chemical Physics*, 153(4), Article 044130. <https://doi.org/10.1063/5.0014475>
- Pohorille, A., Jarzynski, C., & Chipot, C. (2010). Good practices in free-energy calculations. *Journal of Physical Chemistry B*, 114(32), 10235-10253. <https://doi.org/10.1021/jp102971x>.
- Pozdnyakova, I., Guidry, J., & Wittung-Stafshede, P. (2002). Studies of *pseudomonas aeruginosa* Azurin mutants: Cavities in  $\beta$ -barrel do not affect refolding speed. *Biophysical Journal*, 82(5), 2645-2651. [https://doi.org/10.1016/S0006-3495\(02\)75606-3](https://doi.org/10.1016/S0006-3495(02)75606-3)
- Pozdnyakova, I., & Wittung-Stafshede, P. (2001). Copper binding before polypeptide folding speeds up the formation of active (holo) *Pseudomonas aeruginosa* Azurin. *Biochemistry*, 40(45), 13728-13733. <https://doi.org/10.1021/bi011591o>
- Zhu, F., Bourguet, F. A., Bennett, W. F. D., Lau, E. Y., Arrildt, K. T., Segelke, B. W., Zemla, A. T., Desautels, T. A., & Faissol, D. M. (2022). Large-scale application of free energy perturbation calculations for antibody design. *Scientific Reports*, 12, Article 12489, <https://doi.org/10.1038/s41598-022-14443-z>



## Effect of Lysine and Poultry Slaughterhouse by Product Meal on Growth Performance, Feed Efficiency, and Blood Profile of Sangkuriang Catfish (*Clarias gariepinus* var. Sangkuriang)

Diana Rachmawati\*, Tita Elfitasari, Istiyanto Samidjan, Putut Har Riyadi and Dewi Nurhayati

Department of Aquaculture, Faculty of Fisheries and Marine Sciences, Diponegoro University, Semarang 50275, Central Java, Indonesia

### ABSTRACT

The increasing demand for livestock and poultry feeds results in the lack of fish meals (FM). Poultry slaughterhouse by-product (PSB) is one promising strategy due to its high protein content despite the limited content of lysine. Thus, supplementing lysine in dietary fish feed is necessary. The present study aimed to investigate how different lysine doses in feed with PSB and FM as animal protein sources affected protein digestibility, feed utilization, growth, hematology, and body composition of Sangkuriang catfish (*Clarias gariepinus* var. Sangkuriang). Sangkuriang catfish at the grow-out stage ( $15.54 \pm 0.17$  g/fish) were used. The fish were fed six experimental diets with similar protein and energy content but different lysine levels at 1.25%, 1.75%, 2.25%, 2.75%, 3.25%, and 3.75%/kg (treatments 1 to 6). The addition of lysine to feed had a significant ( $P < 0.05$ ) effect on protein digestibility (ADCp), efficiency of feed utilization (EFU), and relative growth rate (RGR) of Sangkuriang catfish at a grow-out stage but had no significant ( $P > 0.05$ ) effect on survival

rate, hematology, and nutrient content. The optimal doses of dietary lysine with PSB and FM to improve ADCp, EFU, and RGR of Sangkuriang catfish were 2.59%, 2.63%, and 2.62%/kg diet, respectively. However, the supplementation of PSB in experimental diets had no significant effect on glucose, triglyceride, total protein, urea, calcium, magnesium, albumin, globulin, hemoglobin, hematocrit, phosphorous, and mean corpuscular hemoglobin concentration (MCHC). The lysine addition in feed

### ARTICLE INFO

#### Article history:

Received: 28 September 2022

Accepted: 25 January 2023

Published: 08 September 2023

DOI: <https://doi.org/10.47836/pjst.31.6.07>

#### E-mail addresses:

[journalsubmission92@gmail.com](mailto:journalsubmission92@gmail.com); [dianarachmawati1964@gmail.com](mailto:dianarachmawati1964@gmail.com)

(Diana Rachmawati)

[titaelfitasari@yahoo.com](mailto:titaelfitasari@yahoo.com) (Tita Elfitasari)

[istiyanto\\_samidjan@yahoo.com](mailto:istiyanto_samidjan@yahoo.com) (Istiyanto Samidjan)

[putut\\_thp@yahoo.co.id](mailto:putut_thp@yahoo.co.id) (Putut Har Riyadi)

[ewinurhayati24@gmail.com](mailto:ewinurhayati24@gmail.com) (Dewi Nurhayati)

\* Corresponding author

formulated with PSB and FM could improve the growth performance and increase the feed digestibility of Sangkuriang catfish at the grow-out stage.

*Keywords:* Feed, food efficiency, growth, lysine, nutrient

---

## INTRODUCTION

Sangkuriang catfish (*Clarias gariepinus* var. Sangkuriang) is a popular freshwater fish species widely cultured in Indonesia. The fish has distinct characteristics, including fast growth, adapting quickly to the environment, delicacy, and high nutrient content (Rachmawati et al., 2019). Feed cost is the most important variable in intensive culture, accounting for 80% of the total production costs of each culture cycle (Rawles et al., 2011). It is because protein is the costliest fish feed component compared to other nutritional components. It is a source of essential amino acids (EAA) for body tissue repair and fish growth (Khan & Abidi, 2011).

Fish meal is widely regarded as the finest animal protein source for feed components due to its stable amino acid profile (National Research Council, 2011). However, due to the rising demand for livestock and poultry feed, fish meals are scarce for fish feed (Suloma et al., 2014). Therefore, alternative protein sources must be found to substitute fish meals in the fish diet. Srour et al. (2016) identified poultry slaughterhouse by-products (PSB) as an alternative protein source due to their high protein content (60%–65%) and lower cost when contrasted to fish meal (Hernández et al., 2014). Poultry slaughterhouse by-product (PSB) differs from poultry by-product meal (PBM) since it still contains ether extract (EE), ash, and non-digestible part (feathers), which reduces degradability (Yones & Metwalli, 2015).

According to Khan & Abidi (2011), most poultry slaughterhouse by-products (PSB) have low lysine content. Thus, adding lysine to dietary feed based on fish requirements becomes one solution for improving fish growth performance (Khan & Abidi, 2011). Lysine is a vital nutrient for fish growth and normal physiological function. Lysine and methionine are involved in synthesizing carnitine, which is used in fatty acid transport activities to produce energy via oxidation (Nguyen & Davis, 2016). Lysine is frequently the first amino acid limiter in fish feed ingredients among the ten essential amino acids (Farhat & Khan, 2013). In fish, an insufficiency of lysine causes slow growth and poor protein utilization. In addition, several fish species have reported appetite loss and increased lipid accumulation (Mai et al., 2006). It has also been reported that excessive lysine and a lack of dietary feed caused lower growth in several fish species (Bicudo et al., 2009).

Although biochemical evaluation of blood and plasma could help assess fish health, there is limited evidence on the effect of dietary lysine on fish blood (Zhou et al., 2010). Therefore, the present study aimed to investigate how different lysine doses in feed with poultry slaughterhouse by-product (PSB) meal and fish meal (FM) as an animal protein

source affected protein digestibility, feed utilization, growth, hematology, and body composition of Sangkuriang catfish (*Clarias gariepinus* var. Sangkuriang) at the grow-out stage.

## MATERIALS AND METHODS

### Preparation of Experimental Fish

Sangkuriang catfish at the grow-out stage were obtained from the Teaching Factory, Faculty of Fisheries and Marine Sciences, University of Diponegoro, Indonesia. Experimental fish were previously acclimatized for one week. During acclimatization, the fish were adapted to an environment with the same water quality as the research environment. The commercial feed has a protein content of 30% and 10% fat. Fish were fed 3 times daily at 7 am, 12 pm, and 4 pm. Fish were fasted one day before the experiment to remove metabolic waste from the fish's body. Experimental fish were chosen based on uniform size, physically healthy, active swimming, and no organ deformation (Rachmawati et al., 2017).

### Experimental Design

The current study was experimental research with a completely randomized design (CRD), 6 treatments, and 3 replicates. This study was conducted in the Wet Laboratory, Department of Aquaculture, Faculty of Fisheries and Marine Sciences, University of Diponegoro, Indonesia. A total of 360 Sangkuriang catfish with an average weight of  $15.54 \pm 0.17$  g/fish at the grow-out stage were used. The fish were then randomly divided into six groups ( $n=60$ ) with a stocking density of 1 fish/liter (20 fish/fiber tank). The experiment was carried out in a plastic fiber tank (capacity of 70 L) filled with 20 L of water at 25–28°C, pH 7.0–7.5, and dissolved oxygen above  $5 \text{ mg L}^{-1}$  (Boyd, 2003). Fish were sampled weekly by calculating the total fish biomass in each plastic fiber tank. At satiation, feeding was given 3 times a day for 42 days at 8 am, 1 pm, and 5 pm. During the experiment, siphoning was done to maintain water quality by removing uneaten feed and collecting fish feces for protein digestibility analysis.

### Feed Preparation

Sangkuriang catfish at the grow-out stage were treated with 6 experimental diets with similar protein (30%) and energy content ( $8.30 \text{ Kcal g}^{-1}$ ) and different lysine levels at 1.25%, 1.75%, 2.25%, 2.75%, 3.25%, and 3.75%/kg (treatment 1 to 6). The proximate and amino acid analyses of animal and plant protein sources are demonstrated in Table 1. The experimental diets containing 30% of protein (Rachmawati et al., 2022) were then added with 0.5% chromium (III) oxide ( $\text{Cr}_2\text{O}_3$ ) as the indicator of protein digestibility. Experimental diets consisted of fish meal, poultry slaughterhouse by-product (PSB) meal as the animal protein source, and soybean meal as a plant protein source. According

Table 1  
*Protein and amino acid content in experimental diet (g/100 g)*

Composition	Fish meal	Soybean meal	Poultry slaughterhouse by-product
Dry matter	89.18	89.18	89.18
Lipid	7.56	3.90	13.14
Crude protein	68.35	39.82	52.31
Alanine	4.96	1.87	2.89
Glutamic acid	5.93	3.99	5.89
Proline	4.30	3.10	5.29
Tyrosine	2.28	1.70	1.87
Serine	2.76	2.20	3.95
Aspartic acid	3.96	2.75	3.87
Glycine	5.87	2.28	3.87
Cystine	0.7	0.69	3.2
Arginine	4.90	3.2	3.06
Histidine	1.51	1.13	0.64
Isoleucine	3.30	1.97	2.70
Leucine	5.18	3.36	4.29
Lysine	5.30	2.76	1.98
Methionine	1.96	8.58	0.50
Phenylalanine	2.80	2.16	2.79
Threonine	4.06	1.80	2.70
Tryptophan	0.69	0.58	0.47
Valine	3.76	2.10	3.47

to El-Husseiny et al. (2018), PSB is high in protein, approximately 61.5%; hence, it is suitable to replace a fish meal with lysine partially. The composition of PSB that replaced fish meal in experimental diets up to 50% and the doses of lysine used in this study based on El-Husseiny et al. (2018) with slight modification, including 1.25%, 1.75%, 2.25%, 2.75%, 3.25%, and 3.75%/kg diet (treatment 1 to 6). PSB meal is a poultry meal derived from the broiler and layer industry sectors, particularly from dead animals and giblets that were heat-peeled at 112°C for 2 h. PSB was obtained from the Animal Slaughterhouse Semarang, Central Java, Indonesia.

Experimental diets were made by mixing feed ingredients until homogenous. The acidity of the mixed experimental diets was neutralized with 6 N sodium hydroxide (NaOH) (Nose et al., 1974) to eliminate the effect of pH on growth performance and feed efficiency (Wilson et al., 1977). Furthermore, the mixed experimental diets were produced using a 4 mm-sized pellet molding machine to be further dried at room temperature and stored at -4°C until use. Formulation and proximate analysis of experimental diets (g/100 g diet) of Sangkuriang catfish is presented in Table 2. Amino acid profiles and AA requirements of experimental diets according to National Research Council (2011) are shown in Table 3.

Table 2  
 Formulation, chemical composition, and proximate analysis of experimental diet (g/100 g diet)

Ingredients Composition	1	2	3	4	5	6
Soybean meal	20.0	20.0	20.0	20.0	20.0	20.0
Fish meal	20.0	20.0	20.0	20.0	20.0	20.0
PSB	22.76	22.76	22.76	22.76	22.76	22.76
Corn	20.0	20.0	20.0	20.0	20.0	20.0
Starch	1.14	1.14	1.14	1.14	1.14	1.14
Wheat	8.7	8.2	7.7	7.2	6.7	6.2
Salt	0.4	0.4	0.4	0.4	0.4	0.4
Vitamin and Mineral Premix <sup>1)</sup>	1.5	1.5	1.5	1.5	1.5	1.5
Chemical composition (g kg <sup>-1</sup> )						
Carboxymethylcellulose	0.6	0.6	0.6	0.6	0.6	0.6
Vitamin C	0.15	0.15	0.15	0.15	0.15	0.15
Soybean oil	3.0	3.0	3.0	3.0	3.0	3.0
Lysine	1.25	1.75	2.25	2.75	3.25	3.75
Cr <sub>2</sub> O <sub>3</sub>	0.5	0.5	0.5	0.5	0.5	0.5
Total	100	100	100	100	100	100
Results of Proximate Analysis						
Dry matter	9.26	9.26	9.26	9.26	9.26	9.26
Crude protein	30.40	30.60	30.60	30.56	30.55	30.60
Crude lipid	12.22	12.32	12.43	12.29	12.37	12.28
Crude Ash	8.23	8.27	8.23	8.25	8.27	8.29
Gross energy (Kcal g <sup>-1</sup> ) <sup>3)</sup>	8.15	8.23	8.30	8.28	8.27	8.25

<sup>1)</sup>Vitamin mix (mg/100 g diet): riboflavin 5.0; cyanocobalamin 0.01; inositol 200; menadione 4.0; folic acid 1.5; b-carotene 15.0; a-tocopherol 2.0; vitamin C-sty 120.0; Ca-pantothenate 10.0; choline chloride 900.0; thiamin-HCl 5.0; niacin 2.0; pyridoxin-HCl 4.0; calciferol 1.9; biotin 0.6; p-aminobenzoic acid 5.0

<sup>2)</sup>Mineral mix (mg/100 g diet): Calcium carbonate (CaCO<sub>3</sub>) 282; Iron (II) chloride tetrahydrate (FeCl<sub>3</sub>·4H<sub>2</sub>O) 166; Magnesium sulfate (MgSO<sub>4</sub>) 240; Manganese sulfate (MnSO<sub>4</sub>) 6.3; Cobalt (II) Sulfate Heptahydrate (CoSO<sub>4</sub>·7H<sub>2</sub>O) 0.05; Potassium dihydrogen phosphate (KH<sub>2</sub>PO<sub>4</sub>) 412; Calcium biphosphate [Ca(H<sub>2</sub>PO<sub>4</sub>)] 618; Zinc sulfate (ZnSO<sub>4</sub>) 9.99; Copper sulfate (CuSO<sub>4</sub>) 2; Potassium iodide (PI) 0.15

<sup>3)</sup>Total energy based on: protein = 4 kcal/g, lipid = 9 kcal/g, and carbohydrate = 4 kcal/g (NRC, 2011)

Table 3  
 Amino acid profile of the experimental diet (g/kg experimental diet)

Amino Acids	1	2	3	4	5	6	Catfish *
Essential amino acids							
Arginine	24.62	24.50	24.72	25.94	24.76	24.56	10.3
Tryptophan	3.80	3.82	3.83	3.89	3.83	3.62	5.3
Threonine	18.23	18.24	18.45	19.20	18.12	18.43	12.0
Methionine	18.10	18.76	18.63	18.87	18.25	18.49	15.0
Isoleucine	18.20	18.27	18.30	18.20	18.13	18.26	6.2
Histidine	7.63	7.65	7.49	7.25	7.48	7.39	3.7

Table 3 (continue)

Amino Acids	1	2	3	4	5	6	Catfish *
Phenylalanine	18.71	18.46	18.53	18.23	18.79	18.84	4.6
Lysine	19.50	22.31	22.50	28.42	32.53	38.56	12.3
Leucine	28.42	28.57	28.10	28.36	28.61	28.47	8.4
Valine	19.15	19.23	19.67	19.39	19.73	19.59	7.1
Non-essential amino acid							
Alanine	22.54	22.19	21.53	21.26	21.38	21.17	–
Serine	20.36	20.53	21.64	20.23	22.62	20.76	–
Glycine	27.63	26.67	24.73	26.13	24.26	24.74	–
Glutamic	35.78	35.39	35.27	35.72	35.87	35.35	–
Aspartic	24.52	24.20	24.72	24.12	24.89	24.75	–
Proline	27.19	29.53	31.36	27.79	29.58	28.47	–
Tyrosine	12.57	12.89	12.78	12.67	12.77	12.57	–

Note. \*NRC (2011)

### Chemical Analysis

Feed ingredients, experimental diets, and the whole body of fish and fish fillet were proximately analyzed through the standard model (Horwitz, 1975). Protein content was measured using the Kjeldahl method (BÜCHI, Auto-KjeldahlK-370, Swiss). Kjeldahl factor 6.25 (100/16) was used to convert total nitrogen into total protein content as a dry mass percentage. The total lipid content of fish was extracted with petroleum benzene using the Soxhlet method (Barnstead/Electrothermal, UK). Fiber content was analyzed with a fiber analyzer (VELP® Scientifica, Italia), while ash content analysis was applied to each dried sample in a porcelain crucible using a muffle furnace (Finetech, Shin Saeng Scientific, South Korea) at 600°C for 8 h. Moisture content was determined using moisture analyzer (AM B5 0, AD AM, UK). Protein digestibility was analyzed using a spectrophotometer (Millipore, Merck KGaA, Germany) at 350 nm.

Amino acid content of experimental diets was analyzed using High-Speed Amino Acid Analyzer LA8080 AminoSAAYA (Hitachi High Technologies, Japan). Approximately  $\pm 1$  mg sample was weighed, put into a closed tube, and hydrolyzed with 6N hydrogen chloride (HCl) for 22 h at 110°C. The sample was filtered through a 0.2 mm filter and further injected into High-Speed Amino Acid Analyzer LA8080 AminoSAAYA (Hitachi High Technologies, Japan) with ion-exchange resin columns at size  $4.6 \times 150$  mm at 53°C. Amino acids were separated by a gradient system using sodium citrate buffer solution of pH 3.3, 4.3, and 4.9 at a flow rate of  $0.225 \text{ mL minute}^{-1}$ . Post-column ninhydrin reagent at a flow rate of  $0.3 \text{ mL min}^{-1}$  was used to identify each amino acid at 570 nm and 440 nm, respectively.

### Protein Digestibility Analysis

The indirect method of adding  $\text{Cr}_2\text{O}_3$  0.5% to the diet was employed to measure protein digestibility (Pérez-Jiménez et al., 2014). Before the feces of the fish were collected, the fish was acclimated to the diet containing chromium for 1 week. After the eighth day, the feces were collected for 49 d every morning, noon, and afternoon after the fish was fed. The feces were collected two hours after feeding that its collection used a small plastic hose with the tip attached to the wooden stick to move around easier and put the collected feces in the bucket. Then the feces were filtered with a plankton cloth net; the filtered feces were placed in small plastic bottles and stored in cold storage. Before the feces were analyzed, it was dried in the oven (Memmert, UF30Plus Universal, Italy) at  $6^\circ\text{C}$  for 24 h. After that, protein and  $\text{Cr}_2\text{O}_3$  content in the feces was analyzed using a spectrophotometer (SSA 320N, Denmark) with a wavelength of 350 nm (Pérez-Jiménez et al., 2014).

### Parameter Observed

All parameters related to fish growth were measured, including weight gain (WG), relative growth rate (RGR) (National Research Council, 2011), feed efficiency expressed by protein digestibility (ADCp) (Fenucci, 1981), the efficiency of feed utilization (EFU), feed conversion ratio (FCR), protein efficiency ratio (PER), protein retention (PR), and survival rate (SR) (National Research Council, 2011). These parameters were calculated based on Equations 1-8:

$$WG (g) = \text{Final body weight (g)} - \text{Initial body weight (g)} \quad (1)$$

$$ADCp (\%) = 100 - \left\{ \frac{100 \times \text{Cr}_2\text{O}_3 \text{ in the fish feed}}{\% \text{Cr}_2\text{O}_3 \text{ in the feces}} \times \frac{\% \text{protein in the feces}}{\% \text{protein in diet}} \right\} \quad (2)$$

$$EFU (\%) = \frac{\text{Final weight} - \text{Initial weight}}{\text{Weight of diet consumed}} \times 100 \quad (3)$$

$$RGR (\%) = 100 \times \frac{(\text{Final weight} - \text{Initial weight})}{(\text{Times of experiment} \times \text{Initial weight})} \quad (4)$$

$$FCR = \frac{\text{Feed intake (g)}}{\text{Body weight gain (g)}} \quad (5)$$

$$PER = 100 \times \frac{(\text{Final weight} - \text{Initial weight})}{\text{The amount of diet consumed} \times \text{Protein content of diet}} \quad (6)$$

$$PR = 100 \times \left( \frac{\text{The total protein in fish body gain (g)}}{\text{The total protein consumed (g)}} \right) \quad (7)$$

$$SR (\%) = 100 \times \left( \frac{\text{Final count}}{\text{Initial count}} \right) \quad (8)$$

## Hematology and Biochemical Analysis

Hematocrit analysis (Hct%) was measured using micro-centrifugation (Barros et al., 2002). The packed cell volume percentage was determined after blood centrifugation in a standard heparinized micro-hematocrit capillary tube of 3500 g for 10 min at room temperature. The concentration of hemoglobin (Hb; g dl<sup>-1</sup>) was measured using a spectrophotometer through the cyanmethemoglobin method (Blaxhall & Daisley, 1973). Blood indices, including (MCHC) were calculated using the formula (g dl<sup>-1</sup>)=Hb(g dl<sup>-1</sup>)/Hct(%) (Dacie & Lewis, 1991). Biochemical parameters were analyzed with automatic analysis tools (Mindray BK-3.00, China) using the commercial clinical kit (Pars Azmoon Kit, USA). Biochemical measurement was conducted for glucose, total protein, albumin, total cholesterol, triglyceride, calcium, magnesium, and inorganic phosphorus, as Kumar et al. (2005) referred to.

## Statistical Analysis

Data on growth, feed intake, feed efficiency, nutrient content, and survival rate of fish were analyzed using the homogeneity test and analysis of variance (ANOVA). Duncan's multiple range test was further applied if ANOVA revealed a very significant difference ( $P<0.01$ ) or a significant difference ( $P<0.05$ ). The optimal dose of lysine was determined with polynomial orthogonal (Steel et al., 1996). All statistical analysis used SPSS ver. 19.0 (Chicago, Illinois, USA).

## RESULTS

### The Efficiency of Feed Utilization and Growth

The initial weight of fish observed for growth and feed efficiency parameter was  $15.54\pm 0.17$  g/fish. There was no statistically significant difference ( $P>0.05$ ) between experimental diet treatments. Protein digestibility (ADCp), efficiency of feed utilization (EFU), relative growth rate (RGR), food conversion ratio (FCR), protein efficiency ratio (PER), and protein retention of fish given experimental diets increased until a certain dose of lysine (2.75%) (Table 4). However, it later decreased along with the increasing lysine dose of higher than 2.75%. The survival rate of Sangkuriang catfish for all treatments was 100% during the study. Moreover, feed intake during the research did not indicate a significant difference between treatments of experimental diets.

The optimum lysine levels in feed with PSB and FM for Sangkuriang catfish at the grow-out stage were measured using the orthogonal polynomial test. Based on EFU, PER, and RGR data, the optimum lysine levels in the diet of Sangkuriang catfish at the grow-out stage were 2.63% (Figure 1), 2.47% (Figure 2), and 2.62% (Figure 3), respectively.



Table 4

Protein digestibility (ADCp), the efficiency of feed utilization (EFU), relative growth rate (RGR), feed conversion ratio (FCR), protein efficiency ratio (PER), protein retention (PR), and survival rate (SR) of Sangkuriang catfish at grow-out stage fed experimental diets contained different lysine level

Parameters	Experimental diets					
	1	2	3	4	5	6
Initial body weight (g)	15.54±0.17	15.58±0.19	15.54±0.15	15.60±0.16	15.50±0.17	15.50±0.18
Final body weight (g)	63.32±0.27 <sup>f</sup>	75.78±0.28 <sup>c</sup>	79.26±0.25 <sup>b</sup>	88.14±0.22 <sup>a</sup>	70.56±0.21 <sup>d</sup>	68.64±0.23 <sup>c</sup>
Weight gain (g/fish) <sup>1</sup>	47.82±0.36 <sup>f</sup>	60.20±0.36	63.72±0.30	72.54±0.34 <sup>a</sup>	55.06±0.37 <sup>d</sup>	53.10±0.31 <sup>c</sup>
Feed intake (g)	276.48±0.23	278.42±0.35	279.75±0.26	274.43±0.27 <sup>a</sup>	276.88±0.32	275.88±0.31
ADCp (%)	58.43±0.21 <sup>f</sup>	65.34±0.27 <sup>d</sup>	69.21±0.20 <sup>b</sup>	76.52±0.25 <sup>a</sup>	67.29±0.20 <sup>c</sup>	61.35±0.23 <sup>c</sup>
EFU (%)	55.34±0.36 <sup>f</sup>	63.29±0.33 <sup>d</sup>	67.46±0.36 <sup>b</sup>	73.82±0.38 <sup>a</sup>	65.31±0.36 <sup>c</sup>	60.37±0.30 <sup>c</sup>
RGR (%/day)	2.03±0.18 <sup>f</sup>	2.36±0.14 <sup>d</sup>	2.94±0.10 <sup>b</sup>	3.48±0.16 <sup>a</sup>	2.73±0.17 <sup>c</sup>	2.25±0.15 <sup>c</sup>
FCR	2.08±0.22 <sup>f</sup>	1.65±0.24 <sup>c</sup>	1.48±0.23 <sup>b</sup>	1.36±0.20 <sup>a</sup>	1.74±0.21 <sup>d</sup>	1.89±0.27 <sup>c</sup>
PER	1.34±0.12 <sup>f</sup>	1.73±0.17 <sup>d</sup>	2.09±0.13 <sup>b</sup>	2.44±0.16 <sup>a</sup>	1.85±0.17 <sup>c</sup>	1.45±0.12 <sup>c</sup>
PR	42.67±0.30 <sup>f</sup>	54.23±0.31 <sup>c</sup>	58.62±0.35 <sup>b</sup>	59.43±0.34 <sup>a</sup>	48.64±0.30 <sup>d</sup>	46.35±0.33 <sup>c</sup>
SR (%)	100±0.00	100±0.00	100±0.00	100±0.00	100±0.00	100±0.00

Note. Mean values with different superscripts showed a significant difference ( $P < 0.05$ )

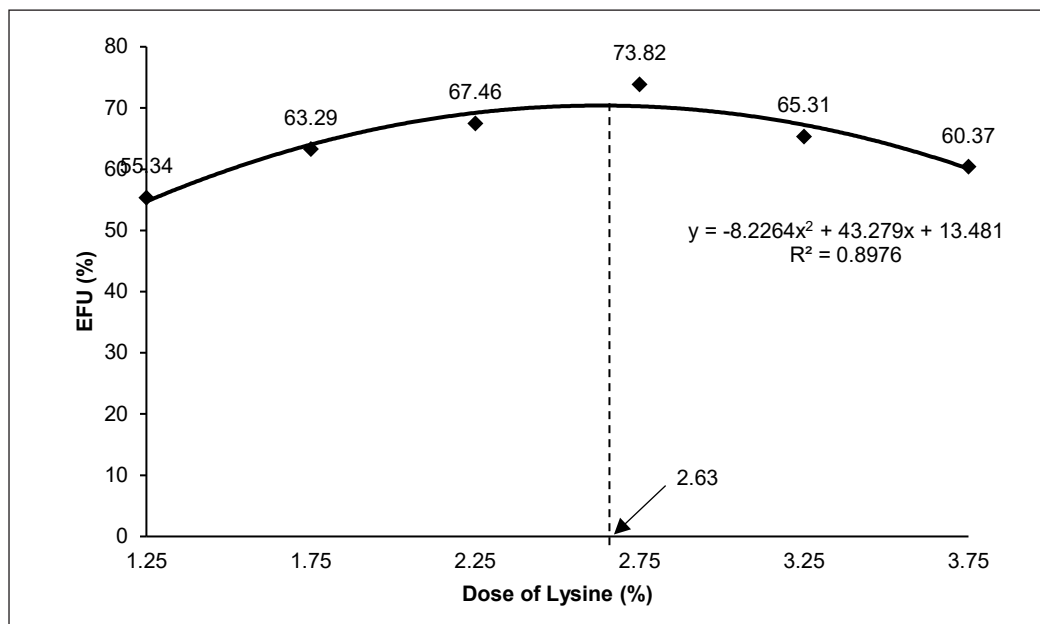


Figure 1. Correlation between dietary lysine level and efficiency of feed utilization (EFU) of Sangkuriang catfish at grow-out stage

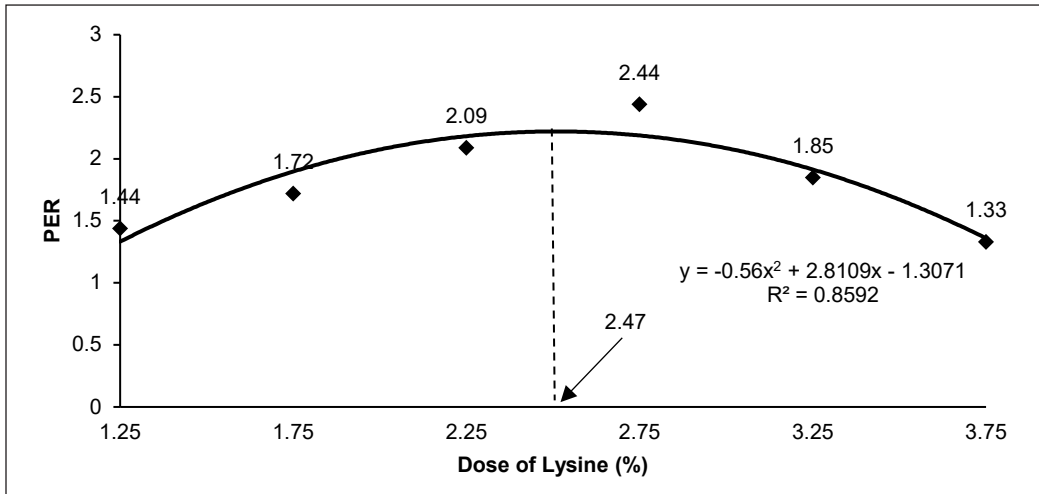


Figure 2. Correlation between dietary lysine level and protein efficiency ratio (PER) of Sangkuriang catfish at the grow-out stage

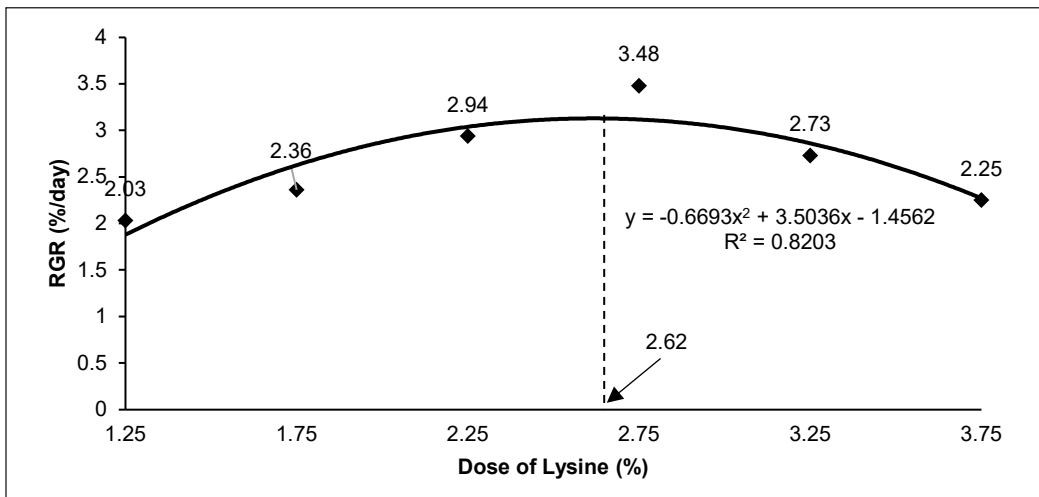


Figure 3. Correlation between dietary lysine level and relative growth rate (RGR) of Sangkuriang catfish at grow-out stage

### Proximate Analysis of Experimental Diets

A proximate analysis of the whole body of fish-fed experimental diets is presented in Table 5. The proximate analysis showed an insignificant difference ( $P < 0.05$ ) in moisture, crude protein, crude lipid, and ash of carcass of fish-fed experimental diets.

### Hematology and Biochemical Parameter

The use of poultry slaughterhouse by-product (PSB) meal added with different doses of lysine in experimental diets had no significant effect on glucose, triglyceride, total protein,

Table 5  
Body chemical composition ( $\text{g kg}^{-1}$ ) of Sangkuriang catfish at grow-out stage fed experimental diets during the study

Composition	Experimental Diets					
	1	2	3	4	5	6
Moisture	751.79±0.2	751.74±0.27	751.78±0.23	751.79±0.28	751.74±0.25	751.78±0.27
Crude protein	153.38±0.20	153.39±0.22	153.39±0.25	153.39±0.24	153.38±0.22	153.39±0.21
Crude lipid	57.54±0.13	57.59±0.10	57.59±0.17	57.54±0.15	57.59±0.13	57.54±0.14
Ash	37.29±0.34	37.28±0.30	37.24±0.35	37.24±0.30	37.29±0.37	37.29±0.33

Note. Mean values with different superscripts showed a significant difference ( $P < 0.05$ )

Table 6  
Results of hematological analysis and biochemical parameters of Sangkuriang catfish at grow-out stage fed experimental diets during the study

Parameters	Experimental Diets					
	1	2	3	4	5	6
Hemoglobin	8.88±0.19	8.47±0.14	8.67±0.71	8.62±0.84	8.34±1.33	8.21±0.63
Hematocrit (%)	43.00±2.16	42.67±2.26	44.67±2.52	43.33±2.31	43.00±2.45	43.33±2.27
MCHC ( $\text{g dl}^{-1}$ )	21.77±1.04	21.87±1.28	21.51±1.23	21.98±1.35	21.01±1.52	21.71±1.14
Total protein	5.67±0.09	5.37±0.12	5.25±0.18	5.41±0.17	5.41±0.16	5.29±0.14
Albumin	0.53±0.12	0.53±0.20	0.58±0.19	0.57±0.17	0.57±0.21	0.57±0.25
Globulin	4.86±0.26	4.61±0.23	4.77±0.24	4.74±0.20	4.34±0.31	4.82±0.30
Glucose	84.67±0.32	85.67±0.37	85.00±0.36	84.67±0.40	85.67±0.39	85.00±0.39
Cholesterol	412.00±3.54 <sup>f</sup>	464.00±3.68 <sup>c</sup>	519.33±3.37 <sup>d</sup>	575.00±3.49 <sup>c</sup>	607.33±3.38 <sup>b</sup>	630.67±3.57 <sup>a</sup>
Triglyceride	252.67±4.35	253.67±4.40	254.33±4.39	258.00±4.2	255.00±4.49	256.33±4.52
Urea	8.63±1.25	8.43±1.15 <sup>a</sup>	8.50±1.32 <sup>a</sup>	8.43±1.04 <sup>a</sup>	8.50±1.13 <sup>a</sup>	8.47±1.41 <sup>a</sup>
Calcium	15.60±0.87	15.50±0.75	15.13±0.54 <sup>a</sup>	15.23±0.65 <sup>a</sup>	15.57±0.73 <sup>a</sup>	15.83±0.69 <sup>a</sup>
Phosphorous	10.87±0.27	10.58±0.29	10.49±0.3	10.33±0.62	10.67±0.34	10.30±0.39
Magnesium	4.80±0.62	4.77±0.63	4.90±0.72	4.50±0.58	4.60±0.63	4.58±0.53

Note. Mean values with different superscripts showed a significant difference ( $P < 0.05$ )

urea, calcium, magnesium, albumin, globulin, hemoglobin, hematocrit, phosphorous, MCHC concentrations. The fish-fed experimental treatment diets 1 and 6 had the lowest and highest cholesterol levels, respectively (Table 6).

## DISCUSSION

The study showed that lysine addition in feed ingredients formulated with PSB and FM as animal protein sources were suitable for Sangkuriang catfish at the grow-out stage. The highest efficiency of feed utilization (EFU) was shown by the fish-fed experimental diet 4 (Table 3). An experimental diet containing lysine levels according to the fish requirement

will support tissue formation, increasing feed efficiency that is further converted into body protein (Marchao et al., 2020). Fish fed with PSB and FM and supplemented with 2.75% lysine (experimental diet 4) possessed a higher EFU than other experimental diets. It occurred since fish fed the treatment diet exhibited the highest protein digestibility (ADCp) compared to other diets. Higher protein digestibility in the diet will result in higher efficiency of feed utilization by fish (National Research Council, 2011). Lysine that is added to dietary feed can increase feed digestibility through the activation of digestive enzymes. Aristasari et al. (2020) stated that lysine addition in the feed would increase ileal (intestine) digestibility. Thus, the nutrient is quickly absorbed, resulting in fish getting full faster, a high growth rate, and improved feed efficiency. Furthermore, Jiang et al. (2015) reported that lysine could increase feed intake, protein digestibility, and growth of grass carp.

Adding 2.75% lysine in feed with PSB and FM (experimental diet 4) was the best treatment, with the highest relative growth rate (RGR) of  $3.48 \pm 0.16\%$ /day. It was expected that treatment diet 4 exhibited the highest protein efficiency ratio (2.44%) compared to other treatments. Lysine supplementation with a dose according to fish diet requirements could increase feed conversion and fish growth while decreasing lipids in the fish body (Obado et al., 2018). Lysine and methionine are also involved in carnitine synthesis (Walton et al., 1984). L-carnitine increases energy production in mitochondria by oxidizing fatty acids and improves the efficiency of energy utilization from fatty acid oxidation of fish to increase growth rate and reduce tissue fat concentration (Suloma et al., 2014).

The supplementation of lysine at different doses in dietary feed with PSB and FM significantly affected ( $P < 0.05$ ) PER of Sangkuriang catfish. It indicated that lysine added to feed could increase feed quality. Thus, the protein of experimental diets is possibly utilized optimally by fish for growth. Table 3 showed that the experimental diets used were of good quality, as seen from the complete essential amino acid profile. The good quality feed contains protein based on fish requirements and a full essential amino acid profile (EAA) (El-Husseiny et al., 2017). An incomplete EAA profile in feed is associated with inhibited protein synthesis and causes slow growth (Hansen et al., 2007). Therefore, one effort to fulfill EAA requirements in fish feed is possibly made by formulating diets that contain balanced essential amino acids according to fish needs (Khan & Abidi 2011). Lu et al. (2014) mentioned that dietary amino acid levels of feed affected protein efficiency ratio (PER), feed efficiency ratio (FER), and crude protein significantly. Furthermore, Xie et al. (2012) reported that PER would increase along with the increasing lysine level in feed but later will remain constant.

Fish-fed experimental diets added with lysine below 2.75% (1.25, 1.75%, and 2.25%) were observed to have lower growth and were expectedly caused by lysine doses that

did not follow fish requirements to support growth. This result was confirmed by de Vareilles et al. (2012) that feed containing lysine that is not following fish needs will result in imbalanced amino acids and poor protein retention. Thus, dietary protein will be used more for energy formation, inhibiting fish growth. Besides, other study results also showed that experimental diets with lysine doses above 2.75% (3.25% and 3.75%) inhibited fish growth due to increased carnitine production in the body. This finding was confirmed by Putra et al. (2019) that high carnitine would lead to excessive oxidation of long-chain fatty acids, thus resulting in fatty acid deficiency that inhibits body protein synthesis. Fatty acid deficiency will induce inhibited fish growth. Akbary et al. (2011) reported that essential fatty acid deficiency resulted in slow growth of fish body weight gain, increased moisture content of muscle, high level of hepatic lipid, and low feed efficiency. Several long-chain fatty acids are required for the growth process. Katan et al. (2020) found that long-chain polyunsaturated fatty acids (LC-PUFA), namely eicosapentaenoic (EPA;20:5 $\omega$ 3), arachidonic acid (ARA; 20:4 $\omega$ 6), and docosahexaenoic acid (DHA;22:6 $\omega$ 3) play an important role in fish body weight gain and metabolism. Cholesterol significantly increased along with the increasing lysine dose in experimental diets, even though the value approached the normal range, as reported in *Sparidentex hasta*-fed PSB-based diets (Mozanzadeh et al., 2016). An increase in cholesterol was also reported in fish given feed with a higher animal protein source (Kjaer et al., 2008; Mozanzadeh et al., 2015) compared to fish-fed plant-protein-based diets (Yaghoubi et al., 2016). According to Gaylord et al. (2007), the protein source is important in controlling cholesterol levels by either increasing or decreasing metabolic rate, hence inducing bile salt synthesis in the liver. The addition of lysine with PSB and FM in the feed of another fish species is required to confirm the efficacy of the feed formulation.

## CONCLUSION

The lysine addition in feed formulated with PSB and FM could improve the growth performance, increase feed digestibility, and have no significant effect on the hematology of Sangkuriang catfish at the grow-out stage. The optimal doses of dietary lysine with PSB and FM as an animal protein source for ADCp, EFU, and RGR parameters of Sangkuriang catfish at the grow-out stage were 2.59%, 2.63%, and 2.62%, respectively.

## ACKNOWLEDGMENTS

The authors thank the Indonesian Government, especially the Ministry of Education, Culture, Research and Technology, for funding this research through the Applied Research Grant sourced from the Deputy of Research and Development Reinforcement, the National Research and Innovation Agency, Fiscal Year 2022 No: 187-57/UN7.6.1/PP/2022.

## REFERENCES

- Akbary, P., Hosseini, S. A., & Imanpoor, M. R. (2011). Enrichment of artemia nauplii with essential fatty acids and vitamin C: Effect on rainbow trout (*Oncorhynchus mykiss*) larvae performance. *Iranian Journal of Fisheries Sciences*, 10(4), 557-569.
- Aristasari, E., Nur' Aini, R. A., Nopita, W., Agustono, A., Lamid, M., & Al-Arif, M. A. (2020). The growth, protein content, and fatty acid of catfish meat (*Pangasius* sp.) with the addition of different lysine doses in commercial feed. *IOP Conference Series: Earth and Environmental Science*, 441(1), 1-7. <https://doi.org/10.1088/1755-1315/441/1/012018>
- Barros, M. M., Lim, C., Evans, J. J., & Klesius, P. H. (2002). Effect of iron supplementation to cotton seed meal diets on growth performance of channel cat fish, *Ictalurus punctatus*. *Journal of Applied Aquaculture*, 10(1), 86-92. [https://doi.org/10.1300/J028v10n01\\_07](https://doi.org/10.1300/J028v10n01_07)
- Bicudo, A. J. A., Sado, R. Y., & Cyrino, J. E. P. (2009). Dietary lysine requirement of juvenile pacu *Piaractus mesopotamicus* (Holmberg, 1887). *Aquaculture*, 297(1-4), 151-156. <https://doi.org/10.1016/j.aquaculture.2009.09.031>
- Blaxhall, P.C., & Daisley, K.W. (1973). Routine hematological methods for use fish with blood. *Fish Biology*, 5(6), 771-781. <https://doi.org/10.1111/j.1095-8649.1973.tb04510.x>
- Boyd, C. E. (2003). Guidelines for aquaculture effluent management at the farm level. *Aquaculture*, 226(1-4), 101-112. [https://doi.org/10.1016/S0044-8486\(03\)00471-X](https://doi.org/10.1016/S0044-8486(03)00471-X)
- Dacie, J. V., & Lewis, S. M. (1991). *Practical Hematology*. Churchill Livingstone.
- de Vareilles, M., Conceição, L. E. C., Gómez-Requeni, P., Kousoulaki, K., Richard, N., Rodrigues, P. M., & Rønnestad, I. (2012). Dietary lysine imbalance affects muscle proteome in zebrafish (*Danio rerio*): A comparative 2D-DIGE study. *Marine Biotechnology*, 14(5), 643-654. <https://doi.org/10.1007/s10126-012-9462-3>
- El-Husseiny, M. O., Hassan, M. I., El-Haroun, E. R., & Suloma, A. (2018). Utilization of poultry by-product meal supplemented with L-lysine as fish meal replacer in the diet of African catfish *Clarias gariepinus* (Burchell, 1822). *Journal of Applied Aquaculture*, 30(1), 63-75. <https://doi.org/10.1080/10454438.2017.1412844>
- Farhat, F., & Khan, M. A. (2013). Dietary L-lysine requirement of fingerling stinging catfish, *Heteropneustes fossilis* (Bloch) for optimizing growth, fish meal conversion, protein and lysine deposition. *Aquaculture Research*, 44(4), 523-533. <https://doi.org/10.1111/j.1365-2109.2011.03054.x>
- Fenucci, J. L. (1981). *Studies on the nutrition of marine shrimp of the Penaeus* [Unpublished Doctoral dissertation]. University of Houston, Texas.
- Gaylord, T. G., Barrows, F. T., Teague, A. M., Johansen, K. A., Overturf, K. E., & Shepherd, B. (2007). Supplementation of taurine and methionine to all-plant protein diets for rainbow trout (*Oncorhynchus mykiss*). *Aquaculture*, 269(1-4), 514-524. <https://doi.org/10.1016/j.aquaculture.2007.04.011>
- Hansen, A. C., Rosenlund, G., Karslen, O., Koppe, W., & Hemre, G. I. (2007). Total replacement of fishmeal with plant proteins in diets for atlantic cod (*Gadus morhua* L.) I: Effects on growth and protein retention. *Aquaculture*, 272(1-4), 599-611. <https://doi.org/10.1016/j.aquaculture.2007.08.034>

- Hernández, C., Osuna-Osuna, L., Benitez-Hernandez, A., Sanchez-Gutierrez, Y., González-Rodríguez, B., & Dominguez-Jimenez, P. (2014). Replacement of fish meal by poultry by-product meal, food grade, in diets for juvenile spotted rose snapper (*Lutjanus guttatus*). *Latin American Journal of Aquatic Research*, 42(1), 111-120. <http://dx.doi.org/10.3856/vol42-issue1-fulltext-8>
- Horwitz, W. (Ed.). (1975). *Official Methods of Analysis* (12th ed.). Association of Official Analytical Chemists.
- Jiang, J., Shi, D., Zhou, X. Q., Feng, L., Liu, Y., Jiang, W. D., & Zhao, Y. (2015). Effects of lysine and methionine supplementation on growth, body composition and digestive function of grass carp (*Ctenopharyngodon idella*) fed plant protein diets using high-level canola meal. *Aquaculture Nutrition*, 22(5), 1126-1133. <https://doi.org/10.1111/anu.12339>
- Katan, T., Xue, X., Caballero-Solares, A., Taylor, R. G., Rise, M. L., & Parrish, C. C. (2020). Influence of dietary long-chain polyunsaturated fatty acids and  $\omega 6$  to  $\omega 3$  ratios on head kidney lipid composition and expression of fatty acid and eicosanoid metabolism genes in atlantic salmon (*Salmo salar*). *Frontiers in Molecular Biosciences*, 7, 1-17. <https://doi.org/10.3389/fmolb.2020.602587>
- Khan, M. A., & Abidi, S. F. (2011). Dietary arginine requirement of *Heteropneustes fossilis* fry (Bloch) based on growth, nutrient retention and hematological parameters. *Aquaculture Nutrition* 17(4), 418-428. <https://doi.org/10.1111/j.1365-2095.2010.00819.x>
- Kjaer, M. A., Todorčević, M., Torstensen, B. E., Vegusdal, A., & Ruyter, B. (2008). Dietary n-3 HUFA affects mitochondrial fatty acid beta-oxidation capacity and susceptibility to oxidative stress in Atlantic salmon. *Lipids*, 43(9), 813-827. <https://doi.org/10.1007/s11745-008-3208-z>
- Kumar, S., Sahu, N. P., Pal, A. K., Choudhury, D., Yengkokpam, S., & Mukherjee, S. C. (2005). Effect of dietary carbohydrate on hematology, respiratory burst activity and histological changes in *L. rohita* juveniles. *Fish & Shellfish Immunology*, 19(4), 331-334. <https://doi.org/10.1016/j.fsi.2005.03.001>
- Lu, J., Hua, Y., Fu, W. Z., Zhou, F., Yang, B. B., Xiao, J. X., & Shao, Q. J. (2014). Effects of supplementation coated lysine and methionine in mixture protein diets on growth performance, digestibility and serum biochemical indices of juvenile black sea bream, *Acanthopagrus schlegelii*. *Turkish Journal of Fisheries and Aquatic Sciences*, 14(3), 633-642. [http://dx.doi.org/10.4194/1303-2712-v14\\_3\\_05](http://dx.doi.org/10.4194/1303-2712-v14_3_05)
- Mai, K. S., Zhang, L., Ai, Q. H., Duan, A. Y., Zhang, C. X., Li, H. T., Wan, J. L., & Liufu, Z. G. (2006). Dietary lysine requirement of juvenile Japanese seabass, (*Lateolabrax japonicus*). *Aquaculture*, 258(1-4), 535-542. <https://doi.org/10.1016/j.aquaculture.2006.04.043>
- Marchao, R. S., Ribeiro, F. B., de Siqueira, J. C., Bomfim, M. A. D., Silva, J. C., de Sousa, T. J. R., & da Costa Sousa, M. (2020). Digestible lysine requirement for tambaqui (*Colossoma macropomum*) juveniles using the diet dilution technique. *Aquaculture Reports*, 18, 1-7. <http://dx.doi.org/10.1016/j.aqrep.2020.100482>
- Mozanzadeh, M. T., Agh, N., Yavari, V., Marammazi, J. G., Mohammadian, T., & Gisbert, E. (2016). Partial or total replacement of dietary fish oil with alternative lipid sources in silvery- black porgy (*Sparidentex hasta*). *Aquaculture*, 451, 232-240. <https://doi.org/10.1016/j.aquaculture.2015.09.022>
- Mozanzadeh, M. T., Marammazi, J. G., Yaghoubi, M., Yavari, V., Agh, N., & Gisbert, E. (2015). Somatic and physiological responses to cyclic fasting and re-feeding periods in sobaity sea bream (*Sparidentex hasta*, Valenciennes 1830). *Aquaculture Nutrition*, 23(1), 181-191. <https://doi.org/10.1111/anu.12379>

- Nguyen, L., & Davis, D. A. (2016). Comparison of crystalline lysine and intact lysine used as a supplement in practical diets of channel catfish (*Ictalurus punctatus*) and Nile tilapia (*Oreochromis niloticus*). *Aquaculture*, 464, 331-339. <https://doi.org/10.1016/j.aquaculture.2016.07.005>.
- Nose, T., Arais, S., Lee, D. L., & Hashimoto, Y. (1974). A note on amino acids essential for growth of young carp. *Bulletin of the Japanese Society of Scientific Fisheries*, 40, 903-908. <https://doi.org/10.2331/SUISAN.40.903>
- National Research Council. (2011). *Nutrient Requirements of Fish and Shrimp*. National Academy Press.
- Obado, E., Sabwa, J. A., Raburu, P., Manyala, J., Ngugi, C., Fitzsimmons, K. M., & Egna, H. (2018). Effects of lysine and methionine supplementation and cost effectiveness in production of Nile tilapia diets (*Oreochromis niloticus*) in Western Kenya. *International Journal of Research Science & Management*, 5(3), 12-23. <http://dx.doi.org/10.5281/zenodo.1193968>
- Pérez-Jiménez, A., Peres, H., & Oliva-Teles, A. (2014). Effective replacement of protein-bound amino acids by crystalline amino acids in Senegalese sole (*Solea senegalensis*) juveniles. *Aquaculture Nutrition*, 20(1), 60-68. <https://doi.org/10.1111/anu.12052>
- Putra, L. V. D., Agustono, U., & Kenconoajati, S. H. (2019). The effect of adding lysine in commercial feed on growth rate, feed efficiency, and feed conversion ratio to tambaqui (*Colossoma macropomum*). *IOP Conference Series: Earth and Environmental Science*, 236(1), 1-6. <https://doi.org/10.1088/1755-1315/236/1/012076>
- Rachmawati, D., Hutabarat, J., Samidjan, I., & Windarto, S. (2019). The effects of papain enzyme-enriched diet on protease enzyme activities, feed efficiency, and growth of fingerlings of sangkuriang catfish (*Clarias gariepinus*) reared in tarpaulin pool. *AACL Bioflux*, 12(6), 2177-2187.
- Rachmawati, D., Istiyanto, S., & Mel, M. (2017). Effect of phytase on growth performance, feed utilization efficiency and nutrient digestibility in fingerlings of *Chanos chanos* (Forsskal 1775). *Philippine Journal of Science*, 146(3), 237-245.
- Rachmawati, D., Sarjito, S., Samidjan, I., Nurhayati, D., & Riyadi, P. H. (2022). Effects of yeast on the growth performance of sangkuriang catfish fingerlings (*Clarias gariepinus* var. Sangkuriang). *Pertanika Journal of Tropical Agricultural Science*, 45(1), 273-284. <https://doi.org/10.47836/pjtas.45.1.16>
- Rawles, S. D., Thompson, K. R., Brady, Y. J., Metts, L. S., Aksoy, M. Y., Gannam, A. L., Twibell, R. G., & Webster, C. D. (2011). Effects of replacing fish meal with poultry by-product meal and soybean meal and reduced protein level on the performance and immune status of pond-grown sunshine bass (*Morone chrysops* × *M. saxatilis*). *Aquaculture Nutrition*, 17(3), 708-721. <https://doi.org/10.1111/j.1365-2095.2010.00831.x>
- Srouf, T. M., Essa, M. A., Abdel-Rahim, M. M., & Mansour, M. A. (2016). Replacement of fish meal with poultry by-product meal (PBM) and its effects on the survival, growth, feed utilization, and microbial load of European seabass, *Dicentrarchus labrax* fry. *Global Advanced Research Journal of Agricultural Science*, 5(7), 293-301.
- Steel, R. G. D., Torrie, J. H., & Dickey, D. A. (1996). *Principles and Procedures of Statistics: A Biometrical Approach* (3rd ed.) McGraw Hill, Inc.



- Suloma, A., El-Husseiny, O. M., Hassane, M. I., Mabroke, R. S., & El-Haroun, E. R. (2014). Complementary responses between hydrolyzed feather meal, fish meal and soybean meal without amino acid supplementation in Nile tilapia *Oreochromis niloticus* diets. *Aquaculture International*, 22, 1377-1390. <https://doi.org/10.1007/s10499-014-9753-y>
- Walton, M. J., Cowey, C. B., & Adron, J. W. (1984). The effect of dietary lysine levels on growth and metabolism of rainbow trout (*Salmo gairdneri*). *British Journal of Nutrition*, 52(1), 115-122. <https://doi.org/10.1079/bjn19840077>
- Wilson, R. P., Harding, E., & Garling Jr, D. L. (1977). Effect of dietary pH on amino acid utilization and the lysine requirement of fingerling channel catfish. *Journal of Nutrition*, 107(1), 166-170. <https://doi.org/10.1093/jn/107.1.166>
- Xie, F., Ai, Q., Mai, K., Xu, W., & Wang, X. (2012). Dietary lysine requirement of large yellow croaker (*Pseudosciaena crocea*, Richardson 1846) larvae. *Aquaculture Research*, 43(6), 917-928. <https://doi.org/10.1111/j.1365-2109.2011.02906.x>
- Yaghoubi, M., Mozanzadeh, M. T., Marammazi, J. G., Safari, O., & Gisbert, E. (2016). Dietary replacement of fish meal by soy products (soybean meal and isolated soy protein) in silvery- black porgy juveniles (*Sparidentex hasta*). *Aquaculture*, 464, 50-59. <https://doi.org/10.1016/j.aquaculture.2016.06.002>
- Yones, A. M. M., & Metwalli, A. A. (2015). Effects of fish meal substitution with poultry by-product meal on growth performance, nutrients utilization and blood contents of juvenile Nile tilapia (*Oreochromis niloticus*). *Journal of Aquaculture Research & Development*, 7(1), 2-6. <http://dx.doi.org/10.4172/2155-9546.1000389>
- Zhou, F., Shao, J., Xu, Z., Ma, J., & Xu, Z. (2010). Quantitative L-lysine requirement of juvenile black sea bream (*Sparus macrocephalus*). *Aquaculture Nutrition*, 16(2), 194-204. <https://doi.org/10.1111/j.1365-2095.2009.00651.x>



## Polynomial Regression Calibration Method of Total Dissolved Solids Sensor for Hydroponic Systems

**Ansar Jamil\***, Teo Sheng Ting, Zuhairiah Zainal Abidin, Maisara Othman, Mohd Helmy Abdul Wahab, Mohammad Faiz Liew Abdullah, Mariyam Jamilah Homam, Lukman Hanif Muhammad Audah and Shaharil Mohd Shah

*Advanced Telecommunication Research Center (ATRC), Universiti Tun Hussein Onn Malaysia, Johor, Malaysia*

### ABSTRACT

Smart hydroponic systems have been introduced to allow farmers to monitor their hydroponic system conditions anywhere and anytime using Internet of Things (IoT) technology. Several sensors are installed on the system, such as Total Dissolved Solids (TDS), nutrient level, and temperature sensors. These sensors must be calibrated to ensure correct and accurate readings. Currently, calibration of a TDS sensor is only possible at one or a very small range of TDS values due to the very limited measurement range of the sensor. Because of this, we propose a TDS sensor calibration method called Sectioned-Polynomial Regression (Sec-PR). The main aim is to extend the measurement range of the TDS sensor and still provide a good accuracy of the sensor reading. Sec-PR computes the polynomial regression line that fits into the TDS sensor values. Then, it divides the regression line into several sections. Sec-PR calculates the average ratio between the polynomial regressed TDS sensor values and the TDS meter in each section. These average ratio values map the TDS sensor reading to the TDS meter. The performance of Sec-PR was determined using mathematical analysis and verified using

experiments. The finding shows that Sec-PR provides a good calibration accuracy of about 91% when compared to the uncalibrated TDS sensor reading of just 78% with Mean Average Error (MAE) and Root Mean Square Error (RMSE) equal to 59.36 and 93.69 respectively. Sec-PR provides a comparable performance with Machine Learning and Multilayer Perception method.

**Keywords:** Calibration, hydroponic, polynomial regression, TDS sensor

### ARTICLE INFO

#### Article history:

Received: 09 October 2022

Accepted: 04 April 2023

Published: 08 September 2023

DOI: <https://doi.org/10.47836/pjst.31.6.08>

#### E-mail addresses:

[ansar@uthm.edu.my](mailto:ansar@uthm.edu.my) (Ansar Jamil)

[shengting97@gmail.com](mailto:shengting97@gmail.com) (Teo Sheng Ting)

[zuhairia@uthm.edu.my](mailto:zuhairia@uthm.edu.my) (Zuhairiah Zainal Abidin)

[maisara@uthm.edu.my](mailto:maisara@uthm.edu.my) (Maisara Othman)

[helmy@uthm.edu.my](mailto:helmy@uthm.edu.my) (Mohd Helmy Abdul Wahab)

[faiz@uthm.edu.my](mailto:faiz@uthm.edu.my) (Mohammad Faiz Liew Abdullah)

[mariyam@uthm.edu.my](mailto:mariyam@uthm.edu.my) (Mariyam Jamilah Homam)

[hanif@uthm.edu.my](mailto:hanif@uthm.edu.my) (Lukman Hanif Muhammad Audah)

[shaharil@uthm.edu.my](mailto:shaharil@uthm.edu.my) (Shaharil Mohd Shah)

\* Corresponding author

## INTRODUCTION

Agriculture is one of the most productive sectors in Malaysia, especially palm oil. As of 2021, Malaysia is the world's second-largest palm oil producer and exporter after Indonesia. It is about 26% of world production and 34% of world export in 2020 (<https://www.trade.gov/malaysia-country-commercial-guide>). As additional land for palm oil production is unavailable, the same goes for other types of agriculture, such as vegetables, paddy, rice, and fruits. Any large-scale deforestation for agriculture is prohibited due to the negative impact on nature. However, food security issues after covid-19 experienced by many countries caused shortages in the supply of food items such as chicken, vegetables, and cooking oil. As a result, the increase in food prices burdens Malaysians, and because of that, agriculture is one of the pillars of Malaysia's economy.

A hydroponic system is a suitable solution to tackle this critical issue. Hydroponic is a subset of horticulture that uses mineral nutrient solution as a medium for the cultivation of crops instead of soil (Domingues et al., 2012; Maucieri et al., 2019). Any medium other than soil, such as sand, gravel, pebbles, perlite, rock wool, or aquatic medium, could also hold the plant (Garg et al., 2021). Hydroponics requires small space areas without the need for a large land clearing. Hydroponics can be installed in a small yard and a building with proper lighting for indoor farming. There are different types of hydroponic systems, which are the Nutrient Film Technique (NFT) (Alipio et al., 2019; Graves, 1983), Ebb and Flow system (Daud et al., 2018); Wick System (Dubey & Nain, 2020), Deep Flow Technique (DFT) (Pramono et al., 2020) and drip hydroponic (Olubanjo et al., 2022). It is very important to manage water and nutrients in the hydroponic system to achieve the optimum growth of crops (Son et al., 2020). The concentration of ions in the nutrient solutions reduces with time as it is absorbed by plants, which is measured according to electrical conductivity (EC) characteristics (Hosseini et al., 2021; Singh & Dunn, 2016). A high concentration of ions provides good electrical conductivity. Otherwise, a low concentration of ions provides poor electrical conductivity. Instead of EC, other parameters such as pH, dissolved oxygen, and temperature should be measured. Analysis of nutrient solutions and adjustment of nutrient ratios must be done every day for a correct nutrient reading. With the advancement of technologies, IoT technology could be implemented to ease collecting these nutrient parameters automatically, which can be viewed using a web server or phone app. IoT technology transforms conventional hydroponic into smart hydroponic systems (Modu et al., 2020; Munandar et al., 2018).

A smart hydroponic system can be realized and applied at all levels, whether on a small scale at home or a large scale commercially. Farmers can be anywhere away from the hydroponic farm but still be able to monitor the condition of their farm, and if needed, they can manually control it themselves. An IoT device is installed in an existing hydroponic system. Sensors are attached to the IoT devices, such as TDS/EC sensors, pH sensors,

oxygen sensors, and liquid level sensors, to measure the parameter of the hydroponic system. It is critical to ensure that these connected sensors are calibrated during the installation and while the system operates. Failure to ensure that each sensor is regularly and accurately calibrated will result in inaccurate sensor readings. If this situation occurs, the IoT device does not work properly, causing a failure to the entire smart hydroponic system that will cause decreases in crop yield.

Let us consider a TDS sensor, the easiest method to calibrate this sensor is using a reference TDS meter. Reference TDS meter means that this instrument has been calibrated using standard solutions (alkaline, neutral, and acidic solutions), which are normally included at the time of purchase. Several brands of TDS meters are available in the market, such as Hanna TDS instrument tester and Xiaomi portable TDS meter. Manual calibration of a TDS sensor is a simple process. First, use a TDS meter to prepare a nutrient solution at the required TDS value measures in ppm (part per million) units. Second, deep the uncalibrated TDS sensor into the solution and take the sensor reading. Third, calculate the offset by deducting the sensor reading from the TDS meter reading, and finally, add the offset to the sensor reading to make the sensor reading almost the same as the TDS meter reading. For example, if the required level is 1000 ppm, a nutrient solution is prepared at this level using the TDS meter. It means the TDS meter reading is also 1000 ppm. When the TDS sensor is deep into the nutrient solution, the sensor reading is 900 ppm. Here, the offset is 100 ppm should be added to the sensor reading to achieve the required level. However, this method is only valid at one TDS value. The calibration process must be repeated if the required TDS value is changed.

Suseno et al. (2020) developed a calibration method for TDS sensors for nutrient concentrations up to 780 ppm. They characterized analog TDS sensor readings and standard TDS values. After that, the calibration is performed by comparing the data read by the analog TDS sensor with data from the standard TDS results. The characterization graph shows the linear equation between the x-axis variable, namely the ADC reading, and the y-axis, the standard multimeter voltage value. The relationship between the ADC reading with the standard voltage value produces an equation.

Wibowo et al. (2019) proposed a nutrient dosing system for aquaponic that is very important to improve the quality of catfish and lettuce yield. The dosing system must ensure that the nutrient level is between 400 ppm and 500 ppm. The TDS sensor was calibrated so the TDS sensor reading is the same as the TDS meter. Then, the calibration accuracy is calculated by observing the systematic errors. The calibration range of the TDS sensor is up to 819 ppm.

Nguyen et al. (2018) shared a case study about calibrating conductivity sensors using Combined Algorithm Selection and Hyperparameter Optimization. A different model of calibration process was carried out by using the Gaussian process (Franchini et al., 2019;

Peršić et al., 2021; Urban et al., 2015), Simple Logistic (Zheng et al., 2019) and Linear Regression (Iida et al., 2020; Koestoer et al., 2019). Based on their finding, the calibration range of the TDS sensor is within 200 ppm to 2000 ppm only. At the same time, the uncalibrated TDS sensor has a minimum of 57 and a maximum of 1756.92.

In this paper, we propose a new TDS calibration method called Sectioned-Polynomial Regression (Sec-PR) to extend the measurement range of the TDS sensor over the specification by the manufacturer. We just considered the calibration range from 0 to 3000 ppm in this research work. However, the Sec-PR calibration range can be extended to more than 3000 ppm, depending on applications. It is expected that Sec-PR will be able to provide a good calibration accuracy when compared to the existing methods, such as linear regression, multi-layer perception, and the Gaussian process. In addition, Sec-PR is expected to be implemented easily into the programming code of smart hydroponic systems.

## METHODOLOGY

The methodology in this work can be divided into three phases: the initial experiment, mathematical analysis, and implementation of Sec-PR. For the initial experiment phase, an experiment was conducted to compare the TDS sensor and TDS meter readings over different concentrations of fertilizer. This step is very important to determine the trend of the TDS sensor and TDS meter reading used in the next phase. In this mathematical analysis phase, the Sec-PR calibration method is designed to make the TDS sensor reading the same as the TDS meter reading over a wide measurement range. Microsoft Excel was used during the design to analyze the calibration accuracy of Sec-PR. Modifications to the Sec-PR design can be optimized to achieve its best performance. The next phase is the process where Sec-PR is applied to the program code, and the performance of Sec-PR is determined in the actual experiment, which is the same experiment as in the first phase. The TDS sensor reading from the Sec-PR is compared with the TDS meter reading, and the accuracy of the reading is determined. After that, the result is verified with the findings from the second phase, which is a mathematical analysis. Furthermore, in this phase, the performance of Sec-PR is compared with the existing calibration methods of the TDS sensor.

Figure 1 shows the experiment configuration to measure a TDS sensor and a TDS meter reading over different concentrations of fertilizer. The experiment configuration consists of a TDS sensor, ESP 32 dev kit, laptop, 25-liter container as the tank, TDS meter, water, and fertilizer AB. The TDS sensor is dipped into the tank, and the other end is connected to the ESP32 dev kit, which is a microcontroller. ESP32 reads the TDS sensor continuously, and the reading is sent to the laptop using serial communication. Then, the reading can be viewed using a serial monitor window. The experiment begins with the container filled with 6 liters of water. Then, the initial reading of the water in the tank, where no fertilizer has

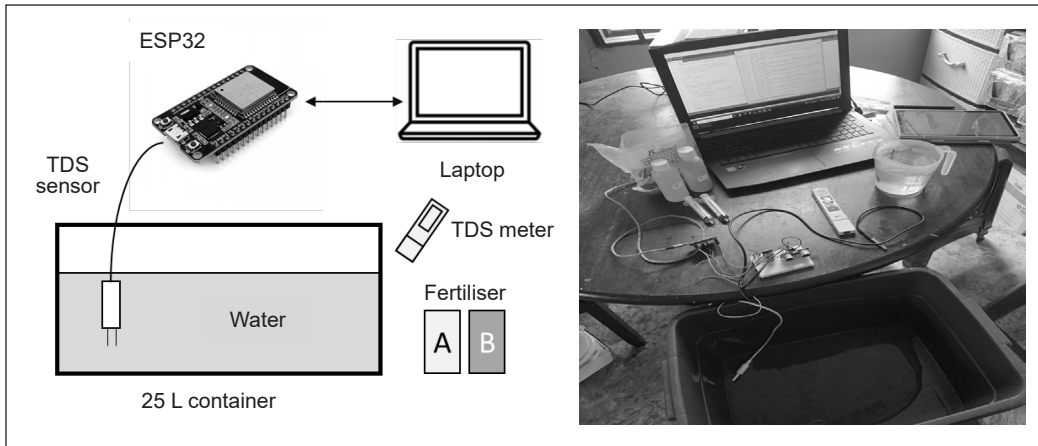


Figure 1. Experiment configuration

been added, is measured using the TDS meter and TDS sensor. After that, add 1 ml of AB fertilizer into the tank using a syringe and stir the solution well. The TDS reading of the nutrient is measured again using the TDS meter and the TDS sensor. This step is repeated by adding another 1 ml of fertilizer AB for fifteen different points until the TDS value is about 3000 ppm. This experiment is repeated five times to increase the accuracy of the data.

TDS value indicates how many milligrams of soluble solids are dissolved in one liter of water. Usually, the higher the TDS value, the higher the number of soluble solids dissolved in water, which means the concentration of the fertilizer is high. Therefore, the TDS value represents one reference point to reflect the fertilizer concentration used widely in hydroponic farms. In this work, we used Gravity Analog TDS Sensors, a consumer-grade product available in the market at an affordable price. The Gravity Analog TDS sensor costs a hundred times cheaper when compared to an industrial-grade TDS sensor. The TDS sensor measures the electrical conductivity of the solution,  $R$ , and then ESP32 converts the sensor reading into the TDS value in ppm unit using Equation 1.

$$TDS\ value = (133.42 \times v^3 - 255.86 \times v^2 + 8.57.39 \times v) \times 0.5\ ppm \quad [1]$$

Where  $v$  is the compensation voltage calculated based on the sensor reading,  $R$  and temperature of the solution,  $T$  using Equation 2.

$$v = R / (1.0 + 0.02 (T - 25.0)) \quad [2]$$

Figure 2 shows the TDS sensor reading and TDS meter reading for different concentrations of fertilizer from the initial experimental phase. The TDS sensor provides a nonlinear increase in TDS value. As fertilizer concentration increases, the increment of

TDS value is reduced significantly. As expected, the TDS meter reading increases linearly with the increase in the concentration of fertilizer. Based on the graph, both devices give the same reading at one TDS value of about 2040 ppm. Otherwise, the TDS sensor reading deviates from the TDS meter for other TDS values. For TDS values below 2040 ppm, the TDS sensor reading is higher than the TDS meter reading. For TDS values over 2040 ppm, the sensor reading is lower than the TDS meter reading. The average deviation of the TDS sensor reading from the TDS meter is equal to 243.4 ppm value. Based on the trend of the graph, the deviation of TDS sensor readings from the TDS meter becomes larger for TDS values more than 3000 ppm.

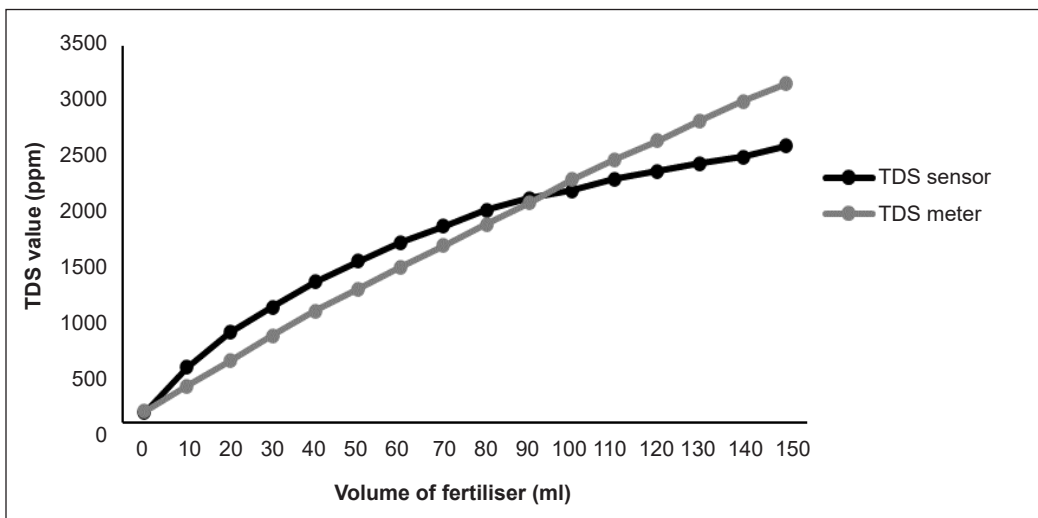


Figure 2. TDS sensor and TDS meter reading over different concentrations of fertilizer

### Sectioned-polynomial Regression of TDS Sensor Calibration

A simple way to calibrate the TDS sensor is to offset the TDS sensor reading to make it equal to the TDS meter reading. For example, if the TDS sensor reading is 1440 ppm and the TDS meter reading is 1671 ppm, offset by 231 ppm is added to the TDS sensor reading. Although it is a simple method, this calibration method is suitable for just one calibration point or a very small calibration range of TDS values. For any changes to the calibration setting of TDS values, the TDS sensor must be recalibrated. Another calibration method is to model the TDS sensor readings using linear regression. Linear Regression is the process of finding a line that best fits the data points available on the plot so that we can use it to predict output values for inputs that are not present in the data set we have, with the belief that those outputs would fall on the line (Hope, 2020). While the Least Squares Regression Line is the line that makes the vertical distance from the data points to the regression line as small as possible. It is called a “least square” because the best line of fit is one that



minimizes the variance (the sum of squares of the errors) (Karunasingha, 2022). Figure 3 shows a line graph computed using linear regression for TDS sensor reading. Deviation from the TDS meter is 210 ppm, which is slightly better when compared to the original sensor reading, which is 243 ppm; however, the deviation value still can be considered high due to the non-linearity characteristic of the TDS sensor reading. Because of that, Sec-PR uses the polynomial regression model that fits into the TDS sensor reading with  $R^2$  equal to 0.9946.

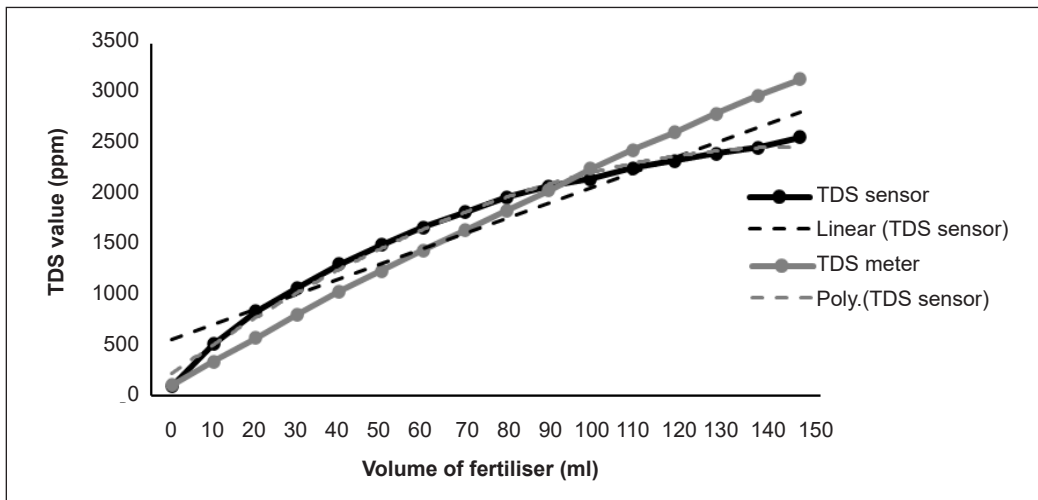


Figure 3. Polynomial regression of TDS sensor reading

Sec-PR maps the TDS sensor reading with the TDS meter reading by dividing the graph into a few sections. The number of sections depends on the TDS sensor reading over different concentrations of fertilizer. The minimum number of sections is two and can exceed several sections required to achieve a wide calibration range with better accuracy. The total TDS sensor readings limit the number of sections. A higher number of sensors reading allows more sections to be created. Otherwise, a smaller number of sensor readings just allows a smaller number of sections. Table 1 shows the Sec-PR calibration algorithm. Each section is labeled as  $S_i$  is numbered and represented by where  $i$  refers to the number of sections starting from 1 to  $n$ . It means that  $n$  is the total number of sections. The average ratio between  $y_i$  and  $y_s$  is calculated for each section and represented by  $R_i$ , which determines the calibrated value for the TDS sensor reading,  $TDS_{cal}$ .  $TDS_{cal}$  is computed by dividing the current TDS sensor reading,  $TDS_{sensor}$ , with  $R_i$ , where  $TDS_{sensor}$  must be within the minimum and maximum TDS value for the  $i^{th}$  section, represented as  $min_i$  and  $max_i$ , respectively. Equation of  $TDS_{cal}$  can be implemented easily in the coding by simply using the if-else-if or case function to determine which the current TDS sensor reading belongs to which section.

Let us consider Sec-PR with 3 sections, as shown in Figure 4. The total number of sections,  $n$ , equals 3, each labeled  $S_1$ ,  $S_2$ , and  $S_3$ . Range of TDS value for  $S_1$  is between and  $min_1 = 98.2$  ppm and  $max_1 = 1309$  ppm. Range of TDS value for  $S_2$  is between  $min_2 = 1310$  and  $max_2 = 2081$  ppm. Range of TDS value for  $S_3$  is between  $min_3 = 2082$  and  $max_3 = 2571$  ppm. Then, Sec-PR calculates the average ratio between the polynomial regression of the TDS sensor with the TDS meter,  $R_i$ , for each section. The calculated results for  $R_1$ ,  $R_2$ , and  $R_3$  are 1.54, 1.13, and 0.89.  $TDS_{cal}$  can be obtained by dividing the current TDS sensor reading with  $R_i$ . For example, if the current TDS sensor reading,  $TDS_{sensor}$ , is 256 ppm, the reading falls into section  $S_1$ .  $TDS_{cal}$  value is calculated by dividing 256 by 1.54, which equals 166 ppm. Another example is if the current TDS sensor reading is 1500 ppm in section  $S_2$ , the  $TDS_{cal}$  value becomes 1327 ppm, calculated by dividing 1500 by 1.13.

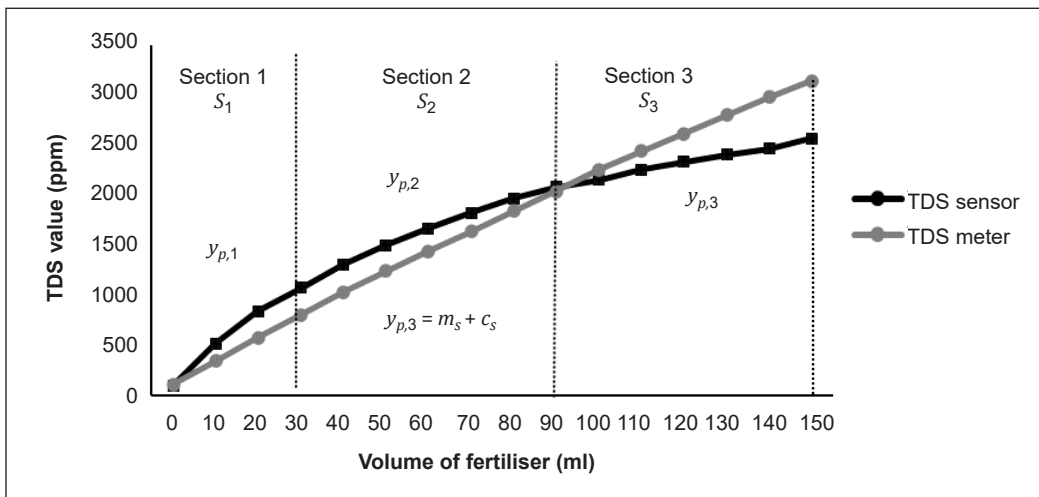


Figure 4. Sec-PR for three sections

Table 1  
Sec-PR calibration algorithm

Sec-PR Algorithm	Parameters
1	$n$ is the total number of sections $x$ is the volume of fertilizer $S_i$ $i^{th}$ section $TDS_{meter}$ measured TDS value using the TDS meter $TDS_{sensor}$ measured TDS value using the TDS sensor $TDS_{cal}$ calibrated TDS value from Sec-PR $y_p = \beta_0x + \beta_1x + c$ the second-order polynomial regression line for the TDS sensor $y_{p,i}$ TDS sensor value on the polynomial regression line at $i^{th}$ section $min_i$ is the minimum range of TDS value at $i^{th}$ section $max_i$ is the maximum range of TDS value at $i^{th}$ section

Table 1 (continue)

Sec-PR Algorithm	
2	<p><b>Measure standard TDS meter reading</b>  <math>y_s = m_s x + c_s</math> the linear line for TDS meter reading.</p>
3	<p><b>Measure TDS sensor reading</b>  <math>y_p = \beta_0 x + \beta_1 x + c</math> the polynomial regression for TDS sensor reading</p>
	<b>Divide TDS sensor reading into <math>n</math> section</b>
4	<p><b>Polynomial regression at <math>i^{th}</math> section</b>  <math>y_{p,i} = \beta_0 x + \beta_1 x + c</math>  <math>i = 1, 2, 3, 4 \dots \dots, n</math></p>
5	<p><b>Mean ratio between TDS sensor value (on the line of the polynomial regression) and TDS meter for <math>i^{th}</math> section, <math>R_i</math></b>  <math display="block">R_i = \text{mean} \left( \frac{y_{p,i}(x)}{y_s(x)} \right)</math></p>
6	<p><b>Calculate the calibration value of the TDS sensor reading for <math>i^{th}</math> section</b>  <math display="block">TDS_{cal} = \frac{TDS_{sensor}}{R_i}, \quad \min_i \leq TDS_{sensor} &lt; \max_i</math></p> <p style="text-align: center;"><b>For <math>n</math> sections, the equation can be written as</b></p> $TDS_{cal} = \begin{cases} \frac{TDS_{sensor}}{R_1}, & \min_1 \leq TDS_{sensor} < \max_1 \\ \frac{TDS_{sensor}}{R_2}, & \min_2 \leq TDS_{sensor} < \max_2 \\ \frac{TDS_{sensor}}{R_3}, & \min_3 \leq TDS_{sensor} < \max_3 \\ \vdots & \vdots \\ \frac{TDS_{sensor}}{R_n}, & \min_n \leq TDS_{sensor} < \max_n \end{cases}$

**RESULTS AND DISCUSSION**

Figure 5 shows the TDS values of Sec-PR for the different number of sections over the different fertilizer volumes. Sec-PR (6 sections) provides the best performance, with the TDS value being very close to the TDS meter. Sec-PR (6 sections) has recorded MAE and RMSE equal to 51.52 and 62.37, respectively (Table 2). It is about

a 78% improvement compared to the uncalibrated TDS sensor value, with MAE and RMSE equal to 243.34 and 285.41, respectively. Besides that, Sec-PR with a higher number of

Table 2  
*Mathematical calculation of MAE and RMSE for Sec-PR*

Algorithm	MAE	RMSE
TDS Sensor	243.34	285.41
Polynomial Regression (PR)	301.12	415.71
Sec-PR (2 Sections)	141.06	182.26
Sec-PR (4 Sections)	66.60	84.99
Sec-PR (6 Sections)	51.52	62.37

sections provides better performance when compared to Sec-PR with a lower number of sections. That means Sec-PR (2 sections) provides the lowest performance with MAE and RMSE equal to 141.06 and 182.26, respectively, but still better when compared to the uncalibrated TDS sensor value.

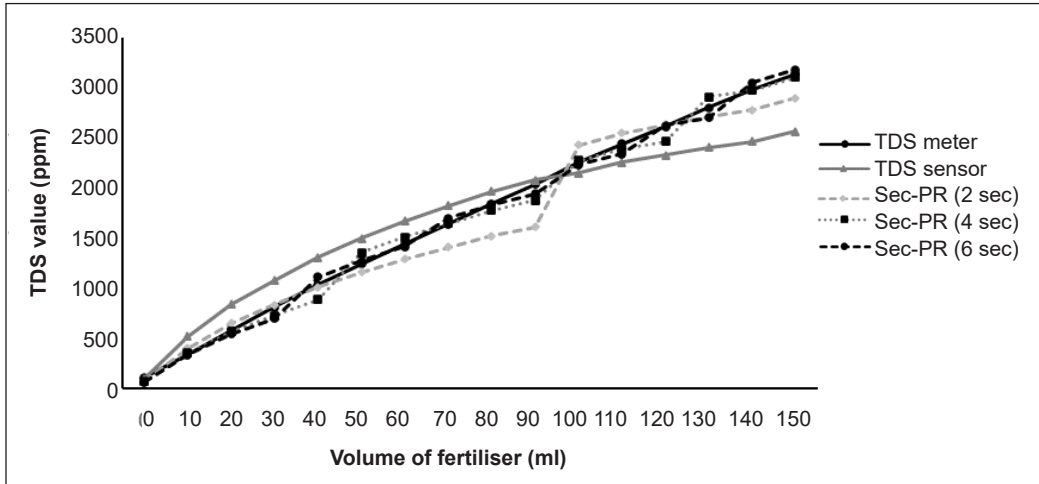


Figure 5. TDS values of Sec-PR for different numbers of sections

Sec-PR was implemented in the experimental setup to determine its performance in the real environment. The findings of the experiment are shown in Figure 6. The graph shows that the performance of Sec-PR in the experiment is comparable with the mathematical analysis. Table 3 shows that Sec-PR has recorded MAE and RMSE equal to 79.94 and 93.96, respectively, about a 67.8% improvement compared to the uncalibrated TDS value.

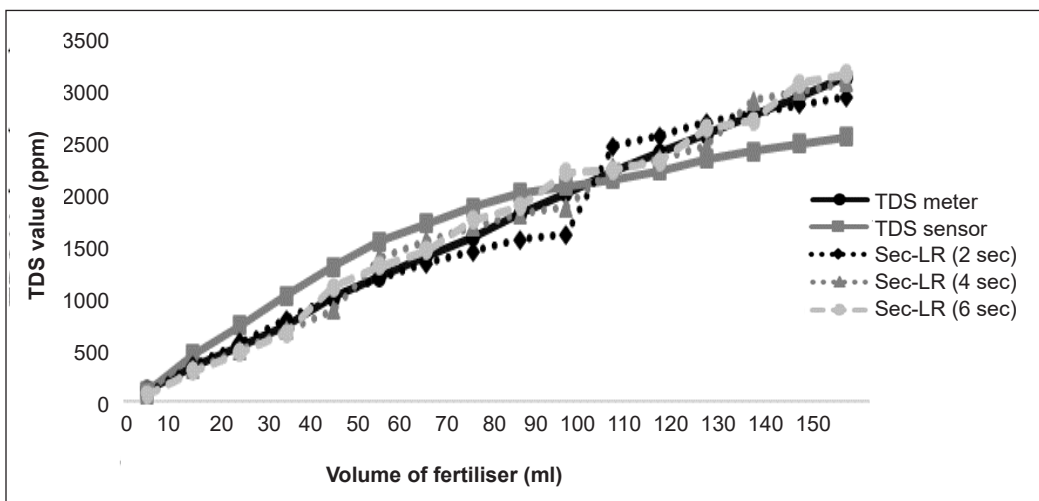


Figure 6. Experimental results of Sec-PR for different numbers of sections

The performance of Sec-PR is compared with other TDS sensor calibration methods (Table 4). Based on the literature, three calibration methods are considered for comparison: machine learning, Gaussian Process, and Multi-layer perception. The recorded MAE and RMSE values are taken directly from the literature. Sec-PR provides

comparable performances when compared to machine learning and multilayer perception. The RMSE value recorded by Sec-PR is just slightly higher when compared to machine learning and multilayer perception, which can be considered a variation in the different experimental setups. In terms of MAE, Sec-PR also gives comparable performance when compared to multilayer perception. Sec-PR and multilayer perception have recorded MAE equal to 79.94 and 40.6973, respectively. However, Sec-PR has recorded a better calibration accuracy when compared to Gaussian Process for both MAE and RMSE. Even though Sec-PR does not provide the best accuracy, Sec-PR covers a wider calibration range compared to other calibration methods.

Table 3  
*Experimental results of MAE and RMSE for Sec-PR*

Algorithm	MAE	RMSE
TDS Sensor	254.16	292.82
Sec-PR (2 Sections)	117.09	161.02
Sec-PR (4 Sections)	82.34	97.80
Sec-PR (6 Sections)	79.94	93.69

Table 4  
*Comparison of Performance between Sec-PR and the existing calibration methods*

Algorithm	MAE	RMSE	Range
Sec-PR	79.94	93.69	0 to 3000 ppm
Machine Learning(Goparaju et al., 2021)	-	27.93	0 to 400 ppm
Gaussian Process (Nguyen et al., 2018)	302.681	352.2483	0 to 2000 ppm
Multilayer perception (Nguyen et al., 2018)	40.6973	46.034	0 to 2000 ppm

## CONCLUSION

Sec-PR is a calibration method of TDS sensor designed for smart hydroponic systems. Sec-PR aims to extend the limited measurement range of the TDS sensor and still provide a good accuracy of sensor readings. In addition, Sec-PR can be implemented easily into any programming code of smart hydroponic systems. Sec-PR computes a polynomial regression line for TDS sensor reading over different fertilizer concentrations collected from the initial experiment. In order to map the TDS sensor reading to the TDS meter reading, the graphs are divided into several sections. Then, the average ratio between the polynomial regressed TDS sensor value, and the TDS meter value is calculated for each section. This average ratio value is implemented in the program code that will be used to calculate the calibrated value of the TDS sensor. The actual TDS sensor reading is divided by the average ratio to ensure that the sensor reading becomes almost the same as the

TDS meter. The performance of Sec-PR was determined using mathematical analysis and verified using experiments. Sec-PR provides a good accuracy of about 91% compared to the uncalibrated TDS sensor reading of just 78% accuracy. Sec-PR has recorded MAE and RMSE equal to 59.36 and 93.69, respectively. Sec-PR provides a comparable performance with Machine Learning and Multilayer Perception method. However, Sec-PR provides better performance when compared to the Gaussian Process. For future work, Sec-PR can be implemented for other types of sensors.

## ACKNOWLEDGEMENTS

The project is financially supported by Universiti Tun Hussein Onn Malaysia (UTHM) under H908-TIER 1 Grant.

## REFERENCES

- Alipio, M. I., Cruz, A. E. M. dela, Doria, J. D. A., & Fruto, R. M. S. (2019). On the design of Nutrient Film Technique hydroponics farm for smart agriculture. *Engineering in Agriculture, Environment and Food*, 12(3), 315-324. <https://doi.org/10.1016/j.eaef.2019.02.008>
- Daud, M., Handika, V., & Bintoro, A. (2018). Design and realization of fuzzy logic control for Ebb and flow hydroponic system. *International Journal of Scientific and Technology Research*, 7(9), 138-144.
- Domingues, D. S., Takahashi, H. W., Camara, C. A. P., & Nixdorf, S. L. (2012). Automated system developed to control pH and concentration of nutrient solution evaluated in hydroponic lettuce production. *Computers and Electronics in Agriculture*, 84, 53-61. <https://doi.org/10.1016/j.compag.2012.02.006>
- Dubey, N., & Nain, V. (2020). Hydroponic - The future of farming. *International Journal of Environment, Agriculture and Biotechnology*, 4(4), 857-864. <https://doi.org/10.22161/ijeab.54.2>
- Franchini, S., Charogiannis, A., Markides, C. N., Blunt, M. J., & Krevor, S. (2019). Calibration of astigmatic particle tracking velocimetry based on generalized Gaussian feature extraction. *Advances in Water Resources*, 124, 1-8. <https://doi.org/10.1016/j.advwatres.2018.11.016>
- Garg, K., Verma, S., & Solanki, H. A. (2021). A review on variety and variability of soil-less media for maximizing yield of greenhouse horticultural crops. *Research and Reviews: Journal of Environmental Sciences*, 3(1), 1-9. <http://doi.org/10.5281/zenodo.4663964>
- Goparaju, S. U. N., Vaddhiparthy, S. S. S., Pradeep, C., Vattem, A., & Gangadharan, D. (2021, Jun 14-July 31). *Design of an IoT system for machine learning calibrated TDS measurement in smart campus*. [Paper presentation]. 2021 IEEE 7th World Forum on Internet of Things (WF-IoT), Los Angeles, USA. <https://doi.org/10.1109/WF-IoT51360.2021.9595057>
- Graves, C. J. (1983). The nutrient film technique. *Horticultural Reviews*, 5(1), 1-44.
- Hope, T. M. (2020). *Machine learning*. Elsevier.
- Hosseini, H., Mozafari, V., Roosta, H. R., Shirani, H., van de Vlasakker, P. C. H., & Farhangi, M. (2021). Nutrient use in vertical farming: Optimal electrical conductivity of nutrient solution for growth of

- lettuce and basil in hydroponic cultivation. *Horticulturae*, 7(9), Article 283. <https://doi.org/10.3390/horticulturae7090283>
- Iida, S., Shimizu, T., Shinohara, Y., Takeuchi, S., & Kumagai, T. (2020). The necessity of sensor calibration for the precise measurement of water fluxes in forest ecosystems. *Forest-Water Interactions*, 240, 29-54. [https://doi.org/10.1007/978-3-030-26086-6\\_2](https://doi.org/10.1007/978-3-030-26086-6_2)
- Karunasingha, D. S. K. (2022). Root mean square error or mean absolute error. *Information Sciences*, 585, 609-629. <https://doi.org/10.1016/j.ins.2021.11.036>
- Koestoer, R., Pancasaputra, N., Roihan, I., & Harinaldi. (2019). A simple calibration methods of relative humidity sensor DHT22 for tropical climates based on Arduino data acquisition system. *AIP Conference Proceedings*, 2062(1), Article 020009. <https://doi.org/10.1063/1.5086556>
- Maucieri, C., Nicoletto, C., van Os, E., Anseeuw, D., van Havermaet, R., & Junge, R. (2019). Hydroponic technologies. In S. Goddek, A. Joyce, B. Kotzen & G. M. Burnell (Eds.), *Aquaponics Food Production Systems* (pp.77-110). Springer. [https://doi.org/10.1007/978-3-030-15943-6\\_4](https://doi.org/10.1007/978-3-030-15943-6_4)
- Modu, F., Adam, A., Aliyu, F., Mabu, A., & Musa, M. (2020). A survey of smart hydroponic systems. *Advances in Science, Technology and Engineering Systems Journal*, 5(1), 233-248. <https://doi.org/10.25046/aj050130>
- Munandar, A., Fakhurroja, H., Anto, I. F. A., Pratama, R. P., Wibowo, J. W., Salim, T. I., & Rizqyawan, M. I. (2018, November 21-22). *Design and development of an IoT-based smart hydroponic system*. [Paper presentation]. 2018 International Seminar on Research of Information Technology and Intelligent Systems (ISRITI), Yogyakarta, Indonesia. <https://doi.org/10.1109/ISRITI.2018.8864340>
- Nguyen, T. D., Nguyen, T. T. S., & Le, N. T. (2018, October 18-20). *Calibration of conductivity sensor using combined algorithm selection and hyperparameter optimization*. [Paper presentation]. 2018 International Conference on Advanced Technologies for Communications (ATC), Ho Chi Minh City, Vietnam. <https://doi.org/10.1109/ATC.2018.8587559>
- Olubanjo, O. O., Adaramola, O. D., Alade, A. E., Azubuike, C. J., & others. (2022). Development of drip flow technique hydroponic in growing cucumber. *Sustainable Agriculture Research*, 11(2), 1-67. <https://doi.org/https://doi.org/10.5539/sar.v11n2p67>
- Peršić, J., Petrović, L., Marković, I., & Petrović, I. (2021). Spatiotemporal multisensor calibration via gaussian processes moving target tracking. *IEEE Transactions on Robotics*, 37(5), 1401-1415. <https://doi.org/10.1109/TRO.2021.3061364>
- Pramono, S., Nuruddin, A., & Ibrahim, M. H. (2020). Design of a hydroponic monitoring system with deep flow technique (DFT). *AIP Conference Proceedings*, 2217(1), Article 030195. <https://doi.org/10.1063/5.0000733>
- Singh, H., & Dunn, B. (2016). *Electrical conductivity and pH guide for hydroponics* (HLA-6722). Division of Agriculture Science and Natural Resources Oklahoma State University. [https://shareok.org/bitstream/handle/11244/331022/oksa\\_HLA-6722\\_2016-10.pdf](https://shareok.org/bitstream/handle/11244/331022/oksa_HLA-6722_2016-10.pdf)
- Son, J. E., Kim, H. J., & Ahn, T. I. (2020). Hydroponic systems. In T. Kozai, G. Niu & M. Takagaki (Eds.), *Plant Factory* (pp.273-283). Academic Press. <https://doi.org/10.1016/B978-0-12-816691-8.00020-0>

- Suseno, J., Munandar, M., & Priyono, A. (2020). The control system for the nutrition concentration of hydroponic using web server. *Journal of Physics: Conference Series*, 1524(1), Article 012068. <https://doi.org/10.1088/1742-6596/1524/1/012068>
- Urban, S., Ludersdorfer, M., & van der Smagt, P. (2015). Sensor calibration and hysteresis compensation with heteroscedastic gaussian processes. *IEEE Sensors Journal*, 15(11), 6498-6506. <https://doi.org/10.1109/JSEN.2015.2455814>
- Wibowo, R. R. D. I., Ramdhani, M., Priramadhi, R. A., & Aprillia, B. S. (2019). IoT based automatic monitoring system for water nutrition on aquaponics system. *Journal of Physics: Conference Series*, 1367(1), Article 012071. <https://doi.org/10.1088/1742-6596/1367/1/012071>
- Zheng, Q., Weng, Q., & Wang, K. (2019). Developing a new cross-sensor calibration model for DMSP-OLS and Suomi-NPP VIIRS night-light imageries. *ISPRS Journal of Photogrammetry and Remote Sensing*, 153, 36-47. <https://doi.org/10.1016/j.isprsjprs.2019.04.019>



## Intelligence System via Machine Learning Algorithms in Detecting the Moisture Content Removal Parameters of Seaweed Big Data

Olayemi Joshua Ibidoja<sup>1,2</sup>, Fam Pei Shan<sup>2</sup>, Mukhtar Eri Suheri<sup>3</sup>, Jumat Sulaiman<sup>4</sup> and Majid Khan Majahar Ali<sup>2\*</sup>

<sup>1</sup>Department of Mathematics, Federal University Gusau, Gusau, Zamfara State, 234, Nigeria

<sup>2</sup>School of Mathematical Sciences, Universiti Sains Malaysia, 11800 USM, Penang, Malaysia

<sup>3</sup>Department of Statistics, University of Sulatan Ageng Tirtayasa, Banten, Indonesia

<sup>4</sup>Faculty of Science and Natural Resources, Universiti Malaysia Sabah, 88400 UMS, Kota Kinabalu, Sabah, Malaysia

### ABSTRACT

The parameters that determine the removal of moisture content have become necessary in seaweed research as they can reduce cost and improve the quality and quantity of the seaweed. During the seaweed's drying process, many drying parameters are involved, so it is hard to find a model that can determine the drying parameters. This study compares seaweed big data performance using machine learning algorithms. To achieve the objectives, four machine learning algorithms, such as bagging, boosting, support vector machine, and random forest, were used to determine the significant parameters from the data obtained from v-GHSD (v-Groove Hybrid Solar Drier). The mean absolute percentage error (MAPE) and coefficient of determination (R<sup>2</sup>) were used to assess the model. The importance of variable selection cannot be overstated in big data due to the large number of variables and parameters that exceed the number of observations. It will reduce the complexity of the model, avoid the curse of dimensionality, reduce cost, remove irrelevant variables, and increase precision. A total of 435 drying parameters determined the moisture content removal, and each algorithm was used to select 15, 25, 35 and 45 significant parameters.

The MAPE and R-Square for the 45 highest variable importance for random forest are 2.13 and 0.9732, respectively. It performed best, with the lowest error and the highest R-square. These results show that random forest is the best algorithm to decide the vital drying parameters for removing moisture content.

**Keywords:** Big data, drying, machine learning, seaweed, variable selection

### ARTICLE INFO

#### Article history:

Received: 18 October 2022

Accepted: 07 March 2023

Published: 08 September 2023

DOI: <https://doi.org/10.47836/pjst.31.6.09>

#### E-mail addresses:

[ojibidoja@fugusau.edu.ng](mailto:ojibidoja@fugusau.edu.ng) (Olayemi Joshua Ibidoja)

[fpeishan@usm.my](mailto:fpeishan@usm.my); [fpeishan@gmail.com](mailto:fpeishan@gmail.com) (Fam Pei Shan)

[mukhtar@untirta.ac.id](mailto:mukhtar@untirta.ac.id) (Mukhtar Eri Suheri)

[jumat@ums.edu.my](mailto:jumat@ums.edu.my) (Jumat Sulaiman)

[majidkhanmajaharali@usm.my](mailto:majidkhanmajaharali@usm.my) (Majid Khan Majahar Ali)

\*Corresponding author

## INTRODUCTION

Globally, the demand for food is increasing every day. The United Nations world population index predicts that by 2050, there will be 9.7 billion people on the planet (Namana et al., 2022). The demand for food will increase due to the rate of population growth and the effect of COVID-19. Rahimi et al. (2022) stated that COVID-19 affected the treatment of animals, while the lockdown affected the production of food and the supply of labour. Bajan et al. (2020) stated that world population growth comes with increased food production demand. It is essential to increase production, which involves increasing energy consumption to meet this demand. The need to meet the demand for food products and the food market is necessary (Safronova et al., 2022). Food is a security to the survival of human beings, and the hunger problem needs to be solved with a breakthrough in biotechnology (Prosekov & Ivanova, 2018). By 2050, the world should be prepared to feed over 9 billion people (Cole et al., 2018). To feed the increasing population, drying or preserving food is an important alternative that can be considered to preserve the nutritional value and quality of food.

Drying food involves the removal of moisture from the food. Solar driers dry many products, especially aquaculture and agriculture (Javaid et al., 2020). Nuroğlu et al. (2019) have used “drying in an oven under the magnetic field” and “drying under the sun and magnetic field” to dry grape samples and chilli pepper. From the results, the chilli pepper was the most contaminated when the traditional drying method was used. In East Africa, the rate of loss of farm produce is high due to the use of sun drying. The authors provided a prototyped modified solar dryer as another option. Multiple metallic solar panels were used to boost the drying performance of the solar drier (Ssemwanga et al., 2020).

The global seaweed industry provides diverse products directly or indirectly for human consumption, with a total value of approximately US\$ 10 billion a year (Bixler & Porse, 2011). Malaysia's seaweed production grew from 1,000 metric tons in 1991 to 14,000 metric tons in 2009; in 2012, it was 33,000 metric tons. It is anticipated to continue growing exponentially over the next 30 years. The nursery, cultivating, drying, harvesting, processing, and marketing are a few processes involved in the carrageenan-bearing seaweed sector. Managing harvested seaweed biomass is essential to the carrageenophyte industry's entire value chain. It is important to understand the drying process for foods (Ali, Fudholi et al., 2017; Ali, Sulaiman et al., 2017). Seaweeds are very important to marine resources and are found in coastal waters. Seaweeds are very beneficial to human beings and fish. Seaweeds can be used as food, fertilizer, cosmetics, biofuel and medicine (Echave et al., 2022; Pradhan et al., 2022).

Machine learning variable selection has been used by many authors (Ali et al., 2021; Arjasakusuma et al., 2020; Gunn et al., 2022; Meyer et al., 2019). Application of the important variables will improve accuracy, reduce overfitting, and ensure robustness. Lim et al. (2020) used ridge regression to determine the drying parameters of fish and included the interaction terms.

As the dimensions of datasets in predictive modelling continue to grow, feature selection becomes increasingly practical. Datasets with complex feature interactions and high levels of redundancy still present a challenge to existing feature selection methods. Variable selection is becoming useful, and the dimensions of data, complexity, volume, interactions, heterogeneity, and the number of irrelevant variables make it a problem for traditional methods. A machine-learning algorithm can model complicated patterns (Solyali, 2020).

To fill the gap in the existing literature, a comparison of performance and evaluation of seaweed big data using four machine learning algorithms, such as bagging, boosting, support vector machine and random forest, will be evaluated.

## MATERIALS AND METHODS

### Model Building

Knowing the important parameters that determine the moisture content of the seaweed after drying is important. We combined the second-order interaction with the main 29 seaweed drying parameters to get 435 drying parameters, to develop an intelligent system. All 435 parameters determine the moisture content of the seaweed after drying. With this limitation, we have 435 parameters to predict the moisture content of seaweed after drying. Therefore, we selected 15, 25, 35, and 45 as the most important variables, and boosting, bagging, random forest, and support vector machines will be used as the algorithms. The system for drying has already been designed and data collected, but no optimization has been done. The flowchart in Figure 1 shows the procedure and the methodology used in this study.

### Stage I

It involves the inclusion of all possible models.

$$\frac{n!}{(n-r)!r!} + \text{number of single factor} \quad (1)$$

where  $n$  is the number of single factors, and  $r$  is the number of orders. Equation 1 can compute the total number of all possible models.

### Stage II

It requires simulation using random forest, boosting, support vector machine, and bagging machine learning algorithms to model the data. Each machine learning algorithm is then used to select the 15, 25, 35 and 45 highest important variables to determine the moisture content removal of the seaweed after drying. If the parameters are significant and satisfy the conditions, they will be imposed in the optimization. Otherwise, it will be removed. Features selection can only provide the rank of relevant variables and not the number of significant factors, and there is no rule for determining how many parameters should be used in a prediction model (Chowdhury & Turin, 2020; Drobnič et al., 2020; Kaneko,

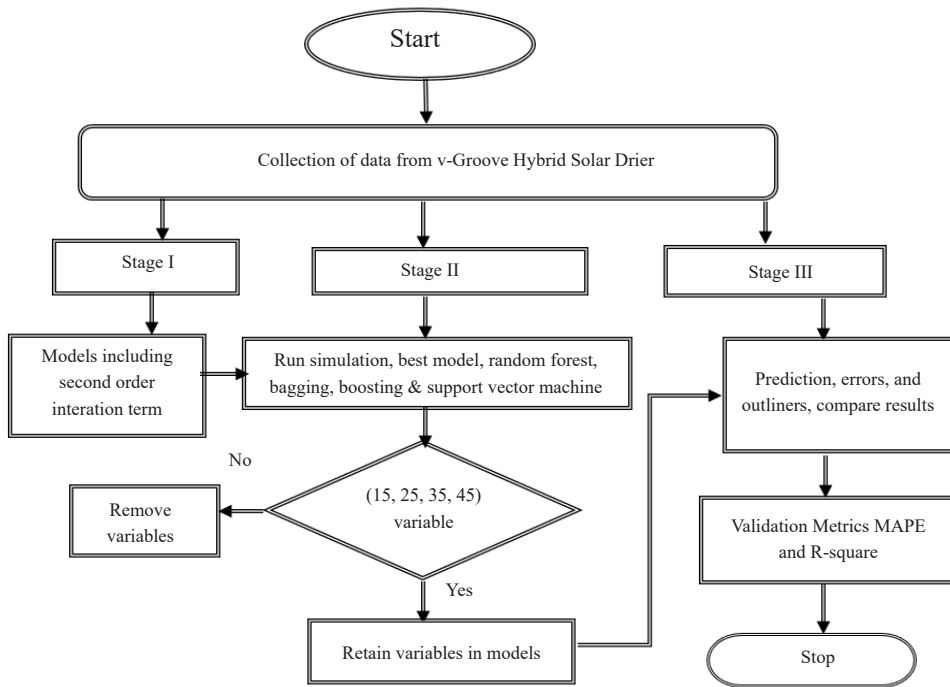


Figure 1. Flowchart of the steps for the study

2021). Hence, if the parameters do not rank among the 15, 25, 35, and 45 highest important variables, they will be removed from the model.

### Stage III

The prediction must be made to achieve the objectives further, and the errors must be calculated. The outliers are also computed using 2 - sigma limits. Outliers are observations far from the measures of location (Leys et al., 2019). The best model is selected using mean absolute percentage error (MAPE) and coefficient of determination (R-square) metric validation.

$$MAPE = \frac{100}{n} \sum_{i=1}^n \left| \frac{y_i - \hat{y}_i}{y_i} \right| \tag{2}$$

Where  $n$  is the number of observations,  $y_i$  is the actual value, and  $\hat{y}_i$  is the forecast value.

$$R^2 = 1 - \frac{\sum (y_i - \hat{y}_i)^2}{\sum (y_i - \bar{y})^2} \tag{3}$$

Where  $y_i$  is the actual value, and  $\hat{y}_i$  is the forecast value.

The metrics were used to assess the model. The formulae for the model metric validations are given in Equations 2 and 3. The lower the MAPE, the better the prediction accuracy. The higher the R-square, the better the prediction accuracy.

## Boosting

Boosting is an ensemble machine learning modelling technique that can create a powerful classifier from a huge number of weak classifiers. Boosting can be used to improve the precision of a machine-learning algorithm. Rahman et al. (2020) stated that boosting algorithms use the training observations that end up in misclassifications. Boosting algorithms use the weight of the samples of the weak classifiers depending on the precision of the preceding boosting rounds (Alshaf et al., 2022). Boosting is to measure the errors in the predecessors of the classifier, which makes it sensitive to outliers. It cannot be scaled- up since the estimator relies on the accuracy of the past predictors. Given the matrix of explanatory variables  $X = [X_1, \dots, X_p] \in \mathbb{R}^{n \times p}$  and the dependent variable vector  $\mathbf{y} \in \mathbb{R}^{n \times 1}$ . In the regression coefficients vector  $\beta \in \mathbb{R}^p$ , the value of the predicted response variable is represented by  $\mathbf{X}\beta$ , and the residuals are denoted by  $\varepsilon = \mathbf{y} - \mathbf{X}\beta$ . The LSB ( $\varepsilon$ ) denotes the least squares for the boosting. The LSB ( $\varepsilon$ ) in regression produces models with interesting statistical properties (Freund et al., 2017). LSB ( $\varepsilon$ ) algorithm is expressed as follows according to Freund et al. (2017) and Friedman (2001).

### Algorithm: LSB ( $\varepsilon$ )

Fix the rate of learning  $\varepsilon > 0$ ; the rate of learning is the rate at which the coefficients produced by LSB ( $\varepsilon$ ) converge to the group of the unregularized least square solutions, and the iterations number M and initialize the  $\hat{\beta}^0 = 0$  and  $\hat{\mathbf{r}}^0 = \mathbf{y}$ .

1. Do the following for  $0 \leq k \leq M$ , do the following:
2. Determine the covariate index  $j_k$  and  $\tilde{u}_{j_k}$  as shown below:

$$j_k \in \operatorname{argmin}_{1 \leq m \leq p} \sum_{i=1}^n (\hat{r}_i^k - x_{im} \tilde{u}_m)^2, \text{ where}$$

$$\tilde{u}_m = \operatorname{argmin}_{u \in \mathbb{R}} \left( \sum_{i=1}^n (\hat{r}_i^k - x_{im} u)^2 \right), \text{ for } m = 1, 2, \dots, p.$$

3. Update the residuals and coefficients of regression as follows:

$$\hat{\mathbf{r}}^{k+1} \leftarrow \hat{\mathbf{r}}^k - \varepsilon X_{j_k} \tilde{u}_{j_k}$$

$$\hat{\beta}_{j_k}^{k+1} \leftarrow \hat{\beta}_{j_k}^k + \varepsilon \tilde{u}_{j_k} \text{ and } \hat{\beta}_j^{k+1} \leftarrow \hat{\beta}_j^k, j \neq j_k$$

Furthermore, the LSB algorithm at the  $k$ th iteration selects the covariate index  $j_k$ , leading to the maximal decrease in the fit of the univariate regression to the present residuals. Suppose the  $X_{j_k} \tilde{u}_{j_k}$  represents the best fit for the univariate regression to the present residuals. In that case, LSB will update the residuals  $\hat{\mathbf{r}}^{k+1} \leftarrow \hat{\mathbf{r}}^k - \varepsilon X_{j_k} \tilde{u}_{j_k}$  and the coefficients of the  $j_k$  th:  $\hat{\beta}_{j_k}^{k+1} \leftarrow \hat{\beta}_{j_k}^k + \tilde{u}_{j_k}$  to minimize the error.

## Bagging

Bagging is an ensemble machine-learning technique that can improve the accuracy and

performance of machine-learning algorithms. A common integration technique known as bagging generates numerous copies of the training set using a bootstrapping procedure, which is then utilized to train several models (Yang et al., 2020). Bagging apply comparable learners to tiny sample populations before calculating the average of all the forecasts (Kabari et al., 2019). Bagging can improve the accuracy of a model, reduce overfitting of data, and deal with data of higher dimensionality effectively. However, bagging is computationally expensive.

Consider a regression setup where the data is represented by  $L_i = (Y_i, X_i)$  ( $i = 1, \dots, n$ ), and  $Y_i$  and  $X_i$  represent the  $p$ -dimensional variables for the  $i$ th instance. In the presence of a new independent variable or covariate  $x$ , a dependent variable for  $\mathbb{E}[Y|X = x] = f(x)$ , the response variable that corresponds to  $x$  can be represented by:

$$\hat{\theta}_n(x) = h_n(L_1, \dots, L_n)(x)$$

The estimator could be a learning algorithm or complex model, for instance, a linear regression via testing, classification, and regression trees. The  $h_n$  denotes the function of the sample  $n$ .

Theoretically, bagging is defined as:

- i. Build a bootstrap sample  $L_i^* = (Y_i^*, X_i^*)$  ( $i = 1, \dots, n$ ) based on the practical distribution of the pairings  $L_i = (Y_i, X_i)$  ( $i = 1, \dots, n$ ).
- ii. Using the plug-in principle to determine the bootstrapped forecaster  $\hat{\theta}_n^*(x)$ , which is,  $\hat{\theta}_n^*(x) = h_n(L_1, \dots, L_n)(x)$ .
- iii.  $\hat{\theta}_{n;B}(x) = \mathbb{E}^*[\hat{\theta}_n^*(x)]$  is the bagged predictor.

The bootstrap expectation in step (III) can be applied by Monte Carlo: Start with step (I) for every bootstrap simulation  $j \in \{1, \dots, J\}$ , to approximate  $\hat{\theta}_{n;B}(x) \approx J^{-1} \sum_{j=1}^J \hat{\theta}_n^*(x)$ , we compute  $\hat{\theta}_n^*(x)$  ( $j = 1, \dots, J$ ) as in step II,  $J$  is frequently chosen in the range of 50, depending on the sample size and computational cost related with assessing the predictor. The plug-in principle is used in bootstrapping by estimating the population's distribution from the information in the sample distribution.

### Random Forest (RF)

RF can be defined as a combination of many classification and regression trees (CARTs), and the aim is to solve the problem of overfitting in individual CART (Georganos et al., 2021). Given that  $\mathcal{L}$  is a learning set with a group of  $\mathbb{N}$  pairs of features, with the response  $x_1, x_2, \dots, x_n$  if  $x_i \in X$ . A group of  $p$ -features  $x_i$  (for  $i = 1, 2, \dots, N$ ) is an  $N \times p$  matrix  $X$ , in which the rows  $i = 1, 2, \dots, N$  relates as  $x_i$ , with columns  $j = 1, 2, \dots, p$  as  $x_j$ . Similarly, the response can be written as a vector  $y = (y_1, y_2, \dots, y_N)$ . In this scenario, the supervised learning job can be indicated as learning the function  $\varphi: X \rightarrow Y$  from the learning set  $\mathcal{L} = (X, y)$ . The goal is to develop a model whose predictions for the variable  $\varphi(x)$ , represented by  $\hat{Y}$ , are as precise

as possible. In this situation, the  $Y$  variable must be continuous. The results of the model can be described as follows, given that the regressor function represents  $\varphi: X \rightarrow Y$ , in which  $Y \in \mathbb{R}$ . During the statistical learning process, the explanatory variables,  $X_1, X_2, \dots, X_p$  and the response variable  $Y$ , are random variables, and the values  $X \times Y$  are selected collectively in respect of the joint probability distribution  $P(XY)$ , the  $X$  is the vector of random  $[X_1], [X_2], \dots, [X_p]$ . RF can handle large data effectively and has high precision over decision tree algorithms. However, more resources are needed for computation, and it takes more time when compared to a decision of the tree algorithm.

Algorithm:

For  $b = 1$  to  $n$

1. Create a bootstrapped sample  $D_b^*$  from the training set  $D$ .
2. Grow the tree by using the  $m$  from the bootstrapped sample  $D_b^*$ .

For a specific mode

- i. Select  $m$  variables randomly.
- ii. Identify the top split variables and values.
- iii. Divide a node using the top divided variables and values.

Replicate steps 1–3 till the stopping conditions are satisfied.

### Support Vector Machine (SVM)

SVM is popularly used to solve regression and classification problems. SVM has the capacity to discover nonlinear connections by using kernel function (Rashidi et al., 2019). Given  $\{(x_1, y_1), \dots, (x_n, y_n)\} \in X \times \mathbb{R}$ ,  $X$  denotes the pattern space of the inputs ( $X = \mathbb{R}^d$ ).

From Cortes and Vapnik (1995), by comparing the standard Gaussian regression with the squared error loss function is minimized with the loss for observations  $i$  given as  $L\{y_i, f(x_i)\} = \{y_i, f(x_i)\}^2$ .

However, in support vector regression, the  $\epsilon$ -insensitive loss function is minimized, and any loss lesser than  $\epsilon$  is set to 0. Outside that bound, a simple linear loss function is applied in Equation 4:

$$L_\epsilon = f(x) = \begin{cases} 0, & \text{if } |y_i - f(x_i)| < \epsilon \\ |y_i - f(x_i) - \epsilon|, & \text{otherwise} \end{cases} \quad (4)$$

For instance, suppose  $f(x)$  is a linear function  $f(x) = \beta_0 + x_i^t \beta$ . Equation 5 represents the loss function given as:

$$\sum_{i=1}^n \max(y_i - x_i^t \beta - \beta_0 - \epsilon, 0) \quad (5)$$

The  $\epsilon$  is the tuning parameter and can be written as the constrained optimization problem: minimize  $\frac{1}{2} ||\beta||^2$ , subject to the constrain in Equation 6:

$$\begin{cases} y_i - x_i^t \beta - \beta_0 \leq \epsilon \\ -(y_i - x_i^t \beta - \beta_0) \leq \epsilon \end{cases} \quad (6)$$

If observations do not lie within the  $\epsilon$  band around that regression line, then there is no solution to the problem. The slack variables  $\zeta_i$  and  $\zeta_i^*$  are used; this allows the observations to fall outside the  $\epsilon$  band around that regression line.

Minimize: 
$$\frac{1}{2} ||\beta||^2 + K \sum_{i=1}^n (\zeta_i + \zeta_i^*) \quad (7)$$

Subject to 
$$\begin{cases} y_i - x_i^t \beta - \beta_0 \leq \epsilon + \zeta_i \\ -(y_i - x_i^t \beta - \beta_0) \leq \epsilon + \zeta_i^* \\ \zeta_i, \zeta_i^* \geq 0 \end{cases} \quad (8)$$

The equation to minimize is shown in Equation 7, and the constraint is provided in Equation 8. However, before,  $K > 0$  regulated how strong it is to prevent observations beyond the  $\epsilon$  band.

**Evaluation Metric**

MAPE is widely used because it is easy to interpret and due to its scale-independency (Kim & Kim, 2016).

$R^2$  is the proportion of variance in the dependent variable that can be predicted from a set of independent variables.  $R^2$  lies between 0 and 1. Moreover, the value determines the performance of the model (Chicco et al., 2021; Gouda et al., 2019; Ibidoja et al., 2016).

The MAPE and R-square are very useful for validating a model. The MAPE is the average difference between predicted and real values. In this study, MAPE is the average percentage error between the moisture content of the seaweed predicted by the model and the real value. The lower the MAPE, the better the model fits the data. R-square is the amount of variance in the dependent variable that the independent variable can describe. The higher the R-square value, the better the dependent variable can be explained. The R-square is also called the coefficient of determination; it is the quantity of variability in a variable explained by changes in the other variable. For a high precision in the model, we expect the error to be small and is the loss function for regression in machine learning (Jierula et al., 2021).

**DATA COLLECTION**

We used primary data on seaweed drying obtained using a v-groove hybrid solar drier. The data was collected using sensors installed on the v-GHSD (v-Groove Hybrid Solar Drier)



in Semporna, Malaysia, on the southeastern coast of Sabah. The data contains 29 different drying parameters that determine the moisture content of the seaweed, and each parameter has 1914 observations. The dependent variable is the moisture content after drying. We have different parameters that represent different relative humidity. Another parameter is the sun, and the remaining parameters are the temperature.

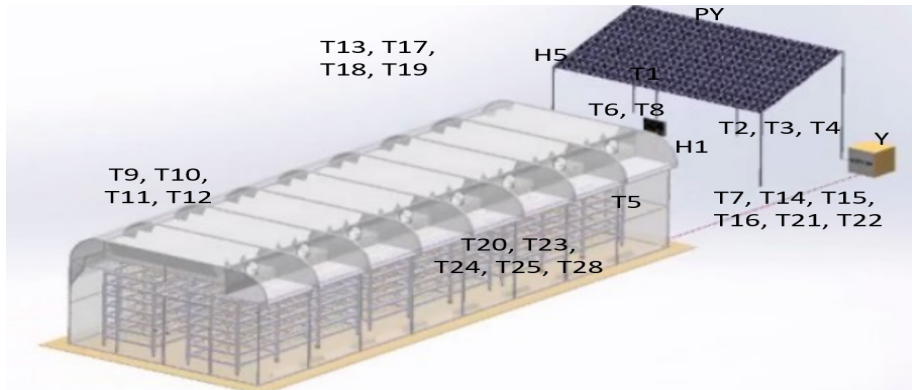


Figure 2. v-GHSD (v - Groove Hybrid Solar Drier)

Figure 2 represents the v-GHSD (v - Groove Hybrid) solar drier used to dry the seaweed and remove moisture. It also shows the positions of the parameters that determine the moisture content removal of the seaweed. The sensors are placed in strategic positions to measure the data. From Table 1, the T's are the temperature, Y is the moisture content, H's are the humidity, and PY is the solar radiation.

Table 1

Representation of parameters

Symbols	Factors	Meanings
Y	Dependent	Moisture Content
H1	Independent	Relative Humidity Ambient
H5	Independent	Relative Humidity Chamber
PY	Independent	Solar Radiation
T1	Independent	Temperature (°C) ambient
T2, T3, T4	Independent	Temperature (°C) prior to entering the solar collector
T5	Independent	Temperature (°C) in opposite the down v-Groove (Solar Collector)
T6, T8	Independent	Temperature (°C) in front of the up v-Groove (Solar Collector)

## RESULTS AND DISCUSSION

Tables 2, 3, 4, and 5 show the variables selected for 15, 25, 35 and 45 for bagging, boosting, support vector machine, and random forest, respectively.

Table 2

*The 15 highest variable importance*

Model	Selected Variables
Bagging	T1, T4, T7, T8, T1*T8, T1*H5, T3*T12, T6*H1, T9*T13, T11*T15, T12*T28, T14*T22, T19*T21, T22*T26, T26*T27
Boosting	T1, T7, H1, H5, T9*PY, T25*T28, H1*H5, T10*H5, T13*T28, T28*T29, T10*H1, T7*H1, T26*T28, T12*H1, T2*T7
Support Vector Machine	T15, T16, T25, T26, T2*T8, T6*T8, T6*T10, T7*T10, T8*T17, T9*H5, T12*PY, T13*T17, T19*H5, T21*H5, T26*H5
Random Forest	T8, T2*T6, T1*T6, T6*T13, T21*H5, T19*H5, T7*T9, T22*H5, T6*T29, H5*PY, T7*H1, T8*H5, T26*H5, T8*H1, T1*T2

Table 3

*The 25 highest variable importance*

Model	Selected Variables
Bagging	T1, T4, T6, T7, T8, T9, T26, T1*T4, T1*T5, T1*T8, T1*H5, T2*T22, T3*T12, T3*PY, T4*T22, T6*H1, T6*H5, T9*T13, T10*PY, T11*T15, T12*T28, T14*T22, T19*T21, T22*T26, T26*T27
Boosting	T1, H1, H5, T7, T9*PY, T25*T28, H1*H5, T10*H5, T13*T28, T28*T29, T10*H1, T7*H1, T26*T28, T12*H1, T2*T7, T10*PY, T6*T7, T8*H1, T11*PY, T8*PY, T1*T4, T3*T5, T9*T21, T5*T26, T6*H5
Support Vector Machine	T15, T16, T25, T26, T28, T1*T17, T2*T8, T3*T17, T6*T8, T6*T10, T7*T10, T8*T17, T9*H5, T10*H1, T11*PY, T12*PY, T13*T17, T15*T16, T15*T25, T19*T22, T19*H5, T21*H5, T25*T28, T26*H5, T27*H5
Random Forest	T7, T8, H1, T1*T2, T1*T6, T1*T7, T1*T9, T2*T6, T2*T7, T2*T13, T6*T13, T6*T29, T7*T9, T7*H1, T8*H5, T8*H1, T14*H5, T19*H5, T21*H5, T22*H5, T25*H5, T26*H5, H1*PY, H1*H5, H5*PY

Table 4

*The 35 highest variable importance*

Model	Selected Variables
Bagging	T1, T4, T6, T7, T8, T9, T22, T26, PY, T1*T4, T1*T5, T1*T8, T1*H5, T2*T22, T3*T12, T3*PY, T4*T22, T5*T11, T5*T28, T6*H1, T6*H5, T6*PY, T7*T22, T7*PY, T8*T9, T9*T13, T10*T19, T10*T27, T10*PY, T11*T15, T12*T28, T14*T22, T19*T21, T22*T26, T26*T27

Table 4 (Continue)

Model	Selected Variables
Boosting	T1, T7, T8, T9, H1, H5, PY, T9*PY, T25*T28, H1*H5, T10*H5, T13*T28, T28*T29, T10*H1, T7*H1, T26*T28, T12*H1, T2*T7, T10*PY, T6*T7, T8*H1, T11*PY, T8*PY, T1*T4, T3*T5, T9*T21, T5*T26, T6*H5, H5*PY, T6*H1, H1*PY, T23*H5, T4*T5, T14*H5, T2*T28
Support Vector Machine	T12, T15, T16, T25, T26, T28, T1*T17, T2*T5, T2*T8, T2*T17, T3*T17, T3*T23, T4*T17, T5*T19, T6*T8, T6*T10, T7*T10, T7*T16, T7*T17, T8*T17, T8*T28, T9*H5, T10*H1, T11*T14, T11*PY, T12*PY, T13*T17, T15*T16, T15*T25, T19*T22, T19*H5, T21*H5, T25*T28, T26*H5, T27*H5
Random Forest	T2, T7, T8, T9, H1, T1*T2, T1*T6, T1*T7, T1*T9, T1*T13, T2*T6, T2*T7, T2*T13, T5*T9, T6*T8, T6*T9, T6*T13, T7*T9, T7*H1, T7*PY, T8*H1, T8*H5, T8*PY, T9*H5, T10*H5, T11*H5, T14*H5, T15*H5, T19*H5, T21*H5, T22*H5, T25*H5, H1*H5, H1*PY, H5*PY

Table 5

*The 45 highest variable importance*

Model	Selected Variables
Bagging	T1, T4, T6, T7, T8, T9, T10, T14, T22, T26, PY, T1*T2, T1*T4, T1*T5, T1*T8, T1*T10, T1*H5, T2*T22, T3*T12, T3*PY, T4*T22, T5*T11, T5*T28, T6*T15, T6*H1, T6*H5, T6*PY, T7*T22, T7*PY, T8*T9, T9*T13, T9*T23, T10*T19, T10*T27, T10*PY, T11*T15, T11*T16, T11*T17, T12*T25, T12*T28, T14*T22, T14*T23, T19*T21, T22*T26, T26*T27
Boosting	T1, T7, T8, T9, H1, H5, PY, T1*T4, T2*T7, T2*T28, T3*T5, T4*T5, T5*T25, T5*T26, T6*T7, T6*H1, T6*H5, T7*T12, T7*H1, T7*H5, T8*H1, T8*PY, T9*T21, T9*T26, T9*H5, T9*PY, T10*T23, T10*H1, T10*H5, T10*PY, T11*PY, T12*H1, T12*H5, T13*T28, T14*H5, T23*H5, T25*T28, T25*T29, T26*T28, T26*T29, T26*H5, T28*T29, H1*H5, H1*PY, H5*PY
Support Vector Machine	T12, T15, T16, T25, T26, T28, PY, T1*T5, T1*T6, T1*T17, T2*T5, T2*T6, T2*T8, T2*T17, T3*T5, T3*T17, T3*T23, T4*T5, T4*T17, T5*T13, T5*T19, T6*T8, T6*T10, T7*T10, T7*T16, T7*T17, T8*T17, T8*T28, T9*T23, T9*H5, T10*T23, T10*H1, T11*T14, T11*T22, T11*PY, T12*PY, T13*T17, T15*T16, T15*T25, T19*T22, T19*H5, T21*H5, T25*T28, T26*H5, T27*H5
Random Forest	T2, T7, T8, T9, H1, T1*T2, T1*T6, T1*T7, T1*T9, T1*T13, T1*H1, T2*T6, T2*T7, T2*T9, T2*T13, T3*T8, T3*H1, T4*T8, T4*H1, T5*T9, T6*T7, T6*T8, T6*T9, T6*T13, T7*T9, T7*H1, T7*PY, T8*H1, T8*H5, T8*PY, T9*H5, T10*H5, T11*H5, T13*H1, T14*H5, T15*H5, T16*H5, T19*H5, T21*H5, T22*H5, T23*H1, T25*H5, H1*H5, H1*PY, H5*PY

Table 6 is a four-dimensional results summary of the single factor the machine learning algorithms selected for the 45 high-ranking variables. Bagging and boosting have 4 single factors in common, bagging and SVM have 2 single factors in common, and bagging and random forest have 3 single factors in common for the first 45 highest important significant factors that determine the moisture content of the seaweed. For every machine learning algorithm, 11 (24.4%), 7 (15.6%), 7 (15.6%), and 5 (11.1%) single parameters are selected for bagging, boosting, support vector machine, and random forest, respectively. Bagging selects the highest number of single variables.

Table 6

*Number of single variables for the 45 selected single factors for each machine learning algorithm*

	Bagging	Boosting	SVM	Random Forest
Bagging	11	4	2	3
Boosting	4	7	-	4
SVM	2	-	7	-
Random Forest	3	4	-	5

Table 7 is a four-dimensional results summary of the second-order factors the machine learning algorithms selected for the 45 high-ranking variables. Bagging and boosting have 4 second-order factors in common, bagging and SVM have 2 second-order factors in common, and bagging and random forest have 2 second-order factors in common. Random forest and boosting have the highest number of second-order factors of 11 in common with the factors selected. For the interaction, bagging, boosting, support vector machine and random forest selected, 34 (75.6%), 38 (84.4%), 38 (84.4%), and 40 (88.9%).

Table 7

*Number of similar variables for the 45 selected interaction factors for each machine learning algorithm*

	Bagging	Boosting	SVM	Random Forest
Bagging	34	4	2	2
Boosting	4	38	7	11
SVM	2	7	38	6
Random Forest	2	11	6	40

The high number of interaction variables selected showed how important it is to consider the interaction in the moisture content removal of agricultural products. The results of the interaction are also supported by the results of (Javaid et al., 2019).

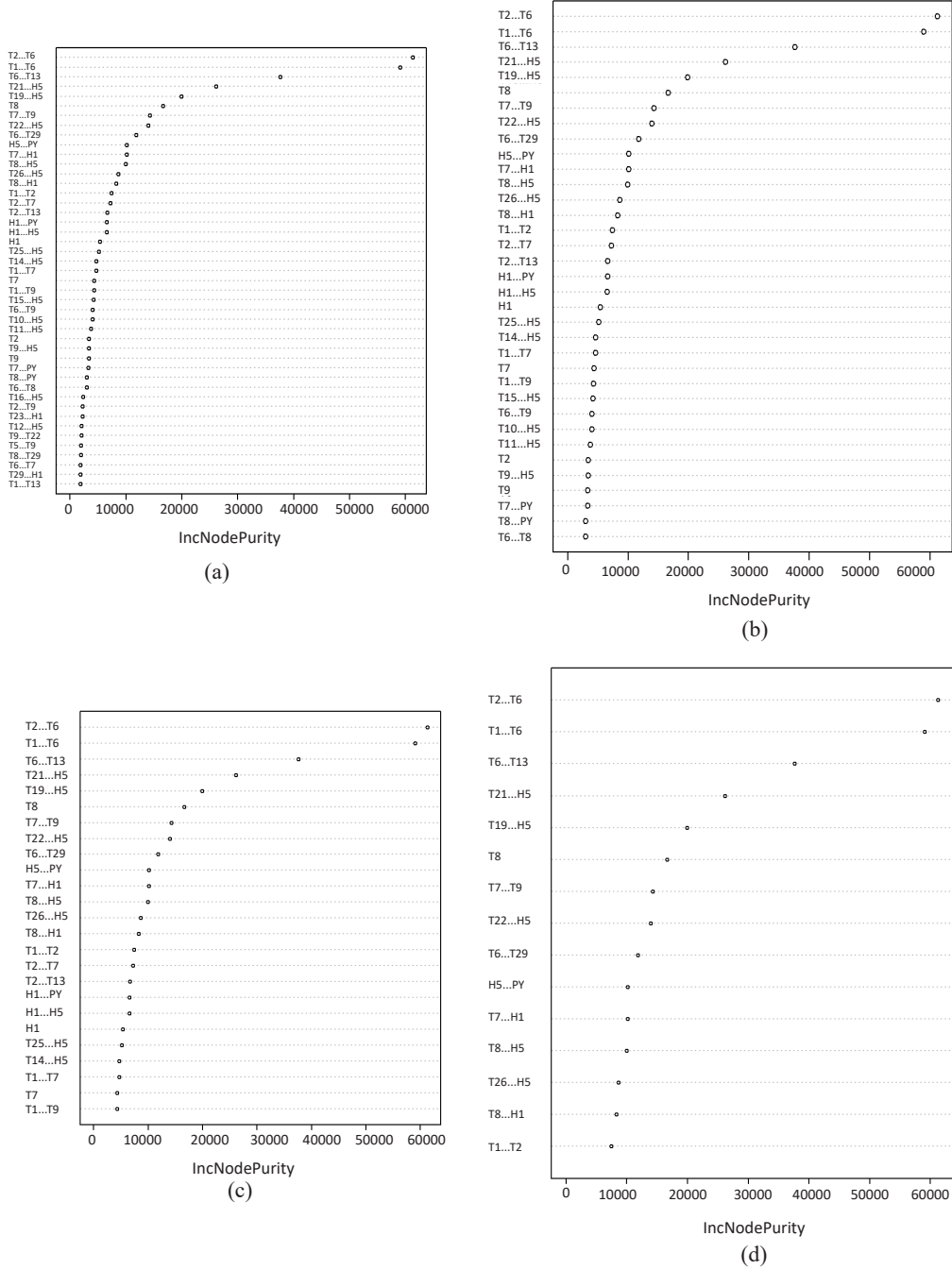


Figure 3. Variable importance for (a) 45, (b) 35, (c) 25, and (d) 15 random forest

Figure 3 shows the plot of the variable importance of the selected 45, 35, 25, and 15 parameters of the seaweed big data using the random forest algorithm. We used the *randomForest* and *caret* packages in the R programming language to achieve this. It reveals how important the variable is in determining the moisture content removal of the seaweed. The five most important factors are the parameters  $T2 * T6$ ,  $T1 * T6$ ,  $T6 * T13$ ,  $T21 * H5$ , and  $T19 * H5$ .  $T2 * T6$  and  $T1 * T6$  rank at the top for the factors.

Figures 4 to 7 show the standardized residual plots of random forest, support vector machine, bagging and boosting, respectively. Each algorithm produced different patterns of plots. Likewise, there were differences when the number of parameters 15, 25, 35 and 45 selected were compared for each algorithm. It also shows the upper and lower control limits to identify outliers. The percentage of outliers is calculated using the number of observations outside the 2-sigma limit.

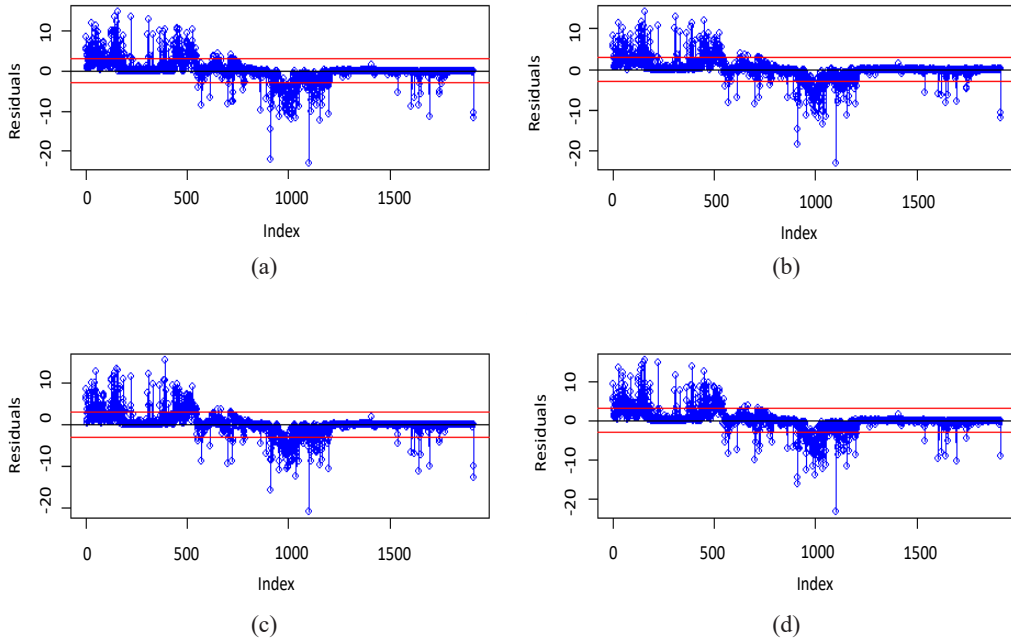


Figure 4. Plot for standardized residuals for (a) 15, (b) 25, (c) 35 and (d) 45 high-ranking variables for random forest

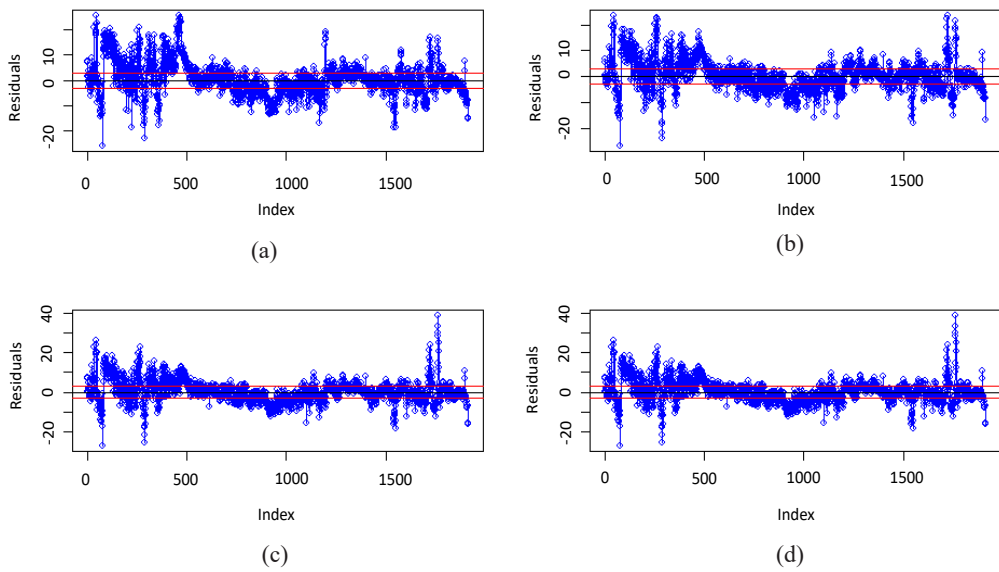


Figure 5. Plot for standardized residuals for (a) 15, (b) 25, (c) 35 and (d) 45 high-ranking variables for support vector machine

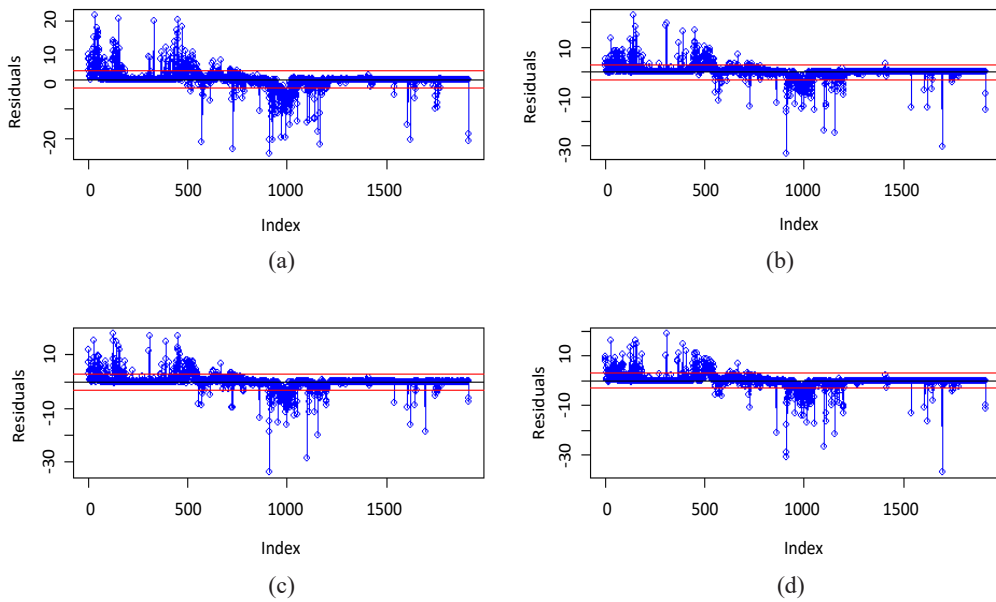


Figure 6. Plot for standardized residuals for (a) 15, (b) 25, (c) 35 and (d) 45 high-ranking variables for bagging

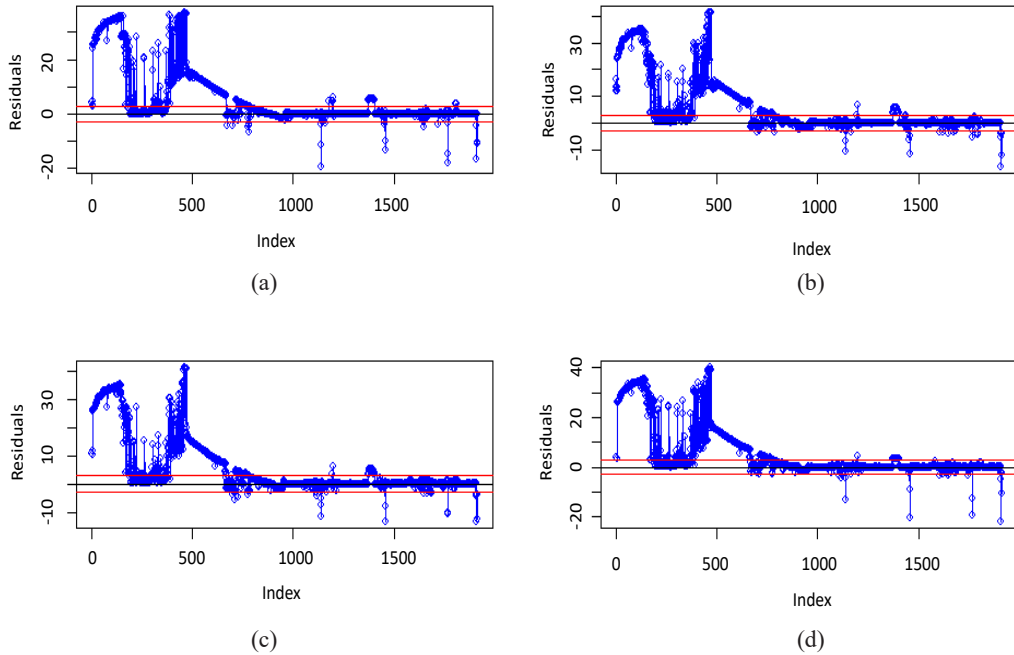


Figure 7. Plot for standardized residuals for (a) 15, (b) 25, (c) 35 and (d) 45 high-ranking variables for boosting

Table 8 shows the evaluation metrics for the 15, 25, 35 and 45 highest important ranking variables. The 45 highest-ranking important variables for random forest have the value of MAPE (2.13) and R-Square (0.9732), which gave the best performance. It is similar to Chen et al. (2020), where random forest performed better than the support vector machine. With these results, random forest is the best to determine the moisture content removal of the seaweed. MAPE (2.13) represents the average percentage error between the moisture content removal of the seaweed predicted by the model and the real value. Sumari et al. (2021) assert that if MAPE is less than 10, it is high prediction accuracy. The value R-square (0.9732) implies that the selected drying parameters can explain 97.32% of the dependent variable moisture content variance.

Table 8  
Evaluation metrics

High Ranking Variables	Bagging		Boosting		Support Vector Machine		Random Forest	
	MAPE	R <sup>2</sup>	MAPE	R <sup>2</sup>	MAPE	R <sup>2</sup>	MAPE	R <sup>2</sup>
15	12.26	0.7284	8.17	0.5310	8.61	0.8348	2.46	0.9638
25	9.78	0.8270	8.70	0.5544	7.98	0.8691	2.33	0.9671



Table 8 (Continue)

High Ranking Variables	Bagging		Boosting		Support Vector Machine		Random Forest	
	MAPE	$R^2$	MAPE	$R^2$	MAPE	$R^2$	MAPE	$R^2$
35	8.41	0.8669	8.18	0.5368	7.57	0.8758	2.18	0.9715
45	8.15	0.8767	8.20	0.5570	8.61	0.8348	2.13	0.9732

Table 9 shows the number of outliers with their percentages using the 2- sigma limits. Data can have outliers due to factors that cannot be controlled, and these outliers will affect the prediction accuracy (Lim et al., 2020; Rajarathinam & Vinoth, 2014). For 15 important variables, boosting has the highest number of outliers, with 185. It represents less than 10% of the total observations. For the 25 highest important variables, boosting has the highest number of outliers, with 152 observations. It represents less than 8% of the total observations. Of the 35 highest important variables, boosting has the highest number of outliers, with 171 observations. It represents less than 9% of the total observations. Of the 45 highest important variables, boosting has the highest number of outliers, with 165 observations. It represents less than 9% of the total observations. Although the random forest has one of the highest outliers, it performs better. This result also aligns with (Liu et al., 2018), where random forest performed better with uncertainties and variances.

Table 9

Percentage of outliers outside 2 - sigma limits

Model	The Highest Variable Importance			
	15	25	35	45
	$\mu \pm 2\sigma$ (%)	$\mu \pm 2\sigma$ (%)	$\mu \pm 2\sigma$ (%)	$\mu \pm 2\sigma$ (%)
Random Forest	123(6.43%)	119(6.22%)	99(5.17%)	92(4.81%)
SVM	106(5.54%)	89(4.65%)	79(4.13%)	80(4.18%)
Bagging	81(4.23%)	84(4.39%)	77(4.02%)	73(3.81%)
Boosting	185(9.67%)	152(7.94%)	171(8.93%)	165(8.62%)

The number outside and inside the parentheses are the number of outliers and the percentage of outliers for the 2-sigma limit, respectively.

## CONCLUSION

This study computed the total number of all possible models to achieve the objectives. Random forest, boosting, support vector machine, and bagging machine learning algorithms were used to model the data. The 15, 25, 35 and 45 highest important variables were selected to determine the moisture content removal of the seaweed big data after the

drying. The errors and outliers were computed using metric validation and 2-sigma limits. The percentage representing the interaction parameters has shown how important it is to determine the moisture content removal of seaweed because the interaction parameters selected by the algorithms are more than the single parameters. From the results, the random forest with 45 highest variable importance gave better results when compared to the bagging, boosting and support vector machine. The values of MAPE (2.13) and R-Square (0.9732) gave the best performance. With these results, an intelligence system based on random forest is the best algorithm to determine the important drying parameters for the moisture content removal of the seaweed with the lowest error.

A few batches of experiments can be used to confirm these results for future work. Missing value implications can also be investigated.

## ACKNOWLEDGEMENT

The authors thank the “Ministry of Higher Education Malaysia for Fundamental Research Grant Scheme with Project Code: FRGS/1/2022/STG06/USM/02/13” for their support. We are also grateful to the anonymous reviewers for their comments and suggestions to improve the clarity and quality of the paper.

## REFERENCES

- Ali, M. K. M., Fudholi, A., Sulaiman, J., Muthuvalu, M. S., Ruslan, M. H., Yasir, S. M., & Hurtado, A. Q. (2017). Post-harvest handling of eucheumatoid seaweeds. In A. Q. Hurtado, A. T. Critchley & L. C. Neish (Eds.), *Tropical Seaweed Farming Trends, Problems and Opportunities* (pp. 131-145). Springer International Publishing. [https://doi.org/10.1007/978-3-319-63498-2\\_8](https://doi.org/10.1007/978-3-319-63498-2_8)
- Ali, M. K. M., Sulaiman, J., Yasir, S. M., Ruslan, M. H., Fudholi, A., Muthuvalu, M. S., & Ramu, V. (2017). Cubic spline as a powerful tools for processing experimental drying rate data of seaweed using solar drier. *Article in Malaysian Journal of Mathematical Sciences*, 11(S), 159-172.
- Ali, M. K. M., Mukhtar, Ismail, M. T., Ferdinand, M. H., & Alimuddin. (2021). Machine learning-based variable selection: An evaluation of bagging and boosting. *Turkish Journal of Computer and Mathematics Education*, 12(13), 4343-4349.
- Alsahaf, A., Petkov, N., Shenoy, V., & Azzopardi, G. (2022). A framework for feature selection through boosting. *Expert Systems with Applications*, 187, Article 115895. <https://doi.org/10.1016/j.eswa.2021.115895>
- Arjasakusuma, S., Kusuma, S. S., & Phinn, S. (2020). Evaluating variable selection and machine learning algorithms for estimating forest heights by combining lidar and hyperspectral data. *ISPRS International Journal of Geo-Information*, 9(9), 1-26. <https://doi.org/10.3390/ijgi9090507>
- Bajan, B., Mrówczyńska-Kamińska, A., & Poczta, W. (2020). Economic energy efficiency of food production systems. *Energies*, 13(21), 1-16. <https://doi.org/10.3390/en13215826>
- Bixler, H. J., & Porse, H. (2011). A decade of change in the seaweed hydrocolloids industry. *Journal of Applied Phycology*, 23(3), 321-335. <https://doi.org/10.1007/s10811-010-9529-3>

- Chen, R. C., Dewi, C., Huang, S. W., & Caraka, R. E. (2020). Selecting critical features for data classification based on machine learning methods. *Journal of Big Data*, 7(1), 1-26. <https://doi.org/10.1186/s40537-020-00327-4>
- Chicco, D., Warrens, M. J., & Jurman, G. (2021). The coefficient of determination R-squared is more informative than SMAPE, MAE, MAPE, MSE and RMSE in regression analysis evaluation. *PeerJ Computer Science*, 7, Article e623. <https://doi.org/10.7717/peerj-cs.623>
- Chowdhury, M. Z. I., & Turin, T. C. (2020). Variable selection strategies and its importance in clinical prediction modelling. *Family Medicine and Community Health*, 8(1), Article e000262. <https://doi.org/10.1136/fmch-2019-000262>
- Cole, M. B., Augustin, M. A., Robertson, M. J., & Manners, J. M. (2018). The science of food security. *Npj Science of Food*, 2(1), 1-8. <https://doi.org/10.1038/s41538-018-0021-9>
- Cortes, C., & Vapnik, V. (1995). Support-vector networks. *Machine Learning*, 20, 273-297.
- Drobníč, F., Kos, A., & Pustišek, M. (2020). On the interpretability of machine learning models and experimental feature selection in case of multicollinear data. *Electronics*, 9(5), Article 761. <https://doi.org/10.3390/electronics9050761>
- Echave, J., Otero, P., Garcia-Oliveira, P., Munekata, P. E. S., Pateiro, M., Lorenzo, J. M., Simal-Gandara, J., & Prieto, M. A. (2022). Seaweed-derived proteins and peptides: Promising marine bioactives. *Antioxidants*, 11(1), 1-26. <https://doi.org/10.3390/antiox11010176>
- Freund, R. M., Grigas, P., & Mazumder, R. (2017). A new perspective on boosting in linear regression via subgradient optimization and relatives. *Annals of Statistics*, 45(6), 2328-2364. <https://doi.org/10.1214/16-AOS1505>
- Friedman, J. H. (2001). Greedy Function approximation: A gradient boosting machine. *The Annals of Statistics*, 29(5), 1189-1232.
- Georganos, S., Grippa, T., Niang Gadiaga, A., Linard, C., Lennert, M., Vanhuysse, S., Mboga, N., Wolff, E., & Kalogirou, S. (2021). Geographical random forests: A spatial extension of the random forest algorithm to address spatial heterogeneity in remote sensing and population modelling. *Geocarto International*, 36(2), 121-136. <https://doi.org/10.1080/10106049.2019.1595177>
- Gouda, S. G., Hussein, Z., Luo, S., & Yuan, Q. (2019). Model selection for accurate daily global solar radiation prediction in China. *Journal of Cleaner Production*, 221, 132-144. <https://doi.org/10.1016/j.jclepro.2019.02.211>
- Gunn, H. J., Rezvan, P. H., Fernández, M. I., & Comulada, W. S. (2022). How to apply variable selection machine learning algorithms with multiply imputed data: A missing discussion. *Psychological Methods*, 28(2), 452-471. <https://doi.org/10.1037/met0000478>
- Ibidoja, O. J., Ajare, E. O., & Jolayemi, E. T. (2016). Reliability measures of academic performance. *International Journal of Science for Global Sustainability*, 2(4), 59-64.
- Javaid, A., Ismail, M. T., & Ali, M. K. M. (2020). Comparison of sparse and robust regression techniques in efficient model selection for moisture ratio removal of seaweed using solar drier. *Pertanika Journal of Science and Technology*, 28(2), 609-625.
- Javaid, A., Muthuvalu, M. S., Sulaiman, J., Ismail, M. T., & Ali, M. K. M. (2019). Forecast the moisture ratio removal during seaweed drying process using solar drier. *AIP Conference Proceedings*, 2184, Article 050016. <https://doi.org/10.1063/1.5136404>

- Jierula, A., Wang, S., Oh, T. M., & Wang, P. (2021). Study on accuracy metrics for evaluating the predictions of damage locations in deep piles using artificial neural networks with acoustic emission data. *Applied Sciences*, *11*(5), 1-21. <https://doi.org/10.3390/app11052314>
- Kabari, L. G., Onwuka, U., & Onwuka, U. C. (2019). Comparison of bagging and voting ensemble machine learning algorithm as a classifier. *International Journal of Computer Science and Software Engineering*, *9*(3), 19-23.
- Kaneko, H. (2021). Examining variable selection methods for the predictive performance of regression models and the proportion of selected variables and selected random variables. *Heliyon*, *7*(6), 1-12. <https://doi.org/10.1016/j.heliyon.2021.e07356>
- Kim, S., & Kim, H. (2016). A new metric of absolute percentage error for intermittent demand forecasts. *International Journal of Forecasting*, *32*(3), 669-679. <https://doi.org/10.1016/J.IJFORECAST.2015.12.003>
- Leys, C., Delacre, M., Mora, Y. L., Lakens, D., & Ley, C. (2019). How to classify, detect, and manage univariate and multivariate outliers, with emphasis on pre-registration. *International Review of Social Psychology*, *32*(1), 1-10. <https://doi.org/10.5334/irsp.289>
- Lim, H. Y., Fam, P. S., Javaid, A., & Ali, M. K. M. (2020). Ridge regression as efficient model selection and forecasting of fish drying using v-groove hybrid solar drier. *Pertanika Journal of Science and Technology*, *28*(4), 1179-1202. <https://doi.org/10.47836/pjst.28.4.04>
- Liu, C., Tang, F., & Bak, C. L. (2018). An accurate online dynamic security assessment scheme based on random forest. *Energies*, *11*(7), Article 1914. <https://doi.org/10.3390/en11071914>
- Meyer, H., Reudenbach, C., Wöllauer, S., & Nauss, T. (2019). Importance of spatial predictor variable selection in machine learning applications - Moving from data reproduction to spatial prediction. *Ecological Modelling*, *411*, Article 108815. <https://doi.org/10.1016/j.ecolmodel.2019.108815>
- Namana, M. S. K., Rathnala, P., Sura, S. R., Patnaik, P., Rao, G. N., & Naidu, P. V. (2022). Internet of things for smart agriculture - State of the art and challenges. *Ecological Engineering and Environmental Technology*, *23*(6), 147-160. <https://doi.org/10.12912/27197050/152916>
- Nuroğlu, E., Öz, E., Bakırdere, S., Bursalıoğlu, E. O., Kavanoz, H. B., & İçelli, O. (2019). Evaluation of magnetic field assisted sun drying of food samples on drying time and mycotoxin production. *Innovative Food Science and Emerging Technologies*, *52*, 237-243. <https://doi.org/10.1016/j.ifset.2019.01.004>
- Pradhan, B., Bhuyan, P. P., Patra, S., Nayak, R., Behera, P. K., Behera, C., Behera, A. K., Ki, J. S., & Jena, M. (2022). Beneficial effects of seaweeds and seaweed-derived bioactive compounds: Current evidence and future prospective. *Biocatalysis and Agricultural Biotechnology*, *39*, Article 102242. <https://doi.org/10.1016/j.bcab.2021.102242>
- Prosekov, A. Y., & Ivanova, S. A. (2018). Food security: The challenge of the present. *Geoforum*, *91*, 73-77. <https://doi.org/10.1016/j.geoforum.2018.02.030>
- Rahimi, P., Islam, M. S., Duarte, P. M., Tazerji, S. S., Sobur, M. A., el Zowalaty, M. E., Ashour, H. M., & Rahman, M. T. (2022). Impact of the COVID-19 pandemic on food production and animal health. *Trends in Food Science and Technology*, *121*, 105-113. <https://doi.org/10.1016/j.tifs.2021.12.003>
- Rahman, S., Irfan, M., Raza, M., Ghori, K. M., Yaqoob, S., & Awais, M. (2020). Performance analysis of boosting classifiers in recognizing activities of daily living. *International Journal of Environmental Research and Public Health*, *17*(3), Article 1082. <https://doi.org/10.3390/ijerph17031082>

- Rajarathinam, A., & Vinoth, B. (2014). Outlier detection in simple linear regression models and robust regression-A case study on wheat production data. *International Journal of Scientific Research*, 3(2), 531-536.
- Rashidi, H. H., Tran, N. K., Betts, E. V., Howell, L. P., & Green, R. (2019). Artificial intelligence and machine learning in pathology: The present landscape of supervised methods. *Academic Pathology*, 6, 1-17. <https://doi.org/10.1177/2374289519873088>
- Safronova, O. V., Polyakova, E. D., Evdokimova, O. V., Demina, E. N., Lazareva, T. N., & Petrova, O. A. (2022). Development of sustainable systems of food production using spirulina platensis dairy technology as a functional filler. *IOP Conference Series: Earth and Environmental Science*, 981(2), Article 022074. <https://doi.org/10.1088/1755-1315/981/2/022074>
- Solyali, D. (2020). A comparative analysis of machine learning approaches for short-/long-term electricity load forecasting in Cyprus. *Sustainability*, 12(9), Article 3612. <https://doi.org/10.3390/SU12093612>
- Ssemwanga, M., Makule, E., & Kayondo, S. I. (2020). Performance analysis of an improved solar dryer integrated with multiple metallic solar concentrators for drying fruits. *Solar Energy*, 204, 419-428. <https://doi.org/10.1016/j.solener.2020.04.065>
- Sumari, A. D. W., Charlinawati, D. S., & Ariyanto, Y. (2021). A simple approach using statistical-based machine learning to predict the weapon system operational readiness. *Proceedings of the International Conference on Data Science and Official Statistics*, 2021(1), 343-351. <https://doi.org/10.34123/icdsos.v2021i1.58>
- Yang, W., Yuan, T., & Wang, L. (2020). Micro-blog sentiment classification method based on the personality and bagging algorithm. *Future Internet*, 12(4), Article 75. <https://doi.org/10.3390/fi12040075>



## Response Surface Methodology: A Versatile Tool for the Optimization of Particle Sizes of Cellulose Beads

Kimberly Wei Wei Tay<sup>1</sup>, Suk Fun Chin<sup>1\*</sup>, Mohd Effendi Wasli<sup>1</sup> and Zaki Musa<sup>2</sup>

<sup>1</sup>Faculty of Resource Science and Technology, Universiti Malaysia Sarawak, 94300 UNIMAS, Kota Samarahan, Sarawak, Malaysia

<sup>2</sup>Malaysian Agricultural Research and Development Institute (MARDI), Jalan Santubong, Petra Jaya, 93050 Kuching, Sarawak, Malaysia

### ABSTRACT

Synthesis parameters are of utmost importance for controlling the particle sizes of cellulose beads. This study aims to investigate the effects of synthesis parameters e.g., stirring speed (250–1250 rpm), surfactant concentrations (0.5–6.0% w/v), cellulose concentrations (1–5% w/v), and reaction temperature (30–100°C) on the particle sizes for micron-sized cellulose beads ( $\mu$ CBs) as well as other parameters e.g. the volume (1.0 mL) and concentration (0.1–1.0% w/v) of cellulose for nanosized ( $n$ CBs) cellulose beads using the response surface methodology (RSM). A total of 27 runs were conducted applying RSM based on the central composite design approach with Minitab-19. Cellulose concentrations were shown to have the most significant effect on both  $\mu$ CBs and  $n$ CBs. Under optimized conditions, the minimum and maximum mean particle size of  $\mu$ CBs that could be achieved were 15.3  $\mu$ m and 91  $\mu$ m, respectively. The predicted mean particle size for  $n$ CBs was obtained at 0.01 nm as the smallest and 200 nm as the biggest particle size under the optimum conditions. This study envisages that RSM and experiments for targeted applications such as biomedicine and agriculture could optimize the particle sizes of cellulose beads.

*Keywords:* Cellulose beads, controlled particle sizes, microbeads, nanobeads, response surface methodology

### ARTICLE INFO

#### Article history:

Received: 19 October 2022

Accepted: 25 January 2023

Published: 03 October 2023

DOI: <https://doi.org/10.47836/pjst.31.6.10>

#### E-mail addresses:

70097@siswa.unimas.my (Kimberly Wei Wei Tay)  
sfchin@unimas.my; sukfunchin@gmail.com (Suk Fun Chin)  
wmeffendi@unimas.my (Mohd Effendi Wasli)  
zakimusa@mardi.gov.my (Zaki Musa)

\* Corresponding author

### INTRODUCTION

Cellulose fibers have attracted tremendous interest as a precursor material for the synthesis of micro-beads and nanobeads due to their vast availability, renewability, cost-effectiveness, biocompatibility,

biodegradability (Balart et al., 2021; Gericke et al., 2013; Jampi et al., 2021; Kalia et al., 2011; Xu & Cho, 2022). Cellulose fibers can be isolated from various cellulosic wastes such as cotton, sawdust, and printed paper (Pang et al., 2011, 2018; Voon et al., 2016). Cellulose beads in nano and micron sizes have a high potential to be used in various technological and biomedical applications such as solid support, ion exchange, and water treatment (Alazab & Saleh, 2022; Saleh, 2021), protein immobilization (Califano et al., 2021; Culica et al., 2021; Guo et al., 2021) and delayed drug release (Gülsu & Yüksesktepe, 2021; Ho et al., 2020; Mohan et al., 2022), slow-release fertilizer (França et al., 2021; Gomes et al., 2022; Machado et al., 2022), dye removal (Hamidon et al., 2022; Harada et al., 2021; Meng et al., 2019) and heavy metal removal (Du et al., 2018; Hu et al., 2018; Liu et al., 2021) due to their versatility and eco-friendliness (Carvalho et al., 2021).

Many researchers have attempted the water in oil microemulsion and nanoprecipitation methods to synthesize  $\mu$ CBs and *n*CBs, respectively. Water in oil (W/O) microemulsion is thermodynamically more stable than oil in water by protecting the water-soluble molecules inside a continuous oil phase (Li et al., 2022; Russell-Jones & Himes, 2011; Song et al., 2020). Surfactant is crucially needed in forming microemulsion (Li et al., 2018). Owing to their adequate cutaneous tolerance, low irritation potential, and less toxicity than anionic surfactants, non-ionic surfactants are preferable, such as sorbitan monooleate, Span 80 as attributed to its biodegradability, biocompatibility, and safe to use in food, cosmetic as well as drug production (Conforti et al., 2021; Lechuga et al., 2016; Roque et al., 2020).

Nanoprecipitation is a straightforward and versatile method that involves the complex interaction between mixing, supersaturation, nucleation, and particle growth (Tay et al., 2012). Thanks to its simplicity and reproducibility, this process is greatly explored to synthesize nanoparticles (Yan et al., 2021). Response surface methodology (RSM) has been widely adopted as it helps achieve optimal conditions with a minimum number of trials (Karri et al., 2018; Sebeia et al., 2021; Shahnaz et al., 2020). Several studies have demonstrated that the RSM method is a very effective and versatile method for determining the effects of multiple synthesis parameters on the morphology and properties of the synthesized products (Allouss et al., 2019; Chin et al., 2021; Jancy et al., 2020; Lee & Patel, 2022; Pal et al., 2022; Wu & Hu, 2021).

The synthesis parameters profoundly affected the particle sizes of the  $\mu$ CBs and *n*CBs (Chin et al., 2018; Voon et al., 2015, 2017b). However, without a proper understanding of the underlying mechanisms between each synthesis parameter and the particle sizes, it is very challenging to precisely and consistently control the particle sizes of the  $\mu$ CBs and *n*CBs. Therefore, a systematic study of the effect of synthesis parameters on the particle sizes for  $\mu$ CBs and *n*CBs by both the experimental method and the RSM is of utmost importance to allow precise control of their particle sizes for targeted applications. In this study, the effects of synthesis parameters on mean particle size for  $\mu$ CBs and *n*CBs were investigated and optimized using the RSM.



## MATERIALS AND METHODS

### Materials and Reagents

Paper wastes were obtained from Universiti Malaysia Sarawak, particularly on the campus of Faculty Resource and Science Technology. Chemical substances such as sodium dihydrogen phosphate or  $\text{NaH}_2\text{PO}_4$  (Sigma Aldrich), alpha-cellulose (Sigma Aldrich), as well as disodium hydrogen phosphate or  $\text{Na}_2\text{HPO}_4$  (Sigma Aldrich) were obtained. Procurement was made for hydrochloric acid or HCl (Merck), sodium hydroxide or NaOH (Merck), urea (Merck), thiourea (Merck), sorbitan oleate or known as Span 80 (Merck), paraffin oil (Merck), absolute ethanol (Merck), as well as sodium dodecyl sulfate or SDS (Merck). No further purification was needed for every chemical applied. Phosphate buffer saline solution, PBS, was prepared using sodium dihydrogen phosphate,  $\text{NaH}_2\text{PO}_4$  (1.0 M), and disodium hydrogen phosphate,  $\text{Na}_2\text{HPO}_4$  (1.0 M) solutions. Ultrapure water ( $\sim 18.2 \text{ M}\Omega \cdot \text{cm}$ ,  $25^\circ\text{C}$ ) was obtained from the Water Purifying System (ELGA, Model Ultra Genetic).

### Extraction of Cellulose Fibres

The extraction of cellulose fibers from paper waste was based on our published methods (Voon et al., 2016, 2017a, 2017b). Approximately 100 g of paper waste was turned into powder by grinding and then sprinkled onto the water with constant stirring of 2000 rpm for 2 hours. A treatment with NaOH solution (12.0 wt%) in 24 hours was required for the slurry and, eventually, with HCl solution (3.0 wt%) at  $80^\circ\text{C}$  for 2 hours to eliminate hemicellulose, lignin together with residual ink. Refined cellulose fibers were then cleaned with ultrapure water, followed by the drying process in an oven ranging from  $60^\circ\text{C}$  to  $100^\circ\text{C}$  for 24 hours to ensure the water content remained below 0.5%. A comparison of the cellulose sample and commercial alpha-cellulose based on the FTIR spectrum was made to confirm the purity of the cellulose sample.

### Dissolution of Cellulose

Dissolution of cellulose fibers was conducted by dissolving and sonicating the measured quantity of cellulose fibers in an aqueous-based solvent system, NTU solvent (100 mL) with the composition proportion at 8: 6.5: 8 (% w/v) of NaOH: thiourea: urea respectively for half an hour. The resulting dispersion was cooled by putting it inside a freezer under  $-20^\circ\text{C}$  for 24 hours to achieve a solid frozen mass and later defrosted at normal room temperature to collect a transparent cellulose solution (Voon et al., 2017a).

### Preparation of Cellulose Beads

**Fabrication of Micron-sized Cellulose Beads ( $\mu\text{CBs}$ ).**  $\mu\text{CBs}$  were synthesized from the cellulose solution by employing the water-in-oil (W/O) microemulsion technique and the

surfactant and precipitating agent, Span 80 and acetic acid, respectively. Span 80 in 0.6 g was commonly dissolved at room temperature in paraffin oil (20 mL). Afterward, half an hour of stirring for the resulting mixture to ensure the homogenized oil phase was attained. Next, microemulsion formation was achieved by adding drop by drop of the cellulose solution (3.5 mL) into the obtained oil phase, along with 1000 rpm of constant stirring for 1 hour. Under vigorous agitation, precipitation of  $\mu$ CBs was observed after incorporating 10% acetic acid. The resulting mixture was used in a separating funnel to obtain cellulose beads and, later, rinsed once with deionized water and two times with absolute ethanol to eliminate the remaining NTU solvent, paraffin oil, and Span 80. The mean particle size of  $\mu$ CBs formed was controlled by modifying the synthesis parameters, which are the stirring speed (250 rpm–1250 rpm), quantity of surfactant (0.5% w/v–6.0% w/v), cellulose concentration (1.0% w/v–5.0% w/v) and reaction temperature (30°C–100°C). Ultimately,  $\mu$ CBs were kept in ethanol (20% v/v) at 0–5°C (Voon et al., 2017a).

**Fabrication of Nanosized Cellulose Beads (*n*CBs).** The cellulose solution (1 mL) of several concentrations (0.1% w/v–1.0% w/v) was added in a drop-by-drop manner to a specified amount of absolute ethanol (6 mL) just when initiating ultrasonication. Precipitation was seen immediately with a cloudy appearance, indicating the formation of *n*CBs. The obtained suspension was centrifuged. After that, the precipitate was washed five times with absolute ethanol to get rid of the excess NaOH, urea, and thiourea to obtain the *n*CBs (Voon et al., 2017a).

### Response Surface Methodology (RSM)

By using Minitab-19 software, a total of 27 runs were made to investigate the effects of synthesis parameters on the mean particle sizes of the  $\mu$ CBs and *n*CBs. Specifically, 22 runs were for  $\mu$ CBs. The p-values for each parameter for both  $\mu$ CBs and *n*CBs are lower than 0.05, as stated in the coded coefficients in Table 1. In addition, the listed p-values in the ANOVA table (Table 2) for the model also provided further validation, deducing that it is statistically significant for all the parameters involved. As shown in Figures 1(a) and (b), the Pareto charts also predicted the same justification. Therefore, the significance of all the synthesis parameters on the mean particle sizes was accurate as estimated by the models applied.

The model's  $R^2$  value and adjusted  $R^2$  (Table 3) for  $\mu$ CBs were estimated to be approximately 92.79% and 88.36%, respectively. As for *n*CBs, the  $R^2$  and adjusted  $R^2$  have the same value of 100%. The evaluation of the goodness of the fit was dependent on statistical parameters like p-value,  $R^2$ , and adjusted  $R^2$  (Kim et al., 2020). In this case, these models displayed low p-values, high  $R^2$ , and adjusted  $R^2$ , indicating that the synthesis parameters used for controlling the particle sizes of the cellulose beads were a good fit with

Table 1  
Coded coefficients table of the synthesis parameters for  $\mu$ CBs and  $n$ CBs

	Term	Coef	SE Coef	T-Value	P-Value	VIF
$\mu$ CBs	Constant	35.17	3.72	9.44	0.000*	
	Stirring speed (rpm)	-14.75	2.51	-5.88	0.000*	1.12
	Span 80 concentration (% w/v)	-7.56	2.27	-3.33	0.005*	1.07
	Cellulose concentration (% w/v)	13.32	2.79	4.77	0.000*	1.00
	Temperature (°C)	17.85	2.21	8.07	0.000*	1.62
	SS <sup>2</sup>	13.19	4.38	3.01	0.010*	1.10
	SC <sup>2</sup>	17.44	3.91	4.46	0.001*	1.10
	CC <sup>2</sup>	-2.51	3.46	-0.73	0.481	1.13
	T <sup>2</sup>	10.28	3.95	2.60	0.022*	1.59
$n$ CBs	Constant	38.23	0.237	161.15	0.004*	
	Cellulose concentration (% w/v)	67.12	0.153	437.51	0.001*	1.75
	VC (mL)	32.90	0.166	197.85	0.003*	2.38
	CC <sup>2</sup>	61.79	0.254	243.54	0.003*	1.50

Note. Superscript \* refers to the statistically significant parameters ( $p < 0.05$ ). SS<sup>2</sup> represents the squared stirring speed, SC<sup>2</sup> is the squared Span 80 concentration, CC<sup>2</sup> is the squared cellulose concentration, T<sup>2</sup> is the squared temperature, and VC is the volume of cellulose.  $\mu$ CBs involve SS (250–1250 rpm), SC (0.5–6.0% w/v), CC (1–5% w/v), and T (30–100°C), while  $n$ CBs are VC (1 mL) and CC (0.1–1.0% w/v).

Table 2  
Analysis of variance (ANOVA) table for  $\mu$ CBs and  $n$ CBs

	Source	DF	Adj SS	Adj MS	F-Value	P-Value
$\mu$ CBs	Model	8	3261.29	407.66	20.92	0.000*
	Linear	4	2633.13	658.28	33.79	0.000*
	Stirring speed (rpm)	1	674.39	674.39	34.61	0.000*
	Span 80 concentration	1	216.52	216.52	11.11	0.005*
	Cellulose concentration	1	443.56	443.56	22.77	0.000*
	Temperature (°C)	1	1269.51	1269.51	65.16	0.000*
	Square	4	754.90	188.73	9.69	0.001*
	SS <sup>2</sup>	1	176.55	176.55	9.06	0.010*
	SC <sup>2</sup>	1	387.36	387.36	19.88	0.001*
	CC <sup>2</sup>	1	10.27	10.27	0.53	0.481
	T <sup>2</sup>	1	131.62	131.62	6.76	0.022*
	Error	13	253.28	19.48		
	Lack-of-Fit	10	175.63	17.56	0.68	0.720
	Pure Error	3	77.65	25.88		
Total	21	3514.57				
$n$ CBs	Model	3	21934.80	7311.60	196270.43	0.002*
	Linear	2	21828.50	10914.20	292979.26	0.001*
	Cellulose concentration (% w/v)	1	7130.60	7130.60	191412.39	0.001*

Table 2 (continue)

Source	DF	Adj SS	Adj MS	F-Value	P-Value
VC (mL)	1	1458.30	1458.30	39146.31	0.003*
Square	1	2209.60	2209.60	59313.64	0.003*
CC <sup>2</sup>	1	2209.60	2209.60	59313.64	0.003*
Error	1	0.00	0.00		
Total	4	21934.80			

Note. Superscript \* refers to the statistically significant parameters ( $p < 0.05$ ). SS<sup>2</sup> represents the squared stirring speed, SC<sup>2</sup> is the squared Span 80 concentration, CC<sup>2</sup> is the squared cellulose concentration, T<sup>2</sup> is the squared temperature, and VC is the volume of cellulose.  $\mu$ CBs involve SS (250–1250 rpm), SC (0.5–6.0% w/v), CC (1–5% w/v), and T (30–100°C), while nCBs are VC (1 mL) and CC (0.1–1.0% w/v).

Table 3

Model summary table of the synthesis parameters for  $\mu$ CBs and nCBs

	S	R-sq**	R-sq(adj)**	R-sq(pred)
$\mu$ CBs	4.41395	92.79%	88.36%	64.17%
nCBs	0.19301	100.00%	100.00%	-

Note. \*\* High values of R-squared and R-squared (adj.) are indicated.  $\mu$ CBs involve SS (250–1250 rpm), SC (0.5–6.0% w/v), CC (1–5% w/v), and T (30–100°C), while nCBs are VC (1 mL) and CC (0.1–1.0% w/v).

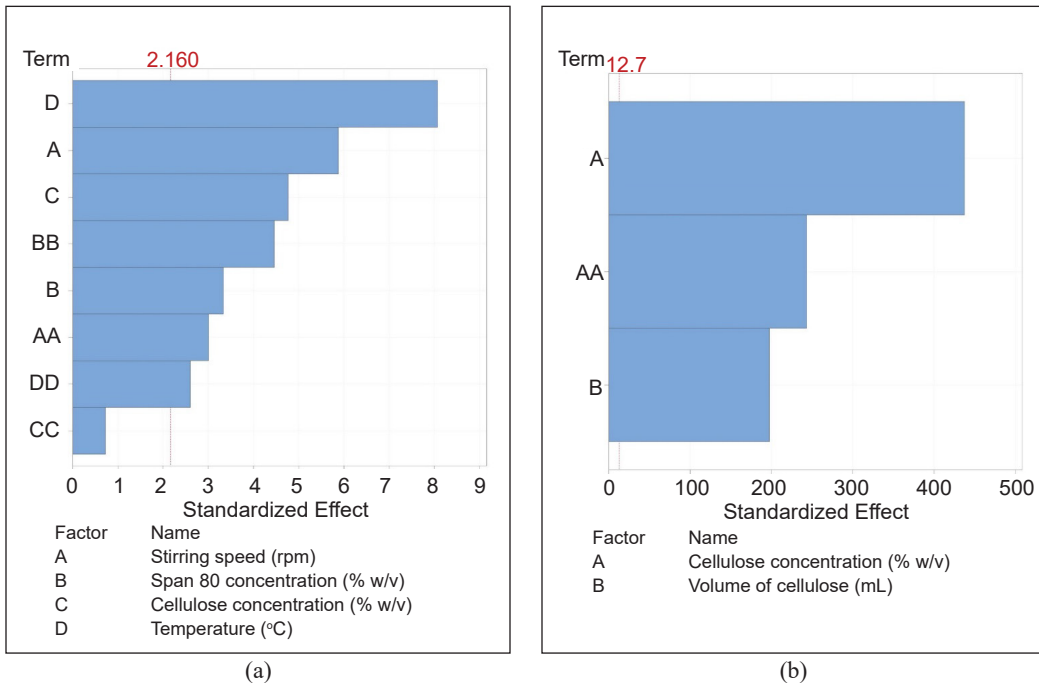


Figure 1. Pareto charts for the mean particle sizes of (a)  $\mu$ CBs and (b) nCBs, where  $\mu$ CBs are SS (250–1250 rpm), SC (0.5–6.0% w/v), CC (1–5% w/v) and T (30–100°C); nCBs are VC (1 mL) and CC (0.1–1.0% w/v)

the model. Equations 1 and 2 demonstrated the regression equations in uncoded units of the models for both sized cellulose beads, respectively.

$$\text{Particle sizes } (\mu\text{m}) = 96.90 - 0.1086(\text{SS}) - 17.74(\text{SC}) + 10.43(\text{CC}) - 0.581(\text{T}) + 0.000053(\text{SS})^2 + 2.306(\text{SC})^2 - 0.629(\text{CC})^2 + 0.00839(\text{T})^2 \quad [1]$$

$$\text{Particle sizes (nm)} = 0.000 - 112.93(\text{CC}) + 65.80(\text{VC}) + 247.17(\text{CC})^2 \quad [2]$$

Where SS is the stirring speed, SC is the Span 80 concentration, CC is the cellulose concentration, T is temperature, and VC is the volume of cellulose.

## RESULTS AND DISCUSSION

### Effect of Synthesis Parameters on the Mean Particle Sizes for $\mu\text{CBs}$

**Effects of Stirring Speeds.** Figures 2(a) and (b) illustrate the respective contour and surface plots for the effects of stirring speed and Span 80 concentration on the mean particle sizes of  $\mu\text{CBs}$ . Both plots anticipated that the minimum mean particle size of 30.2  $\mu\text{m}$  could be attained with a stirring speed of 1023.4 rpm and 3.9% w/v of Span 80 concentration. At the same time, a maximum mean particle size of 87.5  $\mu\text{m}$  was obtained under 254 rpm and 0.5% w/v Span 80 concentration. In our previous study, the smallest 27.6  $\mu\text{m}$  and 64.5  $\mu\text{m}$  particle sizes of  $\mu\text{CBs}$  were produced under 1000 rpm and 250 rpm, respectively, with 2% w/v Span 80 (Voon et al., 2017a). A slow stirring speed would decrease the kinetic energy of particles. Eventually, aggregation of particles may tend to occur. Shi et al. (2011) mentioned the difficulty dispersing the cellulose solution in the oil phase under less than 300 rpm stirring speed. The size of the microsphere would also increase under slower stirring (Luo & Zhang, 2010), whereas an increase of 500 rpm stirring speed could lead to a reduction of at least half in the size of cellulose microspheres (Jo et al., 2019; Lefroy et al., 2022) because aggregates would break apart under higher stirring speeds (Kemin & Chin, 2020). As cellulose contains many hydroxyl groups (Shi et al., 2021), the formation of cellulose molecules' intra and intermolecular hydrogen bonds was likely to occur. However, the strong stirring force produced from the high stirring speed might damage the structure of the beads, causing a reduction of compressive strength (Li et al., 2020).

In the presence of surfactants, the interaction of polymer chains would be hindered, forming various reduced mean particle sizes (Tay et al., 2012). Surface tension between particles could be decreased, preventing coalescence from producing smaller particles when applying an optimum surfactant concentration (Chin et al., 2014). For instance, the presence of a carbonyl group would result, as indicated by a strong absorption peak at around 1700  $\text{cm}^{-1}$  (Essawy et al., 2016; Guan et al., 2017). It further proved the combination of surfactants with the cellulose and the hindrance of the intermolecular hydrogen bond aggregation of the cellulose due to the exposed hydrophobic polymer chains (Wang et al.,

2019). An increment of surfactant concentration can enhance the micelle formation and lead to a larger mean particle size (Ching et al., 2019; Jo et al., 2019). It has resulted in instability and aggregation of particles, thereby producing larger microspheres (Chin et al., 2014; Hakim et al., 2020). As surfactant concentration increased, the number of micelles also increased, which enhanced the formation of surfactant-polymer complexes via the electrostatic and hydrophobic interactions (Bhardwaj et al., 2018).

However, it had been reported that an increase in surfactant concentrations from 0 % to 3% w/v showed a significant reduction in the particle size of microspheres (Alnaief et al., 2011; Voon et al., 2017a). Specifically, 3% w/v of surfactant concentration was an optimum concentration for fully covering the whole surface area of droplets, providing great stabilization in forming smaller particle sizes (Chin et al., 2014). Therefore, the optimal conditions for forming the smallest mean particle size of beads were approximately 1000 rpm, and within 4% w/v Span 80 concentration could be employed, proving a satisfactory agreement exists between the experimental and predicted results.

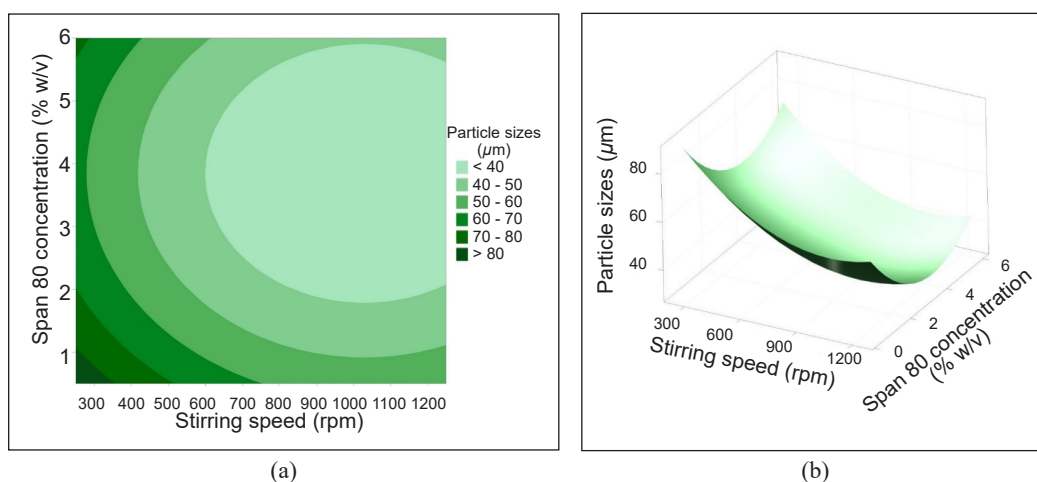


Figure 2. The effects of stirring speed and Span 80 concentration on the mean particle sizes of  $\mu$ CBs: (a) contour; and (b) surface plots (With 3% w/v cellulose concentration; 65°C)

The effects of stirring speed and cellulose concentration on the mean particle sizes of the  $\mu$ CBs are shown in Figures 3(a) and (b). The results showed that the mean particle size would decrease using a lower stirring speed and higher cellulose concentration. The plots estimated a minimum of 15.3  $\mu$ m cellulose beads would be obtained at 1031.4 rpm and 1.0% w/v of cellulose concentration. Conversely, the maximum mean particle size of 73.8  $\mu$ m would be expected to be produced using a stirring speed at 251 rpm and 5.0% w/v cellulose concentration. The smallest particle size achieved experimentally was approximately 14.5  $\mu$ m and the largest at around 42.3  $\mu$ m when cellulose concentration increased from 1.0% w/v to 5% w/v, under 1000 rpm (Voon et al., 2017a).

The viscosity of the cellulose solution is dependent on the cellulose concentrations. An adequate viscosity can be found in a higher concentration of cellulose, which helps to resist the increased deformation forces (Schroeter et al., 2021). The number of cellulose molecules would increase when cellulose concentration increased (Chin et al., 2016). A slower agitation speed was accompanied during the process. It could lead to the formation of many big aggregates accompanied by high strength and resistance to the disintegration of porous structures (Li et al., 2022). Similarly, Druel et al. (2018) reported cellulose concentration as the major contributor to regulating the size of the beads. High cellulose concentration with low stirring speed would promote larger growth of particles, while low cellulose concentration with high stirring speed produced smaller particles. Previous studies highlighted the emulsification process of cellulose, enabling extensive production of microspheres with tailored particle sizes as well as distributions (Costa et al., 2019; Shi et al., 2021; Winuprasith & Suphantharika, 2015). Hence, the experimental results concurred with the predicted RSM data of approximately 15  $\mu\text{m}$  and 70  $\mu\text{m}$  with respect to the minimum and maximum particle sizes of the  $\mu\text{CBs}$ .

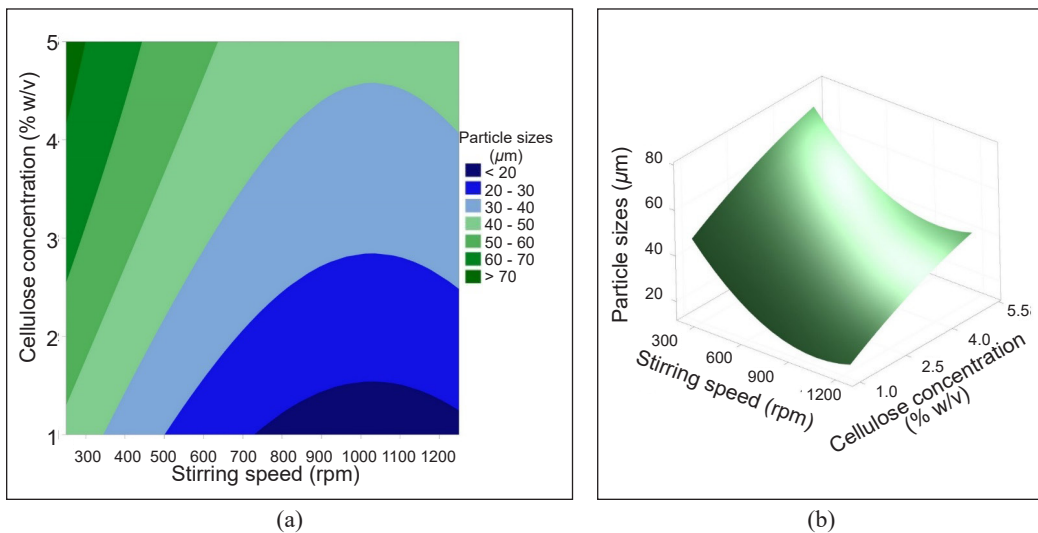


Figure 3. The effects of stirring speed and cellulose concentration on the mean particle sizes of  $\mu\text{CBs}$ : (a) contour; and (b) surface plots (With 3.25% w/v Span 80 concentration; 65°C)

The contour and surface plots for the effects of stirring speed and reaction temperature on the mean particle sizes of  $\mu\text{CBs}$  were presented in Figures 4(a) and (b), respectively. The prediction of the plots for the minimum of 23.3  $\mu\text{m}$  cellulose beads would require 1022 rpm and 34.2°C. When the reaction temperature increased to 100°C and with stirring speed at 251 rpm, a maximum mean particle size of 91  $\mu\text{m}$  could be synthesized. It showed that the higher the stirring speed and the lower the reaction temperature, the smaller the

particle size of cellulose beads. Under an optimum 1000 rpm, the smallest 26.1  $\mu\text{m}$  and the largest 67.2  $\mu\text{m}$  of  $\mu\text{CBs}$  were obtained experimentally when the reaction temperature was at 30°C and 100°C, respectively (Voon et al., 2017a).

As previously stated, a low stirring speed can give rise to the agglomeration of particles. Temperature also had strong influential effects on particle sizes. Increased temperature is capable of speeding up the movement of droplets, increasing the instability of the oil/water interface, elevating the coalescence of the droplets, and eventually, causing phase separation of the emulsions (Tong et al., 2015). It was reported that an increase in temperature could decrease the viscosity of cellulose solution (Bhardwaj et al., 2018). Bigger particle size could be obtained due to decreasing viscosity and increased surface tension when the temperature of the cellulose solution increased (An et al., 2021). At a low temperature, coagulation took place at the inner layer as it enfolded the cellulose molecules densely and caused a little shrinkage of the bead (Trygg et al., 2013). The microemulsion droplets would remain stable under a low temperature and vice versa at higher temperatures, resulting in smaller beads. At the same time, an optimum stirring speed would also be required. Emulsion stability is also associated with the surfactant type and amount (Akbari & Nour, 2018). In addition, Span 80 surfactants are shown to be influenced by temperature due to the critical micelle concentration, whereby droplet size would remain the same above the critical value (Michor & Berg, 2015). Thus, an optimum temperature is critical to achieving the desired particle sizes of cellulose beads. Overall, the estimated RSM data agrees with the experimental work reported (Voon et al., 2017a).

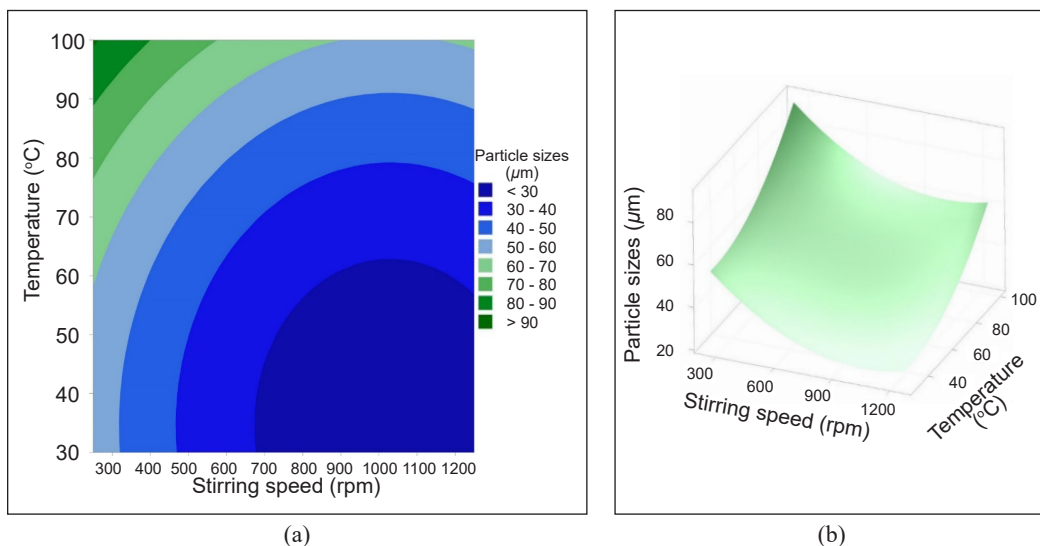


Figure 4. The effects of stirring speed and temperature on the mean particle sizes of  $\mu\text{CBs}$ : (a) contour; and (b) surface plots (3% w/v cellulose concentration; 3.25% w/v Span 80 concentration)



### Effects of Synthesis Parameters on the Particle Sizes of *n*CBs

**Effect of Cellulose Concentration.** Figures 5(a) and (b) showed the contour and surface plots of cellulose concentration on the mean particle sizes of *n*CBs. The plots showed that the mean particle sizes of *n*CBs increased linearly with the volume and concentration of the cellulose solution used in the synthesis. The plots predicted that a minimum of 0.01 nm could be obtained when 0.2 mL of 0.2% w/v cellulose concentration was used. On the other hand, a maximum of 200 nm of *n*CBs could be produced by using 1.0 mL of 1.0% w/v cellulose concentration. As determined experimentally, the smallest 57 nm and largest 200 nm of mean particle sizes of *n*CBs were obtained at 0.1% w/v and 1.0% w/v of cellulose concentration, respectively, using a constant 1.0 mL cellulose solution (Voon et al., 2017a).

The hydrophilicity of cellulose molecules can cause the aggregation of particles via hydrogen bonds and, eventually, the formation of bigger clusters of particles (Ren et al., 2014). Higher cellulose concentration will lead to high viscosity, creating a more firm network (Li et al., 2015). Interaction of cellulose/non-solvent molecules would increase under higher cellulose concentration, causing cellulose accumulation (Chin et al., 2016). Lince et al. (2008) reported the three stages of the formation of nanoparticles using nanoprecipitation: nucleation, growth, and aggregation. The insolubility of cellulose in water prompted nucleation to happen and form a solid nucleus within the drop. The deposition of more molecules will lead the nucleus to develop as mediated via coalescence as well as interchange with other drops (Ethayaraja et al., 2007). Ostwald ripening effect could cause the formation of large agglomerated particles over time (Maity et al., 2008).

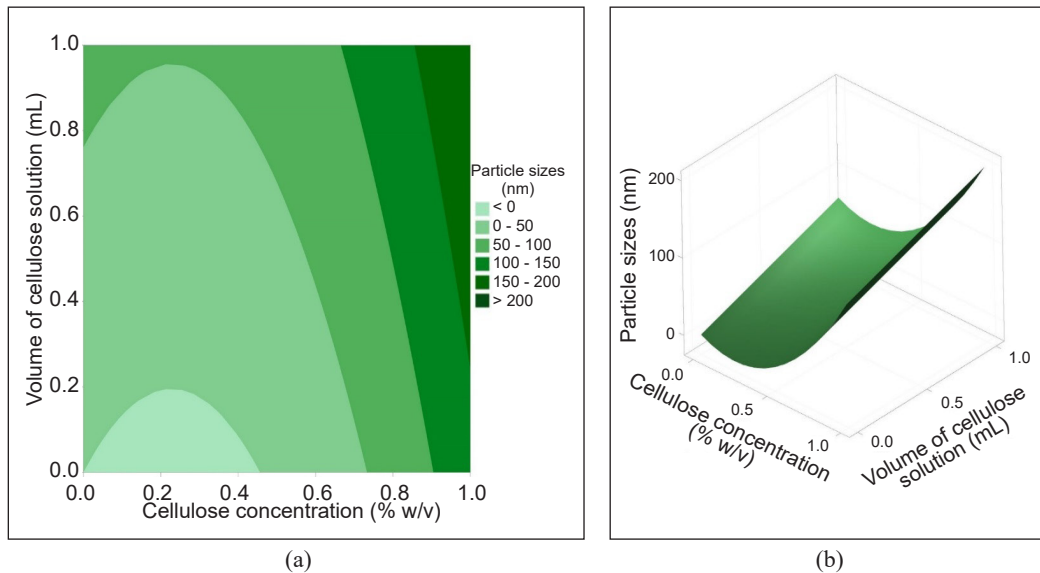


Figure 5. The effects of cellulose concentration on the mean particle sizes of *n*CBs: (a) contour; and (b) surface plots

Hence, bigger *n*CBs would be expected to be produced when more volume of higher cellulose concentration was used, which further verified the consistency of the predicted RSM values with our previous work.

## CONCLUSION

The synthesis parameters of  $\mu$ CBs and *n*CBs were successfully determined using response surface methodology via the central composite design. The effects of several important synthesis parameters such as the stirring speed (250–1250 rpm), Span 80 concentration (0.5–6.0% w/v), cellulose concentration (1–5% w/v) and the reaction temperature (30–100°C) on the mean particle sizes of  $\mu$ CBs were determined, whereas the volume (1 mL) and the concentration (0.1–1.0% w/v) of the cellulose solution were used to tailor the particle sizes of the *n*CBs. The results of this study would allow the control of  $\mu$ CBs and *n*CBs particle sizes via fine-tuning of the synthesis parameters. The model was proven capable of precisely elucidating the experimental data by manipulating the ANOVA, *p*-value,  $R^2$ , and adjusted  $R^2$ . Hence, this study demonstrated that by precisely controlling the synthesis parameters to modulate the particle sizes of the  $\mu$ CBs and *n*CBs.  $\mu$ CBs and *n*CBs with tailored particle sizes would have promising potential as controlled release carriers for drugs or fertilizers in various fields such as biomedical, pharmaceutical, and agricultural.

## ACKNOWLEDGEMENTS

The authors wish to acknowledge the financial support rendered by Kementerian Pengajian Tinggi Malaysia (Malaysian Ministry of Higher Education) via the award of the Fundamental Research Grant Scheme (Grant No. FRGS/1/2020/STG05/UNIMAS/02/1).

## REFERENCES

- Akbari, S., & Nour, A. H. (2018). Emulsion types, stability mechanisms and rheology: A review. *International Journal of Innovative Research and Scientific Studies*, 1(1), 11-17. <https://doi.org/10.53894/ijirss.v1i1.4>
- Alazab, A. A., & Saleh, T. A. (2022). Magnetic hydrophobic cellulose-modified polyurethane filter for efficient oil-water separation in a complex water environment. *Journal of Water Process Engineering*, 50, Article 103125. <https://doi.org/10.1016/j.jwpe.2022.103125>
- Allouss, D., Essamlali, Y., Amadine, O., Chakir, A., & Zahouily, M. (2019). Response surface methodology for optimization of methylene blue adsorption onto carboxymethyl cellulose-based hydrogel beads: Adsorption kinetics, isotherm, thermodynamics and reusability studies. *RSC Advances*, 9(65), 37858-37869. <https://doi.org/10.1039/c9ra06450h>
- Alnaief, M., Alzaitoun, M. A., García-González, C. A., & Smirnova, I. (2011). Preparation of biodegradable nanoporous microspherical aerogel based on alginate. *Carbohydrate Polymers*, 84(3), 1011-1018. <https://doi.org/10.1016/j.carbpol.2010.12.060>

- An, H. J., Park, H., & Cho, B. U. (2021). Effect of temperature of tetraethylammonium hydroxide/urea/cellulose solution on surface tension and cellulose bead size. *Journal of Korea Technical Association of the Pulp and Paper Industry*, 53(6), 69-76. <https://doi.org/10.7584/jktappi.2021.12.53.6.69>
- Balart, R., Garcia-Garcia, D., Fombuena, V., Quiles-Carrillo, L., & Arrieta, M. P. (2021). Biopolymers from natural resources. *Polymers*, 13(15), Article 2532. <https://doi.org/10.3390/polym13152532>
- Bhardwaj, P., Kamil, M., & Panda, M. (2018). Surfactant-polymer interaction: effect of hydroxypropylmethyl cellulose on the surface and solution properties of gemini surfactants. *Colloid and Polymer Science*, 296(11), 1879-1889. <https://doi.org/10.1007/s00396-018-4409-5>
- Califano, D., Patenall, B. L., Kadowaki, M. A. S., Mattia, D., Scott, J. L., & Edler, K. J. (2021). Enzyme-functionalized cellulose beads as a promising antimicrobial material. *Biomacromolecules*, 22(2), 754-762. <https://doi.org/10.1021/acs.biomac.0c01536>
- Carvalho, J. P. F., Silva, A. C. Q., Silvestre, A. J. D., Freire, C. S. R., & Vilela, C. (2021). Spherical cellulose micro and nanoparticles: A review of recent developments and applications. *Nanomaterials*, 11(10), Article 2744. <https://doi.org/10.3390/nano11102744>
- Chin, S. F., Jimmy, F. B., & Pang, S. C. (2016). Fabrication of cellulose aerogel from sugarcane bagasse as drug delivery carriers. *Journal of Physical Science*, 27(3), 159-168. <https://doi.org/10.21315/jps2016.27.3.10>
- Chin, S. F., Azman, A., & Pang, S. C. (2014). Size controlled synthesis of starch nanoparticles by a microemulsion method. *Journal of Nanomaterials*, 2014, Article 763736. <https://doi.org/10.1155/2014/763736>
- Chin, S. F., Jimmy, F. B., & Pang, S. C. (2018). Size controlled fabrication of cellulose nanoparticles for drug delivery applications. *Journal of Drug Delivery Science and Technology*, 43, 262-266. <https://doi.org/10.1016/j.jddst.2017.10.021>
- Chin, S. F., Jong, S. J., & Yeo, Y. J. (2021). Optimization of cellulose-based hydrogel synthesis using response surface methodology. *Biointerface Research in Applied Chemistry*, 12(6), 7136-7146. <https://doi.org/10.33263/BRIAC126.71367146>
- Chin, S. F., Yazid, S. N. A. M., & Pang, S. C. (2014). Preparation and characterization of starch nanoparticles for controlled release of curcumin. *International Journal of Polymer Science*, 2014, Article 340121. <https://doi.org/10.1155/2014/340121>
- Ching, Y. C., Gunathilake, T. M. S. U., Chuah, C. H., Ching, K. Y., Singh, R., & Liou, N. S. (2019). Curcumin/tween 20-incorporated cellulose nanoparticles with enhanced curcumin solubility for nano-drug delivery: Characterization and in vitro evaluation. *Cellulose*, 26(9), 5467-5481. <https://doi.org/10.1007/s10570-019-02445-6>
- Conforti, C., Giuffrida, R., Fadda, S., Fai, A., Romita, P., Zalaudek, I., & Dianzani, C. (2021). Topical dermocosmetics and acne vulgaris. *Dermatologic Therapy*, 34(1), Article e14436. <https://doi.org/10.1111/dth.14436>
- Costa, C., Medronho, B., Filipe, A., Mira, I., Lindman, B., Edlund, H., & Norgren, M. (2019). Emulsion formation and stabilization by biomolecules: The leading role of cellulose. *Polymers*, 11(10), Article 1570. <https://doi.org/10.3390/polym11101570>

- Culica, M. E., Chibac-Scutaru, A. L., Mohan, T., & Coseri, S. (2021). Cellulose-based biogenic supports, remarkably friendly biomaterials for proteins and biomolecules. *Biosensors and Bioelectronics*, *182*, Article 113170. <https://doi.org/10.1016/j.bios.2021.113170>
- Druel, L., Niemeyer, P., Milow, B., & Budtova, T. (2018). Rheology of cellulose-[DBNH][CO<sub>2</sub>Et] solutions and shaping into aerogel beads. *Green Chemistry*, *20*(17), 3993-4002. <https://doi.org/10.1039/c8gc01189c>
- Du, K., Li, S., Zhao, L., Qiao, L., Ai, H., & Liu, X. (2018). One-step growth of porous cellulose beads directly on bamboo fibers via oxidation-derived method in aqueous phase and their potential for heavy metal ions adsorption. *ACS Sustainable Chemistry and Engineering*, *6*(12), 17068-17075. <https://doi.org/10.1021/acssuschemeng.8b04433>
- Essawy, H. A., Ghazy, M. B. M., El-Hai, F. A., & Mohamed, M. F. (2016). Superabsorbent hydrogels via graft polymerization of acrylic acid from chitosan-cellulose hybrid and their potential in controlled release of soil nutrients. *International Journal of Biological Macromolecules*, *89*, 144-151. <https://doi.org/10.1016/j.ijbiomac.2016.04.071>
- Ethayaraja, M., Ravikumar, C., Muthukumar, D., Dutta, K., & Bandyopadhyaya, R. (2007). CdS-ZnS core-shell nanoparticle formation: Experiment, mechanism, and simulation. *The Journal of Physical Chemistry C*, *111*(8), 3246-3252. <https://doi.org/10.1021/jp066066j>
- França, D., de Barros, J. R. S., & Faez, R. (2021). Spray-dried cellulose nanofibrils microparticles as a vehicle for enhanced efficiency fertilizers. *Cellulose*, *28*(3), 1571-1585. <https://doi.org/10.1007/s10570-020-03609-5>
- Gericke, M., Trygg, J., & Fardim, P. (2013). Functional cellulose beads: Preparation, characterization, and applications. *Chemical Reviews*, *113*(7), 4812-4836. <https://doi.org/10.1021/cr300242j>
- Gomes, M. H. F., Callaghan, C., Mendes, A. C. S., Edler, K. J., Mattia, D., de Jong van Lier, Q., & de Carvalho, H. W. P. (2022). Cellulose microbeads: Toward the controlled release of nutrients to plants. *ACS Agricultural Science & Technology*, *2*(2), 340-348. <https://doi.org/10.1021/acsagritech.1c00233>
- Guan, H., Li, J., Zhang, B., & Yu, X. (2017). Synthesis, properties, and humidity resistance enhancement of biodegradable cellulose-containing superabsorbent polymer. *Journal of Polymers*, *2017*, Article 3134681. <https://doi.org/10.1155/2017/3134681>
- Gülsu, A., & Yüksespe, E. (2021). Preparation of spherical cellulose nanoparticles from recycled waste cotton for anticancer drug delivery. *Chemistry Select*, *6*(22), 5419-5425. <https://doi.org/10.1002/slct.202101683>
- Guo, H., Lei, B., Yu, J., Chen, Y., & Qian, J. (2021). Immobilization of lipase by dialdehyde cellulose crosslinked magnetic nanoparticles. *International Journal of Biological Macromolecules*, *185*, 287-296. <https://doi.org/10.1016/j.ijbiomac.2021.06.073>
- Hakim, S. L., Kusumasari, F. C., & Budianto, E. (2020). Optimization of biodegradable PLA/PCL microspheres preparation as controlled drug delivery carrier. *Materials Today: Proceedings*, *22*, 306-313. <https://doi.org/10.1016/j.matpr.2019.08.156>
- Hamidon, T. S., Adnan, R., Haafiz, M. K. M., & Hussin, M. H. (2022). Cellulose-based beads for the adsorptive removal of wastewater effluents: A review. *Environmental Chemistry Letters*, *20*(3), 1965-2017. <https://doi.org/10.1007/s10311-022-01401-4>

- Harada, N., Nakamura, J., & Uyama, H. (2021). Single-step fabrication and environmental applications of activated carbon-containing porous cellulose beads. *Reactive and Functional Polymers*, 160, Article 104830. <https://doi.org/10.1016/j.reactfunctpolym.2021.104830>
- Ho, B. K., Chin, S. F., & Pang, S. C. (2020). pH-responsive carboxylic cellulose acetate nanoparticles for controlled release of penicillin G. *Journal of Science: Advanced Materials and Devices*, 5(2), 224-232. <https://doi.org/10.1016/j.jsamd.2020.04.002>
- Hu, Z. H., Omer, A. M., Ouyang, X. K., & Yu, D. (2018). Fabrication of carboxylated cellulose nanocrystal/sodium alginate hydrogel beads for adsorption of Pb(II) from aqueous solution. *International Journal of Biological Macromolecules*, 108, 149-157. <https://doi.org/10.1016/j.ijbiomac.2017.11.171>
- Jampi, A. L. W., Chin, S. F., Wasli, M. E., & Chia, C. H. (2021). Preparation of cellulose hydrogel from sago pith waste as a medium for seed germination. *Journal of Physical Science*, 32(1), 13-26. <https://doi.org/10.21315/JPS2021.32.1.2>
- Jancy, S., Shruthy, R., & Preetha, R. (2020). Fabrication of packaging film reinforced with cellulose nanoparticles synthesised from jack fruit non-edible part using response surface methodology. *International Journal of Biological Macromolecules*, 142, 63-72. <https://doi.org/10.1016/j.ijbiomac.2019.09.066>
- Jo, S., Park, S., Oh, Y., Hong, J., Kim, H. J., Kim, K. J., Oh, K. K., & Lee, S. H. (2019). Development of cellulose hydrogel microspheres for lipase immobilization. *Biotechnology and Bioprocess Engineering*, 24(1), 145-154. <https://doi.org/10.1007/s12257-018-0335-0>
- Kalia, S., Dufresne, A., Cherian, B. M., Kaith, B. S., Avérous, L., Njuguna, J., & Nassiopoulos, E. (2011). Cellulose-based bio- and nanocomposites: A review. *International Journal of Polymer Science*, 2011, 1-35. <https://doi.org/10.1155/2011/837875>
- Karri, R. R., Tanzifi, M., Yarakı, M. T., & Sahu, J. N. (2018). Optimization and modeling of methyl orange adsorption onto polyaniline nano-adsorbent through response surface methodology and differential evolution embedded neural network. *Journal of Environmental Management*, 223, 517-529. <https://doi.org/10.1016/j.jenvman.2018.06.027>
- Kemin, L. V., & Chin, S. F. (2020). Amino-starch nanoparticles as controlled release nanocarriers for curcumin. *Journal of Physical Science*, 31(2), 1-14. <https://doi.org/10.21315/jps2020.31.2.1>
- Kim, B., Choi, Y., Choi, J., Shin, Y., & Lee, S. (2020). Effect of surfactant on wetting due to fouling in membrane distillation membrane: Application of response surface methodology (RSM) and artificial neural networks (ANN). *Korean Journal of Chemical Engineering*, 37(1), 1-10. <https://doi.org/10.1007/s11814-019-0420-x>
- Lechuga, M., Fernández-Serrano, M., Jurado, E., Núñez-Olea, J., & Ríos, F. (2016). Acute toxicity of anionic and non-ionic surfactants to aquatic organisms. *Ecotoxicology and Environmental Safety*, 125, 1-8. <https://doi.org/10.1016/j.ecoenv.2015.11.027>
- Lee, J., & Patel, R. (2022). Wastewater treatment by polymeric microspheres: A review. *Polymers*, 14(9), Article 1890. <https://doi.org/10.3390/polym14091890>
- Lefroy, K. S., Murray, B. S., & Ries, M. E. (2022). Relationship between size and cellulose content of cellulose microgels (CMGs) and their water-in-oil emulsifying capacity. *Colloids and Surfaces A: Physicochemical and Engineering Aspects*, 647, Article 128926. <https://doi.org/10.1016/j.colsurfa.2022.128926>

- Li, H., Kruteva, M., Dulle, M., Wang, Z., Mystek, K., Ji, W., Pettersson, T., & Wågberg, L. (2022). Understanding the drying behavior of regenerated cellulose gel beads: The effects of concentration and nonsolvents. *ACS Nano*, *16*(2), 2608-2620. <https://doi.org/10.1021/acsnano.1c09338>
- Li, M. C., Wu, Q., Song, K., Lee, S., Qing, Y., & Wu, Y. (2015). Cellulose nanoparticles: Structure-morphology-rheology relationships. *ACS Sustainable Chemistry and Engineering*, *3*(5), 821-832. <https://doi.org/https://doi.org/10.1021/acssuschemeng.5b00144>
- Li, M., Zhang, H., Wu, Z., Zhu, Z., & Jia, X. (2022). DPD simulation on the transformation and stability of O/W and W/O microemulsions. *Molecules*, *27*(4), Article 1361. <https://doi.org/10.3390/molecules27041361>
- Li, Q., Dang, L., Li, S., Liu, X., Guo, Y., Lu, C., Kou, X., & Wang, Z. (2018). Preparation of  $\alpha$ -linolenic-acid-loaded water-in-oil-in-water microemulsion and its potential as a fluorescent delivery carrier with a free label. *Journal of Agricultural and Food Chemistry*, *66*(49), 13020-13030. <https://doi.org/10.1021/acs.jafc.8b04678>
- Li, Z., Wu, W., Jiang, W., Zhang, L., Li, Y., Tan, Y., Chen, S., Lv, M., Luo, F., Luo, T., & Wei, G. (2020). Preparation and regeneration of a thermo-sensitive adsorbent material: Methyl cellulose/calcium alginate beads (MC/CABs). *Polymer Bulletin*, *77*(4), 1707-1728. <https://doi.org/10.1007/s00289-019-02808-w>
- Lince, F., Marchisio, D. L., & Barresi, A. A. (2008). Strategies to control the particle size distribution of poly- $\epsilon$ -caprolactone nanoparticles for pharmaceutical applications. *Journal of Colloid and Interface Science*, *322*(2), 505-515. <https://doi.org/10.1016/j.jcis.2008.03.033>
- Liu, Y., Qiao, L., Wang, A., Li, Y., Zhao, L., & Du, K. (2021). Tentacle-type poly(hydroxamic acid)-modified macroporous cellulose beads: Synthesis, characterization, and application for heavy metal ions adsorption. *Journal of Chromatography A*, *1645*, Article 462098. <https://doi.org/10.1016/j.chroma.2021.462098>
- Luo, X., & Zhang, L. (2010). Creation of regenerated cellulose microspheres with diameter ranging from micron to millimeter for chromatography applications. *Journal of Chromatography A*, *1217*(38), 5922-5929. <https://doi.org/10.1016/j.chroma.2010.07.026>
- Machado, T. O., Grabow, J., Sayer, C., de Araújo, P. H. H., Ehrenhard, M. L., & Wurm, F. R. (2022). Biopolymer-based nanocarriers for sustained release of agrochemicals: A review on materials and social science perspectives for a sustainable future of agri- and horticulture. *Advances in Colloid and Interface Science*, *303*, Article 102645. <https://doi.org/10.1016/j.cis.2022.102645>
- Maity, D., Ding, J., & Xue, J. M. (2008). Synthesis of magnetite nanoparticles by thermal decomposition: Time, temperature, surfactant and solvent effects. *Functional Materials Letters*, *1*(3), 189-193. <https://doi.org/10.1142/S1793604708000381>
- Meng, R., Liu, L., Jin, Y., Luo, Z., Gao, H., & Yao, J. (2019). Recyclable carboxylated cellulose beads with tunable pore structure and size for highly efficient dye removal. *Cellulose*, *26*(17), 8963-8969. <https://doi.org/10.1007/s10570-019-02733-1>
- Michor, E. L., & Berg, J. C. (2015). Temperature effects on micelle formation and particle charging with span surfactants in apolar media. *Langmuir*, *31*(35), 9602-9607. <https://doi.org/10.1021/acs.langmuir.5b02711>
- Mohan, T., Ajdnik, U., Nagaraj, C., Lackner, F., Štiglic, A. D., Palani, T., Amornkitbamrung, L., Gradišnik, L., Maver, U., Kargl, R., & Kleinschek, K. S. (2022). One-step fabrication of hollow spherical cellulose

- beads: Application in pH-responsive therapeutic delivery. *ACS Applied Materials and Interfaces*, 14(3), 3726-3739. <https://doi.org/10.1021/acsami.1c19577>
- Pal, N., Agarwal, M., & Gupta, R. (2022). Green synthesis of guar gum/Ag nanoparticles and their role in peel-off gel for enhanced antibacterial efficiency and optimization using RSM. *International Journal of Biological Macromolecules*, 221, 665-678. <https://doi.org/10.1016/j.ijbiomac.2022.09.036>
- Pang, S. C., Chin, S. F., & Yih, V. (2011). Conversion of cellulosic waste materials into nanostructured ceramics and nanocomposites. *Advanced Materials Letters*, 2(2), 118-124. <https://doi.org/10.5185/amlett.2011.1203>
- Pang, S. C., Voon, L. K., & Chin, S. F. (2018). Controlled depolymerization of cellulose fibres isolated from lignocellulosic biomass wastes. *International Journal of Polymer Science*, 2018, 1-11. <https://doi.org/10.1155/2018/6872893>
- Ren, S., Sun, X., Lei, T., & Wu, Q. (2014). The effect of chemical and high-pressure homogenization treatment conditions on the morphology of cellulose nanoparticles. *Journal of Nanomaterials*, 2014, 168-168. <https://doi.org/10.1155/2014/582913>
- Roque, L., Fernández, M., Benito, J. M., & Escudero, I. (2020). Stability and characterization studies of Span 80 niosomes modified with CTAB in the presence of NaCl. *Colloids and Surfaces A: Physicochemical and Engineering Aspects*, 601, Article 124999. <https://doi.org/10.1016/j.colsurfa.2020.124999>
- Russell-Jones, G., & Himes, R. (2011). Water-in-oil microemulsions for effective transdermal delivery of proteins. *Expert Opinion on Drug Delivery*, 8(4), 537-546. <https://doi.org/10.1517/17425247.2011.559458>
- Saleh, T. A. (2021). Protocols for synthesis of nanomaterials, polymers, and green materials as adsorbents for water treatment technologies. *Environmental Technology and Innovation*, 24, Article 101821. <https://doi.org/10.1016/j.eti.2021.101821>
- Schroeter, B., Yonkova, V. P., Niemeyer, N. A. M., Jung, I., Preibisch, I., Gurikov, P., & Smirnova, I. (2021). Cellulose aerogel particles: Control of particle and textural properties in jet cutting process. *Cellulose*, 28(1), 223-239. <https://doi.org/10.1007/s10570-020-03555-2>
- Sebeia, N., Jabli, M., Ghanmi, H., Ghith, A., & Saleh, T. A. (2021). Effective dyeing of cotton fibers using cynomorium coccineum L. peel extracts: Study of the influential factors using surface response methodology. *Journal of Natural Fibers*, 18(1), 21-33. <https://doi.org/10.1080/15440478.2019.1612302>
- Shahnaz, T., Sharma, V., Subbiah, S., & Narayanasamy, S. (2020). Multivariate optimisation of Cr(VI), Co(III) and Cu(II) adsorption onto nanobentonite incorporated nanocellulose/chitosan aerogel using response surface methodology. *Journal of Water Process Engineering*, 36, Article 101283. <https://doi.org/10.1016/j.jwpe.2020.101283>
- Shi, F., Lin, D. Q., Phottraithip, W., & Yao, S. J. (2011). Preparation of cellulose-tungsten carbide composite beads with ionic liquid for expanded bed application. *Journal of Applied Polymer Science*, 119(6), 3453-3461. <https://doi.org/10.1002/app.33005>
- Shi, W., Ching, Y. C., & Chuah, C. H. (2021). Preparation of aerogel beads and microspheres based on chitosan and cellulose for drug delivery: A review. *International Journal of Biological Macromolecules*, 170, 751-767. <https://doi.org/10.1016/j.ijbiomac.2020.12.214>

- Song, M., Liu, W., Wang, Q., Wang, J., & Chai, J. (2020). A surfactant-free microemulsion containing diethyl malonate, ethanol, and water: Microstructure, micropolarity and solubilizations. *Journal of Industrial and Engineering Chemistry*, 83, 81-89. <https://doi.org/10.1016/j.jiec.2019.11.016>
- Tay, S. H., Pang, S. C., & Chin, S. F. (2012). A facile approach for controlled synthesis of hydrophilic starch-based nanoparticles from native sago starch. *Starch/Staerke*, 64(12), 984-990. <https://doi.org/10.1002/star.201200056>
- Tong, K., Zhao, C., Sun, Z., & Sun, D. (2015). Formation of concentrated nanoemulsion by W/O microemulsion dilution method: Biodiesel, tween 80, and water system. *ACS Sustainable Chemistry & Engineering*, 3(12), 3299-3306. <https://doi.org/10.1021/acssuschemeng.5b00903>
- Trygg, J., Fardim, P., Gericke, M., Mäkilä, E., & Salonen, J. (2013). Physicochemical design of the morphology and ultrastructure of cellulose beads. *Carbohydrate Polymers*, 93(1), 291-299. <https://doi.org/10.1016/j.carbpol.2012.03.085>
- Voon, L. K., Pang, S. C., & Chin, S. F. (2015). Highly porous cellulose beads of controllable sizes derived from regenerated cellulose of printed paper wastes. *Materials Letters*, 164, 264-266. <https://doi.org/10.1016/j.matlet.2015.10.161>
- Voon, L. K., Pang, S. C., & Chin, S. F. (2016). Regeneration of cello-oligomers via selective depolymerization of cellulose fibers derived from printed paper wastes. *Carbohydrate Polymers*, 142, 31-37. <https://doi.org/10.1016/j.carbpol.2016.01.027>
- Voon, L. K., Pang, S. C., & Chin, S. F. (2017a). Optimizing delivery characteristics of curcumin as a model drug via tailoring mean diameter ranges of cellulose beads. *International Journal of Polymer Science*, 2017, Article 2581767. <https://doi.org/10.1155/2017/2581767>
- Voon, L. K., Pang, S. C., & Chin, S. F. (2017b). Porous cellulose beads fabricated from regenerated cellulose as potential drug delivery carriers. *Journal of Chemistry*, 2017, Article 1943432. <https://doi.org/10.1155/2017/1943432>
- Wang, G., Yang, X., & Wang, W. (2019). Reinforcing linear low-density polyethylene with surfactant-treated microfibrillated cellulose. *Polymers*, 11(3), Article 441. <https://doi.org/10.3390/polym11030441>
- Winuprasith, T., & Suphantharika, M. (2015). Properties and stability of oil-in-water emulsions stabilized by microfibrillated cellulose from mangosteen rind. *Food Hydrocolloids*, 43, 690-699. <https://doi.org/10.1016/j.foodhyd.2014.07.027>
- Wu, R., & Hu, C. (2021). Fabrication of magnetic cellulose microspheres by response surface methodology and adsorption study for Cu(II). *Cellulose*, 28(3), 1499-1511. <https://doi.org/10.1007/s10570-020-03640-6>
- Xu, F., & Cho, B. U. (2022). Preparation of porous regenerated cellulose microstructures via emulsion-coagulation technique. *Cellulose*, 29(3), 1527-1542. <https://doi.org/10.1007/s10570-022-04428-6>
- Yan, X., Bernard, J., & Ganachaud, F. (2021). Nanoprecipitation as a simple and straightforward process to create complex polymeric colloidal morphologies. *Advances in Colloid and Interface Science*, 294, Article 102474. <https://doi.org/10.1016/j.cis.2021.102474>



*Review Article*

## **A Review on Analysis Method of Proximal Hyperspectral Imaging for Studying Plant Traits**

**Jian Wen Lin, Mohd Shahrime Mohd Asaari\*, Haidi Ibrahim, Mohamad Khairi Ishak dan Abdul Sattar Din**

*School of Electrical and Electronic Engineering, Universiti Sains Malaysia, 14300 USM, Pulau Pinang, Malaysia*

### **ABSTRACT**

Understanding the response of plant traits towards different growing conditions is crucial to maximizing crop yield and mitigating the effect of the food crisis. At present, many imaging techniques are being explored and utilized within plant science to solve problems in agriculture. One of the most advanced imaging methods is hyperspectral imaging (HSI), as it carries the spectral and spatial information of a subject. However, in most plant studies that utilized HSI, the focus was given to performing an analysis of spectral information. Even though a satisfactory performance was achieved, there is potential for better performance if spatial information is given more consideration. This review paper (1) discusses the potential of the proximal HSI analysis methods for plant traits studies, (2) presents an overview of the acceptance of hyperspectral imaging technology for plant research, (3) presents the basic workflow of hyperspectral imaging in proximal settings concerning the image acquisition settings, image pre-processing, spectral normalization, and spectral analysis, (4) discusses the analysis methods that utilize spatial information, and (5) addresses some technical challenges related to implementing hyperspectral imaging in proximal settings for plant traits analysis.

#### **ARTICLE INFO**

*Article history:*

Received: 21 October 2022

Accepted: 06 March 2023

Published: 03 October 2023

DOI: <https://doi.org/10.47836/pjst.31.6.11>

*E-mail addresses:*

[jianwenapp1996@gmail.com](mailto:jianwenapp1996@gmail.com) (Lin Jian Wen)

[mohdshahrime@usm.my](mailto:mohdshahrime@usm.my) (Mohd Shahrime Mohd Asaari)

[haidi@usm.my](mailto:haidi@usm.my) (Haidi Ibrahim)

[khairiishak@usm.my](mailto:khairiishak@usm.my) (Mohamad Khairi Ishak)

[sattar@usm.my](mailto:sattar@usm.my) (Abdul Sattar Din)

\* Corresponding author

*Keywords:* Deep learning, hyperspectral imaging, machine learning, spatial information, spectral information

### **INTRODUCTION**

Food crisis arises from extreme climates, such as droughts and heat waves, that might cause the crops to yield, unable to meet the supply-demand for human consumption in

the future. The current trends of agriculture yield that increased by 1.6%, 1.0%, 0.9%, and 1.3% each year for maize, rice, wheat, and soybean, respectively, were still insufficient to meet the demand of the projected population by 2050 (Ray et al., 2013). A recent study reported that for each degree-Celsius increase in global mean temperature, crops like wheat, maize, rice, and soybean would decrease at a single-digit percentage rate (Zhao et al., 2017). Therefore, to boost the global crop yield, one of the solutions is to breed more sustainable crops that can survive through extreme biotic and abiotic stresses.

The understanding of the plant's response to different biotic and abiotic stresses is known as plant phenotyping. Plant phenotyping is particularly important to support the decision-making in breeding higher-quality crops (Li et al., 2014). For instance, Sims and Gamon (2002) used measurement of the Xanthophyll-cycle pigment content, which is associated with spectral reflectance in the visible green region (500 nm–570 nm) in plants to estimate photosynthesis efficiency and, thus, could accelerate research of plant resistance towards stress. The discovery of such plant traits towards stress might take years due to the limitation of imaging sensors. Examples of traditional imaging sensors used to obtain plant traits were Red-Green-Blue (RGB), fluorescence, thermal, and multispectral cameras. Comparing these traditional imaging sensors with the promising hyperspectral (HS) camera, the latter captures more information in a single image. As technology advances, HS cameras become more accessible for research imaging purposes, leading to increased studies conducted using HS cameras.

HS camera has been widely used in plant phenotyping due to its capability to capture a wide range of spectral reflectance from samples. Technically, the spectral information acquired by several types of HS cameras ranges from visible light (VIS) to shortwave-infrared (SWIR), which is a wavelength from 400 nm to 2500 nm (Salazar-vazquez & Mendez-vazquez, 2020). As a comparison with the conventional RGB camera, the HS camera provided more information for plant phenotyping as many plant traits and chemical interactions that happened in plants corresponded to electromagnetic waves within the spectrum range of near-infrared (NIR) and SWIR (Nguyen & Lee, 2006; Sims & Gamon, 2003). In most common approaches, many vegetation indices (VI) derived within the NIR-SWIR wavelength region, like normalized difference vegetation index (NDVI), red edge normalized ratio (NR red edge), water index (WI), and moisture stress index (MSI) were used to determine different biophysical conditions of plants (Zhang & Zhou, 2019). Besides, the absorption valley of electromagnetic waves was also used to estimate the water content of corn leaves located between 900 nm and 1700 nm (Sun et al., 2021).

A multispectral camera is another imaging device that works similarly to the HS camera. However, the HS camera was more favored as the HS images carried more detailed information than multispectral images. The spectral signature of HS images can be considered a continuous spectrum as the interval between captured spectral bands was small.

However, this technical feature was less prominent for the multispectral images because the spectral bands were captured far from each other. Therefore, the spectral signature was considered discrete for the multispectral image. The greater spectral dimensionality of HS images allowed a more in-depth examination and discrimination of the plant's responses. The abundant amount of information carried by HS images attracted the attention of researchers and has led to an increase in technical papers discussing hyperspectral imaging (HSI) analysis in the agriculture field compared to past decades (Lu et al., 2020).

Since HSI emerged as a promising method for plant phenotyping, the imaging methods can be categorized into remote sensing and proximal imaging, as Goetz (2009) demonstrated. Remote sensing refers to capturing a large area of objects within a single image. For example, the common Indiana Pines and University of Pavia datasets were obtained from the HSI satellite and, thus, considered remote sensing. Besides, remote sensing includes unmanned aerial vehicles (UAV) and aircraft, which allows a large area of targets to be captured simultaneously. In contrast to remote sensing, proximal imaging denotes the distance of 1 meter between sensors and plants (Mishra, Lohumi et al., 2020). Proximal HSI is usually carried out indoors in a laboratory or greenhouse area. The time taken for proximal HSI is longer for the whole group of samples as the sample image is usually taken one at a time. However, with the development of a high-throughput phenotyping platform (HTPP), the proximal HSI can be performed efficiently and with minimal human intervention.

Mainly, the information carried by HS images can be categorized into two, which are spectral and spatial information (Saha & Manickavasagan, 2021; Zhang & Zhou, 2019). The common downsides of processing HS images are high computational cost and long processing duration. Therefore, numerous studies were carried out to determine the most efficient algorithm for the HS image. However, most studies only utilized the spectral information from HS images for the proximal analysis of plants. It might have wasted a large amount of spatial information, which could play a significant role in studying plant traits.

This paper aims to provide insights into HSI workflow and how spatial information is utilized throughout the proximal HSI analysis.

## **WORKFLOW OF PROXIMAL HYPERSPECTRAL IMAGING**

The spectral and spatial information obtained from HS images can be redundant and frequently accompanied by noises. Therefore, several algorithms were developed for effective information extraction in different use cases, like detecting plant traits when experiencing water stress, disease, or lacking certain nutrients. Even though the set-up of imaging stations and algorithms might differ in these studies, the general technical workflow of proximal HSI analysis of plants was similar. The workflow can be categorized into image acquisition, image pre-processing, and spectral modeling. Illumination correction belongs

to the pre-processing stage. However, as the illumination effect is a major concern in HSI analysis, it will be discussed in more detail later. Figure 1 shows the flowchart of the general workflow of HSI analysis for better illustration.

### Image Acquisition

The acquisition of HS images was challenging as multiple factors needed to be considered before setting up the imaging station to ensure that the obtained HS images had less noise and an efficient acquisition process. Types of HS cameras, illumination sources, and acquisition geometry arrangement were among the factors.

In general, the HS cameras used to capture plant images can be performed in three separate ways, such as whiskbroom, pushbroom, and tunable filter, as shown in Figure 2, in which each method has its advantages and disadvantages (Elmasry et al., 2012). For the whiskbroom method, firstly, a grid of spatial position was predefined on the sample surface. Then, the camera scanned the spectrum of a single point at a time. The advantage of the whiskbroom method was that the illuminations for every point passed through the optical system similarly. However, the whiskbroom method caused spatial distortion in HS images, and the time taken for a complete scan was much longer than other methods (Stuart et al., 2019). The pushbroom method utilized a two-dimensional dispersing element and detector array to obtain the sample's HS image (line by line). Due to their speed and versatility, the pushbroom HS cameras were commonly installed in conveyor-belt systems like HTPP for effective sample image acquisition (Manley et al., 2009). Lastly, the tunable filter HS camera acquired the samples images by capturing the spectrum of all points according to their wavelength by using liquid crystal tunable filters (LCTF) or acousto-optic tunable filters (AOTF) (Gupta et al., 1999; X. Wang et al., 2018). No movement of either the camera or the sample was allowed throughout the process. The acquisition duration of the tunable filter method depended on the number of spectral bands concerned. Therefore, using the tunable filter method was most practical only when the interested spectral bands were less.

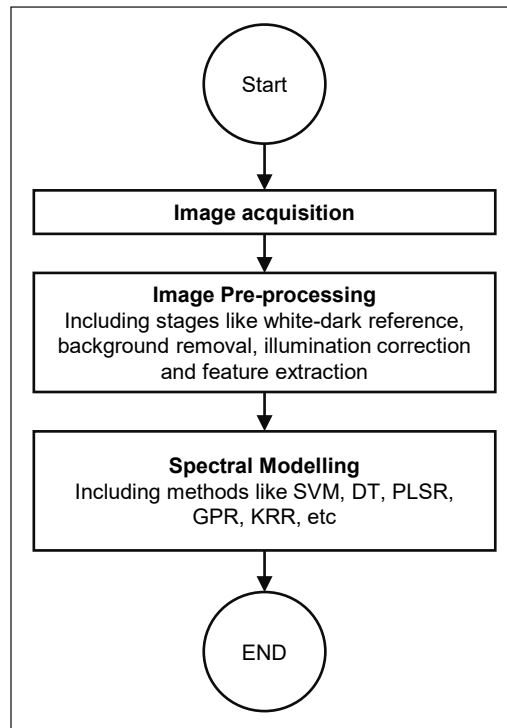


Figure 1. Flowchart for the general workflow of proximal HSI analysis

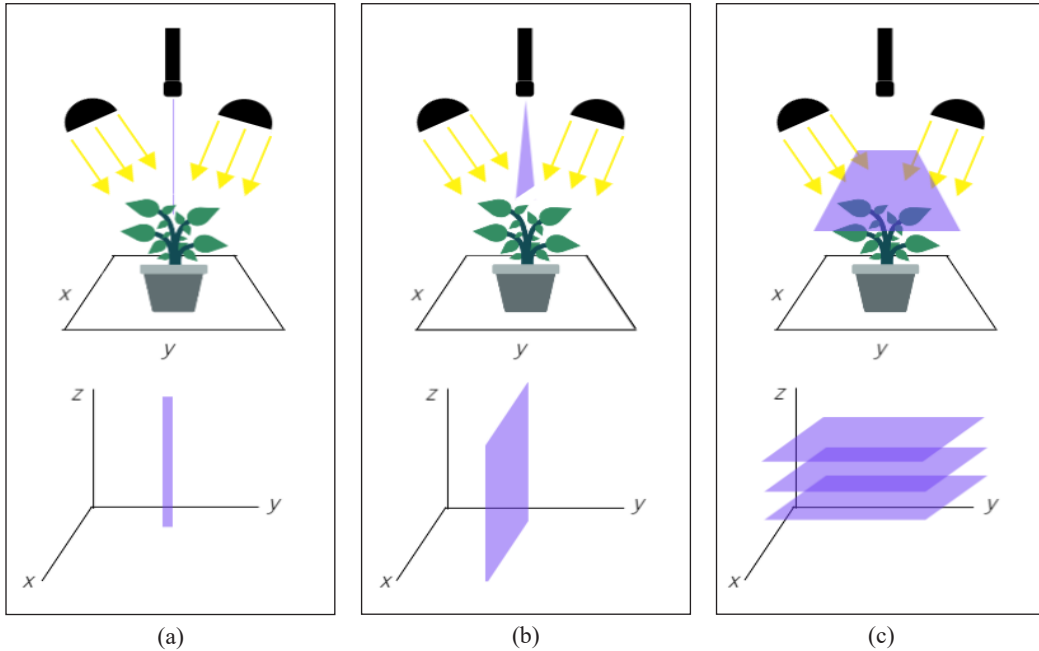


Figure 2. Illustration of: (a) whiskbroom; (b) pushbroom; and (c) tunable imaging method

Another important consideration during image acquisition was the illumination sources. The illumination sources can be categorized into two: passive and active light sources (Grönwall et al., 2016). A passive light source is a natural light, usually used when the image acquisition station is outdoors or in a greenhouse. In some passive light source use cases, special glass was used to filter the sunlight spectrum so that only interested bands were used for analysis. Meanwhile, the active light sources consist of man-made devices, such as tungsten halogen lamps, gas discharge tubes, xenon lamps, and the ubiquitous light-emitting diode (LED) lamps. When choosing an active light source, the set-up convenience, cost, and interest bandwidths need to be considered. Figure 3 shows the set-up of different illumination source directions. In plant phenotyping, halogen lamps were used as their illumination, which ranged from 400 nm–to 2600 nm, which allowed the HS image to be captured (Paulus & Mahlein, 2020). Table 1 lists the image acquisition criteria of studies relevant to proximal HS crop analysis.

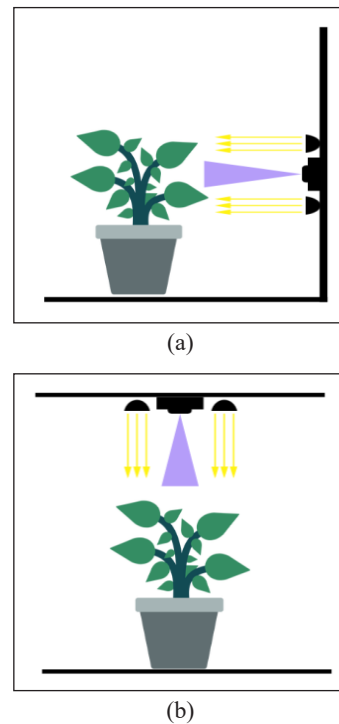


Figure 3. Illustration of image acquisition: (a) Side; and (b) top

## Image Pre-processing

The first HS image obtained by the camera was considered raw data that contained noises and pixels that were not parts of the sample. At this stage, these raw signals were heavily affected by spectral non-uniformities and could not be used directly for quantitative analysis. Therefore, pre-processing steps were required to extract clean and useful data for an accurate analysis. The remaining part will discuss the common steps used to obtain useful data from the HS image of a plant.

Once the HS image was captured, a radiometric calibration of the camera needed to be performed to reduce the effect of uneven illumination. The original reflectance value of each band will be converted to a relative reflectance value by using Equation 1.

$$R = \frac{I-B}{W-B} \quad (1)$$

Where  $R$  represents the calibrated HS image,  $I$  is the raw HS image,  $B$  is the image obtained when the HS camera shutter was completely covered (black reference), and  $W$  is the HS image of a high-reflective whiteboard (white reference). After this step, the relative reflectance value ranged from 0 to 1, and thus, the effect of outliers due to uneven illumination was reduced.

Depending on the position and the distance of the HS camera with the targeted plants, the captured HS image may contain background objects that were not part of the plants, such as soil, pot, and the imaging platform. It was important to focus only on the plant pixels for further analysis. Image segmentation techniques were applied to suppress the background pixels. In studying plant traits' response to drought, Behmann et al. (2016) applied k-mean clustering to segment HS images into plant and background clusters. Plant clusters were defined using a normalized difference vegetation index (NDVI) with a threshold of 0.3 and a near-infra-red (745 nm) threshold of 0.3 for the cluster centroid. For the NDVI calculation, reflectance values of bands 670 nm and 800 nm, within the red visible and near infra-red (NIR) range, respectively, were used in the calculation using Equation 2.

$$NDVI = \frac{R_{800} - R_{670}}{R_{800} + R_{670}} \quad (2)$$

The values calculated after Equation 2 ranged from -1 to +1. The NDVI value must be at least 0.2 or above, in which a higher value represents denser vegetation to ensure that a pixel belongs to a plant. The NDVI value, near 0, usually indicates objects like rock, sand, or snow, while a negative NDVI value indicates water.

## Illumination Correction

**Spectral Averaging.** Spectral averaging is a straightforward illumination correction method (Pandey et al., 2017). It is implemented by averaging the spectral signature of

all pixels that belong to a plant in an HS image. The average spectrum lost all the spatial information, which could be useful for further analysis. Besides, spectral averaging assumes that noise to the spectra will be minimized by mixing normal and noisy spectra. Despite requiring a low computational cost, spectral averaging is not recommended for reducing noise-like illumination effects. The accuracy of spectral averaging is highly dependent on the segmentation step. If the pixels used for averaging are contaminated by pixels not part of the sample, the resulting spectrum will not be able to represent the plant accurately.

**Spectral Smoothing.** Spectral smoothing is a spectral correction method that mitigates the effect of spiky noise in the spectrum caused by the illumination effect. The variations of spectral smoothing are like moving average, first derivatives, second derivatives, and Savitsky-Golay (SG) polynomials filter (Fletcher & Turley, 2017). A smoothed spectrum has a higher Signal-to-Noise Ratio (SNR) as the noise carried by spiky bands is shared among the adjacent reflectance values. The computational power of spectral smoothing can be a few times higher depending on the derivative function used. Besides, the number of bands in the smoothed spectrum will be lesser than in the original spectrum.

**Standard Normal Variate.** The standard normal variate (SNV) normalization improves spectral averaging by retaining the spatial information of HS images. SNV normalization is inspired by chemometrics domains, whereby the formula models light scattering when light is reflected from the sample surface (Asaari et al., 2018; Vigneau et al., 2011). Firstly, the leaf surface was assumed to be a Lambertian surface where the reflectance intensity was similar in all directions. Therefore, the factor that greatly affected the reflectance received by the camera would be the leaf inclination. Coupled Lambert's cosine law with inverse square law (Brownson, 2014). The following Equation 3 describes the SNV normalization computation:

$$Z = \frac{X - X_{mean}}{X_{std}} \quad (3)$$

Where  $X$  is the original processed reflectance value across all bands for one pixel.  $X_{mean}$  and  $X_{std}$  are the mean and standard deviation of  $X$  for all sample pixels, and  $Z$  is the normalized spectra. Note that SNV normalization is performed on the individual spectrum. Thus, no averaging of the spectrum is required.

**Multiple Scattering Correction (MSC).** The Multiple Scattering Correction (MSC) normalization is very similar to SNV normalization as both normalization methods were inspired by chemometrics. The only difference between SNV and MSC is that MSC normalization requires a reference spectrum. Most studies used the average spectrum as a reference spectrum as it is deemed free from noise. However, as mentioned above,

the average spectrum is very sensitive to outliers, which are non-sample spectra. Such characteristic causes MSC normalization to be more susceptible to noise. Even so, MSC normalization is still a popular correction method and has been applied in many HS studies due to its longer history compared to SNV normalization. For instance, Ren et al. (2020) employed it to correct the HS spectrum of black tea samples.

**Variable Sorting Normalization.** Variable sorting normalization (VSN) is a recent development for spectral correction by Mishra, Polder et al. (2020) and was used together with illumination correction methods, such as SNV, MSC, and Detrend. For example, when coupled with SNV, VSN estimated the weight for each wavelength in the computation of weight and standard deviation of the HS image. In another work, Fischler and Bolles (1987) performed estimation via a random sample consensus (RANSAC) algorithm, which calculated the dependency of each wavelength towards size effects (addition and multiplication offsets). With VSN, the illumination correction methods can model the illumination scattering with the least influence of chemical variables.

## Spectral Processing

**Band Selection and Feature Extraction.** Dense sampling due to small band intervals caused another redundancy of information. Not all values were useful for HS analysis, and retaining such data would impose a higher computational cost for the analytic process. Therefore, band selection and feature extraction were two important approaches to remove data that was insignificant to the analysis result.

In-band selection, the number of spectral bands was reduced by selecting a subset of the most discriminating features, which minimized the reconstruction error rate. The common techniques for performing band selection are analysis of variance Fisher (ANOVA F-test), random forest (RF), and sequential forward selection (SFS). The intensity values were grouped according to spectral bands in the ANOVA F-test. Each spectral band group consists of several values equivalent to the number of pixels of an image. Then, the same waveband group of images from different treatment groups was compared using ANOVA. Spectral bands with an F1 score lower than the preset threshold were considered a less significant spectral band and were removed. The ANOVA F-test had successfully been used as one of the pre-processing steps in identifying rice of different genotypes. Sabzi et al. (2021) detected excess nitrogen consumption in cucumbers (Wang et al., 2010). RF was used by Dinç and Aygün (2013), whereby a feature in a supervised self-training classifier formed each classification tree. Each classification tree had its voting result and was combined to form the final voting result. The classification result with the largest number of votes determined the final feature category. Even though RF was a promising classifier, it required a large amount of sampling data and features to prevent overfitting. The trained



RF was used on unlabeled inputs to apply RF as band selection. Certain features were selected, and all their values were shuffled for all the unlabeled inputs before the mean squared error (MSE) was computed. A large MSE indicated an important feature. In the case of SFS, classification was first performed separately for each feature. The feature which had the highest predictive accuracy was added to a subset. Several works have shown the feasibility of SFS in reducing the high-dimensional HS data prior to classification (Bradley et al., 2018).

In feature extraction, a new set of features was created by transforming the data into a new feature space. A common feature extraction technique used on HS data was based on a linear combination of image bands, such as in principle component analysis (PCA) and minimum noise fraction (MNF). As mentioned previously, the HS image consists of more than hundreds of bands, and this information can be redundant. Rodarmel and Shan (2002) stated that PCA works on the assumption that all neighboring bands of the HS vector highly correspond to each other. Therefore, PCA aimed to minimize the correlation between bands and obtain an optimum linear band combination that retained most information in the original data. The dataset obtained from PCA was known as principal components and was arranged by the amount of original information retained descending. In most situations, only the first few principal components would be used for further analysis. Figure 4 illustrates the PCA applied in data with 2 bands, also known as dimensions. In Figure 4, each data contained a value of Band 1 and Band 2, which can be represented as in Equation 4.

$$m_i = (x_{f1}, x_{f2}) \quad (4)$$

Highly correlated data can be represented in a lesser number of bands. Figure 4 shows PCA Band 1, which retained most of the variations of the original data with just a single band. Any further classification processes applied in PCA Band 1 would obtain a similar result as applied in the original data, which consists of Band 1 and Band 2. A more comprehensive mathematical derivation and historical review of PCA can be referred to in a study by Gonzalez and Woods (1993).

Meanwhile, MNF is a 2-step linear transform denoising technique for HS images. The first step is known as ‘noise-whitening,’ using principal components of the noise covariance matrix to decorrelate and rescale the noise in data. After the first

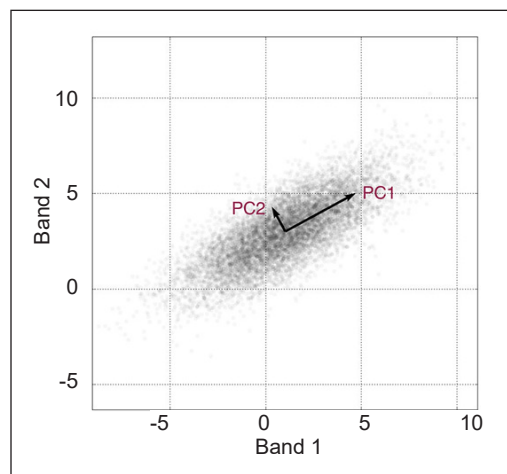


Figure 4. Illustration of PCA

step, the resulting data would have noise with unit variance and minimum correlation between bands. The second step was conducted by applying PCA to the noise-whitened data. A previous study showed that MNF achieved a higher signal-to-noise Ratio (SNR) as compared to PCA for signal-dependent noise (Luo et al., 2016). However, the PCA result had higher SNR than MNF when dealing with Gaussian white noise. The mathematical steps of MNF were explained in detail in a study by Nielsen (2011).

**Spectral Modelling.** Pre-processing data will be fed into machine learning models for either classification or regression approaches. Table 2 shows the spectral modeling methods, illumination correction, and feature extraction implemented in proximal HSI analysis. The classification approach aims to locate inputs into the correct class, respectively, while the regression approach predicts the output quantity for a given input value. Some of the most common classifiers, such as support vector machine (SVM) and decision tree (DT), whereas models like partial least square regression (PLSR), Gaussian process regression (GPR), and kernel ridge regression (KRR) were considered as regression approaches.

**Support Vector Machine (SVM).** SVM classified data into two groups by forming a hyperplane within the high-dimensional data with the largest support vector margin. The hyperplane could be in different shapes by using SVM with kernel functions, such as polynomial, linear, and radial basis functions. Figure 5 shows an illustration of a linear SVM methodology. Data were classified into circle and triangle groups by a decision hyperplane between two support vectors.

Moughal (2013) used SVM together with minimum noise fraction (MNF) to analyze HS data, and the overall accuracy was the highest among maximum likelihood (ML) and spectral angle mapper (SAM) classifiers. In a recent study, Guo et al. (2019) showed that HS data was first reduced using PCA, and the first three PCs were fed into a guided filter in Equation 5 as a noise reduction and image dehazing step.

$$q_i = \alpha_k g_i + b_k \forall i \in \omega_k \quad (5)$$

Where  $q$  is the linear transform of  $g$  in a window  $\omega_k$  centered at pixel  $k$ .  $\alpha_k$  and  $b_k$  are linear coefficients and bias. After the image was filtered, SVM was adopted to classify the image pixel by pixel.

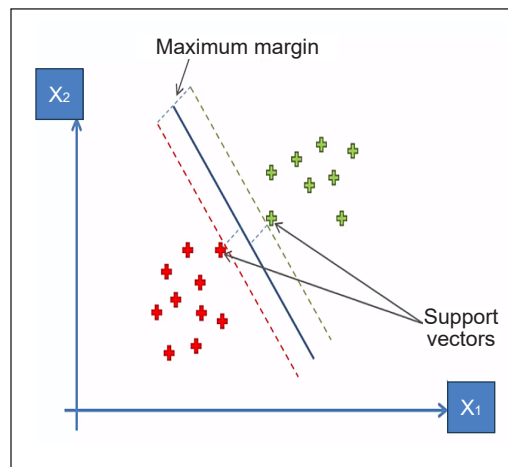


Figure 5. Illustration of SVM

**Decision Tree (DT).** As a comparison with other classifiers, DT was less computationally intensive and provided good readability. It adopted the top-down recursive strategy in which each leaf node denoted the classified class of a feature. The branch with the least conflict with the training data set decided on the input class. The correct classification rate (CCR) using Equation 6 to predict the performance of a DT model.

$$CCR = \frac{N_c}{N_t} \times 100\% \quad (6)$$

Where  $N_c$  is the number of correctly classified samples, while  $N_t$  is the total number of samples. Even though DT can be easily applied, it has a serious overfitting problem. In many cases, DT performed well with training datasets but the opposite in real datasets due to outliers.

**Random Forest (RF).** RF classification was an elaborate method of DT as it is built on multiple DTs. The initial step to build an RF classifier was to perform bootstrapping. A subset of dimensions from each bootstrapped dataset will be used to compute a DT. The final output of an RF was determined by aggregating the outputs of all DTs. Data that was not involved in bootstrapping, known as an out-of-bag dataset, will be used to validate the performance of an RF classifier. By using multiple DTs, the sensitivity towards outliers was reduced and thus provided better performance.

**Partial Least Square Regression (PLSR).** The working principle of PLSR was to reduce many measured collinear spectral variables to a small amount of non-correlated latent variables or factors (Darvishzadeh et al., 2008). As a comparison with spectra, the latent variables were assumed to be the relevant information in the measured spectra and were used to calculate dependent variables, such as biophysical and biochemical characteristics. The final aim of PLSR was to build a linear model, as shown in Equation 7, used to classify data into two groups.

$$Y = X\beta + \varepsilon \quad (7)$$

Where  $Y$  is a mean-centered vector of the dependent variable,  $X$  is a mean-centered matrix of independent variables (spectral bands in the study using HS image),  $\beta$  is a matrix of regression coefficients, and  $\varepsilon$  is a matrix of residuals. PLSR was like principal component regression (PCR), given that Equation 9 was used on latent variables of  $X$ . The difference was the decomposition of PLSR performed on both the spectra and responses simultaneously (Schlerf et al., 2003). A detailed description of PLSR can be reviewed by Geladi and Kowalski (1986).

**Gaussian Process Regression (GPR).** A joint multivariate normal distribution distributed the output values after GPR was applied. The mean vector of the joint distribution was generally assumed as zero vectors, and the covariance matrix was obtained using a covariance function defined over a pair of input values. Several works have successfully applied the GP regression to predict the biochemical characteristics from HS data (Arefi et al., 2021; Gewali & Monteiro, 2016). The details of the mathematical derivation of GPR were provided (Gewali et al., 2019).

**Kernel Ridge Regression (KRR).** KRR extends a simple linear regression by substituting the covariance with a kernel function (Mateo-García et al., 2018). The advantage of adopting KRR was its simplicity, as the aim is to find a parameter value that minimizes the mean square error. Besides, KRR was normally used when the training data was less as the computational cost was expensive for computing KRR for large datasets. The response for input  $x$  is estimated using KRR, as shown in Equation 8.

$$\bar{f}(x) = \sum_{j=1}^n k(x_j, x)\alpha_j \tag{8}$$

Where given training data is  $(x_1, y_1), \dots, (x_n, y_n) \in \chi \times \gamma$ , where  $\chi \subseteq R^d$  is an input domain and  $\gamma \subseteq R^d$  is an output domain.  $\alpha = (\alpha_1 \dots \alpha_n)^T$  is the solution of Equation 9.

$$(\chi^T \chi + \lambda I_n)\alpha = \chi^T \gamma \tag{9}$$

Where  $\lambda$  is the regularization parameter  $> 0$ ,  $\chi^T \chi$  is the entries matrix, and  $\gamma$  is the vector responses. The KRR technique applied for the non-linear learning method for discrimination between healthy and stressed plants was demonstrated (Asaari et al., 2022).

**Spectral Angle Mapper (SAM) classifier.** The Spectral Angle Mapper (SAM) is a supervised classification that treats every spectrum as an  $n$ -th dimension vector in space. The angle between two spectra is computed using Equation 10 (Rashmi et al., 2014) to determine their similarity, where a smaller angle represents a higher similarity between two spectra.

$$\alpha = \cos^{-1} \left( \frac{\sum_{i=1}^{nb} t_i r_i}{\sqrt{\sum_{i=1}^{nb} t_i^2} \sqrt{\sum_{i=1}^{nb} r_i^2}} \right) \tag{10}$$

Where  $nb$  is the number of bands,  $t$  is the spectrum vector,  $r$  is the reference spectrum vector, and  $\alpha$  is the spectral angle. A distinct reference spectrum for each class is always required in HS analysis before SAM is applied.

Table 1  
 List of image acquisition criteria focuses on proximal HSI analysis on crop

Imaging Method	Imaging Condition	Camera Model Name	Spectrum Wavelength	Wavelength Interval	Light Source	Imaging Subject	Authors
Pushbroom	Indoor	ImSpector V10E	400–1000 nm	~ 3 nm	15W tungsten halogen light	Potato plants	Mishra, Polder et al., 2020
					Combination of 105W halogen lamp and 56W LED	Apple slices	Arefi et al., 2021
					Two 3x3 35W halogen lamps	Maize plants	Mohd Asaari et al., 2018
					150W halogen lamp	Wheat plants	Bauriegel et al., 2011
					Two lightlines for homogenous illumination	Sugar beet leaves	Leucker et al., 2016
					Two linear light emitters	Barley leaves	Kuska et al., 2015
					150W fiber halogen lamp	Cucumber downy mildew leaves	Tian & Zhang, 2012
					Not specified	Sugar beet leaves	Behmann et al., 2016
		ImSpector V10E + N25E	400–2500 nm	Not specified	Incandescent light and two 150W halogen lamps	Wheat plants	Moshou et al., 2014
		Specim V9 Spectrograph	460–900 nm	7 nm	Not specified	Potato plants leaves	Sun et al., 2018
		Gaia Hyperspectral Camera V10E	862.9–1704.2 nm	2.8 nm	Not specified	Maize kernels	Manley et al., 2009
		SisuCHEMA Imaging System	1000–2500 nm	6.5 nm	Not specified	Maize plants and soybean plants	Pandey et al., 2017
		Headwall Photonics Spectrometer	550–1700 nm	4.7 nm	Two 35W halogen lamps	Cucumber leaves	Sabzi et al., 2021
		FSR Hyperspectral Camera	400–1000 nm	Not specified	10W tungsten halogen lamp	Chinese congou black tea	Ren et al., 2020
		ImSpector N17E-OWL320	900–1700 nm	5 nm	Two 150W halogen lamps	Barley and corn plants	Romer et al., 2012
		Surface Optics Corp - 700	400–900 nm	4 nm	Six 400W halogen lamps		

Table 1 (continue)

Imaging Method	Imaging Condition	Camera Model Name	Spectrum Wavelength	Wavelength Interval	Light Source	Imaging Subject	Authors
	Outdoor	iXon Imaging Device HySpex VNIR 1600 - 160	450–920 nm 400–1000 nm	2.8 nm 3.7 nm	Two 150W halogen lamps Sunlight	Ruby red grapefruit Wheat plants, wheat leaves, and wheat field	Qin et al., 2009 Vigneau et al., 2011
<b>Snapshot</b>	Indoor	Specim IQ Sensor Hyperspectral Snapshot Mosaic Camera	397–1004 nm 470–1000 nm	3 nm 12 nm	Sunlight Four 50W halogen lamps	Vines Maize seeds	Nguyen et al., 2021 Gao et al., 2018
<b>Not specified</b>	Indoor	ASD Fieldspec FR Spectrometer	350–2500 nm	3nm and 10nm below and above 1000nm, respectively	100W halogen reflector Not specified Not specified 100W halogen lamp 50W halogen lamp Halogen lamp	Sugar beet leaves Corn leaves Rice crops Sugar beet leaves Rice crop leaves Leaf from different species	Mahelein et al., 2010 Sun et al., 2021 Wang et al., 2010 Rumpf et al., 2010 Liu et al., 2007 Sims & Gamon, 2002
	Outdoor	Unispec PP Systems FieldSpec UV/VNIR Spectroradiometer SVC HR-1024 Spectroradiometer ASD Fieldspec FR Spectrometer	350–1100 nm 350–1050 nm 350–1000 nm 350–2500 nm	3.5 nm 3 nm 3.5 nm 3nm and 10nm below and above 1000nm, respectively	Li-1800 integrating sphere Two 500W halogen lamps Sunlight	Avocado plant leaves Winter wheat leaves Maize plants Celery crop Palmar amaranth and cotton seeds Rice crop	Yuan et al., 2014; J. Zhang et al., 2012 Sankaran et al., 2012 Fu et al., 2014 Zhang & Zhou, 2019 Huang & Apan, 2006 Fletcher & Turley, 2017 Nguyen & Lee, 2006
		GER 1500 spectrometer	300–1100 nm	1.55 nm	Sunlight		

Table 2  
*List of illumination correction, feature extraction, and spectral modeling focus on proximal HSI analysis on crop*

<b>Illumination Correction</b>	<b>Feature Extraction</b>	<b>Spectral Modelling</b>	<b>Authors</b>
<b>Average</b>	Not specified	PLSR, PCR	<b>Liu et al., 2007</b>
	Not specified	PLSR	<b>Ge et al., 2016</b> <b>Pandey et al., 2017</b>
<b>SNV</b>	ANOVA	K-means, Computation of ED	<b>Asaari et al., 2018)</b>
	ANOVA	SVM + K-means	<b>Asaari et al., 2019</b>
	Not specified	PLSR	<b>Nguyen &amp; Lee, 2006</b> <b>Vigneau et al., 2011</b>
<b>MSC</b>	Not specified	ANN	<b>Sabzi et al., 2021</b>
	PCA	DT	<b>Ren et al., 2020</b>
<b>Spectral Smoothing</b>	Competitive Adaptive Reweighted Sampling (CARS)	PLSR	<b>Sun et al., 2021</b>
<b>Derivatives</b>	Not specified	PLSR	<b>Huang &amp; Apan, 2006</b> <b>Fu et al., 2014</b>
		Spectral Angle Mapper (SAM)	<b>Leucker et al., 2016</b>
		RF	<b>Fletcher &amp; Turley, 2017</b>
<b>MSC + SNV</b>	PCA	PLS-DA	<b>Manley et al., 2009</b>
<b>VSN + SNV</b>	Not specified	K-means clustering	<b>Mishra, Polder et al., 2020</b>
<b>MSC + Spectral Smoothing</b>	Neighborhood Component Analysis (NCA), PLSR	GPR, Bagging Decision Tree (BDT), Lasso Regression	<b>Arefi et al., 2021</b>
<b>Not specified</b>	PCA	SVM, RF	<b>Nguyen et al., 2021</b>
	PCA	RF, KNN	<b>Gao et al., 2018</b>
	CA, CARS	PLSR	<b>Sun et al., 2018</b>
	ANOVA	Computation of VIs	<b>Mahlein et al., 2010</b>
	Not specified	SVM, least square SVM, MLP	<b>Moshou et al., 2014</b>

## UTILIZATION OF SPATIAL INFORMATION

Each pixel of the HS image was formed by a spectral vector, which consists of multiple bands. Undeniably, many plant traits can be observed by utilizing spectral information alone. However, spatial information should not be overlooked to explore the potential of HS images fully. The spatial information can be from the HS image or obtained from other sensors, commonly the depth sensor. Table 3 summarizes the research works that utilized spatial images in proximal HS analysis.

### Foreground-Background Segmentation

The purpose of foreground-background segmentation in HS images was to remove the pixels not part of the sample under investigation. This approach was used to remove

unwanted background by calculating the NDVI value of each pixel (Asaari et al., 2018; Behmann et al., 2014; Pandey et al., 2017). This method might not be efficient if the background consists of an object that reflected illumination within the NIR or red range.

The background removal performed by using NDVI could be improved by analyzing spatial information to eliminate the remaining pixels that were not part of the sample plant. Williams et al. (2017) eroded the HS image using a 3×3 cross-shaped structural element to remove stray and mixed pixels at the leaf's edge after the NDVI segmentation step. The image erosion determined if a particular pixel belonged to the sample plant via its neighboring pixels. If most neighboring pixels were the plant's pixel, the target pixel would be set to the plant pixel and vice versa. Besides, a graph theory that required a low computational power was also implemented to segmentize the sample from a background that reflected a similar intensity of VNIR illumination as a sample.

Chen et al. (2019) explored object segmentation using the HS lidar sensor system. Nine different materials were aimed to be segmented via 3D point clouds obtained using the lidar sensor. The obtained 3D data were processed using connected-component labeling (CCL), a point cloud segmentation method that did not require a seed point. It was initially used in binary digital images by isolating components that did not overlap spatially, whereby points in each component had similar properties. The same theory could be applied when segmenting objects in a 3D point cloud and sample plant from its background, which had different spectral properties.

### **Noise Reduction and Morphological Profile**

Different kinds of noise can degrade the HS image quality. Huang et al. (2021) set input data within a certain range by comparing it with white and dark references to reduce the effect of noise. Kool et al. (2021) implemented morphological closing to remove noise before the classification. Morphological closing involved a dilation followed by erosion to remove gaps caused by noise. It allowed the noisy pixels to be corrected and used for consequent processing steps.

Morphological profile (MP) is obtained by opening and closing the original image. Small bright pixels could be eliminated by opening, while small dark pixels could be eliminated by closing. Different MPs could be obtained depending on the scale and structural element (SE) that came in different shapes like disk-shaped, linear-shaped, cross-shaped, and so on, depending on the shape that wishes to be removed. MPs were generated by exploring the spatial information of HS images (Liao et al., 2019; Villegas et al., 2017). The MPs were combined with the first few principal components (PCs) for further analysis. Both studies showed that the fusion of MPs and PCs performed better than just utilizing solely spectral information for analysis.



### **Point Clouds for HS 3D Model**

During image acquisition, the reflected illumination was not always towards the camera due to the inclined normal of the complex geometry of the plant. It caused an illumination effect as the reflected illumination might overlap before reaching the camera. In most studies utilizing only spectral data, the spectral information would be corrected with mathematical formulas, such as spectral averaging, standard normal variation (SNV), and variable sorting normalization (VSN), and were able to improve the analysis accuracy to a certain extent. However, modeling the scattering effect of illumination was dependent on the leaves' inclination angle and precise estimation of the inclination angle of every leaf, whereby using spectral information alone was nearly impossible.

One of the promising solutions for this issue was combining spatial and spectral information by using 3D point clouds of HS images. 3D point clouds were generated using different depth sensors and incorporated with HS information for analysis (Behmann et al., 2016; Huang et al., 2018; Villegas et al., 2017). The inclination angle of leaves could be computed with 3D models, reducing the illumination effect. The studies proved that the analysis accuracy was higher by fusing geometry information with the original HS information than by solely analyzing the spectral information. Even though incorporating 3D models provided better analysis results, it did not come without disadvantages. One of the concerns when using this method was the additional requirement of a depth sensor. Besides, acquiring accurate 3D point clouds required precise calibration and more time.

### **Deep Learning for HS Image Classification**

Deep learning utilized the spectral and spatial information of HS images and outperformed the conventional machine learning method in many situations. For instance, Yan et al. (2021) compared the convolutional neural network (CNN) with conventional machine learning methods like logistic regression (LR), standard vector machine (SVM), neural network (NN), and decision tree (DT) on 1D, 2D and 3D data extracted from HS images. The results showed that CNN had the highest accuracy when used on first derivative spectra and HS images to detect the existence of aphids in cotton. Whereas for RGB images (2D), CNN achieved the same accuracy as LR, which was also one of the highest of all five methods.

Deep learning usually refers to a deep neural network consisting of a recurrent neural network (RNN), CNN, and generative adversarial network (GAN). These methods were called 'deep' as data would be processed in many layers, each performing a different function. Amongst various deep neural networks, CNN is the most popular network for image and speech recognition due to its strength in extracting features from complex data. Even though CNN has shown great potential for complex data analysis, it is not completely free from limitations. One of the concerns when implementing CNN to study plant traits is the limited number of samples used for training (Paoletti et al., 2018).

Besides, the limited samples coupled with high data dimensionality also led to another problem, commonly referred to as the Hughes phenomenon, also known as the curse of dimensionality (Khodadadzadeh et al., 2014).

In recent studies, augmented data to tackle a limited number of samples (Z. Wang et al., 2018; Zhao et al., 2021). Techniques for data augmentation include flipping horizontally and vertically and randomly rotating the image quarterly. Besides, Nagasubramanian et al. (2019) cropped the original HS images spatially random into fixed smaller sample sizes to increase the number of training samples. The augmented data generated by these techniques would appear as different inputs to the neural network, as deep learning is a spectral-spatial-based analysis method. As shown in Figure 6, the conventional architecture of CNN can be classified into two parts: the feature learning layer and the classification layer. Feature learning layers consist of convolutional layers, pooling layers, batch normalization, and activation functions. On the other hand, the classification layer is formed by fully connected layers.

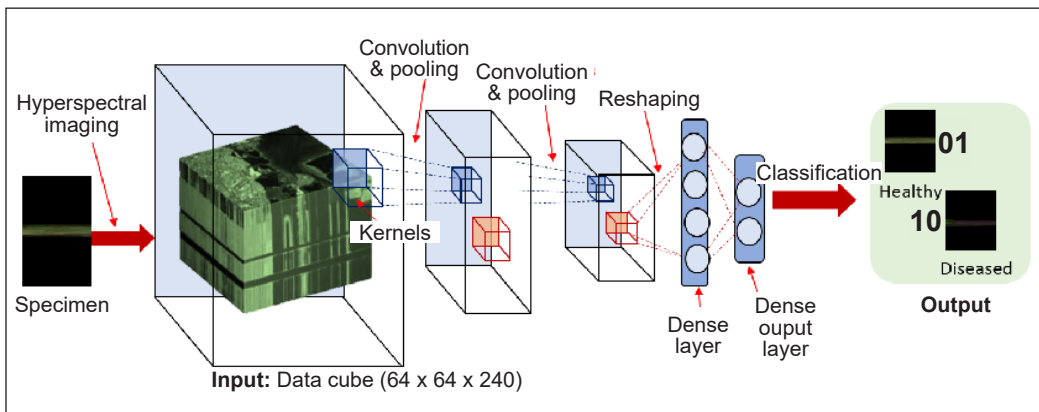


Figure 6. Conventional architecture of CNN of HSI

When pre-processing data is fed into CNN for training, it initially goes through the convolutional layer. If the data is an RGB image, a 2D convolutional kernel would be used to convolute the image so that features like edges, vertices, lines, and so on would be extracted. For the case of HS images, a 3D convolutional kernel would be used to extract spectral-spatial features. The work presented by Nagasubramanian et al. (2019) and Nguyen et al. (2021) used  $3 \times 3 \times 3$  used  $3 \times 3 \times 3$  and  $3 \times 3 \times 16$  pixels kernels, respectively, in all five methods and two convolutional layers. The size of the kernel could affect the model's accuracy. Larger kernels tend to capture high-resolution patterns with the downside of more parameters and computational power. However, the model performance was not proportional to kernel size. The accuracy of the model would drop when the kernel size exceeds a certain threshold. Tan and Le (2020) suggested mixing large and small kernels to capture high- and low-resolution patterns.

Each convolutional layer is normally followed by a batch normalization layer and a pooling layer (Nguyen et al., 2021; Yan et al., 2021, 2019). The purpose of batch normalization is to reduce internal shift, which is the change in network activation distributions due to network parameters change during training (Ioffe & Szegedy, 2015). By doing this, the issue of unstable gradient can be addressed, and the learning rate can be increased. The layer that ensues is the pooling layer, which helps prevent overfitting and reduce the complexity of the network, thus lowering the computational cost. Types of pooling layers are max pooling and average pooling. When the pooling layer is applied to 3D data, the height and width are reduced, but the depth remains unchanged.

Since the output value from every layer is not bounded, a large value might lead to computational issues for the model as the layer gets deeper. The activation function is applied to set the input within a certain range after every layer, normally after the pooling layer in CNN. Besides, the activation function adds non-linearity to a neural network. For example, Equation 11 shows layers of functions stacked within each other. This forms non-linearity, which allows the model to learn patterns from a complex dataset.  $f_n(x)$  can be any non-linear activation function like rectified linear unit (ReLU), Sigmoid, or SoftMax function, represented in Equations 12, 13, and 14, respectively. ReLU is commonly used at the current stage as it requires the least computational costs.

$$o(x) = f_n \left( f_{n-1} (\dots f_1(x)) \right) \tag{11}$$

$$f(x) = \max(0, x) \tag{12}$$

$$f(x) = \frac{1}{1+e^{-x}} \tag{13}$$

$$f(x_i) = \frac{e^{x_i}}{\sum_0^j x_j} \tag{14}$$

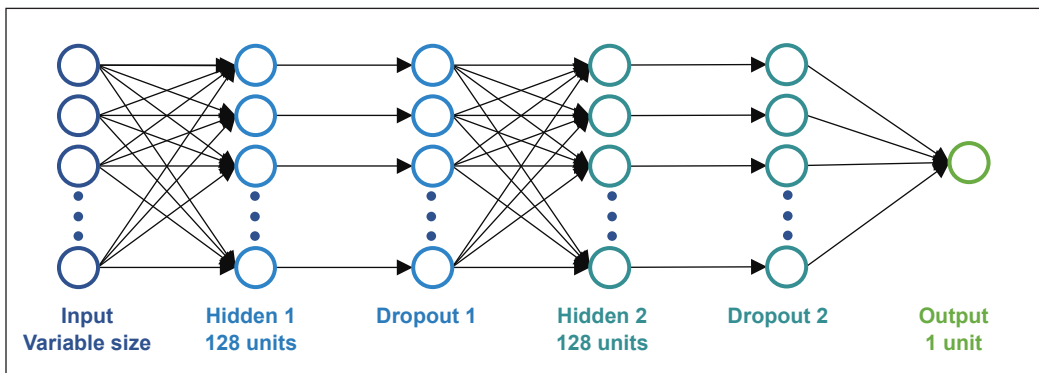


Figure 7. Conventional architecture of fully connected layer (Sun et al., 2019)

The convolutional layer serves as a feature extraction function to work with other ML methods, as demonstrated by Nguyen et al. (2021). In many studies, data after convolutional layers are flattened to a 1D vector and fed into a fully connected layer, also known as a dense layer, in which inputs and outputs are related via learnable weight. Figure 7 shows the conventional architecture with 2 hidden and 2 dropout layers. The dropout layer helps to prevent model overfitting and is used only during training. However, information loss might occur when the parameter of the dropout layer is not correctly set.

Table 3  
List of studies that utilize spatial images in close-range HSI analysis

Spatial Information Use Case	Spectrum Wavelength	Wavelength Interval	Research Subject	Authors
Combine 3D models with HS images to remove geometry-related effects in HS analysis	400–2500 nm	Not specified	Sugar beets	<b>Behmann et al., 2016</b>
	400–1000 nm	7 nm	Aagrow soybean	<b>Huang et al., 2018</b>
	380–2200 nm	4.69 nm	Tomato palnts	<b>Sun et al., 2019</b>
Analyse 3D HS image using CNN, which preserves spectral and spatial information	376–1044 nm	5 nm	Cotton leaves	<b>Yan et al., 2021</b>
	328.81–1113.54 nm	0.78 nm	Blueberry	<b>Wang, Hu et al., 2018</b>
	400–1000 nm	2.5 nm	Glycine max (L.) Merr. soybean	<b>Nagasubramanian et al., 2019</b>
	397–1004 nm	3 nm	Grapevines	<b>Nguyen et al., 2021</b>
Compute mean spectral reflectance from spatially selected ROIs	395–885 nm	2.05 nm	Corn seedlings	<b>Yang et al., 2019</b>
	450–950 nm	3.97 nm	Cotton	<b>Zhao et al., 2021</b>
Morphological process to remove noise spatially	467–900 nm	2.87 nm	Potato plants	<b>Kool et al., 2021</b>
	400–2506nm	1.23 nm and 5.79 nm for below and above 895, respectively	Gien Moy and Latham raspberries	<b>Williams et al., 2017</b>
Generate MPs to support processes like noise removal and combination with PCs	364–1031 nm	4.5 nm	Banana leaves	<b>Liao et al., 2019</b>
	364–1031 nm	4.5 nm	Banana leaves	<b>Villegas et al., 2017</b>
Classification of objects with different material properties in 3D data via CCL	500–820 nm	9.69 nm	Peperomia tetraphylla plant, Sansevieria Trifasciata plant, and other non-living objects	<b>Chen et al., 2019</b>

## REMAINING TECHNICAL CHALLENGES

Even though HS image carries a large amount of information, researchers still faced many challenges during the studies. Each stage poses certain difficulties that need to be tackled before a study is carried out. For instance, the inconsistent natural light makes outdoor data

acquisition more difficult. Therefore, factors like weather forecasts must be considered prior to data acquisition.

Even though the HS camera is decreasing, it is still costly compared to imaging devices like thermal and RGB because the HS camera is still mainly used for research purposes, and there are fewer providers for such cameras. It makes HS a niche device that can hardly be obtained.

Every pixel of an HS image is a vector of spectra information. Unlike RGB images with three bands or multispectral images with 10-20 bands, the pixel vector of HS images can be hundreds of elements long. It leads to costly storage for HS images. Besides, remote data transfer for such a huge amount of data is challenging. One possible solution is to use a compression algorithm where no data loss occurs when compressed data is extracted.

One of the challenges with deep learning adoption for HS analysis is that the amount of training dataset is still insufficient in many studies because the public HS dataset is fewer, and the datasets required are specific, depending on the subject studied. The common approach is via data augmentation, whereby the available training dataset is rotated, scaled, cropped, and added noise to assemble the subject under different conditions.

## **CONCLUSION**

HS image carries much information both spectrally and spatially. In many cases, spatial information is used only in pre-processing steps like segmentation and noise reduction. For model training, the use case of HS spectral-spatial information is demonstrated by deep learning. In many studies, CNN showed better performance as compared to the conventional pixel-based analysis, which treats every pixel independently. Therefore, deep learning methods utilizing spectral and spatial information should be the research focus in future HSI analysis to derive full benefits from HS information.

Besides, one piece of information that can hardly be explored and utilized from HS images is the pixel depth. The depth information is usually provided using an external depth sensor. Currently, most studies about neural network analysis on proximal HSI do not include in-depth information. Hence, there is potential to integrate depth information with HS images trained by neural networks to improve accuracy in studying plant traits.

## **ACKNOWLEDGEMENT**

The authors acknowledged the Ministry of Higher Education Malaysia (MOHE) for the Fundamental Research Grant Scheme with Project Code: FRGS/1/2020/TK0/USM/02/13.

## REFERENCES

- Arefi, A., Sturm, B., von Gersdorff, G., Nasirahmadi, A., & Hensel, O. (2021). Vis-NIR hyperspectral imaging along with Gaussian process regression to monitor quality attributes of apple slices during drying. *LWT*, *152*, Article 112297. <https://doi.org/10.1016/j.lwt.2021.112297>
- Asaari, M. S. M., Mertens, S., Dhondt, S., Inzé, D., & Scheunders, P. (2022). Analysis of plant stress response using hyperspectral imaging and kernel ridge regression. In N. M. Mahyuddin, N. R. M. Noor & H. A. M. Sakim (Eds.), *Proceedings of the 11th International Conference on Robotics, Vision, Signal Processing and Power Application* (pp. 426-431). Springer. [https://doi.org/10.1007/978-981-16-8129-5\\_66](https://doi.org/10.1007/978-981-16-8129-5_66)
- Asaari, M. S. M., Mertens, S., Dhondt, S., Inzé, D., Wuyts, N., & Scheunders, P. (2019). Analysis of hyperspectral images for detection of drought stress and recovery in maize plants in a high-throughput phenotyping platform. *Computers and Electronics in Agriculture*, *162*, 749-758. <https://doi.org/10.1016/j.compag.2019.05.018>
- Asaari, M. S. M., Mishra, P., Mertens, S., Dhondt, S., Inzé, D., Wuyts, N., & Scheunders, P. (2018). Close-range hyperspectral image analysis for the early detection of stress responses in individual plants in a high-throughput phenotyping platform. *ISPRS Journal of Photogrammetry and Remote Sensing*, *138*, 121-138. <https://doi.org/10.1016/j.isprsjprs.2018.02.003>
- Bauriegel, E., Giebel, A., Geyer, M., Schmidt, U., & Herppich, W. B. (2011). Early detection of Fusarium infection in wheat using hyper-spectral imaging. *Computers and Electronics in Agriculture*, *75*(2), 304-312. <https://doi.org/10.1016/j.compag.2010.12.006>
- Behmann, J., Mahlein, A. K., Paulus, S., Dupuis, J., Kuhlmann, H., Oerke, E. C., & Plümer, L. (2016). Generation and application of hyperspectral 3D plant models: Methods and challenges. *Machine Vision and Applications*, *27*(5), 611-624. <https://doi.org/10.1007/s00138-015-0716-8>
- Behmann, J., Steinrücken, J., & Plümer, L. (2014). Detection of early plant stress responses in hyperspectral images. *ISPRS Journal of Photogrammetry and Remote Sensing*, *93*, 98-111. <https://doi.org/10.1016/j.isprsjprs.2014.03.016>
- Bradley, P. E., Keller, S., & Weinmann, M. (2018). Unsupervised feature selection based on ultrametricity and sparse training data: A case study for the classification of high-dimensional hyperspectral data. *Remote Sensing*, *10*(10), Article 1564. <https://doi.org/10.3390/rs10101564>
- Brownson, J. R. S. (2014). *Solar Energy Conversion Systems*. Elsevier Inc. <https://doi.org/https://doi.org/10.1016/C2011-0-07039-4>
- Chen, B., Shi, S., Sun, J., Gong, W., Yang, J., Du, L., Guo, K., Wang, B., & Chen, B. (2019). Hyperspectral lidar point cloud segmentation based on geometric and spectral information. *Optics Express*, *27*(17), 24043-24059. <https://doi.org/10.1364/oe.27.024043>
- Darvishzadeh, R., Skidmore, A., Schlerf, M., Atzberger, C., Corsi, F., & Cho, M. (2008). LAI and chlorophyll estimation for a heterogeneous grassland using hyperspectral measurements. *ISPRS Journal of Photogrammetry and Remote Sensing*, *63*(4), 409-426. <https://doi.org/10.1016/j.isprsjprs.2008.01.001>
- Dinç, S., & Aygün, R. S. (2013). Evaluation of hyperspectral image classification using random forest and Fukunaga-Koontz transform. In P. Perner (Ed.), *Machine Learning and Data Mining in Pattern Recognition* (pp. 234-245). Springer. [https://doi.org/10.1007/978-3-642-39712-7\\_18](https://doi.org/10.1007/978-3-642-39712-7_18)

- Elmasry, G., Kamruzzaman, M., Sun, D. W., & Allen, P. (2012). Principles and applications of hyperspectral imaging in quality evaluation of agro-food products: A review. *Critical Reviews in Food Science and Nutrition*, 52(11), 999-1023. <https://doi.org/10.1080/10408398.2010.543495>
- Fischler, M. A., & Bolles, R. C. (1987). Random sample consensus: A paradigm for model fitting with applications to image analysis and automated cartography. In M. A. Fischler & O. Firschein (Eds.), *Readings in Computer Vision* (pp. 726-740). Morgan Kaufmann Publishers, Inc. <https://doi.org/10.1016/b978-0-08-051581-6.50070-2>
- Fletcher, R. S., & Turley, R. B. (2017). Employing canopy hyperspectral narrowband data and random forest algorithm to differentiate palmer amaranth from colored cotton. *American Journal of Plant Sciences*, 08(12), 3258-3271. <https://doi.org/10.4236/ajps.2017.812219>
- Fu, Y., Yang, G., Wang, J., Song, X., & Feng, H. (2014). Winter wheat biomass estimation based on spectral indices, band depth analysis and partial least squares regression using hyperspectral measurements. *Computers and Electronics in Agriculture*, 100, 51-59. <https://doi.org/10.1016/j.compag.2013.10.010>
- Gao, J., Nuytens, D., Lootens, P., He, Y., & Pieters, J. G. (2018). Recognising weeds in a maize crop using a random forest machine-learning algorithm and near-infrared snapshot mosaic hyperspectral imagery. *Biosystems Engineering*, 170, 39-50. <https://doi.org/10.1016/j.biosystemseng.2018.03.006>
- Ge, Y., Bai, G., Stoerger, V., & Schnable, J. C. (2016). Temporal dynamics of maize plant growth, water use, and leaf water content using automated high throughput RGB and hyperspectral imaging. *Computers and Electronics in Agriculture*, 127, 625-632. <https://doi.org/10.1016/j.compag.2016.07.028>
- Geladi, P., & Kowalski, B. R. (1986). Partial least-squares regression: A tutorial. *Analytica Chimica Acta*, 185, 1-17. [https://doi.org/10.1016/0003-2670\(86\)80028-9](https://doi.org/10.1016/0003-2670(86)80028-9)
- Gewali, U. B., & Monteiro, S. T. (2016, September 25-28). *A novel covariance function for predicting vegetation biochemistry from hyperspectral imagery with Gaussian processes*. [Paper presentation]. International Conference on Image Processing (ICIP), Arizona, USA. <https://doi.org/10.1109/ICIP.2016.7532752>
- Gewali, U. B., Monteiro, S. T., & Saber, E. (2019). Gaussian processes for vegetation parameter estimation from hyperspectral data with limited ground truth. *Remote Sensing*, 11(13), Article 1614. <https://doi.org/10.3390/rs11131614>
- Goetz, A. F. H. (2009). Three decades of hyperspectral remote sensing of the Earth: A personal view. *Remote Sensing of Environment*, 113(SUPPL. 1), S5-S16. <https://doi.org/10.1016/j.rse.2007.12.014>
- Gonzalez, R. C., & Woods, R. E. (1993). *Digital Image Processing* (3rd ed.). Pearson.
- Grönwall, C., Steinvall, O., Göhler, B., & Hamoir, D. (2016). Active and passive imaging of clothes in the NIR and SWIR regions for reflectivity analysis. *Applied Optics*, 55(20), Article 5292. <https://doi.org/10.1364/ao.55.005292>
- Guo, Y., Yin, X., Zhao, X., Yang, D., & Bai, Y. (2019). Hyperspectral image classification with SVM and guided filter. *Eurasip Journal on Wireless Communications and Networking*, 2019(1), 1-9. <https://doi.org/10.1186/s13638-019-1346-z>

- Gupta, N., Dahmanja, R., Gottlieb, M., Denes, L., Kaminsky, B., & Metes, P. (1999). Hyperspectral imaging using acousto-optic tunable filters. *Proceedings AEROSENSE*, 3718, 512-521. <https://doi.org/10.1117/12.359988>
- Huang, J. F., & Apan, A. (2006). Detection of sclerotinia rot disease on celery using hyperspectral data and partial least squares regression. *Journal of Spatial Science*, 51(2), 129-142. <https://doi.org/10.1080/14498596.2006.9635087>
- Huang, P., Luo, X., Jin, J., Wang, L., Zhang, L., Liu, J., & Zhang, Z. (2018). Improving high-throughput phenotyping using fusion of close-range hyperspectral camera and low-cost depth sensor. *Sensors*, 18(8), Article 2711. <https://doi.org/10.3390/s18082711>
- Huang, Y., Li, J., Yang, R., Wang, F., Li, Y., Zhang, S., Wan, F., Qiao, X., & Qian, W. (2021). Hyperspectral imaging for identification of an invasive plant mikania micrantha kunth. *Frontiers in Plant Science*, 12, Article 626516. <https://doi.org/10.3389/fpls.2021.626516>
- Ioffe, S., & Szegedy, C. (2015, July 6-11). *Batch normalization: Accelerating deep network training by reducing internal covariate shift*. [Paper presentation]. 32nd International Conference on Machine Learning (ICML), Lille, France.
- Khodadadzadeh, M., Li, J., Plaza, A., Ghassemian, H., Bioucas-Dias, J. M., & Li, X. (2014). Spectral-spatial classification of hyperspectral data using local and global probabilities for mixed pixel characterization. *IEEE Transactions on Geoscience and Remote Sensing*, 52(10), 6298-6314. <https://doi.org/10.1109/TGRS.2013.2296031>
- Kool, J., Been, T., & Evenhuis, A. (2021, March 24-26). *Detection of latent potato late blight by hyperspectral imaging*. [Paper presentation]. 11th Workshop on Hyperspectral Image and Signal Processing, Evolution in Remote Sensing, Amsterdam, Netherlands. <https://doi.org/10.1109/WHISPERS52202.2021.9484002>
- Kuska, M., Wahabzada, M., Leucker, M., Dehne, H. W., Kersting, K., Oerke, E. C., Steiner, U., & Mahlein, A. K. (2015). Hyperspectral phenotyping on the microscopic scale: Towards automated characterization of plant-pathogen interactions. *Plant Methods*, 11(1), Article 28. <https://doi.org/10.1186/s13007-015-0073-7>
- Leucker, M., Mahlein, A. K., Steiner, U., & Oerke, E. C. (2016). Improvement of lesion phenotyping in cercospora beticola-sugar beet interaction by hyperspectral imaging. *Phytopathology*, 106(2), 177-184. <https://doi.org/10.1094/PHYTO-04-15-0100-R>
- Li, L., Zhang, Q., & Huang, D. (2014). A review of imaging techniques for plant phenotyping. *Sensors*, 14(11), 20078-20111. <https://doi.org/10.3390/s141120078>
- Liao, W., Ochoa, D., Gao, L., Zhang, B., & Philips, W. (2019, July 29- August 2). *Morphological analysis for banana disease detection in close range hyperspectral remote sensing images*. [Paper presentation]. IEEE International Symposium on Geoscience and Remote Sensing (IGARSS), Yokohama, Japan. <https://doi.org/10.1109/IGARSS.2019.8899087>
- Liu, Z. Y., Huang, J. F., Shi, J. J., Tao, R. X., Zhou, W., & Zhang, L. L. (2007). Characterizing and estimating rice brown spot disease severity using stepwise regression, principal component regression and partial least-square regression. *Journal of Zhejiang University Science B*, 8(10), 738-744. <https://doi.org/10.1631/jzus.2007.B0738>



- Lu, B., Dao, P. D., Liu, J., He, Y., & Shang, J. (2020). Recent advances of hyperspectral imaging technology and applications in agriculture. *Remote Sensing*, *12*(16), 1-44. <https://doi.org/10.3390/RS12162659>
- Luo, G., Chen, G., Tian, L., Qin, K., & Qian, S. E. (2016). Minimum noise fraction versus principal component analysis as a preprocessing step for hyperspectral imagery denoising. *Canadian Journal of Remote Sensing*, *42*(2), 106-116. <https://doi.org/10.1080/07038992.2016.1160772>
- Mahlein, A. K., Steiner, U., Dehne, H. W., & Oerke, E. C. (2010). Spectral signatures of sugar beet leaves for the detection and differentiation of diseases. *Precision Agriculture*, *11*(4), 413-431. <https://doi.org/10.1007/s11119-010-9180-7>
- Manley, M., Williams, P., Nilsson, D., & Geladi, P. (2009). Near infrared hyperspectral imaging for the evaluation of endosperm texture in whole yellow maize (*Zea mays* L.) Kernels. *Journal of Agricultural and Food Chemistry*, *57*(19), 8761-8769. <https://doi.org/10.1021/jf9018323>
- Mateo-García, G., Laparra, V., & Gómez-Chova, L. (2018, July 22-27). *Optimizing kernel ridge regression for remote sensing problems*. [Paper presentation]. IEEE International Symposium on Geoscience and Remote Sensing (IGARSS), Valencia, Spain. <https://doi.org/10.1109/IGARSS.2018.8518016>
- Mishra, P., Lohumi, S., Ahmad Khan, H., & Nordon, A. (2020). Close-range hyperspectral imaging of whole plants for digital phenotyping: Recent applications and illumination correction approaches. *Computers and Electronics in Agriculture*, *178*, Article 105780. <https://doi.org/10.1016/j.compag.2020.105780>
- Mishra, P., Polder, G., Gowen, A., Rutledge, D. N., & Roger, J. M. (2020). Utilising variable sorting for normalisation to correct illumination effects in close-range spectral images of potato plants. *Biosystems Engineering*, *197*, 318-323. <https://doi.org/10.1016/j.biosystemseng.2020.07.010>
- Moshou, D., Pantazi, X. E., Kateris, D., & Gravalos, I. (2014). Water stress detection based on optical multisensor fusion with a least squares support vector machine classifier. *Biosystems Engineering*, *117*(1), 15-22. <https://doi.org/10.1016/j.biosystemseng.2013.07.008>
- Moughal, T. A. (2013). Hyperspectral image classification using support vector machine. *Journal of Physics: Conference Series*, *439*(1), Article 012042. <https://doi.org/10.1088/1742-6596/439/1/012042>
- Nagasubramanian, K., Jones, S., Singh, A. K., Sarkar, S., Singh, A., & Ganapathysubramanian, B. (2019). Plant disease identification using explainable 3D deep learning on hyperspectral images. *Plant Methods*, *15*(1), 1-10. <https://doi.org/10.1186/s13007-019-0479-8>
- Nguyen, C., Sagan, V., Maimaitiyiming, M., Maimaitijiang, M., Bhadra, S., & Kwasniewski, M. T. (2021). Early detection of plant viral disease using hyperspectral imaging and deep learning. *Sensors*, *21*(3), Article 742. <https://doi.org/10.3390/s21030742>
- Nguyen, H. T., & Lee, B. (2006). Assessment of rice leaf growth and nitrogen status by hyperspectral canopy reflectance and partial least square regression. *European Journal of Agronomy*, *24*(4), 349-356. <https://doi.org/10.1016/j.eja.2006.01.001>
- Nielsen, A. A. (2011). Kernel maximum autocorrelation factor and minimum noise fraction transformations. *IEEE Transactions on Image Processing*, *20*(3), 612-624. <https://doi.org/10.1109/TIP.2010.2076296>

- Pandey, P., Ge, Y., Stoerger, V., & Schnable, J. C. (2017). High throughput in vivo analysis of plant leaf chemical properties using hyperspectral imaging. *Frontiers in Plant Science*, 8(1348), 1-12. <https://doi.org/10.3389/fpls.2017.01348>
- Paoletti, M. E., Haut, J. M., Plaza, J., & Plaza, A. (2018). A new deep convolutional neural network for fast hyperspectral image classification. *ISPRS Journal of Photogrammetry and Remote Sensing*, 145(Part A), 120-147. <https://doi.org/10.1016/j.isprsjprs.2017.11.021>
- Paulus, S., & Mahlein, A. K. (2020). Technical workflows for hyperspectral plant image assessment and processing on the greenhouse and laboratory scale. *GigaScience*, 9(8), 1-10. <https://doi.org/10.1093/gigascience/giaa090>
- Qin, J., Burks, T. F., Ritenour, M. A., & Bonn, W. G. (2009). Detection of citrus canker using hyperspectral reflectance imaging with spectral information divergence. *Journal of Food Engineering*, 93(2), 183-191. <https://doi.org/10.1016/j.jfoodeng.2009.01.014>
- Ray, D. K., Mueller, N. D., West, P. C., & Foley, J. A. (2013). Yield trends are insufficient to double global crop production by 2050. *PLoS One*, 8(6), Article e66428. <https://doi.org/10.1371/journal.pone.0066428>
- Ren, G., Wang, Y., Ning, J., & Zhang, Z. (2020). Using near-infrared hyperspectral imaging with multiple decision tree methods to delineate black tea quality. *Spectrochimica Acta - Part A: Molecular and Biomolecular Spectroscopy*, 237, Article 118407. <https://doi.org/10.1016/j.saa.2020.118407>
- Rodarmel, C., & Shan, J. (2002). Principal component analysis for hyperspectral image classification. *Surveying and Land Information Science*, 62(2), 115-122.
- Romer, C., Wahabzada M., Ballvora A., Pinto, F., Rossini, M., Panigada, C., Behmann, J., Leon, J., Thureau, C., Baukchage, C., Kersting, K., Rascher, U., & Plumer, L. (2012). Early drought stress detection in cereals: Simplex volume maximisation for hyperspectral image analysis. *Functional Plant Biology*, 39(11), 878-890. <https://doi.org/10.1071/FP12060>
- Rumpf, T., Mahlein, A. K., Steiner, U., Oerke, E. C., Dehne, H. W., & Plümer, L. (2010). Early detection and classification of plant diseases with support vector machines based on hyperspectral reflectance. *Computers and Electronics in Agriculture*, 74(1), 91-99. <https://doi.org/10.1016/j.compag.2010.06.009>
- Sabzi, S., Pourdarbani, R., Rohban, M. H., García-Mateos, G., Paliwal, J., & Molina-Martínez, J. M. (2021). Early detection of excess nitrogen consumption in cucumber plants using hyperspectral imaging based on hybrid neural networks and the imperialist competitive algorithm. *Agronomy*, 11(3), Article 575. <https://doi.org/10.3390/agronomy11030575>
- Saha, D., & Manickavasagan, A. (2021). Machine learning techniques for analysis of hyperspectral images to determine quality of food products: A review. *Current Research in Food Science*, 4, 28-44. <https://doi.org/10.1016/j.crfs.2021.01.002>
- Salazar-vazquez, J., & Mendez-vazquez, A. (2020). HardwareX A plug-and-play Hyperspectral Imaging Sensor using low-cost equipment. *HardwareX*, 7, Article e00087. <https://doi.org/10.1016/j.ohx.2019.e00087>
- Sankaran, S., Ehsani, R., Inch, S. A., & Ploetz, R. C. (2012). Evaluation of visible-near infrared reflectance spectra of avocado leaves as a non-destructive sensing tool for detection of laurel wilt. *Plant Disease*, 96(11), 1683-1689. <https://doi.org/10.1094/PDIS-01-12-0030-RE>

- Schlerf, M., Atzberger, C., Udelhoven, T., Jarmer, T., Mader, S., Werner, W., & Hill, J. (2003, May 13-16). *Spectrometric estimation of leaf pigments in Norway spruce needles using band-depth analysis, partial least-square regression and inversion of a conifer leaf model*. [Paper presentation]. 3rd EARSeL Workshop on Imaging Spectroscopy, Herrsching, Germany.
- Sims, D. A., & Gamon, J. A. (2002). Relationships between leaf pigment content and spectral reflectance across a wide range of species, leaf structures and developmental stages. *Remote Sensing of Environment*, *81*(2-3), 337-354. [https://doi.org/10.1016/S0034-4257\(02\)00010-X](https://doi.org/10.1016/S0034-4257(02)00010-X)
- Sims, D. A., & Gamon, J. A. (2003). Estimation of vegetation water content and photosynthetic tissue area from spectral reflectance: a comparison of indices based on liquid water and chlorophyll absorption features. *Remote Sensing of Environment*, *84*(4), 526-537. [https://doi.org/10.1016/S0034-4257\(02\)00151-7](https://doi.org/10.1016/S0034-4257(02)00151-7)
- Stuart, M. B., McGonigle, A. J. S., & Willmott, J. R. (2019). Hyperspectral imaging in environmental monitoring: A review of recent developments and technological advances in compact field deployable systems. *Sensors*, *19*(14), Article 3071. <https://doi.org/10.3390/s19143071>
- Sun, G., Ding, Y., Wang, X., Lu, W., Sun, Y., & Yu, H. (2019). Nondestructive determination of nitrogen, phosphorus and potassium contents in greenhouse tomato plants based on multispectral three-dimensional imaging. *Sensors*, *19*(23), Article 5295. <https://doi.org/10.3390/s19235295>
- Sun, H., Liu, N., Wu, L., Chen, L., Yang, L., Li, M., & Zhang, Q. (2018). Water content detection of potato leaves based on hyperspectral image. *IFAC-PapersOnLine*, *51*(17), 443-448. <https://doi.org/10.1016/j.ifacol.2018.08.179>
- Sun, J., Yang, W., Zhang, M., Feng, M., Xiao, L., & Ding, G. (2021). Estimation of water content in corn leaves using hyperspectral data based on fractional order Savitzky-Golay derivation coupled with wavelength selection. *Computers and Electronics in Agriculture*, *182*, Article 105989. <https://doi.org/10.1016/j.compag.2021.105989>
- Tian, Y., & Zhang, L. (2012). Study on the methods of detecting cucumber downy mildew using hyperspectral imaging technology. *Physics Procedia*, *33*, 743-750. <https://doi.org/10.1016/j.phpro.2012.05.130>
- Vigneau, N., Ecartot, M., Rabatel, G., & Roumet, P. (2011). Potential of field hyperspectral imaging as a non destructive method to assess leaf nitrogen content in Wheat. *Field Crops Research*, *122*(1), 25-31. <https://doi.org/10.1016/j.fcr.2011.02.003>
- Villegas, G., Liao, W., Criollo, R., Philips, W., & Ochoa, D. (2017). Detection of leaf structures in close-range hyperspectral images using morphological fusion. *Geo-Spatial Information Science*, *20*(4), 325-332. <https://doi.org/10.1080/10095020.2017.1399673>
- Wang, H., Chen, J., Lin, H., & Yuan, D. (2010). Research on effectiveness of hyperspectral data on identifying rice of different genotypes. *Remote Sensing Letters*, *1*(4), 223-229. <https://doi.org/10.1080/01431161.2010.481680>
- Wang, X., Zhang, Y., Ma, X., Xu, T., & Arce, G. R. (2018). Compressive spectral imaging system based on liquid crystal tunable filter. *Optics Express*, *26*(19), Article 25226. <https://doi.org/10.1364/oe.26.025226>
- Wang, Z., Hu, M., & Zhai, G. (2018). Application of deep learning architectures for accurate and rapid detection of internal mechanical damage of blueberry using hyperspectral transmittance data. *Sensors*, *18*(4), Article 1126. <https://doi.org/10.3390/s18041126>

- Williams, D., Britten, A., McCallum, S., Jones, H., Aitkenhead, M., Karley, A., Loades, K., Prashar, A., & Graham, J. (2017). A method for automatic segmentation and splitting of hyperspectral images of raspberry plants collected in field conditions. *Plant Methods*, *13*(1), 1-12. <https://doi.org/10.1186/s13007-017-0226-y>
- Yan, T., Xu, W., Lin, J., Duan, L., Gao, P., Zhang, C., & Lv, X. (2021). Combining multi-dimensional Convolutional Neural Network (CNN) with visualization method for detection of aphis gossypii glover infection in cotton leaves using hyperspectral imaging. *Frontiers in Plant Science*, *12*, Article 604510. <https://doi.org/10.3389/fpls.2021.604510>
- Yang, W., Yang, C., Hao, Z., Xie, C., & Li, M. (2019). Diagnosis of plant cold damage based on hyperspectral imaging and convolutional neural network. *IEEE Access*, *7*, 118239-118248. <https://doi.org/10.1109/ACCESS.2019.2936892>
- Yuan, L., Huang, Y., Loraamm, R. W., Nie, C., Wang, J., & Zhang, J. (2014). Spectral analysis of winter wheat leaves for detection and differentiation of diseases and insects. *Field Crops Research*, *156*, 199-207. <https://doi.org/10.1016/j.fcr.2013.11.012>
- Zhang, F., & Zhou, G. (2019). Estimation of vegetation water content using hyperspectral vegetation indices: A comparison of crop water indicators in response to water stress treatments for summer maize. *BMC Ecology*, *19*(1), 1-12. <https://doi.org/10.1186/s12898-019-0233-0>
- Zhang, J. C., Pu, R. L., Wang, J. H., Huang, W. J., Yuan, L., & Luo, J. H. (2012). Detecting powdery mildew of winter wheat using leaf level hyperspectral measurements. *Computers and Electronics in Agriculture*, *85*, 13-23. <https://doi.org/10.1016/j.compag.2012.03.006>
- Zhao, C., Liu, B., Piao, S., Wang, X., Lobell, D. B., Huang, Y., Huang, M., Yao, Y., Bassu, S., Ciais, P., Durand, J. L., Elliott, J., Ewert, F., Janssens, I. A., Li, T., Lin, E., Liu, Q., Martre, P., Müller, C., ... & Asseng, S. (2017). Temperature increase reduces global yields of major crops in four independent estimates. *Proceedings of the National Academy of Sciences of the United States of America*, *114*(35), 9326-9331. <https://doi.org/10.1073/pnas.1701762114>
- Zhao, J., Pan, F., Li, Z., Lan, Y., Lu, L., Yang, D., & Wen, Y. (2021). Detection of cotton waterlogging stress based on hyperspectral images and convolutional neural network. *International Journal of Agricultural and Biological Engineering*, *14*(2), 167-174. <https://doi.org/10.25165/J.IJABE.20211402.6023>

## Influence of Heat Treatment on the Mechanical Properties and Precipitation Kinetic of Sugar Palm Fiber Ash Reinforced LM26 Al Matrix Composites

Isah Aliyu<sup>1,2</sup>, Mohd Sapuan Salit<sup>1,3\*</sup>, Edi Syams Zainudin<sup>1,3</sup>, Mohd Zuhri Mohamed Yusoff<sup>1,3</sup> and Ridwan Yahaya<sup>4</sup>

<sup>1</sup>Advanced Engineering Materials and Composites Research Centre (AEMC), Department of Mechanical and Manufacturing Engineering, Universiti Putra Malaysia (UPM), 43400 Serdang, Selangor, Malaysia

<sup>2</sup>Department of Metallurgical Engineering, Waziri Umaru Federal Polytechnic, Birnin Kebbi, 860101, Nigeria

<sup>3</sup>Laboratory of Biocomposite Technology, Institute of Tropical Forestry and Forest Products, Universiti Putra Malaysia (UPM), 43400 Serdang, Selangor, Malaysia

<sup>4</sup>Science and Technology Research Institute for Defence (STRIDE), 43400, Kajang, Selangor, Malaysia

### ABSTRACT

Heat treatment is a commonly known treatment subjected to aluminum alloy and their composites to improve their mechanical properties for automotive, aerospace, and marine applications. The heat treatment was carried out to determine the influence of aging time and temperature on the mechanical properties of LM26 Al alloy reinforced with 0, 2, 4, 6, 8, and 10 wt% sugar palm fiber ash (SPFA) and its precipitation kinetics. The LM26 Al/SPFA composites were fabricated through the stir casting technique, solutionized at 500°C for 2 h, and quenched in water at room temperature. The quenched composites were aged at various ageing times and temperatures and allowed to air cool. The hardness, impact energy, tensile, and compression strengths of the aged composites were appraised. In addition, the precipitation kinetics were studied to validate the precipitation temperatures of LM26 Al matrix composites. The hardness of the composites increased with aging time

and temperature, with LM26 Al/10 wt% SPFA composite reaching a hardness peak of 102.10 VH at an aging temperature of 180°C after 5 h, compared to 56.70 VH for LM26 Al alloy. Similarly, after 5 h of aging at 180°C, the LM26 Al/8 wt% SPFA composite achieved maximum tensile and compression strengths of 198.21 MPa and 326.22 MPa, respectively. Precipitation temperature decreased from 584.8°C (LM26 Al alloy)

### ARTICLE INFO

#### Article history:

Received: 25 October 2022

Accepted: 25 January 2023

Published: 03 October 2023

DOI: <https://doi.org/10.47836/pjst.31.6.12>

#### E-mail addresses:

engalisa@yahoo.com (Isah Aliyu)

sapuan@upm.edu.my (Mohd Sapuan Salit)

edisyam@upm.edu.my; edisyam@gmail.com (Edi Syams Zainudin)

zuhri@upm.edu.my (Mohd Zuhri Mohamed Yusoff)

adr266@gmail.com (Ridwan Yahaya)

\* Corresponding author

to 480.46°C (LM26/ 10wt% SPFA), indicating that adding SPFA improved precipitation kinetics. The age-hardened composite with high hardness, tensile strength, and compression strength makes it a promising piston material application in the automotive industry.

*Keywords:* Aging time, LM26 Al alloy, mechanical properties, precipitation kinetics, sugar palm fiber

---

## INTRODUCTION

Metal matrix composites (MMCs) are becoming more popular due to their superior mechanical characteristics over monolithic metals. Aluminum matrix composites (AMCs) have been widely used to replace conventional and monolithic materials in various applications as lightweight structural materials due to their low density, superior creep resistance, high specific strength, excellent malleability, and excellent damping capacity, making them suitable for use in aerospace, electronics, marine, constructions, medical and automotive industries (Varalakshmi et al., 2019; Yuan et al., 2019; Yuan et al., 2017). AMCs have been widely used in various industrial applications, including medical components, automotive components for the production of pistons, brake discs, connecting rods, and aerospace components that include wings and fuselages (Bushlya et al., 2017; Chauhan et al., 2021; Ramasamy et al., 2021).

AMCs are strengthened by reinforcing them with either particles, fibers, or whiskers materials, which act as load-bearing materials. The commonly hard ceramic reinforcement materials used in the fabrication of AMCs include  $B_4C$ , SiC,  $MoS_2$ , and  $Al_2O_3$ , while fiber ashes used include rice husk (Olusesi & Udoeye, 2021), coconut shell (Babu et al., 2020), sugarcane bagasse (Kawin et al., 2020), bamboo leaf (Olaniran et al., 2019), bean pod (Bawa et al., 2020), groundnut shell (Venkatesh et al., 2019), and palm kernel shell (Iyasele, 2018) for strengthening purposes.

The sugar palm tree (*Arenga Pinnata* (Wurmb) Merr.) is a multifunctional tree that belongs to the family of palmea and is mostly found in countries such as Malaysia, China, and Indonesia. The sugar palm tree has dark braided fibers generally weaved from the bottom to the top of its trunk. Sugar palm fiber has many advantages and qualities, including less effort in preparing the fiber with high durability without any secondary processes and good seawater properties, which is suitable for the construction of ropes for ship cordage (Edhirej et al., 2017; Harussani & Sapuan, 2022; Ishak, Leman, et al., 2013). Other applications include shelters for fish breeding, road constructions, roofing materials, cushioning, weaving mats and hats, and making ropes and brooms (Ilyas et al., 2018; Ishak, Sapuan, et al., 2013). The preliminary studies showed that SPFA contained a high amount of refractory materials ( $SiO_2$ , CaO,  $Fe_2O_3$ ,  $Al_2O_3$ ). Agricultural waste contains a high amount of refractory materials, such as  $SiO_2$ , CaO,  $Fe_2O_3$ , and  $Al_2O_3$ , which account for their use as reinforcement material in AMCs (Ikubanni et al., 2022).

In order to achieve greater desirable mechanical properties of AMCs, the selection of good geometry of the reinforcement, such as size, shape, and quantity, is of paramount

importance. The reinforcement in the form of particles has been considered a new technological breakthrough in the fabrication of AMCs (Mabuwa et al., 2022). Selecting suitable reinforcing material and matrix is crucial for achieving the desirable properties of AMCs (Pasha et al., 2022). Moreover, homogeneous dispersion of reinforcement contents in the matrix and fabrication route employed, such as squeeze casting, stir casting, powder metallurgy, chemical vapor deposition pressure infiltration, solid solution precipitation hardening, and other metallurgical techniques, play a significant role in the improvement of the mechanical properties (Sajjadi et al., 2011; Samal et al., 2020; Vencl et al., 2010). Powder metallurgy and stir casting techniques are the most prevalent fabrication routes employed in the production of AMCs due to their cost effectiveness, ease of handle, greater hardness, and refined microstructural grains as compared to other methods (K. Singh et al., 2022; P. Singh et al., 2021; Reddy et al., 2020).

Stir casting eventually reduces the cost of producing AMCs by one-third to half compared to other methods, and the cost of high-volume fabrication decreased by one-tenth (Hashim et al., 1999; Yashpal et al., 2017). Stir casting is an advanced technique that involves stirring the molten metal to ensure uniform distribution of reinforcement before casting it into a prepared mold. The stirring action promotes vortex formation and increases reinforcement wettability with the matrix, thereby improving the bonding between the reinforcement and the matrix (Chak et al., 2020; Shaikh et al., 2019; Natrayan et al., 2017; V. K. Singh et al., 2015; Yuan et al., 2019). Many researchers are now using stir casting mostly in the fabrication of AMCs (Lokesh et al., 2022; Nambiar et al., 2020; Patel et al., 2022; Pasupulla et al., 2022; Velavan et al., 2020). Morampudi et al. (2022) fabricated an AA6061 aluminum matrix composite by reinforcing it with ilmenite ( $\text{FeTiO}_3$ ). Kennedy and Raja (2022) employed the stir casting technique to compare the mechanical characteristics of Al- $\text{B}_4\text{C}$  and Al-SiC composites, with Al- $\text{B}_4\text{C}$  composite having higher tensile and yield strength compared to Al-SiC composite.

LM26 aluminum alloy (Al-Si-Mg casting alloy) is widely used in the fabrication of block engines, pistons, intake manifolds, brake calipers, cylinder blocks, impellers, pumps, and cylinder heads valve components owing their overall performance of high specific-strength, better castability, low thermal expansion coefficient, improve wear resistance, adequate wettability, and superior corrosion resistance (Hiremath & Hemanth, 2018; Nagaraja et al., 2021; G. Singh & Sharma, 2021). When combined with proper heat treatment, the presence of Si and Mg in LM26 aluminum alloy led to the formation of  $\text{Mg}_2\text{Si}$  precipitates, eventually improving the mechanical properties significantly. The precipitation sequence of AMCs is given as supersaturated solid solution (SSSS), Guinier-Preston (GP) zone,  $\beta''$ ,  $\beta'$ , and  $\beta$  precipitates. The age-hardening response of LM26 Al alloy is influenced by many factors, such as chemical composition, solution heat treatment time and temperature, and aging time and temperature, all of which influence mechanical characteristics (Koppad et al., 2020).

Heat treatment, as a hardening process, is applied to metallic materials to improve their mechanical, structural, and physical properties for engineering applications (Somasekhar et al., 2018). Heat treatment resulted in precipitation hardening and improved mechanical properties compared to non-heat-treated AMCs. Heat-treated AMCs were found to have better mechanical characteristics, as well as reduced wear rate, than non-heat-treated AMCs (Mistry & Gohil, 2019).

The influence of aging temperature on wear and mechanical characteristics of the A375 matrix reinforced with large and small-sized SiC particles was investigated by Lakshmikanthan et al. (2020). The reinforcement of fly ash and graphite was uniformly distributed in the matrix of A6061 after T6 treatment with improved mechanical characteristics (B. Singh et al., 2022). The influence of aging temperature on the mechanical characteristics of Al-Si alloy and Al-Si/6% fly ash matrix composite was investigated by Tiwari et al. (2017). The temperatures under consideration for aging were 130°C, 150°C, 175°C, and 200°C. Peak hardness, tensile, and impact strengths were noticed in the alloy and composite at 175°C of aging temperature. Sharma et al. (2019) investigated the influence of T4 and T6 treatment on the wear behavior of Al-based composites and discovered that the wear rate improved with a lower coefficient of friction of T6-treated composites compared to T4-treated and as-cast composites. Sam et al. (2020) studied the effect of T6 treatment compared to TiB<sub>2</sub>, WC, and ZrO<sub>2</sub> as reinforcements on the tribological and mechanical characteristics of LM 25 aluminum alloy. They discovered that incorporating WC as reinforcement significantly improved the hardness and tensile strength of the composites after T6 heat treatment, with a corresponding lower wear rate than incorporating TiB<sub>2</sub> and ZrO<sub>2</sub> as reinforcement. Li et al. (2018) investigated the tribological behavior of Al-5% Si-1.0% Cu-0.5% Mg matrix reinforced with SiC particles by subjecting it to heat treatment. They discovered that after heat treatment, the composite had a lower wear rate and lower coefficient of friction than the base alloy.

The depletion of mineral resources such as synthetic reinforcements, with their high cost, high weight, and limited supply, are major setbacks in most developing countries in the fabrication of AMCs (Ikumapayi et al., 2022; Seetharaman et al., 2022). The reliance on importing synthetic materials from overseas and the high cost of foreign exchange implies that synthetic materials purchased locally are relatively expensive if available. Researchers have shown kin interest in improving the mechanical characteristics of AMC by incorporating cheaper and readily available green reinforcements into AMCs (Khan et al., 2022). According to the literature and to the best of the authors' knowledge, the study of heat treatment on the mechanical behavior and precipitation kinetics of LM26 AMCs reinforced with SPFA has not been explored and requires investigation. This research aims to determine the appropriate aging time and temperature corresponding to optimal hardness, impact energy, tensile, and compression strength, as well as the effect of precipitation temperature on the precipitation kinetics of the LM26 Al/SPFA composite.



## MATERIALS AND METHODS

### Material Preparation

The matrix material used in this investigation was LM26 Al alloy, with a chemical composition of 9.70% Si, 2.40% Cu, 1.2% Mg, 1.10% Fe, 0.91% Zn, 0.83% Ni, 0.50% Mn, 82.86% Al, and 0.50% of other elements. Sugar palm fiber was collected from Jempol, Negeri Sembilan, Malaysia, and used as reinforcement. The sugar palm fiber was washed under running tap water and dried in the laboratory for 48 h before being burnt in an incinerator to produce sugar palm fiber ash (SPFA). The SPFA was collected and heated in an electrical muffler furnace for 4 h at 700°C to remove the volatile and carbonaceous constituents. After being screened with sieve sets arranged in descending order of finest, the SPFA with an average size of less than 75 µm was used, and its chemical composition was analyzed with X-ray fluorescence (SHIMADZU, EDX-720) as shown in Table 1.

Table 1  
*Elemental constituent of LM26 Al-alloy*

Elements	Si	Mg	Cu	Fe	Mn	Zn	Ni	Others	Al
% mass fraction	9.70	1.20	2.40	1.10	0.50	0.91	0.83	0.50	Bal.

The composites were fabricated by using a stir-casting route. The LM26 Al alloy was cut into pieces, placed in the graphite crucible of an induction electrical resistance furnace, and heated above 700°C. After the LM26 Al alloy was completely melted, followed by manually stirring and allowed to cool to a semi-solid state at 580°C. SPFA were preheated in a muffler furnace (up to 500°C) to remove moisture and improve wettability. The preheated SPFA and 1wt% Mg were introduced into the molten LM26 Al alloy vortex to improve its wettability. The molten mixture was stirred for 10 min at 500 rpm to ensure proper reinforcement mixing in the base matrix. After stirring, the molten mixture was degassed with 1% hexachloroethane (C<sub>2</sub>Cl<sub>6</sub>) powder. Then, the mixture was poured into a precast sand mold to produce a standard tensile strength specimen in accordance with ASTM E 8 (ASTM International, 2015). The procedure described was used to produce composites with varying percentages of SPFA content ranging from 0 to 10wt% at 2wt% intervals. There were nine tensile samples made from each composition.

### Heat Treatment Processes

The fabricated LM26 Al alloy and LM26 Al-SPFA composites were packed in a resistance heat treatment furnace, and solution heat treatment (SHT) was carried out at 500°C for 2 h before quenching in water (at room temperature). The quenched samples were divided into three parts to analyze their hardness, impact energy, tensile strength, compression strength, and precipitation kinetic of the AMCs.

One tensile sample, each from the same composition from SHT and quenched samples was machined into eleven hardness samples in accordance with ASTM E383 (ASTM International, 2017).

To determine the aging temperature with peak hardness, five quenched SHT hardness samples, each from the same composition, were aged in the furnace for 2 h, one each at temperatures of 90°C, 120°C, 150°C, 180°C, and 210°C before being cooled at room temperature. Similarly, six quenched SHT hardness samples, each from the same compositions, were aged in the furnace at 180°C, one each for different aging times of 1 h, 2 h, 3 h, 4 h, 5 h, and 6 h, cool outside the furnace in still air to determine the aging time that corresponds to peak hardness.

Three sets each of the same composition of tensile and compression strengths samples from the quenched SHT were aged at 180°C for 5 h and air cool to determine the impact energy, tensile strength, and compression strength.

The SHT and quenched samples containing SPFA content of 0, 2wt%, 8wt%, and 10wt% were filed to obtain 6 mg of powder for the study of precipitation kinetic.

### **X-ray Diffraction**

The X-ray diffraction (PANalytical X'Pert Pro Model: PW3040/60, Netherlands) with Cu-K $\alpha$  radiation, wavelength ( $\lambda$ ) of 1.5406 Å, in an angle range of  $2\theta = (4^\circ-90^\circ)$  working at the rate of 2 °/min was utilized to ascertain the oxides and intermetallic compounds in SPFA, as-cast LM26 Al alloy and LM26 AMCs reinforce with SPFA.

### **Hardness Test**

Micro hardness testing was carried out by using a digital Mirco-vicker's hardness tester (Model: 401MVD, Germany) in accordance with ASTM E384 (ASTM International, 2017). Surface flaws were abraded with 400 grit to 1000 grit papers before being polished with 1200 grit emery cloth. After three indentations on each age-hardened sample, the average hardness values were recorded after the samples were subjected to a 1 kg load for 15 sec.

### **Standard Tensile and Compression Tests**

The tensile strength, compression strength, and impact energy tests were performed on the age-hardened LM26 alloy and its composite reinforced with SPFA. The ultimate tensile strength and compression strengths were evaluated on a computerized Universal Testing Machine (UTM) (Model: INSTRON M/c 5566) with a 100 kN capacity at a strain rate of 1.0 mm/min in accordance with the standard ASTM E-8 and E-9 (ASTM International, 2015a).

### **Impact Energy Test**

The impact energy testing was carried out using a Charpy impact machine of 300J capacity with a pendulum of striking speed of 5 m/s. The samples were machined into impact test specimens with dimensions of 55 mm × 10 mm × 10 mm, with a notch depth of 2 mm and a radius of notch tip 0.02 at 45° according to ASTM E23 standard (ASTM International, 2023). The impact test was performed on three tests of samples, with readings taken and their average values recorded.

### **Microstructural Analysis**

The morphology and EDS spectrum of the aged samples at 180°C for 5 h was characterized by using the scanning electron microscope (JSM 6400, JEOL Ltd, Tokyo, Japan) connected with energy dispersive X-ray spectroscopy (DES) according to ASTM standards E 407 and then, polished with different grades of emery papers according to standard metallographic procedure (ASTM International, 2015b). The samples were etched with Keller's reagent, composed of 95 ml of water, 2.5 ml HNO<sub>3</sub>, 1.5 ml HCl, and 1.0 ml HF, and then subjected to SEM analysis.

### **Differential Scanning Calorimetry (DSC)**

Differential scanning calorimetry (DSC) (Model: Mettler Toledo TGA/DSC HT 3, Swiss) was used to perform thermal analysis on LM26 AMC with SPFA content of 0, 2wt%, 8wt%, and 10wt%. The samples were filed to powder form after SHT at 500°C for 4 h and quenched in water. The 6mg of powder samples were weighed using an electronic balance (AND GF-1000, Model T0380263, Japan) and placed in a pan constructed on a framework in the DSC cell. An empty pure aluminum reference pan was positioned on a symmetric framework with its own constantan disc and chromel-alumel thermocouple beneath it. To minimize oxidation, the samples were heated at 10°C/min in a nitrogen atmosphere supplied at 50 mL/min between 500°C and 700°C. The sample temperature was measured with a chromel-alumel thermocouple, and the heat flow was calculated by comparing the difference in temperature between the composites and the reference pure aluminum. The data from all DSC runs were saved to the instrument memory.

## **RESULTS AND DISCUSSION**

### **X-ray Diffraction Patterns Analysis**

The XRD diffraction patterns of SPFA, LM26 Al-alloy, and fabricated LM26 Al-matrix/8wt% SPFA composite are depicted in Figure 1. The XRD confirmed the presence of SiO<sub>2</sub>, CaO, Fe<sub>2</sub>O<sub>3</sub>, and Al<sub>2</sub>O<sub>3</sub> in SPFA, as determined by XRF. Furthermore, SiO<sub>2</sub> was discovered to be the dominant constituent in SPFA. Similarly, the XRD of LM26 alloy

and LM26 Al/SPFA composite confirmed the presence of Al as the dominant and traces of Si and Mg in the form of  $Mg_2Si$  and  $Al_5FeSi$ . These intermetallic compounds,  $Mg_2Si$  and  $Al_5FeSi$ , formed an excellent bonding with the reinforcement (SPFA). It further validated SPFA as good reinforcing material in an LM26 Al alloy matrix. The major diffraction peak of SPFA is  $29.4^\circ$  with a crystallinity index of 52.76%. The matrix, LM26 Al alloy, has a crystallinity index of 49.75% with three major diffraction peaks of  $28.44^\circ$ ,  $38.44^\circ$ , and  $44.69^\circ$ , which are characteristics of metallic aluminum (Shaikh et al., 2019). The addition of SPFA into LM26 Al alloy caused a decrease in the crystallinity of the LM26 Al alloy to 28.97% with a corresponding major peak of  $38.37^\circ$ ,  $41.76^\circ$  and  $44.72^\circ$ .

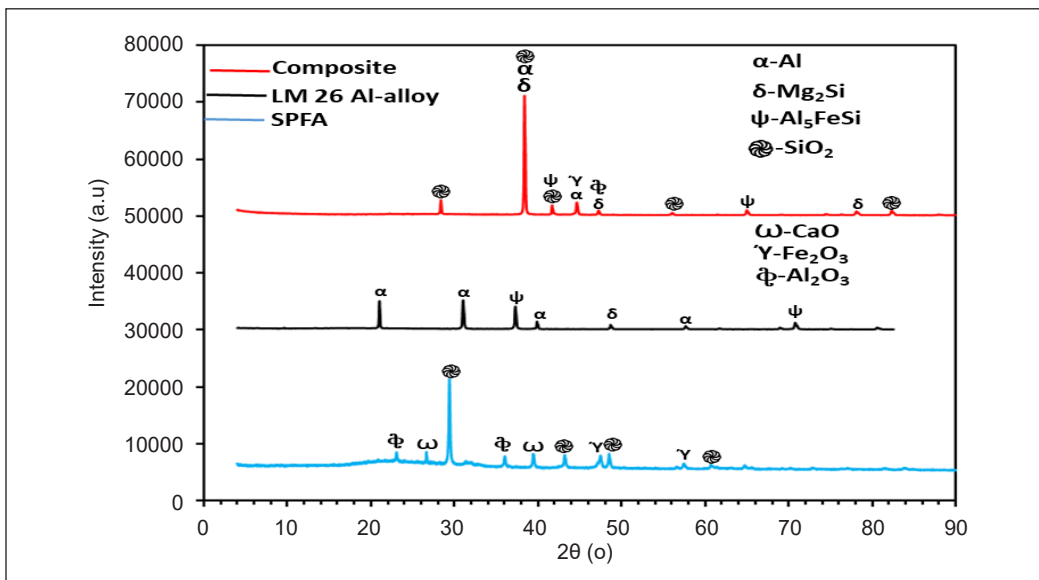


Figure 1. XRD of SPFA, LM26 Al alloy and LM26 Al/SPFA composite

### Hardness Behavior

Hardness testing was performed on the composites to investigate the effects of aging time and temperature. The fabricated composites had a maximum hardness value of 93.62 HV at 10wt% of SPFA addition.

The SHT at  $500^\circ\text{C}$  for 4 h and fast quenching in water led to the formation and retention of a supersaturated single phase, and aging the quenched sample at various temperatures allowed precipitation of the second phase to form, which was metastable. This small metastable precipitate impinged on dislocation movement, thereby increasing the hardness of the alloys and composites (Goudar et al., 2018).

Figure 2 depicts the hardness variation of heat-treated LM26 Al matrix/ (0-10wt%) SPFA composites aged for 2 h at  $90^\circ\text{C}$ ,  $120^\circ\text{C}$ ,  $150^\circ\text{C}$ ,  $180^\circ\text{C}$ , and  $210^\circ\text{C}$ . A study of aging temperature variation was carried out to determine the temperature that results in peak

hardness. It was evident that aging temperature affected the hardness of LM26 Al alloy and its composites (Figure 2). Figure 2 depicts the linear increase in hardness of LM26 Al alloy and its composites reinforced with SPFA with increasing aging temperature at an aging time of 2 h. The increase in hardness with increasing aging temperature could be due to an increase in the number of precipitated forms. The LM26 Al alloy and its composites reinforced with SPFA attained peak hardness after being aged to 180°C. Beyond the aging temperature of 180°C, the hardness of the LM26 Al alloy and its composites dropped due to softening caused by overheating at 210°C (Flanagan et al., 2019).

The hardness variation of age-hardened LM26 Al matrix (0–10wt%) SPFA composites at different aging times of 1 h, 2 h, 3 h, 4 h, 5 h, and 6 h at 180°C is shown in Figure 3. Since the peak hardness was observed at 180°C, this temperature setting was used to investigate the hardness of LM26 Al alloy and its composites over a range of aging times. Figure 3 shows the hardness values in a linear increment of aging times from 1 h to 5 h and then began to drop. The corresponding hardness values of LM26 Al alloy and its composites aged below the aging time of 4 h were lower than the fabricated LM26 Al alloy and its composites and were referred to as under-aged. The lower hardness values observed below 4 h were due to incomplete precipitate formation of the intermetallic compounds. Peak hardness was observed at 5 h (Figure 3) for LM26 Al alloy and its composites. Geetha and Ganesan (2015) reported that peak hardness was attained between 4 h and 6 h aging time. The peak hardness was achieved due to the formation of hard fine precipitate phases of intermetallic compounds ( $Mg_2Si$  and  $Al_3FeSi$ ) and uniformly dispersed SPFA (Figure 8e), which provided resistance to the indenter when indenting the surfaces of LM26 Al alloy and its composite. The precipitation of the intermetallic compounds was enhanced by heating the LM26 Al alloy and its composites to the desired temperature and allowing sufficient time to lapse (Rajasekaran et al., 2012). Figure 3 shows that increasing the aging time beyond 5 h caused a decrease in hardness due to the coarsening of the precipitate formed and its softening at 6 h, referred to as over-aged.

The hardness variation of aged hardened LM26 Al alloy and its composites reinforced with varied amounts of SPFA ranging from 0 to 10wt% in 2wt% intervals at aging times of 1 h, 2 h, 3 h, 4 h, and 5 h is shown in Figure 4. Regardless of the aging time, it was evident that the hardness values increased as the amount of SPFA increased. The increase in hardness values was due to the increase in hard refractory constituents of  $SiO_2$ ,  $Al_2O_3$ ,  $CaO$ , and  $Fe_2O_3$  present in SPFA as a result of its addition [Figure 8 (a-f)]. The hardness value of the aged hardened LM26 Al matrix/10wt% SPFA composite after 5 h was 9.06% higher than that of the fabricated composite counterpart. It was due to the precipitate formed after aging (Figure 8f). A peak hardness value of 102.1 VH was obtained with aged LM26 Al/10wt% of SPFA composite at 5 h and 180°C, while the lowest hardness value of 56.2 VH was achieved with LM26 Al alloy after 1 h aging at 180°C.

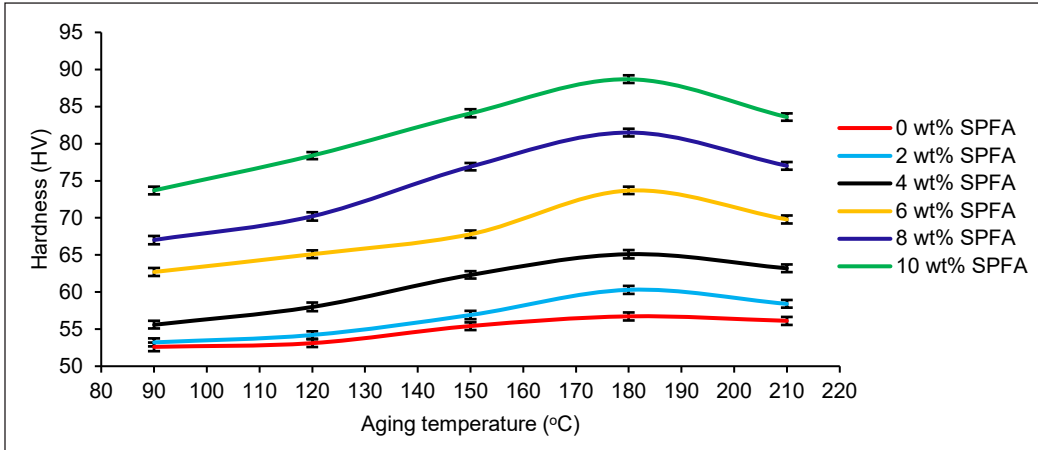


Figure 2. Hardness (VH) of composites at various aging temperatures

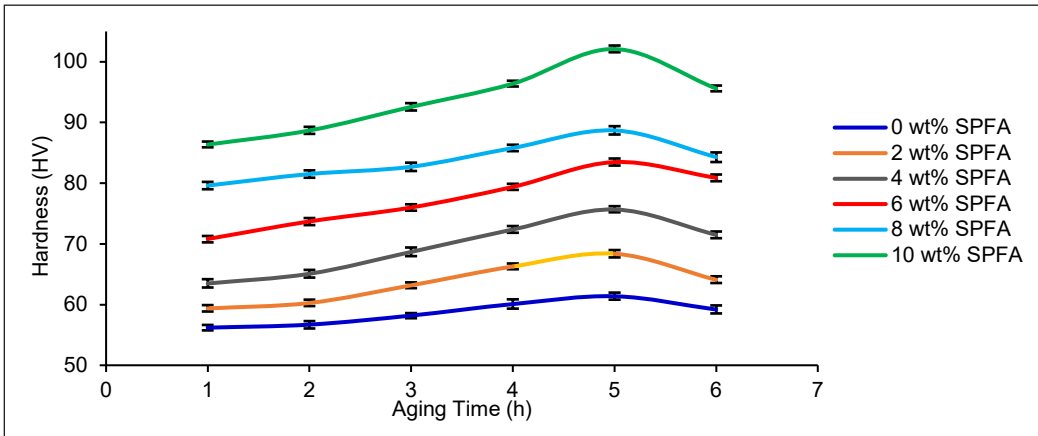


Figure 3. Hardness (VH) of composites at various aging times

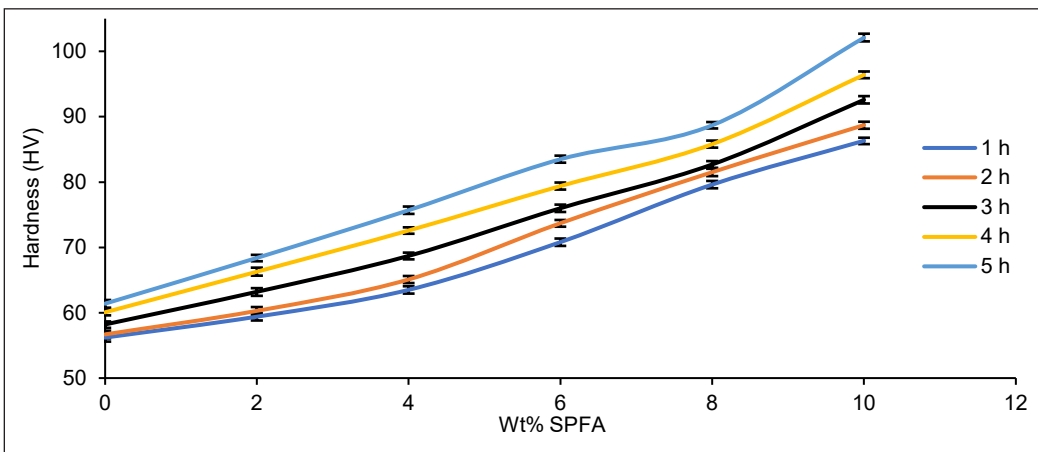


Figure 4. Hardness (VH) of composites at various reinforcement (SPFA) percentages

### Tensile Strength

The stress-strain curves of the materials after 5 h of aging at 180°C are presented in Figure 5. The variation of the volume fraction of reinforcement under tensile conditions was studied. The curves of the SPFA-reinforced composite differ significantly from those of the LM26 Al alloy. The addition of SPFA as reinforcement into the LM26 Al matrix, coupled with age hardening, increased the tensile strength of the composites. It could be explained by the homogeneous distribution of SPFA particles, precipitates that formed after aged hardening, and the SPFA particle's larger surface area within the matrix, which increased interface strength between the reinforcement and the material (Sabry et al., 2020). It was shown in Figure 5 that there was a critical SPFA content above or below which the tensile strength of the composites was lowered. The tensile strength of the composites is greatest when the amount of SPFA particles is up to 8 wt%; above and below this amount, the tensile strength is lowered. Similarly, Manda et al. (2021) reported improved tensile strength with adding molybdenum disulfide in AA6061 and coupled with aging at 180°C for 12 h. The agglomerates formed by the high concentration of SPFA up to 10 wt% act as stress concentration centers. The formation and distribution of the agglomerates within the LM26 Al alloy matrix cause a drop in the tensile strength of the ML26 Al/10 wt% SPFA composite (Al-Salihi & Judran, 2020).

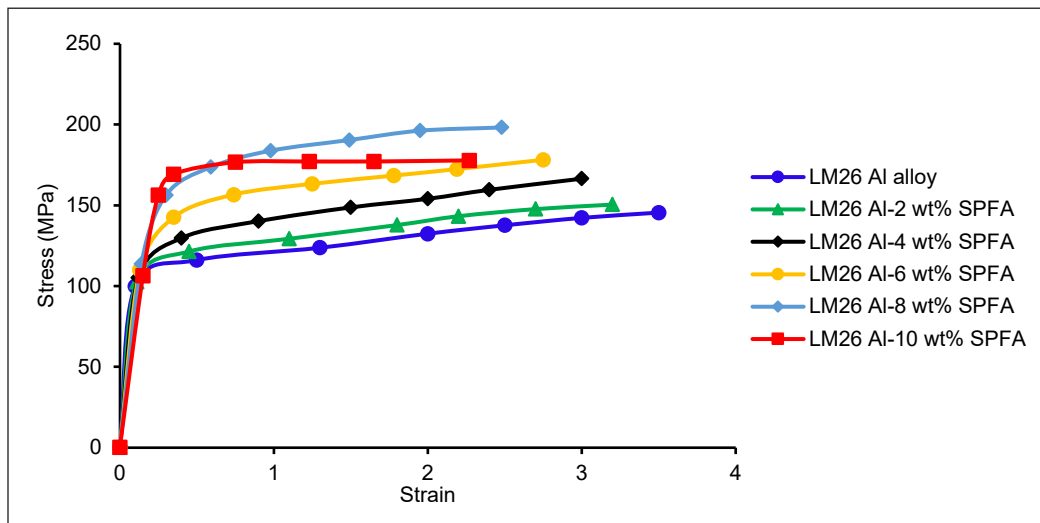


Figure 5. Stress-strain curve of LM26 Al alloy and composites with varying reinforcement content under tension

### Compression Strength

The stress-strain curves of the LM26 Al alloy and LM26 Al/SPFA composites aged at 180°C for 5 h after the compression test as depicted in Figure 6. There was a noticeable difference between the composites reinforced with SPFA and the LM26 Al alloy. The

compression strength of the SPFA-reinforced composite was improved significantly compared to the LM26 Al alloy. The compression strength of LM26 Al with 10 wt% SPFA composite is higher when compared with the composites having 2, 4, and 6 wt% SPFA. LM26 Al composite with 8 wt% SPFA was found to have the highest compression strength. The compression strength of the composites improved significantly with increased volume fraction of the SPFA reinforcement, and precipitates formed as a result of aging. An improvement of 24.36 % in the compression strength was noticed with 8 wt% SPFA reinforced LM26 Al matrix composite compared to the LM26 Al matrix alloy. A study by Das et al. (2019) reported an increase in compression strength with the incorporation of SiC in Al 7075 and aged at 483°C for 2 h compared to the as-cast. It is owing to the SPFA exhibiting a strong bond with LM26 Al matrix alloy, which assists in bearing more compression load as compared to LM26 Al matrix alloy. The increase in compression strength could also be due to increasing dislocation density at the reinforcement matrix interface and load transfer to the strongly bonded SPFA in the LM26 Al matrix (Khan et al., 2022; Rajaram et al., 2022). Similarly, the improvement in compression strength could be a result of a closed pack of the reinforcement in the matrix, the interfacial properties exhibited between the reinforcements and matrix, which are associated with wettability (Arunachalam et al., 2019; Kondoh et al., 2010).

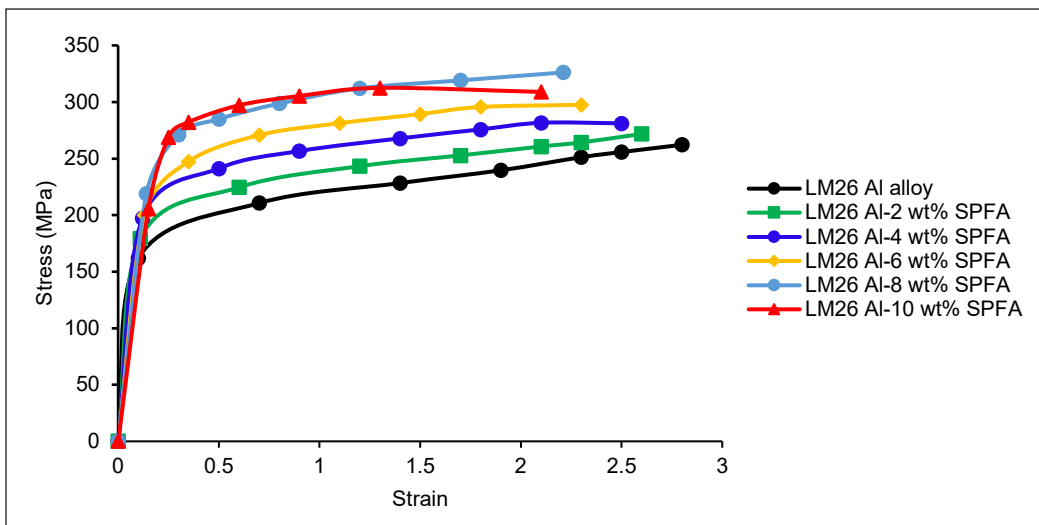


Figure 6. Stress-strain curve of LM26 Al alloy and composite with varying SPFA content under compression

### Impact Energy

An impact strength test was used to appraise the toughness of the composites. The Charpy impact testing was used to determine the energy absorbed by the composites in a single strike before braking. The impact energy of LM26 Al alloy decreased with the increase of



SPFA content to 10wt% SPFA (14.75 J to 6.98 J) (Figure 7). The drop in impact energy could be attributed to the change of ductile matrix of LM26 Al alloy to brittle LM26 Al/10 wt% SPFA composite by the addition of hard ceramic content of SiO<sub>2</sub>, CaO, Fe<sub>2</sub>O<sub>3</sub>, and Al<sub>2</sub>O<sub>3</sub>, present in the SPFA as confirmed by XRF (Table 1) (Manikandan & Arjunan, 2019). The toughness of a material is the amount of energy it absorbs before it fractures. The fracture toughness of LM26 Al alloy was high due to high plastic deformation. The fracture toughness decreased due to the presence of SPFA (SiO<sub>2</sub>, CaO, Fe<sub>2</sub>O<sub>3</sub>, and Al<sub>2</sub>O<sub>3</sub>), which led to a decrease in the plastic deformation energy

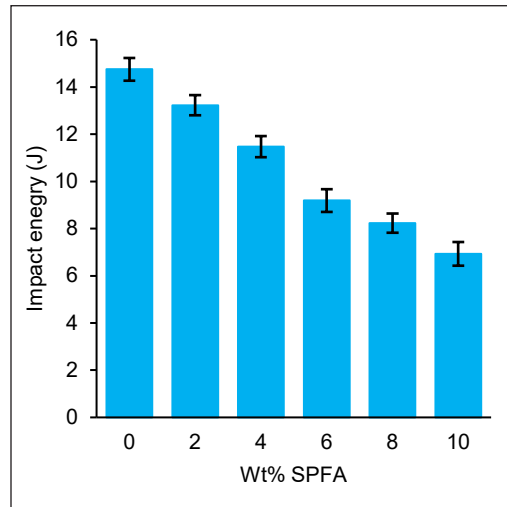


Figure 7. Variation of impact energy with SPFA for LM26 Al/SPFA composite aged for 5 h at 180°C

of the composites. A study by Kumar et al. (2018) reported a decrease in impact strength by incorporating coconut and zirconium oxide in Al 6082 base alloy.

### Microstructural Analysis of LM26 Alloy and LM26 Al/SPFA Composite

Figure 8 depicts the SEM morphology of (a) LM26 Al alloy, (b) LM26 Al/2 wt% SPFA, (c) LM26 Al/4 wt% SPFA, (d) LM26 Al/6 wt% SPFA, (e) LM26 Al/8 wt% SPFA, and (f) LM26 Al/10 wt% SPFA composites solutions at 500°C for 4 h, quenched in water, aged for 5 h at 180°C. The elements such as Al, Si, C, Mg, Fe, K, and O were identified in the elemental analysis of composites in Figure 8. Figure 8a shows the morphology of the alloy that consists of precipitates of intermetallic compounds formed due to aged hardening. The heat treatment transformed fibrous eutectic Si and Mg into fine spheroids uniformly distributed in the LM26 Al matrix. Fine globular eutectic Si and Mg particles were produced during heat treatment and could be seen in the alloy and composites (Figure 8a) (Yang et al., 2018).

Consequently, the heat treatment equally dissolved Mg<sub>2</sub>Si particles in the alloy and composites, leading to structural homogenization, fragmentation of Si particles, an increase in the number of Si particles, and coupling with SPFA particles, resulting in the composites being stronger compared to the corresponding fabricated alloy (Lakshmikanthan et al., 2020). SPFA particles were evenly dispersed in the LM26 Al matrix, as evidenced by all the micrographs (Figure 8 b–e). As shown in Figure 8(a–e) in the micrographs, the composites revealed excellent SPFA particle dispersion with no noticeable porosity or casting defects. However, in the case of the LM26 Al/10wt% SPFA composite, some agglomerates have

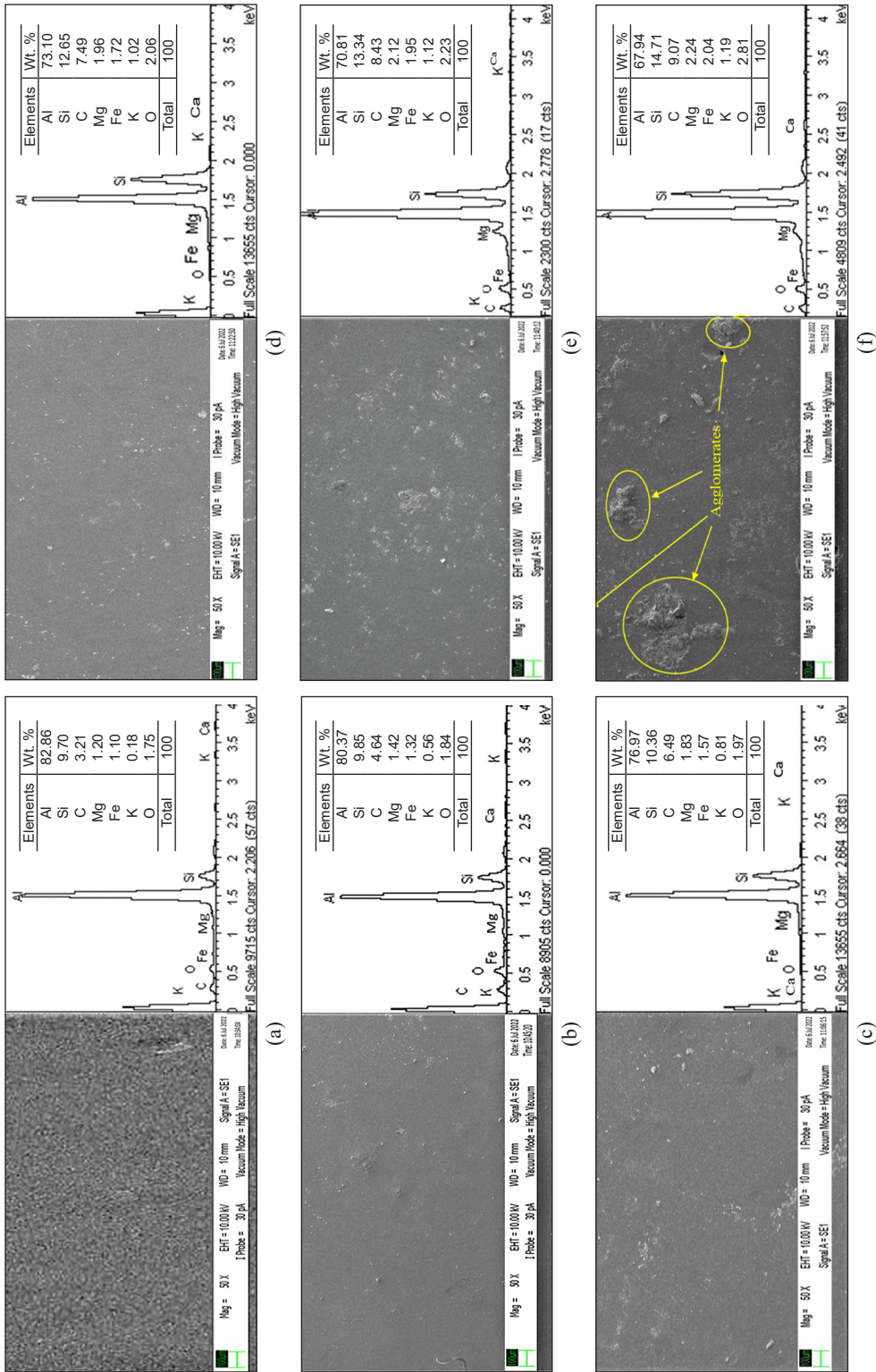


Figure 8. SEM morphology and EDS of age-hardened: (a) LM26 Al alloy, (b) LM26 Al/2 wt% SPFA, (c) LM26 Al/4 wt% SPFA, (d) LM26 Al/6 wt% SPFA, (e) LM26 Al/8 wt% SPFA and (f) LM26 Al/10 wt% SPFA aged for 5 h at 180°C

small SPFA (Figure 8f). SPFA particle agglomerate formation on a smaller scale was observed in a few spots in the LM26 Al/10wt% composite. Amongst all the composites, the overall dispersion of SPFA particles was reasonably uniform, with no notable casting defects such as porosity. The evenly distributed SPFA particles in the LM26 Al matrix alloy were due to the appropriate stir-casting parameters used during the composite fabrication.

### Differential Scanning Calorimeter (DSC)

The DSC thermogram was used to investigate the kinetics during precipitation or dissolution. In Al-Si-Mg alloys, supersaturated solid solution decomposed in the following order: From supersaturated solid solution  $\rightarrow$  Guinier-Preston (GP) zone (rich in Si)  $\rightarrow$   $\beta''$  precipitates  $\rightarrow$   $\beta'$  precipitates  $\rightarrow$   $\beta$  phase and Si particle (He et al., 2018; Rajasekaran et al., 2012; Xia et al., 2020). The DSC thermogram shown in Figure 9 depicted the thermal reactions of LM26 Al composites reinforced with 0, 2wt%, 8wt%, and 10wt% of SPFA at a heating rate of 10 °C/min from 500°C to 700°C in a vacuum with nitrogen gas flowing at a rate of 50 mL/min. The exothermic peaks that normally form indicating the formation of metastable GP zone after solution heat treatment and quenching, were completely absent. Between 550°C and 610°C, a series of endothermic peaks associated with  $\beta''$  and  $\beta'$  precipitates formation were observed from the DSC thermogram (Figure 9) for the samples. The similarities in the DSC curves that overlapped with SPFA addition implied that the precipitation sequence in the alloy was, to some extent, independent of the composition. The assertion was consistent with the  $\beta''$  precipitation formation findings of Fang et al. (2010).

As depicted in Figure 9, the endothermic peaks observed for the alloy and composites were temperature dependent, known as precipitation temperature, the transition temperature, and decreased with increasing percentage of SPFA addition (Table 2). A similar finding has been reported by Fröck et al. (2019). The area between the peaks in Figure 9, which decreased with an increase of SPFA (Table 2), represented the reaction enthalpy, which was proportional to the molar heat of the reaction and the volume fraction of the precipitating or dissolving phases. The corresponding precipitation temperatures were related to precipitate stability and reaction kinetics and decreased as SPFA increased (Table 2). From the DSC thermogram (Figure 9), it was observed that the  $\beta''$  and  $\beta'$  precipitate formation were lower in the composites compared to the matrix alloy. Adding SPFA into LM26 Al alloy decreased the temperature required to attain peak hardness. Therefore, the degree of accelerated precipitation kinetic of LM26 Al alloy was found as follows: LM26 Al + 10wt% SPFA > LM26 Al + 8wt% SPFA > LM26 Al + 2wt% SPFA > LM26 Al alloy. According to the DSC, adding SPFA particles as reinforcement improved aging kinetics, sped up phase transformation reaction, and acted as a seed for precipitation during the heat treatment process, resulting in significant alloy strengthening of the matrix material during the heat treatment process.

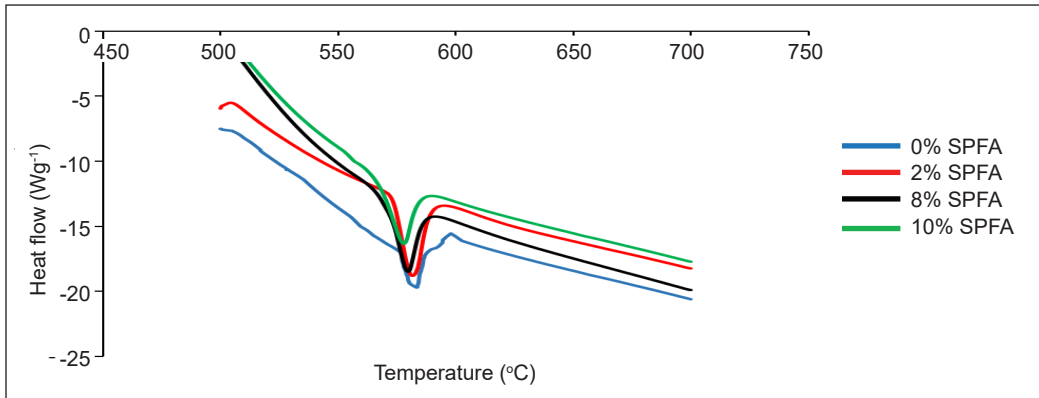


Figure 9. DSC thermogram of quenched LM26 Al matrix composite reinforced with 0, 2 wt%, 8 wt%, and 10 wt% SPFA

Table 2  
DSC characteristics of LM26 Al matrix and its composite reinforced with SPFA

SPFA Content (%)	Precipitation temperature (°C)	Peaks area (Jg <sup>-1</sup> )	Peak height (Wg <sup>-1</sup> )	Peak width (°C)
0	584.80	378.26	6.08	9.42
2	583.98	374.16	6.05	9.30
8	582.39	332.03	5.25	8.71
10	580.46	327.32	4.68	8.56

## CONCLUSION

Stir casting was used to fabricate SPFA successfully reinforced LM26 Al matrix composite, which was then solution heat treated and aged, and their mechanical properties and precipitation kinetics were studied. The most favorable heat treatment for LM26 Al/SPFA composites was the solution heat treated at 500°C for 4 h and aging treatment at 180°C for 5 h. The hardness of the LM26 Al/10 wt% SPFA composite (102.1 HV) increased by 80.07% after 5 h aging at 180 °C in compared to the LM26 Al alloy (56.7 HV). A peak tensile and compression strengths for LM26 Al/8 wt% SPFA composite of 198.21 MPa and 326.22 MPa, respectively was attained after aging at 180°C for 5 h compared to LM26 Al alloy corresponding to 145.46 MPa and 262.31 MPa. The impact energy of the LM26 Al alloy (14.75 J) dropped by 112.84% after 5 h aging at 180°C compared to the impact energy of the LM26 Al/10 wt% composite (6.93 J). The SEM morphology reveals uniform dispersion of SPFA in LM26 Al matrix composite, formation of precipitates after aging, and agglomerate formed is evidenced at a high loading of 10 wt% SPFA. The precipitate formed in the LM26 Al matrix was faster with increasing SPFA addition and occurred at a lower temperature. The precipitate formed after age-hardening was a major contributing factor leading to increased hardness of the aged composite compared to the as-cast composite.

## ACKNOWLEDGEMENT

The authors thank Universiti Putra Malaysia, Malaysia, and Waziri Umaru Federal Polytechnic in Birnin Kebbi, Nigeria. This research was supported financially by Universiti Putra Malaysia (GP/IPS/2021/9697100 and GP/IPS/2021/9702700).

## REFERENCES

- Al-Salihi, H. A., & Judran, H. K. (2020). Effect of Al<sub>2</sub>O<sub>3</sub> reinforcement nanoparticles on the tribological behaviour and mechanical properties of Al6061 alloy. *Materials Science*, 7(4), 486-498. <https://doi.org/10.3934/materci.2020.4.486>
- Arunachalam, R., Piya, S., Krishnan, P. K., Muraliraja, R., Christy, J. V., Mourad, A. I., & Al-Maharbi, M. (2019). Optimization of stir – squeeze casting parameters for production of metal matrix composites using a hybrid analytical hierarchy process - Taguchi-Grey approach. *Engineering Optimization*, 52(7), 1166-1183. <https://doi.org/10.1080/0305215X.2019.1639693>
- ASTM International. (2017). *Standard Test Method for Microindentation Hardness of Materials* (ASTM Standard Version E384-05A). <https://doi.org/10.1520/E0384-05A>
- ASTM International. (2015a). *Standard Test Methods for Tension Testing of Metallic Materials* (ASTM Standard Version E8/E8M- 13A). [https://doi.org/10.1520/E0008\\_E0008M-13A](https://doi.org/10.1520/E0008_E0008M-13A)
- ASTM International (2015b). *Standard Practice for Microetching Metals and Alloys* (ASTM Standard Version E384-05). <https://webstore.ansi.org/standards/astm/astme38405>
- ASTM International. (2023). *Standard Test Methods for Notched Bar Impact Testing of Metallic materials* (ASTM Standard Version E23-18). <https://doi.org/10.1520/E0023-18>
- Babu, P. M., Rajamuneeswaran, S., Pritima, D., Marichamy, S., & Vairamuthu, J. (2020). Spark erosion machining behaviour of coconut shell ash reinforced silicon metal matrix. *Materials Today: Proceedings*, 33, 4602-4604. <https://doi.org/10.1016/j.matpr.2020.08.195>
- Bawa, M. A., Umaru, O. B., Abur, B. T., Salako, I., & Jatau, J. S. (2020). Effect of locust bean pod ash on the hardness and wear rate of heat treated A356 alloy metal matrix composite for production of automobile brake rotor. *International Journal of Research Publication (IJRP.ORG)*, 57(1), 36-43. <https://doi.org/10.47119/IJRP100571720201325>
- Bushlya, V., Lenrick, F., Gutnichenko, O., Petruska, I., Osipov, O., Kristiansson, S., & Stahl, J.-E. (2017). Performance and wear mechanisms of novel superhard diamond and boron nitride based tools in machining Al-SiCp metal matrix composite. *Wear*, 376-377, 152-164. <https://doi.org/10.1016/j.wear.2017.01.036>
- Chak, V., Chattopadhyay, H., & Kumar, A. (2020). Synthesis , characterization and deformation of Al - 4.5Cu / SiCp composites. *Materials Today: Proceedings*, 26, 2833-2838. <https://doi.org/10.1016/j.matpr.2020.02.590>
- Chauhan, A., Vates, U. K., Kanu, J. N., Gupta, E., Singh, G. K., Sharma, B. P., & Gorrepati, S. R. (2021). Fabrication and characterization of novel nitinol particulate reinforced aluminium alloy metal matrix composites (NiTip/AA6061 MMCs). *Materials Today: Proceedings*, 38, 3027-3034. <https://doi.org/10.1016/j.matpr.2020.09.326>

- Das, D., Roy, D. K., Satpathy, M. P., Nanda, B. K., & Nayak, R. K. (2019). Compressive, impact and flexural behaviour of Al based metal matrix composites. *Materials Today: Proceedings*, 18(7), 3080-3086. <https://doi.org/10.1016/j.matpr.2019.07.180>
- Edhirej, A., Sapuan, S. M., Jawaid, M., & Zahari, N. I. (2017). Cassava / sugar palm fiber reinforced cassava starch hybrid composites : Physical , thermal and structural properties. *International Journal of Biological Macromolecules*, 101, 75-83. <https://doi.org/10.1016/j.ijbiomac.2017.03.045>
- Fang, X., Song, M., Li, K., & Du, Y. (2010). Precipitation sequence of an aged Al-Mg-Si alloy. *Journal of Mining and Metallurgy, Section B: Metallurgy*, 46(2), 171-180. <https://doi.org/10.2298/JMMB1002171F>
- Flanagan, S., Main, J., Lynch, P., Vanderwiel, C., & Roth, J. T. (2019). A mechanical evaluation of an overaged overaged aluminum metal-matrix-composite (2009 Al/SiC/15p MMC). *Procedia Manufacturing*, 34, 58-64. <https://doi.org/10.1016/j.promfg.2019.06.117>
- Fröck, H., Reich, M., & Milkereit, B. (2019). Scanning rate extension of conventional DSCs through indirect measurements. *Materials*, 12(7), Article 1085. <https://doi.org/10.3390/ma12071085>
- Geetha, B., & Ganesan, K. (2015). The effects of ageing temperature and time on mechanical properties of A356 aluminium cast alloy with red mud addition and treated by T6 heat treatment. *Materials Today: Proceedings*, 2(4-5), 1200-1209. <https://doi.org/10.1016/j.matpr.2015.07.032>
- Goudar, D. M., Srivastava, V. C., & Rudrakshi, G. B. (2018). Microstructure and mechanical properties of spray formed and hot pressed / heat treated Al- ( 20-30 wt %) Mg<sub>2</sub>Si-2 % Cu Alloy. *Research & Reviews: Journal of Material Sciences*, 6(1), 10-22. <https://doi.org/10.4172/2321-6212.1000211>
- Harussani, M. M., & Sapuan, S. M. (2022). Tensile and flexural properties of compression molded composites of epoxy reinforced with treated sugar palm fibre. *Journal of Natural Fibre Polymer Composites (JNFPC)*, 1(2), 1-13.
- Hashim, J., Looney, L., & Hashmi, M. S. J. (1999). Metal matrix composites: production by the stir casting method. *Journal of materials processing technology*, 92, 1-7. [https://doi.org/10.1016/S0924-0136\(99\)00118-1](https://doi.org/10.1016/S0924-0136(99)00118-1)
- He, H., Zhang, L., Li, S., Wu, X., Zhang, H., & Li, L. (2018). Precipitation stages and reaction kinetics of AlMgSi alloys during the artificial aging process monitored. *Metals*, 8(1), Article 39. <https://doi.org/10.3390/met8010039>
- Hiremath, A., & Hemanth, J. (2018). An exploratory study to evaluate the thermal conductivity of LM25-borosilicate glass (P) composites under the influence of different end chills. *Pertanika Journal of Science & Technology*, 26(4), 1837-1848.
- Ikubanni, P., Oki, M., Adeleke, A., Omoniyi, P., Ajisegiri, E., & Akinlabi, E. (2022). Physico-mechanical properties and microstructure response of hybrid reinforced Al6063 composites to PKSA/SiC Inclusion. *ACTA Metallurgica Slovaca*, 28(1), 25-32. <https://doi.org/10.36547/ams.28.1.1340>
- Ikumapayi, O. M., Afolalu, S. A., Bodunde, O. P., Ugwuoke, C. P., Benjamin, H. A., & Akinlabi, E. T. (2022). Efficacy of heat treatment on the material properties of aluminium alloy matrix composite impregnated with silver nano particle/calcium carbonate Al. *International Journal of Advanced Technology and Engineering Exploration*, 9(89), 523-535. <https://doi.org/10.19101/IJATEE.2021.874829>

- Ilyas, R. A., Sapuan, S. M., & Ishak, M. R. (2018). Isolation and characterization of nanocrystalline cellulose from sugar palm fibres (Arenga Pinnata). *Carbohydrate Polymers*, *181*, 1038-1051. <https://doi.org/10.1016/j.carbpol.2017.11.045>
- Ishak, M. R., Leman, Z., Sapuan, S. M., Rahman, M. Z. A., & Anwar, U. M. K. (2013). Impregnation modification of sugar palm fibres with phenol formaldehyde and unsaturated polyester. *Fibers and Polymers*, *14*(2), 250-257. <https://doi.org/10.1007/s12221-013-0250-0>
- Ishak, M. R., Sapuan, S. M., Leman, Z., Rahman, M. Z. A., Anwar, U. M. K., & Siregar, J. P. (2013). Sugar palm (Arenga pinnata): Its fibres, polymers and composites. *Carbohydrate Polymers*, *91*(2), 699-710. <https://doi.org/10.1016/j.carbpol.2012.07.073>
- Iyasele, E. O. (2018). Comparative analysis on the mechanical properties of a Metal-Matrix Composite (MMC) reinforced with palm kernel/periwinkle shell ash. *Global Scientific Journals*, *6*(8), 1-24.
- Kawin, N., Jagadeesh, D., Saravanan, G., & Periasamy, K. (2020). Optimization of turning parameters in sugarcane bagasse ash reinforced with Al-Si10-Mg alloy composites by Taguchi method. *Materials Today: Proceedings*, *21*, 474-476. <https://doi.org/10.1016/j.matpr.2019.06.634>
- Kennedy, Z. E., & Raja, A. I. (2022). Evaluation of mechanical properties of Al-B<sub>4</sub>C and Al-SiC metal matrix composites - A comparison. *Materials Today: Proceedings*, *55*, 380-383. <https://doi.org/10.1016/j.matpr.2021.08.356>
- Khan, A. H., Shah, S. A. A., Umar, F., Noor, U., Gul, R. M., Giasin, K., & Aamir, M. (2022). Investigating the microstructural and mechanical properties of novel ternary reinforced AA7075 hybrid metal matrix composite. *Materials*, *15*(15), Article 5303. <https://doi.org/10.3390/ma15155303>
- Kondoh, K., Kawakami, M., Imai, H., Umeda, J., & Fujii, H. (2010). Wettability of pure Ti by molten pure Mg droplets. *Acta Materialia*, *58*(2), 606-614. <https://doi.org/10.1016/j.actamat.2009.09.039>
- Kumar, K. R., Pridhar, T., & Balaji, V. S. S. (2018). Mechanical properties and characterization of zirconium oxide (ZrO<sub>2</sub>) and coconut shell ash (CSA) reinforced aluminium (Al6082) matrix hybrid composite. *Journal of Alloys and Compounds*, *765*, 171-179. <https://doi.org/10.1016/j.jallcom.2018.06.177>
- Lakshmikanthan, A., Prabhu, T. R., Babu, U. S., Koppad, P. G., Gupta, M., Krishna, M., & Bontha, S. (2020). The effect of heat treatment on the mechanical and tribological properties of dual size SiC reinforced A357 matrix composites. *Journal of Materials Research and Technology*, *9*(3), 6434-6452. <https://doi.org/10.1016/j.jmrt.2020.04.027>
- Li, N., Yan, H., & Wang, Z. W. (2018). Effects of heat treatment on the tribological properties of SiCp/Al-5Si-1Cu-0.5Mg composite processed by electromagnetic stirring method. *Applied Sciences*, *8*(3), Article 372. <https://doi.org/10.3390/app8030372>
- Lokesh, G. N., Prashanth, K. P., Prasad, G. P., & Venkatesha, B. K. (2022). Mechanical and microstructure evaluation of stir cast Al-4.5%Cu alloy reinforced fly ash/boron carbide hybrid metal matrix composites. *Materials Today: Proceedings*, *54*, 486-491. <https://doi.org/10.1016/j.matpr.2021.11.131>
- Mabuwa, S., Msomi, V., Ndube-Tsolekile, N., & Zungu, V. M. (2022). Status and progress on fabricating automotive-based aluminium metal matrix composites using FSP technique. *Materials Today: Proceedings*, *56*, 1648-1652. <https://doi.org/10.1016/j.matpr.2021.10.179>

- Manda, C. S., Babu, B. S., & Ramaniah, N. (2021). Effect of heat treatment on mechanical properties of aluminium metal matrix composite (AA6061/MoS<sub>2</sub>). *Advances in Materials and Processing Technologies*, 8, 205-222. <https://doi.org/10.1080/2374068X.2020.1860593>
- Manikandan, R., & Arjunan, T. V. (2019). Microstructure and mechanical characteristics of CDA-B4C hybrid metal matrix composites. *Metals and Materials International*, 27, 885-899. <https://doi.org/10.1007/s12540-019-00518-6>
- Mistry, J. M., & Gohil, P. P. (2019). Experimental investigations on wear and friction behaviour of Si<sub>3</sub>N<sub>4</sub>p reinforced heat-treated aluminium matrix composites produced using electromagnetic stir casting process. *Composites Part B: Engineering*, 161, 190-204. <https://doi.org/10.1016/j.compositesb.2018.10.074>
- Morampudi, P., Ramana, V. S. N. V., Bhavani, K., Reddy, C. K., & Vikas, K. S. R. (2022). Wear and corrosion behavior of AA6061 metal matrix composites with ilmenite as reinforcement. *Materials Today: Proceedings*, 52, 1515-1520. <https://doi.org/10.1016/j.matpr.2021.11.228>
- Nagaraja, S., Kodandappa, R., Ansari, K., Kuruniyan, M. S., Afzal, A., Kaladgi, A. A., Asliffattahi, N., Saleel, C. A., Gowda, A. C., & Anand, P. B. (2021). Influence of heat treatment and reinforcements on tensile. *Materials*, 14(18), Article 5261. <https://doi.org/10.3390/ma14185261>
- Nambiar, S., Adhikari, R., Upadhy, N., & Hande, R. (2020). Study on progressive wear of machine reamer while reaming Al6061/SiC Composite. *Pertanika Journal of Science & Technology*, 28(1), 403-420.
- Natrayan, L., Singh, M., & Kumar, M. S. (2017). An experimental investigation on mechanical behaviour of SiCp reinforced Al 6061 MMC using squeeze casting process. *International Journal of Mechanical and Production Engineering Research and Development*, 7(6), 663-668. <https://doi.org/10.24247/ijmperdddec201774>
- Olaniran, O., Uwaifo, O., Bamidele, E., & Olaniran, B. (2019). An investigation of the mechanical properties of organic silica, bamboo leaf ash and rice husk reinforced aluminium hybrid composite. *Material Science & Engineering International Journal*, 3(4), 129-134. <https://doi.org/10.15406/mseij.2019.03.00103>
- Olusesi, O. S., & Udoye, N. E. (2021). Development and characterization of AA6061 aluminium alloy/clay and rice husk ash composite. *Manufacturing Letters*, 29, 34-41. <https://doi.org/10.1016/j.mfglet.2021.05.006>
- Pasha, S. K., Sharma, A., & Tambe, P. (2022). Mechanical properties and tribological behavior of Al7075 metal matrix composites : A review. *Materials Today: Proceedings*, 56, 1513-1521. <https://doi.org/10.1016/j.matpr.2022.01.102>
- Patel, M., Sahu, S. K., Singh, M. K., & Dalai, N. (2022). Micro-structural and mechanical characterization of stir cast AA5052/B4C metal matrix composite. *Materials Today Proceedings*, 56, 1129-1136. <https://doi.org/10.1016/j.matpr.2021.10.331>
- Pasupulla, A. P., Amornphimoltham, P., Charles, P., Sundaram, V. S., & Ramakrishna, M. M. (2022). Taguchi L16 orthogonal array analysis on wear rate parameters for aluminum related hybrid composites. *Materials Today: Proceedings*, 62, 1692-1696. <https://doi.org/10.1016/j.matpr.2021.11.435>
- Rajaram, S., Subbiah, T., Mahali, P. K., & Thangara, M. (2022). Effect of age-hardening temperature on mechanical and wear behavior of furnace-cooled al7075-Tungsten Carbide compositer. *Materials*, 15(15), Article 5344. <https://doi.org/10.3390/ma15155344>
- Rajasekaran, S., Udayashankar, N. K., & Nayak, J. (2012). T4 and T6 Treatment of 6061 Al-15 Vol.% SiCP Composite. *ISRN Materials Science*, 2012, Article 374719. <https://doi.org/10.5402/2012/374719>



- Ramasamy, M., Daniel, A. A., & Nithya, M. (2021). Investigation on surface roughness of aluminium (Al7050/TiC/BN) hybrid metal matrix. *Materials Today: Proceedings*, 46, 852-856. <https://doi.org/10.1016/j.matpr.2020.12.852>
- Sabry, I., Ghafaar, M. A., Hamid, A., Mourad, I., & Idrisi, A. H. (2020). Stir casted SiC-Gr/Al6061 hybrid composite tribological and mechanical properties. *SN Applied Sciences*, 2, Article 943. <https://doi.org/10.1007/s42452-020-2713-4>
- Sajjadi, S. A., Ezatpour, H. R., & Beygi, H. (2011). Microstructure and mechanical properties of Al-Al<sub>2</sub>O<sub>3</sub> micro and nano composites fabricated by stir casting. *Materials Science and Engineering A*, 528(29-30), 8765-8771. <https://doi.org/10.1016/j.msea.2011.08.052>
- Sam, M., Radhika, N., & Sai, K. P. (2020). Effect of heat treatment on mechanical and tribological properties of aluminum metal matrix composites. *Proceedings of the Institution of Mechanical Engineers, Part C: Journal of Mechanical Engineering Science*, 234(22), 4493-4504. <https://doi.org/10.1177/0954406220922253>
- Samal, P., Vundavilli, P. R., Meher, A., & Mahapatra, M. M. (2020). Recent progress in aluminum metal matrix composites: A review on processing, mechanical and wear properties. *Journal of Manufacturing Processes*, 59, 131-152. <https://doi.org/10.1016/j.jmapro.2020.09.010>
- Seetharaman, S., Subramanian, J., Singh, R. A., Wong, W. L. E., Nai, M. L. S., & Gupta, M. (2022). Mechanical properties of sustainable metal matrix composites : A review on the role of green reinforcements and processing methods. *Technologies*, 10, Article 32.
- Shaikh, M. B. N., Arif, S., Aziz, T., Waseem, A., Shaikh, M. A. N., & Ali, M. (2019). Microstructural, mechanical and tribological behaviour of powder metallurgy processed SiC and RHA reinforced Al-based composites. *Surfaces and Interfaces*, 15, 166-179. <https://doi.org/10.1016/j.surfin.2019.03.002>
- Sharma, S., Nanda, T., & Pandey, O. P. (2019). Investigation of T4 and T6 heat treatment on the wear properties of sillimanite reinforced LM30 aluminium alloy composites. *Wear*, 426-427, 27-36. <https://doi.org/10.1016/j.wear.2018.12.065>
- Singh, B., Grewal, J. S., & Sharma, S. (2022). Effect of addition of flyash and graphite on the mechanical properties of A6061-T6. *Materials Today: Proceedings*, 50, 2411-2415. <https://doi.org/10.1016/j.matpr.2021.10.258>
- Singh, G., & Sharma, N. (2021). Study on the influence of T4 and T6 heat treatment on the wear behavior of coarse and fine WC particulate reinforced LM28 Aluminium cast composites. *Composites Part C: Open Access*, 4, Article 100106. <https://doi.org/10.1016/j.jcomc.2021.100106>
- Singh, K., Singh, H., Vardhan, S., & Mohan, S. (2022). An overview on the synthesis of aluminium matrix composites using stir casting technique. *Materials Today: Proceedings*, 60, 868-872. <https://doi.org/10.1016/j.matpr.2021.09.509>
- Singh, P., Gupta, R., Izan, S., Singh, S., Sharma, R., & Dwivedi, S. P. (2021). Tribo-mechanical behaviour of aluminium-based metal matrix composite: A review. *Materials Today: Proceedings*, 47, 3828-3832. <https://doi.org/10.1016/j.matpr.2021.03.092>
- Singh, V. K., Chauhan, S., Gope, P. C., & Chaudhary, A. K. (2015). Enhancement of wettability of aluminum based silicon carbide reinforced particulate metal matrix composite. *High Temperature Materials and Processes*, 34(2), 163-170. <https://doi.org/10.1515/htmp-2014-0043>

- Somashekhar, P. H., Sharma, K. V., & Girisha, H. N. (2018). Effect of heat treatment on tensile and hardness properties of Aluminium-7075 alloy reinforced with graphite and bagasse-ash composites. *IOSR Journal of Engineering*, 8(8), 38-43.
- Reddy, K. S. K., Kannan, M., Karthikeyan, R., Prashanth, S., & Reddy, B. R. (2020). A review on mechanical and thermal properties of aluminum metal matrix composites. *E3S Web of Conferences*, 184, Article 01033. <https://doi.org/10.1051/e3sconf/202018401033>
- Tiwari, K. S., Soni, S., Rana, R. S., & Singh, A. (2017). Effect of aging on mechanical behaviour of ADC12-fly ash particulate composite. *Material Today: Proceedings*, 4(2), 3513-3524. <https://doi.org/10.1016/j.matpr.2017.02.242>
- Varalakshmi, K., Kumar, K. C. K., Babu, P. R., & Sastry, M. R. C. (2019). Characterization of Al 6061-coconut Shell ash metal matrix composites using stir casting. *International Journal of Latest Engineering Science (IJLES)*, 2(3), 41-49. <http://ijlesjournal.org/2019/volume-2%20issue-3/ijles-v2i3p106.pdf>
- Velavan, K., Palanikumar, K., Natarajan, E., & Hong, W. (2020). Implications on the influence of mica on the mechanical properties of cast hybrid (Al+10%B4C+Mica) metal matrix composite. *Journal of Materials Research and Technology*, 10, 99-109. <https://doi.org/10.1016/j.jmrt.2020.12.004>
- Vencl, A., Bobic, I., Arostegui, S., Bobic, B., Marinković, A., & Babić, M. (2010). Structural, mechanical and tribological properties of A356 aluminium alloy reinforced with Al<sub>2</sub>O<sub>3</sub>, SiC and SiC+ graphite particles. *Journal of Alloys and Compounds*, 506(2), 631-639. <https://doi.org/10.1016/j.jallcom.2010.07.028>
- Venkatesh, L., Arjunan, T. V., & Ravikumar, K. (2019). Microstructural characteristics and mechanical behaviour of aluminium hybrid composites reinforced with groundnut shell ash and B4C. *Journal of the Brazilian Society of Mechanical Sciences and Engineering*, 41, Article 295. <https://doi.org/10.1007/s40430-019-1800-1>
- Xia, X., Zhao, Q., Peng, Y., Zhang, P., Liu, L., Ding, J., Luo, X., Huang, L., Zhang, H., & Chen, X. (2020). Precipitation behavior and mechanical performances of A356.2 alloy treated by Al-Sr-La composite refinement-modification agent. *Journal of Alloys and Compounds*, 818, Article 153370. <https://doi.org/10.1016/j.jallcom.2019.153370>
- Yang, K. V., Rometsch, P., Davies, C. H. J., Huang, A., & Wu, X. (2018). Effect of heat treatment on the microstructure and anisotropy in mechanical properties of A357 alloy produced by selective laser melting. *Materials & Design*, 154, 275-290. <https://doi.org/10.1016/j.matdes.2018.05.026>
- Yashpal, Sumankant, Jawalkar, C. S., Verma, A. S., & Suri, N. M. (2017). Fabrication of aluminium metal matrix composites with particulate reinforcement: A review. *Materials Today: Proceedings*, 4(2), 2927-2936. <https://doi.org/10.1016/j.matpr.2017.02.174>
- Yuan, D., Yang, X., Wu, S., Lü, S., & Hu, K. (2019). Development of high strength and toughness nano-SiCp/A356 composites with ultrasonic vibration and squeeze casting. *Journal of Materials Processing Technology*, 269, 1-9. <https://doi.org/10.1016/j.jmatprotec.2019.01.021>
- Yuan, Q., Fu, D., Zeng, X., & Liu, Y. (2017). Fabrication of carbon nanotube reinforced AZ91D composite with superior mechanical properties. *Transactions of Nonferrous Metals Society of China*, 27(8), 1716-1724. [https://doi.org/10.1016/S1003-6326\(17\)60194-8](https://doi.org/10.1016/S1003-6326(17)60194-8)

## Development of a Web-based Application by Employing a Convolutional Neural Network (CNN) to Identify Pests and Diseases on Pakcoy (*Brassica rapa* subsp. *chinensis*)

Achmad Zein Feroza<sup>1</sup>, Nelly Oktavia Adiwijaya<sup>1</sup> and Bayu Taruna Widjaja Putra<sup>2,3\*</sup>

<sup>1</sup>Department of Information Systems Faculty of Computer Science, Jember University, Jember, 68121 Indonesia

<sup>2</sup>Center of Excellence on Artificial Intelligence for Industrial Agriculture, Jember University, Jember, 68121 Indonesia

<sup>3</sup>Laboratory of Precision Agriculture and Geo-informatics, Faculty of Agricultural Technology, Jember University, Jember, 68121 Indonesia

### ABSTRACT

The development of Pakcoy cultivation holds good prospects, as seen from the demand for vegetable commodities in Indonesia. Its cultivation is consistently rising in terms of volume and value of vegetable imports. However, the cultivation process encounters multiple issues caused by pests and diseases. In addition, the volatile climate in Indonesia has resulted in uninterrupted pest development and the potential decline of Pakcoy's productivity. Therefore, the detection system for pests and diseases in the Pakcoy plant is called upon to accurately and quickly assist farmers in determining the right treatment, thereby reducing economic losses and producing abundant quality crops. A web-based application with several well-known Convolutional Neural Network (CNN) were incorporated, such as MobileNetV2, GoogLeNet, and ResNet101. A total of 1,226 images were used for training, validating, and testing the dataset to address the problem in this study. The dataset consisted of several plant conditions with leaf miners, cabbage butterflies, powdery mildew disease, healthy plants, and multiple data labels for pests and diseases presented in the individual image.

The results show that the MobileNetV2 provides a minimum loss compared to GoogLeNet and ResNet-101 with scores of 0.076, 0.239, and 0.209, respectively. Since the MobileNetV2 architecture provides a good model, the model was carried out to be integrated and tested with the web-based application. The testing accuracy rate reached 98% from the total dataset of

### ARTICLE INFO

#### Article history:

Received: 25 October 2022

Accepted: 14 March 2023

Published: 03 October 2023

DOI: <https://doi.org/10.47836/pjst.31.6.13>

#### E-mail addresses:

[feroza.az@mail.unej.ac.id](mailto:feroza.az@mail.unej.ac.id) (Achmad Zein Feroza)

[nelly.oa@unej.ac.id](mailto:nelly.oa@unej.ac.id) (Nelly Oktavia Adiwijaya)

[bayu@unej.ac.id](mailto:bayu@unej.ac.id) (Bayu Taruna Widjaja Putra)

\* Corresponding author

70 testing images. In this direction, MobileNetV2 can be a viable method to be integrated with web-based applications for classifying an image as the basis for decision-making.

*Keywords:* Deep learning, disease, MobileNetV2, pest, precision agriculture

---

## INTRODUCTION

Pakcoy (*Brassica rapa* subsp. *chinensis*) is a leaf vegetable from China usually used for diet remedies (Li et al., 2022). It is cultivated and consumed worldwide due to edible leaves containing complete nutrients, making it a decent option for maintaining a healthy body. The development of Pakcoy cultivation holds good prospects, considering improved community nutrition, expanded job opportunities, developed agribusiness, and higher state income by escalating export growth.

Pakcoy is easy to grow and has good prospects for increasing farmers' income and community health. However, its cultivation encounters a number of issues caused by pests and diseases. The climate in Indonesia, with frequent changes, leads to the massive growth of pests and diseases (Nair, 2000). This circumstance potentially reduces Pakcoy's productivity and even causes crop failure. To that end, accurate and immediate detection of crop pests and diseases can help farmers determine the proper treatment, thereby reducing economic losses and producing abundant quality crops (Rahman et al., 2020).

To properly treat plants, a technology that can provide early warning and recommendations is needed by utilizing artificial intelligence. Previous studies report the extensive use of artificial neural network (ANN) methods for plant classification (Griffel et al., 2023; Sai et al., 2022). This method is known to be substantially faster, which is why it gains popularity among farmers. However, it may not be sufficiently potent in determining the number of hidden layers, particularly as it takes copious epoch parameters and requires high-performance computations (Putra, Wirayuda et al., 2022). Many methods can perform image processing, including the Convolutional Neural Network (CNN) (Putra, Amirudin, et al., 2022; Sujatha et al., 2021). This method has the ability to process visual information by imitating the image recognition system in the visual cortex in humans. Previous studies on image processing using the CNN method have reported decent accuracy. Studies by Kamal et al. (2019) and Rahman et al. (2020), who investigate disease detection, provide a system accuracy of 93% and 98.34%, respectively.

A previous study has documented that the CNN method has gained traction in identifying plant diseases (Rahman et al., 2020) by using lightweight architecture such as MobileNet, NasNet Mobile, and SqueezeNet, which can achieve an accuracy of 93.3% with lightweight model size. A similar study has also been conducted by Esgario et al. (2022) on identifying pests and diseases of coffee plants. The developed system has managed to attain an accuracy rate of 97%.

Another study employing CNN to detect plant diseases has also been carried out by Kamal et al. (2019). This study aims to identify a model with the best depth-wise separable technique to identify plant pests and diseases. The dataset encompasses 82,161 images and 55 classes of healthy as well as diseased plants. The result has found that the MobileNet architectural model offers a better accuracy rate at 98.34% compared to the VGG model. The research above has demonstrated that the CNN method can accurately identify pests and diseases in plants, even significantly better than other methods.

Several studies (Chen et al., 2021; Kumi et al., 2022) develop and evaluate the models to produce the best accuracy. MobileNet architecture seems affordable and lightweight to be implemented in smartphones rather than in other architectures. However, in this study, the development of a relational database management system was also incorporated. This study aims to a) compare the performance of several well-known CNN architectures to address the issues of pest and disease detection; b) Develop a web-based application and deploy the best CNN to classify images and aid in decision-making to help farmers surmount pest and disease problems in Pakcoy.

## MATERIAL AND METHODS

### Dataset

The dataset in this study consisted of multiple images containing information about pests and diseases in Pakcoy. The dataset was obtained from the Kaggle platform, which provided various datasets used for further research by data scientists. The dataset consists of 3 pests and diseases on Pakcoy, including cabbage butterfly, leaf miner, and powdery mildew. The Kaggle data set involved 1,793 images of cabbage butterflies, 333 images of leaf miner pests, and 752 images of powdery mildew. The dataset on Pakcoy was derived from Kaggle along with a label on each image using a CSV file (<https://www.kaggle.com/giane901/chinese-cabbage-disease-detection>). The data were double-checked to re-identify disease availability in each image and store the type of pests and/or disease information. The labeling employed multiple dataset labels, meaning one dataset image could contain more than one infected pest and disease. However, another class, namely the healthy class, was added and collected from local farmers for this purpose. A balanced dataset of four different classes of pest and diseases are required. Thus, 1156 images were used for training and testing for model development. The proposed architectures, namely MobileNetV2, ResNet-101, and GoogLeNet, were carried out using 894 training images and 262 validation images to determine the level of loss function or cost function generated. In addition, 70 images were collected separately from local farmers and unused Kaggle data for model evaluation along with web-based development and implementation.

## Models

**Convolutional Neural Network.** Convolutional Neural Network or CNN is a neural network method in deep learning commonly used for image data (Hendrawan et al., 2022; Koklu et al., 2021). This method can be used to recognize and classify the objects in an image. It integrates several neurons with weight values, activation functions, and bias values almost similar to normal neural networks. Figure 1 shows the base architecture of the CNN.

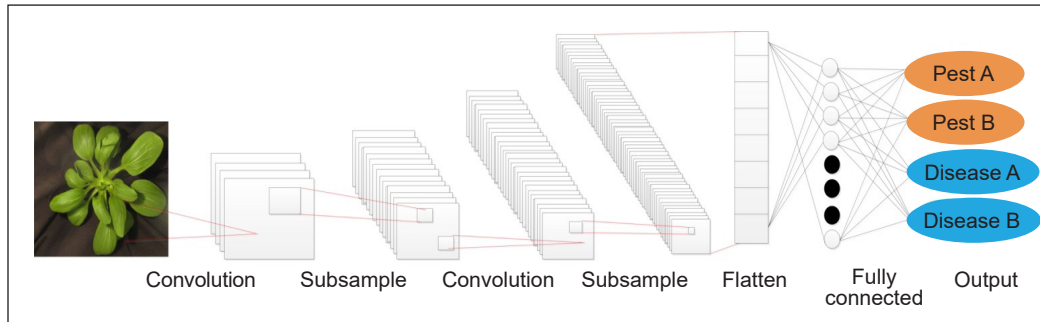


Figure 1. Convolutional neural network

The input layer is the image data input converted into a 3-dimensional matrix with an individual value of each dimension: red, blue, and green. The data are entered at the convolution layer stage, where calculations will occur between the previous layers. As the kernel matrix has been initialized prior to training, the calculation of the number of kernels depends on the number of features generated. Afterward, the rectified linear unit (ReLU) is operative for the activation function. After the activation function, the pooling process will take place. This process is repeated several times until a sufficient feature map is obtained before initiating a fully connected neural network.

**MobileNet V2.** MobileNetV2 is a convolutional neural network (CNN) architecture used to overcome the need for excessive computing resources (Sandler et al., 2018; Sutaji & Yıldız, 2022). In general, the basic difference between MobileNetV2 architecture and CNN architecture is the use of a convolution layer with a filter thickness corresponding to the thickness of the input image. MobileNetV2 divides convolution into depthwise convolution and pointwise convolution. The MobileNetV2 architecture uses the ReLU6 activation function (Figure 2).

Depthwise separable convolution is a block in deep learning consisting of depthwise and pointwise convolution. This depthwise separable convolution layer reduces complexity and parameters upon generating a smaller model (Howard et al., 2017; Kamal et al., 2019). Depthwise convolution is the result of factorization of standard convolution of a number of inputs, and it is capable of individual channel processing. What follows is the

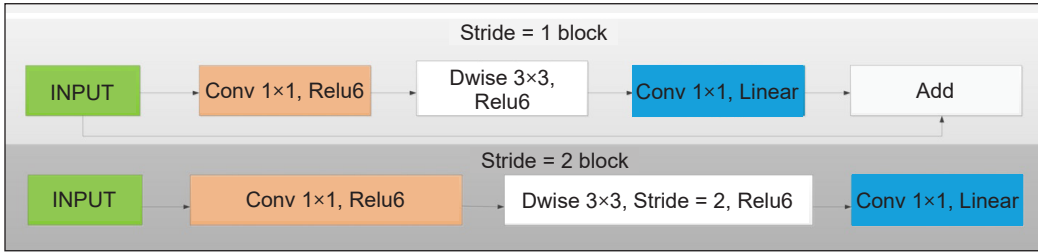


Figure 2. MobileNet V2 architecture

comparison of the total operating costs between depthwise separable convolution and standard convolution. The total cost calculation of standard convolution is formulated as Equation 1.

$$Z_k \cdot Z_k \cdot A \cdot B \cdot Z_f \cdot Z_f \tag{1}$$

By contrast, that of depthwise separable convolution employs the Equation 2

$$Z_k \cdot Z_k \cdot A \cdot Z_f \cdot Z_f + A \cdot B \cdot Z_f \cdot Z_f \tag{2}$$

$Z_k$  denotes the size or dimension of the kernel,  $A$  represents the number of input channels,  $B$  corresponds to the number of output channels, and  $Z_f$  is the size of the feature or filter. As for standard convolution, the computational cost employs the following Equation 3.

$$\frac{Z_k \cdot Z_k \cdot A \cdot Z_f \cdot Z_f + A \cdot B \cdot Z_f \cdot Z_f}{Z_k \cdot Z_k \cdot A \cdot Z_f \cdot Z_f} = \frac{1}{B} + \frac{1}{Z_k^2} \tag{3}$$

Equation 3 implies that a  $3 \times 3$  kernel reduces computation by 8 or 9 times (Howard et al., 2017; Kamal et al., 2019).

After the dataset had gone through data labeling and augmentation, a pre-trained model of the MobileNetV2 architecture was prototyped. Each image data followed the MobileNetV2 architecture (Sandler et al., 2018) and performed convolution according to the architecture (Table 1).

Table 1  
MobileNetV2 architecture

Input	Operator	Expansion factor	Output channels	Number of repeat	Stride
$224^2 \times 3$	conv2d	-	32	1	2
$112^2 \times 32$	bottleneck	1	16	1	1
$112^2 \times 16$	bottleneck	6	24	2	2
$56^2 \times 24$	bottleneck	6	32	3	2
$28^2 \times 32$	bottleneck	6	64	4	2

Table 1 (continue)

Input	Operator	Expansion factor	Output channels	Number of repeat	Stride
$14^2 \times 64$	bottleneck	6	96	3	1
$14^2 \times 96$	bottleneck	6	160	3	2
$7^2 \times 160$	bottleneck	6	320	1	1
$7^2 \times 320$	conv2d $1 \times 1$	-	1280	1	1
$7^2 \times 1280$	avgpool $7 \times 7$	-	-	1	-
$1 \times 1 \times 1280$	conv2d $1 \times 1$	-	k	-	-

**GoogLeNet.** GoogLeNet is an architecture developed by and has a 22-layer deep convolutional neural network (Szegedy et al., 2015). The GoogLeNet architecture usually uses  $224 \times 224$  pixels of each input image. A study conducted by Luo et al. (2021) shows that GoogLeNet works well in classifying weed seeds. However, the use of GoogLeNet needs to be evaluated to classify Pakcoy pests and diseases.

**ResNet-101.** Resnet-101 is an architecture developed by Microsoft with 101 layers of deep convolution neural networks. Also, the size of the input image of this architecture was  $224 \times 224$  pixels. A study by Wu et al. (2021) shows that ResNet-101 performs better than ResNet-50 in segmenting the abnormal leaves in the plants. For Pakcoy pests and diseases classification, we used a ResNet-101 rather than ResNet-50.

## Metrics

As a measuring tool, a confusion matrix is designed to make measurements when analyzing a classifier. It helps to determine whether a classifier is good in terms of recognizing data from different classes. When the classifier is run and generates real-time data, True-Positive and True-Negative values provide that information. Meanwhile, if the classifier encounters an error upon classifying data, the values of False-Positive and False-Negative will provide the required information. In this study, the confusion matrix was employed, and the parameters associated with accuracy (Equation 4), precision (Equation 5), recall (Equation 6), and f1-score (Equation 7). The equations of these constructs are as follows.

$$Accuracy (a) = \frac{TP+TN}{TP+TN+FN+FP} \quad (4)$$

$$Precision (p) = \frac{TP}{TP+FP} \quad (5)$$

$$Recall (r) = \frac{TP}{TP+FN} \quad (6)$$

$$f1 - score (f) = \frac{2 \times precision \times recall}{precision + recall} \quad (7)$$



### Web-based Development and Implementation

**Choosing the Best Model.** Three different architectures (MobileNetV2, GoogLeNet, and ResNet-101) were evaluated, and the best metrics were chosen for inclusion in web-based development and deep learning implementation. The model will be re-trained and re-tested for further use if new information/data is provided.

**Business Process Model Notation (BPMN).** Business Process Model Notation (BPMN) is a graphical representation essential to determine a business process model. BPMN is developed to help readers understand a business process underway. Two main actors, namely user and admin, were involved in the business process. The users can be Pakcoy farmer or stakeholder who wants to predict and recognize the pests and diseases of Pakcoy and its problem-solving. An admin manages users, pests, and disease information, re-train and -tests the model, and applies the best model. Figure 3 shows the BPMN of the pest and disease identification system for Pakcoy in this study.

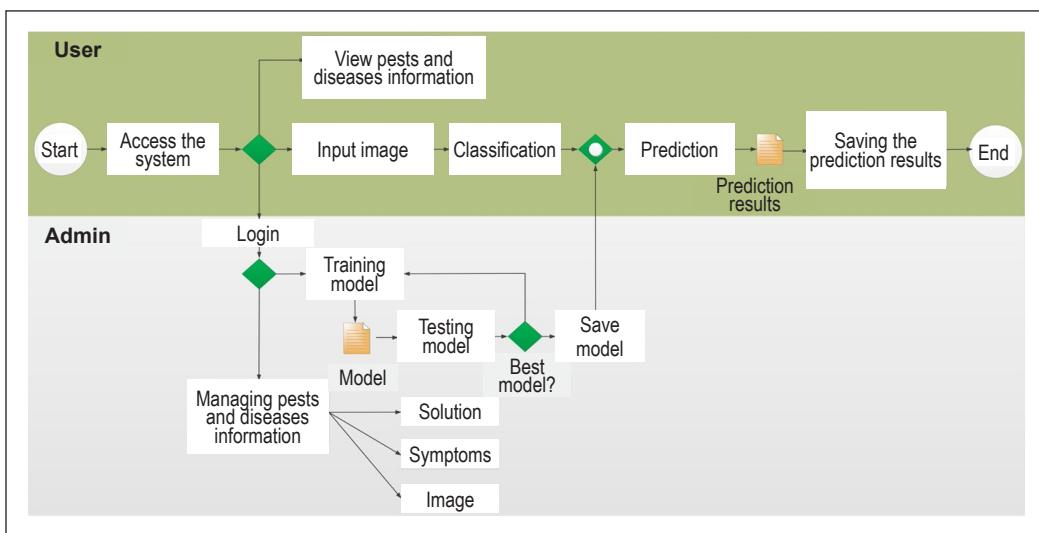


Figure 3. Business Process Model Notation (BPMN)

**Workflow.** The flowchart describes the detailed convolution process. The process is essential in processing image input using a MobileNet architectural model. It plays a key role in producing new features for identifying pests and diseases on Pakcoy plants. Figure 4 displays how input is engaged in the overall convolution of MobileNet.

**Entity Relationship Diagram.** Entity Relationship Diagram (ERD) is a diagram for modeling database requirements. The ERD development should be done before developing the web application. The basic tables, namely the image of infected Pakcoy leaf, pest,

and disease name, symptoms of each pest and disease, and its solutions, need to be provided for identifying the Pakcoy pest and disease. The ERD of the pest and disease identification system developed in this study can be seen in Figure 5.

### RESULTS AND DISCUSSION

Although several studies provide adequate evidence of those architectures (MobileNetV2, GoogLeNet, and ResNet-101) performance in identifying and classifying the pests and diseases of the plant, based on the principle of precision agriculture, which focuses on site-specific management, each agricultural problem/ issue needs to be handled by using the particular treatment and cannot be generalized using the same architecture. Thus, pests and diseases recognition of Pakcoy need to be evaluated.

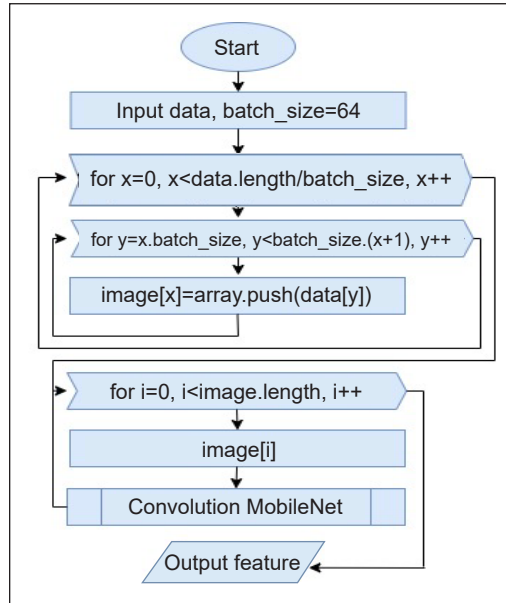


Figure 4. Convolution flowchart

### The Results of Training Model

For this purpose, all well-known architectures, namely MobileNetV2, GoogLeNet, and Resnet101, use batch size, dropout, and early stop patience of 64, 0.085, and 10, respectively. In addition, we also used the learning rate of 0.01, 0.001, 0.0001, and 0.00001 to evaluate the performance of selected architectures and examine the model acquired to

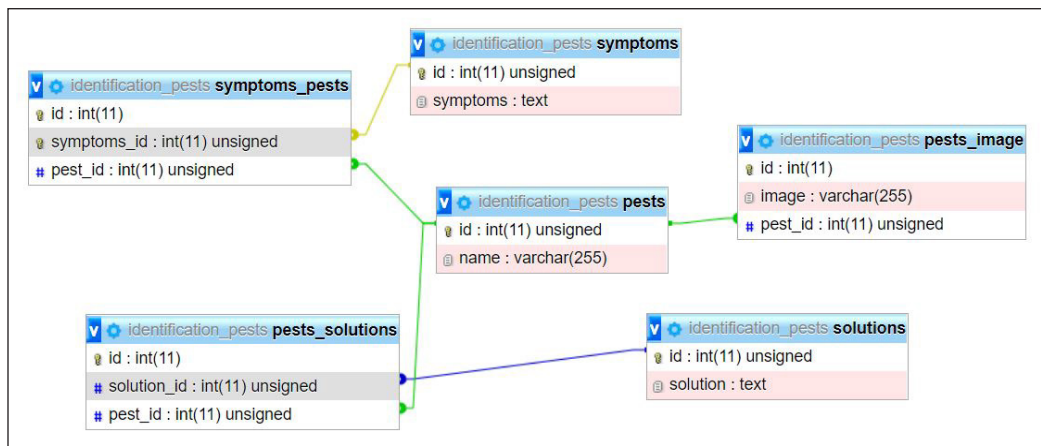


Figure 5. Entity Relationship Diagram (ERD)

recognize the Pakcoy pests and diseases. This study employed multi-label datasets, meaning that one image can indicate more than one pest and disease.

The results have demonstrated that the training process using a learning rate of 0.001 produces the best model and provides the lowest loss function value, especially for MobileNetV2 architecture (Table 2). A good loss function produces the lowest expected error. Since the batch size, dropout, and early stop patience of 64, 0.085, and 10 were used in the training step, these parameter values significantly affect the results, characterized by good results and graphics without overfitting (Figure 6). The results point out that the MobileNetV2 has the best level of loss function compared to ResNet101 and GoogLeNet models. It concludes that the model also markedly affects the success rate of training. Thus, the tested model can be used directly by the user to be implemented into web and mobile applications. Several researchers used a MobileNet architecture for several benefits, such as being lightweight in smartphone implementation and reducing application latency (Chudzik et al., 2020; Li et al., 2021).

Table 2  
Loss function value

Learning Rate	MobileNetV2	ResNet101	GoogLeNet
0.01	0.4496	0.4385	0.3396
0.001	0.0764	0.2091	0.2397
0.0001	0.098	0.1048	0.2107
0.00001	0.075	0.1009	0.0829

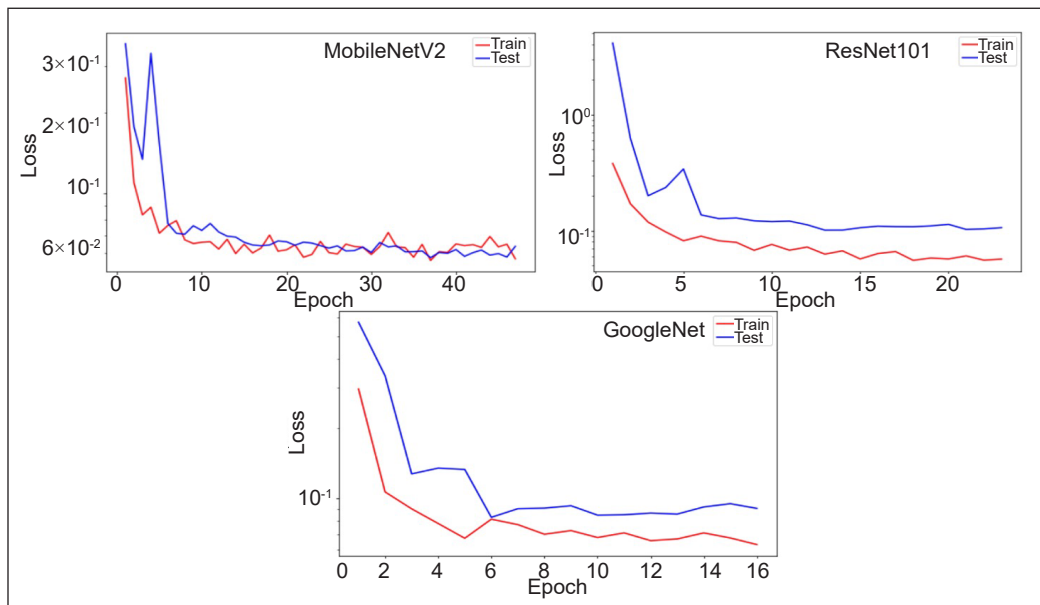


Figure 6. Comparison of different model architectures

## The Results of Model Testing

The model testing with MobileNet was carried out using 70 image datasets. Model evaluation determines whether the model tested is sufficiently decent and can be used directly by farmers. In evaluating the model, the researchers calculated accuracy, precision, recall, and f1-score in the form of a confusion matrix. Here are the evaluation results of the model using the confusion matrix (Table 3).

The average precision, recall, and f1-score of each label were calculated using a macro average and a weighted average. As seen in Table 4, each label has a different value but does not imply a significant gap. The findings highlight that the MobileNet architecture model has stable accuracy, precision, recall, and f1-score values, which are essential for identifying pests and diseases. MobileNet is readily applicable for identifying pests and diseases to aid growing Pakcoy.

Table 3  
*Accuracy, precision, recall, and f1-support*

Label	Accuracy (a)	Precision (p)	Recall (r)	f1-score (f)	Number of Label (s)
Healthy	1.00	1.00	1.00	1.00	6
Cabbage butterfly	0.97	0.95	1.00	0.97	39
Leaf miner	1.00	1.00	1.00	1.00	24
Powdery mildew	0.97	1.00	0.90	0.95	20

Table 4  
*The average of confusion matrix*

	Accuracy	Precision	Recall	f1-score	Number of Labels
Macro Avg	98 %	99 %	97 %	98 %	89
Weighted Avg	98 %	98 %	98 %	98 %	89

## Implementation Results of Web-based System

In this study, the front end and back end of the system were developed (Figure 7). The front end consists of the homepage and pest and disease prediction page. The landing page is directed to the home page, which users can access. This page has a start button to upload images to predict pests and diseases for the backend used for administration. This page presents information on predicted pests and diseases based on the image uploaded by the user. It informs the pests and diseases that possibly affect a certain plant and the solutions to overcome these pests and diseases. In addition, the administrator can upload the types of pests and diseases, symptoms, and recommendations. For new pests and diseases that are not available in the model, the Administrator will re-train the existing and additional dataset of new pests/diseases, then generate a new model and replace the old model.

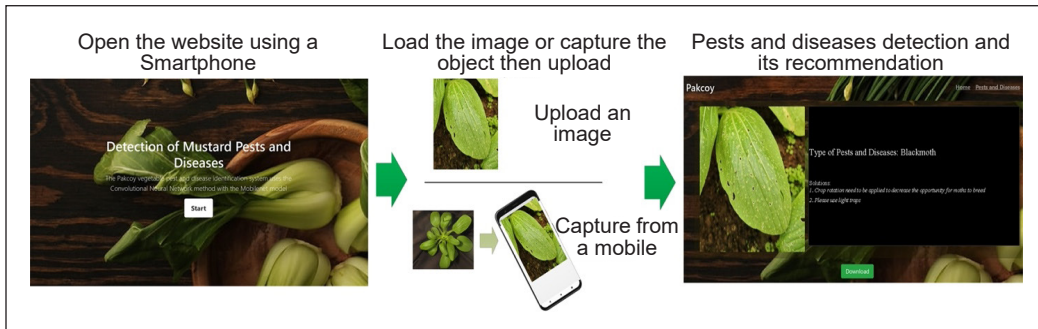


Figure 7. Web-based pests and diseases

## CONCLUSION

In this study, we specify four Pakcoy classifications: healthy, cabbage butterfly, leaf miner, and powdery mildew. Several architectures, namely GoogleNet, ResNet, and MobileNet, were evaluated to predict the type of pests and diseases in an image. We also evaluate a single to multilabel criterion of pests and diseases of Pakcoy. A significant model was obtained using MobileNetV2 architecture for pests and disease recognition.

The convolutional Neural Network method using the MobileNet architecture model coupled with several adjusted parameters comprises an effective system to identify pests and diseases on Pakcoy. Based on the training data, the developed model produces an error rate of 0.076 and an accuracy rate of 98%. The model architecture, along with its parameters, has been proven to generate a low error rate without not overfitting. In addition, we successfully developed a web-based application and supported mobile-based applications. Future study is suggested to develop a pest and disease identification system involving many types of pests and diseases affecting Pakcoy including *spodoptera litura*, *spodoptera exigua*, *Agrotis* sp., *plasmodiophora brassicae*, *plutella xylostella*, and *phytophora* sp.

## ACKNOWLEDGEMENT

We would like to extend our uttermost gratitude to the University of Jember IT Center, Indonesia, for providing the Supercomputer NVIDIA Station DGX A 100 for this project.

## REFERENCES

- Chen, J., Zhang, D., Suzauddola, M., & Zeb, A. (2021). Identifying crop diseases using attention embedded MobileNet-V2 model. *Applied Soft Computing*, 113, Article 107901. <https://doi.org/10.1016/J.ASOC.2021.107901>
- Chudzik, P., Mitchell, A., Alkaseem, M., Wu, Y., Fang, S., Hudaib, T., Pearson, S., & Al-Diri, B. (2020). Mobile real-time grasshopper detection and data aggregation framework. *Scientific Reports*, 10, Article 1150. <https://doi.org/10.1038/s41598-020-57674-8>

- Esgario, J. G. M., de Castro, P. B. C., Tassis, L. M., & Krohling, R. A. (2022). An app to assist farmers in the identification of diseases and pests of coffee leaves using deep learning. *Information Processing in Agriculture*, 9(1), 38-47. <https://doi.org/10.1016/J.INPA.2021.01.004>
- Griffel, L. M., Delparte, D., Whitworth, J., Bodily, P., & Hartley, D. (2023). Evaluation of artificial neural network performance for classification of potato plants infected with potato virus Y using spectral data on multiple varieties and genotypes. *Smart Agricultural Technology*, 3, Article 100101. <https://doi.org/10.1016/J.ATECH.2022.100101>
- Hendrawan, Y., Widyaningtyas, S., Fauzy, M. R., Sucipto, S., Damayanti, R., Riza, D. F. A., Hermanto, M. B., & Sandra, S. (2022). Deep learning to detect and classify the purity level of luwak coffee green beans. *Pertanika Journal of Science & Technology*, 30(1), 1-18. <https://doi.org/10.47836/pjst.30.1.01>
- Howard, A. G., Zhu, M., Chen, B., Kalenichenko, D., Wang, W., Weyand, T., Andreetto, M., & Adam, H. (2017). *MobileNets: Efficient convolutional neural networks for mobile vision applications*. ArXiv. <https://doi.org/10.48550/arxiv.1704.04861>
- Kamal, K. C., Yin, Z., Wu, M., & Wu, Z. (2019). Depthwise separable convolution architectures for plant disease classification. *Computers and Electronics in Agriculture*, 165, Article 104948. <https://doi.org/10.1016/J.COMPAG.2019.104948>
- Koklu, M., Cinar, I., & Taspinar, Y. S. (2021). Classification of rice varieties with deep learning methods. *Computers and Electronics in Agriculture*, 187, Article 106285. <https://doi.org/10.1016/J.COMPAG.2021.106285>
- Kumi, S., Kelly, D., Woodstuff, J., Lomotey, R. K., Orji, R., & Deters, R. (2022). Cocoa companion: Deep learning-based smartphone application for cocoa disease detection. *Procedia Computer Science*, 203, 87-94. <https://doi.org/10.1016/J.PROCS.2022.07.013>
- Li, W., Zheng, T., Yang, Z., Li, M., Sun, C., & Yang, X. (2021). Classification and detection of insects from field images using deep learning for smart pest management: A systematic review. *Ecological Informatics*, 66, Article 101460. <https://doi.org/10.1016/J.ECOINF.2021.101460>
- Li, Z., Zhu, H., Hua, H., Liu, C., Cheng, Y., Guo, Y., Du, P., & Qian, H. (2022). Anti-fatigue activity of *Brassica rapa* L. extract and correlation among biochemical changes in forced swimming mice. *Food Bioscience*, 47, Article 101633. <https://doi.org/10.1016/J.FBIO.2022.101633>
- Luo, T., Zhao, J., Gu, Y., Zhang, S., Qiao, X., Tian, W., & Han, Y. (2021). Classification of weed seeds based on visual images and deep learning. *Information Processing in Agriculture*, 10(1), 40-51. <https://doi.org/10.1016/J.INPA.2021.10.002>
- Nair, K. S. S. (Ed.). (2000). *Insect Pests and Diseases in Indonesian Forest: An Assessment of the Major Threats, Research Efforts and Literature*. Center for International Forestry Research (CIFOR). <https://doi.org/10.17528/CIFOR/000700>
- Putra, B. T. W., Amirudin, R., & Marhaenanto, B. (2022). The evaluation of deep learning using Convolutional Neural Network (CNN) approach for identifying Arabica and Robusta coffee plants. *Journal of Biosystems Engineering*, 47, 118-129. <https://doi.org/10.1007/S42853-022-00136-Y>

- Putra, B. T. W., Wirayuda, H. C., Syahputra, W. N. H., & Prastowo, E. (2022). Evaluating in-situ maize chlorophyll content using an external optical sensing system coupled with conventional statistics and deep neural networks. *Measurement*, *189*, Article 110482. <https://doi.org/10.1016/J.MEASUREMENT.2021.110482>
- Rahman, C. R., Arko, P. S., Ali, M. E., Khan, M. A. I., Apon, S. H., Nowrin, F., & Wasif, A. (2020). Identification and recognition of rice diseases and pests using convolutional neural networks. *Biosystems Engineering*, *194*, 112-120. <https://doi.org/10.1016/J.BIOSYSTEMSENG.2020.03.020>
- Sai, K., Sood, N., & Saini, I. (2022). Classification of various nutrient deficiencies in tomato plants through electrophysiological signal decomposition and sample space reduction. *Plant Physiology and Biochemistry*, *186*, 266-278. <https://doi.org/10.1016/J.PLAPHY.2022.07.022>
- Sandler, M., Howard, A., Zhu, M., Zhmoginov, A., & Chen, L. C. (2018). MobileNetV2: Inverted residuals and linear bottlenecks. In *2018 IEEE/CVF Conference on Computer Vision and Pattern Recognition* (pp. 4510-4520). IEEE Publishing. <https://doi.org/10.1109/CVPR.2018.00474>
- Sujatha, R., Chatterjee, J. M., Jhanjhi, N. Z., & Brohi, S. N. (2021). Performance of deep learning vs machine learning in plant leaf disease detection. *Microprocessors and Microsystems*, *80*, Article 103615. <https://doi.org/10.1016/J.MICPRO.2020.103615>
- Sutaji, D., & Yıldız, O. (2022). LEMOXINET: Lite ensemble MobileNetV2 and Xception models to predict plant disease. *Ecological Informatics*, *70*, Article 101698. <https://doi.org/10.1016/J.ECOINF.2022.101698>
- Szegedy, C., Liu, W., Jia, Y., Sermanet, P., Reed, S., Anguelov, D., Erhan, D., Vanhoucke, V., & Rabinovich, A. (2015). Going deeper with convolutions. In *2015 IEEE Conference on Computer Vision and Pattern Recognition (CVPR)* (pp. 1-9). IEEE Publishing. <https://doi.org/10.1109/CVPR.2015.7298594>
- Wu, Z., Yang, R., Gao, F., Wang, W., Fu, L., & Li, R. (2021). Segmentation of abnormal leaves of hydroponic lettuce based on DeepLabV3+ for robotic sorting. *Computers and Electronics in Agriculture*, *190*, Article 106443. <https://doi.org/10.1016/J.COMPAG.2021.106443>





Review Article

## Renewable Energy Impact on Distance Relay Power Swing Blocking and Fault Discrimination: A Review

Chidiebere Okeke<sup>1</sup>, Othman Mohammad Lutfi<sup>1\*</sup>, Hizam Hashim<sup>1</sup>, Mohd Zainal Abdin Ab Kadir<sup>1</sup>, Noor Izzri Abdul Wahab<sup>1</sup>, Osaji Emmanuel<sup>1,2</sup>, Samuel Nwagbara<sup>1</sup> and Collins Chimeleze<sup>3</sup>

<sup>1</sup>Advanced Lightning, Power and Energy Research (ALPER), Department of Electrical and Electronic Engineering, Faculty of Engineering, Universiti Putra Malaysia, 43400 UPM, Serdang, Selangor, Malaysia

<sup>2</sup>College of Science and Engineering, Department of Electrical and Information Engineering, Landmark University Omu-Aran. P.M.B 1001, Kwara state, Nigeria

<sup>3</sup>College of Computing and Informatics, Universiti Tenaga Nasional, 43000, Kajang, Selangor, Malaysia

### ABSTRACT

The annual increase of the global load demand has led to higher penetration of inverter-based renewable energy resources like wind farms and solar PV into the modern grid system. Distance relay may mal-operate by incorrectly estimating line impedance as fault during swing scenarios considering the infeed contributions impact from renewable sources. The negative impact of these integrated power electronics-based devices on the power swing blocking (PSB) and out-of-steps tripping (OST) functions of the distance relay characteristics has not been extensively discussed in previous studies.

This study divulges a comprehensive review of the various PSB and OST schemes

studies conducted to prevent relay mal-operation during power swing (PS) and symmetrical faults. Also, the large-scale renewable resources penetrations impact the PS characteristic and trip decision operation of the distance relay divulged. The mining of distance relay event records for hidden useful knowledge deployment for intelligent PSB and OST functions is the future research direction. Using the distance relay divulged knowledge will assist in reducing the failure rate level of PSB and OST function distance relaying

#### ARTICLE INFO

*Article history:*

Received: 25 October 2022

Accepted: 06 March 2023

Published: 03 October 2023

DOI: <https://doi.org/10.47836/pjst.31.6.14>

*E-mail addresses:*

chidiebereokeke@gmail.com (Chidiebere Okeke)

lutfi@upm.edu.my (Othman Mohammad)

hhizam@upm.edu.my (Hizam Hashim)

mzk@upm.edu.my (Mohd Zainal Abdin Ab Kadir)

izzri@upm.edu.my (Noor Izzri Abdul Wahab)

osajiemmanuel@gmail.com (Emmanuel Osaji)

sammytotti@gmail.com (Samuel Nwagbara)

chimeleze@uniten.edu.my (Collins Chimeleze)

\* Corresponding author

schemes, hence improving the degree of reliability/dependability of the power system under different operating conditions.

*Keywords:* Distance relay, faults; photovoltaic, power swing, renewable resources, windfarm

---

## INTRODUCTION

In a modern interconnected power system, all generators run in synchronism under steady-state conditions, which leads to a balanced operating condition between generated power, connected loads demand and constant rotor angle (Khadka et al., 2020). However, when the steady-state balance condition between the generator and the load impedance characteristic is disrupted with the emergence of network disturbances (like line switching, faults, large load addition and large load disconnection), then power system instability emerges (Višić et al., 2020). This network's unbalanced state causes a sudden change in the power system operating fundamental parameters like the current, voltage, frequency and power flow resulting from changes in the generator's rotor angle (Mooney & Fischer, 2006). The rotor angle oscillations of the synchronous generator result in a change in power flow, voltage and current signals of the power system. A power swing (PS) is a variation of power system fundamental parameters that oscillates power flow in the electrical networks (Hashemi & Sanaye-Pasand, 2018; Shair et al., 2021). The PS phenomenon affects the smooth operation of the distance relay, resulting in the relay mal-operation. Power system swings can be categorised as stable and unstable swings—the stable swing scenarios enable the recovery of the generators from the transient instability during power system disturbances (Yellajosula et al., 2019). An unstable or out-of-step power swing (OST) causes continuous oscillation in power flow due to continuous changes in the generator rotor angle, which leads to serious power flow oscillation (Mohapatra et al., 2017) and power system breakdown or equipment damage if not addressed (Nasab & Yaghobi, 2020).

Generally, distance relay operates by estimating the line impedance using phasor measurement of voltage, current and phase angle difference between the signals from the relay location under SteadyState (normal) and transient (fault) conditions for informed trip decision (Paladhi et al., 2022; Rao & Pradhan, 2017). The power flow oscillation during PS and fault disturbances are similar in features and function of variations in voltage and current signals, which impacts the estimated impedance at the distance relay location on the high voltage transmission line (Arumuga & Reddy, 2022). The estimated impedance under transient disturbances (like PS and faults) is compared with the earlier preset SteadyState threshold value used for informed trip decision protection characteristic settings (Taheri et al., 2020). The distance relay is expected to initiate a power swing blocking (PSB) function during stable PS to prevent unnecessary tripping of the healthy section of the line even when the estimated impedance is lower than the preset threshold value, forcing

the impedance locus trajectory into the preset protection zones (O'Donovan et al., 2020). However, initiate a trip command to the associated breaker during faults with similar impedance trajectory movement to prevent damage to equipment installation (Alsyoufi & Hajjar, 2019). The PS occurrences may interrupt the protection relay operation when the impedance locus intrudes into the operating zones of the relay characteristics, thereby causing mal-operation of the relay tripping as if it is a fault condition occurrence. For a short circuit fault, the estimated impedance seen by the relay reduces suddenly during short circuit fault interruption and compels sudden movement of the impedance trajectory into the trip operating zones of the relay to initiate tripping of the faulty line section (Kang & Gokaraju, 2016). The distance relay false tripping during stable PS is not expected because it may result in the blackout isolation of healthy sections of the line, compromising the reliability of the power system due to unexpected power outages resulting from protection system compromise (Sorrentino et al., 2018).

The distance relay is not expected to initiate a trip command under stable PS conditions by activating the PSB function of the distance relay. Under unstable swing and symmetrical fault conditions, the distance relay is expected to initiate a coordinated trip command using the out-of-step trip (OST) function of the relay to prevent a serious negative impact on the power system total blackout (Arumuga & Reddy, 2022; Sorrentino et al., 2018). When there is a power system blackout resulting from the relay mal-operation, it takes a longer time to restore the system to its normal operating conditions and creates a huge financial burden on utility companies if not prevented (Elliott et al., 2021). Several studies on power swing blocking (PSB) and OST functions have been conducted and integrated into the relay to detect and prevent unwanted tripping operations of the relaying schemes to address these challenges (Desai & Makwana, 2022).

Integrating renewable energy generation sources into the modern power system grid, like wind farms and solar photovoltaic (PV), is conducted in line with the stipulated grid codes (Cabrera-Tobar et al., 2019; Zheng et al., 2017). These source integrations are facilitated by factors associated with the low global warming impact benefit due to the reduction in the emission levels of greenhouse gases (GHG) and sustainability of renewable natural sources with the ability to self-replenish. The higher penetrations of renewable sources into the conventional grid reduce the grid inertia (Dreidy et al., 2017; Ying et al., 2017) with the shutdown of more fossil-fired generation plants. However, this paradigm shift introduced some power system stability challenges affecting the smooth operation of power flow from the generating sources to the diverse connected load (Choudhury, 2020; Mararakanye & Bekker, 2019). Secondly, huge harmonic contents are introduced, affecting the power quality of the generated electrical power (Benjamin & Jain, 2018). The large harmonic contents injection from the integrated converters and cyclo-converters integration with the renewable sources (like windfarm and PV) negatively impacted the

voltage and current signal waveforms used by the protective device for smooth operation (Choudhury, 2020; Mondal et al., 2020; Shafiullah et al., 2013). This integration impacted large disturbances like short circuit faults, generator disconnections, line switching, and addition and disconnection of large loads, which may compromise the power system stability (Bakar et al., 2010; Gunasegaran et al., 2015).

The increase in the renewable penetration in modern grid networks causes an increase in the swing frequency, voltage and current signal oscillations that adversely impact the time-based discrimination of faults from power swing (Buraimoh & Davidson, 2020). The distance relay's smooth operation is affected by the renewable power sources integration and PS scenarios, which are challenging in the accurate estimations of the line impedance by the distance relay (Ahmed et al., 2020; Mathe & Folly, 2017; Sorrentino et al., 2018). The wrong impedance estimation compromises the accurate trip decision-making that may result in the total system collapse or cascaded tripping of healthy sections of the networks if not addressed. The annual increase in the global load demand has led to higher penetration of inverter-based renewable energy resources into the modern grid system, as demonstrated in recent research (Sinsel et al., 2020). The negative impact of these integrated power electronics devices on the PS characteristics has not been extensively discussed. The higher renewable resource penetrations may adversely impact the trip decision operation of the distance relay if carefully investigated. The deployment of the distance relay assists in reducing the failure rate level and improving the degree of reliability/dependability of the power system. Distance relay may mal-operate by incorrectly estimating line impedance as fault during swing scenarios considering infeed contributions from renewable sources. The unwanted distance relay trip is not expected under stable swing conditions since the network can recover stability.

Given these challenges, this current study divulges a comprehensive review of the various power swing blocking (PSB) and OST schemes studies conducted to prevent relay mal-operation during swings and faults. Also, divulging the impact of high-scale penetration of the renewable energy sources on PS and faults characteristics impact the distance relay accurate trip decision. It is the motivation of this study as no earlier study was conducted in this direction. This review manuscript presents an up-to-date approach to addressing the impact of renewable integrated sources on PS generation and distance relay mal-operation under transient disturbance.

## **POWER SWING SCENARIOS AND CLASSIFICATION**

Power swing is defined as the variation of power flow due to loss in synchronism of generators, which leads to a change in its SG rotor angle (Desai & Makwana, 2022). The large oscillations of the fundamental power system parameters between the sending and receiving ends affect the measured apparent impedance seen by the relay in a power system

(Arumuga & Reddy, 2022). The PS is classified based on the level of disturbances as stable and unstable power swings and also sub-classified based on the swing frequency as slow frequency (1–3 Hz) and fast frequency (4–7 Hz) (Brahma, 2007).

### Power Swing Impact on Different Relays Operation

During PS, the load impedance locus oscillates between the initial position and the protection relay operating characteristic (zones) at the power oscillation frequency speed (Figure 1). The system impedance trajectory during the swing scenario may enter the protection trip zones of the relay characteristic (Rao & Ahmad, 2017). If the impedance locus stays in the protection zone beyond the preset operation time ( $T$ ), a tripping operation is initiated even though no actual short-circuit fault occurred in the system (Torres et al., 2016). Such tripping operation is undesirable because no actual short circuit fault occurred, and tripping may lead to the isolation of healthy line sections and system instability. In this case, the protective relay should block tripping operation during the stable power swing since the oscillation from the rotor angle achieves a new stable operation point under a stable PS, as displayed with the new stable swing impedance locus.

In contrast, an unstable power swing scenario is a balanced three-phase symmetrical disturbance that causes undesired relay operation in a power system network (Camarillo-Peñaranda et al., 2020). It is due to a loss of synchronism as the rotor angle of the generator could not achieve a new equilibrium point, as displayed in Figure 1. Hence, it results in uncontrolled tripping of the protective relay, leading to cascade outages. The impact of a pole slipping from an unstable swing may damage the generator and associated turbines if not addressed. An unstable power swing is associated with low voltage, which may result in motor stalling, generator tripping and damage to connected voltage-sensitive loads. The protection remedy is to isolate the group of generators operating asynchronously to prevent

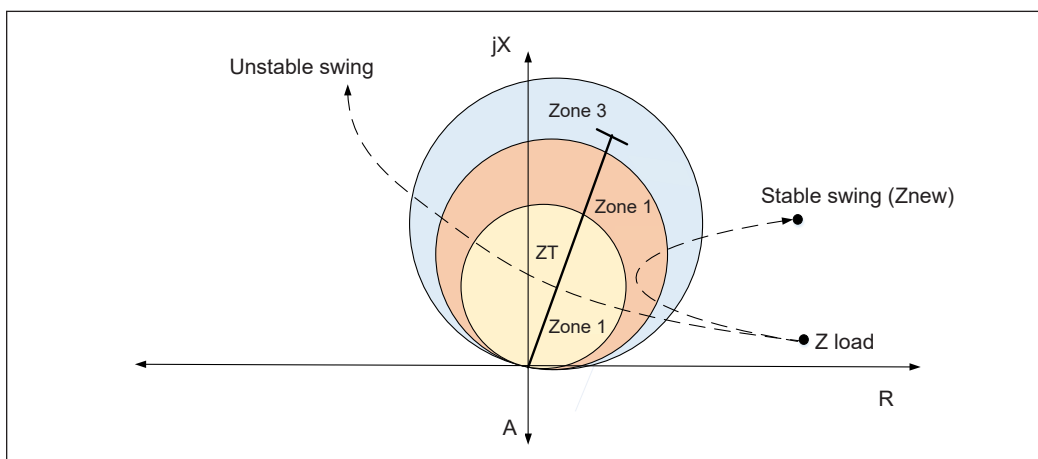


Figure 1. Stable and unstable swing locus trajectory movement

system equipment damage, power system shutdown and stability compromise (Sorrentino et al., 2018). Additional provision of reliable power system protection schemes that constantly monitor the changes in power flow, voltage, current and rotor angle to prevent cascaded outages is also required. The deployment of an OST protective relay function to discriminate between stable and unstable PS conditions is recommended (Gonzalez-Longatt et al., 2021).

The differential protective relay is unaffected by the PS condition and does not respond to unstable power swing conditions on power transmission lines. In contrast, the stability and unstable power swing conditions affect the distance relay, overcurrent relay, and directional relay operations characteristics, resulting in uncontrolled tripping of associated breakers (Moustakas et al., 2020). The current flowing through the transmission line is a function of the two-terminal voltage phase angle difference. The generator rotor angle is directly proportional to the voltage phase difference seen by the distance relay, which influences the line impedance estimated by the distance relay (Jedrzejczak et al., 2016). The distance relay is expected to detect and block its trip operation under stable swing scenarios to improve the power system's stability and reliability. The distance relay compared the estimated line impedance with the preset threshold value under stable conditions by measuring the instantaneous voltage, current and phase angle for fault impedance estimation (Dubey et al., 2016).

The literature has recorded several power system blackouts in a few countries due to protective relay mal-operations, as highlighted in Table 1.

Table 1  
*Distance relay maloperation causes a power system blackout*

Ref	Country	Year	Impact
Corsi and Sabelli, 2004	Italy	2003	The Italian power grid was subjected to 3 hours of blackout that affected over 60 million residences with 180 GWh energy shortfalls.
Bakar et al., 2010	Malaysia	2003, 2005	Two undesirable distance relay mal-operation recorded by the Malaysia TNB power grid system blackout for five hours due to load encroachment.
Ratha, 2013	India	July 30 and 31, 2012	Two different large-scale blackouts affected 350 and 680 million Indians, involving 75% of the total states of India.
Bowen et al., 2018	Brazil	March 21, 2018	Large-scale national grid blackout in Brazil with 19760 MW load disconnected (25% of the country's total connected loads) and 85% of the states.

### **Power Swing Impact Analysis Impact on Distance Relay**

Considering two sources, V is a high voltage powered transmission line with generated voltages  $V_A$  and  $V_B$  at both terminal and voltage drop measurement at the relay location (Figure 2). The system power flow equation in any transmission line is expressed in Equation 1.

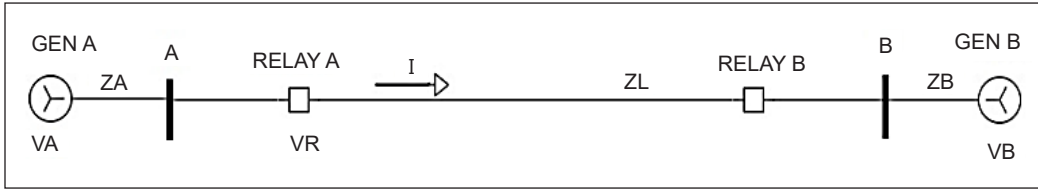


Figure 2. Two-source powered high voltage transmission line test system

$$P = \frac{V_s - V_r}{X} \sin \delta \tag{1}$$

Power swing is the variation of power flow as a result of synchronous generators’ rotor angle changes, which may lead to loss of synchronism if it persists for too long. The current (*I*) flowing through the transmission line can be expressed mathematically in Equation 2.

$$I = \frac{V_A - V_B}{Z_A + Z_L + Z_B} \tag{2}$$

Where, *P*: power flow transfer on the transmission line; *V<sub>A</sub>*: synchronous generator A source voltage; *V<sub>B</sub>*: synchronous generator B source voltage; *V<sub>R</sub>*: voltage drop measured at the relay location; *X*: reactance between the generator and the load; *δ*: rotor angle between the sending and receiving end voltage; *Z<sub>A</sub>*: Impedance of generating source A; *Z<sub>B</sub>*: Impedance of generating source B; *Z<sub>L</sub>*: transmission line impedance; *Z<sub>T</sub>*: total system impedance; and *I*: current flowing through the transmission line.

Substituting *Z<sub>T</sub>* = *Z<sub>A</sub>* + *Z<sub>L</sub>* + *Z<sub>B</sub>* into Equation 2, simplified Equation 3

$$I = \frac{V_A - V_B}{Z_T} \tag{3}$$

Voltage drop at the relay location (*V<sub>R</sub>*) is expressed in Equation 4.

$$V_R = V_A - I \times Z_A \tag{4}$$

The impedance seen by the relay is expressed in Equation 5 based on Ohms’ law:

$$\text{The impedance is seen by the distance relay, } Z_R = \frac{V_R}{I} \tag{5}$$

Substituting Equation 3 and 4 in Equation 5 produced Equation 6.

$$Z_R = \frac{V_A - (I \times Z_A)}{I} = \frac{V_A}{I} - Z_A$$

$$Z_R = \left[ \frac{V_A}{V_A - V_B} \times Z_T \right] - Z_A \quad (6)$$

If the voltage  $V_A$  at terminal A leads to the source voltage  $V_B$  at terminal B by angle  $\delta$ , the ratio  $V_A/V_B = n$ . Substituting these parameters in Equation 6

$$Z_R = \left[ \frac{\left[ \frac{V_A}{V_B} \right]}{\left[ \frac{V_A}{V_B} \right] - 1} \times Z_T \right] - Z_A$$

$$Z_R = \left[ \frac{ne^{i\delta}}{ne^{i\delta} - 1} \times Z_T \right] - Z_A \quad (7)$$

Equation 7 represents the locus of the family of circles seen by the distance relay at the location with  $n$  as the parameter and  $\delta$  as a variable. Where  $n = V_A/V_B$

When  $n = 1$ , the power swing locus is a straight line perpendicular to the total line impedance  $Z_T$  at angle  $90^\circ$  with the locus illustrated in Figure 3.

For  $n > 1$ , the centre of the power swing locus lies on the expansion of the total line impedance. The distance of the terminal end B to the centre of the locus and the radius of the circle are in Equations 8 and 9, respectively, as displayed in Figure 3.

$$\text{Distance of B to the centre of the circle, } D_{BC} = \frac{Z_T}{(n^2 - 1)} \quad (8)$$

$$\text{The radius of the circle, } r_{BC} = \frac{nZ_T}{n^2 - 1} \quad (9)$$

For  $n < 1$ , a distance of A to the centre of the circle and the radius of the circle in Equations 10 and 11, respectively, are displayed in the locus of Figure 3.

Distance of A to the centre of the circle,

$$D_{AC} = \frac{Z_T}{\left( \frac{1}{n^2} - 1 \right)} \quad (10)$$

The radius of the circle,

$$r_{AC} = \frac{\frac{1}{n} Z_T}{\left( \frac{1}{n^2} - 1 \right)} \quad (11)$$



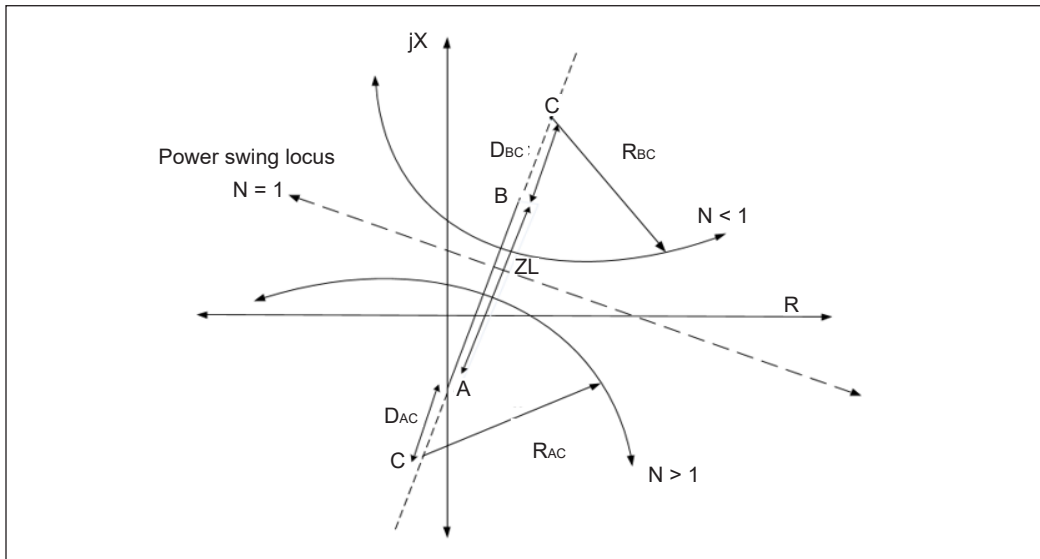


Figure 3. Power swing characteristic locus trajectory

### Distance Relay Characteristic Under Power Swings

Power swing is typically a phase symmetrical event similar to a three-phase symmetrical fault but with longer oscillation time as compared to a short circuit fault with a fast movement response (Mahamedi, 2010). If the locust of the impedance seen by the distance relay during the PS scenario entered and stays in the trip zones of the distance relay R-X characteristics, the relay sees low estimated impedance as a fault and thereby initiates a tripping command. The time the PS locus travels through the relay characteristic and the trip zones determines whether the relay will trip the associated breakers. The current flowing through the transmission line depends on the phase difference between the two sources' terminal voltages. The system voltage phase difference is directly proportional to the generator's rotor angle, influencing the current flow through the relay on the transmission line (Bakar et al., 2010). The electrical current magnitude directly impacts the estimated impedance seen by the distance relay. Furthermore, the PS scenarios influence the performance and operation of the distance relay in a power system since the estimated impedance depends on the source and line impedance magnitudes for an informed decision.

A power swing scenario appears like a short circuit fault that changes its distance from the relay location. The greater the area occupied by the distance relay characteristic on the R-X diagram, the more vulnerable the relay mal-operation impact from the PS. The mho relay characteristic displayed the lowest impact of PS false tripping of the distance relay considering the smallest area coverage of PS impact locus on the relay characteristic plot on the R-X diagram of Figure 4. The impedance characteristics plot with a larger swing impedance locus coverage on the same R-X plot follows it. On the contrary, the reactance

characteristic has the largest PS impact on the distance relay mal-operation, considering the largest area coverage of the swing locus on Figure 4 R-X diagram.

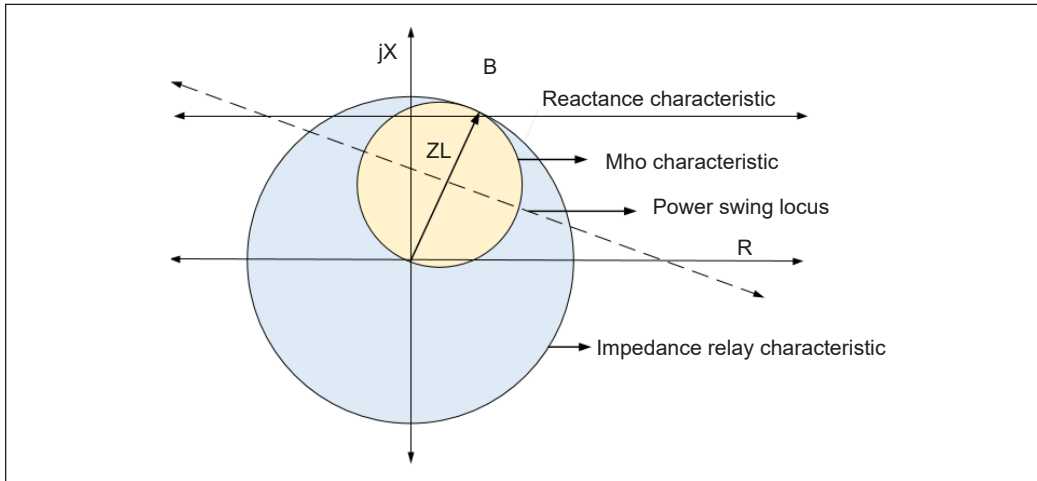


Figure 4. Power swing impact on distance relay characteristics

## POWER SWING BLOCKING (PSB) AND OUT-STEP-TRIPPING (OST) TECHNIQUES

The distance relay has two operating functions, known as power swing blocking (PSB) and out-of-step tripping (OST), that mitigate the impact of PS on the power system (Desai & Makwana, 2021). The PSB discriminates the PS from short-circuit faults by blocking the relay from operation during the PS scenarios and unblocking the relay operation during fault. The PS appears like a fault but changes its location with respect to the relay location because the distance relay measures the impedance to the fault section of the line. The estimated impedance during PS is similar to that of a three-phase symmetrical short circuit fault in characteristics, which initiates the relay mal-operation trip command. The estimated impedance seen by the relay during PS is constantly changing based on the change in the distance of the PS impedance locus from the relay location. One of the primary functions of the distance relay is to discriminate between PS and short circuit faults effectively. The relay PSB function device prevents unwanted tripping of the system for enhanced reliability/dependability and unblocks the scheme during short circuit faults to prevent system damage. Several PSB scheme research studies have been conducted to address this limitation, as seen in the algorithm comparison performance study conducted in this direction (Khoradshadi-Zadeh, 2005). Mooney and Fischer (2006) presented a practical relay setting guideline for the conventional PSB functions in their study to aid smooth PSB implementation, and Nayak et al. (2010) divulged a comparative analysis between existing PSB scheme merits and limitations.

In contrast, the out-of-step tripping (OST) function of distance relay discriminates between stable and unstable PS (types) scenarios based on the swing impedance locus and initiates system partitioning in case of unstable swing occurrences (Holbach, 2006). The OST function prevents the tripping of the distance relay during stable swings. A stable swing is determined if the impedance locus does not enter the OST zone and the relay blocks from the trip operation (Tziouvaras & Hou, 2004). The function initiates a trip operation during an unstable swing if the impedance trajectory enters the OST operating zone.

This section highlights updates on the different PSB and OST protection schemes from literature deployed in preventing the distance relay mal-operation during the PS condition. Numerical relay manufacturers adopt some of these methods in the modern power system network protection scheme.

### Rate of Change in Impedance Methods

It is a conventional approach mostly deployed by relay manufacturers that consider the rate of changes in the impedance estimation by the distance relay. The discrimination is based on the rate of change of the positive sequence component of the impedance locust ( $\Delta Z_{app}/\Delta t$ ) during PS and fault scenarios, as illustrated in Rao et al. (2017). Gao and Wang (1991) established that the rate of change of impedance is gradual and slow in the case of PS compared to an instantaneous change in impedance under fault conditions. Under the normal operating conditions of the system, the load impedance  $Z_{load}$  is located outside the distance relay operation characteristic zones without tripping, as displayed in Figure 5.

On the contrary, the emergence of stable PS conditions generates a slow-moving impedance locus gradually into the relay operation characteristic trip zones, as illustrated

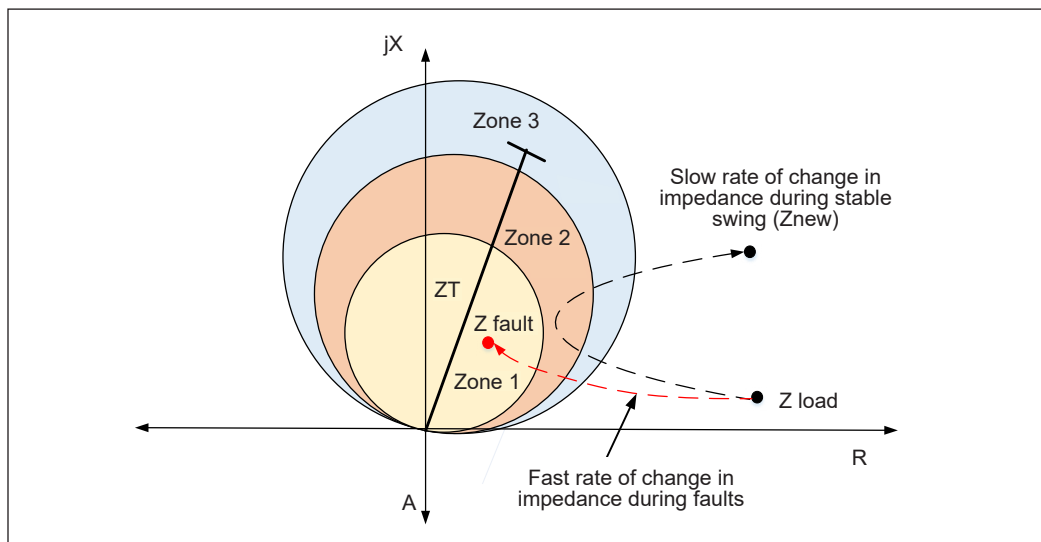
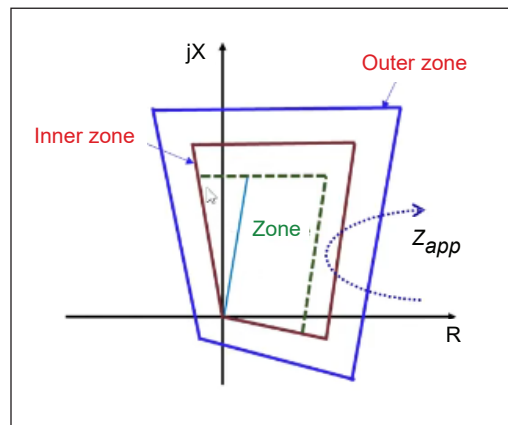


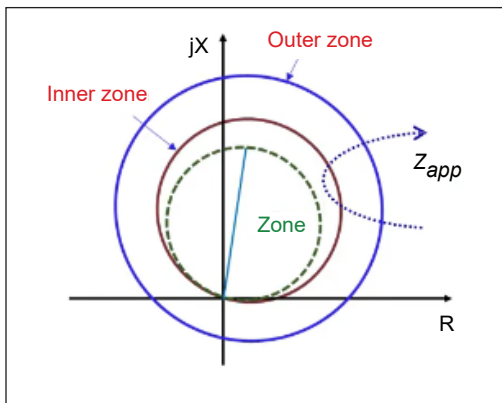
Figure 5. Rate of change in impedance locus in the distance relay

in Figure 5. Hence, the relay mal-operates due to a reduction in the estimated impedance seen by the relay inside the preset trip zones. Under a fault condition, the rate of change in impedance ( $\Delta Z_{app}/\Delta t$ ) seen by the relay is also lower than the preset value but forces the impedance trajectory to transit instantaneously from the load point into the relay operating zones. The operating principle of such a scheme is based on identifying the difference between the time taken for the rate of change in impedance during PS and the fault condition for PSB or fault trip decision (Arumuga & Reddy, 2022).

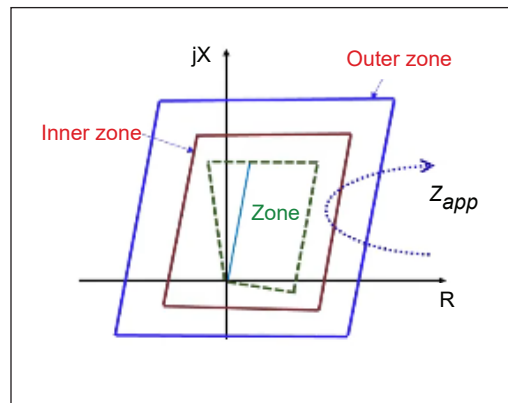
**Concentric Characteristics Approach.** In this approach, two sets of similar concentric characteristics are drawn with reference to the protection characteristic zone of interest displayed for polygon, mho and trapezoidal protection characteristics of distance relay on the R-X characteristics plots of Figure 6. The relay timer estimates the time taken for the estimated impedance locus to cross through the outer and inner concentric characteristics of the relay during PS and faults. The estimated time is then compared with the preset threshold time ( $T$ ) of the relay (Rao et al., 2017). If the recorded duration for crossing the outer and inner concentric characteristic is greater than the preset time ( $T$ ), then the relay classifies such disturbance as PS and then blocks the relay from the trip operation (PSB). In contrast, if the estimated time is shorter than the preset time ( $T$ ), such a scenario is classified as a fault; the relay then unblocks to enable the tripping operation to the associated breaker (Zhu et al., 2004).



(a)



(b)



(c)

Figure 6. Distance relay concentric characteristic plots: (a) polygon; (b) mho; and (c) trapezoidal

**Double Blinder Characteristics Approach.** This approach addresses the existing operating limitations of the rate of change in the impedance and the concentric circle approaches. The scheme draws two sets of inner and outer blinders parallel to the system line impedance after determining the protection zone of interest (mostly demonstrated for zone 3 of the distance relay) (Kang & Gokaraju, 2016). The double blinder scheme is mostly targeted at detecting out-of-step occurrences during PS to prevent relay mal-operation as the impedance locus of the PS is projected perpendicular at an angle of  $90^\circ$  to the total system impedance displayed in Figure 7.

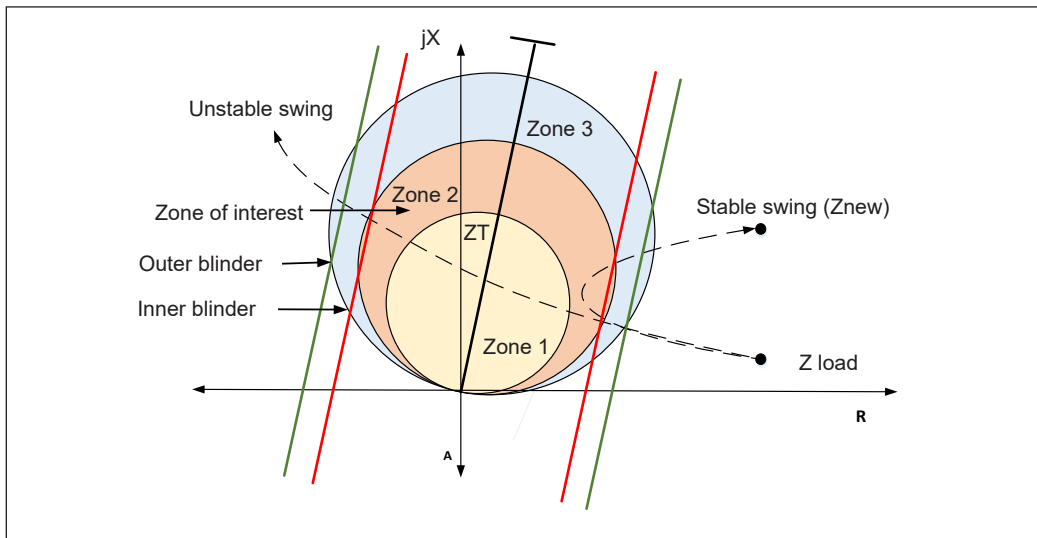


Figure 7. Double blinder scheme for distance relay

**Change in Resistance Monitoring Method.** A resistance monitoring approach is an alternative method introduced to address the challenges in complex grid analysis studies to prevent distance relay mal-operation during a PS scenario. Generally, the relay's resistance component of the measured impedance changes continuously during the PS scenario but changes instantaneously and remains at the new value during fault inception duration (Nayak et al., 2010).

### Rate of Change in System Parameters Methods

These are alternative approaches associated with the rate of changes in three-phase power, voltage variation, frequency and current, as illustrated in this discussion. These PSB and OST schemes are developed using other power system network oscillating parameters associated with PS and fault disturbances. In a study conducted by Taheri et al. (2020), outside the rate of change in impedance deployed, the rate of change of the instantaneous frequency parameter for detection and discrimination of PSB and fault. Taheri and Razavi

(2018) adopted the RMS value of the current signal measurement for detecting PS and fault discrimination as executed. Other adopted similar schemes are the following:

- (i) Power Variation Scheme
- (ii) Power Swing Centre Voltage ( $V\cos\theta$ ) Based Scheme
- (iii) Incremental Current Estimation Scheme
- (iv) Rate of Change in Instantaneous Frequency

### **Signal Analysis Schemes**

The spectrum analysis of parameter variation during power system disturbance can be observed through the extracted signal parameters for comprehensive analysis. Adopting analogue and digital signal analysis methods on the extracted power system parameters' signal or waveform is to hide knowledge in the analysed signal to detect power system feature responses under PS and fault disturbances. With the advent of digital signal analysis tools, which has encouraged various types of research on PS and fault detection, discrimination to address the impending negative impacts on the distance relay mal-operations (Khodaparast & Khederzadeh, 2014; Lazaro et al., 2018; Morais et al., 2015). The list of a few signal analyses approached adopted the time domain, frequency domain, and multiresolution analysis of power system signals from monitored system parameters based on literature are the following:

- (i) Fourier transform Signal Analysis Scheme
- (ii) Wavelet Transform Signal Analysis Scheme
- (iii) S-Transformation Based Scheme

### **Artificial Intelligent-based Schemes**

It is a pattern recognition approach for classifying PS and fault as adopted in modern protection relaying trip function development. The AI methods are deployed for PS and fault detection across conducted studies on the PSB and OST functions development. These have eliminated the rigour of complex impedance estimations and the adoption of operation parameter variation during PS disturbances studies. A few of the conducted research methods are highlighted as follows:

- (i) Neural Network (ANN) Based Scheme
- (ii) Support Vector Machine (SVM)
- (iii) Adaptive neuro-fuzzy inference system (ANFIS)

## **RENEWABLE IMPACT ON DISTANCE RELAY PSB AND OST FUNCTIONS**

The high penetration of renewable energy sources, mostly from PV and wind farms on the transmission network, is due to the high cost, rapid depletion and supply sustainability

challenges of fossil fuel energy resources in the power generation system (Moustakas et al., 2020). These reasons have increased investment in these two renewable energy generation sources with a dramatic increase in the emergence of improved wind turbines, PV panels, batteries and converters development (Lawan et al., 2017). These renewable source penetrations significantly impact the power system disturbance and transient instability resulting from the power swing and faults. The large-scale penetration demands are due to the annual increase in load demand, which has also produced a new set of protection relay operation challenges (Shair et al., 2021). Inverter-based renewable sources from both windfarm and PV affect the PS characteristic, which may result in the mal-operation of the PSB and OST tripping function of the distance relay as reported (Haddadi et al., 2021; Haddadi et al., 2019).

Large-scale grid-connected PV system on the existing traditional power system is due to low maintenance and operation costs compared to the conventional fossil fuels power generation methods (Yang et al., 2010). The solar PV system is made up of solar panels and control power inverters for integration into distributed and transmission grid networks in compliance with the stipulated grid code (Buraimoh & Davidson, 2020; Zheng et al., 2017). In a comparative study on the impact of large-scale penetration of PV on PS generation, the result demonstrated fluctuation in voltage rise on the IEEE 9 bus system. The oscillation impacted the PS characteristic locus, and noticeable oscillations in active and reactive power were recorded before and during the PV penetrations (Yusoff & Abidin, 2013). The study does not account for the impact of the PV integration on the PSB function of the relay as the drawback. Another detailed study by Jia et al. (2017) considered the PV inverter penetrated grid performance impact on the PSB function of a relay under PS and fault conditions investigated to enhance trip characteristics. Furthermore, an adaptive protection scheme is presented to adjust the distance relay settings on a large-scale integrated PV. The voltage and current signal data from the PV source at the relay location are deployed for the impedance boundary setting of the relay to discriminate faults from swing (Mishra et al., 2020). The deployment of variation in the PS phase angle of the fault current for the adaptive relay impedance setting is presented (Liang et al., 2020).

Similarly, the large-scale penetration of wind farms in the modern electrical system has impacted the power system stability (Rampokanyo & Kamera, 2018). The wind farm is made up of several wind turbines that analyse the impact of the wind farm on the PS and distance relay mal-operation. Windfarms, unlike synchronous generators, are mostly designed from an asynchronous generator having the power angle ( $P-\delta$ ) replaced with the torque-speed ( $T-\omega$ ) curve (Samuelsson & Lindahl, 2005). Hence, having the rotor speed and rotating flux at the same speed (equal), the rotor angle is constant and easily obtained under stable conditions.

There is a need to divulge some factors that affect the PS generation level and their impact on the operation of the distance relay PSB and OST functions as divulged in this

current study. Some of these factors are the types of generators, Power Grid Code [Fault-Ride-Through (FRT)], the control scheme used, and harmonic contents.

### **Types of Wind-turbine Generator**

The wind turbine is classified into variable and fixed speeds based on the rotor design, which impacts differently on the PS and distance relay operations (Mathe & Folly, 2017). The fixed-speed wind turbine demonstrated fixed speed during operation, as observed in the Squirrel cage induction generator (SCIG) wind turbine (Sravanthi & Rani, 2014). The impact of the SCIG on the PS has been divulged in (Zare & Azad 2020); the Induction generator (IG) damped PS in the power system network and does not contribute to PS fluctuation resulting from the synchronous generator (SG) due to rotor angle stability (Abbasi & Yaghobi, 2017). The induction-based generator wind turbine performed better than a synchronous generator (Folly & Sheetekela, 2009; Slootweg & Kling, 2003). The comparative study conducted between SCIG and SG illustrates more oscillation from SG than the IG impact on the PSB and OST function of the distance relay. It is because the PS equation for the SG is defined by  $P-\delta$  parameters, while that from IG is represented by  $T-\omega$  in Muljadi et al. (2007).

On the contrary, the variable speed generator design is found in the double-feed induction generator (DFIG) wind turbine with rotor and stator windings connected to the power grid through an electronics converter (Ontiveros et al., 2010). This type of turbine increases the obtained energy from the wind and improves the power quality and mechanical stress reduction (Abdin & Xu, 2000). The study demonstrated low participation of the DFIG wind turbine in the PS generation in any integrated power system (Gautam et al., 2009). In a conducted study by Chowdhury et al. (2013), variable speed wind generators (DFIG) have demonstrated better performance with low swing frequency than the fixed speed (SCIG and synchronous generator-based turbine) under PS conditions. The DFIG windfarm integration separates the mechanical oscillation of the rotor from the electrical oscillation of the power system (Ying et al., 2017). Furthermore, the oscillation in the rotor speed of a fixed-speed wind turbine affects the variation in the active power delivery in the power system. Contrarily, the variable-speed wind turbine delivers the same magnitude of active power at different speeds by controlling the rotor voltage (Chung, 2013). Increasing wind farm penetration decreases the synchronous generator contributions and PS frequency reduction on the existing grid, enhancing system stability (Khoradshadi-Zadeh, 2005).

### **Power Grid Code**

The grid codes that require PV and wind turbines to be permanently connected to the grid during fault and power system disturbances are based on the fault-ride-through (FRT) ability to impact the network stability (Cabrera-Tobar et al., 2019; He et al., 2016). The



FRT is achieved by investigating the PV and wind turbine inverter-based control system to determine the allowable current value that is permitted through the system to ensure system stability under low SG inertial in earlier conducted studies (Liu et al., 2017; Saleh et al., 2015; Tu et al., 2014; Yoosefian & Chabanloo, 2020).

### **Electrical Center Movement**

An electrical centre is a point in a power system where the system voltage becomes zero during PS occurrences. Large-scale penetration of the wind farm changes the PS impedance directory seen by the relay due to the reduced grid inertia from the reduction in the number of SGs. Also, the solar PV penetration impacts the system voltage rise and the relay operation, as presented in Yan et al. (2011), but the impact on the system active power variation is not reported. The changes in the system parameters result in the estimation of the system impedance, leading to mal-operation of the PSB and OST function of the relay with only connected SGs. Hence, it leads to unexpected tripping of a healthy section of the line during a stable swing and may further affect the movement of the system's electrical centre deployed for optimal location setting of the PSB and OST function implementation (Verzosa, 2013). The large-scale wind farm penetration directly influences the movement of the electrical centre of the power system (Haddadi et al., 2019).

### **Control System/Harmonic Content**

The renewable energy system operates with the installations of large-scale inverter-based control systems, which produce harmonic injection into the system's fundamental frequency. Harmonic content in a system can be determined by load characteristic study influenced by the harmonic contents in the sampled current signal waveform. Injected inter-harmonic frequencies from non-linear loads or power inverter systems create a harmonic distortion effect on the measured voltage and current waveforms seen at the relay location for impedance estimation in the trip decision (Tin et al., 2011; Wannous & Toman, 2018). The harmonic content in the current and voltage waveform seen by the relay adversely impacts the relay operation characteristic and also causes the thermoelectric effect of the system (Wannous & Toman, 2018). A simulation study considered harmonic analysis of the power electronics load on the distance relay characteristics to prevent mal-operation of the distance relay PSB and OST function in Saha et al. (2014). Given this adverse impact, a reliability study is conducted to analyse the harmonic contributions from non-linear connected load and their impact on the relay operation characteristic encroachment leading to mal-operation (Jedrzejczak et al., 2016). Wrong impedance estimation due to harmonic frequency contents causes the distance relay to overreach or underreach its operation characteristic within the protection zone coverage (Taheri & Sedighizadeh, 2020).

## **FUTURE RESEARCH PROSPECT**

Modern digital numerical relays are microprocessor-based with the capability to monitor and record operation events data. An automated distance relay performance analysis has been carried out by manipulating the event report domiciled inside the numerical relay in building an Expert system (Othman et al., 2009; Othman et al., 2010; Othman et al., 2016). Event reporting is a standard feature in most microprocessor-based protective relays used as a framework for knowledge discovery in huge database (KDD) records to discover the relay's decision algorithm (prediction rules) and the association rule under different operating conditions and network topological changes. These huge databases contained useful hidden information that can be used in building expert system decision rules as deployed in Othman et al. (2011).

Data mining strategies have assisted in utilising the intelligent electronic devices (IEDs) recorded dataset and divulging the hidden knowledge in the recorded event report at a relay device level in Othman and Aris (2012). The data and useful information saved in these reports are valuable records for testing, measuring performance, analysing problems, and identifying deficiencies before resulting in future relay mal-operation. All necessary relay fault data must be collected and analysed for complete retrospective verification that all elements of the protection relay system characteristics were set properly and operated as anticipated under different operating conditions (normal, PS and faults). A simulation study based on fault discrimination under integrated renewable energy sources using data mining classification model development for relay trip decision-making is presented in Emmanue et al. (2019) and Emmanuel et al. (2020). None of these studies considered relay event data mining under PS scenarios as the major drawback.

Few identified data mining methods for PS detection and fault discrimination only considered developing a model based on an adaptive decision algorithm for distance relay PSB function performance on compensated and uncompensated power transmission systems (Dubey et al., 2016). The renewable integrated network impact was not considered in the study. Machine learning adoption for ensemble model development in fault classification during PS on non-renewable integrated lines is presented in Patil et al. (2019) and Swetapadma and Yadav (2016). No study has been reported on the data mining application on PSB and OST function model development. The data mining and deep learning approach will handle all impeding mathematical complexity in the PSB and OST function modelling of distance relay operation characteristics using hidden information in the historical event records. These unattempted approaches are the future frontier for the novel PSB and OST function model designs for distance relays.

## CONCLUSION

This review has presented additional updated information relevant to earlier studies from the existing body of literature on the impact of renewable integration on the PS generation and distance relay PSB and OST operation characteristic compromise. The system operation was performed under different system topologies with reference to different types of generators (SG, SCIG and DFIG) with different impacts on PS and fault characteristics divulged. Integrating large-scale inverter-based renewable sources from both windfarm and solar PV arrays with interharmonic and subharmonic frequencies could pollute the system voltage and current seen by the distance relay. These polluted signals compromise distance relay operation due to overreach or underreach of the relay operation characteristic zones. The intelligent-based PSB and OST function modelling have been comprehensively divulged, considering a reduction in the mal-operation compromise merits over the conventional methods. Continuous research on PSB and OST functions is important to improve the PS and fault discrimination functions in different distance relay operating characteristics.

Data mining and deep learning methods seem promising because they present a realistic model development based on extracted real-life scenarios and data information with reduced mathematical rigour in complex number handling. Mining hidden knowledge embedded in the relay event records under different network topology changes in the relay operation characteristic is the next discovered frontier added to the existing body of knowledge through this review study.

## ACKNOWLEDGEMENTS

This work was supported by the Geran Putra Berimpak - Universiti Putra Malaysia (GPB-UPM) under Grant UPM/800-3/3/1/GPB/2019/9671700.

## REFERENCES

- Abbasi, M. J., & Yaghobi, H. (2017). A new combined method to diagnosis loss of excitation from stable power swing in doubly fed induction generator. *Journal of Modeling in Engineering*, 15(51), 159-169. <https://doi.org/10.22075/jme.2017.2684>
- Abdin, E. S., & Xu, W. (2000). Control design and dynamic performance analysis of a wind turbine-induction generator unit. *IEEE Transactions on Energy Conversion*, 15(1), 91-96. <https://doi.org/10.1109/60.849122>
- Ahmed, S. D., Al-Ismail, F. S. M., Shafiullah, M., Al-Sulaiman, F. A., & El-Amin, I. M. (2020). Grid integration challenges of wind energy: A review. *IEEE Access*, 8, 10857-10878. <https://doi.org/10.1109/ACCESS.2020.2964896>
- Alsyoufi, Y. R., & Hajjar, A. A. (2019). A high-speed algorithm to discriminate between power swing and faults in distance relays based on a fast wavelet. *Electric Power Systems Research*, 172, 269-276. <https://doi.org/10.1016/j.epsr.2019.03.021>

- Arumuga, M., & Reddy, M. J. B. (2022). Distance protection methodology for detection of faulted phase and fault along with power swing using apparent impedance. *IEEE Access*, 10, 43583-43597. <https://doi.org/10.1109/ACCESS.2022.3168563>
- Bakar, A. H. A., Yatim, F. M., Yusof, S., & Othman, M. R. (2010). Analysis of overload conditions in distance relay under severe system contingencies. *International Journal of Electrical Power & Energy Systems*, 32(5), 345-350. <https://doi.org/10.1016/j.ijepes.2009.11.023>
- Benjamin, A., & Jain, S. K. (2018). A review of literature on effects of harmonics on protective relays. In *2018 IEEE Innovative Smart Grid Technologies-Asia (ISGT Asia)* (pp. 407-412). IEEE Publishing. <https://doi.org/10.1109/ISGT-Asia.2018.8467876>
- Bowen, Z., Qiyu, C., & Dongsheng, Y. (2018). On the power system large-scale blackout in Brazil. *Power Generation Technology*, 39(2), 97-105. <https://doi.org/10.12096/j.2096-4528.pgt.2018.016>
- Brahma, S. M. (2007). Distance relay with out-of-step blocking function using wavelet transform. *IEEE Transactions on Power Delivery*, 22(3), 1360-1366. <https://doi.org/10.1109/TPWRD.2006.886773>
- Buraimoh, E., & Davidson, I. E. (2020). Overview of fault ride-through requirements for photovoltaic grid integration, design and grid code compliance. In *2020 9th International Conference on Renewable Energy Research and Application (ICRERA)* (pp. 332-336). IEEE Publishing. <https://doi.org/10.1109/ICRERA49962.2020.9242914>
- Cabrera-Tobar, A., Bullich-Massagué, E., Aragüés-Peñalba, M., & Gomis-Bellmunt, O. (2019). Active and reactive power control of a PV generator for grid code compliance. *Energies*, 12(20), Article 3872. <https://doi.org/10.3390/en12203872>
- Camarillo-Peñaranda, J. R., Celeita, D., Gutierrez, M., Toro, M., & Ramos, G. (2020). An approach for out-of-step protection based on swing center voltage estimation and analytic geometry parameters. *IEEE Transactions on Industry Applications*, 56(3), 2402-2408. <https://doi.org/10.1109/TIA.2020.2973590>
- Choudhury, S. (2020). A comprehensive review on issues, investigations, control and protection trends, technical challenges and future directions for Microgrid technology. *International Transactions on Electrical Energy Systems*, 30(9), Article e12446. <https://doi.org/10.1002/2050-7038.12446>
- Chowdhury, M. A., Hosseinzadeh, N., Shen, W. X., & Pota, H. R. (2013). Comparative study on fault responses of synchronous generators and wind turbine generators using transient stability index based on transient energy function. *International Journal of Electrical Power & Energy Systems*, 51, 145-152. <https://doi.org/10.1016/j.ijepes.2013.02.025>
- Chung, P. D. (2013). Comparison of steady-state characteristics between DFIG and SCIG in wind turbine. *International Journal of Advanced Science and Technology*, 51, 135-146.
- Corsi, S., & Sabelli, C. (2004). General blackout in Italy sunday september 28, 2003, h. 03: 28: 00. In *IEEE Power Engineering Society General Meeting, 2004* (pp. 1691-1702). IEEE Publishing. <https://doi.org/10.1109/PES.2004.1373162>
- Desai, J., & Makwana, V. (2021). Power swing blocking algorithm based on real and reactive power transient stability. *Electric Power Components and Systems*, 48(16-17), 1673-1683. <https://doi.org/10.1080/15325008.2021.1906794>

- Desai, J. P., & Makwana, V. H. (2022). Modeling and implementation of power swing detection and out-of-step protection. *Journal of The Institution of Engineers (India): Series B*, *103*, 541-548. <https://doi.org/10.1007/s40031-021-00679-2>
- Dreidy, M., Mokhlis, H., & Mekhilef, S. (2017). Inertia response and frequency control techniques for renewable energy sources: A review. *Renewable and Sustainable Energy Reviews*, *69*, 144-155. <https://doi.org/10.1016/j.rser.2016.11.170>
- Dubey, R., Samantaray, S. R., Panigrahi, B. K., & Venkoparao, V. G. (2016). Data-mining model based adaptive protection scheme to enhance distance relay performance during power swing. *International Journal of Electrical Power & Energy Systems*, *81*, 361-370. <https://doi.org/10.1016/j.ijepes.2016.02.014>
- Elliott, R. J. R., Nguyen-Tien, V., & Strobl, E. A. (2021). Power outages and firm performance: A hydro-IV approach for a single electricity grid. *Energy Economics*, *103*, Article 105571. <https://doi.org/10.1016/j.eneco.2021.105571>
- Emmanue, O., Othman, M. L., Hizam, H., Othman, M. M., Aker, E., Chidiebere, A. O., & Samuel, T. N. (2019). Hybrid signal processing and machine learning algorithm for adaptive fault classification of wind farm integrated transmission line protection. *International Journal of Integrated Engineering*, *11*(4), 91-100. <https://publisher.uthm.edu.my/ojs/index.php/ijie/article/view/4562>
- Emmanuel, O., Othman, M. L., Hizam, H., & Othman, M. M. (2020). Single line-to-ground fault special protection scheme for integrated windfarm transmission line using data mining. In *2020 2nd International Conference on Smart Power & Internet Energy Systems (SPIES)* (pp. 76-81). IEEE Publishing. <https://doi.org/10.1109/SPIES48661.2020.9242959>
- Folly, K., & Sheetekela, S. (2009). Impact of fixed and variable speed wind generators on the transient stability of a power system network. In *2009 IEEE/PES Power Systems Conference and Exposition* (pp. 1-7). IEEE Publishing. <https://doi.org/10.1109/PSCE.2009.4840178>
- Gao, Z. D., & Wang, G. B. (1991). A new power swing block in distance protection based on a microcomputer-principle and performance analysis. In *1991 International Conference on Advances in Power System Control, Operation and Management, APSCOM-91* (Vol. 2, pp. 843-847). IET.
- Gautam, D., Vittal, V., & Harbour, T. (2009). Impact of increased penetration of DFIG-based wind turbine generators on transient and small signal stability of power systems. *IEEE Transactions on Power Systems*, *24*(3), 1426-1434. <https://doi.org/10.1109/TPWRS.2009.2021234>
- Gonzalez-Longatt, F., Adiyabazar, C., & Martinez, E. V. (2021). Setting and testing of the out-of-step protection at mongolian transmission system. *Energies*, *14*(23), Article 8170. <https://doi.org/10.3390/en14238170>
- Gunasegaran, M. K., Tan, C., Bakar, A. H. A., Mokhlis, H., & Illias, H. A. (2015). Progress on power swing blocking schemes and the impact of renewable energy on power swing characteristics: A review. *Renewable and Sustainable Energy Reviews*, *52*, 280-288. <https://doi.org/10.1016/j.rser.2015.07.066>
- Haddadi, A., Farantatos, E., Kocar, I., & Karaagac, U. (2021). Impact of inverter based resources on system protection. *Energies*, *14*(4), Article 1050. <https://doi.org/10.3390/en14041050>
- Haddadi, A., Kocar, I., Karaagac, U., Gras, H., & Farantatos, E. (2019). Impact of wind generation on power swing protection. *IEEE Transactions on Power Delivery*, *34*(3), 1118-1128. <https://doi.org/10.1109/TPWRD.2019.2896135>

- Hashemi, S. M., & Sanaye-Pasand, M. (2018). Distance protection during asymmetrical power swings: challenges and solutions. *IEEE Transactions on Power Delivery*, 33(6), 2736-2745. <https://doi.org/10.1109/TPWRD.2018.2816304>
- He, H., Chen, L., Yin, T., Cao, Z., Yang, J., Tu, X., & Ren, L. (2016). Application of a SFCL for fault ride-through capability enhancement of DG in a microgrid system and relay protection coordination. *IEEE Transactions on Applied Superconductivity*, 26(7), 1-8. <https://doi.org/10.1109/TASC.2016.2599898>
- Holbach, J. (2006). New out of step blocking algorithm for detecting fast power swing frequencies. In *2006 Power Systems Conference: Advanced Metering, Protection, Control, Communication, and Distributed Resources* (pp. 182-199). IEEE Publishing. <https://doi.org/10.1109/PSAMP.2006.285388>
- Jedrzejczak, J., Anders, G. J., Fotuhi-Firuzabad, M., Farzin, H., & Aminifar, F. (2016). Reliability assessment of protective relays in harmonic-polluted power systems. *IEEE Transactions on Power Delivery*, 32(1), 556-564. <https://doi.org/10.1109/TPWRD.2016.2544801>
- Jia, K., Gu, C., Xuan, Z., Li, L., & Lin, Y. (2017). Fault characteristics analysis and line protection design within a large-scale photovoltaic power plant. *IEEE Transactions on Smart Grid*, 9(5), 4099-4108. <https://doi.org/10.1109/TSG.2017.2648879>
- Kang, D., & Gokaraju, R. (2016). A new method for blocking third-zone distance relays during stable power swings. *IEEE Transactions on Power Delivery*, 31(4), 1836-1843. <https://doi.org/10.1109/PESGM.2017.8273837>
- Khadka, N., Paudel, R., Adhikary, B., Bista, A., Sharma, S., & Shrestha, A. (2020). Transient stability in renewable energy penetrated power systems: A review. *Proceedings of the RESSD 2020 International Conference on Role of Energy for Sustainable Social Development in 'New Normal' Era, Kathmandu, Nepal*. IEEE PES Nepal Chapter.
- Khodaparast, J., & Khederzadeh, M. (2014). Three-phase fault detection during power swing by transient monitor. *IEEE Transactions on Power Systems*, 30(5), 2558-2565. <https://doi.org/10.1109/TPWRS.2014.2365511>
- Khoradshadi-Zadeh, H. (2005). Evaluation and performance comparison of power swing detection algorithms. In *IEEE Power Engineering Society General Meeting, 2005* (Vol. 2, pp. 1842-1848). <https://doi.org/10.1109/PES.2005.1489280>
- Lawan, M. M. G., Raharijaona, J., Camara, M. B., & Dakyo, B. (2017). Power control for decentralized energy production system based on the renewable energies—using battery to compensate the wind/load/PV power fluctuations. In *2017 IEEE 6th International Conference on Renewable Energy Research and Applications (ICRERA)* (pp. 1132-1138). IEEE Publishing. <https://doi.org/10.1109/ICRERA.2017.8191230>
- Lazaro, C., Marques, J. P., Marchesan, G., & Cardoso, G. (2018). Waveform asymmetry of instantaneous current signal based symmetrical fault detection during power swing. *Electric Power Systems Research*, 155, 340-349. <https://doi.org/10.1016/j.epsr.2017.11.005>
- Liang, Y., Li, W., & Zha, W. (2020). Adaptive mho characteristic-based distance protection for lines emanating from photovoltaic power plants under unbalanced faults. *IEEE Systems Journal*, 15(3), 3506-3516. <https://doi.org/10.1109/JSYST.2020.3015225>

- Liu, S., Bi, T., & Liu, Y. (2017). Theoretical analysis on the short-circuit current of inverter-interfaced renewable energy generators with fault-ride-through capability. *Sustainability*, *10*(1), Article 44. <https://doi.org/10.3390/su10010044>
- Mahamedi, B. (2010). A very fast unblocking scheme for distance protection to detect symmetrical faults during power swings. In *2010 Conference Proceedings IPEC*. IEEE Publishing. <https://doi.org/10.1109/IPECON.2010.5697162>
- Mararakanye, N., & Bekker, B. (2019). Renewable energy integration impacts within the context of generator type, penetration level and grid characteristics. *Renewable and Sustainable Energy Reviews*, *108*, 441-451. <https://doi.org/10.1016/j.rser.2019.03.045>
- Mathe, R., & Folly, K. (2017). Impact of large scale grid-connected wind generators on the power system network. In *2017 IEEE PES PowerAfrica* (pp. 328-333). IEEE Publishing. <https://doi.org/10.1109/PowerAfrica.2017.7991246>
- Mishra, P., Pradhan, A. K., & Bajpai, P. (2020). Adaptive distance relaying for distribution lines connecting inverter-interfaced solar PV plant. *IEEE Transactions on Industrial Electronics*, *68*(3), 2300-2309. <https://doi.org/10.1109/TIE.2020.2975462>
- Mohapatra, S., Mohanty, S. K., & Patel, T. K. (2017). Out-of-step technique based symmetrical fault analysis. In *2017 Innovations in Power and Advanced Computing Technologies (i-PACT)* (pp. 1-5). IEEE Publishing. <https://doi.org/10.1109/IPACT.2017.8244912>
- Mondal, A., Das, S., & Patel, B. (2020). Fault detection during power swing using fast discrete S-transform. In K. Maharatna, M. R. Kanjilal, S. C. Konar, S. Nandi, & K. Das (Eds.), *Lecture notes in electrical engineering: Vol. 575. Computational Advancement in Communication Circuits and Systems* (pp. 73-79). Springer. [https://doi.org/10.1007/978-981-13-8687-9\\_7](https://doi.org/10.1007/978-981-13-8687-9_7)
- Mooney, P. E. J., & Fischer, N. (2006). Application guidelines for power swing detection on transmission systems. In *2006 Power Systems Conference: Advanced Metering, Protection, Control, Communication, and Distributed Resources* (pp. 159-168). <https://doi.org/10.1109/PSAMP.2006.285385>
- Morais, A. P., Júnior, G. C., Mariotto, L., & Marchesan, G. (2015). A morphological filtering algorithm for fault detection in transmission lines during power swings. *Electric Power Systems Research*, *122*, 10-18. <https://doi.org/10.1016/j.epsr.2014.12.009>
- Moustakas, K., Loizidou, M., Rehan, M., & Nizami, A. (2020). A review of recent developments in renewable and sustainable energy systems: Key challenges and future perspective. *Renewable and Sustainable Energy Reviews*, *119*, Article 109418. <https://doi.org/10.1016/j.rser.2019.109418>
- Muljadi, E., Butterfield, C. P., Parsons, B., & Ellis, A. (2007). Effect of variable speed wind turbine generator on stability of a weak grid. *IEEE Transactions on Energy Conversion*, *22*(1), 29-36. <https://doi.org/10.1109/TEC.2006.889602>
- Nasab, M. R., & Yaghobi, H. (2020). A real-time out-of-step protection strategy based on instantaneous active power deviation. *IEEE Transactions on Power Delivery*, *36*(6), 3590-3600. <https://doi.org/10.1109/TPWRD.2020.3045276>
- Nayak, P. K., Rao, J. G., Kundu, P., Pradhan, A. K., & Bajpai, P. (2010). A comparative assessment of power swing detection techniques. In *2010 Joint International Conference on Power Electronics*,

- Drives and Energy Systems & 2010 Power India* (pp. 1-4). IEEE Publishing. <https://doi.org/10.1109/PEDES.2010.5712568>
- O'Donovan, M., Cowhey, E., Barry, N., & Connell, J. (2020). Assessment of Power Swing Blocking Functions. In *2020 55th International Universities Power Engineering Conference (UPEC)* (pp. 1-6). IEEE Publishing. <https://doi.org/10.1109/UPEC49904.2020.9209826>
- Ontiveros, L. J., Mercado, P. E., & Suvire, G. O. (2010). A new model of the double-feed induction generator wind turbine. In *2010 IEEE/PES Transmission and Distribution Conference and Exposition: Latin America (T&D-LA)* (pp. 263-269). IEEE Publishing. <https://doi.org/10.1109/TDC-LA.2010.5762892>
- Othman, M. L., & Aris, I. (2012). Inconsistent decision system: rough set data mining strategy to extract decision algorithm of a numerical distance relay–tutorial. In A. Karahoca (Ed.), *Advances in Data Mining Knowledge Discovery and Applications*. IntechOpen. <https://doi.org/10.5772/50460>
- Othman, M. L., Aris, I., Abdullah, S. M., Bakar, M. L. A. M. A., & Othman, M. R. (2009). Discovering decision algorithm of numerical distance relay using rough-set-theory-based data mining. *European Journal of Scientific Research*, 33(1), 30-56.
- Othman, M. L., Aris, I., Abdullah, S. M., Ali, M. L., & Othman, M. R. (2010). Knowledge discovery in distance relay event report: a comparative data-mining strategy of rough set theory with decision tree. *IEEE Transactions on Power Delivery*, 25(4), 2264-2287. <https://doi.org/10.1109/TPWRD.2010.2055587>
- Othman, M. L., Aris, I., & Ananthapadmanabha, T. (2016). Novel rule base development from IED-resident big data for protective relay analysis expert system. In S. V. Soto, J. M. Luna, & A. Cano (Eds.), *Big Data on Real-World Applications*. IntechOpen. <https://doi.org/10.5772/63756>
- Othman, M. L., Aris, I., Othman, M. R., & Osman, H. (2011). Rough-set-and-genetic-algorithm based data mining and rule quality measure to hypothesize distance protective relay operation characteristics from relay event report. *International Journal of Electrical Power & Energy Systems*, 33(8), 1437-1456. <https://doi.org/10.1016/j.ijepes.2011.06.024>
- Paladhi, S., Pradhan, A. K., & Rao, J. G. (2022). Accurate superimposed component estimation for improved relay performance during power swing. *IEEE Systems Journal*, 16(4), 6119-6129. <https://doi.org/10.1109/JSYST.2021.3138758>
- Patil, D., Naidu, O., Yalla, P., & Hida, S. (2019). An ensemble machine learning based fault classification method for faults during power swing. In *2019 IEEE Innovative Smart Grid Technologies-Asia (ISGT Asia)* (pp. 4225-4230). IEEE Publishing. <https://doi.org/10.1109/ISGT-Asia.2019.8881359>
- Rampokanyo, M., & Kamera, P. (2018). Impact of increased penetration levels of distributed inverter-based generation on transient stability. In *2018 IEEE PES/IAS PowerAfrica* (pp. 573-578). IEEE Publishing. <https://doi.org/10.1109/PowerAfrica.2018.8521139>
- Rao, A. V. K., & Ahmad, A. (2017). Power swing blocking (PSB) function for distance relay using prediction technique. *International Journal of System Assurance Engineering and Management*, 8(2), 301-307. <https://doi.org/10.1007/s13198-016-0434-2>
- Rao, A. V. K., Soni, K. M., Sinha, S. K., & Nasiruddin, I. (2017). Tracking of impedance trajectory for distance protection using neural networks. In *2017 4th IEEE Uttar Pradesh Section International Conference on*



- Electrical, Computer and Electronics (UPCON)* (pp. 289-294). IEEE Publishing. <https://doi.org/10.1109/UPCON.2017.8251062>
- Rao, J. G., & Pradhan, A. K. (2017). Supervising distance relay during power swing using synchrophasor measurements. *IET Generation, Transmission & Distribution*, *11*(17), 4136-4145. <https://doi.org/10.1049/iet-gtd.2016.1110>
- Ratha, A. (2013). India's blackouts of July 2012: What happened and why. *ESI Bulletin on Energy Trends and Development*, *5*(4), 3-6.
- Saha, S., Das, S., & Nandi, C. (2014). Harmonics analysis of power electronics loads. *International Journal of Computer Applications*, *92*(10), 32-36. <https://research.ijcaonline.org/volume92/number10/pxc3895228.pdf>
- Saleh, K. A., Moursi, M. S. E., & Zeineldin, H. H. (2015). A new protection scheme considering fault ride through requirements for transmission level interconnected wind parks. *IEEE Transactions on Industrial Informatics*, *11*(6), 1324-1333. <https://doi.org/10.1109/TII.2015.2479583>
- Samuelsson, O., & Lindahl, S. (2005). On speed stability. *IEEE Transactions on Power Systems*, *20*(2), 1179-1180. <https://doi.org/10.1109/TPWRS.2005.846194>
- Shafiqullah, G. M., Oo, A. M. T., Ali, A. B. M. S., & Wolfs, P. (2013). Potential challenges of integrating large-scale wind energy into the power grid-A review. *Renewable and Sustainable Energy Reviews*, *20*, 306-321. <https://doi.org/10.1016/j.rser.2012.11.057>
- Shair, J., Li, H., Hu, J., & Xie, X. (2021). Power system stability issues, classifications and research prospects in the context of high-penetration of renewables and power electronics. *Renewable and Sustainable Energy Reviews*, *145*, Article 111111. <https://doi.org/10.1016/j.rser.2021.111111>
- Sinsel, S. R., Riemke, R. L., & Hoffmann, V. H. (2020). Challenges and solution technologies for the integration of variable renewable energy sources-A review. *Renewable Energy*, *145*, 2271-2285. <https://doi.org/10.1016/j.renene.2019.06.147>
- Slotweg, J., & Kling, W. L. (2003). The impact of large scale wind power generation on power system oscillations. *Electric Power Systems Research*, *67*(1), 9-20. [https://doi.org/10.1016/S0378-7796\(03\)00089-0](https://doi.org/10.1016/S0378-7796(03)00089-0)
- Sorrentino, E., Navas, G., & Orea, E. (2018). Effect of an additional large disturbance during power swings on the impedance seen by the out-of-step blocking function. *International Journal of Electrical Power & Energy Systems*, *99*, 79-84. <https://doi.org/10.1016/j.ijepes.2017.12.026>
- Sravanthi, P., & Rani, K. R. (2014). Transient stability improvement of SCIG based wind farm with STATCOM. *Journal of Electrical and Electronics Engineering Research (IJEEER)*, *4*(2), 47-57.
- Swetapadma, A., & Yadav, A. (2016). Data-mining-based fault during power swing identification in power transmission system. *IET Science, Measurement & Technology*, *10*(2), 130-139. <https://doi.org/10.1049/iet-smt.2015.0169>
- Taheri, B., & Razavi, F. (2018). Power swing detection using rms current measurements. *Journal of Electrical Engineering and Technology*, *13*(5), 1831-1840.

- Taheri, B., Salehimehr, S., Razavi, F., & Parpaei, M. (2020). Detection of power swing and fault occurring simultaneously with power swing using instantaneous frequency. *Energy Systems, 11*, 491-514. <https://doi.org/10.1007/s12667-018-00320-0>
- Taheri, B., & Sedighzadeh, M. (2020). Detection of power swing and prevention of mal-operation of distance relay using compressed sensing theory. *IET Generation, Transmission & Distribution, 14*(23), 5558-5570. <https://doi.org/10.1049/iet-gtd.2020.0540>
- Tin, H., Abu-Siada, A., & Masoum, M. S. (2011). Impact of harmonics on the performance of over-current relays. In *AUPEC 2011* (pp. 1-4). IEEE Publishing.
- Torres, S., Esponda, H., Andrade, M., Vázquez, E., Paternina, M. R. A., Zamora, A., & Ramirez, J. M. (2016). Unblocking function of distance relay during power swing based on modal analysis. In *2016 IEEE PES Transmission & Distribution Conference and Exposition-Latin America (PES T&D-LA)* (pp. 1-6). IEEE Publishing. <https://doi.org/10.1109/TDC-LA.2016.7805633>
- Tziouvaras, D. A., & Hou, D. (2004). Out-of-step protection fundamentals and advancements. In *57th Annual Conference for Protective Relay Engineers, 2004* (pp. 282-307). IEEE Publishing. <https://doi.org/10.1109/CPRE.2004.238495>
- Tu, D. V., Chaitusaney, S., & Yokoyama, A. (2014). Maximum-allowable distributed generation considering fault ride-through requirement and reach reduction of utility relay. In *2012 10th International Power & Energy Conference (IPEC)* (pp. 127-134). IEEE Publishing. <https://doi.org/10.1109/ASSCC.2012.6523251>
- Verzosa, Q. (2013). Realistic testing of power swing blocking and out-of-step tripping functions. In *2013 66th Annual Conference for Protective Relay Engineers* (pp. 420-449). IEEE Publishing. <https://doi.org/10.1109/CPRE.2013.6822056>
- Višić, I., Strnad, I., & Marušić, A. (2020). Synchronous generator out of step detection using real time load angle data. *Energies, 13*(13), Article 3336. <https://doi.org/10.3390/en13133336>
- Wannous, K., & Toman, P. (2018). Evaluation of harmonics impact on digital relays. *Energies, 11*(4), Article 893. <https://doi.org/10.3390/en11040893>
- Yan, R., Roediger, S., & Saha, T. K. (2011). Impact of photovoltaic power fluctuations by moving clouds on network voltage: A case study of an urban network. In *AUPEC 2011* (pp. 1-6). IEEE Publishing.
- Yang, W., Zhou, X., & Xue, F. (2010). Impacts of large scale and high voltage level photovoltaic penetration on the security and stability of power system. In *2010 Asia-Pacific Power and Energy Engineering Conference* (pp. 1-5). IEEE Publishing. <https://doi.org/10.1109/APPEEC.2010.5448930>
- Yellajosula, J. R. A. K., Wei, Y., Grebla, M., Paudyal, S., & Mork, B. A. (2019). Online detection of power swing using approximate stability boundaries. *IEEE Transactions on Power Delivery, 35*(3), 1220-1229. <https://doi.org/10.1109/TPWRD.2019.2941522>
- Ying, J., Yuan, X., & Hu, J. (2017). Inertia characteristic of DFIG-based WT under transient control and its impact on the first-swing stability of SGs. *IEEE Transactions on Energy Conversion, 32*(4), 1502-1511. <https://doi.org/10.1109/TEC.2017.2698521>

- Yoosefian, D., & Chabanloo, R. M. (2020). Protection of distribution network considering fault ride through requirements of wind parks. *Electric Power Systems Research*, 178, Article 106019. <https://doi.org/10.1016/j.epsr.2019.106019>
- Yusoff, N., & Abidin, A. F. (2013). The effect of solar Photovoltaic (PV) system to the characteristic of power swing. In *2013 IEEE 3rd International Conference on System Engineering and Technology* (pp.99-102). <https://doi.org/10.1109/ICSEngT.2013.6650151>
- Zare, J., & Azad, S. P. (2020). A new distance protection scheme for SCIG-based wind farms. In *2020 IEEE Power & Energy Society General Meeting (PESGM)* (pp. 1-5). IEEE Publishing. <https://doi.org/10.1109/PESGM41954.2020.9281962>
- Zheng, Q., Li, J., Ai, X., Wen, J., & Fang, J. (2017). Overview of grid codes for photovoltaic integration. In *2017 IEEE Conference on Energy Internet and Energy System Integration (EI2)* (pp. 1-6). IEEE Publishing. <https://doi.org/10.1109/EI2.2017.8245501>
- Zhu, S., Gu, Q., & Zheng, L. (2004). New swing-blocking methods for digital distance protection. In *IEEE PES Power Systems Conference and Exposition, 2004* (pp. 587-591). IEEE Publishing. <https://doi.org/10.1109/PSCE.2004.1397484>



## The Influence of Cavity Size and Location Within Insulation Paper on the Partial Discharge Activities

Muhammad Hakirin Roslan<sup>1,2</sup>, Norhafiz Azis<sup>2,3\*</sup>, Mohd Zainal Abidin Ab Kadir<sup>2</sup>,  
Jasronita Jasni<sup>2</sup> and Mohd Fairouz Mohd Yousof<sup>4</sup>

<sup>1</sup>Faculty of Engineering, Universiti Pertahanan Nasional Malaysia, 57000 UPNM, Kuala Lumpur, Malaysia

<sup>2</sup>Advanced Lightning, Power and Energy Research Centre (ALPER), Universiti Putra Malaysia, 43400 UPM, Serdang, Selangor, Malaysia

<sup>3</sup>Institute of Nanoscience and Nanotechnology (ION2), Universiti Putra Malaysia, 43400 UPM, Serdang, Selangor, Malaysia

<sup>4</sup>Faculty of Electrical and Electronics Engineering, Universiti Tun Hussein Onn Malaysia, 86400 UTHM, Parit Raja, Johor, Malaysia

### ABSTRACT

This paper examines the influence of cavity size and location in the insulation paper on the Partial Discharge (PD) activities through Finite Element Method (FEM). The model consisted of a conductor wrapped with insulation paper. Two different locations of the spherical cavities were introduced in this study, namely Location 1 (L1) and Location 2 (L2), located at the center and left corner of the insulation paper. The model introduced two different sizes of cavities with diameters of 0.5 mm and 0.8 mm. An AC voltage source of 17 kV, 50 Hz, was applied at the conductor while the bottom of the insulation paper was grounded. The real and apparent PDs were obtained by integrating the current flowing through the cavity and ground electrode with the respective surface area. The simulation was carried out for 100 cycles. The resultant model was used to study the

PD occurrence, magnitude, and Phase Resolved Partial Discharge (PRPD) within the insulation paper. It is found that the large cavity size produces a lower number of PD occurrences per cycle than the small cavity size. The large cavity size produces a higher charge magnitude as compared with the small cavity size. The PD occurrence per cycle and charge magnitude are higher for the cavity location at L1 compared to L2. The PRPD yields the same pattern for

### ARTICLE INFO

#### Article history:

Received: 27 October 2022

Accepted: 06 March 2023

Published: 03 October 2023

DOI: <https://doi.org/10.47836/pjst.31.6.15>

#### E-mail addresses:

[hakirin@upnm.edu.my](mailto:hakirin@upnm.edu.my) (Muhammad Hakirin Roslan)

[norhafiz@upm.edu.my](mailto:norhafiz@upm.edu.my) (Norhafiz Azis)

[mzk@upm.edu.my](mailto:mzk@upm.edu.my) (Mohd Zainal Abidin Ab Kadir)

[jas@upm.edu.my](mailto:jas@upm.edu.my) (Jasronita Jasni)

[fairouz@uthm.edu.my](mailto:fairouz@uthm.edu.my) (Mohd Fairouz Mohd Yousof)

\* Corresponding author

cavity location at L1 and L2, whereby the differences are only on the charge magnitude and PD occurrence per cycle.

*Keywords:* Insulation paper, partial discharge modeling, spherical cavity, transformer

---

## INTRODUCTION

One of the parameters that can lead to the possible failure of the transformer is Partial Discharge (PD) (Hussain et al., 2021; Naidu & Kamaraju, 2013; Youssef et al., 2022). PD can exist as a result of either a poor manufacturing process or an insulation aging process. One of the sources of the PD is either the cavity or void in insulations. In recent years, PD monitoring has become one of the crucial methods to evaluate the insulation status. The electrical method is one of the conventional methods to evaluate PD within insulations (IEC60270, 2000; Meitei et al., 2021). PD is a complex phenomenon that produces heat, sound, light, chemical reactions, high-frequency waves, and electrical pulses (CIGRE, 2017; Sikorski et al., 2020; Xavier et al., 2021). Even though PD measurement can provide extensive information on the condition of insulations, PD modeling can further enhance the knowledge of its characteristics.

PD modeling can be classified into capacitance, analytical, and Finite Element Method (FEM) model approaches (Afrouzi et al., 2022). The capacitance model is the first PD model introduced to understand the concept of PD (Whitehead, 1952). An analytical model is also proposed, whereby the surface charge accumulation on the cavity surface due to the previous PD is taken into account, which is not considered in the capacitance model (Pedersen et al., 1995; Pedersen et al., 1991). Nowadays, the reliability of numerical modeling software leads to the introduction of PD modeling based on the FEM model (Borghei, 2022; Forss'en, 2008; Forssén & Edin, 2008; Illias, 2011). This method seems promising due to its ability to model the complex geometry of the electrical equipment. The FEM model has been applied to the cables and wide bandgap power module application for the determination of PD activities (Borghei & Ghassemi, 2019; Borghei & Ghassemi, 2020, 2021; Illias et al., 2016; Joseph et al., 2019).

Both external and internal factors can affect PD activities (Illias et al., 2017). Voltage and frequency are known external factors, while cavity condition, design, and PD mechanism characteristics are classified as internal factors (Borghei et al., 2021; Illias et al., 2011, 2012). The cavity condition mainly involves size and location. Insulation thickness, permittivity, and conductivity, as well as the shape of the conductor, can be included in design characteristics. PD mechanisms include the Electron Generation Rate (EGR) and surface charge accumulation on the cavity surface. Due to the complex winding geometry of the transformer, the effect of the cavity location, as well as cavity size in the insulation paper on the PD activities, needs to be further investigated.

This paper presents the investigation of PD activities within a spherical cavity in the insulation paper of a transformer through FEM modeling. The three-dimensional (3D) model consists of a conductor, insulation paper, and a spherical cavity, solved through an electric transient solver. In this study, the simulation of PD activities is carried out based on the 3D modeling of the active part of the high-voltage winding. It is based on disc-layered high voltage winding of a 33/11 kV, 30 MVA transformer. The Phase Resolved Partial Discharge (PRPD) analysis in the insulation paper with consideration of the spherical cavity location and size is evaluated.

## PARTIAL DISCHARGE MECHANISM

Discharge occurs in a defective area, such as a cavity, due to the electron avalanche process, which initiates from the ionization process. Once the electric field in the cavity is sufficient to energize the free electron, it can lead to the multiplication of the number of electrons through collision with neutral atoms. The discharge continues until the electric field in the cavity drops below the extinction field,  $E_{ext}$ . The PD inception field,  $E_{inc}$  is the minimum electric field to initiate the ionization process.  $E_{inc}$  is one of the important mechanisms required to model PD. The second mechanism identifies the number of electrons to initiate the electron avalanche. The final mechanism is the  $E_{ext}$ , the minimum electric field required to stop the discharge process.

### Partial Discharge Inception Field

The ionization process requires sufficient enhancement of the electric field in the cavity to trigger the movement of the free electron to collide with neutral atoms. The first condition to initiate PD is that the electric field in the cavity must exceed the  $E_{inc}$ . In this study, the air-filled cavity was used, which can be calculated based on Equation 1 (Borghesi & Ghassemi, 2020; Borghesi et al., 2021; Callender & Lewin, 2020).

$$E_{inc} = 24.2P \left( 1 + \frac{8.6}{\sqrt{Pd}} \right) \quad \text{unit in } \frac{V}{m} \quad [1]$$

$P$  and  $d$  in Equation 1 referred to the cavity pressure and diameter, which were set to 100 kPa, and 2 different sizes of the cavities with a diameter of 0.5 mm and 0.8 mm.

### Partial Discharge Extinction Field

$E_{ext}$  was determined based on Equation 2, where the value was set to 10% of  $E_{inc}$  value calculated from Equation 1 (Joseph et al., 2019).

$$E_{ext} = 0.1E_{inc} \quad \text{unit in } \frac{V}{m} \quad [2]$$

### Electron Generation Rate

Apart from the electric field in the cavity needing to exceed the  $E_{inc}$ , the availability of the free electron is also required to initiate the ionization process. The lack of the free electron causes the PD occurrence to be delayed even if the first condition, the  $E_{inc}$ , is satisfied. The time delay refers to the statistical time lag,  $\tau_{stat}$ , related to the electron generation. The sources of electron generation are volume ionization and surface emission.

(i) Volume ionization

Electron generation from the volume ionization is normally due to the gas ionization by irradiation of photons (Borghesi et al., 2021). In this study, the electron generation from volume ionization was set as a constant value throughout the simulation, denoted by  $N_{vol}$  (Illias, 2011; Pan et al., 2019).

(ii) Surface emission

Electron Generation Rate (EGR) from surface emission was not considered for the first discharge of PD due to the unavailability of charge accumulation at the surface of the cavity. After the first PD occurrence, the charge from the previous PD accumulates at the surface of the cavity. The effect of the surface charge decay was considered in calculating EGR from the surface emission. In this study, the EGR from surface emission was set as time-dependent, denoted by  $N_{surf}(t)$ , whereby the number of electrons changed with time.

This study calculated the total EGR denoted by  $N_{tot}(t)$  based on Equation 3 (Illias, 2011; Pan et al., 2019).

$$N_{tot}(t) = N_{surf}(t) + N_{vol} \quad , \quad \text{unit in } \frac{1}{s} \quad [3]$$

Where  $N_{vol}$  is a constant value that was set to  $1 \text{ s}^{-1}$ , and  $N_{surf}(t)$  is a time-dependent value that can be calculated based on Equation 4 (Illias, 2011).

$$N_{surf}(t) = N_{PD} \exp\left(\frac{E_{cav}(t)}{E_{inc}}\right) \exp\left(\frac{-(t - t_{PD})}{t_{decay}}\right) \quad , \quad \text{unit in } \frac{1}{s} \quad [4]$$

Where the influence of the electric field on surface emission was represented in the first term of the exponential function, the second exponential function represented the effect of surface charge decay deposited by the previous PD. Based on the previous study, the  $t_{decay}$  was set to 2 ms at ambient temperature conditions (Illias et al., 2012).  $N_{PD}$  is the number of electrons available due to previous PD, which can be calculated by Equation 5 (Illias, 2011).

$$N_{PD} = N_{s0} \frac{E_{cav}(t_{PD})}{E_{inc}} \quad , \quad \text{unit in } \frac{1}{s} \quad [5]$$



Where  $N_{s0}$  is the initial electron available, and its value depends on the polarity of the electric field previous PD,  $E_{cav}(PD1)$ , and the next PD occurrence,  $E_{cav}(PD2)$ , as shown in Equation 6 (Illias, 2011). The  $N_{s0}$  is high when no polarity changes exist between  $E_{cav}(PD1)$  and  $E_{cav}(PD2)$ . Otherwise, the  $N_{s0}$  is low due to the assumption of the effect of surface charge decay. As a result, it can lead to a high statistical time lag.

$$N_{s0} = \begin{cases} N_{s0Low} & \text{when } \frac{E_{cav}(PD2)}{E_{cav}(PD1)} < 0 \\ N_{s0Higher} & \text{when } \frac{E_{cav}(PD2)}{E_{cav}(PD1)} > 0 \end{cases} \quad [6]$$

The values of  $N_{s0Low}$  and  $N_{s0Higher}$  depend on the cavity size, whereby based on the previous study, the values for large cavity size are lower than for small cavity size (Illias et al., 2012).

### FINITE ELEMENT METHOD MODEL

Electric field distribution computation in the dielectric is important in PD modeling. Therefore, the FEM was employed to compute the electric field distribution. In this study, FEM based on Ansys Maxwell was utilized to compute the electric field distribution in the insulation paper as well as a spherical cavity. The electric transient solver was used in this study to solve for the electric potential as well as the electric field distribution.

### Phase Resolved Partial Discharge Simulation

The discharge process used in this study was the conductance method. The discharge process was modeled through increments of the cavity conductivity from the initial state to a high value. Figure 1 shows the flowchart of the PD process algorithm. The process started with the initialization of the modeling parameters in the simulation, as shown in Table 2. The simulation was carried out at each time step during no PD. At each of the time steps, the electric field in the cavity was extracted and compared with the inception field to evaluate the first condition of the PD occurrence. The time step was increased until the electric field in the cavity exceeded the inception field, and the process continued to evaluate the second condition of PD occurrence, which was the availability of the free electron. Once both conditions were satisfied, the total EGR was calculated, and the probability of PD occurrence was determined based on Equation 7 (Forssén & Edin, 2008; Illias, 2011; Pan et al., 2019). Since the PD occurrence was stochastic, the probability was compared with the random number, R, ranging from 0 to 1. If the probability was higher than the R, the discharge process was modeled, increasing the cavity conductivity. Due to the increment of the cavity conductivity, the electric field in the cavity decreased until the electric field

in the cavity was less than the  $E_{ext}$ , whereby the cavity conductivity was reset to the initial value. The apparent and real charges were determined based on the current integration flowing through the ground electrode and cavity center surface area. Once the simulation step reached 100 cycles, the simulation stopped, and PRPD was plotted.

$$P(t) = N_{tot}(t)\Delta t \quad [7]$$

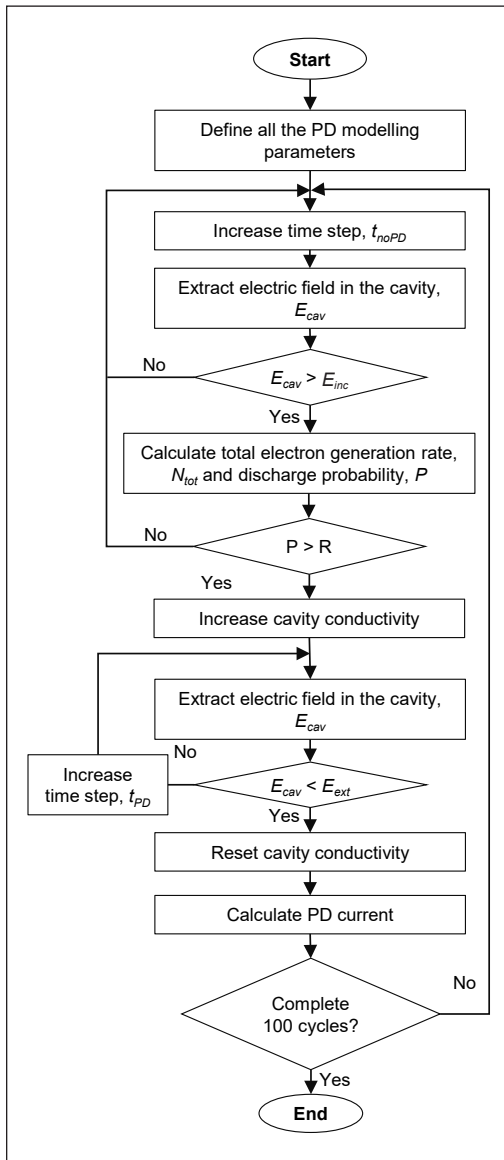


Figure 1. Flowchart of the phase-resolved partial discharge simulation

### Model Geometry and Partial Discharge Model Parameters

The 3D model geometry consists of insulation paper and a conductor, as shown in Figure 2. The model was developed in Ansys Maxwell using an electric transient solver to solve the electric potential distribution in the 3D model. It was modeled based on the active part of the disc-layered high voltage winding in a 33/11 kV, 30 MVA transformer.

The spherical cavity was introduced within the insulation paper to represent the defect area. The details of the geometrical design can be seen in Table 1 (Murthy et al., 2020). The details of the PD modeling parameters for the simulation are shown in Table 2. The relative permittivity of the insulation paper,  $\epsilon_{mat}$ , used in this study was 2.3, according to (Murthy et al., 2020). The

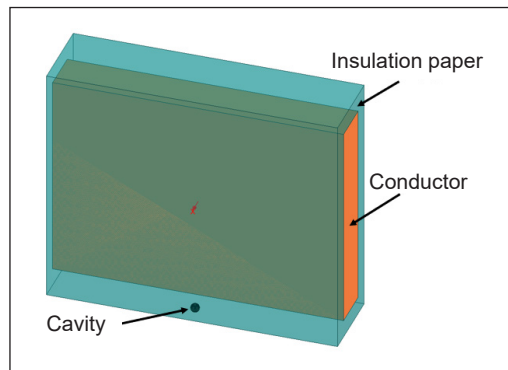


Figure 2. 3D model geometry of insulation paper and conductor

Table 1  
Parameter for 3D finite element method model

Parameters	Values
Height (conductor)	11.5 mm
Width (conductor)	2.4 mm
Length (conductor)	16 mm
The thickness of the insulation paper	1 mm
Cavity diameter	0.5 mm and 0.8 mm
Total mesh elements	255932

Table 2  
Parameter for partial discharge modeling of the insulation paper and cavity

Parameters	Values	Units
Insulation paper (relative permittivity), $\epsilon_{mat}$	2.3	
Cavity (relative permittivity), $\epsilon_{cav}$	1	
Insulation paper (conductivity), $\sigma_{mat}$	$1 \times 10^{-10}$	s/m
Conductivity of cavity during no PD, $\sigma_{cav,0}$	0	s/m
Conductivity of cavity during PD, $\sigma_{cav,PD}$	$5 \times 10^{-3}$	s/m
Simulation time step (no PD), $t_{noPD}$	100	$\mu$ s
Simulation time step during PD, $t_{PD}$	1	ns

relative permittivity of the spherical cavity,  $\epsilon_{cav}$ , was set to 1 since the cavity was assumed to contain only air. The conductivities of insulation paper,  $\sigma_{mat}$ , are reported between  $0.05 \times 10^{-12}$  and  $1.2 \times 10^{-12}$  s/m (Saha & Purkait, 2008; Xiao et al., 2013). However, the electric field distribution in insulation paper is less affected by  $\sigma_{mat}$  if the value is too small based on simulation using the FEM (Illias, 2011). Therefore, the conductivity was set to  $1 \times 10^{-10}$  s/m in the simulation. The conductivity of the cavity during no PD,  $\sigma_{cav,0}$  was 0 s/m since there is no current flowing in the cavity. During the PD occurrence, the conductivity of the cavity,  $\sigma_{cav,PD}$  was set to  $5 \times 10^{-3}$  s/m, according to Illias (2011). This value is found suitable to avoid the fast reduction of the electric field as well as reduce the simulation time. The time step during no PD was set to 100  $\mu$ s, which is suitable to avoid long simulation time. The time step during PD was set to 1 ns since the PD could be initiated in the range between micro and nanoseconds (CIGRE, 2017; Morsalin & Das, 2020). An AC voltage source of 17 kV, 50 Hz AC was supplied at the conductor since it is high enough to exceed the PD inception field in this study. The bottom of the insulation paper was grounded.

In this study, 2 different locations of the spherical cavities were introduced, namely Location 1 (L1) and Location 2 (L2), located at the center and left corner of the insulation papers. In addition, 2 different sizes of cavities with a diameter of 0.5 mm and 0.8 mm were introduced in the model, as shown in Figure 3.

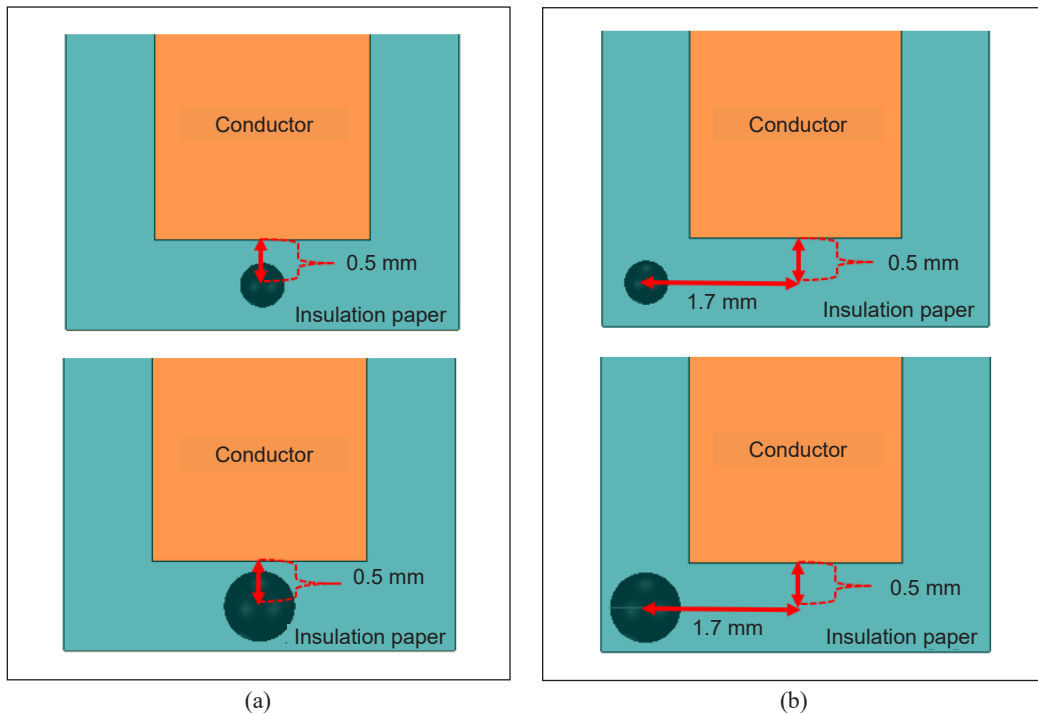


Figure 3. Two different cavity sizes and locations within the insulation paper: (a) Side view (L1); and (b) Side view (L2)

## RESULTS

### Phase Resolved Partial Discharge Pattern for the 0.5 mm Cavity Size in the Insulation Paper

The real charge magnitude PRPD pattern in the insulation paper for the cavity with a diameter of 0.5 mm at L1 is shown in Figure 4. The PD occurrence is mostly generated at the  $E_{inc}$  or minimum charge magnitude with the highest repetition rate. The highest charge magnitude is generated at the phases from  $60^\circ$  to  $90^\circ$  as well as from  $240^\circ$  to  $270^\circ$ . A similar PRPD pattern is recorded for the apparent charge magnitude, as shown in Figure 5. However, the charge magnitude is lower than the real charge magnitude. It is expected due to the apparent charge magnitude is the induced charge calculated at the ground electrode.

The PRPD pattern of real charge magnitude in the insulation paper for the cavity with a diameter of 0.5 mm at L2 is shown in Figure 6. Most of the PD occurrences are recorded at  $E_{inc}$  or at the minimum level charge magnitude with the highest number of repetition rates at the phases from  $45^\circ$  to  $90^\circ$  as well as from  $210^\circ$  to  $270^\circ$ . The highest charge magnitude is generated at the phases from  $60^\circ$  to  $90^\circ$  as well as from  $240^\circ$  to  $270^\circ$ . Figure 7 shows the PRPD pattern of apparent charge magnitude whereby the pattern is similar to the real charge PRPD with the difference only in charge magnitude.

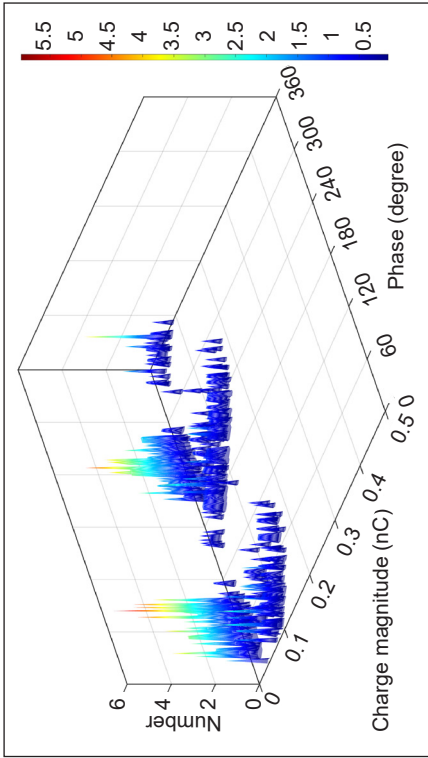


Figure 5. The phase-resolved partial discharge pattern of apparent charge magnitude in the insulation paper for the cavity diameter of 0.5 mm at L1

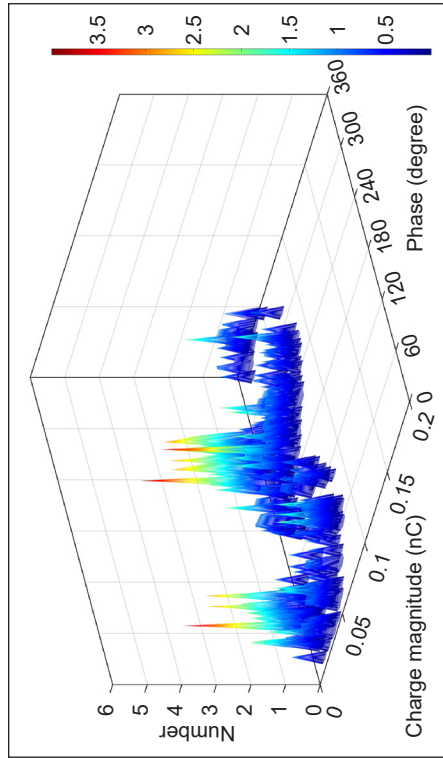


Figure 7. The phase-resolved partial discharge pattern of apparent charge magnitude in the insulation paper for the cavity with a diameter of 0.5 mm at L2

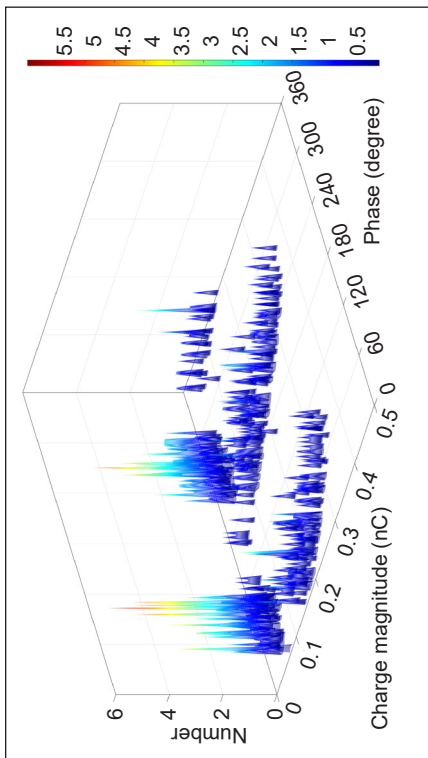


Figure 4. The phase-resolved partial discharge pattern of real charge magnitude in the insulation paper for the cavity diameter of 0.5 mm at L1

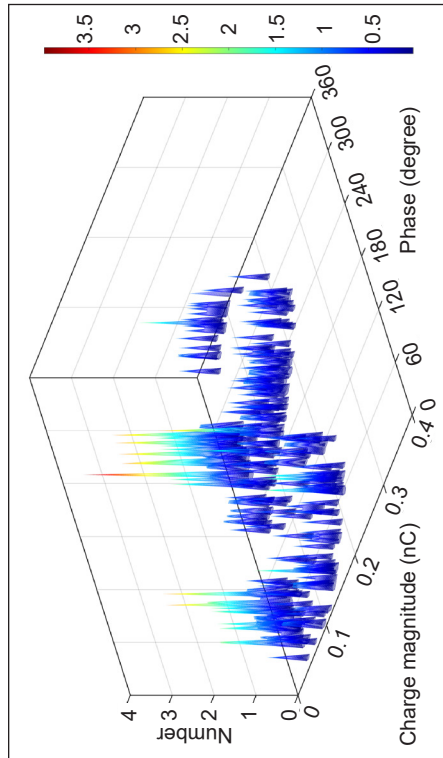


Figure 6. The phase-resolved partial discharge pattern of real charge magnitude in the insulation paper for the cavity diameter of 0.5 mm at L2

### Phased Resolved Partial Discharge Pattern for the 0.8 mm Cavity Size in the Insulation Paper

The PRPD pattern of real and apparent charge magnitudes in the insulation paper for the cavity with a diameter of 0.8 mm at both locations at L1 and L2 are shown in Figures 8, 9, 10, and 11. In terms of cavity location at L1, the PRPD pattern for both real and apparent charge magnitudes are similar, but the differences are only in the amplitude, as shown in Figures 8 and 9. The charge magnitude is highest at the phases from 60° to 120° as well as from 240° and 300°. The charge distribution is evenly distributed over the phase range. The PD repetition rate at each phase and charge magnitude ranges are close to each other, with the repetition rate ranging from 0.5 to 2.

A similar PRPD pattern as L1 is recorded in the insulation paper for the cavity with a diameter of 0.8 mm at L2, as shown in Figures 10 and 11. However, the charge magnitude is slightly lower as compared with L1. The PD occurrence at L1 is also higher than at L2 based on the PRPD pattern intensity, as shown in Figures 8, 9, 10, and 11.

### Partial Discharge Activities for Different Cavity Sizes and Locations

The PD parameters in the insulation paper for different cavity sizes and locations with consideration of  $\tau_{stat}$  are shown in Table 3. The PD occurrence per cycle is 5.12 cycles for both real and apparent charge magnitudes at L1 for the cavity with a diameter of 0.5 mm. However, the PD occurrence per cycle at L2 for the same cavity size is lower than L1 with 3.04 cycles. The PD occurrence per cycle is slightly low for the cavity with a diameter of 0.8 mm at both locations, which are 3.05 cycles at L1 and 2.17 cycles at L2.

The charge magnitude in terms of maximum, minimum, and mean charges for the cavity with a diameter of 0.5 mm are lower than the cavity with a diameter of 0.8 mm, as shown in Table 3. The charge magnitude is higher for the cavity location at L1 as compared with L2, regardless of the cavity size.

Table 4 shows the PD parameters in the insulation paper for different cavity sizes and locations without consideration of  $\tau_{stat}$ . The PD occurrence per cycle is higher for the cavity

Table 3  
Partial discharge parameters in the insulation paper for different cavity sizes and locations considering  $\tau_{stat}$

Parameters	Cavity Location at L1				Cavity location at L2			
	0.5 mm		0.8 mm		0.5 mm		0.8 mm	
Cavity size	Real	Apparent	Real	Apparent	Real	Apparent	Real	Apparent
PD occurrence per cycle	5.12	5.12	3.05	3.05	3.04	3.04	2.17	2.17
Total charge per cycle, pC	684	342	1806	1295	341	124	821	479
Mean Charge, pC	134	67	592	424	112	41	378	221
Maximum charge, pC	368	184	1179	845	240	87	688	402
Minimum charge, pC	50	25	145	104	44	16	113	66

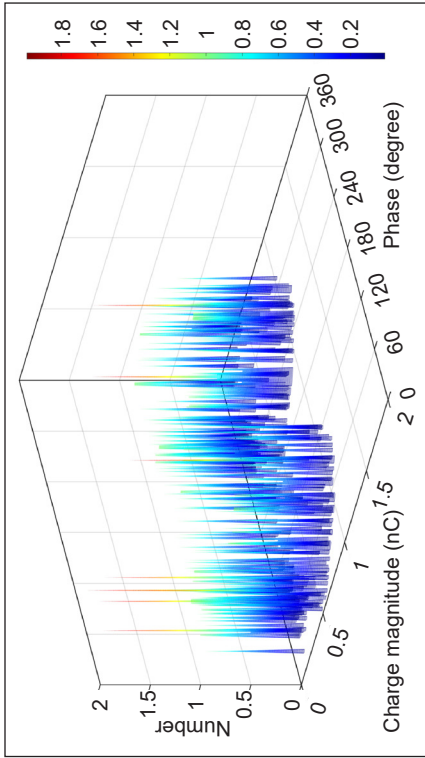


Figure 9. The phase resolved a partial discharge pattern of apparent charge magnitude in the insulation paper for the cavity with a diameter of 0.8 mm at L1

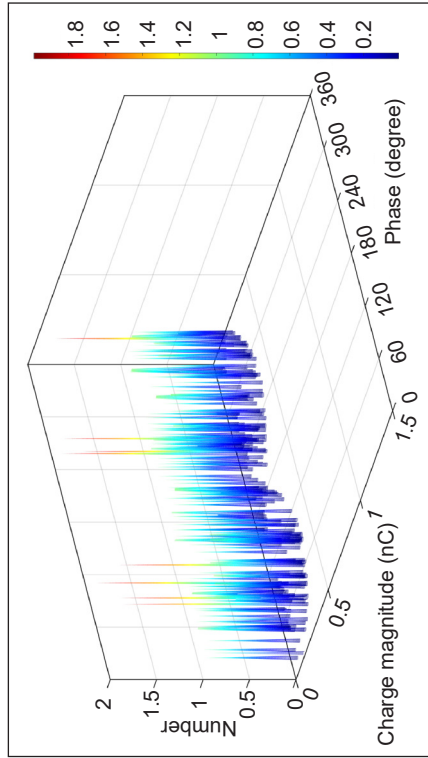


Figure 11. The phased resolved partial discharge pattern of apparent charge magnitude in the insulation paper for the cavity with a diameter of 0.8 mm at L2

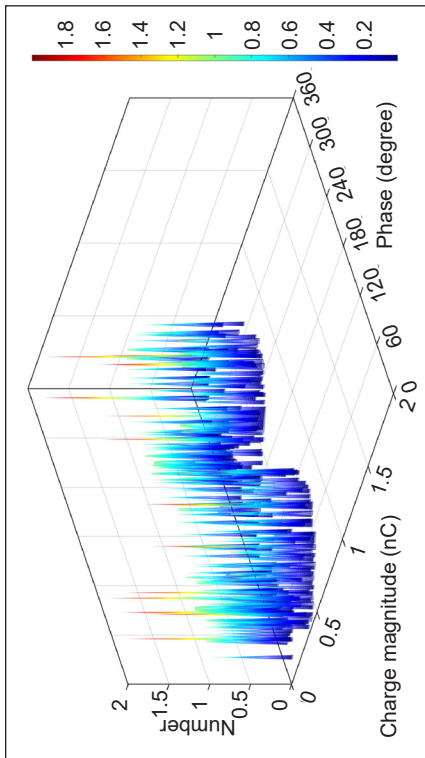


Figure 8. The phase-resolved partial discharge pattern of real charge magnitude in the insulation paper for the cavity with a diameter of 0.8 mm at L1

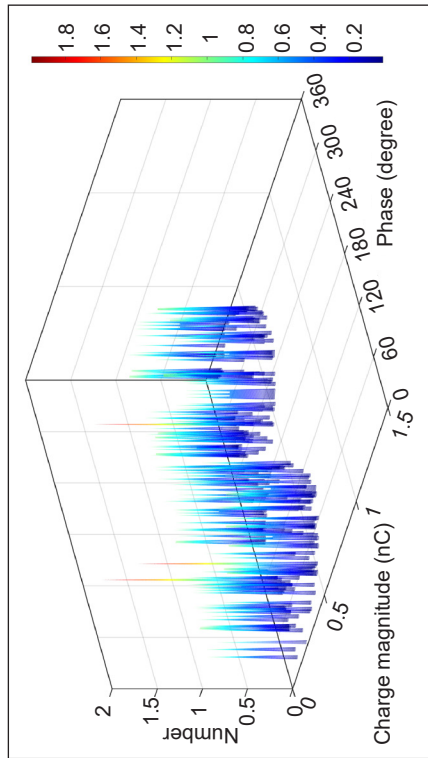


Figure 10. The phase resolved the partial discharge pattern of real charge magnitude in the insulation paper for the cavity with a diameter of 0.8 mm at L2

Table 4  
*Partial discharge parameters in the insulation paper for different cavity sizes and locations without consideration of  $\tau_{stat}$*

Parameters	Cavity Location at L1				Cavity location at L2			
	0.5 mm		0.8 mm		0.5 mm		0.8 mm	
Cavity size	Real	Apparent	Real	Apparent	Real	Apparent	Real	Apparent
PD occurrence per cycle	11.99	11.99	16.00	16.00	7.99	7.99	11.99	11.99
Total charge per cycle, pC	600	300	2320	1664	352	128	1355	791
Mean Charge, pC	50	25	145	104	44	16	113	66
Maximum charge, pC	50	25	145	104	44	16	113	66
Minimum charge, pC	50	25	145	104	44	16	113	66

location at L1 as compared with L2. A similar finding is observed with consideration of  $\tau_{stat}$  (Table 3). In terms of cavity size, the PD occurrence per cycle is higher for the large cavity size as compared with the small size. However, this condition is the opposite when the  $\tau_{stat}$  is considered, whereby the large cavity size produces lower PD occurrence per cycle as compared with a smaller cavity. The maximum, minimum, and mean charge values without consideration of  $\tau_{stat}$  are the same for each of the conditions due to the PD occurrence only at the inception field level at 5.4 kV/mm and 4.75 kV/mm for cavities with diameters of 0.5 mm and 0.8 mm, respectively (Table 4).

**DISCUSSION**

Based on the result in Table 3, the PD occurrence per cycle is higher in the insulation for the cavity location at L1 than in L2, regardless of the cavity size. A similar pattern is found for the charge magnitude whereby the cavity at L1 produces a higher charge magnitude than L2. It is due to the electric field in the cavity is higher at L1 as compared with L2. Figure 12 shows the electric field in the cavity, whereby it is simulated for 1 cycle based on the condition in the absence of PD activity. The electric field in the cavity is higher at L1 than at L2. The sharp edge of the conductor and the location of the cavity within the insulation paper can affect the electric field distribution in the insulation paper even if the same electric potential is injected at the conductor, whereby the electric field at L1 is slightly higher than at L2, as shown in Figure 13. The time to reach the  $E_{inc}$  is faster at L1 ( $t_{L1}$ ) than at L2 ( $t_{L2}$ ), which leads to the increment of the PD occurrence per cycle as well as charge magnitude.

In terms of cavity size, the large cavity size produces a lower PD occurrence per cycle as compared with the small cavity size because the large cavity size can cause a high charge decay rate due to the high free charges accumulated on the cavity surface, which increases the cavity surface conduction. This condition reduces the number of free electrons as well as the EGR. However, the large cavity size generates a higher charge magnitude as



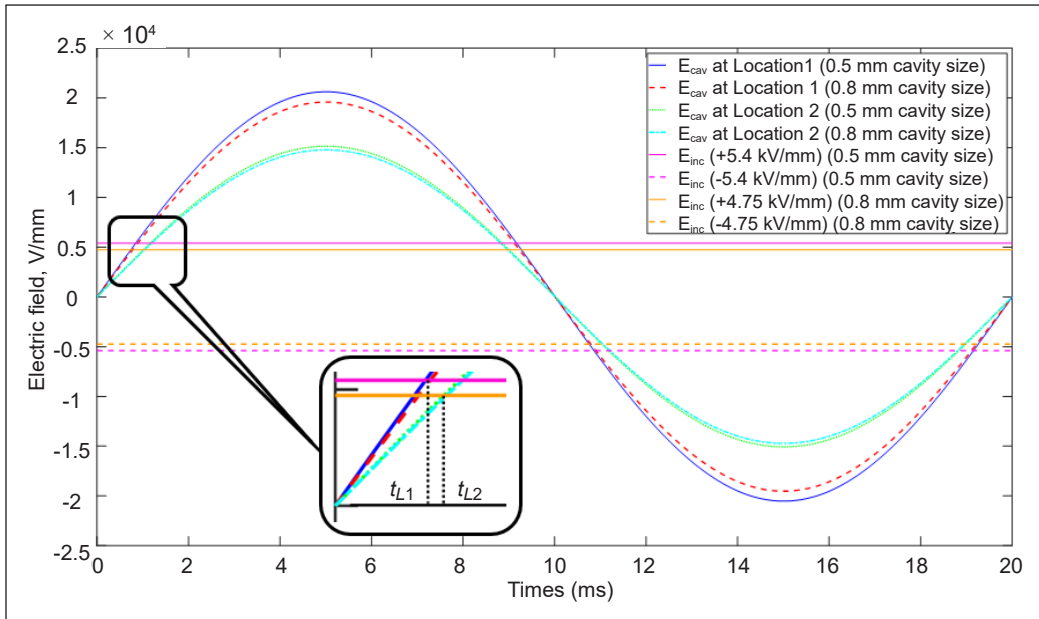


Figure 12. Electric field in the cavity versus time for one cycle in the absence of partial discharge activity

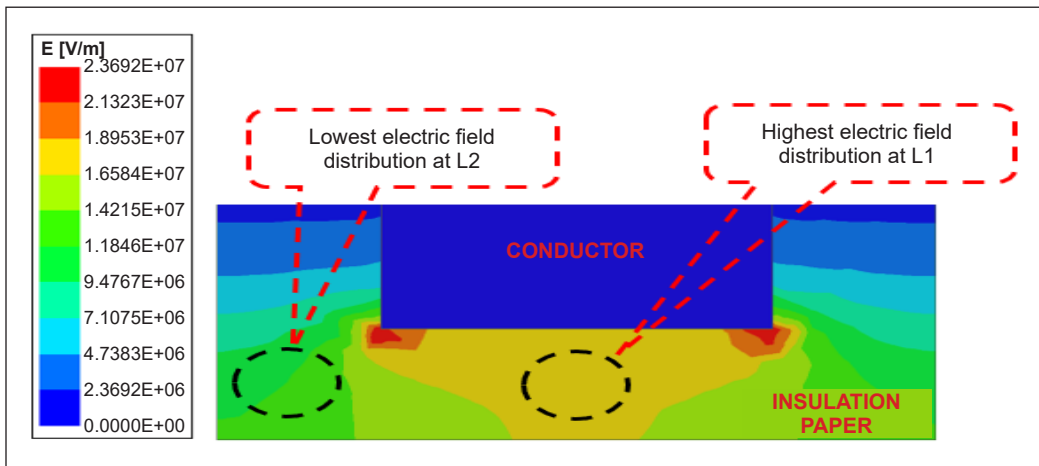


Figure 13. Electric field distribution in the insulation paper in the absence of partial discharge activity

compared with a small cavity. The large cavity size increases the length of the avalanche propagation, leading to high charge magnitude.

### CONCLUSION

PD modeling based on FEM can be used to examine the PD activity in terms of the PRPD pattern within a spherical cavity in the insulation paper. The PRPD pattern for a cavity with a diameter of 0.5 mm produces the same pattern for both locations, L1 and L2, whereby the

PD is distributed mostly at the minimum charge magnitude or PD occurrence at the  $E_{inc}$ . However, the charge magnitude, as well as PD occurrence, is higher at L1 as compared with L2. The PRPD pattern for the cavity with a diameter of 0.8 mm yields the same pattern for both locations, L1 and L2. However, the pattern differs from a cavity with a diameter of 0.5 mm, whereby the PD occurrence is distributed at all phase ranges and produces lower PD occurrence per cycle. On the other hand, the charge magnitude for the cavity with a diameter of 0.8 mm is higher as compared with the cavity with a diameter of 0.5 mm. In conclusion, the cavity location at L1 produces higher charge magnitude and PD occurrence per cycle as compared with L2. In addition, the large cavity size produces a higher charge magnitude but fewer PD occurrences per cycle than a small cavity.

## ACKNOWLEDGMENT

The authors sincerely thank Universiti Putra Malaysia, Inisiatif Putra Berkumpulan GP-IPB (GP-IPB/2022/9717000) funding. Special thanks to Advanced Lightning, Power and Energy Research (ALPER), UPM for technical support to this research.

## REFERENCES

- Afrouzi, H. N., Hassan, A., Chee, D. T. Y., Mehranzamir, K., Malek, Z. A., Mashak, S. V., & Ahmed, J. (2022). In-depth exploration of partial discharge modelling methods within insulations. *Cleaner Engineering and Technology*, 6, Article 100390. <https://doi.org/10.1016/j.clet.2021.100390>
- Borghei, M., & Ghassemi, M. (2019). Partial discharge analysis under high-frequency, fast-rise square wave voltages in silicone gel: A modeling approach. *Energies*, 12(23), Article 4543. <https://doi.org/10.3390/en12234543>
- Borghei, M., & Ghassemi, M. (2020). A finite element analysis model for partial discharges in silicone gel under a high slew rate, high-frequency square wave voltage in low-pressure conditions. *Energies*, 13(9), Article 2152. <https://doi.org/10.3390/en13092152>
- Borghei, M., & Ghassemi, M. (2021). Characterization of partial discharge activities in WBG power converters under low-pressure condition. *Energies*, 14(17), Article 5394. <https://doi.org/10.3390/en14175394>
- Borghei, M., Ghassemi, M., Rodriguez-Serna, J. M., & Albarracin-Sanchez, R. (2021). A finite element analysis and an improved induced charge concept for partial discharge modeling. *IEEE Transactions on Power Delivery*, 36(4), 2570-2581. <https://doi.org/10.1109/tpwr.2020.2991589>
- Borghei, S. M. R. (2022). *Partial discharges: Experimental investigation, model development, and data analytics* [Doctoral dissertation]. Virginia Polytechnic Institute, USA. <http://hdl.handle.net/10919/108321>
- Callender, G., & Lewin, P. L. (2020). Modeling Partial Discharge Phenomena. *IEEE Electrical Insulation Magazine*, 36(2), 29-36.
- CIGRE. (2017). *Partial discharges in transformers* (Working Group D1.29). CIGRE. <https://www.slideshare.net/PowerSystemOperation/partial-discharges-in-transformers>

- Forssén, C. (2008). *Modelling of cavity partial discharges at variable applied frequency* [Doctoral dissertation]. KTH, Sweden. <https://www.diva-portal.org/smash/record.jsf?pid=diva2%3A13791&dswid=6945>
- Forssén, C., & Edin, H. (2008). Partial discharges in a cavity at variable applied frequency Part 2: Measurements and modeling. *IEEE Transactions on Dielectrics and Electrical Insulation*, 15(6), 1610-1616. <https://doi.org/10.1109/TDEI.2008.4712664>
- Hussain, M. R., Refaat, S. S., & Abu-Rub, H. (2021). Overview and partial discharge analysis of power transformers: A literature review. *IEEE Access*, 9, 64587-64605. <https://doi.org/10.1109/access.2021.3075288>
- IEC60270. (2000). *High-voltage test techniques - Partial discharge measurements*. British Standard. <http://teslapishro.ir/wp-content/uploads/2019/12/High-voltage-test-technique.pdf>
- Illias, H. A. (2011). *Measurement and simulation of partial discharges within a spherical cavity in a solid dielectric material* [Doctoral dissertation] University of Southampton, UK. [https://eprints.soton.ac.uk/194921/1/HazleeThesis\\_EPRINTS.pdf](https://eprints.soton.ac.uk/194921/1/HazleeThesis_EPRINTS.pdf)
- Illias, H. A., Chen, G., & Lewin, P. L. (2011). Partial discharge behavior within a spherical cavity in a solid dielectric material as a function of frequency and amplitude of the applied voltage. *IEEE Transactions on Dielectrics and Electrical Insulation*, 18(2), 432-443. <https://doi.org/10.1109/tdei.2011.5739447>
- Illias, H. A., Chen, G., & Lewin, P. L. (2012). Partial discharge within a spherical cavity in a dielectric material as a function of cavity size and material temperature. *IET Science, Measurement & Technology*, 6(2), 52-62. <https://doi.org/10.1049/iet-smt.2011.0091>
- Illias, H. A., Chen, G., & Lewin, P. L. (2017). Comparison between three-capacitance, analytical-based and finite element analysis partial discharge models in condition monitoring. *IEEE Transactions on Dielectrics and Electrical Insulation*, 24(1), 99-109. <https://doi.org/10.1109/tdei.2016.005971>
- Illias, H. A., Tunio, M. A., Bakar, A. H. A., Mokhlis, H., & Chen, G. (2016). Partial discharge phenomena within an artificial void in cable insulation geometry: Experimental validation and simulation. *IEEE Transactions on Dielectrics and Electrical Insulation*, 23(1), 451-459. <https://doi.org/10.1109/tdei.2015.005155>
- Joseph, J., Mohan, S., & Thiruthi Krishnan, S. (2019). Numerical modelling, simulation and experimental validation of partial discharge in cross-linked polyethylene cables. *IET Science, Measurement & Technology*, 13(2), 309-317. <https://doi.org/10.1049/iet-smt.2018.5248>
- Meitei, S. N., Borah, K., & Chatterjee, S. (2021). Partial discharge detection in an oil-filled power transformer using fiber bragg grating sensors: A review. *IEEE Sensors Journal*, 21(9), 10304-10316. <https://doi.org/10.1109/jsen.2021.3059931>
- Morsalin, S., & Das, N. (2020). Diagnostic aspects of partial discharge measurement at very low frequency: A review. *IET Science, Measurement & Technology*, 14(10), 825-841. <https://doi.org/10.1049/iet-smt.2020.0225>
- Murthy, A. S., Azis, N., Jasni, J., Othman, M. L., Mohd Yousof, M. F., & Talib, M. A. (2020). Extraction of winding parameters for 33/11 kV, 30 MVA transformer based on finite element method for frequency response modelling. *PLoS One*, 15(8), Article e0236409. <https://doi.org/10.1371/journal.pone.0236409>

- Naidu, M. S., & Kamaraju, V. (2013). *High Voltage Engineering*. McGraw Hill.
- Pan, C., Chen, G., Tang, J., & Wu, K. (2019). Numerical modeling of partial discharges in a solid dielectric-bounded cavity: A review. *IEEE Transactions on Dielectrics and Electrical Insulation*, 26(3), 981-1000. <https://doi.org/10.1109/tdei.2019.007945>
- Pedersen, A., Crichton, G. C., & McAllister, I. W. (1995). The functional relation between partial discharges and induced charge. *IEEE Transactions on Dielectrics and Electrical Insulation*, 2(4), 535-543. <https://doi.org/10.1109/94.407019>
- Pedersen, A., Crichton, G. C., & McAllister, I. W. (1991). The theory and measurement of partial discharge transients. *IEEE Transactions on Electrical Insulation*, 26(3), 487-497. <https://doi.org/10.1109/14.85121>
- Saha, T. K., & Purkait, P. (2008). Understanding the impacts of moisture and thermal ageing on transformer's insulation by dielectric response and molecular weight measurements. *IEEE Transactions on Dielectrics and Electrical Insulation*, 15(2), 568-582. <https://doi.org/10.1109/TDEI.2008.4483479>
- Sikorski, W., Walczak, K., Gil, W., & Szymczak, C. (2020). On-line partial discharge monitoring system for power transformers based on the simultaneous detection of high frequency, ultra-high frequency, and acoustic emission signals. *Energies*, 13(12), Article 3271. <https://doi.org/10.3390/en13123271>
- Whitehead, S. (1952). Electrical breakdown of solids. *Nature*, 170(4319), Article 219. <https://doi.org/10.1038/170219a0>
- Xavier, G. V. R., Silva, H. S., da Costa, E. G., Serres, A. J. R., Carvalho, N. B., & Oliveira, A. S. R. (2021). Detection, classification and location of sources of partial discharges using the radiometric method: Trends, challenges and open issues. *IEEE Access*, 9, Article 110787-110810. <https://doi.org/10.1109/access.2021.3102888>
- Xiao, L., Ruijin, L., Maochang, L., Lijun, Y., Junkun, Y., & Chaoliang, Q. (2013, October 20-23). *Influence of aging degree on polarization and depolarization currents of oil-paper insulation* [Paper presentation]. Annual Report Conference on Electrical Insulation and Dielectric Phenomena, Chenzhen, China. <https://doi.org/10.1109/CEIDP.2013.6748255>
- Youssef, M. M., Ibrahim, R. A., Desouki, H., & Moustafa, M. M. Z. (2022, March 4-6). *An Overview on Condition Monitoring & Health Assessment Techniques for Distribution Transformers* [Paper presentation]. 6th International Conference on Green Energy and Applications (ICGEA), Singapore. <https://doi.org/10.1109/ICGEA54406.2022.9791900>

## Short-term Ageing Study on the Palm Oil and Mineral Oil in the Presence of Insulation Paper, Moisture, Low Molecular Weight Acid, and Oxygen

Muhammad Muzamil Mustam<sup>1,2</sup>, Norhafiz Azis<sup>2,3\*</sup>, Jasronita Jasni<sup>2</sup>, Rasmina Halis<sup>4</sup>, Mohd Aizam Talib<sup>5</sup>, Robiah Yunus<sup>6</sup>, Nurliyana Abdul Raof<sup>7</sup> and Zaini Yaakub<sup>8</sup>

<sup>1</sup>Faculty of Electrical Engineering, Universiti Teknologi MARA, Pasir Gudang Campus, 81750 UiTM, Seri Alam, Pasir Gudang, Johor, Malaysia

<sup>2</sup>Advanced Lightning, Power and Energy Research Centre (ALPER), Faculty of Engineering, Universiti Putra Malaysia, 43400 UPM, Serdang, Selangor, Malaysia

<sup>3</sup>Institute of Nanoscience and Nanotechnology (ION2), Universiti Putra Malaysia, 43400 UPM, Serdang, Selangor, Malaysia

<sup>4</sup>Department of Natural Resources Industry, Faculty of Forestry and Environment, Universiti Putra Malaysia, 43400 UPM, Serdang, Selangor, Malaysia

<sup>5</sup>Advanced Diagnostic Services, TNB Labs Sdn. Bhd., 43000 Kajang, Selangor, Malaysia

<sup>6</sup>Department of Chemical and Environmental Engineering, Faculty of Engineering, University Putra Malaysia, 43400 UPM, Serdang, Selangor, Malaysia

<sup>7</sup>Department of Chemical Engineering and Energy Sustainability, Faculty of Engineering, Universiti Malaysia Sarawak, 94300 UNIMAS, Kota Samarahan, Sarawak, Malaysia

<sup>8</sup>Hyrax Oil Sdn. Bhd. Lot 4937, Batu 51/2, Jalan Meru, Mukim Kapar, 41050 Klang, Selangor, Malaysia

### ABSTRACT

This study presents the short-term ageing study on refined, bleached and deodorised palm oil (RBDPO) and mineral oil (MO) in the presence of insulation paper, moisture, low molecular weight acid (LMA) and oxygen. The ageing experiment was performed for 7 days at

140°C. The oil was maintained dried while the paper's moisture was varied between 0.5% and 3.5%. In total, 0.2 g of LMA and 20 mbar of oxygen pressure were initially introduced in the oil before the ageing started. Several analyses were conducted after the ageing experiment, which include the AC breakdown voltage (BDV) oil/paper, tensile strength, degree of polymerization (DP) and thermogravimetric analysis and differential scanning calorimetry (TGA-DSC). After being subjected to ageing in the

#### ARTICLE INFO

##### Article history:

Received: 28 October 2022

Accepted: 06 March 2023

Published: 03 October 2023

DOI: <https://doi.org/10.47836/pjst.31.6.16>

##### E-mail addresses:

[muhammadmuzamil@uitm.edu.my](mailto:muhammadmuzamil@uitm.edu.my) (Muhammad Muzamil Mustam)

[norhafiz@upm.edu.my](mailto:norhafiz@upm.edu.my) (Norhafiz Azis)

[jas@upm.edu.my](mailto:jas@upm.edu.my) (Jasronita Jasni)

[rasminal@upm.edu.my](mailto:rasminal@upm.edu.my) (Rasmina Halis)

[aizam.talib@tnb.com.my](mailto:aizam.talib@tnb.com.my) (Mohd Aizam Talib)

[robialh@upm.edu.my](mailto:robialh@upm.edu.my) (Robiah Yunus)

[arnurliyana@unimas.my](mailto:arnurliyana@unimas.my) (Nurliyana Abdul Raof)

[zaini@hyraxoil.com](mailto:zaini@hyraxoil.com) (Zaini Yaakub)

\* Corresponding author

presence of LMA and oxygen, the reduction of AC BDV of RBDPO is lower than MO at all moisture levels. At the same condition, the AC BDV of RBDPO-impregnated paper also maintains higher than MO-impregnated paper. The RBDPO-impregnated paper, in the presence of LMA and oxygen, has higher resistance toward ageing than MO-impregnated paper based on DP and tensile index, even in high moisture. All RBDPO are more resistant to ageing than MO in the presence of LMA and oxygen based on the high onset temperatures of the TGA-DSC analysis.

*Keywords:* Breakdown voltage, degree of polymerization, insulation paper, tensile strength

---

## INTRODUCTION

Recently, vegetable oil (VO) has been identified as a possible substitute for mineral oil (MO) for application in transformers due to its biodegradability, environmental friendliness and fire safety (Maharana et al., 2018; Martin et al., 2006; Matharage et al., 2016; Maharana et al., 2018; Raj et al., 2020; Raymon et al., 2013; Suwarno & Pasaribu, 2017; ). Palm oil (PO) is among the most widely accessible VOs in Asian countries (RSPO, 2015; Suryani et al., 2020). Refined, bleached and deodorised palm oil (RBDPO) is one of the common varieties of PO originating from the oil palm fruit (Azis et al., 2014). Different studies are conducted on RBDPO to explore its application as a dielectric insulating fluid (Makmud et al., 2018; Makmud et al., 2019).

The ageing characteristics of MOs are previously examined, which cover the physiochemical and electrical aspects (Abdelmalik, 2015; Carcedo et al., 2015; Coulibaly et al., 2012; Matharage et al., 2016; Munajad et al., 2017; N'cho et al., 2016). Similar studies are carried out for VOs such as coconut, palm, soya, sunflower, rapeseed and corn oils, whereby among the important finding is that the ageing of cellulose insulation can be retarded as a result of its water scavenging and hydrolytic protection mechanisms (Gomna et al., 2019; Rapp et al., 2005; Vihacencu et al., 2013). The ageing can affect the electrical properties of VOs, such as the electrical dissipation factor and resistivity (Ciuriuc et al., 2014; Wilhelm et al., 2011). In addition, the AC breakdown voltage (BDV) of the natural ester can increase up to 30.96 % after being subjected to ageing (Maharana et al., 2019). A previous study shows that most of the acid generated in MO is low molecular weight acid (LMA). The LMA generated in VO is lower than MO (Azis & Wang, 2011). The presence of LMA can further enhance the degradation of paper (Kouassi et al., 2018).

The ageing characteristics of RBDPO are also examined in recent years (Ismail et al., 2013; Kiasatina et al., 2011; Mohamad et al., 2016; Sinan et al., 2014; Suleiman et al., 2014). A previous study revealed that the AC breakdown voltage of aged RBDPO can decrease between 9.8% and 28.2% after being subjected to ageing (Mohamad et al., 2016). Similarly, it is found that the ageing rate of paper aged in MO can be up to 1.6 higher than

RBDPO and coconut oil samples based on previous ageing models (Mohamad et al., 2015). The percentage of reduction of the tensile index (TI) of RBDPO-impregnated paper is lower than that of MO-impregnated paper at the end of the ageing period (Mohamad et al., 2016). The thermogravimetric analysis and differential scanning calorimetry (TGA-DSC) for aged RBDPO reveals that the onset temperature is 408°C while MO is 297°C (Raof et al., 2019). Currently, the study on the effect of ageing accelerators such as moisture, oxygen and acid on the ageing performance of RBDPO is still lacking.

This paper discusses the impact of short-term ageing on the RBDPO and MO in the presence of insulation paper, moisture, acid and oxygen. The type of acid used in the study is LMA. The properties such as AC BDV of the oil/paper, tensile strength, degree of polymerization (DP) and TGA-DSC are measured and analysed. The ageing factor is derived from the influence of different ageing accelerators. The current study provides a fundamental understanding of the RBDPO and MO aged in the presence of ageing accelerators for possible future applications in transformers.

## METHODOLOGY

### Thermal Ageing Procedure

The MO and RBDPO were initially filtered 3 times using a membrane filter with a pore size of 0.2  $\mu\text{m}$ . The properties and appearances of oils are shown in Figure 1 and Table 1. These oils were dried for 2 days at 85°C in a vacuum oven. All samples were filled with nitrogen to reduce the interaction with oxygen. The final moisture contents of RBDPO and MO were 109 ppm and 12 ppm, respectively. Next, the paper was dried at 90°C or 105°C in a vacuum oven to produce the sample with different moisture contents known as base, low, medium and high moistures. The paper was dried at 105°C for 48 hours, 105°C for 96 hours, 90°C for 48 hours and 90°C for 24 hours to produce base, low, medium and high moisture samples. The final moisture for the base, low, medium and high moisture paper samples are 0.87%, 0.55%, 1.66% and 2.65%. The paper was then impregnated with oils in a vacuum oven for 24 hours at 85°C. These oils were introduced with 0.2 g of formic acid

Table 1  
*Oil properties*

Properties (Unit)	MO	RBDPO
Viscosity, 40°C (mm <sup>2</sup> /s)	7.6	21.2
Density, 150°C (kg/m <sup>3</sup> )	890	915.5
Flashpoint (°C)	154	320
Water content (mg/kg)	<20	60
Breakdown voltage (kV)	40-60	60-70
Acidity (mg KOH/g)	<0.2	<0.06
Dielectric dissipation factor, 90°C	<0.001	0.03



Figure 1. MO and RBDPO

as LMA and 20 mbar of oxygen pressure above the bottle's oil surface. The oil-to-paper ratio was set to 20:1, with 450 g of oil and 22.5 g of paper, and it was aged in borosilicate glass. The bottle cap reinforced with polytetrafluoroethylene tape was used to seal the borosilicate glass containing the oil and paper, aged for 7 days at 140°C to minimise the environmental interaction.

### AC Breakdown Voltage of Oil

An automatic BAUR DPA 75C was used to obtain the AC BDV of oil as per ASTM D1816-12, as shown in Figure 2. The test was conducted at room temperature between 28.4 and 32.9°C (ASTM D1816-12, 2019). The gap spacing between the 36 mm diameter VDE electrodes was fixed to 2.5 mm. In total, 400 ml of oil was carefully poured into the test cell to prevent the formation of any bubbles. The oil was given 15 minutes to rest prior to the test. The voltage was then gradually increased at 0.5 kV/s until the breakdown occurred. Next, the oil was stirred continually using a magnetic stirrer while the interval between breakdowns was set to 5 minutes. In total, 50 measurements of AC BDV were obtained for MO, and the average value was used for the analysis.

### AC Breakdown Voltage of Oil Impregnated Paper

The AC BDV of paper was measured using BAUR DPA 75 C as per IEC 60156, as seen in Figure 3. First, the gap distance of the sphere electrodes with a 12.5 mm diameter was set based on the thickness of the oil-impregnated paper. In total, 2 layers of oil-impregnated paper were used due to the measurement limit caused by the very small gap distance based on the thickness of 1 layer of oil-impregnated paper. Next, 400 ml of pre-processed oil was carefully poured into the test cell, whereby the voltage ramping rate was set to 2 kV/s. The oil-impregnated paper was moved to other positions after each of the breakdowns. In total, 20 measurements of AC BDV were recorded for the oil-impregnated paper, whereby the average value was used for the analysis.

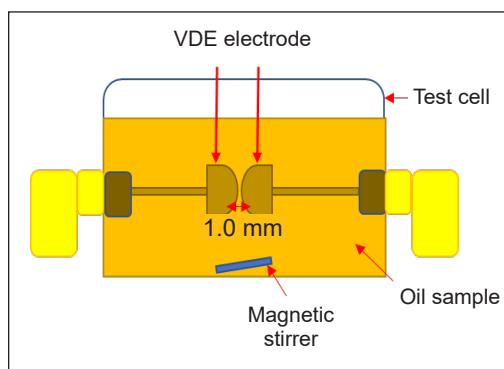


Figure 2. AC breakdown voltage test of oil

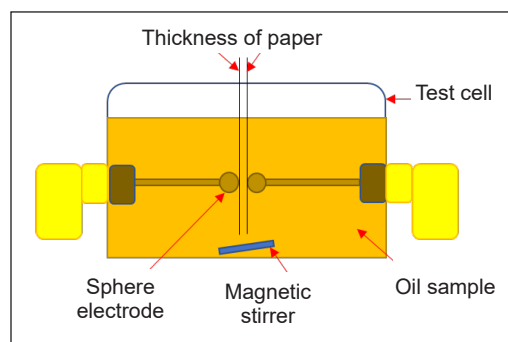


Figure 3. AC breakdown voltage test of oil-impregnated paper



### Tensile Strength

Tensile strength was performed using an Instron 5566 model universal testing machine as per BS EN ISO 1924-2. A 10 kN universal testing machine load cell was used, as shown in Figure 4. The crosshead speed and full-scale load range were adjusted to 20 mm/min and 0.5 kN. The distance between the two clamps was set to 100 mm. The paper width and gap distance of the paper were set to 16 mm ± 0.1 mm and 180 mm ± 0.1 mm, respectively. In total, 5 samples were tested for each type of paper and the average value was used for the analysis. Next, the maximum load of TI was calculated based on Equation 1.

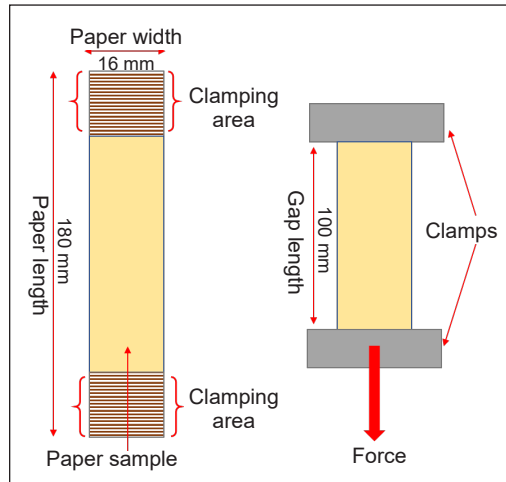


Figure 4. Tensile strength test of paper

$$TI = ((\bar{F}/W) / G) \times 10^3 \quad [1]$$

Whereby TI is the paper’s tensile index in Newton’s metres per gram,  $\bar{F}$  is the maximum load in Newton,  $W$  is the paper’s width in millimetres, and  $G$  is the paper’s grammage in grams per square metre. The paper’s grammage under study was around 51.8 g/m<sup>2</sup>.

### Acidity

The acidity of the oils was determined using a Metrohm 877 oil Titration plus as per ASTM D974 (2023). For each type of oil, 10 g was utilised for the measurement, as seen in Figure 5. In total, 1 measurement was obtained for each type of oil.

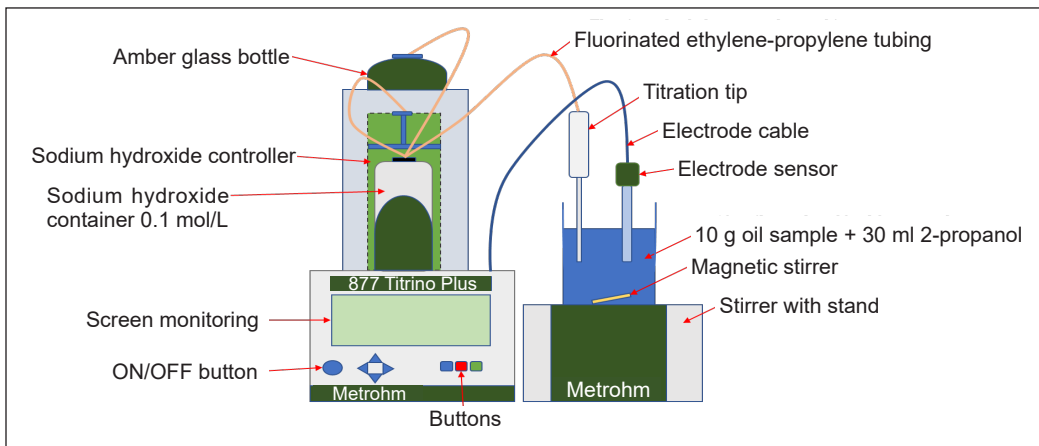


Figure 5. Acidity test of oil

## Moisture in Oil and Paper

A Metrohm 831 Karl Fischer (KF) Coulometer was used to measure the moisture in oil based on ASTM D6304 (2021). For each type of oil, 1 ml of oil was used for the moisture measurement, as shown in Figure 6. A Metrohm 774 Karl Fischer Coulometer measured the moisture content of the insulation paper according to IEC 60814. The moisture in the paper was extracted via an oven technique. The total weight of paper used for the moisture measurement is 0.5 g, as seen in Figure 7. In total, 2 moisture measurements were taken for RBDPO and MO for the insulation paper, where the average value was used for the analysis.

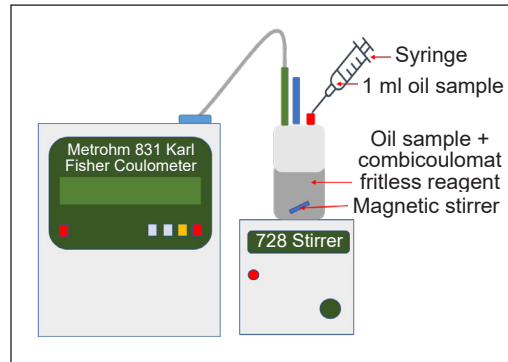


Figure 6. Moisture content test of oil

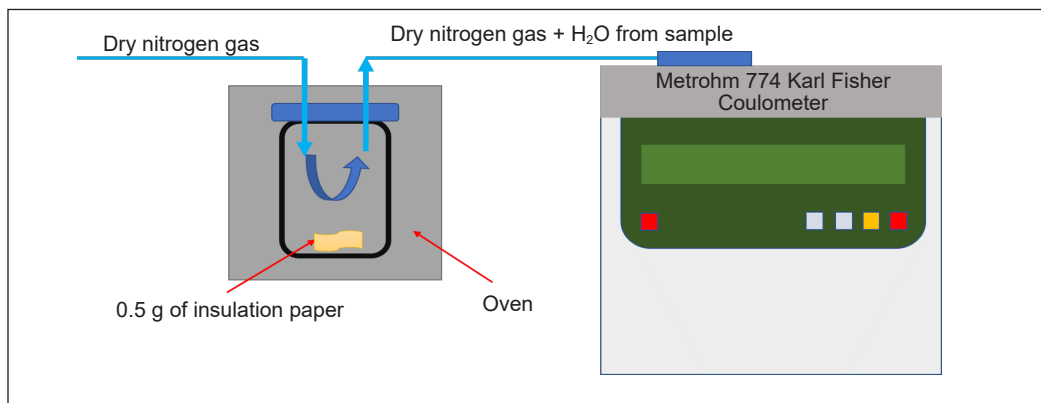


Figure 7. Moisture content test of paper

## Thermogravimetric and Differential Scanning Calorimetry Analysis

The measurements of the oils were performed under non-isothermal conditions based on the standard TGA from Mettler Toledo, TGA-DSC HT 3, as shown in Figure 8. The weight of the oil used was 5 mg. The system was first purged with nitrogen gas at 50 ml/min for around 20 minutes at 25°C to release the trapped gases. The sample was then heated from 25°C to 600°C at a steady rate of 10°C/min, and the temperature was maintained for 10 minutes.

## Degree of Polymerization

The DP of the paper was obtained based on the average intrinsic viscosity according to ASTM D4243 (2023), as seen in Figure 9. The residual oil was removed from the paper through soxhlet extraction using hexane for up to 8 hours to obtain the dry weight value.

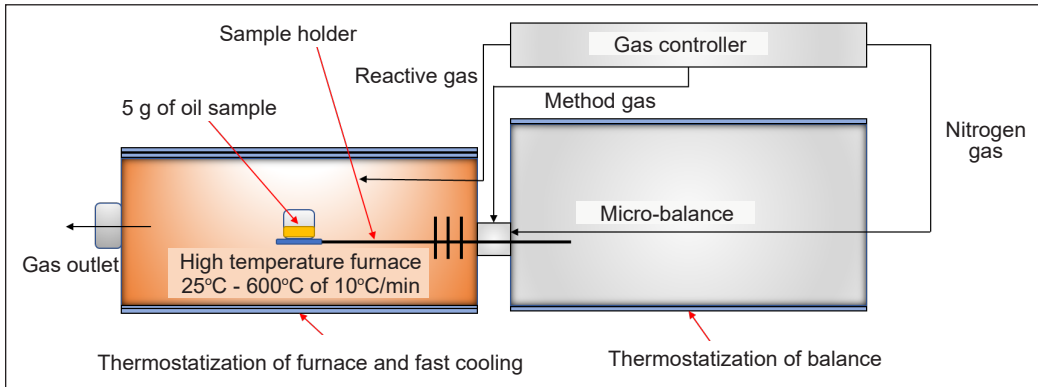


Figure 8. Thermogravimetric analysis and differential scanning calorimetry test of oil

Next, the paper was cut into confetti with dimensions 2 mm before the moisture content was determined using the oven method. In total, 0.1 g of the sample was weighed and mixed with 22.5 ml of distilled water in a beaker. Next, the solution was left for 30 minutes before fragmented in a wet kitchen blender for up to 15 minutes. Next, 22.5 ml Copper (II) ethylenediamine (CED) solution was added and stirred for 2 hours. The mixture was added to the Cannon-Ubbelohde capillary tube viscometer. The viscometer was inserted into a constant water bath at 20°C. Once the tube’s temperature was stabilised, the viscosity measurement was performed. The measurement was carried out for 4 times, whereby the average was used for the analysis. The calibration was performed based on the viscosity determination of the blank solution with a CED-to-water ratio of 50:50.

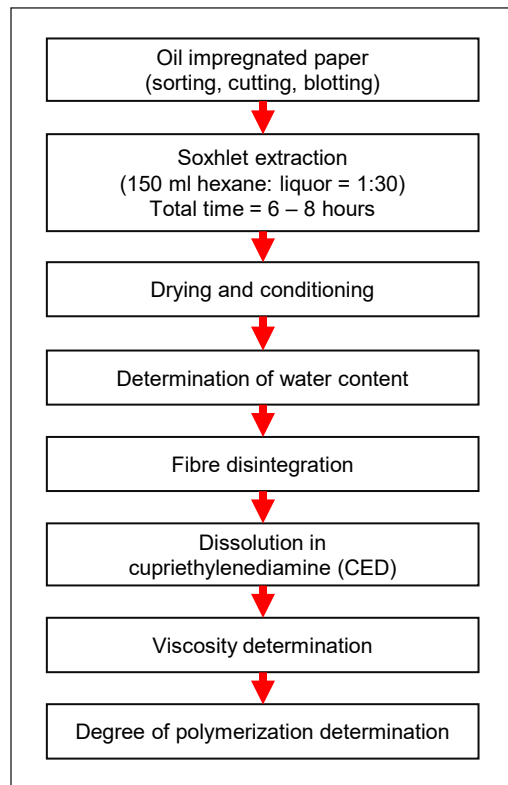


Figure 9. Measurement process of degree of polymerization

From the solution prepared, the concentration (c) was calculated based on Equation 2

$$c = \frac{100m (100 - \%MC)}{4500 + m(\%MC)} \quad [2]$$

Where m is the mass of paper, g, and MC is the moisture content of the paper, %.

DP was calculated based on Mark Houwink constants where  $\alpha$  and K were defined as 1 and  $7.5 \times 10^{-3}$ , respectively (Equation 3).

$$DP^\alpha = \frac{[\eta]}{K} \quad [3]$$

Where  $[\eta]$  is the intrinsic viscosity related to the specific viscosity,  $\eta_s$  and can be determined based on Equation 4.

$$\eta_s = \eta_{rel} - 1 = [\eta](10^{K[\eta]c}) \quad [4]$$

Where  $\eta_{rel}$  is the relative viscosity that can be defined based on Equation 5.

$$\eta_{rel} = \frac{\text{Kinematic viscosity of the solution}}{\text{Kinematic viscosity of CED}} \quad [5]$$

$[\eta].c$  can be obtained from Table 1 in ASTM D4243 (2023). The intrinsic viscosity  $[\eta]$  can be determined using the  $c$  from Equation 2. DP can be estimated based on Equation 3.

## RESULTS AND DISCUSSION

### AC Breakdown Voltage of RBDPO and MO

The AC BDV of RBDPO is higher than MO at all moisture levels after 7 days of ageing, as shown in Figure 10. The decrement pattern of AC BDV for MO is steeper than RBDPO as the moisture increases. In the presence of high moisture, LMA and oxygen, the AC BDV of RBDPO decreases by 12%, while for MO, it decreases by 73%.

### AC Breakdown Voltage of RBDPO and MO-Impregnated Paper

At all moisture levels, the AC BDV of RBDPO-impregnated paper is higher than MO-impregnated paper after 7 days of ageing, as seen in Figure 11. The AC BDV of RBDPO-impregnated paper slightly increases with the introduction of low moisture and decreases with the moisture increment. The same pattern is found for AC BDV of MO-impregnated paper. In the presence of high moisture, LMA and oxygen, the AC BDV of RBDPO and MO-

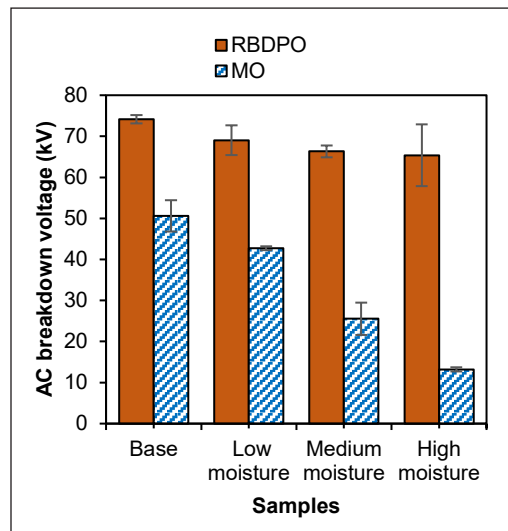


Figure 10. AC breakdown voltage of RBDPO and MO in the presence of moisture, LMA and oxygen

impregnated paper slightly increased by 16.88% and 18.02% compared to the base.

### Tensile Index of RBDPO and MO Impregnated Paper

The reduction pattern of TI is quite similar to DP at all moisture levels after 7 days of ageing, as shown in Figure 12. RBDPO-impregnated paper experiences a lower reduction of TI than MO-impregnated paper. Similar to DP, the TI of both RBDPO and MO-impregnated papers still suffer advanced degradation at low moisture. The lowest TI for RBDPO-impregnated paper is still higher than the 50% retention strength limit per IEEE standard C57.91-2011(IEEE Standards Association, 2012). With high moisture, the TI of MO-impregnated paper exceeds the limit with a percentage reduction of 59.54%. The ageing factor based on TI for RBDPO-impregnated paper in the presence of low, medium and high moistures is 1.41, 1.40 and 1.45. For MO-impregnated paper, the ageing factors are 1.64, 1.80 and 2.47, respectively.

### Degree of Polymerization of RBDPO and MO-Impregnated Paper

The DP reduction of RBDPO-impregnated paper is lower than MO-impregnated paper at all moisture levels after 7 days of ageing, as seen in Figure 13. Even with the introduction of low moisture, both RBDPO and MO-impregnated papers still experience significant degradation, possibly due to the presence of LMA. The lowest DP for RBDPO-impregnated paper is 319 in the presence of high moisture. On the other hand, the DP for MO-impregnated paper decreases lower than 200, reaching the end of its life (Emsley et al., 2000.). The ageing factor based on DP for RBDPO-impregnated paper in the

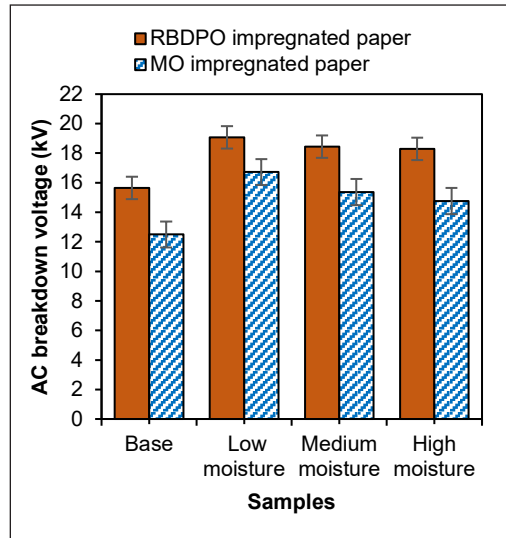


Figure 11. AC breakdown voltage of RBDPO and MO-impregnated paper in the presence of moisture, LMA and oxygen

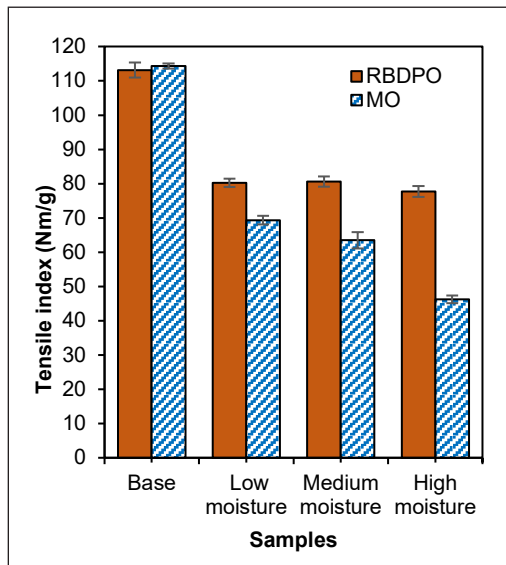


Figure 12. Tensile index of RBDPO and MO-impregnated papers in the presence of moisture, LMA and oxygen

presence of low, medium and high moistures is 2.04, 2.07 and 2.96. For MO-impregnated paper, the ageing factors are 2.47, 4.44 and 4.57, respectively.

### Thermogravimetric and Differential Scanning Calorimetry Analysis of RBDPO and MO

The onset temperature, or the temperature at which degradation begins, is useful for the oil stability (Raof et al., 2019). All RBDPOs are more resistant against degradation as compared to MO since the onset temperatures are high at all moisture levels after 7 days of ageing, as shown in Table 2 and Figure 14. The base RBDPO is stable up to 396°C, whereas base MO is only stable up to 296°C. MO exhibits a high weight loss of 72% in high moisture at 315.5 °C.

The weight loss at the low-temperature range for MO is attributed to the evaporation of low molecular weight hydrocarbons and degradation of the base oil. According to Tripathi & Vinu (2015), the degradation of MO can occur at the temperature range between 150°C and 350°C. For example, the paraffinic chain in the MO molecules can decompose into ethane (C<sub>2</sub>H<sub>6</sub>), ethylene (C<sub>2</sub>H<sub>4</sub>), methane (CH<sub>4</sub>), hydrogen (H<sub>2</sub>) and graphite carbon. At a similar moisture level, the weight loss for RBDPO is only 61% at 431.5°C. RBDPO contains high triglyceride molecules such as palmitic and oleic acids, contributing to its higher thermal stability than MO. The increment of the hydrocarbon chain length and branching in the RBDPO's molecule decreases the weight loss and decomposes much slower (Raof et al.,

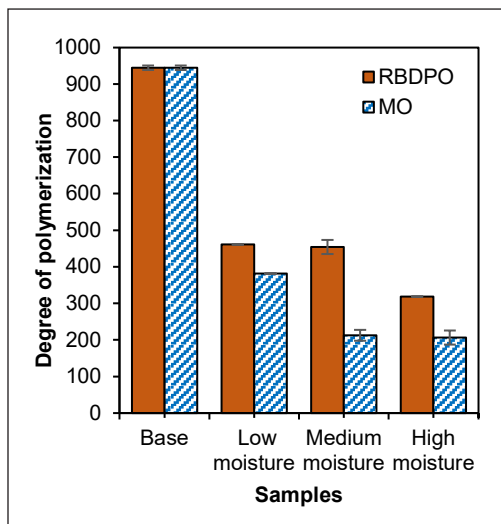


Figure 13. Degree of polymerization of RBDPO and MO-impregnated papers in the presence of moisture, LMA and oxygen

Table 2  
The decomposition temperatures of the RBDPO and MO

Sample	Conditions	Onset temperature (°C)	Peak temperature (°C)	Weight loss (%)
MO	Base	295.6	330.6	57.6
	Low	293.4	329.8	56.1
	Medium	283.3	330.2	62.4
	High	238.5	315.5	72.1
RBDPO	Base	395.7	431.0	59.3
	Low	393.3	429.0	58.4
	Medium	394.4	431.7	61.0
	High	394.6	431.5	61.4

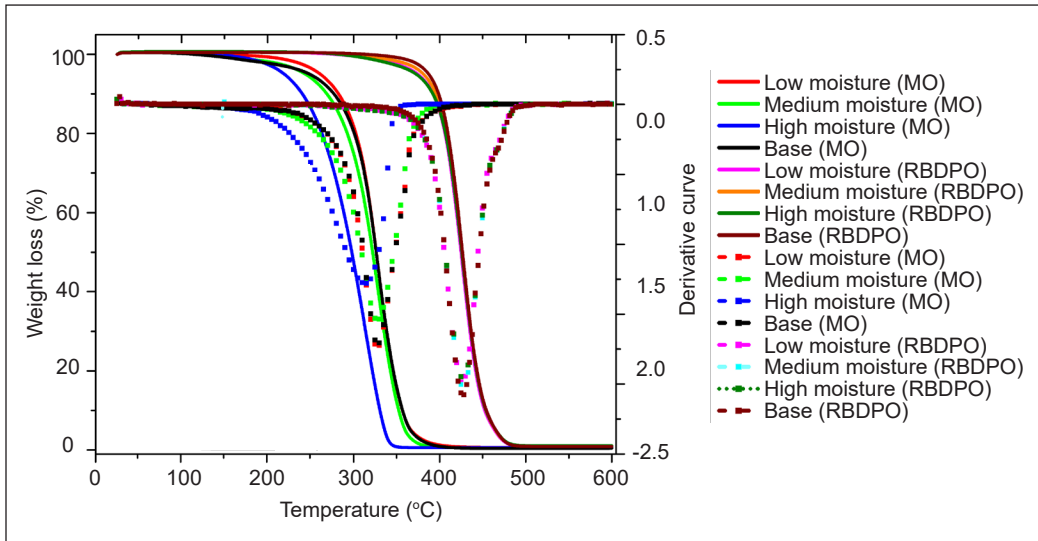


Figure 14. Thermogravimetric analysis and differential scanning calorimetry of the RBDPO and MO for weight loss and derivative curves in the presence of moisture, LMA and oxygen

2019). The relatively low decomposition temperature for RBDPO and MO with high moisture content can be attributed to the high volatility of water at a low temperature.

### Correlation Between Degree of Polymerization and AC Breakdown Voltage of RBDPO and MO Impregnated Paper

The correlation between DP and AC BDV of RBDPO and MO-impregnated paper at all moisture levels after 7 days of ageing can be seen in Figure 15. The result shows that the correlation coefficient,  $R^2$ , for RBDPO and MO-impregnated papers are 0.761 and 0.71, respectively. The correlation coefficient number, which ranges from -1 to 1, describes the strength and direction of the linear link between two quantitative variables. The  $R^2$  from the linear relationship near 1 indicates a strong relationship whereby the range is between 0.7 and 0.99 (Ghoneim, 2021). Meanwhile, positive notation indicates the positive direction, showing that the 2 variables move in the same direction and vice versa. Moreover, it is found that there is a relationship between DP and AC BDV of RBDPO and MO-impregnated papers, which indicates that the reduction of mechanical strength leads to the reduction of electrical strength.

### Correlation Between Degree of Polymerization and Tensile Index

The correlation between DP and TI after being subjected to ageing at all moisture levels after 7 days of ageing can be seen in Figure 16. The result shows that the correlation coefficient,  $R^2$ , for RBDPO and MO-impregnated papers are 0.953 and 0.841, respectively. The positive notation between the decreases and increases of DP and TI can be observed

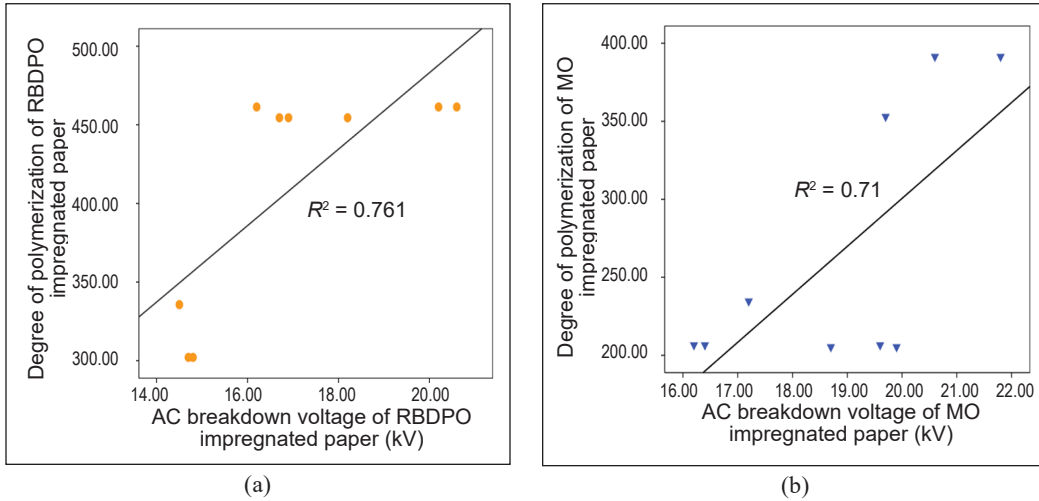


Figure 15. Positive correlation between DP and AC BDV of: (a) RBDPO; and (b) MO-impregnated papers

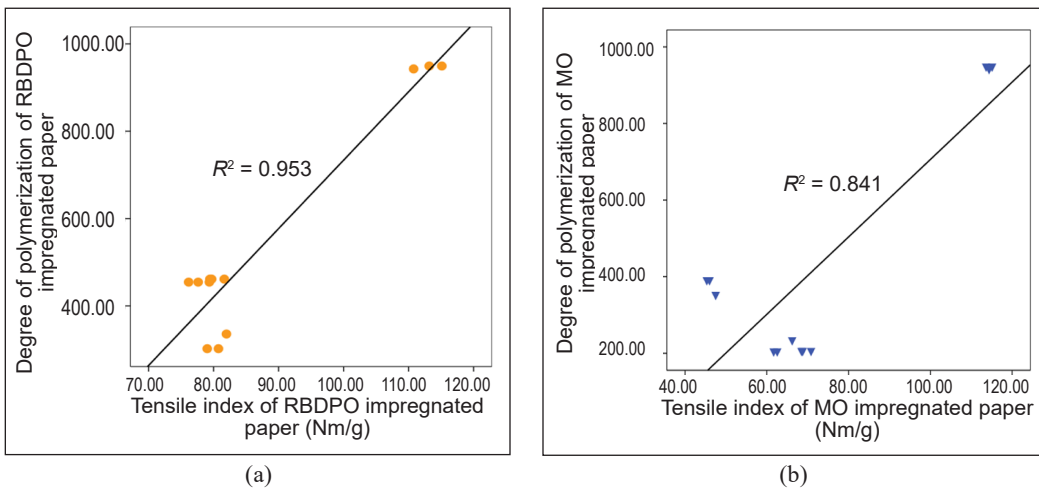


Figure 16. Positive correlation between DP and TI of: (a) RBDPO; and (b) MO-impregnated papers

through the linear regression. The results are in line with the study by (Arroyo et al., 2017), which suggests that the paper strength directly depends on the depolymerization of the cellulose as well as on factors of the inter-fibre bond strength among the cellulose fibres, individual fibre strength and the hierarchical structure of the paper.

## CONCLUSION

This work examines the effects of initial ageing conditions in the presence of LMA, oxygen, and various degrees of moisture content of the paper at 140°C for 7 days are examined. The AC BDV for RBDPO experiences lower reduction than MO with the moisture



increment. The reduction of AC BDV of RBDPO-impregnated paper is still lower than MO-impregnated papers as the moisture level increases from low to high. The reduction trends of both DP and TI of RBDPO-impregnated papers show that the ageing performance is slightly better than MO-impregnated paper, even at high moisture content. RBDPO is more stable and resistant against ageing than the MO with high onset initial temperature. Overall, even with the presence of LMA, oxygen and high moisture, RBDPO is able to perform better than MO based on the condition under study.

## ACKNOWLEDGEMENT

The authors express their gratitude to the Ministry of Higher Education, Malaysia, for the financing provided under the FRGS programme under the designation of FRGS/1/2019/TK07/UPM/02/3 (03-01-19-2071FR), Universiti Teknologi MARA (UiTM), Malaysia, and Majlis Amanah Raya (MARA), Malaysia. Special thanks to Malaysia Transformer Manufacturing Sdn. Bhd., Malaysia, and Hyrax Oil Sdn. Bhd., Malaysia for the technical support.

## REFERENCES

- Abdelmalik, A. A. (2015). Analysis of thermally aged insulation paper in a natural ester-based dielectric fluid. *IEEE Transactions on Dielectrics and Electrical Insulation*, 22(5), 2408-2414. <https://doi.org/10.1109/TDEI.2014.004824>
- Arroyo, O. H., Jalbert, J., Fofana, I., & Ryadi, M. (2017). Temperature dependence of methanol and the tensile strength of insulation paper: Kinetics of the changes of mechanical properties during ageing. *Cellulose*, 24(2), 1031-1039. <https://doi.org/10.1007/s10570-016-1123-7>
- ASTM D1816-12. (2019). *Standard test method for dielectric breakdown voltage of insulating liquids using VDE electrodes*. ASTM International. <https://www.astm.org/Standards/D1816.htm>
- ASTM D974. (2023). *Standard test method for acid and base number by color-indicator titration*. ASTM International. <https://www.astm.org/d0974-22.html>
- ASTM D6304. (2021). *Standard test method for determination of water in petroleum products, lubricating oils, and additives by coulometric karl fischer titration*. ASTM International. <https://www.astm.org/d6304-20.html>
- ASTM D4243. (2023). *Standard test method for measurement of average viscometric degree of polymerization of new and aged electrical papers and boards*. ASTM International. <https://www.astm.org/d4243-16.html>
- Azis, N., & Wang, Z. D. (2011, August 22-26). *Acid generation study of natural ester*. [Paper presentation]. XVII International Symposium on High Voltage Engineering, Hannover, Germany.
- Azis, N., Jasni, J., Ab Kadir, M. Z. A., & Mohtar, M. N. (2014). Suitability of palm based oil as dielectric insulating fluid in transformers. *Journal of Electrical Engineering and Technology*, 9(2), 662-669. <https://doi.org/10.5370/JEET.2014.9.2.662>

- Carcedo, J., Fernández, I., Ortiz, A., Delgado, F., Renedo, C. J., & Pesquera, C. (2015). Aging assessment of dielectric vegetable oils. *IEEE Electrical Insulation Magazine*, 31(6), 13-21. <https://doi.org/10.1109/MEI.2015.7303258>
- Ciuriuc, A., Notingher, P. V., Jovalekic, M., & Tenbohlen, S. (2014, May 22-24). *Experimental study on vegetable and mineral transformer oils properties*. [Paper presentation]. International Conference on Optimization of Electrical and Electronic Equipment (OPTIM), Bran, Romania. <https://doi.org/10.1109/OPTIM.2014.6850907>
- Coulibaly, M. L., Perrier, C., Beroual, A., & Marugan, M. (2012, September 23-27). *Thermal aging of paper and pressboard in mineral and ester oils under air and nitrogen atmospheres*. [Paper presentation]. IEEE International Conference on Condition Monitoring and Diagnosis, Bali, Indonesia. <https://doi.org/10.1109/CMD.2012.6416449>
- Emsley, A. M., Xiao, X., Heywood, R. J., & Aii, M. (2000). Degradation of cellulosic insulation in power transformers. Part 3: Effects of oxygen and water on ageing in oil. *IEE Proceedings-Science, Measurement and Technology*, 147(3), 115-119. <https://doi.org/10.1049/ip-smt:20000021>
- Ghoneim, S. S. M. (2021). The degree of polymerization in a prediction model of insulating paper and the remaining life of power transformers. *Energies*, 14(3), Article 670. <https://doi.org/10.3390/en14030670>
- Gomna, A., N'Tsoukpoe, K. E., Le Pierrès, N., & Coulibaly, Y. (2019). Review of vegetable oils behaviour at high temperature for solar plants: Stability, properties and current applications. *Solar Energy Materials and Solar Cells*, 200, Article 109956. <https://doi.org/10.1016/j.solmat.2019.109956>
- Ismail, N., Arief, Y. Z., Adzis, Z., Azli, S. A., Jamil, A. A. A., Mohd, N. K., Huei, L. W., & Kian, Y. S. (2013). Effect of water on electrical properties of refined, bleached, and deodorized palm oil (RBDPO) as electrical insulating material. *Jurnal Teknologi (Sciences and Engineering)*, 64(4), 97-101. <https://doi.org/10.11113/jt.v64.2108>
- Kiasatina, Kamarol, M., Zulhilmey, M., & Arief, Y. A. (2011, June 21-22). *Breakdown characteristics of RBDPO and soybean oil mixture for transformer application*. [Paper presentation]. International Conference on Electrical, Control and Computer Engineering (InECCE), Kuantan, Malaysia. <https://doi.org/10.1109/INECCE.2011.5953879>
- Kouassi, K. D., Fofana, I., Cissé, L., Hadjadj, Y., Yapi, K. M. L., & Diby, K. A. (2018). Impact of low molecular weight acids on oil impregnated paper insulation degradation. *Energies*, 11(6), Article 1465. <https://doi.org/10.3390/en11061465>
- Maharana, M., Baruah, N., Nayak, S. K., Meher, N., & Iyer, P. K. (2019). Condition assessment of aged ester-based nanofluid through physicochemical and spectroscopic measurement. *IEEE Transactions on Instrumentation and Measurement*, 68(12), 4853-4863. <https://doi.org/10.1109/TIM.2019.2900883>
- Maharana, M., Nayak, S. K., & Sahoo, N. (2018). Karanji oil as a potential dielectrics liquid for transformer. *IEEE Transactions on Dielectrics and Electrical Insulation*, 25(5), 1871-1879. <https://doi.org/10.1109/TDEI.2018.007230>
- Makmud, M. Z.H., Illias, H. A., Chee, C. Y., & Sarjadi, M. S. (2018). Influence of conductive and semi-conductive nanoparticles on the dielectric response of natural ester-based nanofluid insulation. *Energies*, 11(2), Article 333. <https://doi.org/10.3390/en11020333>

- Makmud, M. Z. H., Illias, H. A., Chee, C. Y., & Dabbak, S. Z. A. (2019). Partial discharge in nanofluid insulation material with conductive and semiconductive nanoparticles. *Materials*, *12*(5), Article 816. <https://doi.org/10.3390/MA12050816>
- Martin, D., Wang, Z. D., Darwin, A. W., & James, I. (2006, October 15-18). *A comparative study of the chemical stability of esters for use in large power transformers*. [Paper presentation]. IEEE Conference on Electrical Insulation and Dielectric Phenomena, Kansas City, USA. <https://doi.org/10.1109/CEIDP.2006.311977>
- Matharage, S. Y., Liu, Q., & Wang, Z. D. (2016). Aging assessment of kraft paper insulation through methanol in oil measurement. *IEEE Transactions on Dielectrics and Electrical Insulation*, *23*(3), 1589-1896. <https://doi.org/10.1109/TDEI.2016.005564>
- Mohamad, N. A., Azis, N., Jasni, J., Kadir, M. Z. A. A., Yunus, R., Ishak, M. T., & Yaakub, Z. (2016). Investigation on the dielectric, physical and chemical properties of palm oil and coconut oil under open thermal ageing condition. *Journal of Electrical Engineering and Technology*, *11*(3), 690-698. <https://doi.org/10.5370/JEET.2016.11.3.690>
- Mohamad, N. A., Azis, N., Jasni, J., Kadir, Z. A. A., Yunus, R., Ishak, M. T., & Yaakub, Z. (2015). Analysis on the degradation of insulation paper in palm oil and coconut oil under high temperature ageing. *Jurnal Teknologi*, *72*(1), 1-6.
- Munajad, A., Subroto, C., & Suwarno. (2017). Study on the effects of thermal aging on insulating paper for high voltage transformer composite with natural ester from palm oil using fourier transform infrared spectroscopy (ftir) and energy dispersive x-ray spectroscopy (EDS). *Energies*, *10*(11), Article 1857. <https://doi.org/10.3390/en10111857>
- N'cho, J. S., Fofana, I., Hadjadj, Y., & Beroual, A. (2016). Review of physicochemical-based diagnostic techniques for assessing insulation condition in aged transformers. *Energies*, *9*(5), Article 367. <https://doi.org/10.3390/en9050367>
- Suwarno, & Pasaribu, R. (2017, September 11-15). *Effects of Thermal Aging on Paper Characteristics in Paper-Mineral Oil composite Insulation*. International Symposium on Electrical Insulating Materials (ISEIM), Toyohashi, Japan. <https://doi.org/10.23919/ISEIM.2017.8166587>
- IEEE Standars Associaltion. (2012). *IEEE guide for loading mineraloil-immersed transformers and step-voltage regulators*. IEEE Standars Associaltion. <https://ieeexplore.ieee.org/stamp/stamp.jsp?arnumber=6166928>
- Raj, R. A., Samikannu, R., Yahya Began, A., & Mosalaosi, M. (2020). Comparison of ageing characteristics of superior insulating fluids with mineral oil for power transformer application. *IEEE Access*, *8*, 141111-141122. <https://doi.org/10.1109/ACCESS.2020.3012988>
- Raof, N. A., Yunus, R., Rashid, U., Azis, N., & Yaakub, Z. (2019). Effect of molecular structure on oxidative degradation of ester based transformer oil. *Tribology International*, *140*, Article 105852. <https://doi.org/10.1016/j.triboint.2019.105852>
- Rapp, K. J., McShane, C. P., & Luksich, J. (2005, June 26- July 1). *Interaction mechanisms of natural ester dielectric fluid and kraft paper*. [Paper presntation]. IEEE International Conference on Dielectric Liquids (ICDL), Coimbra, Portugal. <https://doi.org/10.1109/icdl.2005.1490108>

- Raymon, A., Pakianathan, P., E. Rajamani, M. P., & Karthik, R. (2013). Enhancing the critical characteristics of natural esters with antioxidants for power transformer applications. *IEEE Transactions on Dielectrics and Electrical Insulation*, 20(3), 899-912. <https://doi.org/10.1109/TDEI.2013.6518959>
- RSPO. (2015). *Impact Update 2015*. Roundtable on Sustainable Palm Oil. [https://www.helikonia.co.uk/wp-content/uploads/2020/12/FA-RSPO-Impact-Update-2015\\_SINGLE.pdf](https://www.helikonia.co.uk/wp-content/uploads/2020/12/FA-RSPO-Impact-Update-2015_SINGLE.pdf)
- Sinan, S. S., Shawaludin, S. N., Jasni, J., Azis, N., Ab Kadir, M. Z. A., & Mohtar, M. N. (2014, May 23-23). *Investigation on the AC breakdown voltage of RBDPO Olein*. [Paper presentation]. IEEE Innovative Smart Grid Technologies - Asia (ISGT ASIA), Kuala Lumpur, Malaysia. <https://doi.org/10.1109/ISGT-Asia.2014.6873888>
- Suleiman, A. A., Muhamad, N. A., Bashir, N., Murad, N. S., Arief, Y. Z., & Phung, B. T. (2014). Effect of moisture on breakdown voltage and structure of palm based insulation oils. *IEEE Transactions on Dielectrics and Electrical Insulation*, 21(5), 2119-2126. <https://doi.org/10.1109/TDEI.2014.004431>
- Suryani, S., Sariyani, S., Earnestly, F., Marganof, M., Rahmawati, R., Sevindrajuta, S., Indra Mahlia, T. M., & Fudholi, A. (2020). A comparative study of virgin coconut oil, coconut oil and palm oil in terms of their active ingredients. *Processes*, 8(4), Article 403. <https://doi.org/10.3390/PR8040402>
- Tripathi, A. K., & Vinu, R. (2015). Characterization of thermal stability of synthetic and semi-synthetic engine oils. *Lubricants*, 3(1), 54-79. <https://doi.org/10.3390/lubricants3010054>
- Vihacencu, M. Ş., Ciuriuc, A., & Dumitran, L. M. (2013). Experimental study of electrical properties of mineral and vegetable transformer oils. *UPB Scientific Bulletin, Series C: Electrical Engineering*, 75(3), 171-182.
- Wilhelm, H. M., Tulio, L., Jasinski, R., & Almeida, G. (2011). Aging markers for in-service natural ester-based insulating fluids. *IEEE Transactions on Dielectrics and Electrical Insulation*, 18(3), 714-719. <https://doi.org/10.1109/TDEI.2011.5931057>

## Development of Sago-based Analog Rice Using Kansei and Value Engineering

Violetta Putri Rizky Septiani, Mirwan Ushada\* and Suharno

*Department of Agro-industrial Technology, Faculty of Agricultural Technology, Universitas Gadjah Mada, Yogyakarta, 55281 Indonesia*

### ABSTRACT

This study used two product development methods: Kansei and value engineering. Kansei engineering was used to identify and translate consumer psychological impressions or feelings in the form of Kansei words to the design parameters, while value engineering was used to analyze the functional properties by considering cost, reliability, and performance. The consumers determined the priority attributes of analog rice products, namely a good taste, a fluffy and soft texture, as well as a bright color. Three alternative variations of the product development concept were formulated based on these priorities. The concept with the highest value was then concluded as an analog rice produced from 90% Sago flour and 10% MOCAF (Modified Cassava Flour) with a value of 1,131.

*Keywords:* Analog rice, Kansei engineering, product development, value engineering

### INTRODUCTION

According to the World Health Organization (WHO), obesity is a condition characterized by an excessive increase in adipose tissue. It can also be defined as a systemic disease affecting white adipose tissue. Furthermore, obesity has become a global health problem because it can potentially lead to some non-communicable diseases, such as heart disorders,

diabetes, hypertension, stroke, pulmonary emboli, cancers, osteoarthritis, gallbladder diseases, and respiratory abnormalities (Baboota et al., 2013; Mohamed, 2014; Gómez et al., 2021). In The Global Burden of Disease (1996), Muray and Lopez stated that the number of deaths caused by these conditions was predicted to increase by 77%, from 28.1 million in the year 1990 to

#### ARTICLE INFO

##### *Article history:*

Received: 05 November 2022

Accepted: 05 April 2023

Published: 03 September 2023

DOI: <https://doi.org/10.47836/pjst.31.6.17>

##### *E-mail addresses:*

[violettaputri99@mail.ugm.ac.id](mailto:violettaputri99@mail.ugm.ac.id) (Violetta Putri Rizky Septiani)

[mirwan\\_ushada@ugm.ac.id](mailto:mirwan_ushada@ugm.ac.id) (Mirwan Ushada)

[suharno@ugm.ac.id](mailto:suharno@ugm.ac.id) (Suharno)

\* Corresponding author

49.7 million in the year 2020 (Baboota et al., 2013; Blümel et al., 2015; Salleh, 2018). Obesity and metabolic disorders could be influenced by several factors, including genetic and physiological differences, namely gender and age. They can also be influenced by the environment and habits, such as diet, stress, smoking, alcohol, and practice (Shabayek et al., 2022).

Obesity can be prevented using a good diet and healthy lifestyle, such as the regular consumption of functional foods of analog rice (Shao et al., 2017). Analog rice is a non-rice ingredient with high levels of carbohydrates, and it is often produced from carbohydrate-rich flour, such as cassava and corn flour, as well as starch (Park et al., 2021). It also has organoleptic, chemical, and aesthetic characteristics similar to other rice products (Banovic & Sveinsdottir, 2021). These foods have a low glycemic index; hence, the blood sugar was not increased significantly. The product can be used as an alternative to rice consumption. The analog rice product has the physical properties of rice and was made from various formulations of non-rice carbohydrate sources.

Sago is one of the sources of non-rice carbohydrates that can be recommended for its production. The Sago flour has a high carbohydrate content with a competitive yield and affordable price (Nururrahmah et al., 2018; Zhu, 2019; Du et al., 2020). It also has similar energy content to corn and rice, namely 353 kcal, 361 kcal, and 360 kcal per 100 grams, respectively. Sago is gluten-free and has a low glycemic index of 28 (Nururrahmah et al., 2018) compared to corn and rice, with 48 and 68, respectively. Sago starch contains 11.07% dietary fiber and 10.58 mg/100 g resistant starch (Wahjuningsih et al., 2020), which can be developed as a functional food due to its health beneficiary (Azkia et al., 2021). Consumption of dietary fiber can increase productivity activity, enhance the digestive system, increase short-chain fatty acid formulation (SCFA), as well as reduce the risk of cancer and diabetes Mellitus (Kaczmarczyk et al., 2012; Jha et al., 2017; Azkia et al., 2021). The resistant starch also helps to improve digestive health by reducing the number of pathogenic bacteria in the intestine (Azkia et al., 2021).

Analog rice is considered a valuable functional food that the community can consume. However, convincing people to consume the analog as a staple food substitute for rice was difficult. The taste of rice is considered the most delicious and easy to process with a relatively stable price. One of the ways that can be used to increase the consumption of these analog products is to produce them based on the consumer's needs in terms of good physical properties and affordable prices. Therefore, this study aims to identify the quality attributes of analog rice and determine the best alternative concept for developing its products based on consumer needs.

The Kansei engineering method is a new product development technology carried out by identifying the Kansei words, which describe or represent consumer feelings towards a product, service, and technology (Ushada, Amalia, et al., 2023; Ushada, Trapsilawati et al., 2023). The data obtained are then translated into a product design element (Jiang et al.,

2021). The value engineering method can be used to analyze the minimum costs of analog rice. It is also a creative technique used to achieve the function of a product by applying the optimal cost and production system (Hidayat et al., 2021). The method is often used to determine the best functional balance between cost, reliability, and performance.

## MATERIALS AND METHODS

### Materials

The analog rice in this study was produced from the main ingredients of Sago flour collected from Sago tree starch. Additional ingredients that align with the identification of the product specifications were also used for the process. Furthermore, other additives used to develop the texture and aroma of analog rice include 2% Glycerol Mono Stearate (GMS), 1% Carboxy Methyl Cellulose (CMC), 5% palm oil, 1% salt, and 30% water. The type of Sago flour used was the local brand in the Yogyakarta Special Region, Indonesia.

### Respondents

The population for the study was Indonesian society, with the inclusion criteria being people aged 18–60 years willing to fill out the questionnaire. Data was collected from the respondents using a questionnaire in the form of Google Forms. The sample size used in this study was determined with Cochran's formula because some populations were unknown (Seyyedamiri & Khosravani, 2020) (Equation 1).

$$n = \frac{z^2 pq}{e^2} \quad [1]$$

Where  $n$  is the minimum sample size,  $z$  is the confidence level (90%),  $p$  is the presumed proportions,  $q$  is  $1-q$ , and  $e$  is the margin error (0,5). Based on the calculation results, the minimum sample size was 272 respondents. The validity and reliability of the questionnaire were assessed with a pilot test on 30 respondents.

### Methods

This study combined two product development methods, namely Kansei and value engineering. Integration of the methods is presented in Figure 1.

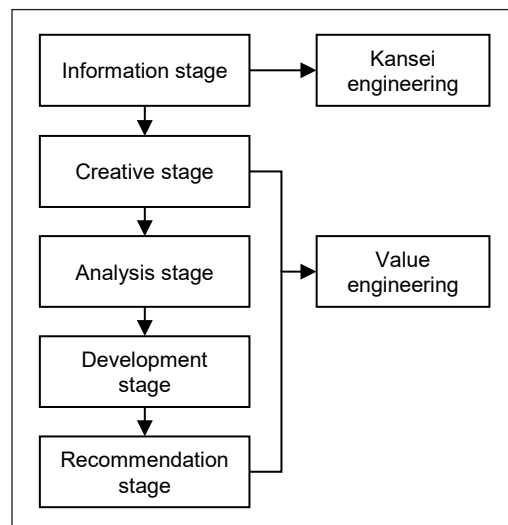


Figure 1. Integration method diagram

**Information Stage.** At this stage, data collection consists of primary and secondary data. The primary data were obtained through direct observation from the field and interviews with respondents using a preliminary questionnaire. Meanwhile, the secondary data were obtained from other sources related to the study object, and they were in the form of documents, files, literature, and company records.

Data processing was carried out with the following steps:

- Collecting consumers' voices based on Kansei's words about product attributes.
- Arranging a semantic differential questionnaire to measure the words obtained in numbers.
- Factor analysis of the questionnaire answers. The selected Kansei words had the highest utility value and served as the basis for product development attributes. In factor analysis, the Kaiser-Meyer-Olkin Measure of Sampling Adequacy (KMO MSA) test and the Bartlett test were used to summarize or reduce Kansei words. The cut-off value of KMO MSA is between the range of 0.5 to 1 (Djaali et al., 2008).

**Creative Stage.** The factor analysis results were used to measure the level of consumer importance in the selected product attributes. Identifying their needs was also carried out to determine the product specification to be developed by giving multiple-choice questions to the respondents. Data was collected through interviews using a questionnaire, results of the development of information stage. Furthermore, the questionnaire was divided into two parts: (1) the level of consumers' importance and (2) the identification of needs. The measurement of the importance level was carried out using a Likert scale with five response points: 1 (very unimportant), 2 (unimportant), 3 (neutral), 4 (important), and 5 (very important). Table 1 indicates the questionnaire for consumer needs. The questionnaire consisted of 4 primary and 4 secondary attributes.

Table 1  
*Questionnaire for consumer needs*

No.	Primary Attributes	Secondary Attributes
1	Texture	Fluffier
2	Texture	Mushy
3	Taste	Tasty
4	Color	Bright

**Analysis Stage.** The Function Analysis System Technique (FAST) diagram was used to develop several alternative ideas to fulfill the requirement based on the information obtained in the previous stage. Furthermore, the diagram consists of four functions, namely the main, derivative, and objective functions, as well as product specifications. The combination results of the attributes gave variations of the product concepts based on the modification design.

**Development Stage.** The development stage was carried out by determining the alternative variations of the product concepts and the attributes to be developed. Determination of the



alternative concept variations was performed using the zero-level diagram. Subsequently, a prototype as the product sample was developed for each concept.

**Recommendation Stage.** Panelists' assessments were carried out on the concept variations, which were determined and had a prototype. The results were used to calculate the performance, cost, and value analysis. Determination of the best alternative concept was performed by looking for the highest value. The value engineering method is often used to obtain the best value in a project or process by defining the functions needed to achieve the target at the lowest cost with good quality and performance (Hidayat et al., 2021).

### **Statistical Analysis**

Pearson Correlation and Cronbach's Alpha were carried out using SPSS 24 for Windows™ (IBM SPSS Inc., Chicago, IL, USA) to obtain the validity and reliability of Kansei word analysis. Factor analysis was also performed using the Kaiser-Meyer-Olkin Measure of Sampling Adequacy (KMO MSA) and Bartlett tests to summarize or reduce the words. This step helped to focus on the attributes of analog rice development that were considered important by the respondents.

### **Sensory Analysis**

Sensory testing was carried out with the hedonic test of acceptance to determine the level of acceptance or consumer preference for the prototype of analog rice products. A total of 32 untrained panelists recruited from the Faculty of Agricultural Technology, Universitas Gadjah Mada, were used for this process. The panelists consisted of 5 males and 27 females aged 20 to 25. They were instructed to evaluate three formulations based on sensory analysis: color, aroma, texture, and taste. The samples were prepared with three-digit random numbers in the containers as a code, and each sample was prepared with a different number. Panelists were asked to evaluate the rice analog samples for sensory parameters such as color, aroma, texture, and taste using the 7-point hedonic scale (Ong et al., 2022). The rating scale used is a score of 1 for the lowest and 7 for the highest: 1 (dislike very much), 2 (dislike moderately), 3 (dislike slightly), 4 (neither like nor dislike), 5 (like slightly), 6 (like moderately), and 7 (like very much).

## **RESULTS AND DISCUSSION**

### **Socio-demographic of Participants**

Among 297 respondents who completed the questionnaire, 69.5% were female, 45.5% were highly educated with bachelor's and postgraduate degrees, 75.9% were below 26 years old, and 24.1% had a high income. Table 2 shows the socio-demographic profile of

the consumers. The results showed that the items were closely related, and the scales were unidimensional.

**Information Stage**

Kansei words of analog rice were obtained by distributing interview questionnaires to thirty people, literature, and social media, such as Instagram, YouTube, and Twitter. A total of 57 words were collected and described in Table 3.

The Kansei words were then filtered or grouped by selecting words with close adjective and visual meanings to the study objects and subjectively selected. Hence, 27 were obtained. Subsequently, they were

paired with antonyms and arranged in a semantic differential questionnaire. It was then distributed to 292 respondents to measure the psychological meaning of word pairs with analog rice. The semantic differential questionnaire is presented in Table 4.

The semantic differential questionnaire was carried out using a pilot test on thirty respondents, followed by a validity test. The results showed that there were 6 invalid

Table 2  
*Respondents' characteristics*

Characteristics	N	%
Gender		
Male	67	30.5
Female	153	69.5
Age (years)		
Teenagers (18–25)	167	75.9
Adults (26–45)	37	16.8
Elderly (>46)	16	7.3
Education level		
Low education	120	54.5
High education	100	45.5
Income		
Low income	167	75.9
High income	53	24.1

Table 3  
*Kansei words of analog rice*

Kansei word	Kansei Word	Kansei Word	Kansei Word
Special	Certified	Strong scent	Destroyed
Healthy	Standardized	Easy stale	Clot
Diet	Quality	Expensive	Fine
Satisfied	Tasteless	Safe	Bright
Variety	Sweet	Easily obtained	Gentle
Delicious	Tasty	Steady	Bitter
Curious	Rough	Hygienic	Typical
Organic	Mushy	Cool	Oily
Interesting	Hard	Practical	Alternative
Halal	Sticky	Clear	Native
Unique	Springy	Affordable	Obesity
Trend	Cheap	Local	Diabetes
Simple	Fluffier	White	
Dry	Pera	Fragrant	
Functional	Watery	Durable	

questions because  $r$ -calculate  $<$   $r$ -table. The details of the validity test are presented in Table 5. The number of pairs was reduced to 21 because 6 questions were invalid ( $27-6 = 21$ ). Subsequently, a reliability analysis was carried out to assess the remaining words. The test results showed that the Cronbach Alpha value was 0,894, greater than 0,6. This finding indicates that the 21 pairs are reliable.

Kansei word pairs declared valid and reliable were analyzed using factor analysis. The KMO and Bartlett Test results were 0,864 with a significance of 0,000, indicating that the variables can be processed using the analysis method. The next step was to eliminate the pair of Kansei words that can represent each factor. Elimination was carried out to simplify the study attributes further, making it easier to carry out designs focusing on important variables. The factor analysis results are presented in Table 6; the highest value of component 1 was 'not-delicious-delicious.' The lowest value was 'not certified-certified.'

Table 5  
Invalid Kansei word

Kansei Word	$r$ -calculate	$r$ -table
Not curious – Curious	0,177	0,361
Ancient – Trend	0,337	0,361
Unvariety – Variety	0,277	0,361
Alternative – Primary	-0,013	0,361
Sticky – Dry	-0,006	0,361
Watery - Rought	0,347	0,361

Table 4  
Pair of Kansei word

Pair of Kansei Word	Pair of Kansei Word
Unhealthy – Healthy	Mushy – Solid
Not efficient – Efficient	Sticky – Dry
Normal – Unique	Clot - Not clumping
Disappointed – Satisfy	Watery - Rough
Not curious – Curious	Dull – Bright
Ancient – Trend	Unscented – Fragrant
Inorganic – Organic	Temporary – Durable
Alternative – Primary	Destroyed – Intact
Not certified – Certified	General – Typical
Tasteless – Tasty	Hard to get - Easy to get
Not delicious – Delicious	Unvariety – Variety
Pera – Fluffier	Rigid – Springly
Expensive – Affordable	Rude – Fine
Complicated – Simple	

Table 6  
Factor analysis of analog rice product

Kansei Word	Component 1
Disappointed – satisfied	0,739
Inorganic – organic	0,670
Not certified – certified	0,657
“Pera” – fluffier	0,686
Not delicious – delicious	0,834
Mushy – solid	0,742
Unbright – bright	0,694

## Creative Stage

The ranking or determination of the priority of consumer needs attributes based on information from 107 respondents was used to calculate the importance level and weight values (Table 7).

Based on the ranking of each attribute of consumer needs, the priority of the attributes desired by consumers is the attribute of goods taste, followed by attributes of fluffier, texture,

bright color, and soft texture. The identification of consumer needs is carried out to find out the specifications of a product to be developed. The basis for determining the material formulation for the development of analog rice in this study is to form the color and taste of analog rice according to the needs of respondents. In addition, it also considers the price and nutritional content of the material for making an analog rice prototype.

Identification of consumer needs was performed to determine the specifications of the product to be developed. The results obtained from 66.4% of the 107 respondents served as a reference for producing prototypes of analog rice. From Table 8, the consumer needs white analog rice. Hence, a prototype was made from the combination of Sago and MOCAF.

Table 7  
*Importance level of analog rice attributes*

Primary attribute	Secondary attribute	Level of importance	Weight	Rank
Texture	Fluffier	4.1869	0.2819	2
	Mushy	2.6449	0.1781	4
Flavor	Delicious	4.2991	0.2895	1
Color	Bright	3.7196	0.2505	3

Table 8  
*Specification of analog rice*

Question	Development Alternatives	Percentage (%)
Favorite product color	White is made from the formulation of Sago and MOCAF (Modified Cassava Flour).	66.4%
	Orange is made from the formulation of Sago and corn flour.	13.1%
	Purple is made from the formulation of Sago and purple sweet potato.	21.5%

### Analyze Stage

The formulation of creative product ideas for the development concept was performed by mapping out the required product functions. The analysis of the interrelationships between the functions was carried out using a FAST diagram to facilitate the preparation of the ideas. The FAST diagram of analog rice is presented in Figure 2.

Based on the FAST diagram image above, the scope of the problem and its solution have been described through the interrelationships between functions arranged in the diagram. The basic function, the scope of the problem to be solved, is analog rice. There is an objective function to complete the basic functions of analog rice, namely quality and aesthetic functions, to get a design that suits consumer needs.

The quality function consists of primary attributes of texture and taste, while the aesthetic function consists of primary attributes of color. The secondary function of fluffier and mushy can be fulfilled by determining the appropriate dough composition and the right

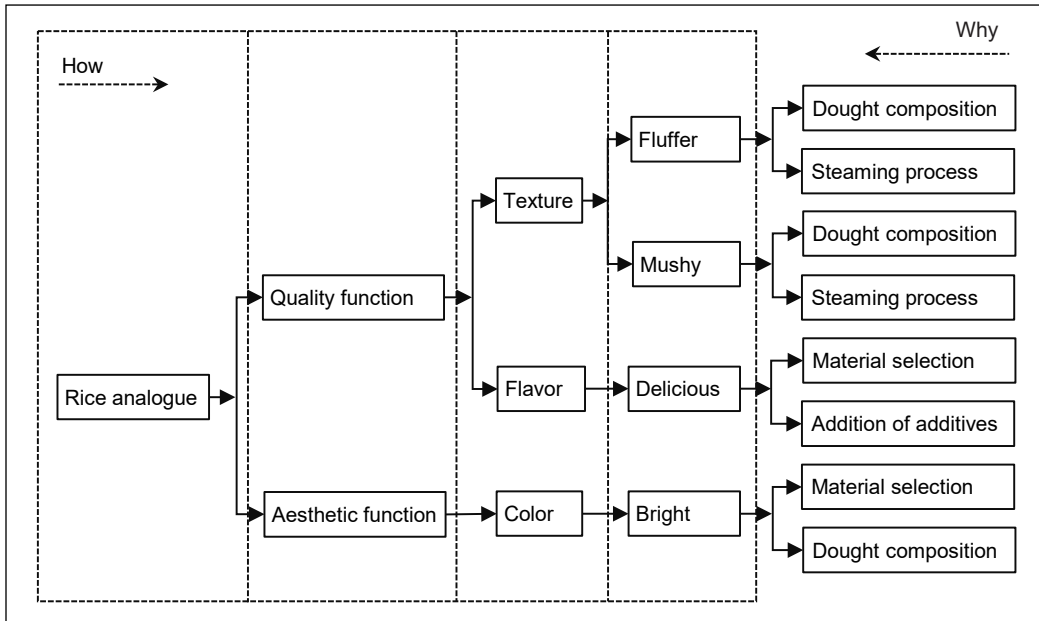


Figure 2. FAST diagram

steaming process, namely by paying attention to the time and temperature during steaming. The secondary function of good taste can be fulfilled by selecting the ingredients for making analog rice, paying attention to dough consumption, and adding additional ingredients to create a good taste from analog rice. Then, the secondary function of the bright color of analog rice can be fulfilled by determining the choice of materials to be used and paying attention to the appropriate dough composition.

### Development Stage

In the development stage, the concept of analog rice consists of 3 variations of alternative concepts as 10%, 20%, and 30% additive composition (Figure 3).

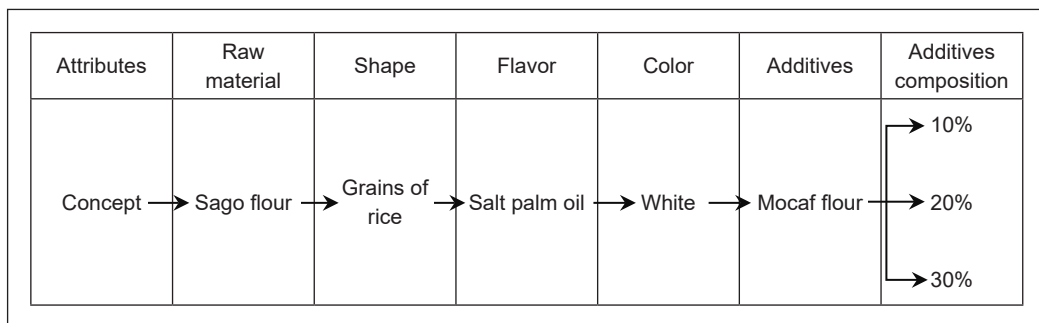


Figure 3. Zero level concept diagram

Based on the Zero Level Concept diagram, Sago flour is the raw material used to develop analog rice products. The expected attributes of analog rice form are similar to rice grains in general. The formulation of grains like rice in the dough is carried out by adding 2% GMS and 1.5% CMC, which function as an emulsifier or adhesive to the material, so that when the extrusion process is carried out, it makes the material stronger, not sticky, and crumbles. The taste attribute is the priority in the development of analog rice products. Consumers want good taste, so they add 1% salt and 5% palm oil.

**Recommendation Stage**

The alternative design concepts were assessed based on the questionnaire on the preference level of 32 panelists. The result was then used to obtain a score for the calculation of weight and performance. Attributes of the level of preference assessment include color, aroma, taste, and texture. The prototype of analog rice, which was developed based on the alternative concept variations, is presented in Table 9. The concepts were developed based on the varied composition of Sago flour and MOCAF.

In the analysis of product performance values using an evaluation matrix, the total weight of the attributes was obtained by dividing the score on each of them by the total score. Furthermore, the product performance was calculated by multiplying the total score by the weight of each attribute. The results of the performance calculation are presented in

Table 9  
*The prototype figure of the alternative concept variations*



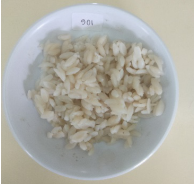
Concept	Prototype figure	Description
1		The analog rice was produced with 90% Sago flour and 10% MOCAF
2		The analog rice was produced with 80% Sago flour and 20% MOCAF
3		The analog rice was produced with 70% Sago flour and 30% MOCAF

Table 10. Table 10 indicates that the best performance is Concept 1, with a performance value 164,510.

This study selected the alternative concept with the highest value as the best alternative concept. The performance value in the formula above does not have units, while the costs have units, namely rupiah. Therefore, the performance needs to be converted into rupiah to calculate the value of each alternative. The formula used for the conversion can be obtained from Equation 2 (Hidayat et al., 2021):

$$Pn' = \frac{P_n C_0}{P_0} \quad [2]$$

Where  $P_n'$  is converting alternative performance to rupiah,  $P_n$  is alternative performance  $n$ ,  $P_0$  is alternative average performance, and  $C_0$  is the alternative average cost.

The results showed that the best concept in developing analog rice products can meet 70% of consumer needs. Based on the sensory tests, the attributes tested were adjusted to others generated from identifying consumer needs, namely taste, texture, color, and aroma. Furthermore, Table 11 shows that the panelist's assessment is in the moderately favorable range for alternative concept 1. Table 11 confirmed Table 10 that the best value is concept 1 of 1,131. The research concluded that the best material formulation is 90% Sago and 10% MOCAF.

Table 10  
*Performance of analog rice concept*

Quality attributes	Color	Aroma	Texture	Flavor	Performance
Attribute weight (%)	24,424	23,695	25,884	25,997	
Concept 1	175	157	162	164	164,510
Concept 2	142	233	148	149	143,240
Concept 3	118	132	151	150	138,178

Table 11  
*Value of analog rice concept*

Concept	Performance	Converted performance	Production cost	Value	Rank
1	31,101	31,101	27,501	1,131	1
2	27,080	27,080	28,101	0,964	2
3	26,123	26,123	28,701	0,910	3

## CONCLUSION

The Sago-based analog rice was developed using Kansei and value engineering. The research results concluded the quality attributes of Sago-based analog rice as delicious, fluffier, and mushy texture, as well as bright color with the specification of white. Three

alternative variations of the product development concept were formulated based on these priorities. The best alternative concept was produced from 90% Sago flour and 10% MOCAF (Modified Cassava Flour) with a value of 1,131.

## ACKNOWLEDGEMENT

This study is part of Violetta Putri Rizky Septiani's thesis 'Development of Rice Analogue Products Using Kansei and Value Engineering Methods.' It was supported and funded by the incubator laboratory research program 2021 from the Faculty of Agricultural Technology, Universitas Gadjah Mada, Indonesia, number 160/UN1/FTP/SK/SDM/2020.

## REFERENCES

- Azkiya, M. N., Wahjuningsih, S. B., & Wibowo, C. H. (2021). The nutritional and functional properties of noodles prepared from sorghum, mung bean and sago flours. *Food Research*, 5(2), 65-69. [https://doi.org/10.26656/fr.2017.5\(S2\).002](https://doi.org/10.26656/fr.2017.5(S2).002)
- Baboota, R. K., Bishnoi, M., Ambalam, P., Kondepudi, K. K., Sarma, S. M., Boparai, R. K., & Podili, K. (2013). Functional food ingredients for the management of obesity and associated co-morbidities - A review. *Journal of Functional Foods*, 5(3), 997-1012. <https://doi.org/10.1016/j.jff.2013.04.014>
- Banovic, M., & Sveinsdóttir, K. (2021). Importance of being analogue: Female attitudes towards meat analogue containing rapeseed protein. *Food Control*, 123, Article 107833. <https://doi.org/10.1016/j.foodcont.2020.107833>
- Blümel, J. E., Chedraui, P., Aedo, S., Fica, J., Mezones-Holguín, E., Barón, G., Bencosme, A., Benitez, Z., Bravo, L. M., Calle, A., Flores, D., Espinoza, M. T., Gomez, G., Hernandez-Bueno, J. A., Laribezcoa, F., Martino, M., Lima, S., Monterrosa, A., Mostajo, D., & Zúñiga, M. C. (2015). Obesity and its relation to depressive symptoms and sedentary lifestyle in middle-aged women. *Maturitas*, 80(1), 100-105. <https://doi.org/10.1016/j.maturitas.2014.10.007>
- Djaali, H., Muljono, P., & Sudarmanto. (2008). *Pengukuran dalam Bidang Pendidikan* [Measurement in the Field of Education]. Grasindo.
- Du, C., Jiang, F., Jiang, W., Ge, W., & Du, S. K. (2020). Physicochemical and structural properties of sago starch. *International Journal of Biological Macromolecules*, 164, 1785-1793. <https://doi.org/10.1016/j.ijbiomac.2020.07.310>
- Gómez, J. C., Ena, J., Lorido, J. A., Ripoll, J. S., Carrasco-Sánchez, F. J., Gómez-Huelgas, R., Soto, M. I. P., Lista, J. D., & Martínez, P. P. (2021). Obesity is a chronic disease. Positioning statement of the Diabetes, Obesity and Nutrition Workgroup of the Spanish Society of Internal Medicine (SEMI) for an approach centred on individuals with obesity. *Revista Clínica Española (English Edition)*, 221(9), 509-516. <https://doi.org/10.1016/j.rceng.2020.06.013>
- Hidayat, K., Nasikin, M. K., & Rakhmawati. (2021). Product development of corn rice using value engineering method. In *IOP Conference Series: Earth and Environmental Science* (Vol. 733, No. 1, p. 012039). IOP Publishing. <https://doi.org/10.1088/1755-1315/733/1/012039>



- Jha, S. K., Singh, H. R., & Prakash, P. (2017). Dietary fiber and human health: An introduction. In R. A. Samaan (Ed.), *Dietary Fiber for the Prevention of Cardiovascular Disease* (pp. 1-22). Academic Press. <https://doi.org/10.1016/B978-0-12-805130-6.00001-X>
- Jiang, T., Yang, C., Zhou, L., & Xue, C. (2021). Using Kansei Engineering to analyze consumers' product attribute preferences. In F. Rebelo (Ed.), *International Conference on Applied Human Factors and Ergonomics* (pp. 990-997). Springer. [https://doi.org/10.1007/978-3-030-79760-7\\_118](https://doi.org/10.1007/978-3-030-79760-7_118)
- Kaczmarczyk, M. M., Miller, M. J., & Freund, G. G. (2012). The health benefits of dietary fiber: Beyond the usual suspects of type 2 diabetes mellitus, cardiovascular disease, and colon cancer. *Metabolism*, *61*(8), 1058-1066. <https://doi.org/10.1016/j.metabol.2012.01.017>
- Mohamed, S. (2014). Functional foods against metabolic syndrome (obesity, diabetes, hypertension, and dyslipidemia) and cardiovascular disease. *Trends in Food Science & Technology*, *35*(2), 114-128. <https://doi.org/10.1016/j.tifs.2013.11.001>
- Nururrahmah, H., & Sudarno, U. (2018). Physicochemical characteristic of sago hampas and sago wastewater in Luwu Regency. In *E3S Web of Conferences* (Vol. 73, p. 07007). EDP Sciences. <https://doi.org/10.1051/e3sconf/20187307007>
- Ong, Y. Q., Harith, S., Shahril, M. R., Shahidan, N., & Hapidin, H. (2022). Organoleptic, hypoglycaemic, and *in vitro* starch digestion effects of formulated melon manis Terengganu peel powder. *International Food Research Journal*, *29*(6), 1293-1303. <https://doi.org/10.47836/ifrj.29.6.06>
- Park, S., Choi, M., & Lee, M. (2021). Effects of anthocyanin supplementation on reduction of obesity criteria: A systematic review and meta-analysis of randomized controlled trials. *Nutrients*, *13*(6), Article 2121. <https://doi.org/10.3390/nu13062121>
- Salleh, M. R. (2018). The burden of mental illness: An emerging global disaster. *Journal of Clinical and Health Sciences*, *3*(1), 1-8. <https://ir.uitm.edu.my/id/eprint/30072>
- Seyyedamiri, N., & Khosravani, A. (2020). Identification of the effective e-promotional tools on improving destination brand image. *Journal of Global Information Management (JGIM)*, *28*(3), 169-183. <https://doi.org/10.4018/JGIM.2020070109>
- Shabayek, D. A., Rimbawan, R., & Budijanto, S. (2022). The potential of red kidney beans and brown rice-based flakes for breakfast to reduce obesity. *Journal of Food, Agriculture, and Society*, *10*(1), 1-14. <https://doi.org/10.17170/kobra-202110144903>
- Shao, A., Campbell, W. W., Chen, C. O., Mittendorfer, B., Rivas, D. A., & Griffiths, J. C. (2017). The emerging global phenomenon of sarcopenic obesity: Role of functional foods: A conference report. *Journal of Functional Foods*, *33*, 244-250. <https://doi.org/10.1016/j.jff.2017.03.048>
- Ushada, M., Amalia, R., Trapsilawati, F., & Putro, N. A. S. (2023). Group preference decision-making for the implementation of Industry 4.0 in food and beverage SMEs. In *Technology Analysis & Strategic Management* (pp. 1-18). Taylor & Francis. <https://doi.org/10.1080/09537325.2022.2117600>
- Ushada, M., Trapsilawati, F., Amalia, R., & Putro, N. A. S. (2023). Modeling trust decision-making of Indonesian food and beverage SME groups in the adoption of Industry 4.0. In *Cybernetics and Systems* (pp. 1-17). Taylor & Francis. <https://doi.org/10.1080/01969722.2022.2122011>

- Wahjuningsih, S. B., Azkia, M. N., & Anggraeni, D. (2020). The study of sorghum (*Sorghum bicolor* L.), mung bean (*Vigna radiata*) and sago (*Metroxylon sagu*) noodles: Formulation and physical characterization. *Current Research in Nutrition and Food Science Journal*, 8(1), 217-225. <https://dx.doi.org/10.12944/CRNFSJ.8.1.20>
- Zhu, F. (2019). Recent advances in modifications and applications of sago starch. *Food Hydrocolloids*, 96, 412-423. <https://doi.org/10.1016/j.foodhyd.2019.05.035>

## Utilizing Rainwater Harvesting System for Water Scarcity at a Double-Story Residential House

Muhammad Izzuddin Rosli<sup>1</sup>, Sharifah Abdullah<sup>1\*</sup> and Nur Asmaliza Mohd Noor<sup>2</sup>

<sup>1</sup>*School of Civil Engineering, College of Engineering, Universiti Teknologi MARA, 40450 UiTM, Shah Alam, Selangor, Malaysia*

<sup>2</sup>*School of Civil Engineering, College of Engineering, Universiti Teknologi MARA Pahang, 26400 UiTM, Jengka, Pahang, Malaysia*

### ABSTRACT

The use of rainwater is widely recognized as a dependable solution to reduce and mitigate the effects of water scarcity. Research on rainwater harvesting systems has increased significantly in recent years, especially on methods and treatment systems. A rainwater harvesting system can be described as collecting and storing rainwater that can be used rather than waste as runoff. A rainwater collection system might lessen the reliance on the public water supply. This study aims to determine the suitability of a rainwater harvesting system at a double-story house, thus identifying the suitable tank size for installation. This study's analysis used the Tangki NAHRIM 2.0 with localized input data such as rainfall, suitable roof area, and roof runoff coefficient. Findings from this study indicate that installing the rainwater harvesting system at a double-story house is suitable, and the optimum tank size is 3 m<sup>3</sup> by considering all the activities that contribute to water usage. Concisely, installing a rainwater harvesting system can reduce the monthly water bill and minimize the usage of treated water, thus preventing water scarcity in the future.

*Keywords:* Rainwater harvesting, residential building, runoff, water scarcity

### ARTICLE INFO

*Article history:*

Received: 08 November 2022

Accepted: 14 March 2023

Published: 03 October 2023

DOI: <https://doi.org/10.47836/pjst.31.6.18>

*E-mail addresses:*

[izzuddin273@gmail.com](mailto:izzuddin273@gmail.com) (Muhammad Izzuddin)

[sharifah.abdullah@uitm.edu.my](mailto:sharifah.abdullah@uitm.edu.my) (Sharifah Abdullah)

[nurasmaliza@uitm.edu.my](mailto:nurasmaliza@uitm.edu.my) (Nur Asmaliza)

\* Corresponding author

### INTRODUCTION

Water security can be defined as the capability of a population to access the acceptable quality of water sufficiently. Nowadays, scarcity of freshwater has become a vital issue in sustainable development and has worsened in terms of its potential impact, thus leading to extreme global risk. The key factors contributing to the increasing

demand for freshwater are the increasing global population, improving the standard of living, shifting the consumption pattern, and the increment of the irrigated agriculture area. Furthermore, the mismatch between demand and availability of freshwater is the principle of global water scarcity (Lani et al., 2018). The United Nations (UN) World Water Development Report (WWDR) in 2018 revealed that the availability of unpolluted, clean water and future opportunities had become a major issue as the global population reached 7.7 billion (UN Report, 2018).

However, the water system problem has worsened, and it is predicted that it will worsen by 2050 as the world population increases by 22 to 34%, from 9.4 to 10.2 billion people, due to the availability of local resources not in line with the population growth. For example, most of the rapid growth in the population is expected in developing countries (Africa and Asia) where the problem of potable water has already appeared (Boretti & Rosa, 2019). Several factors contribute to water shortages as a result of climate change, including changing weather (drought or floods), increasing pollution-producing activities, increasing human demands, and water consumption. The water scarcity issue should not be taken lightly because it can greatly impact a nation or even state and become a major concern worldwide, but little is known about how it has developed over time.

Malaysia is blessed with abundant annual rainfall, which will be wasted if not collected and recycled. Moreover, water collected from the rainfall can be used during water disruption; hence, this may reduce the water scarcity problem. Malaysia is heading towards a crisis due to increasing water demand, poor river basin management, and population growth. The problem can be prolonged when there is a shortage of treated water, irregular water demand, and suspension of investment in maintenance work such as repairs, improvements, or modifications to facilities and current water distribution (Rahman, 2014). The problem of water scarcity in Malaysia recently affected people across the nation, for example, the crucial water crisis in several states, especially Selangor, where it received the highest complaints about unscheduled water disruption. The analysis of the fundamental concept of water scarcity and water stress indicated the difficulties between population demands and excess use of resources to be met (Kummu et al., 2016). Thus, it is important to take precautionary plans such as improving water system management, finding a new alternative water source, and taking strict action on river pollution to reduce the possibilities of water scarcity.

Rainwater harvesting (RHW) can be an alternative source to reduce the water shortage problem. Water from RHW can be used for gardening, toilet flushing, and cleaning areas around the house, reducing water bills and saving more money. If the residents apply this method, it can reduce the water demand or water usage per day. Besides, by applying this method, the citizens supported the worldwide campaign known as the Sustainable Development Goal (SDG), which supports the sustainability of the water supply. RHW,

also known as rainwater collection system, is a technology that collects and stores rainwater for human use. The rainfall can be fully utilized by collecting and storing rainwater rather than wasting it as surface runoff. The system can be as simple as rain barrels to complex structures with pumps, tanks, and purification systems.

The collected water can be used for watering gardens, washing cars and clothes, flushing toilets, and even being treated for human use (Struck, 2011). Generally, the RWH system is divided into surface runoff and rooftop. The advantages of implementing RWH are reducing the dependency on potable water and reducing floods in urban areas, thus reducing the nutrient loading to the river (Nguyen et al., 2018). RWH has many advantages in economy, technology, environment, and society. The benefits in terms of economics, through the implementation of the system, provided annual household cost savings of up to RM 240 per household as the installation of RWH was estimated to be cheaper compared to the higher water price (Lani et al., 2018). Moreover, it is well known that RWH could reduce peak water demand in urban water supply. The application of RWH in New South Wales, Australia, has indicated a significant result in the water savings from the main supply, even during the small rainfall intensity (Lani et al., 2018).

The benefits of reducing volume and peak demand can be interpreted as the smaller infrastructure size and savings in terms of operation and maintenance costs. It can be seen through the application of RWH in a suburb of Melbourne, where this application is able to reduce network pipe size and operating costs by up to 18% and 53%, respectively (Hajani & Rahman, 2014). Furthermore, implementing RWH can significantly lessen the operating costs and greenhouse discharge from the regional water supply systems (Lani et al., 2018). The application of RWH in Malaysia is suitable and just in time due to several water issues such as increased demand on water supply, high rainfall volume, and too dependable on surface water. In lieu of that, there is evidence that RWH can provide various socio-economic and environmental benefits, such as saving on utility bills, flow reduction during flash floods, and delaying the need to build new water supply facilities.

The implementation of RWH by the Malaysian government was implemented a long time ago, especially for public and government buildings. However, the overall success remains insufficient, mainly due to relatively higher investment, low water tariffs, lack of incentive from the government, low awareness among the public, and poor enforcement by the government. In reality, implementing RWH on a larger scale, such as in commercial buildings, can be more cost-effective compared to small-scale systems, such as residential areas, because the large roof area can provide sufficient volume for higher consumption in commercial buildings where higher water tariffs for commercial buildings than domestic tariffs. However, it is a good start to introduce the implementation of RWH in residential areas and educate the public on the advantages of the implementation of RWH. Thus, this study is developed to analyze the rainfall intensity in the targeted place to determine

suitable RWH for a double-story residential house. The collected rainwater can be used for non-potable daily activities such as gardening and washing a car; thus, indirectly, the public can reduce the monthly water bill. It also can reduce and minimize water demand for daily use to reduce water scarcity in the future.

## METHODOLOGY

Figure 1 indicates the study area, which focused on the location in Selangor due to frequent unscheduled water disruption. The application of the rainwater harvesting system for residential houses would be a great help during water disruption, and a double-story terrace house located at Jalan 3/12, Taman Seri Jaromas, 42600 Jenjarom, Selangor Darul Ehsan, has been selected to be as a reference and catchment area in order to do all the design work (Figure 2).

The data analysis used the Tangki NAHRIM 2.0, where the first Tangki NAHRIM was developed in 2008 using the visual basic and widely used in Malaysia to calculate and analyze optimal rainwater tank size (Lani et al., 2018). Tangki NAHRIM 2.0 (TN2) is developed based on established rainwater storage tank modeling methods, and the simulation model was developed in an R computing environment (R Core Team, 2013)

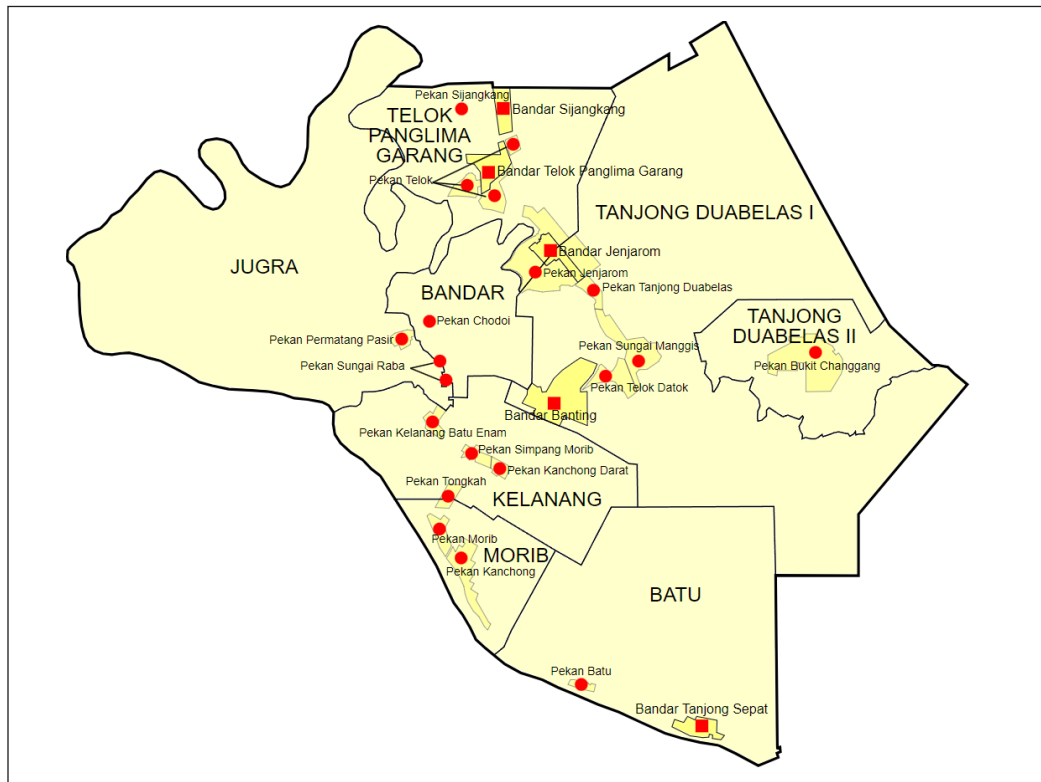


Figure 1. Map of Kuala Langat

with the simplified web-based graphical user interface using the R Shiny framework (Chang et al., 2019). It also includes the built-in rainfall data for both Peninsular and East Malaysia, and the model inputs are rainfall data, harvestable roof area, roof runoff coefficient, first flush depth, water demand, and proposed tank capacity.

Input data related to rainfall data, such as Rain Day versus No Rain Day, Monthly Rainfall, and Annual Rainfall, are used as built-in rainfall data for station Sungai Manggis (station number 2815001), available from 1971 until 2017. The station was selected because it was identified as nearest to the site, Taman Sri Jaromas,

Jenjarom, Selangor. The predetermined roof area, runoff coefficient, tank capacity, and water consumption from the tank selected to simulate the behavior of a rainwater tank. The runoff coefficient, which refers to the type of roof and the runoff coefficient, would be varied such as 0.50 for the thatched roof and 0.90 for the corrugated roof, but Liaw and Tsai (2004) suggested coefficients for all types of roofs 0.82, and for this study, we chose the average value as 0.8 and this similar with a study conducted by Goh and Ideris (2021).

TN2 adopts the yield-after-spill (YAS) water balance model from Jenkins et al. (1978) and Mitchell (2007) by assuming the RWH was utilized after spillage from the roof runoff inflow. The effectiveness of installing the RWH system can be assessed through a few parameters, such as the stored volume of rainwater in the storage tank, the efficiency of the tank, and average annual and monthly rainfall. It is important because the volume should be enough to be used for at least 2 days if water disruption happens, and this should be synchronized with average rainfall in that area; thus, a suitable storage tank can be provided. Next is the flow of water or discharge, which is the volume of water that moves toward a designated point over a specified period. This parameter should be the focus because the discharge of the water should be enough to carry all the water through the pipe and go to the outlet. The assessments of the parameters are the volume of water that can be stored (m<sup>3</sup>), the efficiency of the water tank (%), and average annual and monthly rainfall (mm). Equations 1 and 2 indicate the formula volumetric water saving efficiency and efficiency of the water tank, respectively.

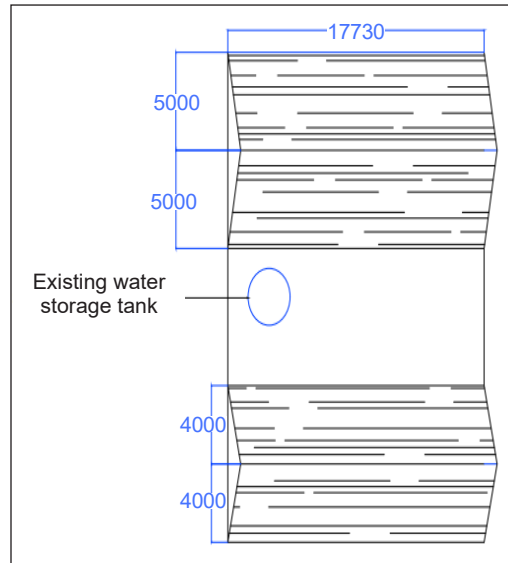


Figure 2. Catchment area

$$E_{ws} = \frac{\sum_{i=1}^n Y_i}{\sum_{i=1}^n D_i} \times 100 \tag{1}$$

n equals the total time interval in simulation, Y is the rainfall volume yielded for the water demand, D is the water demand for the rainwater harvesting system

$$E_s = \left[ 1 - \frac{\sum_{i=1}^n Qs_i}{\sum_{i=1}^n R_i} \right] \times 100 \tag{2}$$

R is the runoff volume, and Qs is the spillage or overflow.

## RESULTS AND DISCUSSION

### Rainfall Pattern

Rainfall collected around the area or basin is an important parameter that needs to be considered when determining how much water is available to support various demands such as agriculture, industry, irrigation, hydroelectric power production, and other human activities. The size or type of RWH relies on the rainfall pattern to forecast the frequency of rainfall. The forecasting uses the historical records of hydrological data and statistical analysis to increase the probability of extreme events such as floods, droughts, and severe storms that will occur in the future. The frequency or probability distribution can be used to relate the magnitude of such incidents to their frequency of recurrence. The monthly, seasonal, and yearly rainfall records are established by everyday rainfall collected at the individual stations, presented in the bulk of data concerning the rainfall climatology at any region or basin that has been stated (Nandargi & Mulye, 2012). Hence, it is very important to have an overview of the rainfall pattern for the respective study area to evaluate the suitability of installing the RWH. Figure 3 shows the comparison between rain days and no rain days from 1971 to 2017. The lowest number of rain days was recorded in 1983,

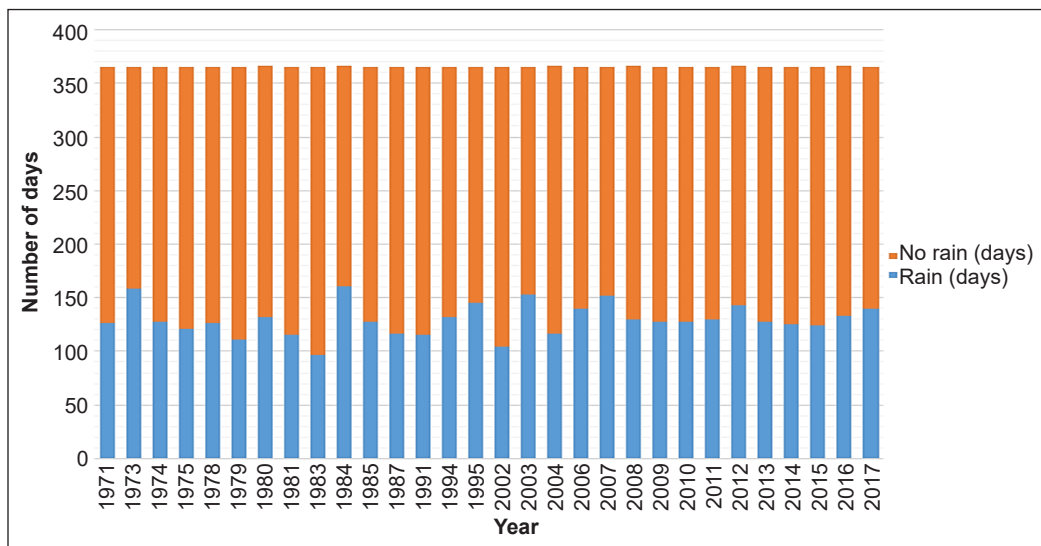


Figure 3. Average number of rain day versus no rain day for each year



with 97 days, while the highest number of rainy days ever recorded was 161 in 1984, and this data shows the potential of installing the RWH in that particular study area.

Meanwhile, Figure 4 depicts the monthly rainfall data from January to December 2017. It shows that the end of the quarter year, September to December, received the highest rainfall due to the location of Malaysia, either Peninsular or East, which has experienced a tropical climate influenced by the tropical airstreams, which have extreme heat and humidity, higher amounts of rainfall, and a climatic year centered on the northeast and southwest monsoons. The northeast monsoon (from November or December to March), the first inter-monsoon period (from March to April or May), the southwest monsoon (from May or June to September or early October), and the second inter-monsoon period are the four seasons of the climatic year (October to November).

The two monsoons' beginning and retreat are not well defined. Meanwhile, Figure 5 indicates annual rainfall at that particular station, and according to the JPS Sg Manggis or station number (2815001), however, there is no data recorded for

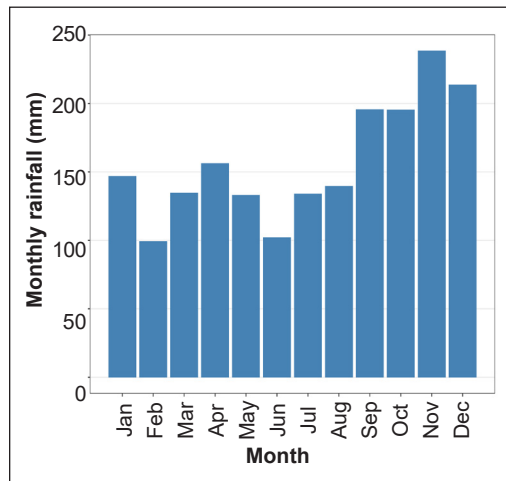


Figure 4. Monthly rainfall

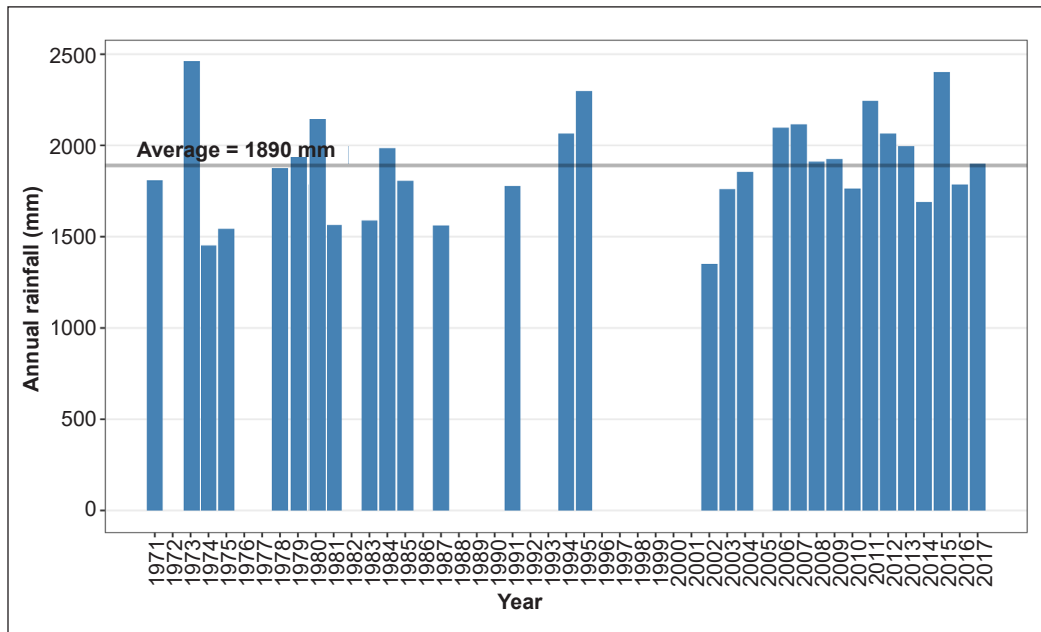


Figure 5. Annual rainfall

rainfall in the years 1976, 1977, 1982, 1986, 1988, 1989, 1990, 1992, 1993, 1996, 1997, 1998, 1999, 2000, 2001, and 2005 due to faulty of rain gauge and no rainfall during that time. Based on Figure 5, the average rainfall for 45 years of observation data was 1890 mm, and the lowest annual rainfall was in 2002, where the amount of rainfall was only 1350.3 mm per year, while the highest rainfall was in 1973, with the rainfall was 2455.2 mm per year.

The determination of the dependability of the water supply from the tank was based on the chosen parameters in which inflow, spillage, and outflow are calculated, which is crucial when working with discretized periods (Allen & Haarhoff, 2015). Therefore, it is required to channel the rainfall to the tank and concurrently withdraw the water needed to portray the rainwater tank accurately.

### Optimum Sizing of Tank

The outputs generated using the TN2 were Percentage tank volume, Water-Saving, and Storage Efficiency, Yield versus Spillage by Volume, and Yield versus Spillage by Day, which later can be applied to determine the optimum size of the tank.

**Percentage Tank Volume.** The sizing of the tank can be determined through the percentage tank volume of rainfall captured from the roof area flow to the rainwater harvesting system. The optimum size of the tank increases when the annual rainfall at that particular area is less than 2000 mm, while it remains nearly constant for the higher rainfall area. The proposed size for the rainwater storage tank for this study was 3 m<sup>3</sup> (256 L) according to the simulated result, as depicted in Figure 6. When the percentage of tank volume was 0% to 25%, the percentage of the time was 12.7%, and for 25% to 50%, the percentage of tank

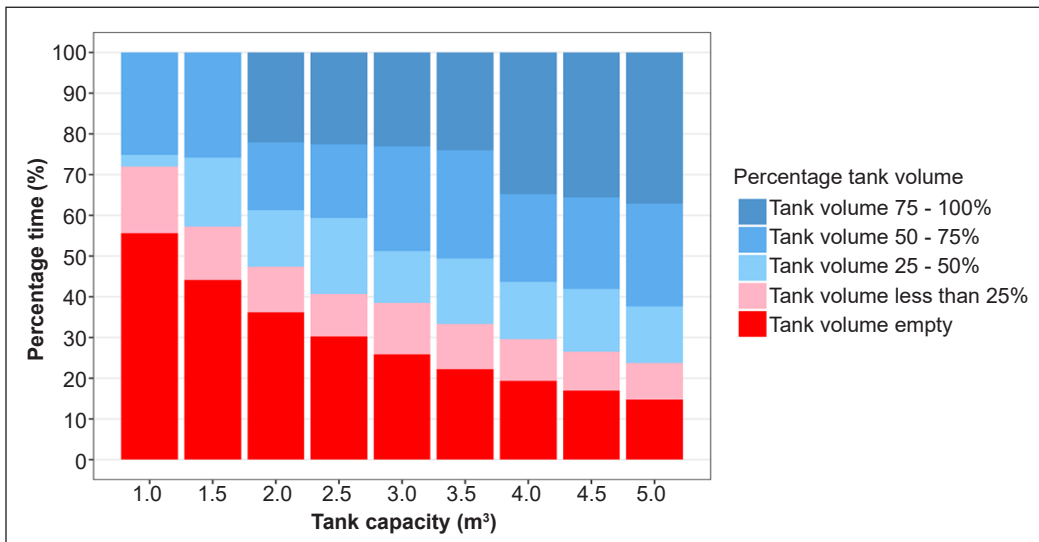


Figure 6. Percentages of tank volume

volume indicated the same percentage of time. Meanwhile, 50% to 75% of the tank volume obtained around 25.7% of the percentage time, and when the percentage volume of the tank reached 75% to 100%, it took 23% for the percentage of the time. In conclusion, the larger tank can store rainwater for a longer period compared to the smaller tank due to the small tank experiencing overflow when a larger volume of rainwater flows into the system.

**Water-Saving and Storage Efficiency.** Evaluation of the optimum size of the tank for the respective house was made according to the shape of water-saving and storage-efficiency curves. Figure 7 shows the shape of water-saving and storage-efficiency curves, and the results indicated a growth line between water-saving efficiency, storage efficiency, and tank capacity. When the water-saving and storage efficiency increased, the tank capacity also increased. Both efficiencies increase when the tank capacity is, at certain points, indicated by the marginal increase for the respective efficiencies (Daud et al., 2021; Goh & Ideris, 2021). For the proposed size tank capacity, which was 3 m<sup>3</sup>, the water-saving efficiency was 77.3%, and the storage efficiency was 31%. This finding was slightly lower compared to the study conducted by Goh and Ideris (2021), which indicated that a tank sized 3 m<sup>3</sup> and above was able to obtain more than 90% water-saving efficiency and 38% storage efficiency fulfilled by the harvested rainwater.

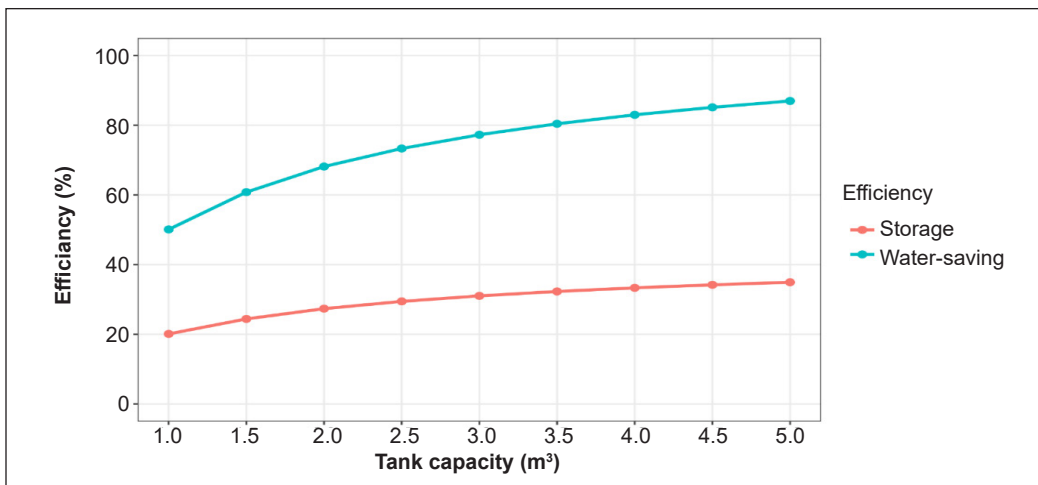


Figure 7. Water saving and storage efficiency

**Yield Versus Spillage by Volume and Yield Versus Spillage by Day.** TN2 implemented the yield principle after spillage, where the rainwater is added into the tank, and the spillage is immediately removed by limiting the tank volume (Khan et al., 2017). The data for yield versus spillage by volume for different tank capacities has been displayed in Figure 8. The result indicated contradictory results between the yield and the spill towards the tank capacity. When the tank capacity increased, the volume of yield increased as well;

however, as for spillage, the spill volume decreased when the tank capacity was increased. For tank size 3 m<sup>3</sup>, the volume for yield was 128.4 m<sup>3</sup>/year, and the volume for the spill was 285.6 m<sup>3</sup>/year. A higher volume of spillage was reported compared to the volume of yield, and this was due to the rainfall pattern, as shown previously in Figure 5, which is influenced by the inter-monsoon seasons (Bakar et al., 2020).

Figure 9 shows the result of yield versus spillage by day against tank capacity. The number of days for spillage and the number of days for yield that are able to fulfill the demand was calculated and averaged by year. The result displayed that the spillage decreased, but at the same time, the yield increased when the tank capacity was bigger. Based on the proposed tank sizing, which is 3 m<sup>3</sup>, the amount of spillage indicated 75.4 days per year; meanwhile, yield indicated 270.8 days per year. The capacity of the tank plays a big role because the capacity of the tank influences the water-saving efficiency and the volume of the water that can be stored. The 3 m<sup>3</sup> capacity of the tank has been proposed and is suitable for domestic usage because, from the obtained data, it can support the daily water demand for toilet flushing, general cleaning, and laundry. According to Campisano et al. (2017) and the Department of Statistics Malaysia (2014), around 5 toilet flushes per day per capita and 7 L per flush with an average of a resident of 4, the total water demand was around 140 L/day, and this can be up to 200 L/day when adding to the general cleaning and gardening (Goh & Ideris, 2021). Thus, installing this tank would reduce the usage of treated water and make the residence sustainable during the water disruption.

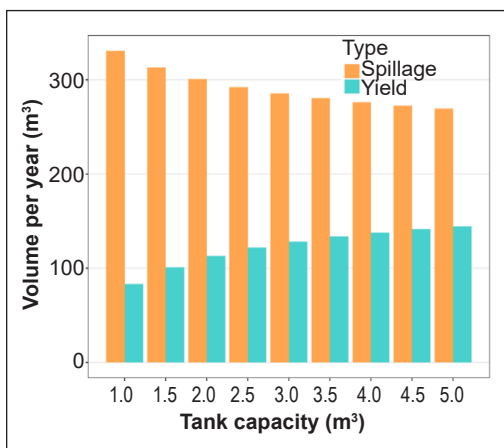


Figure 8. Yield versus spillage by volume

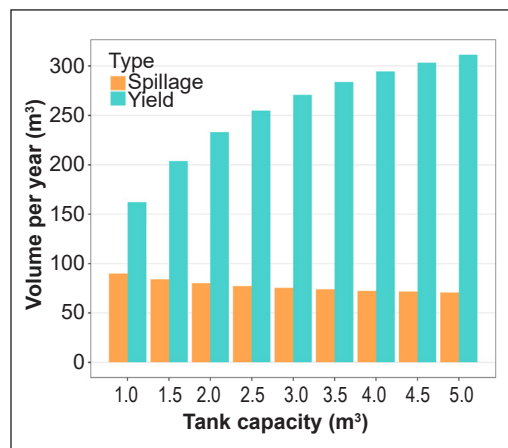


Figure 9. Yield versus spillage by day

## CONCLUSION

Analysis of RWH using the TN2 can calculate the efficiency of a range of tank sizes based on several inputs to determine the optimal tank size. The utilization of RWH can be a good choice due to the abundant source of rainfall, thus reducing water scarcity in Malaysia. From

the study, installing the RWH at a double-story house is suitable, and it can be concluded that water saving is also efficient when the tank sizes increase. Besides, the larger the size of tanks would be, the longer the period can store the rainwater. The optimum tank size for a double-story residential house is 3 m<sup>3</sup>, considering all the activities that may contribute to water usage. Furthermore, to encourage the installation of RWH among residents in Malaysia, an awareness program on the advantages of using the RWH, such as being able to reduce the monthly water bill and good incentives from the government, can be implemented. Future studies on the application of rainwater harvesting among commercial and educational premises can be ventured.

## ACKNOWLEDGEMENTS

The authors express their gratitude to those involved directly and indirectly in this study. This research received no specific grant from any funding agency in the public, commercial, or not-for-profit sectors.

## REFERENCES

- Allen, J., & Haarhoff, J. (2015). A proposal for the probabilistic sizing of rainwater tanks for constant demand. *Journal of the South African Institution of Civil Engineering*, 57(2), 22-27. <https://doi.org/10.17159/23098775/2015/v57n2a3>
- Bakar, M. A. A., Ariff, N. M., Jemain, A. A., & Nadzir, M. S. M. (2020). Cluster analysis of hourly rainfalls using storm indices in Peninsular Malaysia. *Journal of Hydrologic Engineering*, 25(7), 1-11. [https://doi.org/10.1061/\(ASCE\)HE.1943-5584.0001942](https://doi.org/10.1061/(ASCE)HE.1943-5584.0001942)
- Boretti, A., & Rosa, L. (2019). *Water demand by 2050*. Reassessing the Projections of the World Water Development Report. <https://www.nature.com/articles/s41545-019-0039-9>
- Campisano, A., Butler, D., Ward, S., Burns, M. J., Friedler, E., DeBusk, K., Fisher-Jeffes, L. N., Ghisi, E., Rahman, A., Furumai, H., & Han, M. (2017). Urban rainwater harvesting systems: research, implementation and future perspectives. *Water Research*, 115, 195-209.
- Chang, W., Cheng, J., Allaire, J. J., Xie, Y., & McPherson, J. (2019). *Shiny: Web Application Framework for R*. <https://CRAN.R-project.org/package=shiny>
- Daud, N. M., Mahiran, N. N., Ruslan, A. K., Hamzah, N., Bakar, A. A. A., Badrealam, S., Manan, E. A., & Hamzah, A. F. (2021). Effect of roof size on the rainwater harvesting tank sizes and performances using Tangki NAHRIM 2.0. In *IOP Conference Series: Earth and Environmental Science* (Vol. 920, No. 1, p. 012035). IOP Publishing. <https://doi.org/10.1088/1755-1315/920/1/012035>
- Department of Statistics Malaysia. (2014). *Characteristics of Household 2010*. <https://www.mycensus.gov.my/index.php/census-product/publication/census-2010/685-characteristic-of-household-2010>
- Goh, Y. C., & Ideris, M. (2021). Tangki NAHRIM 2.0: An R-based water balance model for rainwater harvesting tank sizing application. *Water Practice & Technology*, 16(1), 182-195. <https://doi.org/10.2166/wpt.2020.106>

- Hajani, E., & Rahman, A. (2014). Reliability and cost analysis of a rainwater harvesting system in peri-urban regions of Greater Sydney, Australia. *Water*, 6(4), 945-960. <https://doi.org/10.3390/w6040945>
- Jenkins, D., Pearson, F., Moore, E., Kim, S. J., & Valentine, R. (1978). *Feasibility of rainwater collection systems in California* [Final Technical Report]. Water Resources Centre, University of California. <https://ntrl.ntis.gov/NTRL/dashboard/searchResults/titleDetail/PB288378.xhtml>
- Khan, S. T., Baksh, A. A., Papon, M. T. I., & Ali, M. A. (2017). Rainwater harvesting system: An approach for optimum tank size design and assessment of efficiency. *International Journal of Environmental Science and Development*, 8(1), 37-43 <https://doi.org/10.18178/ijesd.2017.8.1.917>
- Kummu, M., Guillaume, J. H. A., de Moel, H., Eisner, S., Flörke, M., Porkka, M., Siebert, S., Veldkamp, T. I. E., & Ward, P. J. (2016). The world's road to water scarcity: Shortage and stress in the 20th century and pathways towards sustainability. *Scientific Reports*, 6(1), Article 38495. <https://doi.org/10.1038/srep38495>
- Lani, N. H. M., Yusop, Z., & Syafuddin, A. (2018). A review of rainwater harvesting in Malaysia: Prospects and challenges. *Water*, 10(4), Article 506. <https://doi.org/10.3390/w10040506>
- Liaw, C. H., & Tsai, Y. L. (2004). Optimum storage volume of rooftop rainwater harvesting systems for domestic use. *Journal of the American Water Resources Association*, 40(4), 901-912. <https://doi.org/10.1111/j.1752-1688.2004.tb01054.x>
- Mitchell, V. G. (2007). How important is the selection of computational analysis method to the accuracy of rainwater tank behaviour modelling? *Hydrological Processes: An International Journal*, 21(21), 2850-2861. <https://doi.org/10.1002/hyp.6499>
- Nandargi, S., & Mulye, S. S. (2012). Relationships between rainy days, mean daily intensity, and seasonal rainfall over the Koyna catchment during 1961–2005. *The Scientific World Journal*, 2012, 1-10. <https://doi.org/10.1100/2012/894313>
- Nguyen, V. M., Icikawa, Y., & Ishidaira, H. (2018). Exploring optimal tank size for rainwater harvesting systems in Asian tropical climates. *Hydrological Research Letters*, 12(1), 1-6. <https://doi.org/10.3178/hrl.12.1>
- R Core Team. (2013). *R: A language and environment for statistical computing*. R Foundation for Statistical Computing, Vienna, Austria. <http://www.R-project.org/>
- Rahman, H. (2014). Water shortage in Malaysia: Again? *International Journal of Recent Trends in Engineering and Research*, 4(1), 319-322. <https://doi.org/10.23883/ijrter.2018.4038.8jr8f>
- Struck, S. (2011). *Rainwater Harvesting for Non-potable Use and Evidence of Risk Posed to Human Health Background: General Hazards found in Rainwater*. [https://www.ccnc.ca/sites/default/files/BCCDC-Rainwater\\_Harvesting\\_Oct\\_2011.pdf](https://www.ccnc.ca/sites/default/files/BCCDC-Rainwater_Harvesting_Oct_2011.pdf)
- UN Report. (2018). *UN World Water Development Report*. <https://www.unwater.org/publications/world-water-development-report-2018>

## Measuring Vulnerability Assessment Tools' Performance on the University Web Application

Pita Jarupunphol, Suppachochai Seatun and Wipawan Buathong\*

*Department of Digital Technology, Phuket Rajabhat University, 83000, Phuket, Thailand*

### ABSTRACT

This research measured vulnerability assessment tools' performance on a university web application, including Burp Suite and OWASP ZAP. There are three measurement criteria: (1) the number of vulnerabilities classified under risk and confidence metrics, (2) the number of vulnerability types and URL alerts classified under risk and confidence metrics, and (3) the number of vulnerabilities classified in the 2021 OWASP Top 10 vulnerabilities. Results showed that Burp Suite detected more vulnerabilities and alerts than OWASP ZAP, with a higher proportion of high-risk vulnerabilities. However, OWASP ZAP had a higher proportion of medium-confidence vulnerabilities. The comparison also revealed that the vulnerabilities identified by both tools were ranked differently within the OWASP Top 10, and there were variations in risk prioritisation between the tools. Despite these differences, the vulnerability assessment results obtained from these tools are still helpful for the university's security analysts and administration, as mitigating cyber threats to the web application is paramount.

*Keywords:* Cybersecurity, cyber threats, risks, vulnerability assessment, web application

### ARTICLE INFO

*Article history:*

Received: 19 October 2022

Accepted: 06 March 2023

Published: 03 October 2023

DOI: <https://doi.org/10.47836/pjst.31.6.19>

*E-mail addresses:*

[p.jarupunphol@pkru.ac.th](mailto:p.jarupunphol@pkru.ac.th) (Pita Jarupunphol)

[s6281423108@pkru.ac.th](mailto:s6281423108@pkru.ac.th) (Suppachochai Seatun)

[w.buathong@pkru.ac.th](mailto:w.buathong@pkru.ac.th) (Wipawan Buathong)

\* Corresponding author

### INTRODUCTION

During the COVID-19 pandemic, most academic Institutions must transform their teaching and learning methods to 100% online. These online teaching and learning methods rely on efficient Internet and network systems to fulfil learning activities, such as learning via online meeting applications, sending and storing teaching materials, submitting assignments, and taking online examinations. In the

meantime, academic institutions have become more vulnerable to cyber threats evolving together with the advancement of Internet technologies. Schools and colleges worldwide are targeted by cyber threats, e.g., abusive content, denial of service (DoS), fraud or deception, information gathering, intrusion attempts, unauthorised access, alteration of important information, and malicious code (Alexei & Alexei, 2021; Pavlova, 2020). As a result, academic institutions must take steps to prevent and mitigate potential risks of cyber threats.

Vulnerability assessment and penetration testing are two different security assessment techniques, but they are crucial in web application vulnerability assessment due to the increasing cyber threats (Darus et al., 2020; Disawal & Suman, 2021; Malekar & Ghode, 2020; Nagpure & Kurkure, 2017). While web application vulnerability assessment is related to flaw detection and analysis and alerts organisations about vulnerable components in the web application, penetration testing is about vulnerability exploitation attempts to determine the feasibility of cyber threats that can affect organisations. Today, various vulnerability assessment tools are available to detect and analyse potential risks associated with web applications. Utilising vulnerability assessment tools may not comprehensively identify vulnerabilities and may produce false positives (FPs). Furthermore, various tools exhibit variability in the vulnerabilities and false positives they report, with some overlap (Alsaleh et al., 2017; Mburano & Si, 2018). These vulnerability assessment tools are varied from proprietary to open-source, which can detect, analyse, and report website vulnerabilities. In addition, the web vulnerability assessment tools provide detailed reports for system administrators to detect and address security issues before any threats occur, according to Khera et al. (2019). However, comparing web vulnerability assessment tools is still inadequate in the literature (Mburano & Si, 2018).

According to cyber threat statistics in 2021 reported by the Thai Computer Emergency Response Team (<https://www.etcha.or.th/th/Our-Service/thaicert/stat.aspx>), there were 939 intrusion attempts, 841 frauds, 570 intrusions, 540 availability, and 271 malicious codes. The results differ from the statistics of the same threats in 2020, in which there were 145 intrusion attempts, 576 frauds, 173 intrusions, 101 availability, and 687 malicious codes. Since the nature of these cyber attacks on public and private organisations may not differ from that on academic sectors, academic institution web applications in Thailand are also vulnerable to cyber threats. This article conducts a web application vulnerability assessment of a university in the south of Thailand using a proprietary tool 'Burp Suite' and an open-source tool 'OWASP ZAP' based on the hypotheses: (1) the university's web application contains high-risk vulnerabilities that might be susceptible to cyber threats, (2) proprietary and open-source tools provide different vulnerability assessment results but are helpful for threat mitigation, and (3) vulnerabilities identified from both tools can be classified into the 2021 OWASP Top 10 (<https://owasp.org/Top10/>) vulnerabilities.



## LITERATURE REVIEW

### Cyber Threats in Education

Malekar and Ghode (2020) state that web applications are vulnerable to complex cyber threats. Academic institutions have become an attractive target for cyber-attacks because of several factors. For example, most academic institutions do not invest in information security infrastructure due to limited budgets from the government. Therefore, outdated information systems can be an easy target for attackers. Furthermore, most academic institutions have online databases that collect and store student and staff information varying from personal to financial information (Ulven & Wangen, 2021). Recently, there have been several security incidents in academic sectors. As a result, many schools and colleges have become victims of cyber threats (Naagas et al., 2018; Rahamathullah & Karthikeyan, 2021). For example, an increase in DDoS primarily targets educational institution information systems (Rahamathullah & Karthikeyan, 2021).

Moreover, ransomware attacks can have severe consequences for academic institution operations due to taking much time to restore critical services. The past academic semesters were impacted by ransomware, causing the loss of students' personal information, the institution's financial history, and related information. For instance, the ransomware incident at the University of Northumbria in England, where attackers ransomed the university information system, ceased the university's internal information systems for several weeks (Muncaster, 2020). In addition, ransomware attacks on US schools in 2020 resulted in more than \$6 billion in damages from 77 attacks reported by US educational institutions nationwide (Muncaster, 2021).

### Vulnerability Assessment

Vulnerability assessment includes techniques and tools to identify information system vulnerabilities and determine the risk of vulnerabilities and the risk assessment objective (Abdullah, 2020; Malekar & Ghode, 2020). Vulnerability assessment has been applied to different aspects of digital technology. For instance, network security assessment involves evaluating an organisational network infrastructure to identify vulnerabilities in public and private networks that may be exposed to threats (McNab, 2016). This assessment checks for vulnerabilities that may interrupt or affect the availability of network services and ports open to access under the host. Similarly, web application vulnerability assessment evaluates potential cyber threats to an online information system that numerous organisations use communication and public relations tools and online services. Since the web application nature is open to users at all times, attackers can take this opportunity to exploit several web application vulnerabilities (Amankwah, Chen, Kudjo et al., 2020). These vulnerabilities can pose security threats to the organisational assets. The vulnerability assessment can help

maintain web application security aspects such as confidentiality, integrity, and availability and mitigate threats by reducing risks arising from the system. In addition, vulnerability assessment can prioritise the most severe vulnerabilities to avoid exploitation (Vibhandik & Bose, 2015).

### **Web Application Vulnerability Assessment Tools**

Web application vulnerability assessment tools are available in proprietary and open-source software that can automate the vulnerability testing process and operate on different operating systems (Diogenes & Ozkaya, 2018). Performing vulnerability assessment can be manual or automatic. However, most vulnerability assessment tools can automatically scan and analyse vulnerabilities and provide detailed reports to help address vulnerabilities that cyber threats can potentially exploit. In addition, the tools collect details about vulnerabilities in their web databases, facilitating further actions for vulnerability assessment. Most web application vulnerability assessment tools collect information within the web application and scan for vulnerabilities that may be exploited within the web application. Once the tool completes all operations, the same procedures will be repeated to increase the accuracy of randomisation of attacks on web applications.

In particular, the proxy is an integral part of web vulnerability assessment tools, allowing the tools to access web applications. For example, Burp Suite, developed by PortSwigger Co., Ltd., is one of the most widely used proprietary web vulnerability assessment tools (Wear, 2018). Acunetix is another proprietary vulnerability assessment tool with advanced crawling technology to search for vulnerabilities in web applications (Ibrahim & Kant, 2018). On the other hand, OWASP ZAP (<https://www.zaproxy.org/>) is an open-source web vulnerability assessment tool developed by the Open Web Application Security Foundation (OWASP), a non-profit foundation working on several web security improvement projects. OWASP is widely recognised for its OWASP Top 10 vulnerabilities ranking. For example, SQL Injection, Cross-Site Scripting (XSS), and Cross-Site Request Forgery (CSRF) are well-known web vulnerabilities in the 2021 OWASP Top 10.

### **Vulnerability Assessment Criteria**

Vulnerability assessment covers several criteria to analyse, classify and prioritise vulnerabilities.

**Risk Levels.** Most vulnerability assessment tools classify vulnerabilities into high-risk, medium-risk, and low-risk (Popov et al., 2016). For example, in information security, high risk refers to vulnerabilities that might expose high levels of threats that can affect security requirements in terms of confidentiality, integrity and availability, making the information system unable to operate. This type of risk requires time and a high level of competence

to address issues and bring the information system back to normal. On the other hand, medium risk refers to vulnerabilities that might expose moderate threats affecting some parts of the information security services, such as confidentiality, integrity, and availability. For example, there may be a partial shutdown to repair security issues requiring time and ability to recover, wherein the information system can continue.

Besides, low risk refers to vulnerabilities that expose low-level threats that might affect minimal parts of the system regarding confidentiality, integrity, and availability but without the extended time and the ability to perform corrective actions. As a result, the information system can continue to operate normally. In some vulnerability risk assessments, however, the risk levels can be further extended to ‘critical,’ which is more severe than the high level. In addition, some vulnerabilities cannot be categorised into these risk levels but are unignorable. For example, informational risk refers to vulnerabilities not susceptible to high, medium, or low-level threats without directly affecting the information system. However, the attacker may exploit these informational-level vulnerabilities to attack the system.

**Confidence Levels.** Web application vulnerability assessment tools also provide confidence levels to confirm the identified risk level. These confidence levels are also classified into different degrees, e.g., high, medium, low, certain, firm, and tentative. These confidence levels help security administrators determine and prioritise vulnerabilities categorised into risk levels. In this case, the confidence is comparable to likelihood, a significant indicator for risk identification.

**The OWASP Top 10 Web Application Security Risks.** In addition to the above criteria, the OWASP Top 10 Web Application Security Risks or the OWASP Top 10 vulnerabilities have been web vulnerability assessment criteria widely acknowledged by researchers and practitioners. The OWASP Top 10 ranks vulnerabilities according to severe web application security risk levels. There have been different versions of the OWASP Top 10. Several web vulnerability research articles have widely discussed the 2017 OWASP Top 10 ([https://owasp.org/www-project-top-ten/2017/Top\\_10](https://owasp.org/www-project-top-ten/2017/Top_10)). Nevertheless, the 2021 OWASP Top 10, a recently updated version, is still unfamiliar in web application vulnerability research. While the 2017 OWASP Top 10 vulnerabilities were selected based on the likelihood, impact, and exploitability determined by experts, the 2021 OWASP Top 10 vulnerabilities were ranked using the same criteria but based on the use of data, if possible.

Significant vulnerability positions and names change from the 2017 OWASP Top 10 to the 2021 OWASP Top 10 (e.g., sensitive data exposure to cryptographic failures). Furthermore, several vulnerability criteria in the 2017 OWASP Top 10 are amalgamated into a new vulnerability type. For example, XML external entities (XXE) are amalgamated with security misconfiguration in the 2017 OWASP Top 10 to only security misconfiguration

in the 2021 OWASP Top 10. There are three new vulnerability categories in the 2021 OWASP Top 10: insecure design, software and data integrity failures, and Server-Side Request Forgery (SSRF).

## Related Works

Several research works have been on different web vulnerability assessment perspectives (Abdullah, 2020; Alsaleh et al., 2017; Darus & Awang, 2020; Disawal & Suman, 2021; Karumba et al., 2016). For example, Khalid et al. (2019) proposed a method to predict legitimate or vulnerable code based on six classifiers on a training set consisting of software metrics and text features. The experiment was conducted on three web applications in which 223 vulnerabilities were identified in PHPMyAdmin, Moodle and Drupal. In addition, Darus and Awang (2020) proposed a web assessment tool, 'SNEAKERZ', that automatically detected and analysed vulnerabilities that may arise from the security loophole in web applications based on three software vulnerability categories, including software defects, software bugs, and software errors. The authors asserted that SNEAKERZ could list web vulnerabilities and propose solutions to address the vulnerabilities. In Disawal and Suman (2021), different vulnerabilities were discovered during the web application development process, and a web application vulnerability assessment should be conducted during the web application development to identify factors affecting the web application security, such as weakness, countermeasure, confidentiality impact, access complexity, and severity level. Amankwah, Chen, Kudjo, and Towey (2020) compared the performance of eight web vulnerability assessment tools, including Acunetix, HP WebInspect, IBM AppScan, OWASP ZAP, Skipfish, Arachni, Vega, and Iron Wasp, using two vulnerable web applications. The evaluation was based on multiple evaluation metrics. The results show that commercial and open-source vulnerability assessment tools effectively detect vulnerability.

Several research scholars evaluate the performance of open-source web vulnerability assessment tools (Abdullah, 2020; Alsaleh et al., 2017; Amankwah, Chen, Kudjo, & Towey 2020; Karumba et al., 2016; Mburano & Si, 2018). For example, Karumba et al. (2016) introduced a hybrid algorithm for detecting web application vulnerabilities and compared its performance with other open-source vulnerability scanners. The comparison comprises three metrics: time taken to scan, detection accuracy and consistency. In Abdullah (2020), two open-source web application vulnerability scanners, including Paros and OWASP ZAP, were experimented with for checking vulnerabilities in two vulnerable web applications. The author suggested that the vulnerability assessment tools must constantly be updated to support the discovery of new vulnerabilities that may open up an opportunity for cyber threats. Furthermore, Alsaleh et al. (2017) evaluate the detection performance of two open-source web vulnerability scanners from different perspectives. While the results could

not indicate significant differences between the two scanners, there were differences and inconsistencies between the scanner reports.

Several works on web vulnerability assessment propose tools and techniques to measure vulnerabilities against the 2017 OWASP Top 10 (Amankwah, Chen, Kudjo, & Towey 2020; Khera et al., 2019; Mburano & Si, 2018; Nagpure & Kurkure, 2017; Vibhandik & Bose, 2015). For example, a web vulnerability assessment approach based on a combination of W3AF and Nikto tools was introduced to address security issues in Vibhandik and Bose (2015). The vulnerability assessment performance was measured against the 2017 OWASP Top 10. The authors asserted that combining W3AF and Nikto tools is more effective in detecting vulnerabilities in web applications since a single tool is inadequate to detect different vulnerability types. In addition, the combination can help narrow the scope of security vulnerability detection for complex web applications and servers.

Moreover, Khera et al. (2019) assessed a website's vulnerability in India by applying the 2017 OWASP Top 10 criteria to determine the risk of corporate website threats. Various tools such as Wire shark, Nmap, Metasploit, and Air crack were utilised to assess network security. In the experiment, the attacker can access files within the server by exploiting open ports unrelated to the website's specific operations. Likewise, Nagpure and Kurkure (2017) assessed website vulnerabilities and compared the performance of different tools based on the 2017 OWASP Top 10 criteria, including Burp Suite, OWASP ZAP and Acunetix, according to the tool capabilities in both manual and automation testing methods. High volume and low complexity vulnerability detection and automation testing provide accurate and efficient results. In addition, Amankwah, Chen, Kudjo and Towey (2020) performed a web application vulnerability assessment using open-source software against the 2017 OWASP Top 10 and prioritised vulnerabilities according to severity. The effectiveness of open-source web vulnerability scanners was measured against the 2017 OWASP Top 10 in Mburano and Si (2018). The results were compared further with those from the Web Application Vulnerability Security Evaluation Project (WAVSEP) benchmark.

## **METHODOLOGY**

There are four methodological steps to achieve the research objectives. Figure 1 shows methodological steps in the university's web application vulnerability assessment.

### **Research Scope Identification**

The researchers determined the scope of the university's primary web applications and contacted the person who could authorise the vulnerability assessment. The permission request letter was sent to the university's president, who authorised the university's information technology centre (ITC) director to provide resources as requested for the

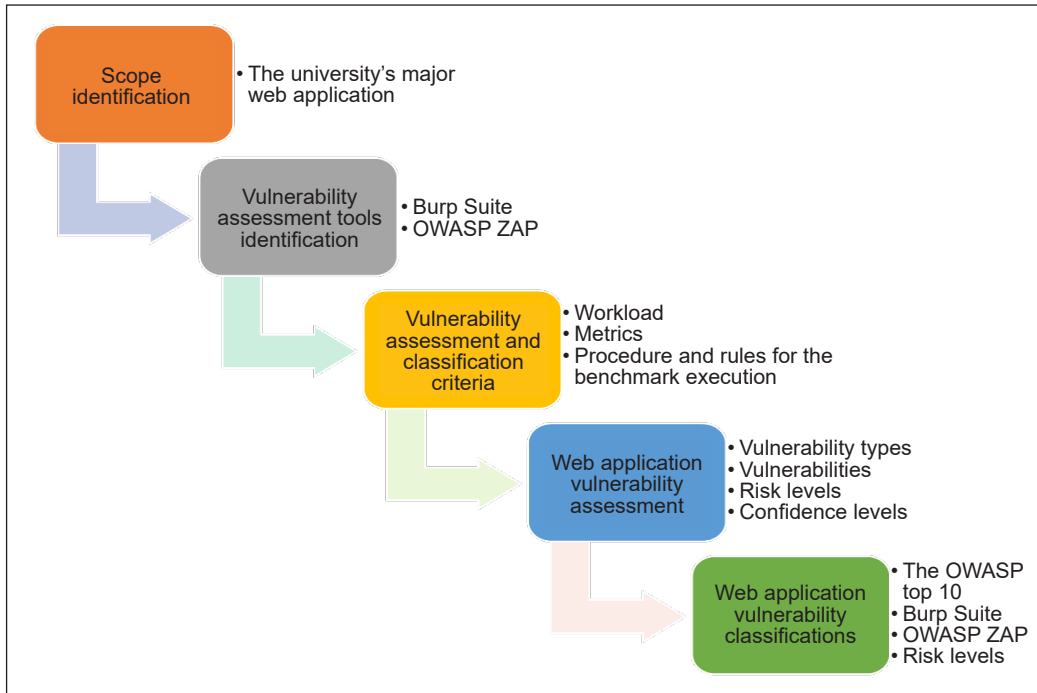


Figure 1. Web application vulnerability assessment methodology

vulnerability assessment. The experiment duration was between January 1, 2022, and February 28, 2022. The experiment was conducted on a system simulated from the university's existing web application to avoid affecting the existing web application and preventing legal offences, according to Thai Netizen Network (2017) and ETDA (2022).

The vulnerability assessment target is one of the university's major web applications storing staff and student personal data. The experiment was conducted on a simulated system to prevent potential issues from the vulnerability assessment in a permitted testing area to search for existing vulnerabilities that may be exposed to cyber threats. The web browser proxy is configured to support the assessment. In addition, boundaries are set within the vulnerability testing program to prevent the program from interfering with other web applications.

### Vulnerability Assessment Tools Identification

After identifying the assessment scope, Burp Suite and OWASP ZAP are two vulnerability assessment tools selected for the experiment. The researchers selected these two web vulnerability assessment tools because one is a widely used proprietary software and another is popular open-source software. In addition, these tools similarly classify vulnerabilities into four risk levels: high, medium, low, and informational. The tools also provide confidence levels to support the risk level reliability. While Burp Suite confidence levels

include certain, firm, and tentative, OWASP ZAP confidence levels are high, medium, and low. However, OWASP ZAP also adds ‘user confirmed’, another confidence level in which users manually confirm vulnerabilities.

### **Vulnerability Assessment and Classification Criteria**

To perform a vulnerability assessment and classification, workload, metrics procedures and rules for the benchmark execution are required as the criteria allow the assessment to be consistent and measurable for identifying and evaluating vulnerabilities (Nunes et al., 2018).

1. Workload is the set of tasks or operations used to evaluate the performance of the system or process, e.g., data processing, database queries, network communication, or other system operations. The university’s web application utilises PHP programming language supported by the MySQL database. The application comprises a total of 8,059 files organised within 773 folders. The overall size of the application is 765 MB. However, the quantity of LOC (Lines of Code) for a given file size and number can fluctuate significantly based on several factors (e.g., the programming language, the intricacy of the code, and the use of libraries and data files).
2. Metrics are the measures used to quantify a system’s or process’s performance, e.g., response time, throughput, CPU utilisation, memory usage, and other performance characteristics. Our vulnerability assessment and classification metrics are the number and percentage of vulnerabilities classified into risk and confidence levels. These metrics can help us prioritise which vulnerabilities need to be addressed and what level of effort should be put into mitigating them.
3. Procedures and rules are the steps for conducting a benchmarking study, e.g., setting up the test environment, configuring the system or process being tested, running the workload, collecting performance data, and analysing the data. Since vulnerability assessment and classification is a process that involves identifying, categorising, and prioritising vulnerabilities, the procedures include both an automatic process, performed by a system such as Burp Suite and OWASP ZAP, and a manual process, performed by a human. In this process, the vulnerabilities reported by the automatic tools are first collected and consolidated. Then, the reported vulnerabilities are manually compared regarding their risk and confidence levels. Please note that vulnerabilities reported by the automatic tools must be triaged and prioritised by a human, helping the organisation focus on the most critical vulnerabilities. When such vulnerabilities identified by both tools must be categorised into the OWASP Top 10, they are manually performed via a repository of vulnerabilities linking to the OWASP Top 10.

## **Web Application Vulnerability Assessment**

Burp Suite and OWASP ZAP were experimented with, and compared their vulnerability assessment performances. This step is critical to test the hypothesis that the university's web application is vulnerable to potential cyber threats and compare the performance of web vulnerability assessment tools. The vulnerability assessment of Burp Suite and OWASP ZAP was conducted utilising a computer system equipped with an Intel(R) Core(TM) i7-10510U CPU, clocked at 2.30 GHz and 16 GB of RAM, running the Windows 10 Pro operating system. The Burpsuite tool typically requires 4 hours to complete a vulnerability assessment, with an average of 10-13 crashes occurring during each assessment. In contrast, the Owasp ZAP tool can complete a vulnerability assessment in approximately 2 hours, with a lower frequency of crashes, averaging 6-8 instances per assessment.

The scanning process of each tool repeats at least three times to ensure that the vulnerability assessment results remain stable. After that, the performance of the two tools in vulnerability assessment will be compared. The reported vulnerabilities are compared at this stage to find similarities and differences. The comparison results at this stage will illustrate how many vulnerabilities are classified into high, medium, and low and what types of vulnerability are discovered.

## **Web Application Vulnerability Classifications**

The vulnerabilities discovered by Burp Suite and OWASP Zap were further classified into the 2021 OWASP Top 10 criteria. First, the vulnerability reports from the two vulnerability assessment tools will be deliberately checked for essential components in the reports. In particular, most web vulnerability reports contain CWE IDs, identifiers referring to vulnerabilities listed by Common Weakness Enumeration (CWE), a widely recognised community listing software and hardware vulnerabilities and their ramifications. For example, CWE-89 means improper neutralisation of special elements used in an SQL Command or 'SQL Injection.' Then, the OWASP Top 10 criteria, their definitions and CWE IDs will also be examined. This step investigates how many university web application vulnerabilities can be categorised in the OWASP Top 10. After that, the classified vulnerabilities between the two tools will be compared.

## **RESULTS**

There are differences in vulnerability assessment performances between Burp Suite and OWASP ZAP.

### **Risk and Confidence Levels**

Burp Suite and OWASP ZAP provide comprehensive reports of vulnerability assessment in which detected vulnerabilities are ranked in risk and confidence metrics. The report,



generated by Burp Suite and depicted in Table 1, presents a university web application’s overall vulnerability risk assessment. The assessment revealed 203 vulnerabilities, classified into four categories: high, medium, low, and informational. Additionally, the report indicated three confidence levels in the identified vulnerabilities: certain, firm, and tentative. Five vulnerabilities are at high risk, four at certain confidence and one at firm confidence. In addition, 130 information-level vulnerabilities are at a certain confidence level.

A report was generated utilising OWASP ZAP (Table 2), encompassing 22 vulnerabilities classified into high, medium, low, and informational severity categories. Additionally, the report includes four levels of confidence, specifically user confirmed, high, medium, and low. There is one vulnerability at high risk with medium confidence. In addition, there are 11 vulnerabilities at medium risk with different confidence levels, including two high, seven medium, and two low.

Table 1  
*Burp Suite vulnerability risk assessment report*

		Confidence			
		Certain	Firm	Tentative	Total
Severity	High	4 (2.0%)	1 (0.5%)	0 (0.0%)	5 (2.5%)
	Medium	0 (0.0%)	4 (2.0%)	3 (1.5%)	7 (3.5%)
	Low	3 (1.5%)	2 (1.0%)	8 (3.9%)	13 (6.4%)
	Information	130 (64.0%)	39 (19.2%)	9 (4.4%)	178 (87.6%)
Total		137 (67.5%)	46 (22.7%)	20 (9.8%)	203 (100.0%)

Table 2  
*OWASP ZAP vulnerability risk assessment report*

		Confidence				
		User Confirmed	High	Medium	Low	Total
Risk	High	0 (0.0%)	0 (0.0%)	1 (4.5%)	0 (0.0%)	1 (4.5%)
	Medium	0 (0.0%)	2 (9.1%)	7 (31.8%)	2 (9.1%)	11 (50.0%)
	Low	0 (0.0%)	1 (4.5%)	3 (13.6%)	1 (4.5%)	5 (22.7%)
	Informational	0 (0.0%)	1 (4.5%)	3 (13.6%)	1 (4.5%)	5 (22.7%)
Total		0 (0.0%)	4 (18.2%)	14 (63.6%)	4 (18.2%)	22 (100.0%)

Both tools generate vulnerability assessment reports that display risk and confidence levels of vulnerabilities. While Burp Suite's report includes the total of each vulnerability risk level, OWASP ZAP's report presents a summary of risk and confidence levels. Additionally, both tools express identified risk and confidence levels in percentages. In this case, the vulnerability risk and confidence levels reported by Burp Suite and OWASP ZAP are summarised in Table 3.

Table 3  
*A summary of the vulnerability risk and confidence levels determined by Burp Suite and OWASP ZAP*

No.	Risk	Confidence	Burp Suite	(%)	OWASP ZAP	(%)
1	High	High	4	2.0	0	0.0
2	High	Medium	1	0.5	1	4.5
3	High	Low	0	0.0	0	0.0
4	Medium	High	0	0.0	2	9.1
5	Medium	Medium	4	2.0	7	31.9
6	Medium	Low	3	1.5	2	9.1
7	Low	High	3	1.5	1	4.5
8	Low	Medium	2	1.0	3	13.7
9	Low	Low	8	3.9	1	4.5
10	Information	High	130	64.0	1	4.5
11	Information	Medium	39	19.2	3	13.7
12	Information	Low	9	4.4	1	4.5
<b>Total</b>			<b>203</b>	<b>100.0</b>	<b>22</b>	<b>100.0</b>

### Vulnerabilities, URL Alerts, and Risk and Confidence Levels

Table 4 shows a report from Burp Suite, which shows the level of threats categorised from High, Medium, Low, and Information levels, along with the number of vulnerabilities discovered. The results also reveal vulnerabilities in different categories.

URLs. As indicated in Table 4, the Burp Suite vulnerability assessment identified 23 distinct vulnerabilities from No.1 to No.23 and generated 203 alerts of URLs. Five vulnerabilities, including No. 1 'SQL Injection' with three alerts and No. 2 'Cleartext Submission of Password' with two alerts, receive high risk and a certain confidence. Three vulnerabilities with 16 alerts are categorised as medium risk, and most confidence is tentative. However, it is essential to note that the vulnerabilities enumerated from No. 12 through No. 23 pertain to informational risks, with a level of confidence ranging from tentative to certain.

A report from OWASP ZAP (Table 5) shows the risk levels categorised into high, medium, low, and informational and the number of vulnerabilities discovered. The results also reveal vulnerabilities in different categories with vulnerable URL alerts. For example, while OWASP ZAP identified 22 vulnerabilities from No.1 to No.22 with 792 URL alerts,

‘Cross-Site Scripting’ (No.1) is the only vulnerability at high risk with two alerts. There are 11 vulnerabilities at medium risk, with the confidence level from low to high. However, informational risk vulnerabilities receive the highest alerts. In particular, 170 alerts for ‘Cookie Slack Detector’ (No.18) and 354 for ‘User Agent Fuzzer’ (No.22).

Table 4  
*Burp Suite URL alerts report*

No.	Burp Suite	Alerts	(%)	Risk	Confidence
1	SQL Injection	3	1.5	High	Certain
2	Cleartext Submission of Password	2	1.0	High	Certain
3	Cross-Site Request Forgery	11	5.4	Medium	Tentative
4	Password Returned in Later Response	1	0.5	Medium	Tentative
5	Session Token in URL	4	2.0	Medium	Firm
6	Vulnerable JavaScript Dependency	7	3.4	Low	Tentative
7	Cookie without HTTP Only Flag Set	1	0.5	Low	Firm
8	Password Field with Autocomplete Enabled	2	1.0	Low	Certain
9	Client-Side HTTP Parameter Pollution (Reflected)	1	0.5	Low	Firm
10	Source Code Disclosure	1	0.5	Low	Tentative
11	Unencrypted Communications	1	0.5	Low	Certain
12	Path-Relative Style Sheet Import	19	9.4	Informational	Firm
13	User Agent-Dependent Response	1	0.5	Informational	Firm
14	Long Redirection Response	6	3.0	Informational	Firm
15	Input Returned in Response (Reflected)	106	52.1	Informational	Certain
16	Cross-Domain Referrer Leakage	4	2.0	Informational	Certain
17	Cross-Domain Script Include	6	3.0	Informational	Certain
18	Frameable Response (Potential Clickjacking)	5	2.5	Informational	Firm
19	HTTP TRACE Method is Enabled	1	0.5	Informational	Certain
20	Backup File	2	1.0	Informational	Certain
21	Email Addresses Disclosed	8	3.9	Informational	Certain
22	Base64-Encoded Data in Parameter	8	3.9	Informational	Firm
23	HTML Does Not Specify Charset	3	1.5	Informational	Certain
<b>Total</b>		<b>203</b>	<b>100.0</b>		

Table 5  
*OWASP ZAP URL alerts report*

No.	OWASP ZAP	Alerts	(%)	Risk	Confidence
1	Cross-Site Scripting (Reflected)	2	0.3	High	Medium
2	Absence of Anti-CSRF Tokens	2	0.3	Medium	Low
3	Anti-CSRF Tokens Check	101	12.8	Medium	Medium
4	Application Error Disclosure	1	0.1	Medium	Medium
5	Backup File Disclosure	3	0.4	Medium	Medium

Table 5 (continue)

No.	OWASP ZAP	Alerts	(%)	Risk	Confidence
6	Content Security Policy (CSP) Header Not Set	1	0.1	Medium	High
7	HTTP Only Site	1	0.1	Medium	Medium
8	Hidden File Found	1	0.1	Medium	High
9	Insecure HTTP Method - TRACE	77	9.7	Medium	Medium
10	Missing Anti-clickjacking Header	1	0.1	Medium	Medium
11	Parameter Tampering	12	1.5	Medium	Low
12	Relative Path Confusion	32	4.0	Medium	Medium
13	Cross-Domain JavaScript Source File Inclusion	5	0.6	Low	Medium
14	Server Leaks Information via "X-Powered-By" HTTP Response Header Field(s)	1	0.1	Low	Medium
15	Server Leaks Version Information via "Server" HTTP Response Header Field	1	0.1	Low	High
16	Timestamp Disclosure - Unix	1	0.1	Low	Low
17	X-Content-Type-Options Header Missing	1	0.1	Low	Medium
18	Cookie Slack Detector	170	21.5	Informational	Low
19	GET for POST	22	2.8	Informational	High
20	Information Disclosure - Suspicious Comments	2	0.3	Informational	Medium
21	Modern Web Application	1	0.1	Informational	Medium
22	User Agent Fuzzer	354	44.7	Informational	Medium
<b>Total</b>		<b>792</b>	<b>100.0</b>		

It can be observed that the number of vulnerability types for URLs generated by Burp Suite and OWASP ZAP is relatively similar, with Burp Suite identifying 1–23 types and OWASP ZAP identifying 1–22 types. However, it should be noted that mapping the vulnerability types between the two tools can be challenging. For example, although Burp Suite categorises 'SQL Injection' and 'Cleartext Submission of Password' as high risk and with a high level of confidence, they are not explicitly included in OWASP ZAP alerts. Besides, some vulnerabilities may be referred to as different issues even though they pertain to the same elements. Additionally, while some vulnerability types may be similarly comprehensible between the two tools, others may differ. For instance, Burp Suite ranks Cross-site request forgery as No. 3 with 11 alerts, while OWASP ZAP ranks Cross Site Scripting (Reflected) as No. 1 with 2 alerts. Furthermore, Burp Suite ranks the Backup file as No. 20 with 2 alerts, while OWASP ZAP ranks the Backup File Disclosure as No. 5 with 3 alerts. Additionally, it is worth noting that the number of URL alerts discovered by both tools is significantly different, with Burp Suite identifying 203 alerts and OWASP ZAP identifying 792 alerts.

In transitioning from a comprehensive vulnerability assessment report to a URL alerts report, a discrepancy regarding the representation of vulnerability numbers has

been identified. Upon comparing vulnerability data, it was observed that Burp Suite identified a consistent number of vulnerabilities across the vulnerability risk assessment (203) and URL alerts (203) reports. However, a discrepancy was identified in the number of vulnerabilities reported by OWASP ZAP in the vulnerability risk assessment (22) and URL alerts (792) reports. Notably, the distribution of vulnerability risk and confidence levels detected by Burp Suite in Table 3 is congruent with the number of URL alerts reported by Burp Suite in Table 4. Conversely, the distribution of vulnerability risk and confidence levels reported by OWASP ZAP in Table 3 is consistent with the number of vulnerability types listed from No.1 to No. 22 in Table 4, suggesting that Burp Suite may have considered vulnerability risk and confidence levels as URL alerts, while OWASP ZAP treated them as distinct vulnerability types.

### **The 2021 OWASP Top 10 Vulnerabilities**

The researchers categorised the vulnerabilities Burp Suite and OWASP ZAP identified according to the 2021 OWASP Top 10 criteria. However, there is a slight difference between the two tools when the detected vulnerabilities must be categorised in the OWASP Top 10. In the Burp Suite vulnerability report, each vulnerability contains an issue background, remediation background, references, and vulnerability classifications. In this case, Burp Suite vulnerability CWE IDs in references will be manually compared with the OWASP Top 10 CWE IDs. If both Burp Suite and the OWASP Top 10 CWE IDs are similar, the Burp Suite vulnerabilities will be classified according to the OWASP Top 10 criteria.

On the other hand, OWASP ZAP provides a descriptive vulnerability report with vulnerability type, source, CWE ID, WASC ID, and reference. Several report components are similar to Burp Suite, containing vulnerability references linking to their definitions and guidelines for reducing risks. However, the significant difference is that the OWASP ZAP report contains sources and their direct links to appropriate criteria of the OWASP Top 10 automatically. In this sense, the authors can understand the criteria and the associated vulnerabilities and effortlessly categorise vulnerabilities according to the OWASP Top 10. The reason might be due to OWASP ZAP being developed by the organisation defining the OWASP Top 10 criteria. Table 6 compares the vulnerabilities reported by the two tools and categorises them by the 2021 OWASP Top 10 criteria.

For example, the number of vulnerabilities from Burp Suite was 189, listed from high to informational risks. There were 5 high risks associated with 2 vulnerabilities, including two for 'Cryptographic Failures' and three for 'Injection'. For 'Broken Access Control' considered as the first rank in the OWASP Top 10, Burp Suite identified 15 medium risks, 3 low risks, and 12 informational risks. Please note that there were 1 low risk and 106 informational risks for 'Injection' in addition to 3 high risks detected by

Table 6  
*Vulnerabilities classified into the 2021 OWASP Top 10*

No.	OWASP Top 10 (2021)	Burp Suite				Total	(%)	OWASP ZAP				Total	(%)
		H	M	L	I			H	M	L	I		
1	Broken Access Control	0	15	3	12	30	15.9	0	2	2	2	6	1.4
2	Cryptographic Failures	2	0	1	8	11	5.8	0	0	0	0	0	0.0
3	Injection	3	0	1	106	110	58.2	2	0	0	0	2	0.5
4	Insecure Design	0	0	0	0	0	0.0	0	12	0	22	34	7.8
5	Security Misconfiguration	0	0	1	24	25	13.2	0	217	2	170	389	89.2
6	Vulnerable and Outdated Components	0	0	7	0	7	3.7	0	0	0	0	0	0.0
7	Identification and Authentication Failures	0	0	0	0	0	0.0	0	0	0	0	0	0.0
8	Software and Data Integrity Failures	0	0	0	6	6	3.2	0	0	5	0	5	1.1
9	Security Logging and Monitoring Failures	0	0	0	0	0	0.0	0	0	0	0	0	0.0
10	Server-Side Request Forgery	0	0	0	0	0	0.0	0	0	0	0	0	0.0
<b>Total</b>		<b>5</b>	<b>15</b>	<b>13</b>	<b>156</b>	<b>189</b>	<b>100.0</b>	<b>2</b>	<b>231</b>	<b>9</b>	<b>194</b>	<b>436</b>	<b>100.0</b>

Burp Suite. Meanwhile, 436 vulnerabilities reported by OWASP ZAP were categorised in the OWASP Top 10. In this case, ‘Injection’ is the only vulnerability at high risk with two items. In addition, 389 vulnerabilities were classified as ‘Security Misconfiguration’, of which 231 were medium risks, 9 were low risks, and 194 were informational risks. Burp Suite classifies detected vulnerabilities into six vulnerabilities in the OWASP Top 10, and OWASP ZAP classifies detected vulnerabilities into five vulnerabilities in the OWASP Top 10. As an illustration, Burp Suite identifies 11 vulnerabilities related to ‘Cryptographic Failures’ classified into two high-risk, one low-risk, and eight informational risk categories. However, this specific vulnerability type is not identified by OWASP ZAP.

Based on the results, certain vulnerabilities identified through Burp Suite and OWASP ZAP can be categorised within the OWASP Top 10. However, it should be noted that there are also instances where both tools detect vulnerabilities, yet they do not fall within the classification of the OWASP Top 10. Those vulnerabilities may include vulnerabilities not considered as severe or widespread as those in the OWASP Top 10. In this case, the OWASP Top 10 is a helpful tool for identifying and prioritising web application security risks, but it is not an exhaustive list of all possible vulnerabilities that tools like Burp Suite and OWASP ZAP can detect.

## **DISCUSSION**

### **The Number of Informational Risks**

Most vulnerabilities not classified in the OWASP Top 10 belong to informational risk but may be worthy of consideration. For example, ‘Password Returned in a Later Response’ means the web application returns a password in an unencrypted form to the user. ‘User-Agent Fuzzer’ implies potential bugs in the website code because of response messages to the same URL with a different ‘User Agent’ header. ‘Long Direction Response’ means the web application might return a redirection response with ‘longer’ message content that sometimes contains sensitive information. Moreover, ‘Frameable Response (Potential Clickjacking)’ should also be considered since this vulnerability might allow the attacker to avoid cross-site request forgery detection, resulting in unauthorised access.

### **The Reliability of Results**

Some limitations might affect the accuracy of vulnerability assessment tools. For example, the number of vulnerabilities assessed against the existing web application may have different results than this study in which the simulated system is placed in front of the firewall to avoid legal issues and impact other network services. Therefore, some types of vulnerabilities might be manipulated and denied entry into the system. These limitations are consistent with Karumbat et al. (2016), who asserted that web vulnerability scanners are not 100% accurate. In addition, there are other potential sources of validity concerns. One example is using web applications with different vulnerabilities, such as those that do not present ‘Insecure Design’ or ‘Security Misconfiguration’ issues. In this scenario, the overall number of vulnerabilities identified by Burp Suite may decrease from 436 to 13, while the total number of vulnerabilities identified by OWASP ZAP may decrease from 189 to 164. As a result, it may be challenging to determine which vulnerability assessment tool is more reliable.

### **The Importance of Medium Risk Vulnerabilities**

By comparing the two tools against the OWASP Top 10, Burp Suite could detect more high-risk vulnerabilities than OWASP ZAP. However, on the other hand, OWASP ZAP detected a significantly greater number of vulnerabilities than Burp Suite. Mainly, OWASP ZAP detected medium-risk vulnerabilities more than Burp Suite could several times. Besides, the number of medium risks in OWASP ZAP is more than that of informational risks in OWASP ZAP. The OWASP ZAP medium risk detection is vital, as described by Liu and Wang (2018), who asserted that second-order vulnerabilities are usually ignored but more severe than first-order vulnerabilities. Consequently, the number of medium risk detection should be considered an issue that should be mitigated to protect the university web application from cyber threats.

## **Inconsistencies**

The results also show that some vulnerabilities detected by the two tools are similar and share the same CWE ID but are named differently. In addition, the tools might detect similar vulnerabilities but identify different risk severities. Therefore, using a single tool to assess vulnerabilities may not yield satisfactory results in mitigating cyber threats. Therefore, the benefit of this research is not only the detection and classification of the university web vulnerabilities based on the OWASP Top 10 but also supports some research scholars (Alsaleh et al., 2017; Mburano & Si, 2018), who claim that each vulnerability assessment tool produces different outcomes for the number and severity of vulnerabilities due to detection algorithm differences. Combining different tools is more desirable for detecting more vulnerabilities than a single tool alone, given that web security is paramount.

## **Vulnerability Risk Mitigation**

Vulnerabilities reported from both tools were sent to the responsible IT administrators to assign network security administrators to take action based on the recommendations presented in the report. Therefore, the contributions of this research are not only the classification and comparison of vulnerabilities in the university web application but also the mitigation of risks that cyber threats can exploit.

## **CONCLUSION**

The results confirm that the university web application has vulnerabilities exposed to cyber threats at high and low-risk levels. The vulnerability assessment was experimented with computer-related acts in Thailand, including the Computer Crime Act and Personal Data Protection Act, to avoid any potential effects on the existing university web application. The researchers have measured and compared the performance of web vulnerability assessment tools between Burp Suite and OWASP ZAP in detecting and analysing vulnerabilities in three scenarios, including overall vulnerability risk reports in risk and confidence metrics, vulnerabilities and URL alerts with risk and confidence metrics, vulnerabilities classified into the 2021 OWASP Top 10 vulnerabilities.

Several vulnerabilities were discovered in the university web application. Combining two vulnerability assessment tools, including Burp Suite and OWASP Zap, could detect more vulnerabilities essential for mitigating risks from cyber threats. In this case, Burp Suite and OWASP Zap differ in their vulnerability assessment performance. There are advantages and disadvantages of the tools. The results have revealed differences and inconsistencies in vulnerabilities assessed by both tools. These differences and inconsistencies, however, highlighted advantages and disadvantages helpful for security analysts and administrators to mitigate vulnerability risks to cyber threats. Therefore, combining these two vulnerability assessment tools could detect numerous vulnerabilities with different results and be valuable



for mitigating security risks to the university web application. This research is consistent with Vibhandik and Bose (2015), who conducted various vulnerability assessment tools to test web application vulnerabilities.

## ACKNOWLEDGEMENT

The authors express their gratitude to Phuket Rajabhat University, Thailand, for providing support in completing the study.

## REFERENCES

- Abdullah, H. S. (2020). Evaluation of open source web application vulnerability scanners. *Academic Journal of Nawroz University*, 9(1), 47-52. <https://doi.org/10.25007/ajnu.v9n1a532>
- Alexei, L. A., & Alexei, A. (2021). Cyber security threat analysis in higher education institutions as a result of distance learning. *International Journal of Scientific & Technology Research*, 10(3), 128-133.
- Alsaleh, M., Alomar, N., Alshreef, M., Alarifi, A., & Al-Salman, A. M. (2017). Performance-based comparative assessment of open source web vulnerability scanners. *Security and Communication Networks*, 2017, Article 6158107. <https://doi.org/10.1155/2017/6158107>
- Amankwah, R., Chen, J., Kudjo, P. K., & Towey, D. (2020). An empirical comparison of commercial and open-source web vulnerability scanners. *Software - Practice and Experience*, 50(9), 1842-1857. <https://doi.org/10.1002/spe.2870>
- Amankwah, R., Chen, J., Kudjo, P. K., Agyemang, B. K., & Amponsah, A. A. (2020). An automated framework for evaluating open-source web scanner vulnerability severity. *Service Oriented Computing and Applications*, 14, 297-307. <https://doi.org/10.1007/s11761-020-00296-9>
- Darus, M. Y., Omar, M. A., Mohamad, M. F., Seman, Z., & Awang, N. (2020). Web vulnerability assessment tool for content management system. *International Journal of Advanced Trends in Computer Science and Engineering*, 9(1.3), 440-444.
- Diogenes, Y., & Ozkaya, E. (2018). *Cybersecurity – Attack and defense strategies: Infrastructure security with Red Team and Blue Team tactics*. Packt Publishing.
- Disawal, S., & Suman, U. (2021, March 17-19). *An analysis and classification of vulnerabilities in web-based application development*. [Paper presentation]. 2021 International Conference on Computing for Sustainable Global Development (INDIACom), New Delhi, India.
- ETDA. (2022). *Personal data protection act*. Electronic Transactions Development Agency. <https://ictlawcenter.elda.or.th/laws/detail/DP-Act-2562>
- Ibrahim, A. B., & Kant, S. (2018). Penetration testing using SQL injection to recognise the vulnerable point on web pages. *International Journal of Applied Engineering Research*, 13(8), 5935-5942.
- Karumba, M. C., Ruhiu, S., & Moturi, C. A. (2016). A hybrid algorithm for detecting web based applications vulnerabilities. *American Journal of Computing Research Repository*, 4(10), 15-20. <https://doi.org/10.12691/ajcrr-4-1-3>

- Khalid, M. N., Farooq, H., Iqbal, M., Alam, M. T., & Rasheed, K. (2019). Predicting web vulnerabilities in web applications based on machine learning. In I. S. Bajwa, F. Kamareddine & A. Costa (Eds.), *Intelligent Technologies and Applications* (pp.473-484). Springer.
- Khera, Y., Kumar, D., Sujay., & Garg, N. (2019, February 14-19). *Analysis and impact of vulnerability assessment and penetration testing*. [Paper presentation]. International Conference on Machine Learning, Big Data, Cloud and Parallel Computing (COMITCon), Faridabad, India.
- Liu, M., & Wang, B. (2018). A web second-order vulnerabilities detection method. *IEEE Access*, 6, 70983-70988. <https://doi.org/10.1109/ACCESS.2018.2881070>
- Malekar, V., & Ghode, S. (2020). A review on vulnerability assessment and penetration testing open source tools for web application security. *International Journal of Advanced Research in Science & Technology (IJARST)*, 2(3), 30-33.
- Mburano, B., & Si, W. (2018, December 18-20). *Evaluation of web vulnerability scanners based on OWASP benchmark*. [Paper presentation]. International Conference on Systems Engineering (ICSEng), Sydney, Australia. <https://doi.org/10.1109/ICSENG.2018.8638176>
- McNab, C. (2016). *Network Security Assessment: Know your Network* (3rd ed.). O'Reilly Media.
- Muncaster, P. (2020, September 3). *Northumbria Uni Campus closed after serious cyber-attack*. Information Security Magazine. <https://www.infosecurity-magazine.com/news/northumbria-uni-campus-closed/>
- Muncaster, P. (2021, August 31). *Ransomware may have cost US schools over \$6bn in 2020*. Information Security Magazine. <https://www.infosecurity-magazine.com/news/ransomware-cost-us-schools-6bn-2020/>
- Naagas, M. A., Mique Jr, E. L., Palaoag, T. D., & Cruz, J. D. (2018). Defence-through-deception network security model: Securing university campus network from DoS/DdoS attack. *Bulletin of Electrical Engineering and Informatics*, 7(4), 593-600. <https://doi.org/10.11591/eei.v7i4.1349>
- Nagpure, S., & Kurkure, S. (2017, August 17-18). *Vulnerability assessment and penetration testing of web application*. [Paper presentation] International Conference on Computing, Communication, Control and Automation (ICCUBEA), Pune, India. <https://doi.org/10.1109/ICCUBEA.2017.8463920>
- Nunes, P. J., Medeiros, I., Fonseca, J. M., Neves, N. F., Correia, M. P., & Vieira, M. P. (2018). Benchmarking static analysis tools for web security. *IEEE Transactions on Reliability*, 67(3), 1159-1175. <https://doi.org/10.1109/TR.2018.2839339>
- Pavlova, E. (2020). Enhancing the organisational culture related to cyber security during the university digital transformation. *Information & Security*, 46(3), 239-249. <https://doi.org/10.11610/isij.4617>
- Popov, G., Lyon, B. K., & Hollcroft, B. (2016). *Risk Assessment: A Practical Guide to Assessing Operational Risks*. Wiley.
- Rahamathullah, U., & Karthikeyan, E. (2021, May 25). *Distributed denial of service attacks prevention, detection and mitigation - A review*. [Paper presentation]. Proceedings of the International Conference on Smart Data Intelligence (ICSMDI 2021), Tamil Nadu, India. <http://dx.doi.org/10.2139/ssrn.3852902>
- Thai Netizen Network. (2017). *Computer crime act 2017 Thai-English Thailand's computer-related crime act 2017 bilingual*. Thai Netizen Network. <https://thainetizen.org/docs/cybercrime-act-2017>

- Ulven, J. B., & Wangen, G. (2021). A systematic review of cybersecurity risks in higher education. *Future Internet*, 13(2), Article 39. <https://doi.org/10.3390/fi13020039>
- Vibhandik, R., & Bose, A. K. (2015, September 21-23). *Vulnerability assessment of web applications - A testing approach*. [Paper presentation] International Conference on e-Technologies and Networks for Development (ICeND), Lodz, Poland. <https://doi.org/10.1109/ICeND.2015.7328531>
- Wear, S. (2018). *Burp Suite Cookbook: Practical Recipes to Help you Master Web Penetration Testing with Burp Suite*. Packt Publishing.



## Nitrogen Dynamics in Soil Treated with Plant-growth Promoting Bacteria and Urea Fertilizer

Amaily Akter<sup>1</sup>, Ali Tan Kee Zuan<sup>1\*</sup>, Susilawati Kasim<sup>1</sup>, Adibah Mohd Amin<sup>1</sup>, Zakry Fitri Ab Aziz<sup>2</sup>, Noor Md Rahmatullah<sup>3</sup>, Buraq Musa Sadeq<sup>1</sup>, Sayma Serine Chompa<sup>1</sup> and Md Ekhlaur Rahman<sup>1,4</sup>

<sup>1</sup>Department of Land Management, Faculty of Agriculture, Universiti Putra Malaysia, 43400 UPM, Serdang, Selangor, Malaysia

<sup>2</sup>Faculty of Agriculture and Food Sciences, Universiti Putra Malaysia Bintulu Campus, 97008, Sarawak, Malaysia

<sup>3</sup>Department of Agricultural Statistics, Faculty of Agribusiness Management, Sher-e-Bangla Agricultural University, Dhaka-1207, Bangladesh

<sup>4</sup>Divisional Laboratory, Soil Resource Development Institute, Krishi Khamar Sarak, Farmgate, Dhaka-1215, Bangladesh

### ABSTRACT

The mineralization of urea fertilizer significantly impacts nitrogen movement in the soil. An incubation study was done on a lab scale basis to examine nitrogen dynamics in soil inoculated with plant growth-promoting bacteria (PGPB) supplemented with varying levels of nitrogen fertilizer in the form of urea (0% N, 25% N, 50% N, 75% N, and 100% N). In the present experiment, sandy clay loam soil was used and incubated for four weeks, and the concentrations of  $\text{NH}_4^+\text{-N}$  and  $\text{NO}_3^-\text{-N}$  were monitored using the destructive method (Kjeldahl) to determine the mineralization rate of urea. Results showed higher  $\text{NH}_4^+\text{-N}$  (11.880 mg/kg mineralized with UPMRB9N50 treatment) and  $\text{NO}_3^-\text{-N}$  (20.060

mg/kg mineralized with UPMRB9N50 treatment) concentrations in the bacteria-treated soil compared to the uninoculated control. Urea-N remains higher (0.0353% and 0.0253% from UPMRB9N50 treatment in the first and second weeks, respectively) in bacteria-treated soil during the first two weeks, then gradually becomes zero towards the end of the observing period. Nitrogen (N) leaching loss was lower in bacterial inoculated soil compared to the control, and the leaching loss of N was greater with the

### ARTICLE INFO

#### Article history:

Received: 01 November 2022

Accepted: 12 April 2023

Published: 09 October 2023

DOI: <https://doi.org/10.47836/pjst.31.6.20>

#### E-mail addresses:

amailyakter2554@gmail.com (Amaily Akter)

tkz@upm.edu.my (Ali Tan Kee Zuan)

susilawati@upm.edu.my (Susilawati Kasim)

adibahamin@upm.edu.my (Adibah Mohd Amin)

zakryfitri@upm.edu.my (Zakry Fitri Ab Aziz)

rahmatnm@sau.edu.bd (Noor Md Rahmatullah)

buraqmosa1991@gmail.com (Buraq Musa Sadeq)

serinesayma@gmail.com (Sayma Serine Chompa)

ekhlaurahman02@gmail.com (Md Ekhlaur Rahman)

\* Corresponding author

increased N fertilizer rates. Cumulative N leaching loss is higher (29.797 mg/kg) in 100% N-treated soil than in other treatments. The findings observed that the beneficial bacteria could enhance the N mineralization to make the nutrient available for the crop while, at the same time, reducing leaching losses of fertilizer when supplied with a minimum amount of chemical fertilizer, thereby saving the input cost and protecting the environment.

*Keywords:* Ammonium ion, nitrate ion, nitrogen leaching, nitrogen mineralization, plant growth-promoting bacteria

---

## INTRODUCTION

A vital component of plants, nitrogen (N) is also a major component of genetic material, amino acids, chlorophyll, and adenosine triphosphate (ATP); it enhances agricultural productivity by 30–50% globally (Leghari et al., 2016). The primary source of N fertilizer that substantially affects agricultural productivity worldwide is urea (Kira et al., 2019). It is the most frequently utilized N fertilizer due to its simplicity and high N content (46%) (Motasim et al., 2021). About 73.4% of all nitrogen fertilizer used worldwide is urea (Heffer & Prud'homme, 2016). However, the worrisome issue with using granular urea fertilizer is its significant nitrogen loss and inefficient use of nitrogen fertilizer, which varies from 10% to 50% (Almaz et al., 2017). When urea is broadcast onto the field, more than 50% of the nitrogen in urea cannot be taken up by plants if fertilization management is not done properly (Rochette et al., 2009). It turns into a risk factor for environmental deterioration, which includes loss of stratospheric ozone, acidic precipitation, the excessive richness of nutrients in a lake or other body of water, water contamination,  $\text{NH}_3$  volatilization loss, and  $\text{N}_2\text{O}$  emissions (Puga et al., 2020). A significant gaseous loss is reported when granular urea is applied to the surface (Lichiheb et al., 2019; Motasim et al., 2021) and nitrogen loss via leaching (Puga et al., 2020).

Due to these situations, people are beginning to learn about an additional or alternative greener approach (Ladha et al., 1997), and using soil microorganisms is one of the techniques. This eco-friendly method utilizes the beneficial microorganisms called plant growth-promoting rhizobacteria (PGPR), which promotes biological nitrogen fixation (BNF), inorganic phosphate solubilization, the synthesis of phytohormones, siderophores, and hydrolyzing enzymes to promote plant development and productivity (Ali-Tan et al., 2017). These microbes play a crucial role in the nitrogen transformation that enhances nitrification in the soil, which leads to an increase in  $\text{NO}_3^-$  production (Mandal et al., 2016). Nitrogen in the soil is relatively more stable in  $\text{NO}_3^-$  form than in  $\text{NH}_4^+$  form (Wang et al., 2018). Loss of  $\text{NH}_4^+-\text{N}$  and  $\text{NO}_3^--\text{N}$  in topsoil was positively correlated, according to (Shan et al., 2015). Ineffective techniques and without proper urea use management encourage nitrogen losses (Zhao et al., 2015). With the optimization of N fertilizer rates and the application of PGPR, it is possible to maximize crop productivity, minimize N losses, and improve mineralization and nutrient uptake. Only a few research have been reported

regarding the results of optimum N fertilizer levels with PGPB-treated soil, especially on the nitrogen mineralization on tropical acidic soils. Thus, this study aims to assess the N mineralization pattern that microbial inoculation affects to better understand and reduce urea-N losses from soils in tropical climates.

## MATERIALS AND METHODS

### Sampling and Preparation of Soils

In this study, sandy clay loam soil was used, and they were based on the USDA's soil classification (Table 1). The top 15 cm of the soil was sampled and air-dried in the drying room at the Department of Land Management, Faculty of Agriculture, Universiti Putra Malaysia. The soils were ground by laboratory pestle and mortar, followed by sieving with a 2.0 mm metallic sieve and stored in a clean container for analysis.

Table 1  
*Physicochemical characteristics of soils*

Features of the soil	Values	References
USDA's class for soil texture	Sandy clay loam	
Sand (%)	52.36 ± 0.012	
Silt (%)	12.46 ± 0.012	(Teh & Talib, 2006)
Clay (%)	35.12 ± 0.006	
Moisture content at field capacity (%)	23.95 ± 0.006	(Richards & Fireman, 1943)
pH	4.91 ± 0.003	(Jones, 2001; Sharifuddin et al., 1990)
Total C (%)	2.31 ± 0.003	
Total N (%)	0.199 ± 0.001	(LECO., 2018)
CEC (cmol+/kg)	8.7 ± 0.115	(Chapman, 1965; Keeney & Nelson., 1982)
K (me/ 100g)	0.23 ± 0.003	
Ca (me/100g)	0.31 ± 0.012	
Mg (me/100g)	0.10 ± 0.003	
P (mg/kg)	39.71 ± 0.012	(Sharifuddin et al., 1990)

### Experimental Design

The incubation study used a completely randomized design (CRD) with two factors: Nitrogen levels (0%, 25%, 750%, 75%, and 100%) and PGPB strains (*Bacillus subtilis* and *Bacillus tequilensis*).

### Characterization of the Soil

**Analysis of Soil Particle Size.** The particle size distribution of soil was analyzed by pipette method (Teh & Talib, 2006) with modifications. In a 1000 ml beaker, 20 g of sieved soil was taken, and H<sub>2</sub>O<sub>2</sub> was added in a 50-milliliter amount and left overnight. After 24 hours,

the mixture was heated at 100°C for about one hour, and the remaining quantities of H<sub>2</sub>O<sub>2</sub> were added until no frothing remained. In case of bubbling from the heated mixer, some drops of alcohol were added. It was followed by adding 0.2 N HCl in 50 milliliters and making the volume 200 milliliters by adding distilled water. After an hour, the mixture was allowed to cool and washed twice with distilled water of 200 milliliters. The mixture was then set on a mechanical agitator by adding 40 mL Calgon solution for 5 minutes, and then the mixture was passed through a 50 µm sieve for collecting sand fraction. Then, the mixture was transposed to a 1000-milliliter cylinder, and distilled water was used to get the volume at the mark. A hot water bath at 23°C was used to place the cylinders, and a plunger thoroughly mixed the solution for a minute. Then, the suspensions were left to settle for 7 hours; after that, a pipette was placed at 10 cm depth, and an aliquot was pipetted and transferred into a porcelain pot. These pots containing soil suspension were dried for 24 hours at 105°C in the oven, then transferred into a 200-milliliter desiccator and cooled before weighing. The previously collected sand fraction was also dried in the oven at 105°C, transferred to a desiccator, and allowed to cool before weighing.

The sand, silt, and clay percentages were calculated by the following Equations 1, 2, and 3:

$$\% \text{ Sand} = \text{weight of oven dried sand particles}(g) \times \frac{100}{\text{weight of the soil}(g)} \quad [1]$$

$$\% \text{ Clay} = \left\{ \frac{\text{weight of oven dried clay}(g) \times 1000}{\text{volume pipetted}} - C \right\} \times \frac{100}{\text{weight of the soil}(g)} \quad [2]$$

$$\% \text{ Silt} = 100 - (\% \text{ sand} + \% \text{ clay}) \quad [3]$$

where; C = weight of Calgon in the solution (g)

The textural classes were determined using the USDA textural triangle.

### **Bulk Density and Moisture Content Determination of Soils**

The soil core method (Okalebo et al., 2002) was used during bulk density determination. A metallic core/ring (known as weigh-w<sub>1</sub> and volume-v) was inserted into the soil after removing the surface layer in the field. The ring was excavated around the soil, and cut excess soil beneath the ring, followed by the removal of excess soil at the ends of the ring with a knife. Immediately, the soil was dried for 24 hours at 105°C in the oven and weighed (w<sub>2</sub>).

$$\text{Bulk density, } Db \text{ (g/cm}^3\text{)} = \frac{[w_2 \text{ (g)} - w_1 \text{ (g)}]}{v \text{ (cm}^3\text{)}} \quad [4]$$



For moisture content determination, in a porcelain pot, 10 g of soil that had been air-dried was weighed and dried in an oven for 24 hours at 105°C, and then the pot was cooled after transferring from the oven to the desiccator.

The following Equation 5 was used to determine the soil's moisture content:

$$\text{Soil moisture content (\%)} = \frac{[\text{initial soil weight (g)} - \text{ovendried soil weight (g)}]}{\text{oven dried soil weight (g)}} \times 100 \quad [5]$$

### Determination of Water Content at Field Capacity

The water at field capacity was estimated using a pressure plate method (Richards & Fireman, 1943). A core sampler was used at the desired depth, and the pressure was maintained at 33 kPa. From the top, pound into the earth a core ring with a known weight of approximately 7.6 cm in diameter and 4.0 cm deep. Carefully remove the core ring from the ground; clean off any excess soil up to the level of the core ring's two ends. Take the core ring and use the plastic caps to seal the ends before bringing it to the lab for analysis. On the porous plates, place the retaining rings for 33 kPa pressure. Five pieces of nearly identical sizes should be created from the undisturbed core samples. One sample piece should be placed in a holding ring on a coarse wire mesh, and one piece should be placed on a porous plate for water saturation (0 bar pressure). Keep the water below the ring edge while soaking ceramic plates for 24 hours. Insert the plate containing the samples into the 33 kPa pressure chamber and attach the outlet tube. Apply pressure by closing the chamber. Equilibrium is attained when no more water outflows and opens the chamber by releasing the pressure slowly. Take away the samples from the chamber and take the weight. The samples should be oven-dried for 24 hours at 105°C, then weighed again.

### Soil pH Determination

The pH of the soil was determined (Jones, 2001; Sharifuddin et al., 1990) 'by adding water into soil at a ratio of 1:2.5 (soil to water)', 50 milliliters of deionized distilled water and 20 g of soil were added to a 100 milliliters plastic vial, and the mixture was agitated for 30 minutes and allowed to be settled, and then pH value was measured using Metrohm827 pH meter, Metrohm AG, Switzerland.

### Cation Exchange Capacity Determination of Soil

The leaching method determined the soil's cation exchange capacity (Chapman, 1965). A hundred ml of 1 M NH<sub>4</sub>OAC was introduced to 10 g of soil sample in a leaching tube (pH 7). After discarding the leachate that had been collected, two rounds of 95% alcohol washing were performed on the soil to remove any remaining NH<sub>4</sub>OAC. Then 100 ml of

0.1 N  $K_2SO_4$  was added, the leachate was collected, and reading was taken following the distillation (Keeney & Nelson., 1982) method.

### **Total N, remaining N (%) and C Content of Soil**

The initial total C, N content in soil and remaining N (%) after the end of the study periods in the soils were estimated by LECO's new TruMac CNS Macro Analyser (LECO., 2018), LECO FP-2000 (LECO Corp. Michigan, USA). By putting around 0.10 g of soil in a C-free combustion boat and burning it at 1350°C in an  $O_2$  environment, the total (%) of C, N, and S was determined. The boat was inserted into the TruMac CNS analysis machine using an auto-sampler stand.

### **Preparation of Inoculants for Soil Application**

The microorganisms UPMB10 and UPMRB9 were inoculated into a 250 ml conical flask containing 100 ml of tryptic soy broth (TSB). The flask was incubated after inoculation in an orbital shaking incubator (Model OSI-503 LD; Firstek Scientific, Japan) for 48 hours at 28°C with 150 rpm of shaking. A UV-Visible spectrophotometer set the optical density ( $OD_{600}$ ) of the two strains to 1.

### **Treatments of the Soil Sample**

There were fifteen treatments used for this incubation study, below mentioned as follows:

B0N0 = Control

B0N25 = Uninoculated control with 25% of nitrogen fertilizer applied @ 180 kg/ha

B0N50 = Uninoculated control with 50% of nitrogen fertilizer applied @ 180 kg/ha

B0N75 = Uninoculated control with 75% of nitrogen fertilizer applied @ 180 kg/ha

B0N100 = Uninoculated control with 100% of nitrogen fertilizer applied @ 180 kg/ha

UPMB10N0 = *Bacillus subtilis* ( $10^8$  CFU/mL) inoculated without nitrogen fertilizer

UPMB10N25 = *Bacillus subtilis* ( $10^8$  CFU/mL) inoculated with 25% nitrogen fertilizer applied @180 kg/ha

UPMB10N50 = *Bacillus subtilis* ( $10^8$  CFU/mL) inoculated with 50% nitrogen fertilizer applied @180 kg/ha

UPMB10N75 = *Bacillus subtilis* ( $10^8$  CFU/mL) inoculated with 75% nitrogen fertilizer applied @180 kg/ha

UPMB10N100 = *Bacillus subtilis* ( $10^8$  CFU/mL) inoculated with 100% nitrogen fertilizer applied @180 kg/ha

UPMRB9N0 = *Bacillus tequilensis* ( $10^8$  CFU/mL) inoculated without nitrogen fertilizer

UPMRB9N25 = *Bacillus tequilensis* ( $10^8$  CFU/mL) inoculated with 25% nitrogen fertilizer applied @180 kg/ha

UPMRB9N50 = *Bacillus tequilensis* ( $10^8$  CFU/mL) inoculated with 50% nitrogen fertilizer applied @180 kg/ha

UPMRB9N75 = *Bacillus tequilensis* ( $10^8$  CFU/mL) inoculated with 75% nitrogen fertilizer applied @180 kg/ha

UPMRB9N100 = *Bacillus tequilensis* ( $10^8$  CFU/mL) inoculated with 100% nitrogen fertilizer applied @180 kg/ha

### **Determination of N Mineralization of Soil**

Finely ground and air-dried samples were analyzed for  $\text{NH}_4^+\text{-N}$ ,  $\text{NO}_3^-\text{-N}$ , and urea-N concentration after extracting the soil with 2M potassium chloride-phenyl mercuric acetate (KCl-PMA) solution. The soil surface in the 100 cm<sup>3</sup> plastic pots received the 15 treatments listed below. Fifty grams of sieved, air-dried soil was left open to preserve the aerobic environment. Adding water to retain the initial weight allowed the moisture content to be kept at a field-capacity level throughout the observing period. Weekly analyses of the N mineralization were conducted using destructive methods (Junejo et al., 2011; Keeney & Nelson., 1982). This procedure involved extracting 20 g of soil with 40 mL of a potassium chloride-phenyl mercuric acetate (KCl-PMA) solution, distilling it with a micro-Kjeldahl steam distillation unit, titrating it against a solution of 0.01 N HCl, and then determining the amount of mineral N (Keeney & Nelson, 1982) and urea-N (using a colorimetric method) (Douglas & Bremner, 1970).

### **Urea-N Determination of Soil Samples**

Twenty grams of soil were extracted with the help of 40 mL of KCl-PMA solution to determine the amount of urea-N. Di-acetyl monoxime and Thio-semi-carbazide were used to color the solution, and the intensity of color was evaluated using a calibrated spectrophotometer at 528 nm wavelength (Douglas & Bremner, 1970).

### **Leaching Loss of N Determination in Soil**

The 100 g of sieved, air-dried soil used in the leaching investigation was placed in leachate tubes (10 cm in diameter and 60 cm in height). The bottom of the leachate tubes was closed with ash flock and filter paper to allow only liquid to be leached. In the soil sample, twenty-eight soil columns with 8 cm depth were made by adding the dried, ground, and 2.00 mm sieved soil samples. Fifteen levels of treatments were added to soil samples. A blank treatment was used for the study. The soil columns were moistened by adding distilled water overnight, and the field-capable moisture level remained. After two days of treatment, a hundred mL of distilled water was added, and the leachate was kept until 10 volumes of pore (Zadeh, 2010). From the leachate, 10 mL was taken for analysis using a distillation plant, and steam was collected in a boric acid solution. The trapped solution

was titrated against 0.01N HCL solution. The leached solutions were analyzed for  $\text{NH}_4^+\text{-N}$  and  $\text{NO}_3^-\text{-N}$  concentration (Keeney & Nelson., 1982). The incubation room's temperature was kept at  $25 \pm 0.5^\circ\text{C}$  throughout the investigation. The experimental units were set up in a completely randomized design with three replicates, and the experiment was carried out as a complete factorial design.

### Analysis of Statistics

The data was statistically examined using ANOVA analysis by Statistical analysis software (SAS) 9.4 (SAS Institute Inc., Cary, NC, USA, 2013) at a 5% level of confidence; the treatment means were compared using Duncan's Multiple Range Test (DMRT).

## RESULTS

### Effects of Treatments on $\text{NH}_4^+\text{-N}$ and $\text{NO}_3^-\text{-N}$ Concentrations in Soil

An increase in  $\text{NH}_4^+\text{-N}$  and  $\text{NO}_3^-\text{-N}$  concentrations were observed in B0N100, UPMRB9N50, and UPMB10N50 treated soils compared to other treatments (Tables 2 and 3). The concentrations of  $\text{NH}_4^+\text{-N}$  declined, whereas concentrations of  $\text{NO}_3^-\text{-N}$  were higher with the increased incubation time, and concentrations of both were higher with

Table 2  
 *$\text{NH}_4^+\text{-N}$  concentration (mg/kg) in soil treated with different levels of N with 2 strains of PGPB throughout the observing period of four weeks*

Treatments	$\text{NH}_4^+\text{-N}$ concentrations (mg/kg)			
	1 <sup>st</sup> week	2 <sup>nd</sup> week	3 <sup>rd</sup> week	4 <sup>th</sup> week
B0N0	2.127n	1.257n	0.0827m	0.085i
B0N25	3.017k	2.177k	1.443j	0.383g
B0N50	6.643g	4.803g	3.157g	0.843f
B0N75	8.123d	5.873d	3.863d	1.033d
B0N100	10.507c	7.593c	4.987c	1.333c
UPMB10N0	2.187m	1.583m	1.040l	0.283h
UPMB10N25	6.973f	5.027f	3.313f	0.883ef
UPMB10N50	11.243b	8.117b	5.353b	1.417b
UPMB10N75	3.113i	2.250i	1.483i	0.393g
UPMB10N100	3.053j	2.203j	1.453j	0.383g
UPMRB9N0	2.227l	1.607l	1.057k	0.283h
UPMRB9N25	7.303e	5.267e	3.467e	0.923e
UPMRB9N50	11.880a	8.583a	5.653a	1.500a
UPMRB9N75	3.227h	2.333h	1.527h	0.407g
UPMRB9N100	3.113i	2.253i	1.483i	0.393g

Note. Using Duncan's multiple range test (DMRT) at the 0.05 confidence level, different letters within a column indicate significant variations between means

Table 3

$NO_3^-$ -N concentration (mg/kg) in soil treated with different levels of N with 2 strains of PGPB throughout the observing period of four weeks

Treatments	$NO_3^-$ -N concentrations (mg/kg)			
	1 <sup>st</sup> week	2 <sup>nd</sup> week	3 <sup>rd</sup> week	4 <sup>th</sup> week
B0N0	1.4867n	1.4933n	1.5033n	1.4767d
B0N25	3.3933k	4.2533k	5.1033k	4.9267c
B0N50	7.4567g	9.3533g	11.2167g	10.8533b
B0N75	9.1233d	11.4333d	13.7167d	13.2567b
B0N100	11.8033c	14.7933c	17.7467c	17.1567a
UPMB10N0	1.5533m	1.5633m	1.6167m	1.5400d
UPMB10N25	7.8333f	9.8167f	11.7833f	11.3933b
UPMB10N50	12.6267b	15.8267b	18.9867b	18.3567a
UPMB10N75	3.4933i	4.3833i	5.2533i	5.0833c
UPMB10N100	3.4333j	4.3033j	5.1633j	4.9857c
UPMRB9N0	1.5867l	1.6000l	1.6533l	1.5757d
UPMRB9N25	8.2067e	10.2933e	12.3433e	11.9367b
UPMRB9N50	13.3333a	16.1333a	20.0600a	17.3933a
UPMRB9N75	3.6333h	4.5533h	5.4633h	5.2767c
UPMRB9N100	3.4933i	4.3833i	5.2533i	5.0767c

Note. Using Duncan's multiple range test (DMRT) at the 0.05 confidence level, different letters within a column indicate significant variations between means

more fertilizer-N applied. Among the treatments,  $NH_4^+$ -N and  $NO_3^-$ -N concentrations were greater in bacteria-treated soil than in the uninoculated control. The concentrations of  $NH_4^+$ -N were greater in the first week and then gradually declined afterward, which is true in all treatments. As opposed to that, the concentrations of  $NO_3^-$ -N were lower in the first week, then increased significantly and peaked in the third week. Similar results were found in both soils, with and without bacterial inoculations. In bacteria-treated soil, the amount of  $NH_4^+$ -N concentrations and level of urea mineralization (%) in the soils were greater during the initial incubation and then became zero incubation in the fourth week (Table 2). Soil applied with 50% of fertilizer-N and inoculated with UPMRB9 showed 15.15%, 10.95%, 7.21%, and 1.91% of mineralized urea into  $NH_4^+$ -N in the week of the first, second, third, and fourth of incubation respectively which, when compared to all treatments, were the highest. Similar patterns were observed with the inoculation of UPMB10. This study revealed that the application of 50% fertilizer-N along with bacterial inoculations mineralized the highest N amount compared to other treatments, and interestingly, the mineralization rate became lower with the increase in N rate (Tables 2 and 3). The highest  $NO_3^-$ -N mineralization rate was recorded in soil treated with UPMRB9 supplied with 50% fertilizer-N. The highest mineralization rates of  $NH_4^+$ -N and  $NO_3^-$ -N occur in the first and third weeks, respectively (Tables 2 and 3).

### Effect of Treatments on Remaining Urea-N in the Soil (%)

With time, less urea-N was left in the soil. The soil treated with bacteria had a larger amount of urea-N remaining compared to the uninoculated treatments. The quantities of remaining urea-N in both bacteria and without bacteria-treated soils were high in the first week of incubation and afterward became lower towards the end of the incubation (Table 4). During the first week of incubation, treatments with UPMB10 and UPMRB9 with 50% N recorded 0.0333% and 0.0353% of N remained in the soil, whereas the control with 100% N recorded 0.0307% of urea-N remained, all three are significantly higher than other treatments. A similar pattern was observed throughout the incubation period.

Table 4

*Urea-N remaining (%) in the soil treated with different levels of N with bacteria throughout the observing period of four weeks*

Treatments	Urea-N remaining (%)			
	1 <sup>st</sup> week	2 <sup>nd</sup> week	3 <sup>rd</sup> week	4 <sup>th</sup> week
B0N0	0.0000j	0.0000j	0.0000h	0.0000f
B0N25	0.0093i	0.0073i	0.0050g	0.0023e
B0N50	0.0203h	0.0137h	0.0083f	0.0033d
B0N75	0.0243d	0.0167de	0.0103e	0.0037d
B0N100	0.0307c	0.0223c	0.0147c	0.0050bc
UPMB10N0	0.000j	0.0000j	0.0000h	0.0000f
UPMB10N25	0.0213fg	0.0153g	0.0103e	0.0033d
UPMB10N50	0.0333b	0.0243b	0.0167b	0.0063b
UPMB10N75	0.0227def	0.0170de	0.0110de	0.0050c
UPMB10N100	0.0217efg	0.0157fg	0.0103e	0.0040d
UPMRB9N0	0.000j	0.0000j	0.0000h	0.0000f
UPMRB9N25	0.0217efg	0.0163ef	0.0110de	0.0040d
UPMRB9N50	0.0353a	0.0253a	0.0177a	0.0093a
UPMRB9N75	0.0237de	0.0173d	0.0117d	0.0057bc
UPMRB9N100	0.0233ef	0.0170de	0.0110de	0.0053c

*Note.* Using Duncan's multiple range test (DMRT) at the 0.05 confidence level, different letters within a column indicate significant variations between means

### N Leaching (NH<sub>4</sub><sup>+</sup>-N and NO<sub>3</sub><sup>-</sup>-N) from Soil

The NH<sub>4</sub><sup>+</sup>-N and NO<sub>3</sub><sup>-</sup>-N leaching loss were greater in the treatment with just fertilizer-N alone than in inoculated soil. The amount of leached N is higher as the amount of N applied is higher (Table 5 and Figure 1). Leachate was greater in the second and third pores and significantly reduced in bacteria and without bacteria-treated soil. In the fertilizer-treated soil, NH<sub>4</sub><sup>+</sup>-N leaching loss was low in the first two pores, which is insignificant. In the third to fifth pore, noticeably greater quantities of NH<sub>4</sub><sup>+</sup>-N were lost by leaching

Table 5  
Leaching loss of  $\text{NH}_4^+ - \text{N}$  (mg/kg) in soil treated with different levels of N with bacteria in 10 pore volumes

Treatments	Leaching loss of $\text{NH}_4^+ - \text{N}$ (mg/kg) in soil									
	1 <sup>st</sup> pore	2 <sup>nd</sup> pore	3 <sup>rd</sup> pore	4 <sup>th</sup> pore	5 <sup>th</sup> pore	6 <sup>th</sup> pore	7 <sup>th</sup> pore	8 <sup>th</sup> pore	9 <sup>th</sup> pore	10 <sup>th</sup> pore
B0N0	0.195l	0.382m	0.416g	0.366l	0.344m	0.322j	0.304j	0.304j	0.304j	0.304j
B0N25	0.391i	0.458j	2.326defg	1.424i	0.522j	0.321kl	0.301k	0.301k	0.301k	0.301k
B0N50	0.861f	1.008g	5.118bcd	3.134f	1.15g	0.690g	0.662g	0.662g	0.662g	0.662g
B0N75	1.053d	1.232d	6.247ab	3.832c	1.406d	0.844d	0.809d	0.809d	0.809d	0.809d
B0N100	1.363a	1.594a	8.097a	4.958a	1.819a	1.092a	1.046a	1.046a	1.046a	1.046a
UPMB10N0	0.192lm	0.372n	0.412g	0.354m	0.337n	0.314k	0.297l	0.297l	0.297l	0.297l
UPMB10N25	0.372j	0.435k	2.21efg	1.353j	0.496k	0.297m	0.285n	0.285n	0.285n	0.285n
UPMB10N50	0.801g	0.937h	4.76bbcd	2.915g	1.063h	0.642h	0.615h	0.615h	0.615h	0.615h
UPMB10N75	1.05d	1.195e	6.071ab	3.717d	1.364e	0.819e	0.785e	0.785e	0.785e	0.785e
UPMB10N100	1.347b	1.575b	8.003a	4.898b	1.797b	1.079b	1.033b	1.033b	1.033b	1.033b
UPMRB9N0	0.188m	0.367o	0.408g	0.352m	0.333n	0.308l	0.291m	0.291m	0.291m	0.291m
UPMRB9N25	0.352k	0.412l	1.531fg	1.281k	0.47l	0.282n	0.270o	0.270o	0.270o	0.270o
UPMRB9N50	0.749h	0.877i	3.105cdefg	2.726h	1.001i	0.600i	0.575i	0.575i	0.575i	0.575i
UPMRB9N75	0.977e	1.146f	4.017bcdef	3.564e	1.308f	0.785f	0.752f	0.752f	0.752f	0.752f
UPMRB9N100	1.322c	1.546c	5.372abc	4.958b	1.764c	1.053c	1.015c	1.015c	1.015c	1.015c

Note. Using Duncan's multiple range test (DMRT) at the 0.05 confidence level, different letters within a column indicate significant variations between means

through fertilizer-treated soil compared to bacteria-treated soil, with the same levels of fertilizer-N application (Table 5). The greatest total  $\text{NH}_4^+\text{-N}$  concentrations of  $\text{NH}_4^+\text{-N}$  were observed in leachate from B0N100 treated soil (23.109 mg/kg) compared to treatments of UPMB10N100 and UPMRB9N100 at (22.834 mg/kg) and (22.023 mg/kg) respectively (Table 6). The  $\text{NO}_3^-\text{-N}$  leachate was greater in the second pore volumes and drastically reduced afterward. In the first three pore volumes, noticeably more  $\text{NO}_3^-\text{-N}$  was leached through fertilizer-treated soil, and the cumulative loss was greater with the increase in fertilizer-N application rates (Figure 1).

Table 6  
*The cumulative leaching loss of N ( $\text{NH}_4^+\text{-N}$  and  $\text{NO}_3^-\text{-N}$ ) from soil*

Treatments	$\text{NH}_4^+\text{-N}$ (mg/kg)	$\text{NO}_3^-\text{-N}$ (mg/kg)
B0N0	3.244 ± 0.006 f	0.622 ± 0.005m
B0N25	6.639 ± e	1.919 ± 0.005j
B0N50	14.608 ± c	4.229 ± 0.003g
B0N75	17.852 ± b	5.169 ± 0.007d
B0N100	23.109 ± 0.006 a	6.688 ± 0.009a
UPMB10N0	3.172 ± 0.006f	0.574 ± 0.005n
UPMB10N25	6.305 ± 0.006e	1.823 ± 0.005k
UPMB10N50	13.580 ± 0.013cd	3.930 ± 0.005h
UPMB10N75	17.358 ± 0.007b	5.016 ± 0.005e
UPMB10N100	22.834 ± 0.003a	6.610 ± 0.005b
UPMRB9N0	3.122 ± 0.006f	0.538 ± 0.004o
UPMRB9N25	5.411 ± 0.568ef	1.726 ± 0.004l
UPMRB9N50	11.360 ± 1.354d	3.897 ± 0.003i
UPMRB9N75	14.807 ± 1.813c	4.809 ± 0.006f
UPMRB9N100	20.023 ± 2.500b	6.490 ± 0.007c

*Note.* Using Duncan's multiple range test (DMRT) at the 0.05 confidence level, different letters within a column indicate significant variations between means

### Total N (%) Remaining in Soils

The total N remaining in the soil was greater in the inoculated treatment than in fertilizer—the amount of N still in the soil correlated with the amount of urea applied. The greatest quantities of remaining N were revealed in soil treated through UPMRB9 with 100% N (0.202%), significantly higher than other treatments. The smallest quantities were found through 25% N with and without bacterial inoculations (Figure 2).

## DISCUSSION

Applying urea to soils causes it to go through hydrolysis, which produces  $\text{NH}_4^+$  and  $\text{HCO}_3^-$  (Mariano et al., 2019). The urease enzyme catalyzes the entire reaction. According



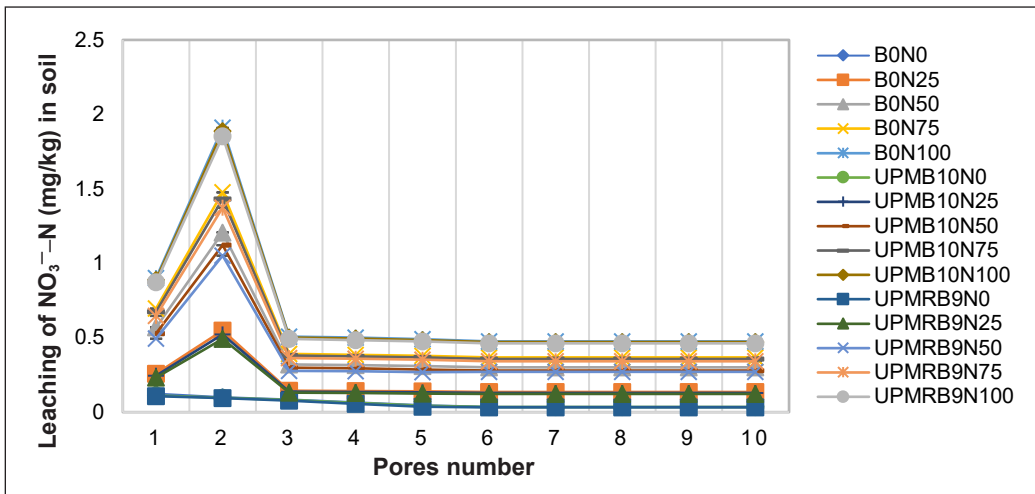


Figure 1. Leaching loss of NO<sub>3</sub><sup>-</sup>-N (mg/kg) in soil treated with different N levels with bacteria in 10 pore volumes. Using Duncan’s multiple range test (DMRT) at the 0.05 confidence level, the standard errors are displayed as vertical bars on the graphs

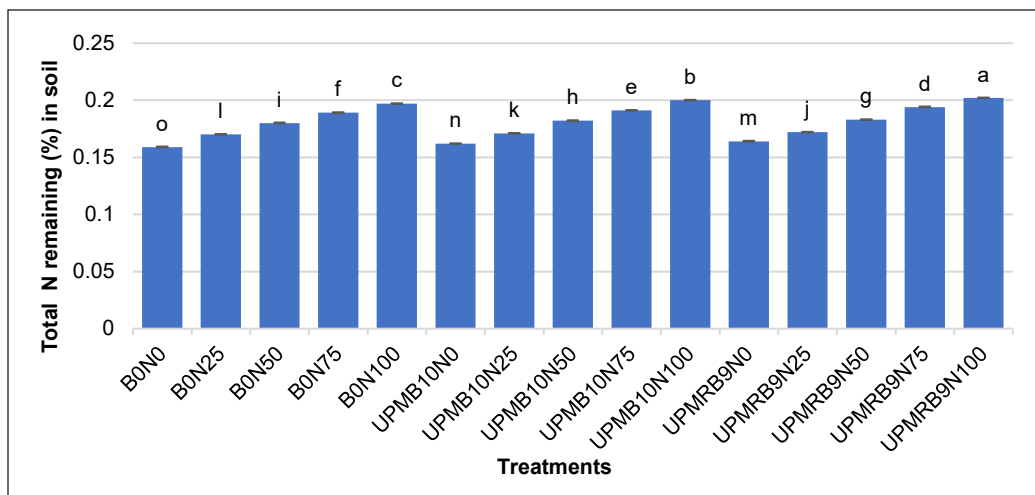


Figure 2. Total remaining N (%) in soil applied with different levels of N fertilizer with bacteria at the end of 30 days of observing period. Using Duncan’s multiple range test (DMRT) at the 0.05 confidence level, different letters within a column indicate significant variations between means. The standard errors are displayed as vertical bars on the bar chart

to reports, urea hydrolysis was said to be initiated by soil moisture (Abera et al., 2012). Depending on the soil characteristics, the NH<sub>4</sub><sup>+</sup> can either be absorbed by soil colloids or converted further to NO<sub>3</sub><sup>-</sup> and NH<sub>3</sub>. Within a few days, there is quick hydrolysis, and during the first four days following treatment, 80% of the urea that has been applied can be hydrolyzed (Bundy, 2001; Cardenas et al., 2013). Urea mineralization in PGPB-treated soil was faster compared to without bacterial inoculation. The soil treated with PGPB has

evenly distributed urea throughout it since it is liquid (PGPB applied as broth where urea gets  $H_2O$  to transform and soil urease enzyme able to release available form of  $NH_4^+$ ). As a result, the soil colloids absorb more  $NH_4^+$ , which may prevent  $NH_4^+$  to  $NH_3$  conversion (Rochette et al., 2013). Increased  $NH_4^+-N$  conversion to increase N volatilization loss is promoted by surface application of urea in soil (Rochette et al., 2009). The process of urea mineralization had an impact on how much urea-N was still present in the soils. If  $NH_4^+-N$  mineralization is increased and the nitrification process is quicker, the amount of applied urea-N that remains in the soil decreases (Junejo et al., 2011). Compared to soil treated with N-fertilizer alone, the soil treated with bacteria had a faster rate of N and higher  $NH_4^+-N$  mineralization, hence less urea-N left in the soils. Unlike uninoculated treatments, bacteria-treated soil had more  $NH_4^+-N$  and  $NO_3^--N$  concentrations.

According to the findings of our investigation, soil treated with uninoculated treatments lost considerably more  $NH_4^+-N$  through leaching than soil treated with PGPB ( $p \leq 0.05$ ). More  $NH_4^+-N$  concentration was present in the first few pore volumes because more urea hydrolysis in the first few days after treatment was applied before declining (Cardenas et al., 2013). Faster urea breakdown encourages greater N leaching (Gioacchini et al., 2002; Zuki et al., 2020). In contrast to the bacteria-treated soil, where urea distribution was more uniform, the urea in the uninoculated soil is more localized. The leaching loss was greater in the soil treated with fertilizer because the urea was more concentrated across a smaller soil area (Omar et al., 2015). In contrast to bacteria-treated soil, the amount of  $NH_4^+-N$  leached from uninoculated soil was greater due to the lack of bacterial inoculation, leading to a lesser and slower nitrification process (Table 6). The nitrification process can convert a lot of  $NH_4^+-N$  into  $NO_3^--N$ . In contrast to relatively heavy textured (clay loam) soil, (Gioacchini et al., 2002) observed that increased N leaching occurred in light textured (sandy loam) soil.

The soil treated with fertilizer alone leached more  $NO_3^--N$  compared to soil treated with PGPB, and with an increase in the rate of urea applications, the  $NO_3^--N$  leaching also rose. In the second pore volume of the incubation research,  $NO_3^--N$  leaching was found to be at its maximum because of the more concentrated urea in the uninoculated applied soil; increased  $NO_3^--N$  leaching was induced (Ma et al., 2019) than PGPB treated soil, which lower  $NO_3^--N$  resulted from the more urea even distribution throughout the soil. It was associated with increased  $NH_3$  volatilization and soil pH (Motasim et al., 2021). Unlike bacteria-treated soil, uninoculated soil lost more of the total N ( $NH_4^+-N$  and  $NO_3^--N$ ) through leaching (Table 6). The remaining total N was greater in the inoculated treatments; possibly, the soil can absorb more  $NH_4^+-N$ . The findings of this investigation indicate that the bacteria-treated soil could retain more  $NH_4^+-N$  and  $NO_3^--N$  concentrations, as a result, reduces loss of leaching due to more mineralization of N in the PGPB-treated soil and increased soil particle adsorption of  $NH_4^+-N$ .

## CONCLUSION

According to our research findings, the beneficial bacteria UPMRB9, along with 50% of N fertilizer from the recommended rate, prove to be a better fertilization combination, mainly due to the increased  $\text{NH}_4^+\text{-N}$  and  $\text{NO}_3^-\text{-N}$  concentrations and reduced loss of leaching, compared to the single urea fertilizer treatment. The findings provide the opportunity and benefits of a better NUE, lower N losses, and reduced input cost while keeping the environment safe. These preliminary findings should be validated with a series of glasshouse and field trials for further confirmation.

## ACKNOWLEDGEMENTS

The authors sincerely acknowledge grants of the Fundamental Research Grant Scheme (FRGS) (FRGS/1/2020/STG01/UPM/02/6) by the Ministry of Higher Education, Malaysia, and Putra Grant (GP-IPS/2022/9709700) by the Universiti Putra Malaysia, Malaysia. The authors are also grateful to the Bangabandhu Science and Technology Fellowship Trust, sponsored by the Ministry of Science and Technology, Government of the People's Republic of Bangladesh, Bangladesh.

## REFERENCES

- Abera, G., Wolde-meskel, E., Beyene, S., & Bakken, L. R. (2012). Nitrogen mineralization dynamics under different moisture regimes in tropical soils. *International Journal of Soil Science*, 7(4), 132-145. <https://doi.org/10.3923/ijss.2012.132.145>
- Ali-Tan, K. Z., Radziah, O., Halimi, M. S., Abdul Rahim, K. B., Abdullah, M., & Shamsuddin, Z. H. (2017). Growth and yield responses of rice cv. MR219 to rhizobial and plant growth-promoting rhizobacterial inoculations under different fertilizer-n rates. *Bangladesh Journal of Botany*, 46(1), 481-488.
- Almaz, M. G., Halim, R. A., Martini, M. Y., & Samsuri, A. W. (2017). Integrated application of poultry manure and chemical fertiliser on soil chemical properties and nutrient uptake of maize and soybean. *Malaysian Journal of Soil Science*, 21(1), 13-28.
- Bundy, L. G. (2001, November 27-December 6). *Managing urea-containing fertilizers*. [Paper presentation]. Proceedings of the Fertilizer Dealer Meeting, Madison, USA.
- Cardenas, L. M., Hatch, D. J., Scholefield, D., Jhurreca, D., Clark, I. M., Hirsch, P. R., Salazar, F., Rao-Ravella, S., & Alfaro, M. (2013). Potential mineralization and nitrification in volcanic grassland soils in Chile. *Soil Science and Plant Nutrition*, 59(3), 380-391. <https://doi.org/10.1080/00380768.2013.789395>
- Chapman, H. D. (1965). Cation-exchange capacity. In A. G. Norman (Ed.), *Methods of Soil Analysis: Part 2 Chemical and Microbiological Properties*, 9.2 (Vol. 9). Wiley Online Library. <https://doi.org/10.2134/agronmonogr9.2.c6>.
- Douglas, L. A., & Bremner, J. M. (1970). Extraction and colorimetric determination of urea in soils. *Soil Science Society of America Journal*, 34(6), 859-862. <https://doi.org/10.2136/sssaj1970.03615995003400060015x>

- Gioacchini, P., Nistri, A., Marzadori, C., Giovannini, C., Vittori Antisari, L., & Gessa, C. (2002). Influence of urease and nitrification inhibitors on N losses from soils fertilized with urea. *Biology and fertility of soils*, 36(2), 129-135. <https://doi.org/10.1007/s00374-002-0521-1>
- Heffer, P., & Prud'homme, M. (2016). *Short-term fertilizer outlook 2016–2017*. International Fertilizer Industry Association.
- Jones, J. B. (2001). *Laboratory Guide for Conducting Soil Tests and Plant Analysis* (Issue BOOK). CRC press.
- Junejo, N., Khanif, M. Y., Hanfi, M. M., Dharejo, K. A., & Wan, Z. W. Y. (2011). Reduced loss of NH<sub>3</sub> by coating urea with biodegradable polymers, palm stearin and selected micronutrients. *African Journal of Biotechnology*, 10(52), 10618-10625. <https://doi.org/10.5897/AJB10.394>.
- Keeney, D. R., & Nelson, D. W. (1982). Nitrogen-Inorganic forms. In A. L. Page (Ed.), *Methods of Soil Analysis, Agronomy Monograph 9, Part 2* (2nd ed., pp. 643-698). ASA, SSSA.
- Kira, O., Shaviv, A., & Dubowski, Y. (2019). Direct tracing of NH<sub>3</sub> and N<sub>2</sub>O emissions associated with urea fertilization approaches, using static incubation cells. *Science of The Total Environment*, 661, 75-85. <https://doi.org/10.1016/j.scitotenv.2019.01.128>
- Ladha, J. K., De Bruijn, F. J., & Malik, K. A. (1997). Introduction: Assessing opportunities for nitrogen fixation in rice-a frontier project. *Plant and Soil*, 194(1), 1-10. <https://doi.org/10.1023/A:1004264423436>
- LECO. (2018). *LECO Corporation, USA*. <https://www.leco.com/elemental-analysis>
- Laghari, S. J., Wahocho, N. A., Laghari, G. M., HafeezLaghari, A., MustafaBhabhan, G., & HussainTalpur, K. (2016). Role of nitrogen for plant growth and development: A review. *Advances in Environmental Biology*, 10(9), 209-219.
- Lichiheb, N., Myles, L., Personne, E., Heuer, M., Buban, M., Nelson, A. J., Koloutsou-Vakakis, S., Rood, M. J., Joo, E., Miller, J., & Bernacchi, C. (2019). Implementation of the effect of urease inhibitor on ammonia emissions following urea-based fertilizer application at a Zea mays field in central Illinois: A study with SURFATM-NH<sub>3</sub> model. *Agricultural and Forest Meteorology*, 269-270, 78-87. <https://doi.org/10.1016/j.agrformet.2019.02.005>
- Ma, Z., Yue, Y., Feng, M., Li, Y., Ma, X., Zhao, X., & Wang, S. (2019). Mitigation of ammonia volatilization and nitrate leaching via loss control urea triggered H-bond forces. *Scientific Reports*, 9(1), Article 15140. <https://doi.org/10.1038/s41598-019-51566-2>
- Mandal, S., Thangarajan, R., Bolan, N. S., Sarkar, B., Khan, N., Ok, Y. S., & Naidu, R. (2016). Biochar-induced concomitant decrease in ammonia volatilization and increase in nitrogen use efficiency by wheat. *Chemosphere*, 142, 120-127. <https://doi.org/10.1016/j.chemosphere.2015.04.086>
- Mariano, E., de Sant Ana Filho, C. R., Bortoletto-Santos, R., Bendassolli, J. A., & Trivelin, P. C. (2019). Ammonia losses following surface application of enhanced-efficiency nitrogen fertilizers and urea. *Atmospheric Environment*, 203, 242-251. <https://doi.org/10.1016/j.atmosenv.2019.02.003>
- Motasim, A. M., Samsuri, A. W., Sukor, A. S. A., & Adibah, A. M. (2021). Gaseous nitrogen losses from tropical soils with liquid or granular urea fertilizer application. *Sustainability*, 13(6), Article 3128. <https://doi.org/10.3390/su13063128>

- Okalebo, J. R., Gathua, K. W., & Paul, L. W. (2002). Soil bulk density and water holding capacity. In *Laboratory Methods of Soil and Plant Analysis: A Working Manual Second Edition* (pp.25-260). Sacred Africa.
- Omar, L., Ahmed, O. H., & Majid, N. M. A. (2015). Improving ammonium and nitrate release from urea using clinoptilolite zeolite and compost produced from agricultural wastes. *The Scientific World Journal*, 2015, Article 574201. <https://doi.org/10.1155/2015/574201>
- Puga, A. P., Grutzmacher, P., Cerri, C. E. P., Ribeiro, V. S., & de Andrade, C. A. (2020). Biochar-based nitrogen fertilizers: Greenhouse gas emissions, use efficiency, and maize yield in tropical soils. *Science of the Total Environment*, 704, Article 135375. <https://doi.org/10.1016/j.scitotenv.2019.135375>
- Richards, L. A., & Fireman, M. (1943). Pressure-plate apparatus for measuring moisture sorption and transmission by soils. *Soil Science*, 56(6), 395-404.
- Rochette, P., Angers, D. A., Chantigny, M. H., Gasser, M. O., MacDonald, J. D., Pelster, D. E., & Bertrand, N. (2013). NH<sub>3</sub> volatilization, soil concentration and soil pH following subsurface banding of urea at increasing rates. *Canadian Journal of Soil Science*, 93(2), 261-268. <https://doi.org/10.4141/cjss2012-095>
- Rochette, P., Angers, D. A., Chantigny, M. H., MacDonald, J. D., Gasser, M. O., & Bertrand, N. (2009). Reducing ammonia volatilization in a no-till soil by incorporating urea and pig slurry in shallow bands. *Nutrient Cycling in Agroecosystems*, 84(1), 71-80. <https://doi.org/10.1007/s10705-008-9227-6>
- Shan, L., He, Y., Chen, J., Huang, Q., & Wang, H. (2015). Ammonia volatilization from a Chinese cabbage field under different nitrogen treatments in the Taihu Lake Basin, China. *Journal of Environmental Sciences*, 38, 14-23. <https://doi.org/10.1016/j.jes.2015.04.028>
- Sharifuddin, H. A. H., Fauziah, I., & Zaharah, A. R. (1990). Technique of soil testing and plant analysis and their utilization for crop production in Malaysia. *Communications in Soil Science and Plant Analysis*, 21(13-16), 1959-1978. <https://doi.org/10.1080/00103629009368350>
- Teh, C. B. S., & Talib, J. (2006). *Soil and Plant Analyses Vol. I Soil Physics Analyses*. Department of Land Management, Faculty of Agriculture, Universiti Putra Malaysia.
- Wang, X., Xu, S., Wu, S., Feng, S., Bai, Z., Zhuang, G., & Zhuang, X. (2018). Effect of *Trichoderma viride* biofertilizer on ammonia volatilization from an alkaline soil in Northern China. *Journal of Environmental Sciences*, 66, 199-207. <https://doi.org/10.1016/j.jes.2017.05.016>
- Zadeh, F. S. (2010). *Sorptiob-desorption, degradation and leaching of napramide in selected malaysian soils* [Unpublish doctoral thesis]. University Putra Malaysia, Malaysia.
- Zhao, M., Tian, Y., Ma, Y., Zhang, M., Yao, Y., Xiong, Z., Yin, B., & Zhu, Z. (2015). Mitigating gaseous nitrogen emissions intensity from a Chinese rice cropping system through an improved management practice aimed to close the yield gap. *Agriculture, Ecosystems & Environment*, 203, 36-45. <https://doi.org/10.1016/j.agee.2015.01.014>
- Zuki, M. M. M., Jaafar, N. M., Sakimin, S. Z., & Yusop, M. K. (2020). N-(n-Butyl) thiophosphoric triamide (NBPT)-coated urea (NCU) improved maize growth and nitrogen use efficiency (NUE) in highly weathered tropical soil. *Sustainability*, 12(21), Article 8780. <https://doi.org/10.3390/su12218780>



## Chitosan Dissolution in [BMIM]Cl Ionic Liquid: An Optimisation and Bacterial Ecotoxicity Study

Mok Shue Yee<sup>1</sup>, Magaret Sivapragasam<sup>2</sup> and Maisara Shahrom Raja Shahrom<sup>2\*</sup>

<sup>1</sup>School of Postgraduate Studies, Research and Internationalisation (SPRINT), Faculty of Integrated Life Sciences, QUEST International University, 30250 Ipoh, Perak, Malaysia

<sup>2</sup>School of Integrated Sciences, Faculty of Integrated Life Sciences, QUEST International University, 30250 Ipoh, Perak, Malaysia

### ABSTRACT

Chitosan is formed from chitin deacetylation, but its insolubility remains challenging for industrial applications. An alternative would be employing Ionic Liquids (ILs) as a potential green solvent to dissolve chitosan. Hence, this research aims to study the optimum conditions of chitosan-[BMIM]Cl dissolution using Response Surface Methodology (RSM) and evaluate the ecotoxicity of chitosan-[BMIM]Cl mixture against Gram-positive and Gram-negative bacteria. Chitosan was obtained from heterogenous N-deacetylation of chitin using 50% sodium hydroxide solution at 100°C for 2.5 h. Chitosan dissolution in [BMIM]Cl was optimised using Central Composite Design (CCD) via RSM based on three independent factors: temperature, initial chitosan loading and dissolution time. Ecotoxicity of chitosan-[BMIM]Cl was evaluated using broth microdilution test against *Escherichia coli* and *Staphylococcus aureus*. Chitosan with a degree of deacetylation (DD) of 83.42% was obtained after three successive alkali treatments. Fourier Transform Infrared Spectroscopy (FTIR) revealed the presence of free hydroxyl groups, additional amino groups, and reduced C=O and C-H stretch intensity, indicating successful chitin deacetylation. The regression model for chitosan dissolution in [BMIM]Cl was significant ( $p < 0.05$ ) with a non-significant lack of fit ( $p > 0.05$ ). The optimised conditions to dissolve chitosan in [BMIM]Cl was 130°C, 1 wt. % and 72 h with a mean relative error of 1.78% and RMSE of 5.0496 wt. %. The toxicity of 10 wt. % chitosan-[BMIM]Cl mixture was “relatively harmless” ( $EC_{50} > 1000$  mg/L) with an  $EC_{50}$  value of 3.1 wt. % for *Escherichia coli* and 3.2 wt. % for *Staphylococcus aureus*.

### ARTICLE INFO

#### Article history:

Received: 10 November 2022

Accepted: 10 May 2023

Published: 09 October 2023

DOI: <https://doi.org/10.47836/pjst.31.6.21>

#### E-mail addresses:

shueyee.mok@qiu.edu.my (Mok Shue Yee)

magaret\_62@yahoo.co.uk (Magaret Sivapragasam)

maisarahshahrom@hotmail.com (Maisara Shahrom Raja Shahrom)

\* Corresponding author

**Keywords:** Bacterial ecotoxicity, chitosan, dissolution, ionic liquids, optimisation

## INTRODUCTION

The seafood industry generates approximately  $10^6$  tonnes of seafood waste annually, the major source of chitin extraction, particularly from crustaceans such as shrimp and crab shell residues (Schmitz et al., 2019). Chitin is a natural polysaccharide first discovered in 1811 by Henri Braconnot that can be found abundantly in crustaceans, the exoskeleton of arthropods and the cell walls of fungi and yeast (Rinaudo, 2006).

Chitin is the second most abundant biomass found naturally in the environment after cellulose. Like cellulose, chitin is highly insoluble and has a low chemical reactivity. In recent years, biorefinery has been one of the most important aspects of the circular bioeconomy, referring to an ingenious and efficient route to fully utilise the accessible biomass resources (IEA Bioenergy, 2020) for the following reasons: cost-effectiveness, mitigation of environmental impacts, and optimising the impacts on socio-economic development. Hence, chitin biomass is the perfect candidate due to its high abundance, continuous supply, ease of accessibility, and versatility (Manzanares, 2020). Partial deacetylation of chitin under alkaline conditions produces chitosan, the most important chitin derivative widely used in the industry (Elieh-Ali-Komi & Hamblin, 2016).

Chitosan is a linear polysaccharide comprising monomers of N-acetyl D-glucosamine and D-glucosamine. The properties of chitosan, such as its biodegradability, biocompatibility, toxic-free, film-forming and antibacterial property, encourages the usage of chitosan in various fields such as agricultural (Zhang et al., 2022), biomedical (Zhao et al., 2018), cosmetics (Aranaz et al., 2018), beverages (Liu et al., 2022), water and waste treatment (Morin-Crini et al., 2019). Chitosan has extensive intermolecular and intramolecular hydrogen bonds that contribute to the poor solubility of chitosan. It is insoluble in neutral or basic solutions but readily dissolved in dilute acidic solutions (Rinaudo, 2006). Chitosan is usually dissolved in 0.1 M acetic acid, but it is also soluble in organic acids such as formic acid, lactic acid, L-ascorbic acid and inorganic acids such as hydrochloric acid and phosphorous acid (Roller & Covill, 1999; Romanazzi et al., 2009). However, the industrial applications of chitosan are still scarce due to its insolubility in most conventional organic solvents. In addition, conventional solvent systems are highly volatile, corrosive, toxic and have limited reusability (Sun, Tian et al., 2014). Therefore, more environmentally friendly solvents to dissolve chitosan is most required.

Ionic liquids (ILs) have been used extensively as an alternative solvent in chemical reactions due to their negligible vapour pressure, greater thermal stability, and highly versatile nature (Claros et al., 2010). The physicochemical properties of ILs can be altered by selecting an appropriate anion or cation of ILs, making them useful in a wider range of applications (Thomas & Marvey, 2016). Previous studies have explored the usage of ILs in the context of biomass processing, such as the fractionation of softwood and wheat straw into sugars such as glucose and pentose, respectively, as well as facilitating the separation



between lignin and cellulose (da Costa Lopes et al., 2018; Gschwend et al., 2019). ILs had been shown capable of dissolving natural polymers such as cellulose (Swatloski et al., 2002; Wu et al., 2004), carbohydrates (Forsyth et al., 2002), chitin (Wang et al., 2010) and chitosan (Zhuang et al., 2020) because ILs have outstanding solvation potential and the role of anion within ILs to disrupt extensive hydrogen bonds within these macromolecules (Rosatella et al., 2009; Zakrzewska et al., 2010).

ILs are widely recognised as green solvents due to their insignificant vapour pressure. However, being non-volatile does not mean that ILs are toxic-free (Lei et al., 2017). Therefore, the ecotoxicity of ILs has been assessed by several researchers (Egorova & Ananikov, 2014; Bubalo et al., 2017; Sivapragasam et al., 2019; Sivapragasam et al., 2020). ILs are very soluble in water, readily dissociate into their respective ions and migrate easily into an aqueous system. Accumulation in water systems may directly affect aquatic organisms and indirectly affect higher organisms, such as humans, upon consumption of contaminated fish. Therefore, it is important to evaluate the ecotoxicity of ILs to determine the value of  $EC_{50}$ , defined as the effective concentration that inhibits the growth of organisms by 50%, which can be achieved using microorganisms due to shorter generation time, faster growth rate and easily available (Sivapragasam et al., 2020).

The present study used RSM to study the optimisation of chitosan dissolution in ILs, [BMIM]Cl. The optimised chitosan dissolution was subjected to ecotoxicity assessment to establish the toxicity of the chitosan-ILs mixture on Gram-positive bacteria and Gram-negative bacteria, *Staphylococcus aureus* and *Escherichia coli*. From this research, the optimised conditions to dissolve chitosan in [BMIM]Cl was established based on three factors (temperature, initial chitosan loading and dissolution time) and the ecotoxicity of chitosan-[BMIM][Cl] was determined.

The impact of this research helps realise a few of the Sustainable Development Goals (SDGs) initiated by the United Nations, which are the sixth, fourteenth and fifteenth goals, which are Clean Water and Sanitation, Life Below Water and Life on Land, respectively. Complete biomass dissolution is desirable for the valorisation and fractionation of biomass macromolecules into their respective constituents, thus enhancing the competency and economic viability of biorefinery products (Rodríguez, 2021), such as the dissolution of chitosan in ILs for various applications such as glucose biosensor,  $CO_2/N_2$  separation and the adsorption of malachite green dye from aqueous solutions (Zhang et al., 2013; Santos et al., 2016; Naseeruteen et al., 2018).

## MATERIALS AND METHODS

Coarse chitin flakes from shrimp shells, practical grade ( $\geq 95\%$  acetylated) and pure silicone oil (cSt 1000) were purchased from Sigma-Aldrich (Missouri, United States) and used without further purification. Sodium hydroxide (NaOH) pellets, A.R grade ( $\geq 96\%$ ) was

purchased from Bendosen (Selangor, Malaysia). Dimethyl sulfoxide (DMSO), A.R grade ( $\geq 99.8\%$ ), was purchased from System Chemicals (Selangor, Malaysia). Acetone, A.R grade ( $\geq 99.7\%$ ), was purchased from QReC (Selangor, Malaysia). Mueller-Hinton broth and potassium bromide KBr powder were purchased from Sisco Research Laboratories Pvt. Ltd (Mumbai, India) and PIKE Technologies (Wisconsin, United States), respectively. KBr powder was dried at  $100^\circ\text{C}$  for 2 h before its use. 1-butyl-3-methylimidazolium chloride, [BMIM]Cl (0.85%  $\text{H}_2\text{O}$ ) was obtained from the Centre of Research in Ionic Liquids, Universiti Teknologi PETRONAS, Malaysia, as a gift.

### Deacetylation of Chitin

Deacetylation of chitin was performed using the protocol described by El Knidri et al. (2016). Chitosan was obtained by deacetylating chitin flakes from shrimp shells with 50% (w/v) concentrated NaOH at  $100^\circ\text{C}$  for 2 h 30 min, using a ratio of chitin to NaOH of 1:20 (g:mL). After the reaction, the product was washed with distilled water until the pH of chitosan became neutral. Partial deacetylation of chitosan was repeated another two times to obtain chitosan with a higher deacetylation degree (DD). Chitosan was dried in an oven at  $80^\circ\text{C}$  for 24 h after repeated alkali treatments.

### Characterisation of Chitosan Using Fourier Transform Infrared (FTIR) Spectroscopy

Chitin and chitosan were characterised using FTIR (Bruker Alpha II, Massachusetts, United States) in the  $4000$  to  $650\text{ cm}^{-1}$  range using the KBr pellet method (Poerio et al., 2021). For each sample, 16 scans were performed with a resolution of  $4\text{ cm}^{-1}$ . The DD of chitosan was calculated using FTIR using the absorption band at  $1320$  and  $1420\text{ cm}^{-1}$ , corresponding to a characteristic band of acetylated amine or amide and a reference band, respectively (Brugnerotto et al., 2021). The deacetylation degree, DD % of chitosan, was calculated using Equation 1, where  $A_{1320}$  and  $A_{1420}$  are the absorption bands at  $1320\text{ cm}^{-1}$  and  $1420\text{ cm}^{-1}$  respectively.

$$DD\% (\%) = 100\% - \frac{\frac{A_{1320}}{A_{1420}} - 0.3822}{0.03133} \quad (1)$$

### Optimisation of Dissolution Parameters Using Response Surface Methodology (RSM)

Parameters for chitosan dissolution in [BMIM]Cl were optimised via RSM using Design Expert version 12.0.3.0 (Stat-Ease, Minnesota, United States). This study explored the effects of three independent variables towards chitosan dissolution in [BMIM]Cl using the CCD model. The three independent variables were temperature ( $X_1$ ,  $90^\circ\text{C}$  to  $130^\circ\text{C}$ ), initial chitosan loading ( $X_2$ , 1 wt. % to 7 wt. %) and dissolution time ( $X_3$ , 24 h to 72 h).

The highest and lowest values for each variable were selected based on previous studies by Sun, Xue et al. (2014), Islam et al. (2015) and Xu et al. (2016). The dependent variable was dissolution percentage (Y, wt. %). A total of 20 randomly suggested experiments generated by the CCD model were performed. Table 1 shows the level of parameters of chitosan dissolution in [BMIM]Cl. The relative error calculation for the RSM model was carried out by conducting the optimised conditions in triplicates.

Table 1  
Level of parameters for chitosan dissolution in [BMIM]Cl using CCD model

Variables	Coding	Unit	Coded Levels of Experimental Factors		
			-1	0	1
Temperature	$X_1$	°C	90	110	130
Initial chitosan loading	$X_2$	wt. %	1	4	7
Time of dissolution	$X_3$	h	24	48	72

### Dissolution of Chitosan in ILs, [BMIM]Cl

The dissolution of chitosan in [BMIM]Cl was performed according to the methodology outlined by Sun et al. (2009) using parameters suggested by RSM. Approximately 2 g of [BMIM]Cl was added to a universal bottle and immersed in an oil bath with a temperature instability of  $\pm 2^\circ\text{C}$ . Prior to dissolution, chitosan was dried in an oven at  $80^\circ\text{C}$  for 24 h to remove moisture. An appropriate amount of chitosan (wt. %) was added and stirred continuously at 500 rpm, and the RSM model suggested the temperature and dissolution time.

Undissolved chitosan was removed according to procedures described by Sun et al. (2009). Briefly, 10 mL of DMSO was added to the universal bottle containing undissolved precipitate and chitosan-ILs solution. The solution was vortexed vigorously and centrifuged at 100 g for 10 min. The supernatant was kept in a separate Falcon tube for regeneration of dissolved chitosan. The precipitate was washed again with DMSO 3 times and subsequently washed with 20 mL of distilled water for another 3 times. The precipitate was dried in an oven at  $60^\circ\text{C}$  for 24 h and weighed after drying. Equation 2 was used to compute the dissolution percentage of chitosan, where  $w_o$  and  $w_p$  are the initial weight of chitosan and undissolved chitosan, respectively.

$$\text{Dissolution \% (wt. \%)} = \frac{[W_o - W_p]}{W_o} \times 100 \quad (2)$$

### Regeneration of Dissolved Chitosan

Chitosan dissolved in [BMIM]Cl was regenerated using procedures described in Rahim et al. (2018). The chitosan-ILs solution was mixed with 15 mL of acetone (9:1) and vortexed vigorously. The mixture was centrifuged at 4000 rpm for 15 min, and the supernatant was

discarded. The pellet formed was washed again with 15 mL of acetone solution (9:1), vortexed and centrifuged at 4000 rpm for 15 min. The precipitate was washed another 3 times and left to air dry in a fume hood to remove residual acetone solution from the regenerated chitosan. Regenerated chitosan was dried in an oven at 60°C for 24 h.

### **Characterisation of Chitosan-IL Using Fourier Transform Infrared (FTIR) Spectroscopy**

Chitosan (pure) and pre-treated chitosan (after dissolution in ILs) were analysed using FTIR Spectroscopy (Bruker Alpha II, Massachusetts, United States) to check any chemical changes that occurred during the dissolution. Chitosan-ILs solution was analysed to see the incorporation of chemical compounds of ILs and chitosan. FTIR spectra were measured in the 4000-650  $\text{cm}^{-1}$  range using the KBr pellet method adapted from Poerio et al. (2021) with some modifications. Sample and KBr were mixed in a ratio of 1:100 and placed into a pellet die to form a transparent pellet. For each sample, 16 scans were taken with a resolution of 4  $\text{cm}^{-1}$ .

### **Broth Microdilution Method**

Ecotoxicity of the chitosan-ILs mixture was assessed using broth microdilution method according to standard procedure CLSI-M07-A9, 2008, developed by Clinical and Laboratory Standard Institute (CLSI), USA. Chitosan-ILs solution was diluted using two-fold serial dilution and added to each 96-well plate. Two-fold chitosan-ILs solutions were added to each well from 100,000 ppm (10 wt. %) to 200 ppm (0.020 wt. %). Bacterial suspensions of *Staphylococcus aureus* ATCC 12600 and *Escherichia coli* ATCC 8739 were prepared by transferring a loopful of colonies from a 24-hour bacteria culture to Mueller-Hinton broth. About 100  $\mu\text{L}$  of *Staphylococcus aureus* and *Escherichia coli* dilutions were added into each well containing 100  $\mu\text{L}$  of chitosan-ILs mixture in a separate microdilution plate. About 100  $\mu\text{L}$  of bacteria suspension was used as blank and dispensed into the well A1. Microdilution plates were incubated at 37°C for 24 h, and the absorbance value of each well was determined using a microplate reader (CYBERLAB™ Cyber ELISA-R01, Millbury, United States) at a wavelength of 550 nm. Minimum inhibitory concentration (MIC) and  $\text{EC}_{50}$  values of chitosan-ILs solution were determined by plotting the absorbance values in a graph generated by Prism version 9.0.0 (GraphPad Software, San Diego, California).

## **RESULTS AND DISCUSSIONS**

### **Deacetylation of Chitin into Chitosan**

Alkaline deacetylation of chitin into chitosan was carried out using 50% NaOH at 100°C for 2.5 h for three successive alkali treatments. Deacetylation of chitin was represented by Equation 3, where the acetamide group in chitin underwent hydrolysis in the presence

of strong NaOH and elevated temperature to form an acetyl group and a reactive amino group, the key functional group that differentiates chitin from chitosan (Fatima, 2020).

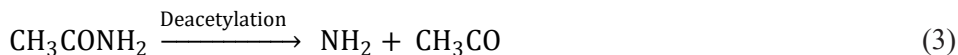


Figure 1 shows chitin flakes before deacetylation and chitosan obtained after partial deacetylation. Chitin flakes before deacetylation were larger (0.4–1.0 cm) and yellowish. Chitosan obtained after three successive alkali treatments was smaller (0.1–0.3 cm) and white, which is in accordance with Kusuma et al. (2015) that chitosan produced has a more pronounced white colour than chitin. Chitosan produced was also odourless and present in the crystalline flakes, which was also observed by Ahing and Wid (2016).

Tamzi et al. (2020) corroborate findings where chitin and chitosan prepared from shrimp (*Panaeusmonodon monodon*), and crab shells (*Scylla serrata*) were yellowish-white and off-white, respectively—the change in colour from yellowish-white to brighter was related to removing acetyl groups during chitin deacetylation.

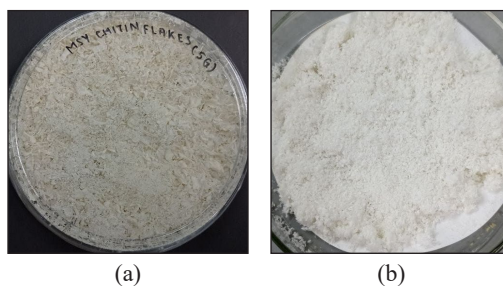


Figure 1. (a) Chitin flakes before deacetylation; (b) and chitosan obtained after three successive alkali treatments

**Characterisation of Chitin and Chitosan Using FTIR.** The structure of chitin and chitosan was analysed by identifying the functional groups and bonds obtained from the spectrum generated using FTIR. The functional groups present in chitin are hydroxyl group (-OH), acetamide group (-CH<sub>3</sub>CONH) and an ether group (C-O-C) between neighbouring glucosamine residues (Elieh-Ali-Komi & Hamblin, 2016). Figure 2 shows the transmittance spectrum of chitin. A strong, broad peak at 3444 cm<sup>-1</sup> represented the O-H stretch of chitin, indicating the presence of a hydroxyl group in the structure of chitin, which was also observed by Puspawati and Simpen (2010). The sharp peak at 3106 cm<sup>-1</sup> was attributed to the N-H stretch. Three peaks recorded at 2961, 2932, and 2891 cm<sup>-1</sup> were due to sp<sup>3</sup> C-H stretch, previously reported by Kusuma et al. (2015) and Matute et al. (2013). The peak at 1655 cm<sup>-1</sup> overlapped the C=O stretch and N-H bend, the characteristic band of amide I (Rumengan et. al., 2014). The peak at 1560 cm<sup>-1</sup> was due to N-H in-plane bend and C-N stretch, a characteristic band of amide II in secondary amide. The 1280 to 1070 cm<sup>-1</sup> peaks were due to C-O-C stretch (Puspawati & Simpen, 2010; Akakuru et al., 2018).

The functional groups that were present in partially deacetylated chitosan are hydroxyl group (-OH), acetamide group (-CH<sub>3</sub>CONH), amino group (-NH<sub>2</sub>) and ether group (C-O-C) between neighbouring glucosamine residues (Akakuru et al., 2018). Figure 3 shows the

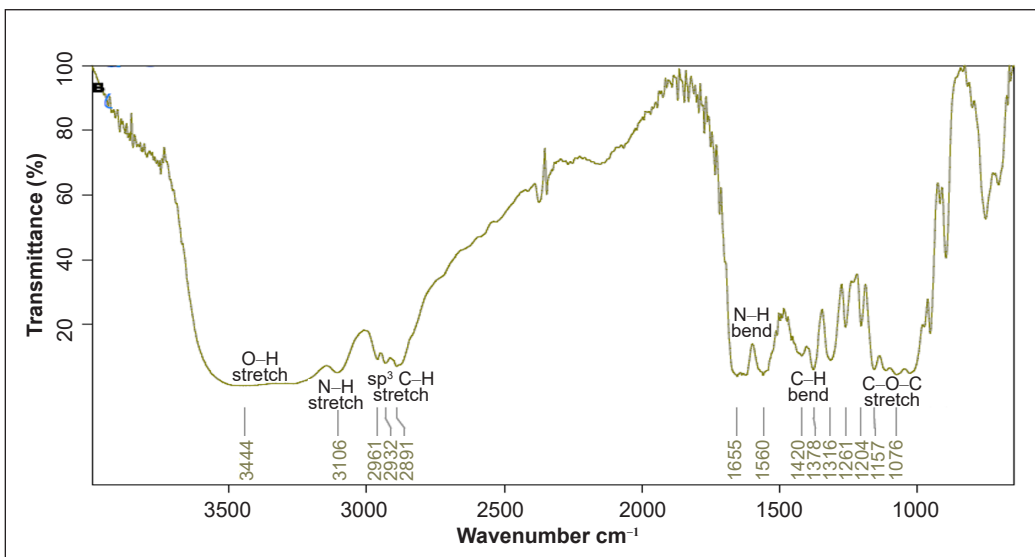


Figure 2. FTIR transmittance spectrum generated by chitin

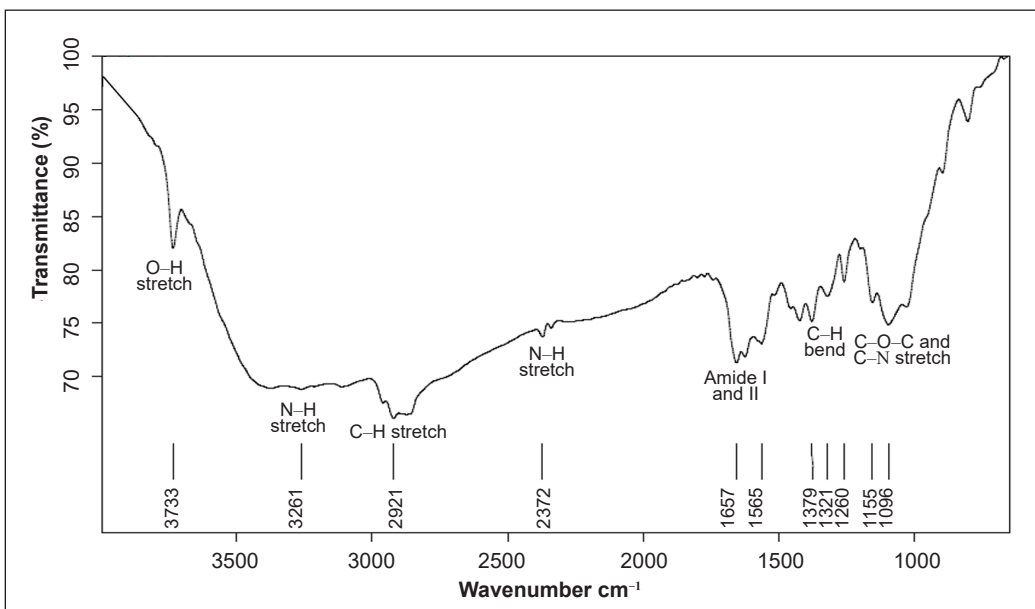


Figure 3. FTIR transmittance spectrum generated by chitosan

transmittance spectrum of chitosan obtained from partial deacetylation of chitin. The sharp peak at  $3733\text{ cm}^{-1}$  was due to the stretch of the free OH group. The peak at  $3261$  and  $2372\text{ cm}^{-1}$  was due to the N-H stretch, as Matute et al. (2013) reported. The peak at  $2921\text{ cm}^{-1}$  was attributed to C-H stretch in the aliphatic compound, particularly symmetric  $\text{CH}_3$  and asymmetric  $\text{CH}_2$  (Palpandi et al., 2009). The peak at  $1657$  and  $1565\text{ cm}^{-1}$  was caused by

the absorption of amide I and II bands, respectively. Amide I band still appears in the FTIR spectrum because chitin was not completely deacetylated to form chitosan with a DD of 100 %. Three peaks recorded at 1260, 1155 and 1096  $\text{cm}^{-1}$  were due to C-O and C-N stretch (Kusuma et al., 2015).

Several peaks in the FTIR spectrum of chitin and chitosan can be used to distinguish between the functional groups in chitin and chitosan. The hydroxyl group in chitosan is a free hydroxyl group attributed by a sharp peak at 3733  $\text{cm}^{-1}$ , while the hydroxyl group in chitin is bonded to hydrogen, attributed by the peak of 3444  $\text{cm}^{-1}$ . One peak was observed at 3106  $\text{cm}^{-1}$  due to N-H stretch in chitin, but there were two peaks at 3261 and 2372  $\text{cm}^{-1}$  caused by N-H stretch in chitosan due to additional amino groups. In addition, C-N stretch was also observed in the range of 1250 to 1020  $\text{cm}^{-1}$  in the FTIR spectrum of chitosan but absent in the chitin spectrum. Lastly, the absorption of infrared radiation by C-H stretch and amide I band in chitin was greater than that in chitosan as there were more acetyl ( $-\text{C}_2\text{H}_3\text{O}$ ) and acetamide groups respectively in the crystalline chain of chitin. Larger absorption at 2885  $\text{cm}^{-1}$  in chitin was due to higher C-H bonds (Rumenagan et al., 2014). In our study, the peak at 2891  $\text{cm}^{-1}$  attributed to C-H stretch in chitin disappeared in the FTIR spectrum of chitosan after partial deacetylation of chitin. It correlated well with the findings from Ahyat et al. (2017), indicating a successful elimination of acetyl group in the chemical structure of chitin during deacetylation. Dennis et al. (2016) reported reduced peaks due to the loss of acetyl groups in their FTIR spectrum- which correlates well with this study.

**Determination of Degree of Deacetylation of Chitosan Using FTIR.** DD was obtained from FTIR using the  $A_{1320}/A_{1420}$  tallies ratio with the degree of deacetylation obtained using  $^1\text{H}$  and  $^{13}\text{C}$ NMR. The absorption band at 1320 and 1420  $\text{cm}^{-1}$  was unaffected by the humidity of the sample (Czechowska-Biskup et al., 2012). Figure 4 shows the absorbance spectrum of chitosan obtained from the heterogenous N-deacetylation of chitin flakes. Based on Figure 4, the absorbance at 1320  $\text{cm}^{-1}$  and 1420  $\text{cm}^{-1}$  was 0.11 and 0.122, respectively.

$$DD\% (\%) = 100\% - \frac{\frac{A_{1320}}{A_{1420}} - 0.3822}{0.03133} \quad (4)$$

$$DD\% = 100\% - \frac{\frac{0.11}{0.122} - 0.3822}{0.03133} = 83.42\% \quad (5)$$

Based on Equation 4, proposed by Brugnerotto et al. (2001), the DD of chitosan from this study was 83.42%, as shown in Equation 5. With a DD of 83.42%, it has 83.42% of the amino group and 16.58% of the acetyl group in its chain.

Based on the FTIR spectrums obtained from both chitin and chitosan samples, it can be confirmed that chitosan was successfully synthesised ( $DD \geq 60\%$ ) from heterogenous

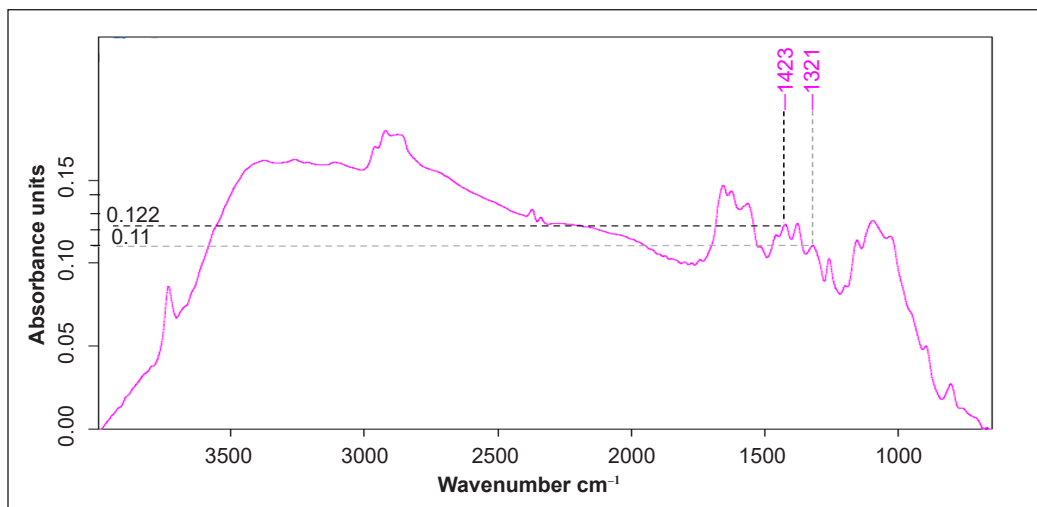


Figure 4. FTIR absorbance spectrum generated by chitosan

N-deacetylation of chitin flakes from shrimp shell using 50% concentrated NaOH solution. Synthesised chitosan was used in RSM to optimise the dissolution of chitosan in [BMIM]Cl based on three independent factors: temperature, initial chitosan loading and dissolution time.

### Optimisation of Chitosan Dissolution Using Response Surface Methodology (RSM)

RSM was applied to optimise the dissolution of chitosan in [BMIM]Cl. This study's experiment design was CCD based on three independent factors: temperature, initial chitosan loading and dissolution time. The suggested experimental runs generated by the RSM model and experimental results are shown in Table 2. The highest dissolution percentage was obtained in standard run 6 with a value of 95 wt. % ( $X_1 = 130^\circ\text{C}$ ,  $X_2 = 1$  wt. %,  $X_3 = 72$  h), followed by standard run 2 with a dissolution percentage of 94.5% ( $X_1 = 130^\circ\text{C}$ ,  $X_2 = 1$  wt. %,  $X_3 = 24$  h). The lowest dissolution percentage of 17.79 wt. % was obtained in standard run 3 ( $X_1 = 90^\circ\text{C}$ ,  $X_2 = 7$  wt. %,  $X_3 = 24$  h).

Design-Expert version 12.0.3.0 was employed to study the experimental data's regression analysis and plot the response surface curves. The statistical parameters were evaluated using analysis of variance (ANOVA), and the fitness of the regression model was evaluated using a lack of fit test, as demonstrated in Table 3. A model will fit the experimental data well if the regression model is significant and the lack of fit test is not significant with a 95% confidence level.

According to Table 3, the regression model for the dissolution percentage of chitosan was significant, with a F-value of 99.24 and a p-value  $< 0.0001$ . The model F-value of 99.24 indicated that there was only a 0.01% chance that the model F-value could occur due to noise. All the independent variables tested in this study were significant, with p-value  $< 0.05$ . The



lack of fit test was insignificant, with an F-value of 2.11 and a p-value of 0.2114, respectively. Significant regression and non-significant lack of fit test indicated that the experimental data fits the data well and can be used to optimise the dissolution of chitosan in [BMIM]Cl. The experimental data was fitted into a linear model, suggested by the RSM software. It showed that there were no interactions between the independent variables.

Table 2  
*Experimental design for dissolution of chitosan in [BMIM]Cl generated by RSM*

Standard	Run	Factor 1 $X_1$ : Temperature (°C)	Factor 2 $X_2$ : Initial Chitosan Loading (wt. %)	Factor 3 $X_3$ : Dissolution Time (h)	Response Dissolution Percentage (wt. %)
1	20	90	1	24	71.500
2	7	130	1	24	94.500
3	14	90	7	24	17.790
4	5	130	7	24	20.640
5	18	90	1	72	89.500
6	15	130	1	72	95.000
7	9	90	7	72	27.570
8	11	130	7	72	43.210
9	8	90	4	48	50.500
10	2	130	4	48	49.750
11	4	110	1	48	83.000
12	1	110	7	48	30.070
13	16	110	4	24	45.000
14	12	110	4	72	66.250
15	13	110	4	48	59.320
16	6	110	4	48	60.625
17	19	110	4	48	55.750
18	3	110	4	48	67.250
19	17	110	4	48	55.750
20	10	110	4	48	60.250

Table 3  
*Analysis of variance (ANOVA) for dissolution percentage*

Source	Sum of Squares	df	Mean Square	F-value	p-value	Remarks
Model	9390.20	3	3130.07	99.24	< 0.0001	Significant
$X_1$ : Temperature	213.81	1	213.81	6.78	0.0192	
$X_2$ : Initial Chitosan Loading	8656.54	1	8656.54	274.45	< 0.0001	
$X_3$ : Dissolution Time	519.84	1	519.84	16.48	0.0009	
Residual	504.67	16	31.54			
Lack of Fit	415.25	11	37.75	2.11	0.2114	Not significant
Pure Error	89.42	5	17.88			
Cor Total	9894.87	19				

Table 4 shows the fit statistics of the regression model for the dissolution percentage of chitosan in [BMIM]Cl. The adequacy of the model was determined using the coefficient determination value,  $R^2$ . The  $R^2$  value of the regression model was 0.9490, suggesting a good correlation between experimental and predicted values. Adjusted  $R^2$  measures the variation of the mean obtained from the model. Predicted  $R^2$  refers to the  $R^2$  value estimated from the regression model (Behera et al., 2018). The adjusted and predicted  $R^2$  value was 0.9394 and 0.9155, respectively, with a difference of only 0.0239, indicating that the  $R^2$  predicted from the regression model agreed reasonably with the adjusted  $R^2$  value. The actual and predicted values for dissolution percentage are as per Figure 5, which showed a reasonably good response estimate and indicated the model's good performance.

Signal to noise ratio was calculated by determining the value of adequate precision. Adequate precision greater than 4 is desirable and can be utilised to navigate design space. The adequate precision obtained from this regression model is 32.8517, greater than 4. Therefore, the regression model can predict the dissolution percentage of chitosan in [BMIM]Cl.

Figures 6, 7 and 8 show the contour plots for dissolution percentage at 24, 48 and 72 h dissolution times, respectively. From Figures 6, 7 and 8, the dissolution of chitosan increases with temperature and dissolution time but decreases with initial chitosan loading.

Table 4  
Fit statistics for dissolution percentage

Standard Deviation	5.62	$R^2$	0.9490
Mean	57.16	<b>Adjusted <math>R^2</math></b>	0.9394
C.V. %	9.83	<b>Predicted <math>R^2</math></b>	0.9155
		<b>Adequate Precision</b>	32.8517

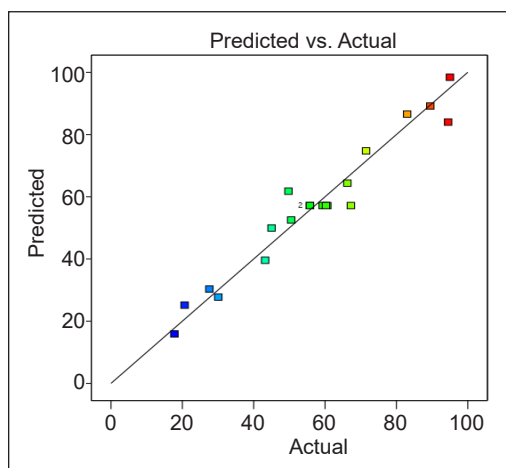


Figure 5. Actual and predicted values for dissolution percentage

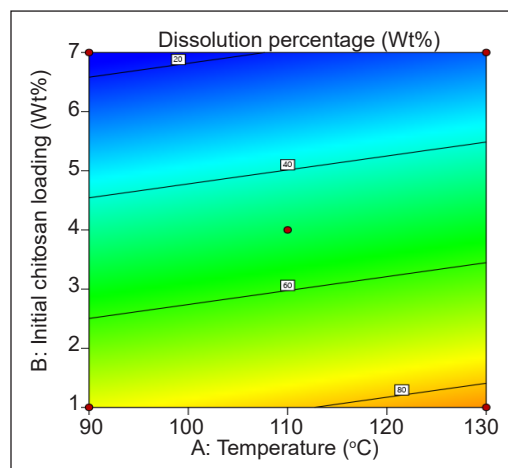


Figure 6. Contour plots at a dissolution time of 24 h

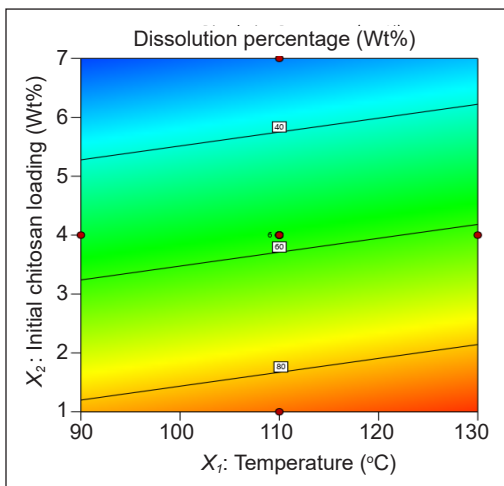


Figure 7. Contour plots at a dissolution time of 48 h

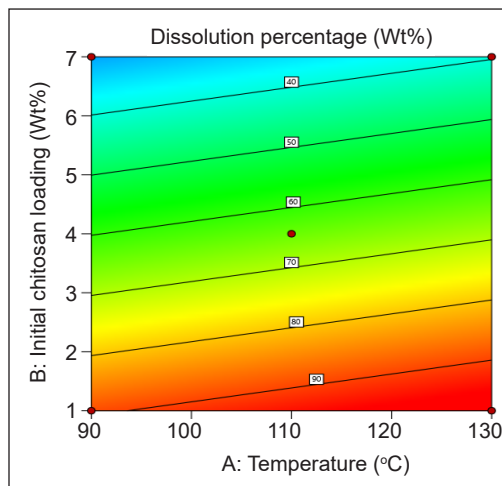


Figure 8. Contour plots at a dissolution time of 72 h

**Effect of Temperature on Dissolution Percentage of Chitosan in [BMIM]Cl.** Chitosan dissolution in [BMIM]Cl increases with 90 to 130°C temperature was relatively the least important among the tested variables that affected the dissolution percentage of chitosan, with the smallest F-value of 6.78. Increasing the temperature decreased the viscosity of [BMIM]Cl and accelerated the swelling of chitosan and mixing of chitosan-[BMIM]Cl (Tan & Lee, 2012). The increase in temperature also caused hydrogen bonds within chitosan to be partially disrupted. The effect of temperature on the dissolution of chitosan in [BMIM][Ac] has been studied by Chen et al. (2011), who observed that chitosan solubility increased with increasing temperatures. Chitosan solubility in [BMIM][Ac] at 150°C (14.4 wt. %) was enhanced by 9 times that at 70°C (1.6 wt. %). Enhanced chitosan dissolution showed that a temperature rise had partially disrupted some of the hydrogen bonds. Sun, Tian et al. (2014) reported that relatively high temperatures improved chitosan dissolution by accelerating the evaporation of remaining water from the ILs, which acted as an anti-solvent during the solubilisation reaction. They also observed that a temperature increment by 10°C decreased the viscosity of ILs by half, with a greater dissolving ability of chitosan in ILs.

**Effect of Initial Chitosan Loading on Dissolution Percentage of Chitosan in [BMIM]Cl.** Initial chitosan loading is inversely proportional to the dissolution of chitosan in [BMIM]Cl. Initial chitosan loading was the most important variable that affected the dissolution percentage of chitosan due to a high F-value of 274.45. The ratio of biopolymer to ILs strongly impacted the dissolution reaction. At lower chitosan loading, chitosan was more dispersed, facilitating the diffusion of [BMIM]Cl into the crystalline region of chitosan, subsequently increasing the dissolution rate and dissolution percentage due to enhanced frequency of effective collisions between chitosan and ILs (Chowdhury et al., 2014). Similar

findings had been reported by Sun et al. (2009) by dissolving various amounts of wood in [EMIM][Ac] from 4 wt. % to 10 wt. %. They observed that as the initial wood loading increases, a lower percentage of wood was dissolved in the ILs from 99.5% in 4 wt. % of the wood in [EMIM][Ac] to 40% in 10 wt. % of wood in [EMIM][Ac].

**Effect of Dissolution Time on Dissolution Percentage of Chitosan in [BMIM]Cl.** As the dissolution time increases, the dissolution percentage of chitosan increases, represented by an upward slope. Dissolution time was the second most important variable after initial chitosan loading, with a F-value of 16.48. Longer dissolution time, they encouraged the diffusion of ILs into the pores of the biomass matrix, improving the dissolution of chitosan in [BMIM]Cl (Ma et al., 2019). Wang et al. (2011) reported the enhancement in the rate of dissolution and regeneration of wood samples in [AMIM]Cl with the increase in reaction time. Pine wood's dissolution and regeneration rates increased from 19% to 26% and 9% to 19 %, respectively, when dissolution time was prolonged from 6 h to 24 h.

**Optimisation of Chitosan Dissolution in [BMIM][Cl].** Optimisation of chitosan dissolution was performed via numerical optimisation in Design-Expert software. The final equation in terms of actual factors for dissolution percentage ( $Y$ , wt. %) was shown in Equation 6, where  $X_1$ ,  $X_2$  and  $X_3$  refer to temperature ( $^{\circ}\text{C}$ ), initial chitosan loading (wt. %) and dissolution time (h), respectively.

$$\text{Dissolution Percentage } (Y, \text{ wt. } \%) = 56.53858 + 0.2312X_1 - 9.80733X_2 + 0.300417X_3 \quad (6)$$

To find the best conditions to dissolve chitosan in [BMIM]Cl, all three independent variables, temperature ( $X_1$ ,  $^{\circ}\text{C}$ ), initial chitosan loading ( $X_2$ , wt. %) and dissolution time ( $X_3$ , h), were set within the range. The response variable, dissolution percentage ( $Y$ , wt. %), was set at maximum values. Out of 100 solutions suggested by RSM, solution 1 ( $X_1 = 130^{\circ}\text{C}$ ,  $X_2 = 1$  wt. % and  $X_3 = 72$  h) was chosen due to the highest dissolution percentage of 98.417 wt. % with desirability of 1.000.

The regression model for the dissolution percentage of chitosan was verified by calculating the relative error and root mean square error (RMSE). The relative error of the regression model for dissolution percentage was calculated by carrying out the optimised solution in triplicates and computed using Equation 7.

$$\text{Relative error } (\%) = \frac{\text{Predicted value} - \text{Experimental value}}{\text{Predicted value}} \times 100 \% \quad (7)$$

The relative error of the three runs was shown in Table 5 and was in the range of 0.42 to 3.47%. The mean of relative error for the regression model was 1.78%, indicating

Table 5  
Relative error for dissolution percentage

Independent Variables			Dissolution Percentage (wt. %)		Relative Error (%)
$X_1$ (°C)	$X_2$ (wt. %)	$X_3$ (h)	Predicted	Experimental	
130	1	72	98.417	98	0.42
130	1	72	98.417	97	1.44
130	1	72	98.417	95	3.47

that the values of the dissolution percentage of chitosan predicted were close to that of chitosan obtained experimentally. It validates a good correlation between the predicted and experimental values.

Root mean square error (RMSE) is a commonly used performance metric for evaluating regression models that measure the average difference between the predicted and actual values of the dependent variable (Ali & Abustan, 2014), which can be calculated using Equation 8.

$$RMSE = \sqrt{\frac{(\text{Predicted value} - \text{actual value})^2}{N}} \quad (8)$$

Table 6 compares predicted and actual values of the dissolution percentage of chitosan in [BMIM]Cl, along with the sum of squares of the residuals.

$$RMSE = \sqrt{\frac{509.9734}{20}} = 5.0496 \text{ wt. \%} \quad (9)$$

In the regression model of chitosan dissolution in [BMIM]Cl, the RMSE value obtained is 5.0496 wt. % (Equation 9) suggests that there was approximately a 5 wt. % variation between the predicted values by the regression model and the observed experimental values obtained during the optimisation of chitosan dissolution in [BMIM]Cl.

Although the optimisation of chitosan dissolution in ILs has yet to be reported, numerous studies have attempted to dissolve chitosan in different ILs. [BMIM]Cl was first used to dissolve chitosan with an initial chitosan loading of 10 wt. % by Xie et al. (2006) at 110°C for 5 h in an oil bath in an inert N<sub>2</sub> atmosphere. Meanwhile, more ILs such as [AMIM]Cl, [BMIM]Cl, and [BMIM][Ac] were used to dissolve chitosan with an initial chitosan loading of 8, 10, and 12 wt. %, respectively, at the same temperature and dissolution time (Wu et al., 2008). In our study, we attempted to dissolve chitosan with an initial loading of 4 wt. % at 110°C under continuous stirring in an oil bath in a normal atmosphere for 24 and 72 h, respectively, with an efficiency of 45 and 66.25%.

Table 6  
*Predicted and actual values of the dissolution percentage of chitosan in [BMIM]Cl*

Standard Order	Run Order	Predicted Value (wt. %)	Actual Value (wt. %)	Residual (wt. %)	Square of Residuals (wt. %)
1	20	74.39	71.50	-2.8900	8.3521
2	7	84.49	94.50	10.0100	100.2001
3	14	14.71	13.55	-1.1600	1.3456
4	5	24.81	20.64	-4.1700	17.3889
5	18	88.52	89.50	0.9832	0.9667
6	15	98.62	95.00	-3.6200	13.1044
7	9	28.83	27.57	-1.2600	1.5876
8	11	38.94	43.25	4.3100	18.5761
9	8	51.61	50.50	-1.1100	1.2321
10	2	61.72	49.75	-11.9700	143.2809
11	4	86.51	83.00	-3.5100	12.3201
12	1	26.82	30.07	3.2500	10.5625
13	16	49.60	45.00	-4.6000	21.16
14	12	63.73	60.50	-3.2300	10.4329
15	13	56.66	59.32	2.6600	7.0756
16	6	56.66	60.63	3.9600	15.6816
17	19	56.66	55.75	-0.9138	0.8350
18	3	56.66	67.25	10.5900	112.1481
19	17	56.66	55.75	-0.9138	0.8350
20	10	56.66	60.25	3.5900	12.8881
					$\Sigma = 509.9732$

**FTIR of Regenerated Chitosan.** Untreated chitosan and chitosan regenerated from optimised solution ( $X_1 = 130^\circ\text{C}$ ,  $X_2 = 1$  wt. % and  $X_3 = 72$  h) were characterised using FTIR to analyse for chemical changes that occurred during the dissolution of chitosan in [BMIM]Cl as illustrated in Figure 9.

No observable chemical changes occurred between chitosan before and after dissolution in [BMIM]Cl, as all the spectra depicted in Figure 9 were similar. The only difference in chitosan after regeneration was the disappearance of free hydroxyl groups in chitosan at  $3733\text{ cm}^{-1}$  after dissolution in ILs. However, the O-H stretch can be observed at  $3443\text{ cm}^{-1}$  of the regenerated chitosan. The spectra for the regenerated chitosan showed more distinct functional groups, such as peaks representing the N-H stretch and amide II band at  $3108$  and  $1561\text{ cm}^{-1}$ . It showed that the dissolution of chitosan in [BMIM]Cl aids in obtaining chitosan of higher purity and enhances the deacetylation process. It also has been noticed in the case of Islam et. al. (2015), where the regenerated chitosan produced clearer and sharper peaks at  $3359\text{ cm}^{-1}$  and in  $1030\text{-}1155\text{ cm}^{-1}$  indicating enhanced O-H and N-H stretch and C-O stretch, respectively. Shifts in O-H and N-H stretch in regenerated chitosan also indicated an enhancement of hydrogen bonding (Qi et al., 2004).

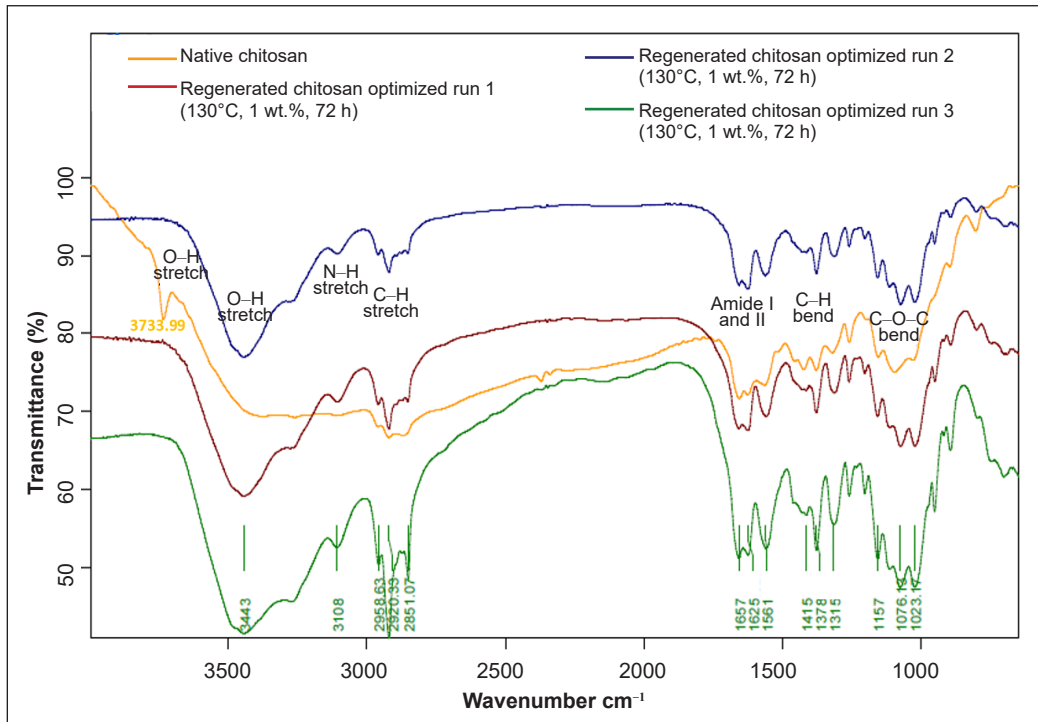


Figure 9. FTIR of chitosan and regenerated chitosan obtained from optimised solution

Due to the similarity between the FTIR spectra of native and regenerated chitosan, results show no chemical reaction between chitosan and [BMIM]Cl during dissolution. In addition, there was no absorption peak observed at  $1520\text{ cm}^{-1}$ , indicating the formation of ammonium salt. Therefore, the main chitosan chain was not disrupted after dissolution in [BMIM]Cl as the direct solvent to solubilise chitosan in ILs. Similar results were also reported by Chen et al. (2011), who attempted to study the dissolution of chitosan in [BMIM][Ac].

The ability of ILs to dissolve chitosan is associated with the ability of ILs to accept hydrogen atoms from chitosan to form H-bonds with the anion (Zhang et al., 2005). Yang et al. (2016) stated that the anion of ILs,  $\text{Cl}^-$  interacts with hydrogen atoms in both the hydroxyl and amino groups, while the cation of ILs,  $[\text{BMIM}]^+$ , interacts with oxygen atoms in hydroxyl and nitrogen atoms. Besides H-bond, intermolecular forces such as ion-induced dipole forces were also observed between the physical interaction of [BMIM]Cl and chitosan. Ion-induced dipole forces occurred when the presence of an ion,  $[\text{BMIM}]^+$  or  $\text{Cl}^-$  distorted the electron distribution of a non-polar molecule or atom such as oxygen or hydrogen atom found in hydroxyl and nitrogen atom in the amino group, inducing the formation of a dipole. It was seen by the free hydroxyl group observed at  $3733\text{ cm}^{-1}$  in native chitosan but shifted to  $3443\text{ cm}^{-1}$  in all the regenerated chitosan, demonstrating the interaction between the cations and anions of ILs with chitosan.

### Ecotoxicity of Chitosan-[BMIM]Cl Solution

The ecotoxicity of the chitosan-[BMIM]Cl mixture was assessed against two bacteria species, *Escherichia coli* (Gram-negative) and *Staphylococcus aureus* (Gram-positive), using broth microdilution assay. MIC values were determined to obtain the range (upper and lower limit) of  $EC_{50}$  values, which refers to the concentration of chitosan-[BMIM]Cl that inhibits 50% of the bacteria growth. The  $EC_{50}$  dose-response curve of chitosan-[BMIM]Cl against *E. coli* and *S. aureus* with a 95% confidence level was shown in Figures 10 and 11, respectively. Based on Figure 10, the  $EC_{50}$  values of chitosan-[BMIM]Cl for *Escherichia coli* were 2.699 to 4.790 wt. %, with an  $EC_{50}$  of 3.1 wt. %. The  $EC_{50}$  values of chitosan-[BMIM]Cl for *Staphylococcus aureus* shown in Figure 11 were 2.711 to 3.700 wt. %, with an  $EC_{50}$  value of 3.2 wt. %.

The toxicity of chitosan-[BMIM]Cl mixture was ranked according to the hazard assessment scores developed by Passino and Smith (1987), who ranked toxicity to be 100-1000 mg/L as being “practically harmless,” 10–100 mg/L as being “moderately toxic,” 1–10 mg/L – “slightly toxic” and 0.1–1 mg/L being “highly toxic.” The toxicity of chitosan-[BMIM]Cl mixture for both *E. coli* and *S. aureus* falls in the category of “relatively harmless” ( $EC_{50} > 1000$  mg/L). There were no distinct differences in the toxicity of the chitosan-[BMIM]Cl mixture despite the cell wall differences between Gram-positive and Gram-negative bacteria, which was a common phenomenon for imidazolium-based ILs (Megaw et al., 2013; Sivapragasam et al., 2019).

In the past, authors have mentioned that the toxicological effects of ILs were not due to the characteristics of bacteria cell walls but various strategies to overcome stress, such as efflux pumps, variations in the plasma membrane and enhanced production of osmolyte (Csonka, 1989; Ma et al., 2019). It was further verified by Mester et al. (2015) that these

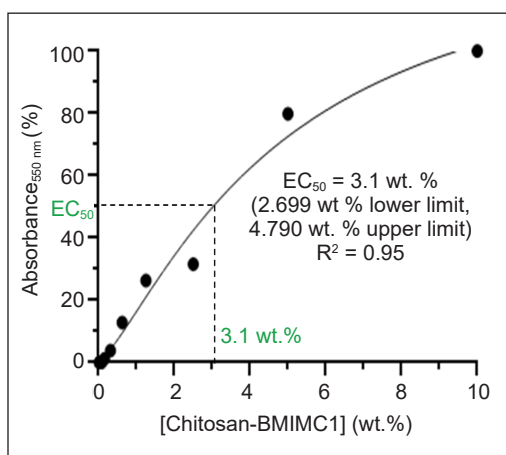


Figure 10.  $EC_{50}$  dose-response curve of chitosan-[BMIM]Cl mixture against *Escherichia coli*

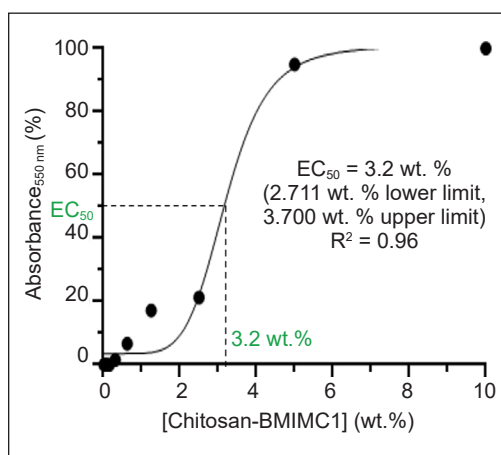


Figure 11.  $EC_{50}$  dose-response curve of chitosan-[BMIM]Cl mixture against *Staphylococcus aureus*



strategies caused huge differences in the susceptibility of bacterial strains towards the respective ILs.

The ecotoxicity of [BMIM]Cl towards *E. coli* and *S. aureus* were also studied by Ghanem et al. (2015) using the standard microbroth dilution test. The EC<sub>50</sub> of [BMIM]Cl towards *E. coli* and *S. aureus* were 14409±9.9 mg/L and 12454.2±11.16 mg/L, respectively, which showed that [BMIM]Cl was “relatively harmless.” Mean minimum inhibitory concentration (MIC) of [BMIM]Cl towards *E. coli* and *S. aureus* were both greater than 50000 mg/L, suggesting that it was “relatively harmless” ecologically (Weyhing-Zerrer et al., 2017).

The ecotoxicity of [BMIM]Cl has been studied using organisms from different trophic levels, such as marine bacteria, *Photobacterium phopshoreum* (Docherty, 2005), yeast, *Saccharomyces cerevisiae* (Zhu et al., 2013), duckweed, *Lemna minor* (Peric et al., 2013), Zebrafish, *Danio rerio* (Zhang et al., 2017) and human cervical carcinoma epithelial cells, HeLa cells (Stepnowski et al., 2004). Toxicity results revealed that [BMIM]Cl was “moderately toxic” to *L. minor* (48.98 mg/L), “practically harmless” to *P. phopshoreum* (898 mg/L), *S. cerevisiae* (530 mg/L) and *D. rerio* (633 mg/L) and lastly “relatively harmless” to HeLa cells.

Factors contributing to chitosan-[BMIM] Cl’s toxicity were due to the structure and length of the alkyl chain on the imidazolium cation. [BMIM]<sup>+</sup> cation has a 4-carbon alkyl chain attached to the nitrogen atom in the aromatic ring. The alkyl chain and aromatic ring structure increase the hydrophobicity of [BMIM]Cl and, therefore, increases the toxicity of chitosan-[BMIM]Cl mixture towards both *Escherichia coli* and *Staphylococcus aureus* (Borkowski et al., 2016).

## CONCLUSION

Chitosan (DD = 83.42%) was successfully synthesised via partial deacetylation of chitin. FTIR results of chitosan revealed the presence of free hydroxyl group and additional amino groups and reduced intensity of C=O stretch and C-H stretch, indicating the successful removal of acetyl groups from acetamide groups in chitin to form chitosan. Chitosan dissolution in [BMIM]Cl was then optimised using CCD in RSM. The optimised conditions revealed by the regression model were 130°C ( $X_1$ , temperature), 1 wt. % ( $X_2$ , initial chitosan loading), and 72 h ( $X_3$ , dissolution time). The regression model for dissolution percentage was significant ( $p < 0.05$ ) with a non-significant lack-of-fit ( $p > 0.05$ ). The R<sup>2</sup> value of the model was 0.9490 with a mean relative error of 1.78 % and RMSE of 5.0496 wt. %, indicating a good correlation between experimental and predicted values for the dissolution percentage of chitosan. No chemical changes were observed in regenerated chitosan, indicating the role of [BMIM]Cl as a direct solvent for chitosan dissolution. Lastly, the ecotoxicity of chitosan-[BMIM]Cl was evaluated

using broth microdilution assay on *Escherichia coli* and *Staphylococcus aureus*—the EC<sub>50</sub> value on 10 wt. % (100,000 mg/L) chitosan-[BMIM]Cl against *E. coli* and *S. aureus* was relatively harmless, with values of 3.1 wt. % (31,000 mg/L) and 3.2 wt. % (32,000 mg/L), respectively, indicating no differences in toxicity despite cell wall variation of Gram-positive and Gram-negative bacteria.

## ACKNOWLEDGMENT

This research was funded by the Ministry of Higher Education (MOHE), Malaysia, through the Fundamental Research Grant Scheme (FRGS/1/2021/STG01/QUEST/03/1). The authors thank QUEST International University, Malaysia, for the laboratory facilities and funding provided and the Centre of Research in Ionic Liquids, Universiti Teknologi PETRONAS, Malaysia, for the ILs provided.

## REFERENCES

- Ahing, F. A., & Wid, N. (2016). Optimization of shrimp shell waste deacetylation for chitosan production. *International Journal of Advanced and Applied Sciences*, 3(10), 31-36. <https://doi.org/10.21833/ijaas.2016.10.006>
- Ahyat, N. M., Mohamad, F., Ahmad, A., & Azmi, A. A. (2017). Chitin and chitosan extraction from *Portunus pelagicus*. *Malaysian Journal of Analytical Sciences*, 21(4), 770-777. <https://doi.org/10.17576/mjas-2017-2104-02>
- Akakuru, O. U., Louis, H., Amos, P. I., Akakuru, O., Nosike, E. I., & Ogulewe, E. F. (2018). The chemistry of chitin and chitosan justifying their nanomedical utilities. *Biochemistry & Pharmacology*, 7, Article 1000241. <https://doi.org/10.4172/2167-0501.1000241>
- Ali, M. H., & Abustan, I. (2014). A new novel index for evaluating model performance. *Journal of Natural Resources and Development*, 4, 1-9. <https://doi.org/10.5027/jnrd.v4i0.01>
- Aranaz, I., Acosta, N., Civera, C., Elorza, B., Mingo, J., Castro, C., Gandia, M. D. I. L., & Caballero, A. H. (2018). Cosmetics and cosmeceutical applications of chitin, chitosan and their derivatives. *Polymers*, 10(2), Article 213. <https://doi.org/10.3390/polym10020213>
- Behera, S. K., Meena, H., Chakraborty, S., & Meikap, B. C. (2018). Application of response surface methodology (RSM) for optimization of leaching parameters for ash reduction from low-grade coal. *International Journal of Mining Science and Technology*, 28, 621-629. <https://doi.org/10.1016/j.ijmst.2018.04.014>
- Borkowski, A., Ławniczak, L., Cłapa, T., Narożna, D., Selwet, M., Peziak, D., Markiewicz, B., & Chrzanowski, L. (2016). Different antibacterial activity of novel theophylline-based ionic liquids - Growth kinetic and cytotoxicity studies. *Ecotoxicology and Environmental Safety*, 130, 54-64. <https://doi.org/10.1016/j.ecoenv.2016.04.004>
- Brugnerotto, J., Lizardi, J., Goycoolea, F. M., Argüelles-Monal, W., Desbrières, J., & Rinaudo, M. (2001). An infrared investigation in relation with chitin and chitosan characterization. *Polymer*, 42(8), 3569-3580. [https://doi.org/10.1016/S0032-3861\(00\)00713-8](https://doi.org/10.1016/S0032-3861(00)00713-8)

- Bubalo, M., Radošević, K., Redovniković, L., Slivac, I., & Srček, V. (2017). Toxicity mechanisms of ionic liquids. *Arhiv za Higijenu Rada I Toksikologiju*, 68(3), 171-179. <https://doi.org/10.1515/aiht-2017-68-2979>
- Chen, Q., Xu, A., Li, Z., Wang, J., & Zhang, S. (2011). Influence of anionic structure on the dissolution of chitosan in 1-butyl-3-methylimidazolium-based ionic liquids. *Green Chemistry*, 13(12), 3446-3452. <https://doi.org/10.1039/C1GC15703E>
- Chowdhury, Z., Zain, S. M., Hamid, S. B. A., & Khalid, K. (2014). Catalytic role of ionic liquids for dissolution and degradation of biomacromolecules. *Bioresources*, 9(1), 1787-1823. <https://doi.org/10.15376/BIORES.9.1.1787-1823>
- Claros, M., Graber, T. A., Brito, I., Albanez, J., & Gavin, J. A. (2010). Synthesis and thermal properties of two new dicationic ionic liquids. *Journal of the Chilean Chemical Society*, 55(3), 396-398. <https://doi.org/10.4067/S0717-97072010000300027>
- Csonka, L. N. (1989). Physiological and genetic responses of bacteria to osmotic stress. *Microbiological Reviews*, 53, 121-147. <https://doi.org/10.1128/mr.53.1.121-147.1989>
- Czechowska-Biskup, R., Jarosińska, D., Rokita, B., Ulański, P., & Rosiak, J. (2012). Determination of degree of deacetylation of chitosan - Comparison of methods. *Progress on Chemistry and Application of Chitin and its Derivatives*, 2012, 5-20.
- da Costa Lopes, A. M., Lins, R. M. G., Rebelo, R. A., & Łukasik, R. M. (2018). Biorefinery approach for lignocellulosic biomass valorisation with acidic ionic liquid. *Green Chemistry*, 20(17), 4043-4057. <https://doi.org/10.1039/C8GC01763H>
- Dennis, G., Harrison, W., Agnes, K., & Erastus, G. (2016). Effect of biological control antagonists adsorbed on chitosan immobilized silica nanocomposite on *Ralstonia solanacearum* and growth of tomato seedlings. *Advances in Research*, 6(1), 1-23. <https://doi.org/10.9734/AIR/2016/22742>
- Docherty, K. M. (2005). Toxicity and antimicrobial activity of imidazolium and pyridinium ionic liquids. *Green Chemistry*, 7, 185-189. <https://doi.org/10.1039/B419172B>
- Egorova, K. S., & Ananikov, V. P. (2014). Toxicity of ionic liquids: Eco(cyto)activity as complicated, but unavoidable parameter for task-specific optimization. *Chemistry-Sustainability-Energy-Materials*, 7(2), 336-360. <https://doi.org/10.1002/cssc.201300459>
- El Knidri, H., El Khalfaouy, R., Laajeb, A., & Lahsini, A. (2016). Eco-friendly extraction and characterization of chitin and chitosan from the shrimp shell waste via microwave irradiation. *Process Safety and Environmental Protection*, 104, 395-405. <https://doi.org/10.1016/j.psep.2016.09.020>
- Elieh-Ali-Komi, D., & Hamblin, M. R. (2016). Chitin and chitosan: Production and application of versatile biomedical nanomaterials. *International Journal of Advanced Research*, 4(3), 411-427. <https://pubmed.ncbi.nlm.nih.gov/27819009>
- Fatima, B. (2020). Quantitative analysis by IR: Determination of chitin/chitosan DD. In M. Khan (Ed.), *Modern Spectroscopic Techniques and Applications* (pp. 1-24). IntechOpen. <https://doi.org/10.5772/intechopen.89708>
- Forsyth, S. A., MacFarlane, D. R., Thomsom, R. J., & Itzstein, M. V. (2002). Rapid, clean and mild o-acetylation of alcohols and carbohydrates in an ionic liquid. *Chemical Communications*, 7(7), 714-715. <https://doi.org/10.1039/b200306f>

- Ghanem, O. B., Mutalib, M. I. A., El-Harbawi, M., Gonfa, G., Chong, F. K., Alitheen, N. B. M., & Lévêque, J. M. (2015). Effect of imidazolium-based ionic liquids on bacterial growth inhibition investigated via experimental and QSAR modelling studies. *Journal of Hazardous Materials*, 297, 198-206. <https://doi.org/10.1016/j.jhazmat.2015.04.082>
- Gschwend, F. J. V., Chambon, C. L., Biedka, M., Brandt-Talbot, A., Fennell, P. S., & Hallett, J. P. (2019). Quantitative glucose release from softwood after pretreatment with low-cost ionic liquids. *Green Chemistry*, 21, 692-703. <https://doi.org/10.1039/C8GC02155D>
- IEA Bioenergy. (2020). *Annual Report 2019 IEA Bioenergy*. <https://www.ieabioenergy.com/wp-content/uploads/2020/05/IEA-Bioenergy-Annual-Report-2019.pdf>
- Islam, S., Arnold, L., & Padhye, R. (2015). Comparison and characterization of regenerated chitosan from 1-butyl-3-methylimidazolium chloride and chitosan from crab shells. *BioMed Research International*, 2015, Article 874316. <https://doi.org/10.1155/2015/874316>
- Kusuma, H. S., Agasi, H., & Darmokoesoemo, H. (2015). Effectiveness inhibition of fermentation legen using chitosan nanoparticles. *Journal of Molecular and Genetic Medicine*, 9(3), Article 1000173. <https://doi.org/10.4172/1747-0862.1000173>
- Lei, Z., Chen, B., Koo, Y. M., & MacFarlane, D. R. (2017). Introduction: Ionic liquids. *Chemical Reviews*, 117(10), 6633-6635. <https://doi.org/10.1021/acs.chemrev.7b00246>
- Liu, L., Wang, Y., Xie, H., Zhang, B., & Zhang, B. (2022). Enhancing the antioxidant ability of *Momordica grosvenorii* saponin to resist gastrointestinal stresses via microcapsules of sodium alginate and chitosan and its application in beverage. *Beverages*, 8(4), Article 70. <https://doi.org/10.3390/beverages8040070>
- Ma, Q., Gao, X., Bi, Z., Han, Q., Tu, L., Yang, Y., Shen, Y., & Wang, M. (2019). Dissolution and deacetylation of chitin in ionic liquid tetrabutylammonium hydroxide and its cascade reaction in enzyme treatment for chitin recycling. *Carbohydrate Polymers*, 230, Article 115605. <https://doi.org/10.1016/j.carbpol.2019.115605>
- Manzanares, P. (2020). The role of biorefining research in the development of a modern bioeconomy. *Acta Innovations*, 37, 47-56. <https://doi.org/10.32933/ActaInnovations.37.4>
- Matute, A. I. R., Cardelle-Cobas, A., García-Bermejo, A. B., Montilla, A., Olano, A., & Corzo, N. (2013). Synthesis, characterization and functional properties of galactosylated derivatives of chitosan through amide formation. *Food Hydrocolloids*, 33, 245-255. <https://doi.org/10.1016/j.foodhyd.2013.03.016>
- Megaw, J., Busetti, A., & Gilmore, B. F. (2013). Isolation and characterization of 1-alkyl-3-methylimidazolium chloride ionic liquid-tolerant and biodegrading marine bacteria. *PLoS One*, 8(4), Article e60806. <https://doi.org/10.1371/journal.pone.0060806>
- Mester, P., Wagner, M., & Rossmann, P. (2015). Antimicrobial effects of short chained imidazolium-based ionic liquids - Influence of anion chaotropicity. *Ecotoxicology and Environmental Safety*, 111, 96-101. <https://doi.org/10.1016/j.ecoenv.2014.08.032>
- Morin-Crini, N., Lichtfouse, E., Torri, G., & Crini, G. (2019). Applications of chitosan in food, pharmaceuticals, medicine, cosmetics, agriculture, textiles, pulp and paper, biotechnology, and environmental chemistry. *Environmental Chemistry Letters*, 17, 1667-1692. <https://doi.org/10.1006/s10311-019-00904-x>

- Naseeruteen, F., Hamid, N. S. A., Suah, F. B. M., Ngah, W. S. W., & Mehamod, F. S. (2018). Adsorption of malachite green from aqueous solution by using novel chitosan ionic liquid beads. *International Journal of Biological Macromolecules*, *107*, 1270-1277. <https://doi.org/10.1016/j.ijbiomac.2017.09.111>
- Palpandi, C., Shanmugam, V., & Shanmugam, A. (2009). Extraction of chitin and chitosan from shell and operculum of mangrove gastropod *Nerita (Dostia) crepidularia* Lamarck. *International Journal of Medical Sciences*, *1*(5), 198-205.
- Passino, D. R. M., & Smith, S. B. (1987). Acute bioassays and hazard evaluation of representative contaminants detected in great lakes fish. *Environmental Toxicology and Chemistry*, *6*(11), 901-907. <https://doi.org/10.1002/etc.5620061111>
- Peric, B., Sierra, J., Martí, E., Cruañas, R., Garau, M. A., Arning, J., Bottin-Weber, U., & Stolte, S. (2013). (Eco)toxicity and biodegradability of selected protic and aprotic ionic liquids. *Journal of Hazardous Materials*, *261*, 99-105. <https://doi.org/10.1016/j.jhazmat.2013.06.070>
- Poerio, A., Girardet, T., Petit, C., Eleutot, S., Jehl, J., Arab-Tehrany, E., Mano, J. F., & Cleymand, F. (2021). Comparison of the physicochemical properties of chitin extracted from *Cicada orni* sloughs harvested in three different years and characterization of the resulting chitosan. *Applied Sciences*, *11*, Article 11278. <https://doi.org/10.3390/app112311278>
- Puspawati, N. M., & Simpen, I. N. (2010). Optimasi deasetilasi khitin dari kulit udang dan cangkang kepiting limbah restoran seafood menjadi khitosan melalui konsentrasi NaOH [Optimization of deacetylation of chitin from seafood restaurant waste shrimp skin and crab shell into chitosan through NaOH concentration]. *Jurnal Kimia*, *4*, 79-90. <https://ojs.unud.ac.id/index.php/jchem/article/view/2760>
- Qi, L., Xu, Z., Jiang, X., Hu, C., & Zou, X. (2004). Preparation and antibacterial activity of chitosan nanoparticles. *Carbohydrate Research*, *339*(16), 2693-2700. <https://doi.org/10.1016/j.carres.2004.09.007>
- Rahim, A. H. A., Yunus, N. M., Man, Z., Sarwono, A., Hamzah, W. S. W., & Wilfred, C. (2018). Ultrasonic assisted dissolution of bamboo biomass using ether-functionalized ionic liquid. *AIP Conference Proceedings*, *2016*, Article 020010. <https://doi.org/10.1063/1.5055412>
- Rinaudo, M. (2006). Chitin and chitosan: Properties and application. *Progress in Polymer Science*, *31*(7), 603-632. <https://doi.org/10.1016/j.progpolymsci.2006.06.001>
- Rodríguez, H. (2021). Ionic liquids in the pretreatment of lignocellulosic biomass. *Acta Innovations*, *38*, 23-26. <https://doi.org/10.32933/ActaInnovations.38.3>
- Roller, S., & Covill, N. (1999). The antifungal properties of chitosan in laboratory media and apple juice. *International Journal of Food Microbiology*, *47*(1-2), 67-77. [https://doi.org/10.1016/S0168-1605\(99\)00006-9](https://doi.org/10.1016/S0168-1605(99)00006-9)
- Romanazzi, G., Gabler, F. M., Margosan, D., Mackey, B. E., & Smilnick, J. L. (2009). Effect of chitosan dissolved in different acids on its ability to control postharvest gray mold of table grape. *Phytopathology*, *99*(9), 1028-1036. <https://doi.org/10.1094/PHYTO-99-9-1028>
- Rosatella, A. A., Branco, L. C., & Afonso, C. A. M. (2009). Studies on dissolution of carbohydrates in ionic liquids and extraction from aqueous phase. *Green Chemistry*, *11*, 1406-1413. <https://doi.org/10.1039/b900678h>

- Rumenagan, I., Suryanto, E., Modaso, R., Wullur, S., Tallei, T., & Limbong, D. (2014). Structural characteristics of chitin and chitosan isolated from the biomass of cultivated rotifer, *Brachionus rotundiformis*. *International Journal of Fisheries and Aquatic Sciences*, *3*, 12-18.
- Santos, E., Rodríguez-Fernández, E., Casado-Coterillo, C., & Irabien, A. (2016). Hybrid ionic liquid-chitosan membranes for CO<sub>2</sub> separation: Mechanical and thermal behavior. *International Journal of Chemical Reactor Engineering*, *14*(3), 713-718. <https://doi.org/10.1515/ijcre-2014-0109>
- Schmitz, C., Auza, L. G., Koberidze, D., Rache, S., Fischer, R., & Bortesi, L. (2019). Conversion of chitin to defined chitosan oligomers: current status and future prospects. *Marine Drugs*, *17*(8), Article 452. <https://doi.org/10.3390/md17080452>
- Sivapragasam, M., Jaganathan, J. R., Levêque, J., Moniruzzaman, M., & Mutalib, M. I. A. (2019). Microbial biocompatibility of phosphonium- and ammonium-based ionic liquids. *Journal of Molecular Liquids*, *273*, 107-115. <https://doi.org/10.1016/j.molliq.2018.10.022>
- Sivapragasam, M., Moniruzzaman, M., & Goto, M. (2020). An overview on the toxicological properties of ionic liquids towards microorganisms. *Biotechnology Journal*, *15*(4), Article e1900073. <https://doi.org/10.1002/biot.201900073>
- Stepnowski, P., Składanowski, A. C., Ludwiczak, A., & Laczyńska, E. (2004). Evaluating the cytotoxicity of ionic liquids using human cell line HeLa. *Human & Experimental Toxicology*, *23*, 513-517. <https://doi.org/10.1191/0960327104ht480oa>
- Sun, N., Rahman, M., Qin, Y., Maxim, M. L., Rodríguez, H., & Rogers, R. D. (2009). Complete dissolution and partial delignification of wood in the ionic liquid 1-ethyl-3-methylimidazolium acetate. *Green Chemistry*, *11*, 646-655. <https://doi.org/10.1039/B822702K>
- Sun, X., Tian, Q., Xue, Z., Zhang, Y., & Mu, T. (2014). The dissolution behaviour of chitosan in acetate-based ionic liquids and their interactions: From experimental evidence to density functional theory analysis. *RSC Advances*, *4*, 30282-30291. <https://doi.org/10.1039/c4ra02594f>
- Sun, X., Xue, Z., & Mu, T. (2014). Precipitation of chitosan from ionic liquid solution by the compressed CO<sub>2</sub> anti-solvent method. *Green Chemistry*, *16*, 2102-2106. <https://doi.org/10.1039/C3GC42166J>
- Swatloski, R. P., Spear, S. K., Holbrey, J. D., & Rogers, R. D. (2002). Dissolution of cellulose with ionic liquids. *Journal of the American Chemical Society*, *124*(18), 4974-4975. <https://doi.org/10.1021/ja025790m>
- Tamzi, N. N., Faisal, M., Sultana, T., & Ghosh, S. K. (2020). Extraction and properties evaluation of chitin and chitosan prepared from different crustacean waste. *Bangladesh Journal of Veterinary and Animal Sciences*, *8*(2), 69-76.
- Tan, H. T., & Lee, K. (2012). Understanding the impact of ionic liquid pretreatment on biomass and enzymatic hydrolysis. *Chemical Engineering Journal*, *183*, 448-458. <https://doi.org/10.1016/j.cej.2011.12.086>
- Thomas, P. A., & Marvey, B. B. (2016). Room temperature ionic liquids as green solvent alternatives in the metathesis of oleochemical feedstocks. *Molecules*, *21*(2), Article 184. <https://doi.org/10.3390/molecules21020184>
- Wang, W. T., Zhu, J., Wang, X. L., Huang, Y., & Wang, Y. Z. (2010). Dissolution behavior of chitin in ionic liquids. *Journal of Macromolecular Science, Part B*, *49*(3), 528-541. <https://doi.org/10.1080/00222341003595634>

- Wang, X., Li, H., Cao, Y., & Tang, Q. (2011). Cellulose extraction from wood chip in an ionic liquid 1-allyl-3-methylimidazolium chloride (AmimCl). *Bioresource Technology*, *102*, 7959-7965. <https://doi.org/10.1016/j.biortech.2011.05.064>
- Weyhing-Zerrer, N., Gundolf, T., Kalb, R., Oßmer, R., Rossmannith, P., & Mester, P. (2017). Predictability of ionic liquid toxicity from a SAR study on different systematic levels of pathogenic bacteria. *Ecotoxicology and Environmental Safety*, *139*, 394-403. <https://doi.org/10.1016/j.ecoenv.2017.01.055>
- Wu, J., Zhang, J., Zhang, H., He, J., Ren, Q., & Guo, M. (2004). Homogenous acetylation of cellulose in a new ionic liquid. *Biomacromolecules*, *5*(2), 266-268. <https://doi.org/10.1021/bm034398d>
- Wu, Y., Sasaki, T., Irie, S., & Sakurai, K. (2008). A novel biomass-ionic liquid platform for the utilization of native chitin. *Polymer*, *49*, 2321-2327. <https://doi.org/10.1016/j.polymer.2008.03.027>
- Xie, H., Zhang, S., & Li, S. (2006). Chitin and chitosan dissolved in ionic liquids as reversible sorbents of CO<sub>2</sub>. *Green Chemistry*, *8*(7), 630-633. <https://doi.org/10.1039/B517297G>
- Xu, B., Li, Q., Zhuang, L., Wang, Q., Li, C., Wang, G., Xie, F., & Halley, P. J. (2016). Dissolution and regeneration behavior of chitosan in 3-methyl-1-(ethylacetyl)imidazolium chloride. *Fibers and Polymer*, *17*(11), 1741-1748. <https://doi.org/10.1007/s12221-016-6747-6>
- Yang, X., Qian, C., Li, Y., & Li, T. (2016). Dissolution and resourefulization of biopolymers in ionic liquids. *Reactive and Functional Polymers*, *100*, 181-190. <https://doi.org/10.1016/j.reactfunctpolym.2016.01.017>
- Zakrzewska, M. E., Bogel-Lukasik, E., & Bogel-Lukasik, R. (2010). Solubility of carbohydrates in ionic liquids. *Energy Fuels*, *24*, 737-745. <https://doi.org/10.1021/ef901215m>
- Zhang, C., Shao, Y., Zhu, L., Wang, J., Wang, J., & Guo Y. (2017). Acute toxicity, biochemical toxicity and genotoxicity caused by 1-butyl-3-methylimidazolium chloride and 1-butyl-3-methylimidazolium tetrafluoroborate in zebrafish (*Danio rerio*) livers. *Environmental Toxicology and Pharmacology*, *51*, 131-137. <https://doi.org/10.1016/j.etap.2017.02.018>
- Zhang, H., Wu, J., Zhang, J., & He., J. (2005). 1-allyl-3-methylimidazolium chloride room temperature ionic liquid: A new and powerful nonderivatizing solvent for cellulose. *Macromolecules*, *38*(20), 8272-8277. <https://doi.org/10.1021/ma0505676>
- Zhang, M., Zhang, F., Li, C., An, H., Wan, T., & Zhang, P. (2022). Application of chitosan and its derivative polymers in clinical medicine and agriculture. *Polymers*, *14*, Article 958. <https://doi.org/10.3390/polym14050958>
- Zhang, Y., Liu, Y, Chu, Z., Shi, L., & Jin, W. (2013). Amperometric glucose biosensor based on direct assembly of prussian blue film with ionic liquid-chitosan matrix assisted enzyme immobilization. *Sensors and Actuators B: Chemical*, *176*, 978-984. <https://doi.org/10.1016/j.snb.2012.09.080>
- Zhao, D., Yu, S., Sun, B., Gao, S., Guo, S., & Zhao, K. (2018). Biomedical applications of chitosan and its derivative nanoparticles. *Polymers*, *10*(4), Article 462. <https://doi.org/10.3390/polym10040462>
- Zhu, S., Yu, P., Lei, M., Tong, Y., Zheng, L., Zhang, R., Ji, J., Chen, Q., & Wu, Y. (2013). Investigation of the toxicity of the ionic liquid 1-butyl-3-methylimidazolium chloride to *Saccharomyces cerevisiae* AY93161 for lignocellulosic ethanol production. *Polish Journal of Chemical Technology*, *15*(2), 94-98. <https://doi.org/10.2478/pjct-2013-0029>

Zhuang, L., Zhong, F., Qin, M., Sun, Y., Tan, X., Zhang, H., Kong, M., Hu, K., & Wang, G. (2020). Theoretical and experimental studies of ionic liquid-urea mixtures on chitosan dissolution: Effect of cationic structure. *Journal of Molecular Liquids*, 317, Article 113918. <https://doi.org/10.1016/j.molliq.2020.113918>



## Novel Pre-treatment for Lignocellulosic Biomass Delignification Using Alkaline-Assisted Ohmic Heating

Izzah Farhana Ab Aziz<sup>1</sup>, Hasfalina Che Man<sup>1,2\*</sup>, Muhammad Hazwan Hamzah<sup>1,2</sup>, Nur Syakina Jamali<sup>3</sup> and Rozita Omar<sup>3</sup>

<sup>1</sup>Department of Biological and Agricultural Engineering, Faculty of Engineering, Universiti Putra Malaysia, 43400 UPM, Serdang, Selangor, Malaysia

<sup>2</sup>SMART Farming Technology Research Centre, Faculty of Engineering, Universiti Putra Malaysia, 43400 UPM, Serdang, Selangor, Malaysia

<sup>3</sup>Department of Chemical and Environmental Engineering, Faculty of Engineering, Universiti Putra Malaysia, 43400 UPM, Serdang, Selangor, Malaysia

### ABSTRACT

Lignocellulosic biomass (LCB) is a common substrate for biogas and bioethanol production due to its significant properties and abundance. However, it has a unique recalcitrant structure that can inhibit the production of biogas, which necessitates pre-treatment of the substrate to obtain higher cellulose or sugars ready for microbial hydrolysis in producing biogas. In this study, a novel approach for empty fruit bunch (EFB) pre-treatment has been made: ohmic heating pre-treatment. This method is conventionally used in the food industry for pasteurization and extraction. It involves electric current and resistance inside the material that releases heat (Joule effect). A preliminary study has been done to figure out the potential of alkaline assisted with ohmic heating (AA-OH) pre-treatment for EFB. Lignin reduction for AA-OH EFB is higher than EFB that undergoes only size reduction (SR) pre-treatment, which are 15.54% and 11.51%, respectively. After confirming the potential of ohmic heating as one of the pre-treatment methods for EFB, three

parameters were investigated (reaction time, temperature, and solvent concentration) by one factor at a time (OFAT) testing to obtain the optimum condition for AA-OH pre-treatment. The optimal condition for achieving a high reduction in lignin (86.9%) and hemicellulose (75%) while also showing a significant increase in cellulose (63.2%), which is desirable for the fermentation process, is achieved by using 4% w/v of

### ARTICLE INFO

#### Article history:

Received: 14 November 2022

Accepted: 04 April 2023

Published: 09 October 2023

DOI: <https://doi.org/10.47836/pjst.31.6.22>

#### E-mail addresses:

[izzahfarhana95@gmail.com](mailto:izzahfarhana95@gmail.com) (Izzah Farhana Ab Aziz)

[hasfalina@upm.edu.my](mailto:hasfalina@upm.edu.my) (Hasfalina Che Man)

[hazwanhamzah@upm.edu.my](mailto:hazwanhamzah@upm.edu.my) (Muhammad Hazwan Hamzah)

[syakina@upm.edu.my](mailto:syakina@upm.edu.my) (Nur Syakina Jamali)

[rozitaom@upm.edu.my](mailto:rozitaom@upm.edu.my) (Rozita Omar)

\* Corresponding author

NaOH, ohmic-heated at a temperature of 120°C for 25 minutes. To sum up, this developed ohmic heating pre-treatment technique can be applied to LCB prior to biogas or bioethanol production.

*Keywords:* Biogas, empty fruit bunch (EFB), lignocellulosic, ohmic heating, pre-treatment, recalcitrant

---

## INTRODUCTION

Exploration of alternative sustainable energy sources is actively carried out by researchers worldwide out of concern for the scarcity of conventional energy resources such as coal, petroleum, and others (Diyanilla et al., 2020). In addition to that, the increasing world population and high demand for energy consumption are also the main concerns (Hoekstra & Wiedmann, 2014). Agricultural waste is mainly comprised of lignocellulosic biomass wastes, considered a cheap source for renewable biogas production, and has excellent potential to overcome the spike in energy demand in the future. As the second largest crude palm oil (CPO) producer and exporter (Ezechi & Muda, 2019), Malaysia also generates abundant oil palm waste, estimated to be more than 80 million tons annually. Palm oil plantation has become one of Malaysia's emerging main agricultural sectors, making the country recognizable in the world as one of the biggest palm oil producers. Significant production of palm kernel shell (PKS), an oil palm frond (OPF), mesocarp fiber (MF), empty fruit bunch (EFB), and palm oil mill effluent (POME) are by-products of the processing of palm oil production.

EFB is chosen in this study due to its lignocellulosic properties, which are highly obtainable, excellent compositional characteristics, and huge biogas production potential. It is a lignocellulosic material consisting mainly of cellulose and hemicellulose (about 80%), made of sugars that can be fermented and converted into biogas (Palamae et al., 2017). However, lignocellulosic biomass (LCB) has uniquely structured lignin, making it recalcitrant towards microbial activity or enzymatic hydrolysis during fermentation or biogas production. Cellulose, the complex lignin-hemicellulose bond, hinders the main component for biofuel generation due to its high molecular weight, branched amorphous compound, and substituted polymer (Karunakaran et al., 2020). Therefore, selecting suitable pre-treatment methods is intrinsic to enhancing biofuel production at a low cost on processing and environmentally friendly.

Alkaline pre-treatment of EFB is already proven to be one of the excellent options among other chemical methods. They are less caustic than dilute acid and can be performed at ambient pressure, eliminating the need for specialized equipment that is corrosion-resistant, or that can withstand high pressures. Several alkaline reagents commonly used are hydroxides of sodium, potassium, calcium, and ammonium (Baruah et al., 2018), of which sodium hydroxide (NaOH) was the most effective (Kim et al., 2016). Cleavage

of the intermolecular ester linkages between lignin and hemicellulose resulted from the saponification reaction, which then allows the alkaline solution to solubilize both fragments (Hu & Ragauskas, 2012; Sun et al., 2016). The degradation of cellulose cell walls will allow for more enzyme interaction (Varga et al., 2003). This pre-treatment can also reduce the crystallinity and degree of polymerization of EFB by cellulose swelling, which increases the internal surface area (Baruah et al., 2018; Behera et al., 2014). Another main benefit of this method is that it requires only mild pre-treatment conditions with minimal inhibitor production and sugar degradation (Alvira et al., 2010; Xu et al., 2010; Zhao et al., 2008). However, this pre-treatment method is usually paired with other methods to shorten its processing time and reduce the usage of chemical and energy input (Conde-Mejía et al., 2012).

The utilization of ohmic heating in LCB pre-treatment is still novel and not yet explored despite its excellent potential in food processing (Rodríguez et al., 2021; Perasiriyan et al., 2016; Pires et al., 2020; Ríos-Ríos et al., 2021; Sengun et al., 2014; Wang et al., 2021). The state-of-the-art OH utilization emerging in the last 15 years, comprehensively included in the extraction process of essential oil (Karunanithi, 2019; Sofi'I et al., 2021; Tunç & Koca, 2021), food-grade (Gavahian et al., 2015; Pare et al., 2014), phytochemicals (Pereira et al., 2016), and phenolic compounds (Kutlu et al., 2021). Ohmic heating is one of the electro-heating methods successfully developed from conventional heating (Aurina & Sari, 2022; Lee & Jun, 2011). Also known as Joule, direct electrical, resistance, electro-heating, and electroconductive heating (Indiarto & Rezaharsanto, 2020; Perasiriyan et al., 2016; Sastry, 2008), alternating electric current (AC) electric fields are passed through materials. Hence, evolving from a single conventional pre-treatment process, researchers explored integrating pre-treatment methods simultaneously into combinations of two or more processes (Hassan et al., 2018; Ummalyima et al., 2019).

The most favored methods in trend for EFB pre-treatment are acid/alkaline-assisted microwave heating which combines the physical (microwave heating) and chemical pre-treatments, where chemical solvents used such as sodium hydroxide, NaOH (Hamzah et al., 2020; Nomanbhay et al., 2013; Yaser et al., 2017), sulphuric acid, H<sub>2</sub>SO<sub>4</sub> (Akhtar et al., 2015; Fatriasari et al., 2017) and ferric (III) chloride, FeCl<sub>3</sub> (Hassan et al., 2021). Electrochemical (EC) pre-treatment is also categorized as one option for 'greener' alternative technologies for delignification (Tamburini et al., 2011) and has started to venture into the reduction in the recalcitrance of LCB (Panigrahi et al., 2021). 64% lignin reduction in wheat straw was obtained by Tamburini et al. (2011) using hypochlorous acid (HOCl) as an electrolyte, and 46% reduction for yard waste using NaOH, done by Panigrahi et al. (2021). At the same time, Sun et al. (2020) incorporated this EC method into organosolv pre-treatment with 73% delignification of sawdust. EC pre-treatment applies a direct current to the system by the principle of electrophoresis, ohmic heating, and electro-osmosis with the aid of chemical reagents as electrolytes for electron transfer

mediators (Panigrahi & Dubey, 2019; Rochefort et al., 2004). Particles will be disintegrated where organic matter solubilization happens due to bonds breaking among polymers in the LCB (Panigrahi & Dubey, 2019).

In this study, ohmic heating is chosen as the pre-treatment method to be assisted with alkaline reagents as electrolytes. The potential of AA-OH to delignify EFB structures was investigated and compared with the performance of SR. Following that, optimization of parameters for AA-OH was also carried out for optimum EFB delignification and cellulose recovery. OFAT approach allows researchers to explore a wide range of values, providing a rough estimation of the optimal levels for a particular factor (Hu et al., 2016) without considering the interactions between different factors. It can help identify which factors have the most significant impact on the outcome variable and which ones can be ignored, especially for this novel study. These pre-treatment method combinations are more economical and environmentally friendly by reason of a reduction in the number of operational steps. Moreover, they also demonstrated an excellent delignification efficiency of feedstock (Diyaniilla et al., 2020) for biogas production while minimizing the presence of inhibitors that can interrupt the performance of biogas production (Kumar & Sharma, 2017; Zhai et al., 2018).

## **MATERIALS AND METHODS**

### **Preparation of Samples**

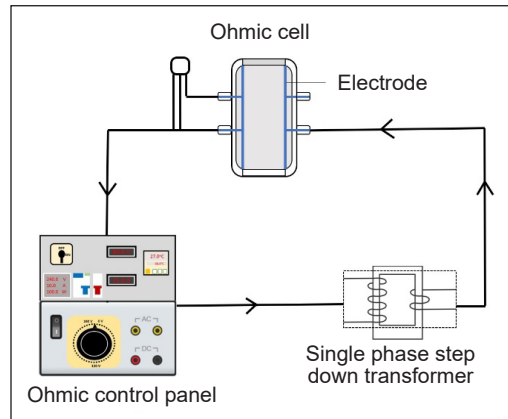
Freshly processed EFB was collected from Seri Bandar Palm Oil Mill (Banting, Selangor, Malaysia). The shredded EFB were then separated from debris and kernel shell before being dried in a drying oven at 50°C for 24 hours to reach a moisture content of less than 10% (Simanungkalit et al., 2017) for fungal proliferation prevention (Marçal et al., 2018). After drying, the EFB was cut and sieved into desired particle sizes (0.5 mm and 1-2 mm) and kept in a proper storage container at room temperature until further use.

### **Ohmic Heater Design and Fabrication**

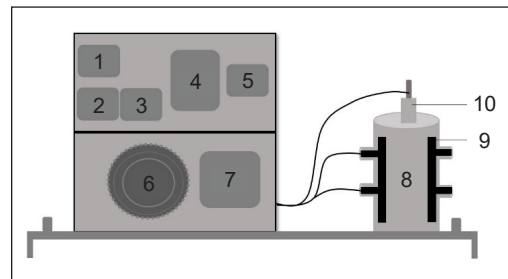
The ohmic heater used in this study was designed and fabricated by Hamzah et al. (2011) for the delignification of LCB at a lab scale, which consisted of a 1 L size cylindrical process chamber with a maximum 800 mL holding capacity, fixed with a pair of titanium electrodes in the process chamber. The main compartments of the ohmic heater consist of an ohmic heated cell, a power supply (transformer), and a temperature sensor. The electrodes are connected to a single-phase alternating current step-down transformer with a 3kW power supply rated at 15 kVA with a maximum working current of 10 A. The electrical energy is converted into thermal energy, and the heat generated is distributed evenly inside the treated materials. With almost 100% energy transfer efficiency, the resulting energy instigates

temperature rise in the system (Gavahian et al., 2019; Lee & Jun, 2011; Picart-Palmade et al., 2019; Shim et al., 2010).

The main advantage of ohmic heating (OH) over conventional and microwave heating (MW) is widely known for its short time of the treatment process, which demonstrated high efficiency in both processing time and heating rate (Alkanan et al., 2021; Gavahian et al., 2019; Lee et al., 2013; Pires et al., 2020; Sakr & Liu, 2014). Less energy consumption with better quality products makes the OH system highly efficient in energy usage, especially compared to microwave and other high-pressure processes (Pires et al., 2020; Rinaldi et al., 2020). In food pasteurization, the thermal effects combined with electric effects can increase cell membrane permeability and destroy bacterial cells (Cappato et al., 2017). Figure 1 shows the design and fabrication of the ohmic heater from the schematic diagram (a) to the fabrication of the ohmic heater (c). From the computer-aided design front view of ohmic heater (b), parts stated are 1: ohmic switch, 2: input power, 3: main switch, 4: ohmic power, 5: temperature controller, 6: ohmic voltage selector, 7: single-phase transformer behind the main cover, 8: ohmic cell, 9: titanium electrode, and 10: thermocouple probe.



(a)



(b)



(c)

Figure 1. Design and fabrication of ohmic heater: (a) schematic diagram of ohmic heater; (b) computer-aided design front view ohmic heater; and (c) fabricated ohmic heater

### Pre-treatment of EFB

A complete series of tests was done to study the potential of ohmic heating pre-treatment on the EFB delignification by comparing the effect of size reduction (SR) and alkaline-assisted ohmic heating (AA-OH) pre-treatment on the composition of cellulose, hemicellulose, and lignin for untreated and pre-treated EFB. Prior to the ohmic heating process, 7 g of prepared native EFB was soaked in 700 mL of 1% w/v sodium hydroxide (NaOH) for 2

hours. This step was necessary to let the fibrous EFB sample absorb the liquid until its equilibrium state. Then, the sample mixture was transferred into the ohmic cell and ohmic heated for 5 minutes at 80°C at a fixed solid-to-liquid ratio of 1:100. The determination of chemical composition for native, size reduced, and ohmic heated EFB was carried out using the Technical Association of the Pulp and Paper Industry (TAPPI) method to see if there was any significant potential for ohmic heating pre-treatment (Hamzah et al., 2020; Mohammad et al., 2020). From the result, further optimization of AA-OH parameters on EFB was done accordingly to one factor at a time (OFAT) for three different variables such as reaction time (5–25 mins), temperature (80–120°C), and concentration of NaOH (1–5% w/v).

### **Morphological and Compositional Analysis of EFB**

Morphological studies to observe the changes of untreated and pre-treated EFB were done by using a Scanning Electron Microscope (SEM), S-3400N model (Hitachi, Japan) equipped with an Energy Dispersive Spectroscopy (EDS) system. The samples were dried in a drying oven at 60°C for 24 hours before undergoing gold coating by a sputtering process, which was done to avoid the charging effect during SEM analysis to ensure their low moisture content. The analysis of morphological changes in the lignin structure of the fibrous sample was recorded at 25 kV acceleration voltage for 250× magnification with a working distance (WD) of 6.3 to 6.4 mm. 5 g of EFB samples were prepared and dried before compositional analysis. TAPPI standard methods (TAPPI, 1950) were followed in the determination of lignin (T-222), holocellulose (T-249-75), and  $\alpha$ -cellulose (T-203) content in all untreated and pre-treated EFB samples. At the same time, hemicellulose content was obtained by subtracting the content of  $\alpha$ -cellulose from the holocellulose.

## **RESULTS AND DISCUSSION**

### **Physical And Morphological Changes of Pre-treated EFB**

Native EFB originally comprises 24–65% cellulose, 17–34% hemicellulose, and 13–37% lignin (Khalil et al., 2012; Chang, 2014; Palamae et al., 2017; Yimlamai et al., 2021). In this work, the chemical compositions of native EFB obtained were comparable to the reported ranges of 22% cellulose, 32% lignin, and 36% hemicellulose. The composition of EFB may vary as this substrate is a natural plant fiber, mainly due to the maturity and freshness level of the empty bunch collected for recovery as well as the geographic factor of the plantation site (Palamae et al., 2017). Figure 2 shows the differences in the physical appearance of the size-reduced EFB (b) and alkaline-assisted ohmic heated EFB (c) compared to the untreated native EFB (a). After the severe grinding process, the size color reduced EFB has gone darker in its powdery form due to the friction created during grinding, resulting in heat generation. The color was slightly lighter for the ohmic-heated EFB, becoming more brittle than its original form.

Morphological and structural changes of pre-treated and untreated EFB were analyzed using Scanning Electron Microscopy (SEM), as shown in Figure 3. Morphologically, one peculiar characteristic can be observed in native EFB, where this fiber has a higher rigidity index than other fibrous plant types, mainly due to its thick cell wall, which is much like the structures of wood cell walls compared to other types of plant cells. From the SEM image results, Figure 3(a), the raw fiber had a relatively smooth surface from the lignin or wax layer cover that protected it from rupture. On the other hand, both pre-treatments significantly altered the fiber morphology and caused some structural damage. Extreme

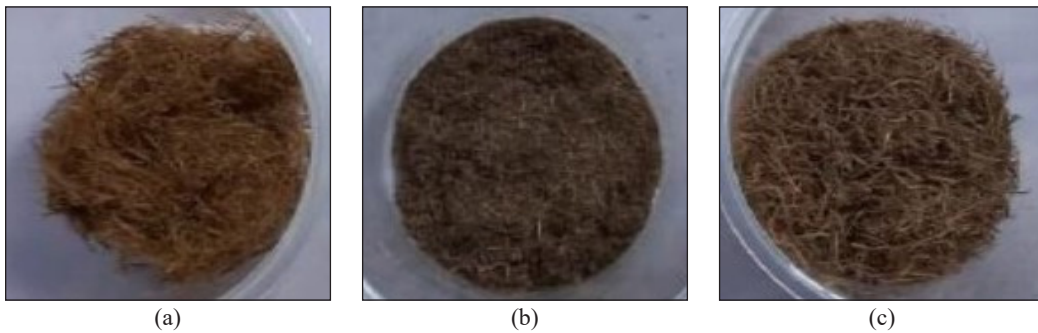


Figure 2. Physical appearances: (a) native EFB; (b) SR-EFB; and (c) AA-OH EFB

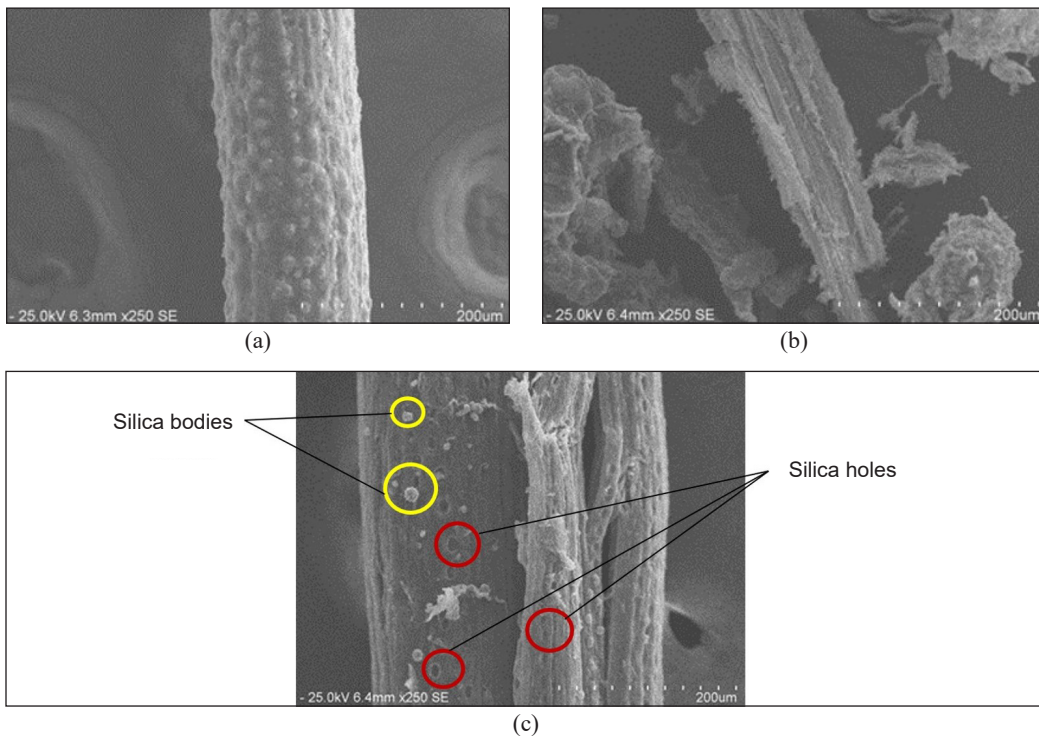


Figure 3. SEM images under 250 $\times$  magnification: (a) native EFB; (b) SR EFB; and (c) AA-OH EFB

size reduction of the EFB led to the tearing of the fiber wall surrounding the cellulose and hemicellulose components, as seen in Figure 3(b). This tearing or fracturing increases the surface area of EFB, which exposes more cellulose and hemicellulose to the subsequent pre-treatment processes. At the same time, a significant effect can be seen after the alkaline-assisted ohmic-heating (AA-OH) process, as in Figure 3(c). Most of the outer layer of lignin was deteriorated and eliminated (Palamae et al., 2017; Azelee et al., 2014) where the cell walls were shattered, and lignin and cellulose were hydrolyzed, creating pores (Iberahim et al., 2013).

Pores formed when pre-treatment using sodium hydroxide (NaOH) formed silica holes (Hamzah et al., 2020), as most of the silica components were removed with extractives on the EFB surface. Removing silica is crucial (Głazowska et al., 2018) because it may create precipitation of insoluble compounds, contributing to biomass recalcitrance. As the silica is deposited in the cell wall, it will protect the plant from enzymatic hydrolysis and microbial attack, acting as one of the physical barriers for fiber, which can cause problems during biomass utilization for bioenergy production (Hamzah et al., 2020; Le et al., 2015). Furthermore, after removing the lignin surfaces of the fiber, circular silica bodies were revealed to be deposited on the surfaces (Palamae et al., 2017). Hence, AA-OH pre-treatment was managed by exposing the cellulose fibers and removing several inter-fiber materials, which opened spaces between the cellulose. It allowed better contact of cellulose to microbial or hydrolytic enzyme activity for an increment of glucose and biogas yield.

### **Lignocellulosic Composition of Untreated and Pre-treated EFB**

The compositional analysis of native, size-reduced (SR), and alkaline-assisted ohmic heated (AA-OH) EFB was determined for lignin, cellulose, and hemicellulose content by using the TAPPI method. The native EFB was prepared accordingly at a particle size ranging from 1 to 2 mm, whereas further size reduction of less than 0.5 mm was done for the SR EFB samples. The EFB samples (1–2 mm) were treated at 300 W of ohmic heating for 5 minutes at 80°C for AA-OH pre-treatment. The electrolyte solvent used was 1% w/v NaOH with a solid-to-liquid ratio of 1:100. After the ohmic heating pre-treatment, the ohmic cell was allowed to cool down first, then de-attached from the electrodes' connecting. The slurry was then filtered through Whatman filter paper No. 1 and washed with distilled water to neutralize the sample. After sample drying at 60°C for 24 hours, the pre-treated samples were stored at room temperature for further analysis.

From the chemical compositional analysis, as shown in Table 1, native EFB comprised lignin (23%), hemicellulose (36%), and cellulose (32%). Another 8% was comprised of extractives and other removal components in the sample. The results obtained were in the ranges found in the literature, which were 15%–30% lignin, 20%–45% hemicellulose, and 20%–65% cellulose (Hamzah et al., 2020; Krishnan et al., 2017; Mohammad et al.,



Table 1  
*Chemical composition of native EFB and pre-treated EFB*

Components (w/w) %	Native EFB	SR EFB	AA-OH EFB
Extractives	4.23	4.11	4.1
Lignin	22.85	20.22	19.30
Hemicelluloses	36.45	34.40	33.98
Cellulose	32.15	36.48	35.78
Removal (others)	4.32	4.79	6.85

2020; Wadchasit et al., 2020). The holocellulosic component in the EFB was the highest by combining the portion of hemicellulose and cellulose (68%). It proved that EFB is one of the perfect substrates for biogas production. On the other hand, the amount of lignin was comparable to the lignin content of hardwoods, which was in the range of 15%–30% (Lourenço & Pereira, 2018; Tarasov et al., 2018) and considered to be high, which necessitates pre-treatment before being utilized as a substrate for biogas production.

From the initial study to investigate the ability of AA-OH pre-treatment on EFB delignification, chemical composition analysis, as in Table 1, has shown a significant positive effect. After SR pre-treatment, it was observed that reducing the particle size of EFB would lead to degradation of both lignin (1.1-fold decrease) and hemicellulose (1.0-fold decrease) content compared to Native EFB. Meanwhile, cellulose composition increased by 1.1-fold. The reduction of EFB's particle size led to a decrease in its polymerization degree and crystalline structure of EFB (Diyanilla et al., 2020). Following that, the surface area of the substrate was increased (Mohammad et al., 2020), which would assist in more efficient enzymatic and microbial hydrolysis (Nabilah-Jansar et al., 2018). However, the cost of this size reduction for feedstock is quite expensive due to the notably high usage of energy for machinery operation, especially in large-scale utilization (Baruah et al., 2018; Cardona et al., 2018; Nabilah-Jansar et al., 2018).

A higher reduction in lignin composition was observed for EFB pre-treated with AA-OH, at a 1.2-fold reduction (19.3%), followed by SR (20.2%), compared to its original lignin content, which was 22.9%. In a similar situation for hemicellulose content, AA-OH reduced the component further than SR pre-treatment, with about a 1.1-fold reduction from 36.5% to 33.98% and 34.40%, respectively. At the same time, the composition of cellulose was increased in the pre-treated EFB for SR and AA-OH, which went up to 36.48% (1.1-fold increase) and 35.78%, respectively. The lignin and hemicellulose reduction and cellulose increment of the EFB after AA-OH pre-treatment are comparable to the SR pre-treatment. Even though there was no significant difference in lignin, hemicellulose, and cellulose content after both pre-treatments, the result still showed that even under mild conditions of treatment and without reducing the size of the substrate, AA-OH has good potential

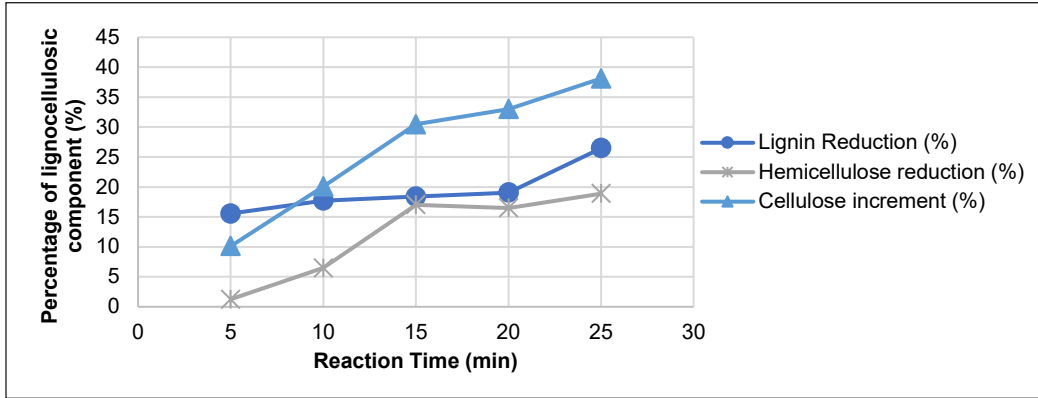
as a new pre-treatment method for EFB delignification. Hence, AA-OH parameters were optimized to find out the optimum condition for high delignification of EFB.

One Factor at A Time (OFAT) optimization approach was selected as the initial methodology for examining and validating the range of values assigned to each parameter under investigation in the delignification process of EFB. The parameters selection and value range for set parameters were referred to another delignification method, microwave-assisted alkaline pre-treatment. Microwave-assisted alkaline delignification is a process that uses microwave irradiation and alkaline solutions to remove lignin from lignocellulosic biomass (Irmak et al., 2018). The process involves treating the EFB with an alkaline solution, followed by exposure to microwave radiation. The microwave radiation causes the alkali solution to heat up rapidly and efficiently penetrate the biomass, resulting in the breakdown of lignin and the release of hemicellulose and cellulose (Alexander et al., 2020). Nomanbhay et al. (2013) obtained 74% of lignin removal by microwave-assisted alkaline pre-treatment on EFB at 12 minutes of reaction time with 3% of NaOH used. Ying et al. (2014) required 60 minutes of reaction time using 2% NaOH solution at 120°C to achieve 42% of lignin removal. Another study by Hamzah et al. (2020), showed an increment in the cellulose composition of EFB after microwave-assisted alkaline pre-treatment from 37% to 49% of cellulose at 120°C for 1 hour reaction time, with 4% NaOH concentration.

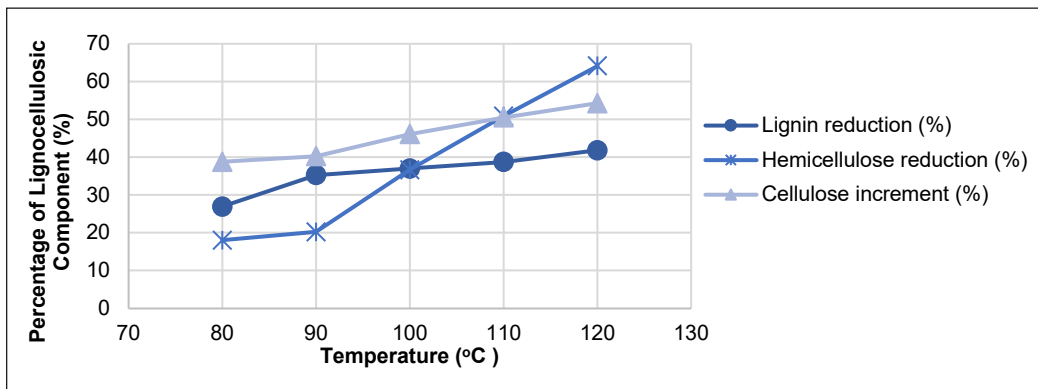
Hence, for this study, three factors for alkaline-assisted ohmic heating were selected: reaction times, F1 (5–25 mins), temperature, F2 (80–120°C), and concentration of NaOH, F3 (1–5 % w/v). The good ohmic heating condition depends mainly on the heat generation rate, system design, the electrical conductivity of the substrate used, electrical field strength, and treatment time (Timsit & Lutten, 2016). It was found that at EFB pre-treated using AA-OH at 300 W, 120°C for 25 minutes had the highest lignin (86.9%) and hemicellulose (75%) removal with the highest cellulose increment (63.2%), as represented in Figure 4. However, at a concentration of 3% w/v of NaOH, significant lignin and hemicellulose removal was already significant enough to utilize a moderate percentage of an alkaline reagent in EFB pre-treatment.

This AA-OH showed better results than past studies using alkaline-assisted microwave heating (AA-MH). Akhtar et al. (2015) pre-soaked EFB in 8% v/v of sulphuric acid, H<sub>2</sub>SO<sub>4</sub>, then the slurry was autoclaved for an hour and followed with AA-MH using 2.5M NaOH solution, microwaved at 10000W, 110°C for 90 minutes. The method managed to remove only 72% of lignin content. Pre-treated EFB using AA-MH with 1% w/v NaOH at 550W microwave power for 12.5 minutes, successfully removing 59% of lignin (Fatriasari et al., 2017). The study revealed that extending the reaction time beyond 25 minutes and increasing the temperature beyond 120°C resulted in the highest removal of lignin and hemicellulose and an expected increase in cellulose yield. However, to gain further insight into the limitations of each parameter in EFB delignification, the study

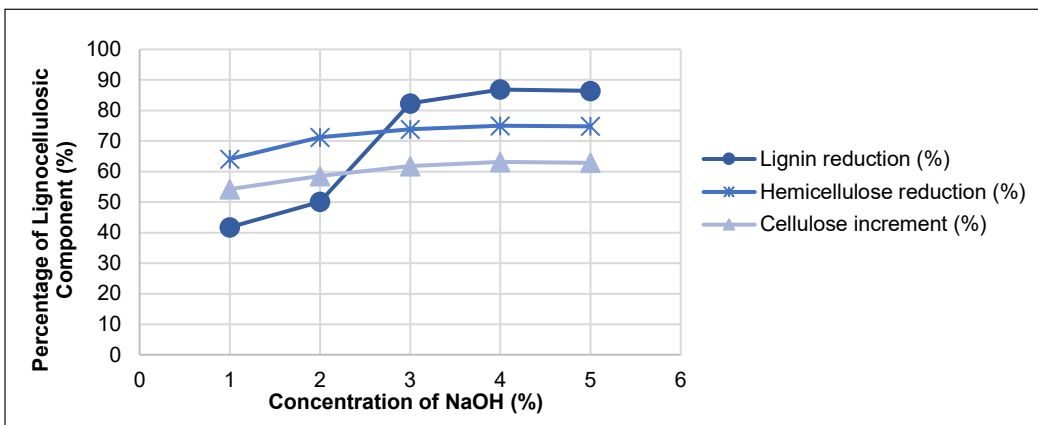
will be further optimized using the Response Surface Methodology (RSM) optimization method. This approach will enable a more comprehensive analysis of outliers within the designated parameter range.



(a)



(b)



(c)

Figure 4. Lignocellulosic composition of OFAT optimization for AA-OH EFB by parameters of: (a) reaction time; (b) temperature; and (c) concentration of NaOH

When the alternating electric (AC) current passes through the EFB samples, it causes the ions in the electrolyte (NaOH) to move towards electrodes with opposite charges (Alkanan et al., 2021; Aurina & Sari, 2022). The ions will collide among them, causing them to be restricted from moving, thereby increasing kinetic energy in the system and generating heat instantly and volumetrically inside the lignocellulosic structure of EFB. The longest residence time (25 minutes) of EFB showed higher lignin reduction (26.5%) even at low temperatures (80°C) and low NaOH concentration. The long contact time of EFB with the electric current that passes through it at constant temperature will enhance the rupture of lignin and hemicellulose structure, producing higher cellulose content. The heat generated depends on the current induced by the field's voltage gradient and the substrate's electrical conductivity (EC). Whereas EC increases with the presence of ionic substances (Bhagwan et al., 2019; Ozkan et al., 2019; Zhuiykov, 2018), thus explaining the high lignin and hemicellulose removal at high NaOH concentrations due to high electrical conductivity. Therefore, heat and kinetic energy generation will increase the system's temperature.

At a higher temperature (120°C), while keeping the ohmic heating power and time constant at 300W and 25 minutes, respectively, results obtained demonstrate better cellulose production (54%) and removal of lignin (42%) and hemicellulose (64%). AC power is utilized in the ohmic heater, so the heating occurs continuously (Aurina & Sari, 2022). OH involves internal mass heating, where heat is generated and transferred from the internal treated medium into the system, which differs from conventional heating in that heat is transferred from the device into the medium (Hamzah et al., 2020). Therefore, such rapid, intense internal heating caused the rupture of the lignocellulosic structure, which allowed more access for cellulose solubilization by alkaline reagent, disrupting the crystalline structure (Akhtar et al., 2015).

## CONCLUSION

In conclusion, AA-OH pre-treatment is suitable for the delignification of EFB with high lignin and hemicellulose removal and high cellulose recovery. Morphological and lignocellulosic compositional analysis of pre-treated EFB showed positive results with significant lignin reduction even at low pre-treatment conditions. These method combinations are more economical and environmentally friendly by reason of a reduction in the number of operational steps. Moreover, they also demonstrated an excellent delignification efficiency of feedstock. This study will be further developed to optimize processing parameters using Response Surface Methodology (RSM), analysis for reducing sugar, and inhibitors for biogas production by anaerobic digestion and dark fermentation process.

## ACKNOWLEDGMENTS

The authors would like to acknowledge the Department of Biological and Agricultural Engineering, Faculty of Engineering UPM, and Malaysia Ministry of Higher Education (MOHE) for the financial and laboratory support through the grant of the Fundamental Research Grant Scheme [FRGS/1/2020/TK0/UPM/02/7].

## REFERENCES

- Akhtar, J., Teo, C. L., Lai, L. W., Hassan, N., Idris, A., & Aziz, R. A. (2015). Factors affecting delignification of oil palm empty fruit bunch by microwave-assisted dilute acid/alkali pretreatment. *BioResources*, *10*(1), 588-596.
- Alexander, R. A., Innasimuthu, G. M., Rajaram, S. K., Jeganathan, P. M., & Somasundarar, S. C. (2020). Process optimization of microwave-assisted alkali pretreatment for enhanced delignification of *Prosopis juliflora* biomass. *Environmental Progress and Sustainable Energy*, *39*(1), Article 13289. <https://doi.org/10.1002/ep.13289>
- Alkanan, Z. T., Altemimi, A. B., Al-Hilphy, A. R. S., Watson, D. G., & Pratap-Singh, A. (2021). Ohmic heating in the food industry: Developments in concepts and applications during 2013-2020. *Applied Sciences*, *11*(6), Article 2507. <https://doi.org/10.3390/app11062507>
- Alvira, P., Tomás-Pejó, E., Ballesteros, M., & Negro, M. J. (2010). Pretreatment technologies for an efficient bioethanol production process based on enzymatic hydrolysis: A review. *Bioresource Technology*, *101*(13), 4851-4861. <https://doi.org/10.1016/j.biortech.2009.11.093>
- Aurina, K., & Sari, A. (2022). Ohmic heating: A review and application in food industry. *Advances in Biological Sciences Research*, *19*, 107-113.
- Azelee, N. I. W., Jahim, J. M., Rabu, A., Murad, A. M. A., Bakar, F. D. A., & Illias, R. M. (2014). Efficient removal of lignin with the maintenance of hemicellulose from kenaf by two-stage pretreatment process. *Carbohydrate Polymers*, *99*, 447-453. <https://doi.org/10.1016/j.carbpol.2013.08.043>
- Baruah, J., Nath, B. K., Sharma, R., Kumar, S., Deka, R. C., Baruah, D. C., & Kalita, E. (2018). Recent trends in the pretreatment of lignocellulosic biomass for value-added products. *Frontiers in Energy Research*, *6*, Article 141. <https://doi.org/10.3389/fenrg.2018.00141>
- Behera, S., Arora, R., Nandhagopal, N., & Kumar, S. (2014). Importance of chemical pretreatment for bioconversion of lignocellulosic biomass. *Renewable and Sustainable Energy Reviews*, *36*, 91-106. <https://doi.org/10.1016/j.rser.2014.04.047>
- Bhagwan, J., Kumar, N., & Sharma, Y. (2019). Fabrication, characterization, and optimization of Mn<sub>x</sub>O<sub>y</sub> nanofibers for improved supercapacitive properties. In Y. B. Pottathara, S. Thomas, N. Kalarikkal, Y. Grohens & V. Kokol (Eds.), *Nanomaterials Synthesis: Design, Fabrication and Applications* (pp. 451-481). Elsevier. <https://doi.org/10.1016/B978-0-12-815751-0.00013-4>
- Cappato, L. P., Ferreira, M. V. S., Guimaraes, J. T., Portela, J. B., Costa, A. L. R., Freitas, M. Q., Cunha, R. L., Oliveira, C. A. F., Mercali, G. D., Marzack, L. D. F., & Cruz, A. G. (2017). Ohmic heating in dairy processing: Relevant aspects for safety and quality. *Trends in Food Science and Technology*, *62*, 104-112. <https://doi.org/10.1016/j.tifs.2017.01.010>

- Cardona, E., Llano, B., Peñuela, M., Peña, J., & Rios, L. A. (2018). Liquid-hot-water pretreatment of palm-oil residues for ethanol production: An economic approach to the selection of the processing conditions. *Energy*, *160*, 441-451. <https://doi.org/10.1016/j.energy.2018.07.045>
- Chang, S. H. (2014). An overview of empty fruit bunch from oil palm as feedstock for bio-oil production. *Biomass and Bioenergy*, *62*, 174-181. <https://doi.org/10.1016/j.biombioe.2014.01.002>
- Conde-Mejía, C., Jiménez-Gutiérrez, A., & El-Halwagi, M. (2012). A comparison of pretreatment methods for bioethanol production from lignocellulosic materials. *Process Safety and Environmental Protection*, *90*(3), 189-202. <https://doi.org/10.1016/j.psep.2011.08.004>
- Diyanilla, R., Hamidon, T. S., Suryanegara, L., & Hussin, M. H. (2020). Overview of pretreatment methods employed on oil palm biomass in producing value-added products: A review. *BioResources*, *15*(4), 9935-9997. <https://doi.org/10.15376/biores.15.4.diyaniilla>
- Ezechi, E. H., & Muda, K. (2019). Overview of trends in crude palm oil production and economic impact in Malaysia. *Sriwijaya Journal of Environment*, *4*(1), 19-26. <https://doi.org/10.22135/sje.2019.4.1.19-26>
- Fatriasari, W., Anita, S. H., & Risanto, L. (2017). Microwave assisted acid pretreatment of oil palm empty fruit bunches (EFB) to enhance its fermentable sugar production. *Waste and Biomass Valorization*, *8*(2), 379-391. <https://doi.org/10.1007/s12649-016-9573-6>
- Gavahian, M., Farhoosh, R., Farahnaky, A., Javidna, K., & Shahidi, F. (2015). Ohmic-assisted hydrodistillation of essential oils from *Mentha piperita*. *Iranian Food Science and Technology Research Journal*, *11*(3), 236-246.
- Gavahian, M., Tiwari, B. K., Chu, Y. H., Ting, Y., & Farahnaky, A. (2019). Food texture as affected by ohmic heating: Mechanisms involved, recent findings, benefits, and limitations. *Trends in Food Science and Technology*, *86*, 328-339. <https://doi.org/10.1016/j.tifs.2019.02.022>
- Głazowska, S., Baldwin, L., Mravec, J., Bukh, C., Hansen, T. H., Jensen, M. M., Fangel, J. U., Willats, W. G. T., Glasius, M., Felby, C., & Schjoerring, J. K. (2018). The impact of silicon on cell wall composition and enzymatic saccharification of *Brachypodium distachyon*. *Biotechnology for Biofuels*, *11*, Article 171. <https://doi.org/10.1186/s13068-018-1166-0>
- Hamzah, F., Idris, A., & Sarif, M. (2020). Effect of microwave-alkali techniques on the morphology and physical changes of treated oil palm empty fruit bunches fiber. *Materials Science Forum*, *987*, 124-128. <https://doi.org/10.4028/www.scientific.net/msf.987.124>
- Hamzah, M. H., Sudin, S. S., Mutalib, T. N. A. T. A., Malek, N. F. H. A., Yusof, N., Jamaludin, H., Man, H. C., & Abidin, Z. Z. (2011). Preliminary study of ohmic heated hydro distillation for essential oil's plant extraction Malaysia. In *2011 IEEE Student Conference on Research and Development* (pp. 211-214). IEEE Publishing. <https://doi.org/10.1109/SCOReD.2011.6148737>
- Hassan, N., Tan, L. W., Anwar, N. A. K., & Idris, A. (2021). Ionic solution pretreatment of oil palm empty fruit bunch to produce sugars. *BioResources*, *16*(1), 1816-1824.
- Hassan, S. S., Williams, G. A., & Jaiswal, A. K. (2018). Emerging technologies for the pretreatment of lignocellulosic biomass. *Bioresource Technology*, *262*, 310-318. <https://doi.org/10.1016/j.biortech.2018.04.099>

- Hoekstra, A. Y., & Wiedmann, T. O. (2014). Humanity's unsustainable environmental footprint. *Science*, *344*(6188), 1114-1117. <https://doi.org/10.1126/science.1248365>
- Hu, F., & Ragauskas, A. (2012). Pretreatment and lignocellulosic chemistry. *Bioenergy Research*, *5*(4), 1043-1066. <https://doi.org/10.1007/s12155-012-9208-0>
- Hu, Y., Qin, H., Zhan, Z., Dun, Y., Zhou, Y., Peng, N., Ling, H., Liang, Y., & Zhao, S. (2016). Optimization of *Saccharomyces boulardii* production in solid-state fermentation with response surface methodology. *Biotechnology & Biotechnological Equipment*, *30*, 173-179. <https://doi.org/10.1080/13102818.2015.1086689>
- Iberahim, N. I., Jahim, J. M., Harun, S., Nor, M. T. M., & Hassan, O. (2013). Sodium hydroxide pretreatment and enzymatic hydrolysis of oil palm mesocarp fiber. *International Journal of Chemical Engineering and Applications*, *4*(3), 101-105. <https://doi.org/10.7763/ijcea.2013.v4.272>
- Indiarto, R., & Rezaharsamto, B. (2020). A review on ohmic heating and its use in food. *International Journal of Scientific & Technology Research*, *9*(2), 485-490.
- Irmak, S., Meryemoglu, B., Sandip, A., Subbiah, J., Mitchell, R. B., & Sarath, G. (2018). Microwave pretreatment effects on switchgrass and miscanthus solubilization in subcritical water and hydrolysate utilization for hydrogen production. *Biomass and Bioenergy*, *108*, 48-54. <https://doi.org/10.1016/J.BIOMBIOE.2017.10.039>
- Karunakaran, V., Abd-Talib, N., & Yong, T. L. K. (2020). Lignin from oil palm empty fruit bunches (EFB) under subcritical phenol conditions as a precursor for carbon fiber production. *Materials Today: Proceedings*, *31*, 100-105. <https://doi.org/10.1016/j.matpr.2020.01.252>
- Karunanithi, S. (2019). Optimization of process parameters of ohmic heating for improving yield and quality of tomato seed oil. *International Journal of Pure & Applied Bioscience*, *7*(3), 104-114. <https://doi.org/10.18782/2320-7051.7477>
- Khalil, H. P. S. A., Jawaid, M., Hassan, A., Paridah, M. T., & Zaido, A. (2012). Oil palm biomass fibres and recent advancement in oil palm biomass fibres based hybrid biocomposites. In N. Hu (Ed.), *Composites and Their Applications* (pp. 187-220). InTech. <https://doi.org/10.5772/48235>
- Kim, J. S., Lee, Y. Y., & Kim, T. H. (2016). A review on alkaline pretreatment technology for bioconversion of lignocellulosic biomass. *Bioresource Technology*, *199*, 42-48. <https://doi.org/10.1016/j.biortech.2015.08.085>
- Krishnan, Y., Bong, C. P. C., Azman, N. F., Zakaria, Z., Othman, N., Abdullah, N., Ho, C. S., Lee, C. T., Hansen, S. B., & Hara, H. (2017). Co-composting of palm empty fruit bunch and palm oil mill effluent: Microbial diversity and potential mitigation of greenhouse gas emission. *Journal of Cleaner Production*, *146*, 94-100. <https://doi.org/10.1016/j.jclepro.2016.08.118>
- Kumar, A. K., & Sharma, S. (2017). Recent updates on different methods of pretreatment of lignocellulosic feedstocks: A review. *Bioresources and Bioprocessing*, *4*, Article 7. <https://doi.org/10.1186/s40643-017-0137-9>
- Kutlu, N., Isci, A., Sakiyan, O., & Yilmaz, A. E. (2021). Effect of ohmic heating on ultrasound extraction of phenolic compounds from cornelian cherry (*Cornus mas*). *Journal of Food Processing and Preservation*, *45*(10), Article e15818. <https://doi.org/10.1111/jfpp.15818>

- Le, D. M., Sørensen, H. R., Knudsen, N. O., & Meyer, A. S. (2015). Implications of silica on biorefineries - interactions with organic material and mineral elements in grasses. *Biofuels, Bioproducts and Biorefining*, 9(1), 109-121. <https://doi.org/10.1002/bbb.1511>
- Lee, S. H., & Jun, S. (2011). Enhancement of sugar release from taro waste using ohmic heating and microwave heating techniques. *Transactions of the ASABE*, 54(3), 1041-1047.
- Lee, S. Y., Ryu, S., & Kang, D. H. (2013). Effect of frequency and waveform on inactivation of *Escherichia coli* O157:H7 and *Salmonella enterica* serovar typhimurium in salsa by ohmic heating. *Applied and Environmental Microbiology*, 79(1), 10-17. <https://doi.org/10.1128/AEM.01802-12>
- Lourenço, A., & Pereira, H. (2018). Compositional variability of lignin in biomass. In M. Poletto (Ed.), *Lignin - Trends and Applications* (pp. 65-98). InTech. <https://doi.org/10.5772/intechopen.71208>
- Marçal, F. A., França, L. F., & Fernandes Corrêa, N. C. (2018). Empty fruit bunch treatment. *BioResources*, 13(3), 6911-6921.
- Mohammad, I. N., Ongkudon, C. M., & Misson, M. (2020). Physicochemical properties and lignin degradation of thermal-pretreated oil palm empty fruit bunch. *Energies*, 13(22), Article 5966. <https://doi.org/10.3390/en13225966>
- Nabilah-Jansar, K., Roslan, A. M., & Hassan, M. A. (2018). Appropriate hydrothermal pretreatment of oil palm biomass in palm oil mill. *Pertanika Journal of Scholarly Research Reviews*, 4(1), 31-40. <http://pjsrr.upm.edu.my/index.php/pjsrr/article/view/119>
- Nomanbhay, S. M., Hussain, R., & Palanisamy, K. (2013). Microwave-assisted alkaline pretreatment and microwave assisted enzymatic saccharification of oil palm empty fruit bunch fiber for enhanced fermentable sugar yield. *Journal of Sustainable Bioenergy Systems*, 03(01), 7-17. <https://doi.org/10.4236/jsbs.2013.31002>
- Ozkan, G., Guldiken, B., & Capanoglu, E. (2019). Effect of novel food processing technologies on beverage antioxidants. In A. M. Grumezescu & A. M. Holban (Eds.), *Processing and Sustainability of Beverages* (pp. 413-449). Elsevier. <https://doi.org/10.1016/b978-0-12-815259-1.00012-4>
- Palamae, S., Dechatiwongse, P., Choorit, W., Chisti, Y., & Prasertsan, P. (2017). Cellulose and hemicellulose recovery from oil palm empty fruit bunch (EFB) fibers and production of sugars from the fibers. *Carbohydrate Polymers*, 155, 491-497. <https://doi.org/10.1016/j.carbpol.2016.09.004>
- Panigrahi, S., & Dubey, B. K. (2019). Electrochemical pretreatment of yard waste to improve biogas production: Understanding the mechanism of delignification, and energy balance. *Bioresource Technology*, 292, Article 121958. <https://doi.org/10.1016/j.biortech.2019.121958>
- Panigrahi, S., Sharma, H. B., Tiwari, B. R., Krishna, N. V., Ghangrekar, M. M., & Dubey, B. K. (2021). Insight into understanding the performance of electrochemical pretreatment on improving anaerobic biodegradability of yard waste. *Renewable Energy*, 180, 1166-1178. <https://doi.org/10.1016/j.renene.2021.08.123>
- Pare, A., Nema, A., Singh, V. K., & Mandhyan, B. L. (2014). Combined effect of ohmic heating and enzyme assisted aqueous extraction process on soy oil recovery. *Journal of Food Science and Technology*, 51(8), 1606-1611. <https://doi.org/10.1007/s13197-012-0685-0>



- Perasiriyana, V., Priya, S., Gowri, A. M., Ramasamy, D., & Sivakumar, T. (2016). Design and evaluation of electrical resistance unit (ohmic heating) for food processing. *International Research Journal of Engineering and Technology*, 3, 1357-1361.
- Pereira, R. N., Rodrigues, R. M., Genisheva, Z., Oliveira, H., de Freitas, V., Teixeira, J. A., & Vicente, A. A. (2016). Effects of ohmic heating on extraction of food-grade phytochemicals from colored potato. *LWT*, 74, 493-503. <https://doi.org/10.1016/j.lwt.2016.07.074>
- Picart-Palmade, L., Cunault, C., Chevalier-Lucia, D., Belleville, M. P., & Marchesseau, S. (2019). Potentialities and limits of some non-thermal technologies to improve sustainability of food processing. *Frontiers in Nutrition*, 5, Article 130. <https://doi.org/10.3389/fnut.2018.00130>
- Pires, R. P. S., Cappato, L. P., Guimarães, J. T., Rocha, R. S., Silva, R., Balthazar, C. F., Freitas, M. Q., Silva, P. H. F., Neto, R. P. C., Tavares, M. I. B., Granato, D., Raices, R. S. L., Silva, M. C., & Cruz, A. G. (2020). Ohmic heating for infant formula processing: Evaluating the effect of different voltage gradient. *Journal of Food Engineering*, 280, Article 109989. <https://doi.org/10.1016/j.jfoodeng.2020.109989>
- Rinaldi, M., Littardi, P., Paciulli, M., Ganino, T., Cocconi, E., Barbanti, D., Rodolfi, M., Aldini, A., & Chiavaro, E. (2020). Impact of ohmic heating and high pressure processing on qualitative attributes of ohmic treated peach cubes in syrup. *Foods*, 9(8), Article 1093. <https://doi.org/10.3390/foods9081093>
- Ríos-Ríos, K. L., Gaytán-Martínez, M., Rivera-Pastrana, D. M., Morales-Sánchez, E., Villamiel, M., Montilla, A., Mercado-Silva, E. M., & Vázquez-Barrios, M. E. (2021). Ohmic heating pretreatment accelerates black garlic processing. *LWT*, 151, Article 112218. <https://doi.org/10.1016/j.lwt.2021.112218>
- Rocheffort, D., Leech, D., & Bourbonnais, R. (2004). Electron transfer mediator systems for bleaching of paper pulp. *Green Chemistry*, 6(1), 14-24. <https://doi.org/10.1039/b311898n>
- Rodríguez, L. M. N., Arias, R., Soteras, T., Sancho, A., Pesquero, N., Rossetti, L., Tacca, H., Aimaretti, N., Cervantes, M. L. R., & Szerman, N. (2021). Comparison of the quality attributes of carrot juice pasteurized by ohmic heating and conventional heat treatment. *LWT*, 145, Article 111255. <https://doi.org/10.1016/j.lwt.2021.111255>
- Sakr, M., & Liu, S. (2014). A comprehensive review on applications of ohmic heating (OH). *Renewable and Sustainable Energy Reviews*, 39, 262-269. <https://doi.org/10.1016/j.rser.2014.07.061>
- Sastry, S. (2008). Ohmic heating and moderate electric field processing. *Food Science and Technology International*, 14(5), 419-422. <https://doi.org/10.1177/1082013208098813>
- Sengun, I. Y., Yildiz Turp, G., Icier, F., Kendirci, P., & Kor, G. (2014). Effects of ohmic heating for pre-cooking of meatballs on some quality and safety attributes. *LWT*, 55(1), 232-239. <https://doi.org/10.1016/j.lwt.2013.08.005>
- Shim, J. Y., Lee, S. H., & Jun, S. (2010). Modeling of ohmic heating patterns of multiphase food products using computational fluid dynamics codes. *Journal of Food Engineering*, 99(2), 136-141. <https://doi.org/10.1016/j.jfoodeng.2010.02.009>
- Simanungkalit, S. P., Mansur, D., Nurhakim, B., Agustin, A., Rinaldi, N., Muryanto, & Fitriady, M. A. (2017). Hydrothermal pretreatment of palm oil empty fruit bunch. *AIP Conference Proceedings*, 1803(1), Article 020011. <https://doi.org/10.1063/1.4973138>

- Sofi'I, I., Arifin, Z., & Oktafrina. (2021). Energy Consumption for Patchouli Oil Extraction Using Ohmic Heating. *IOP Conference Series: Earth and Environmental Science*, 1012(1), Article 012062. <https://doi.org/10.1088/1755-1315/1012/1/012062>
- Sun, S., Sun, S., Cao, X., & Sun, R. (2016). The role of pretreatment in improving the enzymatic hydrolysis of lignocellulosic materials. *Bioresource Technology*, 199, 49-58. Elsevier Ltd. <https://doi.org/10.1016/j.biortech.2015.08.061>
- Sun, W., Greaves, T. L., & Othman, M. Z. (2020). Electro-assisted pretreatment of lignocellulosic materials in ionic liquid-promoted organic solvents. *ACS Sustainable Chemistry and Engineering*, 8(49), 18177-18186. <https://doi.org/10.1021/acssuschemeng.0c06537>
- Tamburini, E., Bernardi, T., Castaldelli, G., Tumiatti, G., & Ferro, S. (2011). Green electrochemical approach for delignification of wheat straw in second-generation bioethanol production. *Energy and Environmental Science*, 4(2), 551-557. <https://doi.org/10.1039/c0ee00226g>
- TAPPI. (1950). *T.A.P.P.I. Standards: Testing Methods, Recommended Practices, Specifications of the Technical Association of the Pulp and Paper Industry*. Technical Association of the Pulp and Paper Industry.
- Tarasov, D., Leitch, M., & Fatehi, P. (2018). Lignin-carbohydrate complexes: Properties, applications, analyses, and methods of extraction: A review. *Biotechnology for Biofuels*, 11(1), 1-28. <https://doi.org/10.1186/s13068-018-1262-1>
- Timsit, R. S., & Luttgen, A. (2016). Temperature distribution in an ohmic-heated electrical contact at high signal frequencies. *Applied Physics Letters*, 108(12), Article 121603. <https://doi.org/10.1063/1.4944535>
- Tunç, M. T., & Koca, İ. (2021). Optimization of ohmic heating assisted hydrodistillation of cinnamon and bay leaf essential oil. *Journal of Food Process Engineering*, 44(3), Article e13635. <https://doi.org/10.1111/jfpe.13635>
- Ummalyma, S. B., Supriya, R. D., Sindhu, R., Binod, P., Nair, R. B., Pandey, A., & Gnansounou, E. (2019). Biological pretreatment of lignocellulosic biomass-current trends and future perspectives. In A. Basile & F. Dalena (Eds.), *Second and Third Generation of Feedstocks: The Evolution of Biofuels* (pp. 197-212). Elsevier Inc. <https://doi.org/10.1016/B978-0-12-815162-4.00007-0>
- Varga, E., Schmidt, A. S., Réczey, K., & Thomsen, A. B. (2003). Pretreatment of corn stover using wet oxidation to enhance enzymatic digestibility. *Applied Biochemistry and Biotechnology - Part A Enzyme Engineering and Biotechnology*, 104(1), 37-50. <https://doi.org/10.1385/ABAB:104:1:37>
- Wadchasit, P., Siripattana, C., & Nuithitikul, K. (2020). The effect of pretreatment methods for improved biogas production from oil-palm empty fruit bunches (EFB): Experimental and model. *IOP Conference Series: Earth and Environmental Science*, 463, Article 012126. <https://doi.org/10.1088/1755-1315/463/1/012126>
- Wang, C., Llave, Y., Sakai, N., & Fukuoka, M. (2021). Analysis of thermal processing of liquid eggs using a high frequency ohmic heating: Experimental and computer simulation approaches. *Innovative Food Science and Emerging Technologies*, 73, Article 102792. <https://doi.org/10.1016/j.ifset.2021.102792>
- Xu, J., Cheng, J. J., Sharma-Shivappa, R. R., & Burns, J. C. (2010). Sodium hydroxide pretreatment of switchgrass for ethanol production. *Energy and Fuels*, 24(3), 2113-2119. <https://doi.org/10.1021/ef9014718>

- Yaser, A. Z., Jananun, J., Chong, K. P., & Haywood, S. K. (2017). Effect of pre-treatment and inoculant during composting of palm oil empty fruit bunches. *ASEAN Journal of Chemical Engineering*, 17(2), 1-16. <https://doi.org/10.22146/ajche.49551>
- Yimlamai, B., Choorit, W., Chisti, Y., & Prasertsan, P. (2021). Cellulose from oil palm empty fruit bunch fiber and its conversion to carboxymethylcellulose. *Journal of Chemical Technology and Biotechnology*, 96(6), 1656-1666. <https://doi.org/10.1002/jctb.6689>
- Ying, T. Y., Teong, L. K., Abdullah, W. N. W., & Peng, L. C. (2014). The effect of various pretreatment methods on oil palm empty fruit bunch (EFB) and kenaf core fibers for sugar production. *Procedia Environmental Sciences*, 20, 328-335. <https://doi.org/10.1016/j.proenv.2014.03.041>
- Zhai, R., Hu, J., & Saddler, J. N. (2018). Minimizing cellulase inhibition of whole slurry biomass hydrolysis through the addition of carbocation scavengers during acid-catalyzed pretreatment. *Bioresource Technology*, 258, 12-17. <https://doi.org/10.1016/j.biortech.2018.02.124>
- Zhao, Y., Wang, Y., Zhu, J. Y., Ragauskas, A., & Deng, Y. (2008). Enhanced enzymatic hydrolysis of spruce by alkaline pretreatment at low temperature. *Biotechnology and Bioengineering*, 99(6), 1320-1328. <https://doi.org/10.1002/bit.21712>
- Zhuykov, S. (2018). Semiconductor nano-crystals in environmental sensors. In S. Zhuykov (Ed.), *Nanostructured Semiconductors* (pp. 475-538). Elsevier Ltd. <https://doi.org/10.1016/b978-0-08-101919-1.00009-x>



## Numerical Analysis and Validation of Characterization of Polydimethylsiloxane Using Hyper-elastic Constitutive Models

Sana Zulfiqar<sup>1</sup>, Abdullah Aziz Saad<sup>1\*</sup>, Zulkifli Ahmad<sup>2</sup>, Feizal Yusof<sup>1</sup> and Zuraihana Bachok<sup>1</sup>

<sup>1</sup>*School of Mechanical Engineering, Universiti Sains Malaysia, Nibong Tebal, 14300, Pulau Penang, Malaysia*

<sup>2</sup>*School of Materials & Mineral Resources Engineering, Universiti Sains Malaysia, Nibong Tebal, 14300, Pulau Penang, Malaysia*

### ABSTRACT

The most researched elastomer in recent years is polydimethylsiloxane (PDMS), which has several uses in various engineering industries. One of the PDMS's key characteristics is its hyper-elasticity nature, which enables the production of sensors, flexible electrical circuits, transducers, and antennas. This study used the hyper-elastic constitutive models to predict the mechanical behavior of incompressible, isotropic, and hyper-elastic material PDMS under uniaxial tension. These models are curve-fitting tools that consist of strain energy density and stress functions. To pursue the analysis, a new formulation of PDMS substrate was proposed, and a tensile test was performed to evaluate its stress-strain behavior. The experimental data was implemented on various hyper-elastic models using Abaqus, like Mooney-Rivlin, Yeoh, Ogden, and reduced polynomial models. The goodness of fit of every model was evaluated by calculating  $R^2$  values. Consequently, among these models, the reduced polynomial model with 6 material constants possessed the highest  $R^2$  value (0.9936) and was considered the best-fit model among the other models. Furthermore, the material constants of this model were applied to the 3D dumbbell-shaped model of PDMS in Abaqus for its validation. The boundary conditions were applied on the model similar to the experimental setup, as 33 mm displacement on one end and the other was fixed with all DOF. For mesh quality and mesh

sensitivity of the material, various mesh sizes with the linear formulation (C3D8RH) were utilized, and the best mesh size was selected to evaluate very close results with the experimental.

*Keywords:* Characterization of material, FEM analysis, hyper-elastic material models, material parameters, polydimethylsiloxane

### ARTICLE INFO

#### Article history:

Received: 16 November 2022

Accepted: 14 March 2023

Published: 09 October 2023

DOI: <https://doi.org/10.47836/pjst.31.6.23>

#### E-mail addresses:

[zulfiqar.sana@ymail.com](mailto:zulfiqar.sana@ymail.com) (Sana Zulfiqar)

[azizsaad@usm.my](mailto:azizsaad@usm.my) (Abdullah Aziz Saad)

[zulkifli@usm.my](mailto:zulkifli@usm.my) (Zulkifli Ahmad)

[mefeizal@usm.my](mailto:mefeizal@usm.my) (Feizal Yusof)

[zuraihana@usm.my](mailto:zuraihana@usm.my) (Zurairhana Bachok)

\* Corresponding author

## INTRODUCTION

Recently, the most popular building material of the siloxane family is polydimethylsiloxane (PDMS). Much work has been done on the applications of PDMS based on its several characteristics and properties like flexibility, elastomeric properties, high chemical resistivity, gas permeability, optical transparency (Izdihar et al., 2021; Martin & Bhushan, 2017), corrosion resistance, bio-compatible (Hassler et al., 2011), thermally stable and viscoelastic nature (Roh et al., 2016). It can easily mold into any shape and is cheaper than other elastomers. In addition, PDMS is non-toxic, non-flammable, and inert. It has a large variety of applications in mechanical, electrical, electronics and biomedical fields (Jewkes et al., 2018) such as stretchable electronic circuits (Zulfiqar et al., 2020; Zulfiqar et al., 2021), mechanical & electrochemical sensors (Casanova-Moreno et al., 2017), robotics, micro-fluid channels (Akther et al., 2020; Bashirzadeh et al., 2018) and Micro-electromechanical systems (MEMS)/Nano Electro-Mechanical System (NEMS) (Yu & Zhao, 2009).

PDMS, a rubber-like hyper-elastic material, is characterized by low elastic and high bulk modulus. The hyper-elastic materials possess large elastic strain and deformation under small volumetric changes. These materials are generally incompressible and do not obey Hooke's law, but they retain excellent energy absorption properties. The mechanical behavior of hyper-elastic materials can be characterized by implementing two methods: experimental and numerical simulation (Aziz et al., 2020; Íñiguez-Macedo et al., 2019; Sugihardjo et al., 2018; S Zulfiqar et al., 2022). Hence, several tests are available for the mechanical characterization of PDMS, such as tensile, fatigue, and creep tests (Doan & Mertiny, 2020; Martins et al., 2010).

Universal Tensile Machine (UTM) is used for different tensile tests. However, for rubber-like materials, ASTM D412 Type C standard (ASTM D412-16, 2021) is opted to make samples. The dog bone-shaped sample is fixed in the two holding grips of the machine in which one side is fixed, and the other is movable, having incremental displacement. This test's main objective is to determine a material's elastomeric properties. From this approach, the more realistic results with higher accuracy are obtained. On the other hand, using numerical software, like Abaqus, Ansys, and SolidWorks, has become more trending (Ribeiro et al., 2018; Souza et al., 2020; Xue et al., 2016). Several hyper-elastic material models for incompressible and isotropic materials, based on the experimental stress-strain data (uniaxial and biaxial) have been proposed in the last 80 years (Anssari-Benam & Bucchini, 2021; Beda, 2007; Bien-aimé et al., 2020; López-Campos et al., 2019; Nunes, 2011; Sattarian & Ghassemi, 2019; Tansel et al., 2020) that give better agreement with uniaxial tensile test data and pure shear data (Beda & Chevalier, 2003; Pucci & Saccomandi, 2002). The popular hyper-elastic material models based on classical Gaussian law (Boyce & Arruda, 2000; Meissner & Matějka, 2002; Wineman, 2005) are Neo-Hookean, Mooney-Rivlin, Yeoh, and Ogden models. The selection of these models depends on experimental

data and working strain range such as Neo-Hookean 30%, Mooney-Rivlin 30% compression & 200% tension, and Ogden up to 700% or more (Faghihi et al., 2014; Gonzalez et al., 2008; Kim et al., 2012; Yu & Zhao, 2009).

The main objective of this study is to characterize the mechanical behavior, in terms of modulus of elasticity and strength, of the proposed PDMS substrate by implementing uniaxial tensile test data on Mooney-Rivlin, Ogden, Yeoh, and reduced polynomial models. The uniaxial tensile test is done to calculate the elastic modulus and tensile strength of the PDMS substrate. Based on stress-strain experimental results, the most suitable constitutive model is selected to simulate the behavior of PDMS further. Finally, FEM analysis is carried out in Abaqus/CAE software to validate material characterization using the material parameters of selected hyper-elastic models on a 3D dumbbell-shaped model under the same boundary conditions used in uniaxial tensile testing. The accuracy of simulated results will be improved by mesh sensitivity and mesh quality analysis.

## HYPER-ELASTIC CONSTITUTIVE MATERIAL MODELS

The mechanical behavior of hyper-elastic materials is calculated by FEM analysis. The accurate constitutive material model is selected to reproduce the non-linear hyper-elastic behavior of a material. The hyper-elastic models are categorized into two types of models: micro-mechanical and macro-mechanical models. Micro-mechanical models work on the methodology of unit cells and manufactured by using different chemicals, while on the other hand, macro-mechanical models study the material's behavior on an experimental data basis. The tensile test is very important for macro-mechanical models to get the experimental data.

Hyper-elastic material models determine the non-linear behavior of hyper-elastic materials like elastomers and rubbers. These models do not work under simple Hooke's law and have a non-linear stress-strain relationship. The hyper-elastic materials are considered to be isotropic and incompressible and have the capability to come to their original shape after unloading, and their flexibility is independent of strain rate (Ali et al., 2010). Such materials also have non-linear mechanical properties under high strain rates. The theory of hyper-elastic materials is defined as a function of strain energy or Helmholtz free energy. Helmholtz free energy measures the work output in the closed thermodynamics system under constant volume and temperature (Wriggers, 2008). The strain energy function plays a very important role in developing a hyper-elastic model by assuming different shapes based on the type of material used. It is also known as the stored energy function obtained by considering thermodynamics and symmetry (Wriggers, 2008). Mathematically, for isotropic and incompressible materials, the strain energy ( $W$ ) function depending on three strain invariants is  $W = f(I_1, I_2, I_3)$ . The strain invariants in terms of principal stretches ( $\lambda$ ) are given as Equations 1–3:

$$I_1 = \lambda_1^2 + \lambda_2^2 + \lambda_3^2 \tag{1}$$

$$I_2 = \lambda_1^2 \lambda_2^2 + \lambda_2^2 \lambda_3^2 + \lambda_3^2 \lambda_1^2 \tag{2}$$

$$I_3 = \lambda_1^2 \lambda_2^2 \lambda_3^2 \tag{3}$$

For incompressible materials, the strain energy function can be written in terms of deviatoric strain energy ( $W_d$ ) and volumetric ( $W_v$ ) strain energy, as given in Equation 4. Hence, the general strain energy ( $W$ ), stress ( $\sigma$ ), and stretch ratio ( $\lambda$ ) equations are expressed in Equations 5–7.

$$W = W_d(I_1, I_2) + W_v(J) \tag{4}$$

$$W = \sum_{i+j=1}^N C_{ij} (I_1 - 3)^i (I_2 - 3)^j + \sum_{k=1}^N \frac{1}{D_k} (J - 1)^{2k} \tag{5}$$

$$\sigma = \lambda_i \frac{\delta W}{\delta \lambda_j} - pI \tag{6}$$

$$\lambda_i = 1 + \varepsilon_i = \left( L_i / L_o \right)_i \tag{7}$$

Where  $J$  is the Jacobean determinant,  $C_{ij}$  and  $D_k$  are material constants. In the case of incompressible materials,  $J = I_3 = \det F = 1$  and hydrostatic pressure ( $p$ ) are negligible, so Equations 5 and 6 are reduced to Equations 8 and 9, respectively.

$$W = \sum_{i+j=1}^N C_{ij} (I_1 - 3)^i (I_2 - 3)^j \tag{8}$$

$$\sigma = \left[ \frac{\delta W}{\delta I_1} + I_1 \frac{\delta W}{\delta I_2} \right] B - 2 \frac{\delta W}{\delta I_2} B^2 \tag{9}$$

Further, the simple stress equation for hyper-elastic deformation behavior in uniaxial, equi-biaxial, and pure shear extension are expressed in Equations 10-12 (Bien-aimé et al., 2020). In case of uniaxial,  $\lambda_2 = \lambda_3 = 1/\sqrt{\lambda}$ .

$$\sigma_{uniax} = 2 \left[ \lambda_1^2 - \frac{1}{(\lambda_1 \lambda_2)^2} \right] \left[ \frac{\delta W}{\delta I_1} + \lambda_2^2 \frac{\delta W}{\delta I_2} \right] \tag{10}$$

$$\sigma_{biax} = 2 \left[ \lambda_2^2 - \frac{1}{(\lambda_1 \lambda_2)^2} \right] \left[ \frac{\delta W}{\delta I_1} + \lambda_1^2 \frac{\delta W}{\delta I_2} \right] \tag{11}$$

$$\sigma_{shear} = 0 \tag{12}$$



### Mooney-Rivlin Model

Mooney-Rivlin model is a phenomenological type model that gives better convergence for a relatively large deformation rate than the Neo-Hookean model (Guo & Sluys, 2006). It is the extension of the Neo-Hookean model, which provides more accurate results. The Mooney-Rivlin model is limited to the uniaxial loading and does not work under biaxial or shear and complex loadings. This model has different forms based on the number of parameters, namely material constants. The selection of a number of parameters of this model depends on the type of stress-strain curve (Guo & Sluys, 2006). The general form of strain energy function ( $W$ ) of the Mooney-Rivlin model is given in Equation 13, and the uniaxial stress ( $\sigma_{uniax}$ ) with  $N$  number of material constants ( $C_{ij}$ ) is defined in Equation 14 for incompressible materials.

$$W = \sum_{i,j=0}^N C_{ij} (I_1 - 3)^i (I_2 - 3)^j \quad [13]$$

$$\sigma_{uniax} = 2C_{10} \left( \lambda^2 - \frac{1}{\lambda} \right) + 2C_{01} \left( \lambda - \frac{1}{\lambda^2} \right) \quad [14]$$

### Ogden Model

The Ogden material model is chosen to describe the non-linear behavior of complex materials like polymers, rubber, and tissues. It usually works under a larger deformation strain rate of up to 700%. The strain energy and uniaxial stress functions are generally expressed by Equations 15 and 16, respectively.

$$W = \sum_{i=1}^N \frac{\mu_i}{\alpha_i} (\lambda_1^{\alpha_i} + \lambda_2^{\alpha_i} + \lambda_3^{\alpha_i} - 3) \quad [15]$$

$$\sigma_{uniax} = \sum_{i=1}^N \mu_i \left( \lambda^{\alpha_i-1} - \lambda^{-1/2\alpha_i-1} \right) \quad [16]$$

Where  $W$  is the strain energy density function,  $N$  is the number of terms in series,  $\lambda_i$  ( $i = 1,2,3$ ) is deviatoric principal stretches,  $\mu_i$ , and  $\alpha_i$  are temperature dependent material constants.

### Yeoh Model

The most appropriate model used for incompressible materials is the Yeoh model because it only involves a third-order polynomial with  $I_1$  dependence (first invariant deformation). It also produces more accurate results than the Neo-Hookean model due to its higher-order first invariant terms. However, it is very difficult to determine the dependence of Helmholtz energy on second or more invariant deformation terms. Therefore, Yeoh neglected  $I_2$  and

higher-order terms. This model is also known as a reduced polynomial model ( $N=3$ ), and for incompressible materials, the strain energy function and uniaxial stress can be expressed in Equations 17 and 18, respectively.

$$W = \sum_{i=1}^{N=3} C_{i0} (I_1 - 3)^i = C_{10} (I_1 - 3) + C_{20} (I_1 - 3)^2 + C_{30} (I_1 - 3)^3 \quad [17]$$

$$\sigma_{uniax} = 2[C_{10} + 2C_{20}(I_1 - 3) + 3C_{30}(I_1 - 3)^2] \quad [18]$$

### Polynomial and Reduced Polynomial Model

A phenomenological model of rubber elasticity is the polynomial hyper-elastic material model. The elastic characteristics of compressible materials can also be described using this approach. It is also a general form of the Neo-Hookean, Mooney-Rivlin, and Yeoh hyper-elastic models and can be extended up to six orders. The polynomial model's strain energy density function is defined in Equation 5 (Ju et al., 2014). The strain energy equation becomes the Mooney-Rivlin model for  $N - 1$ , and the incompressibility factor equals zero. However, if all the  $C_{ij}$  parameters are equal to zero except  $j \neq 0$ , then the final form of the polynomial hyper-elastic model is converted to a reduced polynomial hyper-elastic model. The strain energy equation is reduced to the general form of the Yeoh model (Equation 17). The respective uniaxial stress equation of this model is given in Equation 19.

$$\sigma_{uniax} = 2[C_{10} + 2C_{20}(I_1 - 3) + 3C_{30}(I_1 - 3)^2 + 4C_{40}(I_1 - 3)^3 + 5C_{50}(I_1 - 3)^4 + 6C_{60}(I_1 - 3)^5] \quad [19]$$

## MATERIALS AND METHODS

### Materials and Sample Preparation

The properties and functions of these materials are illustrated in Table 1: Poly(dimethylsiloxane) hydroxyl-terminated (PDMS-OH), fume silica, (3-glycidyoxypropyl) trimethoxysilane (ETMS), toluene, and dibutyltin dilaurate (DBDTL).

The substrate was prepared using PDMS-OH (hydroxyl terminated) as a base polymer and (3-glycidyoxypropyl) trimethoxysilane (ETMS) as cross-linking agent in a ratio of 33:1 (33 parts base polymer and 1 part cross-linking agent). The base polymer was mixed with a viscosity controller (fume silica) and solvent (toluene) for 30 minutes. After that, ETMS was added and mixed for the next 10 minutes. Finally, DBDTL catalyst was mixed into the solution to boost the reaction. The solution was then poured into a rectangular mold to get the rectangular-shaped sheet after curing for 24 hours at room temperature. The three samples of cured PDMS sheets were cut into dumbbell shapes of ASTM D412 Type C standard (Figure 1).

Table 1  
Materials with their properties and functions

Materials	Function	Properties
PDMS-OH	Epoxy resin (binder)	Mol. wt.: $110 \times 10^3$ g/mol Viscosity: $50 \times 10^3$ cSt
Fume silica	Viscosity controller	Particle size: 5–50 nm Specific gravity: 2.2–2.3 g/ml
Toluene	Organic solvent	Mol. wt.: 92.14 g/mol Purity: 99% Density: 0.867 g/ml
ETMS	Cross-linking agent	Mol. wt.: 236.34 g/mol Purity: $\geq 98\%$ Specific gravity: 1.07 g/ml
DBDTL	Catalyst	Mol. wt.: 631.56 g/mol Purity: 95% Density: 1.066 g/ml

### EXPERIMENTAL AND CURVE FITTING OF HYPER-ELASTIC MODELS

PDMS samples were subjected to uniaxial tensile testing under a 10 mm/min loading rate and 10 kN load cell at room temperature. The test samples were gripped at the two ends with 33 mm length. The modulus of elasticity was obtained from the stress-strain curve at small strain values where stress is directly proportional to the strain (validate Hooke’s law). Figure 2 shows the non-linear behavior of PDMS substrate in uniaxial tensile testing.

The engineering stress-strain data was introduced into Abaqus/CAE software to perform the FEM analysis and curve fitting of material (Ali et al., 2010; Subhani & Kumar, 2009) using different built-in hyper-elastic models such as Mooney-Rivlin, Yeoh, Ogden, and reduced polynomial. The

curve fittings of all these models with respect to the experimental data are depicted in Figure 3. In addition, every hyper-elastic model’s accuracy or goodness of fit was examined by coefficient of determination ( $R^2$ ) values. For the best fit hyper-elastic model, the value of



Figure 1. PDMS sample based on ASTM D412 type C standard

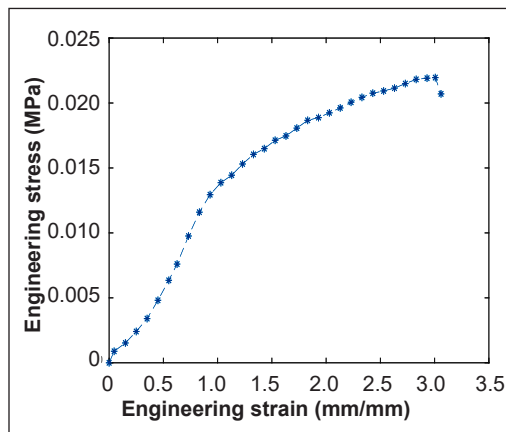


Figure 2. Engineering stress-strain curve of uniaxial tensile data of PDMS material

$R^2$  must be obtained as 1 or very close to 1. However, the general formula for calculating  $R^2$  is given in Equation 20.

$$R^2 = 1 - \frac{\sum_{i=1}^n (Y_{i,exp} - Y_{i,model})^2}{\sum_{i=1}^n (Y_{i,exp} - \overline{Y_{i,exp}})^2} \quad [20]$$

The parameters used in Equation 20 are defined as n is the total number of data points, I represent the integer values from 1 to n,  $Y_{exp}$  demotes the experimental stress values w.r.t. the stretch ratio ( $\lambda_{exp}$ ),  $\overline{Y_{exp}}$  is the average value of experimental stress data, and  $Y_{model}$  gives the stress values obtained by curve fitting of hyper-elastic model w.r.t. the stretch ratio ( $\lambda_{model}$ ).

According to Figure 3, the reduced polynomial ( $N = 6$ ) hyper-elastic model shows stability for all strain values and volumetric data, whereas the other hyper-elastic models are not stable under small and large deformations with the particular uniaxial tensile test data. Hence, the material coefficients and accuracy of respective hyper-elastic constitutive models obtained by curve fitting analysis are listed in Tables 2 and 3.

From Tables 2 and 3, it can be seen that the lowest coefficient of determination value ( $R^2$ ), i.e., 0.8991, was obtained by using Mooney-Rivlin ( $N = 2$ ), while the highest  $R^2$  value using a reduced polynomial model with 6 number of material constants was calculated as 0.9963. This value explained the accuracy of the hyper-elastic model w.r.t. to the experimental test data. Thus, based on its accuracy and curve fitting graph, the reduced polynomial hyper-elastic model was selected as the best fit hyper-elastic model (Figure 3).

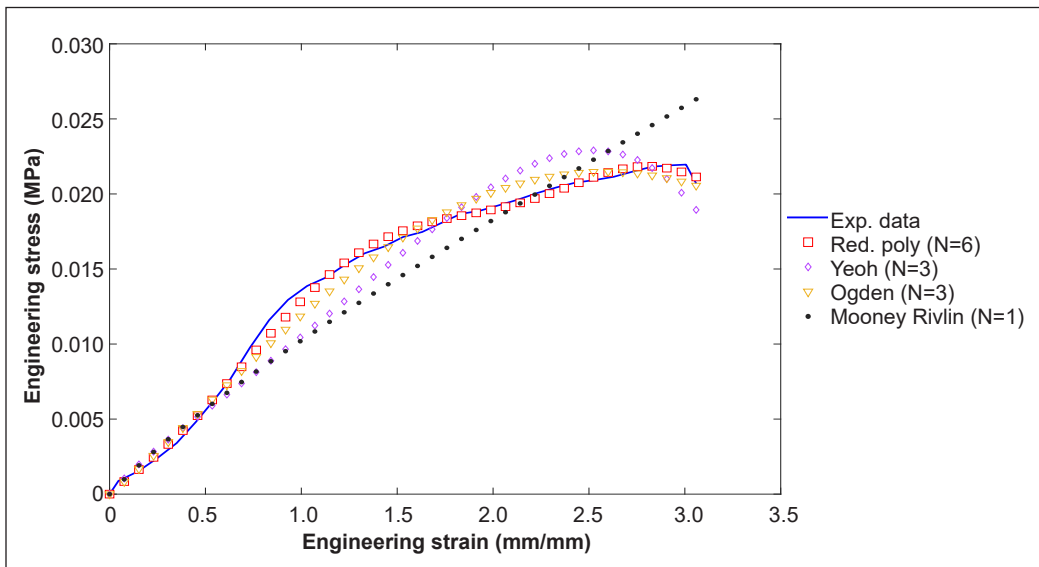


Figure 3. Curve fitting of experimental tensile data for PDMS material using different hyper-elastic constitutive models

Table 2  
Material constants and accuracy of Mooney-Rivlin, Yeoh, and Reduced Polynomial models

FE Models	Material Constants [ $C_{ij}$ , MPa]							$R_2$
	$C_{10}$	$C_{20}$	$C_{30}$	$C_{40}$	$C_{50}$	$C_{60}$	$C_{01}$	
Mooney-Rivlin ( $N = 1$ )	$3.65 \times 10^{-3}$	-	-	-	-	-	$-1.44 \times 10^{-3}$	0.8991
Yeoh ( $N = 3$ )	$2.45 \times 10^{-3}$	$1.61 \times 10^{-4}$	$-7.83 \times 10^{-6}$	-	-	-	-	0.9474
Reduced Polynomial ( $N = 6$ )	$1.94 \times 10^{-3}$	$8.20 \times 10^{-4}$	$-1.65 \times 10^{-4}$	$1.57 \times 10^{-5}$	$-7.18 \times 10^{-7}$	$1.28 \times 10^{-8}$	-	0.9963

Table 3  
Material constants and accuracy of the Ogden model

FE Model	Material Constants						$R^2$
	$\mu_1$ (MPa)	$\mu_2$ (MPa)	$\mu_3$ (MPa)	$\alpha_1$	$\alpha_2$	$\alpha_3$	
Ogden ( $N = 3$ )	0.347	-0.149	-0.194	1.998	2.269	1.698	0.9814

**NUMERICAL ANALYSIS AND VALIDATION OF BEST FIT HYPER-ELASTIC MODEL**

In this study, the numerical analysis was simulated initially by considering only the elastic region of the specimen. The goal of employing PDMS’ elastic characteristics in FEM simulation was to acquire strain values in the elastic area. A 3D dumbbell-shaped model based on the ASTM D412 type C standard was developed, as shown in Figure 4.

The material properties of PDMS were implemented on the above model. These properties include modulus of elasticity as 0.48 MPa and Poisson’s ratio as 0.499. The material constants of reduced polynomial ( $N=6$ ), such as  $C_{10} = 0.00194$ ,  $C_{20} = 0.00082$ ,  $C_{30} = -0.000165$ ,  $C_{40} = 1.57 \times 10^{-5}$ ,  $C_{50} = -7.18 \times 10^{-7}$  and  $C_{60} = 1.28 \times 10^{-8}$ , were chosen based on its high accuracy value than the other hyper-elastic models. The element type 8-node linear brick, hybrid formulation, constant pressure, reduced integration, and hourglass control (C3D8RH) opted for meshing. After meshing, the boundary conditions, as per uniaxial tensile testing, were set as all degree of freedom (DOF) was fixed at the one end of the model, which illustrates that all number of nodes were restricted to move in any direction, making that end equivalent to the fixed lower jaw of UTM. On the other hand, the displacement of about 33 mm was applied on the other end

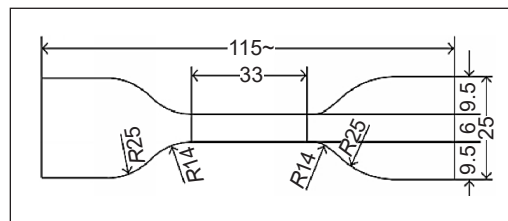


Figure 4. 3D model for PDMS material as per ASTM D412 type C standard  
Note. Dimension unit in mm

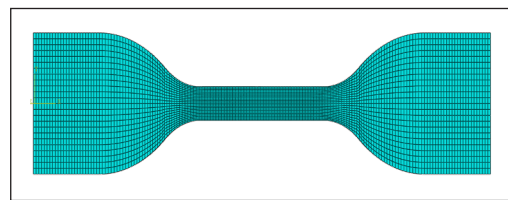
of the model in the x-direction. There would be no displacement in the other two directions, i.e., the y and z directions were fixed ( $U_y = U_z = 0$ ). The boundary conditions and meshing of the proposed parametrized FE model of PDMS material are depicted in Figure 5.

In the C3D8RH element type, the pressure or stress is considered an independent interpolated solution variable connected with displacement solution via constitutive theory (Shahzad et al., 2015). The mesh sensitivity analysis for the uniaxial tensile test was investigated upon establishing the FE model. This analysis aims to determine the ideal element size, type, and numerical formulation to get good results with the least computational work. Different mesh sizes, such as from 2 mm to 0.5 mm of linear formulation, were utilized to evaluate the stress-strain values of the PDMS model along the x-direction. The simulated stress-strain values were then compared with the experimental values to validate the best-fit hyper-elastic model with the respective mesh size. To determine the quality and convergence of mesh size for the simulated results with experimental data, the mean absolute error (MAE) against each mesh size (Martinez et al., 2018; Gómez et al., 2017; Lorza et al., 2017) was calculated using Equation 21.

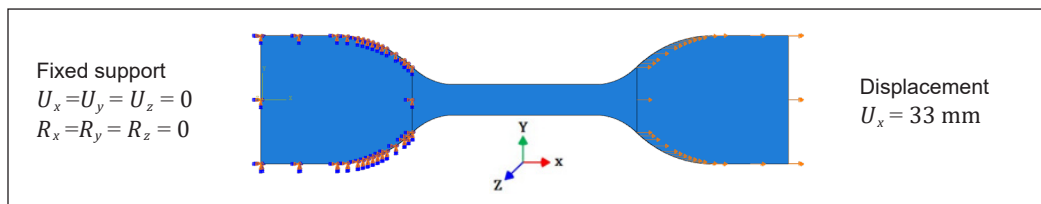
$$MAE = \frac{1}{k} \sum_{m=1}^k |Y_{m,exp} - Y_{m,FE}| \quad [21]$$

Where  $k$  represents the total number of stress-strain data points with  $m = 1, 2, 3, \dots, k$  integers. The experimental and FE stress values with  $m$  number of points are denoted by  $Y_{m,exp}$  and  $Y_{m,FE}$ , respectively.

In addition, the mesh quality enhancement of different mesh sizes is a significant issue for various real-world problems. The results obtained after simulation can be affected by the analysis of the element quality of the mesh. There are variable methods used to improve the quality of mesh sizes, such as aspect ratio (Parthasarathy & Kodiyalam, 1991), Jacobean ratio, and maximum/minimum angles (Chen et al., 2003; Dassi et al., 2016; Ma & Wang, 2021). This research examined the aspect ratios of all the mesh sizes, i.e.,



(a)



(b)

Figure 5. 3D dumbbell-shaped model of PDMS material: (a) Meshing; and (b) boundary conditions

from 2 mm to 0.5 mm, to determine the mesh quality factor. The aspect ratio is, however, defined as the ratio of the longest edge and the shortest normal dropped from a vertex to the opposite face of the element. A good quality mesh must possess an aspect ratio value of less than 5 for the majority of its elements, i.e., equal to or greater than 90% (SYSTEMES, 2021). The high aspect ratios are related to the greater discrepancies of the FE modeling and negatively influenced the convergence of the simulation results. Maintaining the ideal aspect ratio value of 1 for complicated geometries is impossible. Therefore, the modest values of aspect ratios can be retained in the crucial regions of the domain to ensure the fidelity of the simulated results. To highlight the elements with an aspect ratio larger than a certain value, the user must set a criterion in the Verify Mesh tool of Abaqus. Nonetheless, the two aspect ratios greater than 10 and greater than 3 were chosen for the mesh quality analysis of different mesh sizes of the PDMS material.

Besides, the simulated stress-strain values of the reduced polynomial hyper-elastic model were acquired in the natural logarithmic scale. The obtained stress-strain data were converted into engineering stress-strain using Equations 21 and 22 to compare with the experimental data. However, Table 4 shows the simulated engineering stress-strain values at different mesh sizes along with the respective number of nodes, elements, computational cost, aspect ratios, and *MAE* error.

$$\sigma^{true} = \sigma^{eng} e^{\varepsilon^{true}} = \sigma^{eng} (1 + \varepsilon^{eng}) \quad [21]$$

$$\varepsilon^{true} = \ln(1 + \varepsilon^{eng}) \quad [22]$$

The parameters in Equations 21 and 22 are as follows:  $\sigma^{true}$  gives the true stress values,  $\sigma^{eng}$  represents the engineering stress, and  $\varepsilon^{true}$  and  $\varepsilon^{eng}$  denote the true strain and engineering stress values, respectively.

It is worth noticing from Table 4 that by decreasing the mesh sizes from 2 mm to 0.5 mm, the number of nodes and elements increased, which provides the stress-strain simulated results very close to the experimental results. The accuracy of the results increased by increasing the number of nodes and elements, but the main purpose of meshing was to validate the stress-strain data of the best-fit hyper-elastic model with the experimental data. 0.6 mm and 0.5 mm mesh sizes possessed the lowest *MAE* of 0.049% than the other mesh sizes, but it is not enough to select the mesh size based on *MAE* only. Therefore, other factors such as aspect ratio and computational cost are also very important in choosing the best mesh size for PDMS material. For this purpose, 0.8 mm mesh size exhibited the lowest aspect ratio of 1.93 with the acceptable *MAE* (0.053%) and computational cost of 331 seconds. The maximum von Mises engineering stress and strain were obtained at 0.8 mm as 0.009890 MPa and 0.783718, respectively. Consequently, these simulated stress-strain values agree with the experimental stress (0.011140 MPa) and strain (0.78450). Based on

these results, a 0.8 mm mesh size of C3D8RH linear formulation was opted to validate the best-fit hyper-elastic model, i.e., reduced polynomial ( $N = 6$ ). Thus, the contour plots of von Mises true stress and maximum principal true strain along x–the direction for the particular mesh size and element type are illustrated in Figure 6.

According to the contour plots, the maximum variation in stress and strain occurred at the necking of the 3D dumbbell-shaped model of the PDMS material because the boundary conditions with 33 mm gauge length, were applied simultaneously at the two ends of the sample, i.e., 33 mm displacement along x-direction at one end and all degree of freedom fixed on another end.

Table 4  
Various mesh sizes with aspect ratio and mean absolute error of PDMS

Mesh Size (mm)	Nodes	Elements	Computational cost (sec)	Aspect Ratio	Max. von Mises engineering stress (MPa)	Max. principal engineering strain	MAE (%)
2.0	1026	448	27	2.23	0.009081	0.728519	0.082
1.8	1560	704	44	2.21	0.009154	0.733456	0.075
1.6	2064	935	56	2.01	0.009537	0.759615	0.063
1.4	2790	1288	71	2.15	0.009647	0.767076	0.061
1.2	3328	1545	78	2.29	0.009679	0.769281	0.060
1.0	6840	4284	215	2.18	0.009794	0.777118	0.058
0.8	10296	6510	331	1.93	0.009890	0.783718	0.053
0.7	12600	8016	419	1.99	0.009968	0.789038	0.053
0.6	24480	17661	1026	2.0	0.010043	0.794167	0.049
0.5	33740	24480	1870	1.94	0.010110	0.798581	0.049

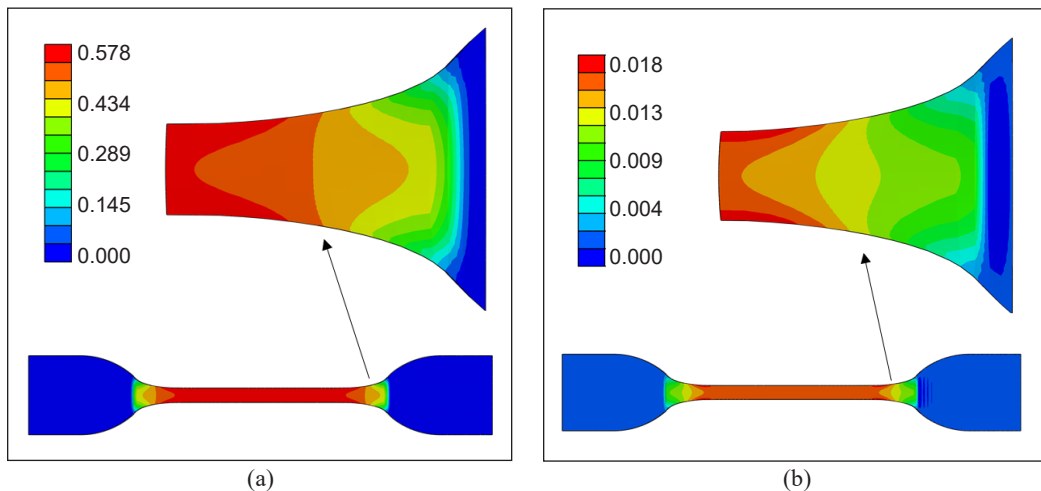


Figure 6. Contour plots of the Reduced Polynomial ( $N = 6$ ) model: (a) Simulated true strain; and (b) simulated true stress



## CONCLUSION

In this work, the mechanical behavior of PDMS was characterized through uniaxial tensile test and hyper-elastic material models. The uniaxial tensile test data obtained by UTM was imported into Abaqus, and curve fitting for different hyper-elastic material models was carried out. Among these hyper-elastic models, the reduced polynomial ( $N = 6$ ) model was the most adequate solution for fitting the maximum points of experimental data according to the evaluation of the coefficient of determination ( $R^2$ ) value of every hyper-elastic model. However, the reduced polynomial model exhibited the highest  $R^2$  value (0.9963) than others. The FE simulation was then conducted on the PDMS sample to validate the reduced polynomial model. For this purpose, the analysis was carried out under the same boundary conditions as in the experimental analysis, i.e., fixed all DOF at one end, and 33 mm displacement was applied on the other end along the x-direction. The material constants of the best-fit hyper-elastic model were implemented on the 3D model. The simulation used different mesh sizes (2 mm to 0.5 mm) of C3D8RH linear formulation element type. The accuracy of the simulated results was improved by performing mesh quality analysis in terms of aspect ratio, and the MAE error of every mesh was also calculated. Based on these criteria, 0.8 mm mesh size possessed the lowest MAE error (0.053%) with 331 seconds computational cost and the lowest aspect ratio of about 1.93 than other mesh sizes. Consequently, the stress-strain data of the reduced polynomial model with 6 material constants agreed with the experimental stress-strain data points. Thus, this model can better fit the test and simulated data with the same boundary conditions. The results of numerical simulation might be different from experimental values if the displacement and thickness values of the material change.

## ACKNOWLEDGEMENT

This paper is a part of a research project supported through Research University Grant 1001.PMEKANIK.8014067 and Short-Term Grant 304.PMEKANIK. 6315494 by Universiti Sains Malaysia (USM). The authors thank the Polymer Lab and Rubber Lab of the School of Materials and Mineral Resources Engineering, USM, for providing experimental services to pursue this study.

## REFERENCES

- Akther, F., Yakob, S. B., Nguyen, N. T., & Ta, H. T. (2020). Surface modification techniques for endothelial cell seeding in PDMS microfluidic devices. *Biosensors*, 10(11), Article 182. <https://doi.org/10.3390/bios10110182>
- Ali, A., Hosseini, M., & Sahari, B. B. (2010). A review of constitutive models for rubber-like materials. *American Journal of Engineering and Applied Sciences*, 3(1), 232-239. <https://doi.org/10.3844/ajeassp.2010.232.239>

- Anssari-Benam, A., & Bucchi, A. (2021). A generalised neo-Hookean strain energy function for application to the finite deformation of elastomers. *International Journal of Non-Linear Mechanics*, 128, Article 103626. <https://doi.org/https://doi.org/10.1016/j.ijnonlinmec.2020.103626>
- ASTM D412-16. (2021). *Standard test methods for vulcanized rubber and thermoplastic elastomers-tension*. ASTM International. <https://doi.org/10.1520/D0412-16R21>
- Aziz, N. A., Saad, A. A., Ahmad, Z., Zulfiqar, S., Ani, F. C., & Samsudin, Z. (2020). Chapter 8 - Stress analysis of stretchable conductive polymer for electronics circuit application. In A. S. H. Makhlof & M. Aliofkhaezrai (Eds.), *Handbook of Materials Failure Analysis* (pp. 205-224). Butterworth-Heinemann. <https://doi.org/https://doi.org/10.1016/B978-0-08-101937-5.00008-7>
- Bashirzadeh, Y., Qian, S., & Maruthamuthu, V. (2018). Non-intrusive measurement of wall shear stress in flow channels. *Sensors and Actuators, A: Physical*, 271, 118-123. <https://doi.org/10.1016/j.sna.2018.01.012>
- Beda, T. (2007). Modeling hyperelastic behavior of rubber: A novel invariant-based and a review of constitutive models. *Journal of Polymer Science, Part B: Polymer Physics*, 45(13), 1713-1732. <https://doi.org/10.1002/polb.20928>
- Beda, T., & Chevalier, Y. (2003). Hybrid continuum model for large elastic deformation of rubber. *Journal of Applied Physics*, 94(4), 2701-2706. <https://doi.org/10.1063/1.1586471>
- Bien-aimé, L. K. M., Blaise, B. B., & Beda, T. (2020). Characterization of hyperelastic deformation behavior of rubber-like materials. *SN Applied Sciences*, 2(4), Article 648. <https://doi.org/10.1007/s42452-020-2355-6>
- Boyce, M. C., & Arruda, E. M. (2000). Constitutive models of rubber elasticity: A review. *Rubber Chemistry and Technology*, 73(3), 504-523. <https://doi.org/10.5254/1.3547602>
- Casanova-Moreno, J., To, J., Yang, C. W. T., Turner, R. F. B., Bizzotto, D., & Cheung, K. C. (2017). Fabricating devices with improved adhesion between PDMS and gold-patterned glass. *Sensors and Actuators, B: Chemical*, 246, 904-909. <https://doi.org/10.1016/j.snb.2017.02.109>
- Chen, Z., Tristano, J. R., & Kwok, W. (2003, September 14-17). Combined laplacian and optimization-based smoothing for quadratic mixed surface meshes. In *Proceedings of the 12th International Meshing Roundtable, IMR 2003* (pp. 360-370). Santa Fe, New Mexico, USA.
- Dassi, F., Kamenski, L., & Si, H. (2016). Tetrahedral mesh improvement using moving mesh smoothing and lazy searching flips. *Procedia Engineering*, 163, 302-314. <https://doi.org/10.1016/j.proeng.2016.11.065>
- Doan, H. G. M., & Mertiny, P. (2020). Creep testing of thermoplastic fiber-reinforced polymer composite tubular coupons. *Materials*, 13(20), 1-17. <https://doi.org/10.3390/ma13204637>
- Faghihi, S., Karimi, A., Jamadi, M., Imani, R., & Salarian, R. (2014). Graphene oxide/poly(acrylic acid)/gelatin nanocomposite hydrogel: Experimental and numerical validation of hyperelastic model. *Materials Science and Engineering C*, 38(1), 299-305. <https://doi.org/10.1016/j.msec.2014.02.015>
- Gómez, F. S., Lorza, R. L., Bobadilla, M. C., & García, R. E. (2017). Improving the process of adjusting the parameters of finite element models of healthy human intervertebral discs by the multi-response surface method. *Materials*, 10(10), Article 1116. <https://doi.org/10.3390/ma10101116>

- Gonzalez, M., Axisa, F., Bulcke, M. Vanden, Brosteaux, D., Vandeveldel, B., & Vanfleteren, J. (2008). Design of metal interconnects for stretchable electronic circuits. *Microelectronics Reliability*, 48(6), 825-832. <https://doi.org/10.1016/j.microrel.2008.03.025>
- Guo, Z., & Sluys, L. J. (2006). Application of a new constitutive model for the description of rubber-like materials under monotonic loading. *International Journal of Solids and Structures*, 43(9), 2799-2819. <https://doi.org/10.1016/j.ijsolstr.2005.06.026>
- Hassler, C., Boretius, T., & Stieglitz, T. (2011). Polymers for neural implants. *Journal of Polymer Science, Part B: Polymer Physics*, 49(1), 18-33. <https://doi.org/10.1002/polb.22169>
- Íñiguez-Macedo, S., Lostado-Lorza, R., Escribano-García, R., & Martínez-Calvo, M. A. (2019). Finite element model updating combined with multi-response optimization for hyper-elastic materials characterization. *Materials*, 12(7), Article 1019. <https://doi.org/10.3390/ma12071019>
- Izdihar, K., Razak, H. R. A., Supion, N., Karim, M. K. A., Osman, N. H., & Norkhairunnisa, M. (2021). Structural, mechanical, and dielectric properties of polydimethylsiloxane and silicone elastomer for the fabrication of clinical-grade kidney phantom. *Applied Sciences*, 11(3), 1-13. <https://doi.org/10.3390/app11031172>
- Jewkes, R., Burton, H. E., & Espino, D. M. (2018). Towards additive manufacture of functional, spline-based morphometric models of healthy and diseased coronary arteries: *In vitro* proof-of-concept using a porcine template. *Journal of Functional Biomaterials*, 9(1), Article 15. <https://doi.org/10.3390/jfb9010015>
- Ju, M. L., Jmal, H., Dupuis, R., & Aubry, E. (2014). A Comparison among polynomial model, reduced polynomial model and Ogden model for polyurethane foam. *Material Science and Engineering Technology II*, 856, 169-173. <https://doi.org/10.4028/www.scientific.net/AMR.856.169>
- Kim, B., Lee, S. B., Lee, J., Cho, S., Park, H., Yeom, S., & Park, S. H. (2012). A comparison among Neo-Hookean model, Mooney-Rivlin model, and Ogden model for Chloroprene rubber. *International Journal of Precision Engineering and Manufacturing*, 13(5), 759-764. <https://doi.org/10.1007/s12541-012-0099-y>
- López-Campos, J. A., Segade, A., Casarejos, E., Fernández, J. R., & Días, G. R. (2019). Hyperelastic characterization oriented to finite element applications using genetic algorithms. *Advances in Engineering Software*, 133, 52-59. <https://doi.org/10.1016/j.advengsoft.2019.04.001>
- Lorza, R. L., Bobadilla, M. C., Calvo, M. Á. M., & Roldán, P. M. V. (2017). Residual stresses with time-independent cyclic plasticity in finite element analysis of welded joints. *Metals*, 7(4), Article 136. <https://doi.org/10.3390/met7040136>
- Ma, Y., & Wang, M. (2021). An efficient method to improve the quality of tetrahedron mesh with MFRC. *Scientific Reports*, 11(1), Article 22802. <https://doi.org/10.1038/s41598-021-02187-1>
- Martin, S., & Bhushan, B. (2017). Transparent, wear-resistant, superhydrophobic and superoleophobic poly(dimethylsiloxane) (PDMS) surfaces. *Journal of Colloid and Interface Science*, 488, 118-126. <https://doi.org/10.1016/j.jcis.2016.10.094>
- Martinez, R. F., Lorza, R. L., Delgado, A. A. S., & Pullaguari, N. O. P. (2018). Optimizing presetting attributes by softcomputing techniques to improve tapered roller bearings working conditions. *Advances in Engineering Software*, 123, 13-24. <https://doi.org/10.1016/j.advengsoft.2018.05.005>

- Martins, P., Peña, E., Calvo, B., Doblaré, M., Mascarenhas, T., Jorge, R. N., & Ferreira, A. (2010). Prediction of nonlinear elastic behaviour of vaginal tissue: Experimental results and model formulation. *Computer Methods in Biomechanics and Biomedical Engineering*, 13(3), 327-337. <https://doi.org/10.1080/10255840903208197>
- Meissner, B., & Matějka, L. (2002). Comparison of recent rubber-elasticity theories with biaxial stress-strain data: The slip-link theory of Edwards and Vilgis. *Polymer*, 43(13), 3803-3809. [https://doi.org/10.1016/S0032-3861\(02\)00150-7](https://doi.org/10.1016/S0032-3861(02)00150-7)
- Nunes, L. C. S. (2011). Mechanical characterization of hyperelastic polydimethylsiloxane by simple shear test. *Materials Science and Engineering: A*, 528(3), 1799-1804. <https://doi.org/https://doi.org/10.1016/j.msea.2010.11.025>
- Parthasarathy, V. N., & Kodiyalam, S. (1991). A constrained optimization approach to finite element mesh smoothing. *Finite Elements in Analysis and Design*, 9(4), 309-320. [https://doi.org/10.1016/0168-874X\(91\)90004-I](https://doi.org/10.1016/0168-874X(91)90004-I)
- Pucci, E., & Saccomandi, G. (2002). A note on the gent model for rubber-like materials. *Rubber Chemistry and Technology*, 75(5), 839-851. <https://doi.org/10.5254/1.3547687>
- Ribeiro, J., Fernandes, C. S., & Lima, R. (2018). Numerical simulation of hyperelastic behaviour in aneurysm models. *Lecture Notes in Computational Vision and Biomechanics*, 27, 937-944. [https://doi.org/10.1007/978-3-319-68195-5\\_102](https://doi.org/10.1007/978-3-319-68195-5_102)
- Roh, C., Lee, J., & Kang, C. K. (2016). Physical properties of PDMS (polydimethylsiloxane) microfluidic devices on fluid behaviors: Various diameters and shapes of periodically-embedded microstructures. *Materials*, 9(10), Article 836. <https://doi.org/10.3390/ma9100836>
- Sattarian, M., & Ghassemi, A. (2019). Identifying the poly methyl methacrylate behavior during free thermoforming using experimental tests and numerical simulation. *Journal of Theoretical and Applied Mechanics*, 57(4), 909-921. <https://doi.org/10.15632/jtam-pl/112414>
- Shahzad, M., Kamran, A., Siddiqui, M. Z., & Farhan, M. (2015). Mechanical characterization and FE modelling of a hyperelastic material. *Materials Research*, 18(5), 918-924. <https://doi.org/10.1590/1516-1439.320414>
- Souza, A., Marques, E., Balsa, C., & Ribeiro, J. (2020). Characterization of shear strain on PDMS: Numerical and experimental approaches. *Applied Sciences*, 10(9), Article 3322. <https://doi.org/10.3390/app10093322>
- Subhani, P. M., & Kumar, R. K. (2009). A new stored energy function for rubber like materials for low strains. *Mechanics of Advanced Materials and Structures*, 16(5), 402-416. <https://doi.org/10.1080/15376490902781167>
- Sugihardjo, H., Tavio, T., & Lesmana, Y. (2018). FE model of low grade rubber for modeling housing's low-cost rubber base isolators. *Civil Engineering Journal*, 4(1), 24-45. <https://doi.org/10.28991/cej-030966>
- SYSTEMES, D. (2021). *Mesh Quality Checks*. DASSAULT SYSTEMES. [https://help.solidworks.com/2021/english/SolidWorks/cworks/c\\_Mesh\\_Quality\\_Checks.htm#:~:text=A good-quality mesh has,Aspect ratio of all elements](https://help.solidworks.com/2021/english/SolidWorks/cworks/c_Mesh_Quality_Checks.htm#:~:text=A good-quality mesh has,Aspect ratio of all elements)

- Tansel, D. Z., Brenneman, J., Fedder, G. K., & Panat, R. (2020). Mechanical characterization of polydimethylsiloxane (PDMS) exposed to thermal histories up to 300 C in a vacuum environment. *Journal of Micromechanics and Microengineering*, 30(6), Article 67001. <https://doi.org/10.1088/1361-6439/ab82f4>
- Wineman, A. (2005). Some results for generalized neo-Hookean elastic materials. *International Journal of Non-Linear Mechanics*, 40(2), 271-279. <https://doi.org/https://doi.org/10.1016/j.ijnonlinmec.2004.05.007>
- Wriggers, P. (2008). *Nonlinear Finite Element Methods*. Springer Berlin Heidelberg. <https://doi.org/10.1007/978-3-540-71001-1>
- Xue, L., Pham, J. T., Iturri, J., & Del Campo, A. (2016). Stick-slip friction of PDMS surfaces for bioinspired adhesives. *Langmuir*, 32(10), 2428-2435. <https://doi.org/10.1021/acs.langmuir.6b00513>
- Yu, Y. S., & Zhao, Y. P. (2009). Deformation of PDMS membrane and microcantilever by a water droplet: Comparison between Mooney-Rivlin and linear elastic constitutive models. *Journal of Colloid and Interface Science*, 332(2), 467-476. <https://doi.org/10.1016/j.jcis.2008.12.054>
- Zulfiqar, S., Saad, A. A., Chek, M. W., Sharif, M. F. M., Samsudin, Z., & Ali, M. Y. T. (2020). Structural and random vibration analysis of LEDs conductive polymer interconnections. *IOP Conference Series: Materials Science and Engineering*, 815, Article 012003. <https://doi.org/10.1088/1757-899X/815/1/012003>
- Zulfiqar, S., Saad, A. A., Ahmad, Z., Yusof, F., & Fakpan, K. (2022). Analysis and characterization of polydimethylsiloxane (PDMS) substrate by using uniaxial tensile test and Mooney-Rivlin Hyper-elastic model. *Journal of Advanced Manufacturing Technology*, 16(1), 61-72.
- Zulfiqar, S., Saad, A. A., Ahmad, Z., Yusof, F., & Bachok, Z. (2021). Structural analysis and material characterization of silver conductive ink for stretchable electronics. *International Journal of Integrated Engineering*, 13(7), 128-135.



## The Design of an Efficient Low-cost FPGA-based Unit for Generation Ultrasound Beamforming

Soufiane Dangoury<sup>1\*</sup>, Mouncef El marghichi<sup>2</sup>, Mohamed Sadik<sup>1</sup> and Abderrahim Fail<sup>1</sup>

<sup>1</sup>Department of Electrical Engineering, NEST Research Group, LRI Lab, École Nationale supérieure d'Electricité et Mécanique ENSEM, Hassan II University of Casablanca, Boulevard Abdellah Ibrahim (Ex. Route d'El Jadida) Casablanca, Morocco

<sup>2</sup>Faculty of Sciences and Technology, Hassan first University, FST of Settat, Km 3, B.P: 577 Road to Casablanca, Settat, Morocco

### ABSTRACT

One of the most critical steps in forming an ultrasound image is beamforming, which determines the nature and shape of the sound waves produced. It allows for generating either sound waves focused on a specific depth in the area to be explored (focused beam) or plane waves. The control of the piezoelectric elements forming the probe causes the difference between these modes. In this paper, we focus on generating the commands for the beamforming transmission for both focused and plane wave techniques. The produced signals of the command were applied to the transducers to achieve the desired sound beam. Eventually, we design and implement the algorithm using a low-cost Altera DE10-lite development board. The results show that despite not optimizing the hardware, the board was able to generate the necessary signals efficiently with less than 4% as logic elements requirement and used memory of 0% in the most complex and demanding scenario. Given the speed of access they present, we replace the use of memory with registers.

*Keywords:* Focused beamforming, low-cost FPGA platform, plane waves, ultrasound

### ARTICLE INFO

*Article history:*

Received: 21 November 2022

Accepted: 04 April 2023

Published: 09 October 2023

DOI: <https://doi.org/10.47836/pjst.31.6.24>

*E-mail addresses:*

s.dangoury@ensem.ac.ma (Soufiane Dangoury)

Elmarghichi.mouncef@gmail.com (Mouncef El marghichi)

m.sadik@ensem.ac.ma (Mohamed Sadik)

A.fail@ensem.ac.ma (Abderrahim Fail)

\* Corresponding author

### INTRODUCTION

Ultrasound is one of the most used medical imaging modalities thanks to its multiple benefits, including ease of use, patient and doctor safety, and, most importantly, portability (Maeda et al., 2012). Thanks to its underlying technology and principal component, the probe -often small in size-

makes it easy to carry and move; ultrasound is considered one of the highly coveted tools in medical imaging.

Nevertheless, the major disadvantage of this medical imaging technique lies in the image quality compared to MRI or even X-ray. The ultrasound image suffers from artifacts that decrease its quality in resolution and contrast; consequently, several works have been done to improve the quality of the image. These works have targeted one or more specific parts of the ultrasound image production process.

Beamforming is among the most scrutinized areas for potential enhancements of ultrasound image resolution. Many works have been published in this area showing the beamforming impact on image quality. Demi (2018) presents a work as a guide for Ultrasound Beamforming where the quality of each technique is discussed. Agarwal et al. (2016) propose an architecture of a real-time delay calculator for digital-focused beamforming in an ultrasound imaging system using a curved probe. In Tanter and Fink (2014), the authors have presented plane waves (PW) as an ultrafast imaging technique that directly affects signal processing speed. Tang et al. (2021) admit the ability of PW to improve frame rate; they accordingly suggest a reconstruction method via attention mechanism and U-net-based GAN (AUGAN) to improve the resolution quality. Liebgott et al. (2016) have launched a challenge that presented a cornerstone for all the work that has followed and prompted us to develop a suitable interface command to generate PW.

FPGA provides a very appealing option that balances high flexibility, design cycle, affordability, and performance (Seng et al., 2021). Nowadays, (FPGA) can be realized in millions of logic gates thanks to the new advances in IC design technology (Babu & Parthasarathy, 2021). The FPGA has configurable logic blocks (CLBs) that contain flip-flops and look-up tables (LUTs), allowing the platform to perform various logic functions.

Several works have been carried out to optimize the implementation of different architectures to reduce the resources used or refine the results obtained. Assef et al. (2012) present a digital beamformer system transmission for generating simultaneous arbitrary waveforms to command just 8 channels. In this respect, we have achieved an implementation of 8 times more efficient and 15 times cheaper. Almekkawy et al. (2014) used a mid-range FPGA chip Altera Arria V FPGA to implement a full dynamic beamformer by using the implementation of the delay summation through a bulk (coarse) delay and fractional (fine) delay in the reception process.

Agarwal et al. (2021) proposed implementing a compact architecture of the reception beamformer using a hardware-efficient dynamic delay calculator. They use an adaptive apodization system architecture based on an IEEE single-precision arithmetic and a focusing mechanism to produce high-quality B-mode images, and the presented architecture uses only 60% of the Xilinx Virtex5 XC5VLX330 FPGA hardware resources. Risser et al. (2021) used a very powerful device: the 1024-channel DiPhAS compared to the FPGAs mentioned



above regarding channel handling, with the main advantage of controlling all elements simultaneously without multiplexers. The DiPhAS consists of four individual 256-channel systems. Kidav et al. (2022) propose a hardware solution integrating the analog front-end using mid-range FPGA Xilinx® Kintex-7 to command 128 channels. Boni et al. (2018) present an open-source platform where all the different parts responsible for producing the sound waves, as well as the reception of the echoes and their treatment until the formation of the ultrasound image, were well described. This work deeply dissects a commercial ultrasound scanner that clearly shows the separation between its parts, motivating us to produce this paper.

In this article, we propose the implementation of an efficient, low-cost FPGA to generate commands, allowing the production of two beamforming techniques, focused beam and plane wave (PW). The implementation is done on a low-cost FPGA DE10-lite Development Board. In addition, the MAX 10 FPGA on the DE10 lite board used in this work has hardcore memory blocks called SDRAM to address the rising demand for memory to execute complex mathematical operations and sequential tasks. Also, it provides a 32-bit processor called NIOS II.

### Ultrasound Hardware

The ultrasonic medical image creation chain encompasses the probe, control system, transmission process, reception process, switch, and monitor, which are the essential components of an ultrasonic image system, as depicted in the block diagram (Figure 1). Transducers, piezoelectric components that emit wave sound and translate received echoes into a signal, make up the probe, a crucial component of an ultrasonic system; it presents a central part of the probe (Figure 2).

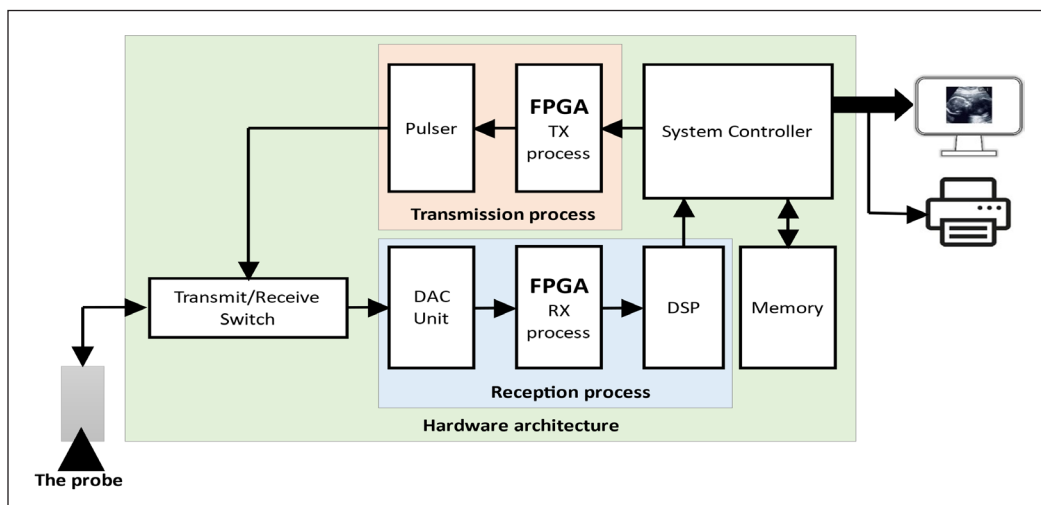


Figure 1. Block diagram of the ultrasound imaging system

The probe consists of small adjacent elements called transducers, as shown in Figure 2 (Powles et al., 2018); the transducer activities will be split into two stages, the first of which is known as the excitation stage and lasts 1% of the total duration (Hoskins et al., 2010). During this phase, the transducer only creates soundwave pulses. The second stage is the hearing phase, when the transducer gets echoes; this phase is critical for picture quality.

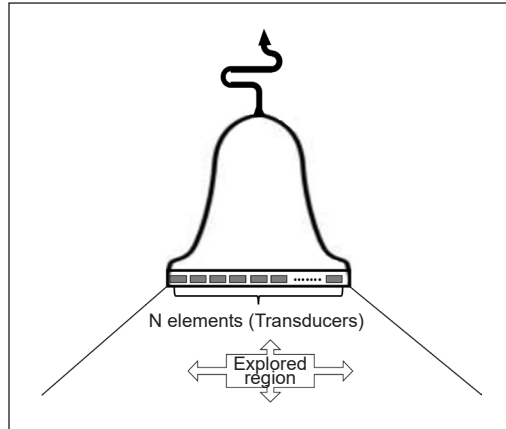


Figure 2. The probe

The sound beam used in the ultrasound could be of different shapes, depending on the way the transducers are controlled. Each specific control of the transducers gives a sound beam of a specific shape (Figure 3), from which comes the necessity to dedicate this work to generating the different controls that could be applied to the probe elements. This mission is entrusted to an FPGA board able to control simultaneously a consequent number of elements.

Pulser is a driver that excites transducers and controls frequency and voltage amplitude, the two components of an electric pulse (Tan et al., 2020). It is a dedicated circuit to generate high-voltage short-time pulses needed to generate ultrasound, particularly in high-power and high-frequency ultrasonic waves (over a frequency of 1 MHz). Our work focused on

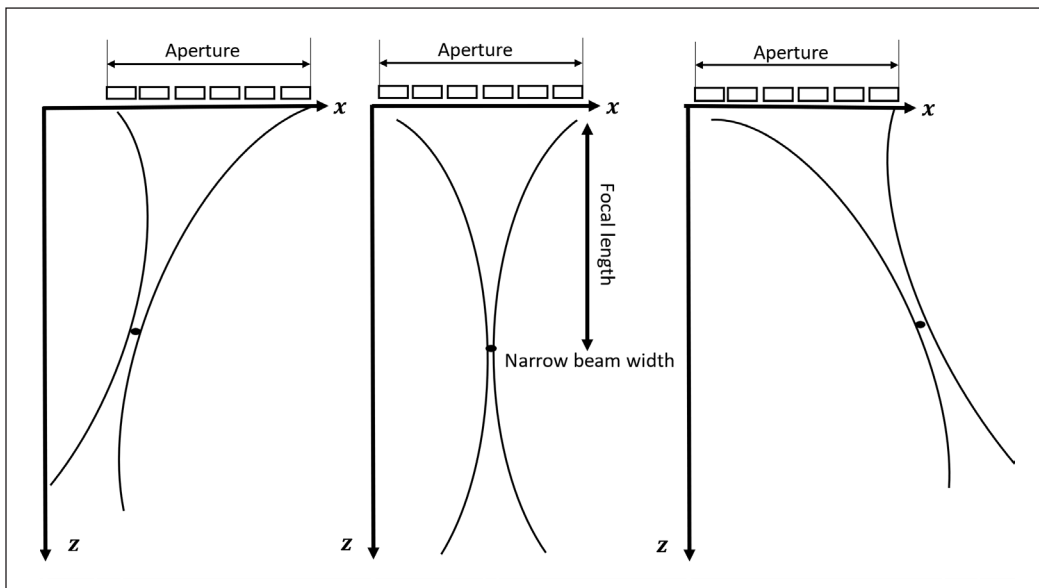


Figure 3. Phased array beam focusing

developing a pulser command system that controls the time when the pulser triggers the transducer.

The reception process by Rossi and Boni (2021) represents the process of data acquisition from the transducers; at its input, we find in general DAC an analog-to-digital converter that samples the signals of the echoes acquired by the elements of the probe, then it converts these samples into digital information, considering the number of transducers to manage simultaneously, it is consistent, the management of different DAC is relegated to an FPGA board often more powerful than that one used in the pulser command generation. As mentioned earlier, the acquired data is processed using a DSP, a processor dedicated to signal processing, which the FPGA also manages.

The system controller's role is to manage the tasks between the transmission and reception parts, the storage of the data on memory, and the display of the ultrasound information in B-mode, and it prints the image if required. The System controller is generally a sequential processing unit, a microprocessor, or a microcontroller whose program is written in a memory, often of the flash type.

The Switcher module is used to multiplex the transmitter/receiver and protects the receiver against high voltage pulses generated by the pulser.

## **METHODS**

### **Ultrasound Beams**

After we have discussed the primary component that formed the ultrasound system, in this part, we write about the probe command method, which influences the lateral resolution. Thus, the lateral resolution is high when the width of the ultrasound beam is narrow (Dangoury et al., 2020). The shape of the ultrasound beam is crucial for detecting more details at all the image depths. However, unfortunately, we cannot keep control of the shape of the beam because it diverges rapidly after being transmitted.

There are several techniques to control the beam shape; they differ in the performance that each presents.

### **Focusing**

This method allows the probe to focus the beam on a single point at a given scan line, resulting in a very narrow beam with concentrated power throughout this point (Figure 3), which is likely to increase lateral resolution significantly in the specific area but at the expense of frame rate due to its computational demands.

To get a focused signal at a certain point, every single pulser transmission from the active aperture must reach that point simultaneously, which we might accomplish by adjusting the excitation delay between the various elements that make up the aperture

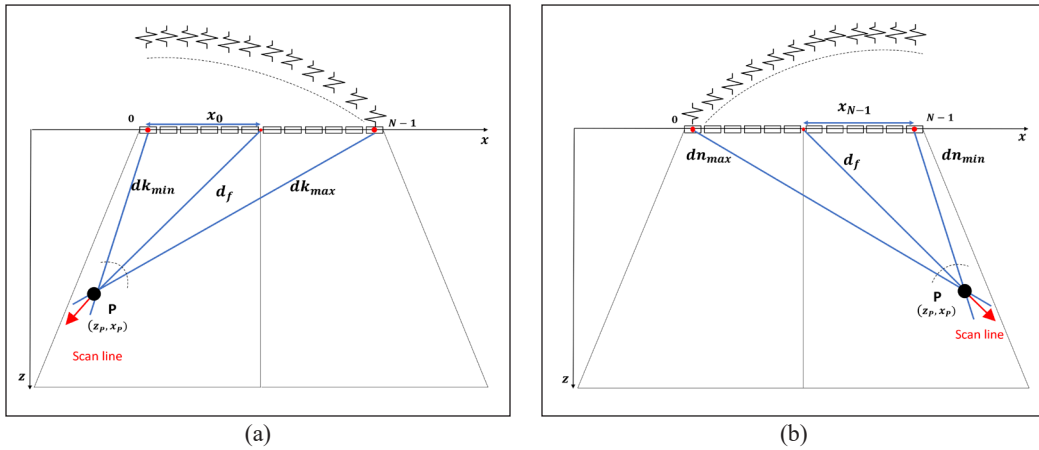


Figure 4. Creating a transmission focus for a phased array: (a) focusing on a left targeted point; and (b) focusing on a right targeted point

(Figure 4). The farthest elements from the scan line are fired first, followed by the center-most elements, the final element to fire. The delay between the applied pulses defines the depth of the focal point; a deeper focal point is achieved by closing the delay difference between the elements, and a closer focal point to the probe is reached by increasing the delay difference between elements.

The practical calculation of the necessary delay for each element will be calculated according to the procedure presented in Figure 5.

Assuming the speed of sound is constant through the explored region, to know the value of the applied delay for each probe's element, we need to determine the distance between a specific element and the focal point (Figure 5) using Equation 1.

$$d_k = \sqrt{x_k^2 + d_f^2 + 2x_k d_f \sin \alpha} \tag{1}$$

Where  $x_k$  is the distance from the center of the array to the  $k$  element concerned with excitation, we have Equation 2:

$$x_k = \left(\frac{N-1}{2} - k\right) d \tag{2}$$

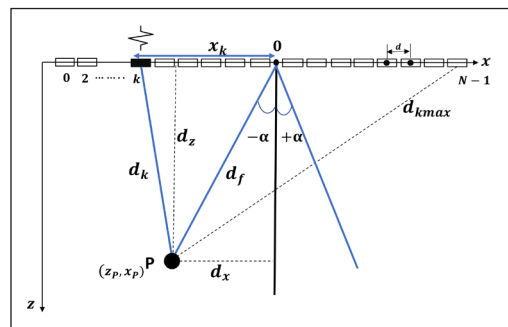


Figure 5. Array geometry for transmission of a focused beam

Note.  $N$ : is the number of elements of the array;  $k$ : is the index of the array element;  $d$ : is the pitch or center-to-center distance between two consecutive elements [m];  $d_f$ : is the distance to the center of the array [m];  $d_k$ : is the distance to the  $k$  element of the array [m];  $x_k$ : is the distance from the  $k$  element's center to the center of the array [m].

$$d_k = \sqrt{(d_f \cos \alpha)^2 + (d_f \sin \alpha + (\frac{N-1}{2} - k)d)^2} \tag{3}$$

From all of the above, we express delay as in Equation 4:

$$\tau_k = t_o - \frac{d_k}{c} \tag{4}$$

where  $c$  is the sound speed, and  $t_o$  is the time required for a sound wave to reach the focal point from the first excited element.

### The Plane Wave

Plane Wave is a technique yielding ultrafast imaging; it uses one generated ultrasound beam through the entire medium by firing all the probe’s elements simultaneously, using parallel processing.

Lack of focusing the beam on the transmission phase, the received echoes provide weak information about the heterogeneities of the medium, which leads to forming a b-mode image with low resolution. Coherent Plane-Wave Compounding (CPWC) Imaging is proposed at the expense of temporal resolution to enhance image quality. CPWC consists of coherently adding echoes from the same scatter from different angles (Rodriguez-Molares et al., 2015).

Coherent Plane-Wave Compounding Imaging is a multi-image approach that involves capturing shots of an object from several angles. The idea is to transmit ultrasound waves at different angles through the medium (Figure 6) and combine all collected echoes to generate one image with fewer speckles and better contrast (Couture et al., 2012).

By using plane waves, the received signal is altered as a result of the presence of several excitation angles. When the waves are perpendicular to the edge of the organ, they

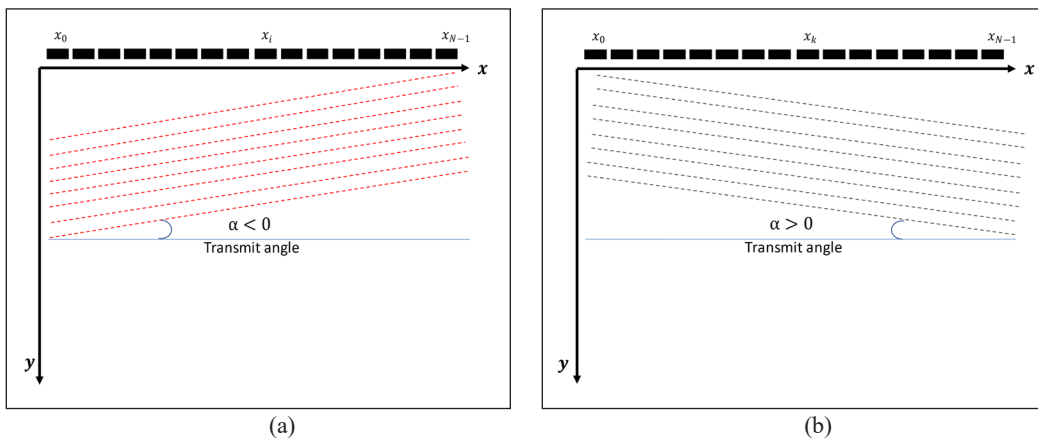


Figure 6. PW imaging, all transducer elements are fired with different delays: (a) negative excitation angle; and (b) positive excitation angles

become harder, and the ultrasound image quality changes better, resulting in good reflection; however, when they are parallel to the edge, their image becomes hazy due to reduced reflection. Taking multiple images from various angles solves the problem by offering a clear view of the orange edge, reducing the frame rate significantly (Montaldo et al., 2009).

In order to transmit a plane wave at an angle  $\alpha$ , (Figure 7), it is necessary to diphas the excitation signals applied to the different elements, which corresponds to applying a delay  $\tau_{TX}$  that is calculated according to the following Equation 5:

$$\tau_{TX} = \frac{z \times \cos \alpha + x_k \times \sin \alpha}{c} \quad (5)$$

The time  $\tau_{RX}$  required to receive reflected echoes from a point in the explored medium with the following coordinate  $(x, z)$  is expressed as shown in Equation 6:

$$\tau_{RX} = \frac{z \times \cos \alpha + x_k \times \sin \alpha}{c} \quad (6)$$

with  $c$  is the sound velocity in the explored medium,  $x_k$  the  $k$ 'th element's position, as illustrated in Figure 7. As a result, the total time  $\tau_{Total}$  it takes a plane wave with emission angle  $\alpha$  to travel through the explored medium to target with coordinates  $(x, z)$  and rebound to the transducer element  $k$ , as shown in Figure 7, is expressed as Equation 7:

$$\tau_{Total} = \tau_{TX} + \tau_{RX} \quad (7)$$

### FPGA Implementation

The command program is implemented in the platform DE10-lite Development Board from the Altera family (Figure 8). The platform has on MAX 10 10M50DAF484C7G FPGA chip with the capacity of 50K programmable logic elements (combinational logic functions (CLFs)) and logic registers (LRs)). The board runs at the speed of a 50 MHz main clock. It can be increased a few more times with the four PLLs -phase lock loop- embedded on the FPGA chip. The board also includes dual ADCs; each ADC supports 1 dedicated analog input and 8 dual function pins. The board provides 36 GPIO and 16 others GPIO, which are fitted for Arduino uses; if there is a need for any additional pins,

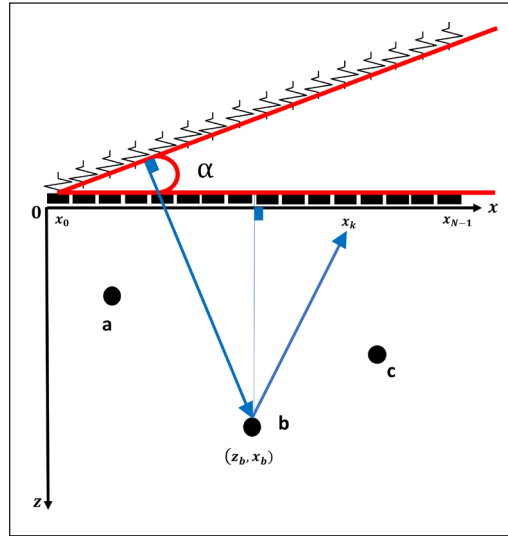


Figure 7. Geometrical model for delay calculation of plane-wave transmission in a linear probe

the ones allocated for switches, buttons, and LEDs could be used without any problem because 10M50DAF484C7G have 380 GPIO. The algorithm is written in VHDL hardware description language (HDL) and Cpp on eclipse using Quartus Prime 16.1 Lite Edition development platform.

This work is designed to control probes as The P4-2v, a 64-element phased array transducer from Verasonics, which can be used for Cardiac, Paediatrics, and Abdominal applications. Table 1 presents the probe parameters; it allows us to produce a scanning region from reaching 60 mm in depth with an aperture of 60° ( $\alpha_{max} = \pm 30^\circ$ ).

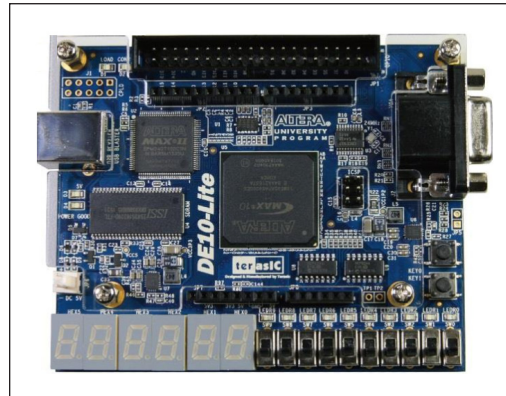


Figure 8. DE10-lite development board

## RESULTS AND DISCUSSION

### Plan Wave Command

For the calculation of delay applied to the individual elements to generate a plane wave with the expected angle, we assume that the probe is located at the point  $z = 0$  (Figure 7), which will significantly simplify Equation 5. Thus, to transmit, in this case, the waves with different angles, the delay applied must be adjusted according to the following new Equation 8:

$$\tau_k = \begin{cases} x_k \sin(\alpha)/c, & \text{for } \alpha < 0 \\ (x_k - N) \sin(-\alpha)/c, & \text{for } \alpha > 0 \end{cases} \quad (8)$$

Where:  $\tau_k$  is the time delay for the element  $k$ ;  $x_k$  is the lateral coordinate of  $k$ , the element.;  $N$ : is the number of elements of the array;  $\alpha$ : is the transmission angle; and  $c$ : represents the speed of sound.

Due to the well-known complexity of the calculation of trigonometric functions and the possible resources that this requires, we have opted for a look-up table that grouped the fraction of sine divided by the velocity, which represent a constant for the same plane wave throughout the all-probe's elements, that was later used in the calculation of the appropriate delays. The total angle of sweep is of the order of 32°; considering the center of the probe as a reference, this results in two sections: the one on the left has a sweep

Table 1  
The probe parameters

Parameter	Value
Number of elements	64
Pitch	0.30 mm
Element width	0.27 mm
Aperture width	19.2 mm
Elevation focus	50–70 (mm)
Transmit frequency	1.0 MHz–5.2 MHz

angle from  $-16^\circ$  to  $0$ , and the one on the right  $0$  to  $+16^\circ$ , having chosen 75 Waves plane this gives a progression of  $0.426^\circ$ , taking into account all of these parameters we need to store 38 different values for  $\alpha > 0$ , we assign them the plus sign and the opposite for alpha  $\alpha < 0$ , in sum the constant part of the expression to store using Equation 9:

$$\sin(\alpha)/c \tag{9}$$

After computing the appropriate delays to be applied to the different elements of the probe, we subsequently have to convert each delay found to a multiple of the minimum time unit that the clock of our board can generate, in our case, is 20 ns, the value obtained will represent the counting base of a 20 bit counter or a down-counter, for each new wave plane the counter is loaded with the appropriate value when it reaches the value the control pulse is triggered (Equation 10).

$$\text{counter}_k = \frac{\text{delay}_k}{20} \tag{10}$$

The counters do not start counting until they are all loaded; the same clock signal controls them (Figure 9).

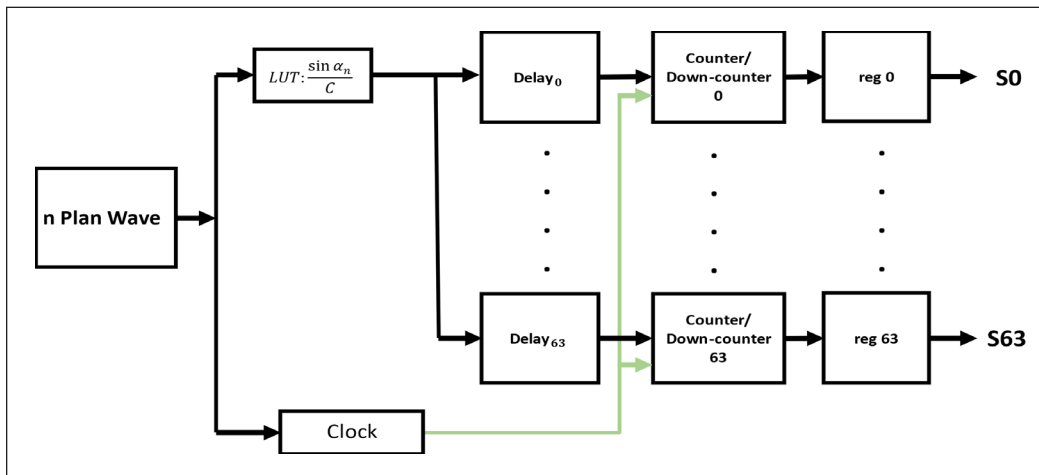


Figure 9. Block diagram of the hardware implementation for plane wave command

The simulation of the command pulses generated by our board was performed under ModelSim, illustrated in Figure 10. Tables 2 and 3 show samples of the results obtained from the application of Equations 8 to 10; the signals applied to the elements

Table 2  
The following table shows a sample of the angles produced for the PW and the resulting constant

The angle $\alpha$	$\sin(\alpha)$	$\sin(\alpha)/c$
0	0	0
0,2158	0,003766412	2,44572E-06
16	0,275637356	0,000178985



are shown in Figures 10 to 12. However, given the inability to simultaneously display a single image containing all 64 controlled elements, we will show only samples of what the screenshot can show.

According to the result obtained from the simulation (Figures 10, 11 and 12), we can see that our FPGA has been able to create the necessary delays to generate the PW of the desired angle, for example, according to Table 3, to be able to generate

Table 3

The following table gives the necessary delay and the value of the counter that allows it to have a PW of  $10^\circ$

Element number	$\tau_k$	counter <sub>k</sub>
63	0	0
62	0,000178985	8949,2648
61	0,000357971	17898,5296
60	0,000536956	26847,7944
3	0,010739118	536955,888
2	0,010918103	545905,153
1	0,011097088	554854,418
0	0,011276074	563803,682

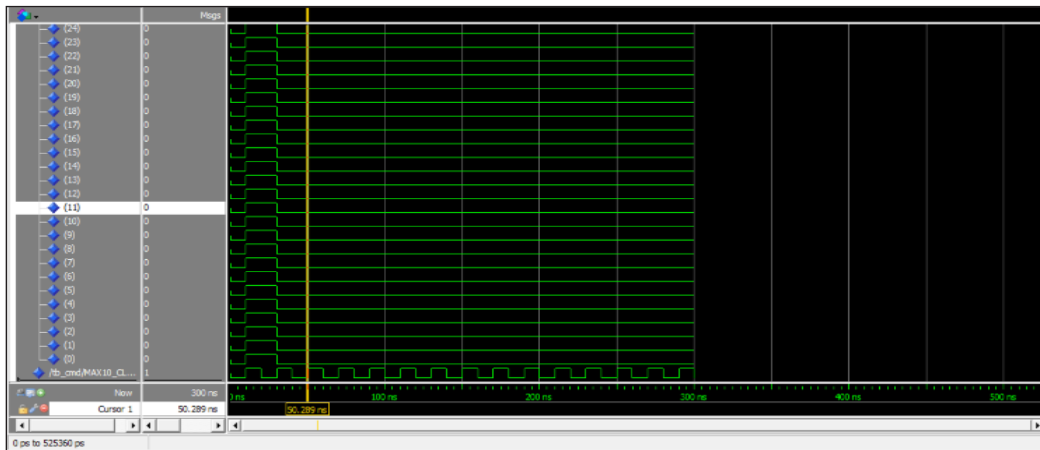


Figure 10. Shows the first 25 elements controlled to generate a PW at  $0^\circ$ ; all elements will fire once, and no delay is required

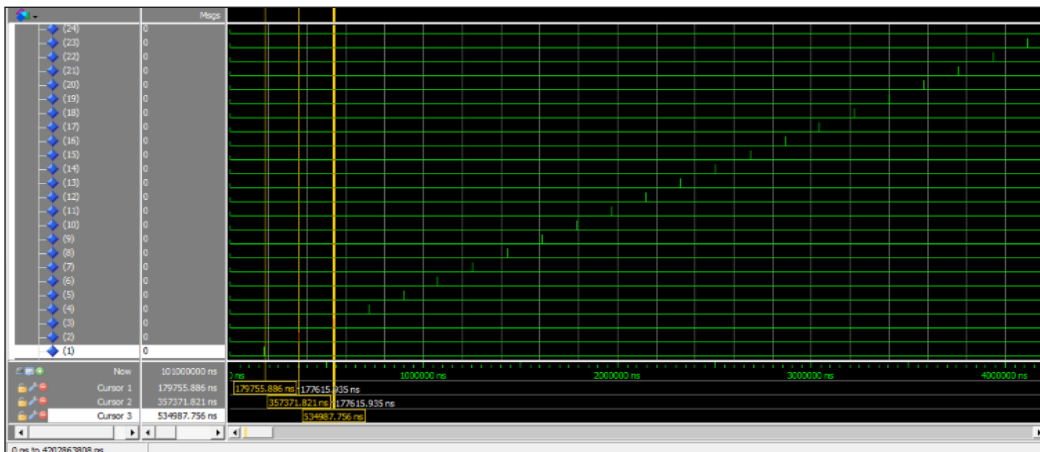


Figure 11. shows the first 25 elements controlled to generate a PW at  $-16^\circ$

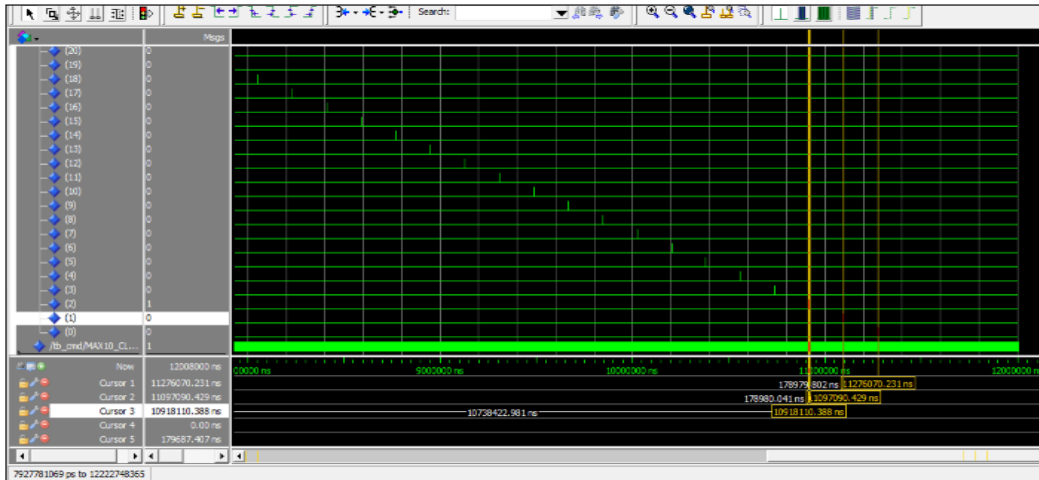


Figure 12. Shows the first 25 elements controlled to generate a PW at +16°

a PW of 16° we must apply a delay of 0,011276074 s (11276074 ns) to the third element, to accomplish this, the counter must be loaded with the value 26847, we will only take the integer part, nevertheless, the value produced by our card corresponds to 11276074 (Figure 12) with an error of 4 ns and 2 ns error for the next elements.

### Focused Command

In this second part, we are interested in the production of focused beams; this type of beamforming requires another command different from that used previously in the case of PW. In this step, we will concretize what we have already introduced; the calculation of different delays applied to the transducers will be carried out according to the algorithm [Figure 13 (b)], the result obtained will be recorded in a look-up table, after that the outputs will be triggered as indicated in according to the algorithm [Figure 13 (a)].

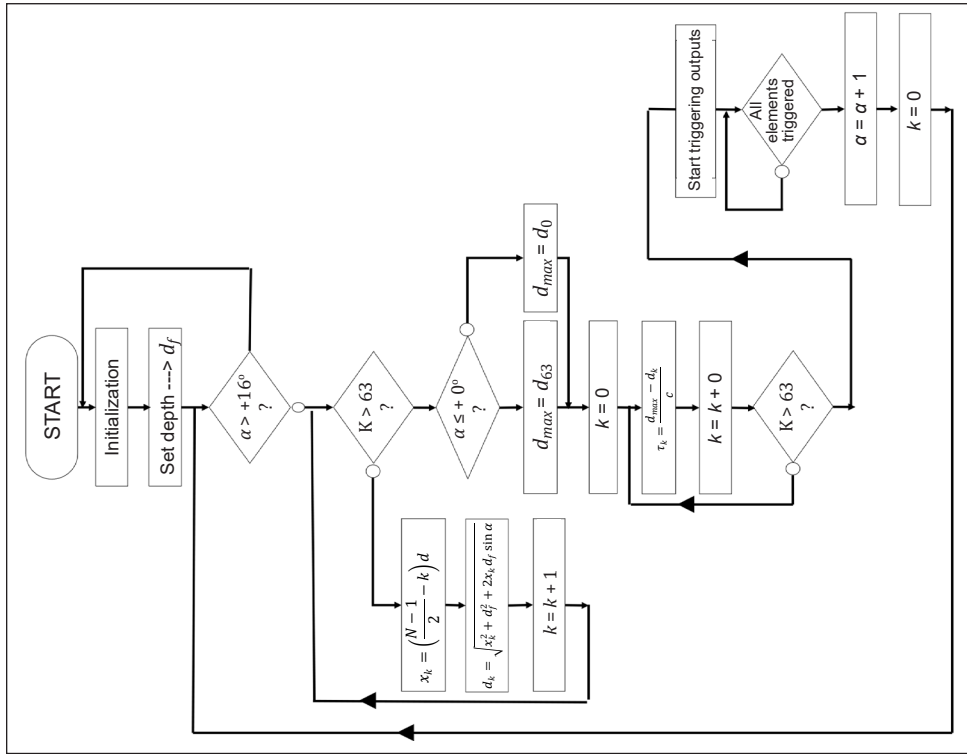
For the first implementation relating to the PW, in accordance with Table 4, filled by values taken from the compilation report, the consumed circuit is of the average of 4% max; however, at this stage, the hard is not optimized; we have not used specific IP or PLL for PW for example, which suggests that all the performances of the card are not or less exploited. Therefore, we conclude that this inexpensive card could ensure applications of control of probes larger than that of 64 elements proposed in this work, for example, the control of a linear probe that goes up to 192 elements. Our work is compared to previous work cited in the literature in Table 5.

### CONCLUSION

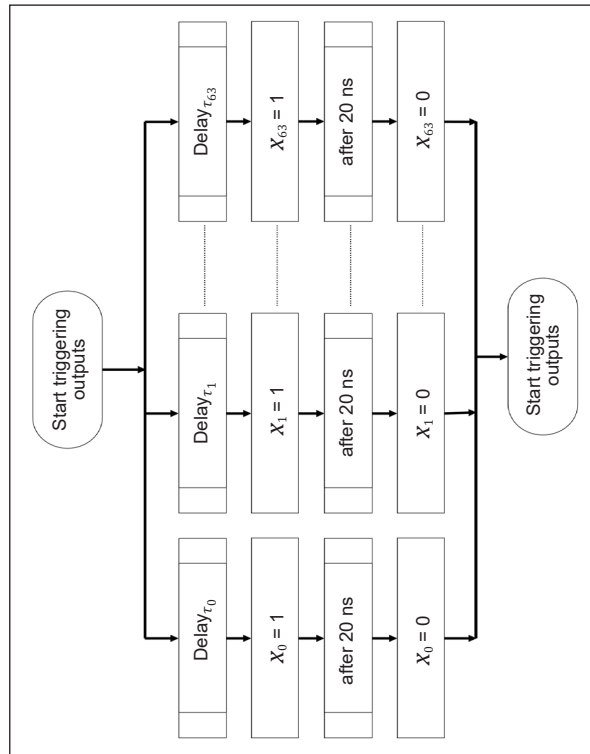
The primary goal of this paper was to investigate the performance of the DE10-lite Development Board for controlling and commanding probe applications. Although this

Table 4  
The resources used by the board for the two proposed implementations

Element number	PW	Focusing
Logic elements	378/49,760 (< 1%)	1,645/49,760 (3%)
Registers	295	1219
Pins	185/360 (51%)	185/360 (51%)
Memory bits	0	0/1,677,312 (0%)
PLLs	0	0/4 (25%)
ADC blocks	0	0/2 (50%)



(b)



(a)

Figure 13. (a) and (b) are the organigram implemented in software application

Table 5  
Comparison to previous work in the literature

	<b>Our project</b>	<b>(Assef et al., 2012)</b>	<b>(Almekkawy et al., 2014)</b>	<b>(Agarwal et al., 2021)</b>	<b>(Kidav et al., 2022)</b>
Device	Altera MAX 10 FPGA	Altera Cyclone III FPGA	Altera Arria V FPGA	Xilinx Virtex 5 FPGA	Xilinx Kintex-7 FPGA
Channel	64	8	64	64	128
Logic cells	50K	-	64,986	-	162,240
Frequency	50 MHz	20 MHz	12 MHz	40 MHz	65 MHz
Phase adjustment:	32°	0° ± 360	-	-	-
The angular resolution	0.426°	7.5° per step	-	-	-
Price	82 \$	1512 \$	+800 \$	+109\$	+450\$

work did not fully utilize all the board’s capabilities and features, it demonstrated that low-cost FPGAs are adequate for controlling the excitation of transducers. The excitation produced by the board was consistent with the study’s analysis and adhered to all the instructions in the study’s theory.

The test results showed that the board could effectively produce the desired signals using less than 4% of the required logic components and 0% of the total memory usage in the most demanding scenario, the focused beam (Figure 14). The optimization of the algorithm’s implementation using only logical registers allowed for fast access and memory savings for other tasks. It suggests reserving a more powerful board solely for acquisition and signal processing.

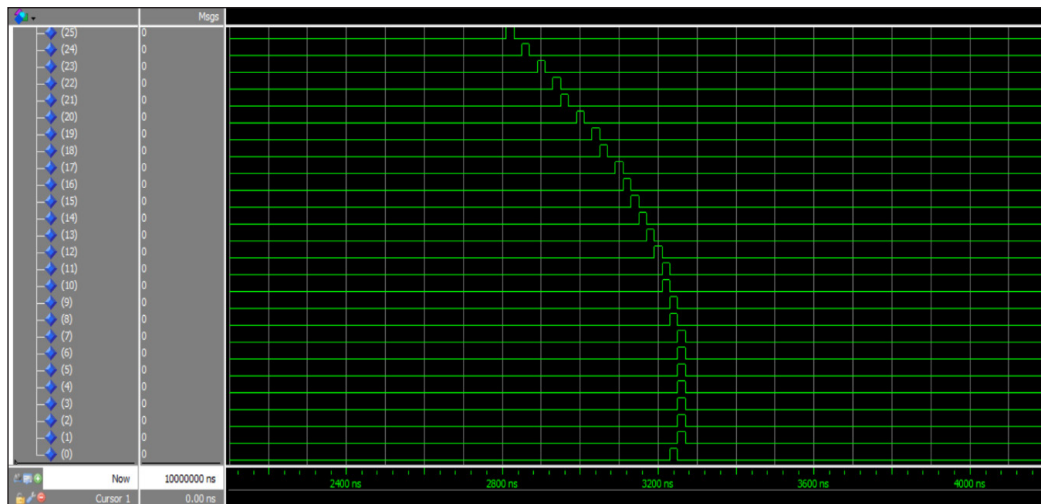


Figure 14. Shows the first 25 elements controlled to generate a focused beam at the point with a depth of 30 mm and -16°

Future work will investigate modifying the PLLs provided by the FPGA board to control larger probes while increasing the frequency. Overall, this work has demonstrated that the DE10-lite Development Board is a suitable and cost-effective option for controlling and commanding probe applications. The results presented in this paper provide valuable insights for researchers and engineers working on similar projects.

## ACKNOWLEDGEMENT

The authors thank all those who participated in the production of this work; we acknowledge the tutorial lessons available at <https://www.coursera.org/learn/intro-fpga-design-embedded-systems>.

## REFERENCES

- Agarwal, M., De, A., & Banerjee, S. (2016). Architecture of a real-time delay calculator for digital beamforming in ultrasound system. *IET Circuits, Devices and Systems*, 10(4), 322-329. <https://doi.org/10.1049/iet-cds.2015.0189>
- Agarwal, M., Tomar, A., & Kumar, N. (2021). An IEEE single-precision arithmetic based beamformer architecture for phased array ultrasound imaging system. *Engineering Science and Technology, an International Journal*, 24(5), 1080-1089. <https://doi.org/10.1016/j.jestch.2021.03.005>
- Almekkawy, M., Xu, J., & Chirala, M. (2014). An optimized ultrasound digital beamformer with dynamic focusing implemented on FPGA. In *2014 36th Annual International Conference of the IEEE Engineering in Medicine and Biology Society* (pp. 3296-3299). IEEE Publishing. <https://doi.org/10.1109/EMBC.2014.6944327>
- Assef, A. A., Maia, J. M., Schneider, F. K., Costa, E. T., & Button, V. L. D. S. N. (2012). A programmable FPGA-based 8-channel arbitrary waveform generator for medical ultrasound research activities. In *2012 Annual International Conference of the IEEE Engineering in Medicine and Biology Society* (pp. 515-518). IEEE Publishing. [https://doi.org/10.0/Linux-x86\\_64](https://doi.org/10.0/Linux-x86_64)
- Babu, P., & Parthasarathy, E. (2021). Reconfigurable FPGA Architectures: A Survey and Applications. In *Journal of The Institution of Engineers (India): Series B* (Vol. 102, Issue 1, pp. 143-156). Springer. <https://doi.org/10.1007/s40031-020-00508-y>
- Boni, E., Yu, A. C. H., Freear, S., Jensen, J. A., & Tortoli, P. (2018). Ultrasound open platforms for next-generation imaging technique development. *IEEE Transactions on Ultrasonics, Ferroelectrics, and Frequency Control*, 65(7), 1078-1092. <https://doi.org/10.1109/TUFFC.2018.2844560>
- Couture, O., Fink, M., & Tanter, M. (2012). Ultrasound contrast plane wave imaging. *IEEE Transactions on Ultrasonics, Ferroelectrics, and Frequency Control*, 59(12), 2676-2683. <https://doi.org/10.1109/TUFFC.2012.2508>
- Dangoury, S., Sadik, M., Alali, A., & Abouzahir, S. (2020). Ultrasound Imaging: Beamforming Techniques. In *Proceedings of the 2nd International Conference on Advanced Technologies for Humanity - Volume 1: ICATH* (pp. 103-109). SciTePress. <https://doi.org/DOI:10.5220/0010428901030109>

- Demi, L. (2018). Practical guide to ultrasound beam forming: Beam pattern and image reconstruction analysis. In *Applied Sciences (Switzerland)* (Vol. 8, Issue 9). MDPI AG. <https://doi.org/10.3390/app8091544>
- Hoskins, P. R., Martin, K., & Thrush, A. (Eds.). (2010). *Diagnostic Ultrasound: Physics and Equipment* (2nd ed.). Cambridge University Press.
- Kidav, J., Pillai, P. M., Deepak, V., & Sreejeesh S., G. (2022). Design of a 128-channel transceiver hardware for medical ultrasound imaging systems. *IET Circuits, Devices and Systems*, 16(1), 92-104. <https://doi.org/10.1049/cds2.12087>
- Lieb Gott, H., Rodriguez-Molares, A., Cervenansky, F., Jensen, J. A., & Bernard, O. (2016). Plane-wave imaging challenge in medical ultrasound. In *2016 IEEE International Ultrasonics Symposium (IUS)* (pp. 1-4). IEEE Publishing. <https://doi.org/10.1109/ULTSYM.2016.7728908>
- Maeda, K., Kurjak, A. K., & Chervenak, F. (2012). The safe use of diagnostic ultrasound in obstetrics and gynecology. *Donald School Journal of Ultrasound in Obstetrics & Gynecology*, 6, 313-317.
- Montaldo, G., Tanter, M., Bercoff, J., Benech, N., & Fink, M. (2009). Coherent plane-wave compounding for very high frame rate ultrasonography and transient elastography. *IEEE Transactions on Ultrasonics, Ferroelectrics, and Frequency Control*, 56(3), 489-506. <https://doi.org/10.1109/TUFFC.2009.1067>
- Powles, A. E., Martin, D. J., Wells, I. T., & Goodwin, C. R. (2018). Physics of ultrasound. In *Anaesthesia and Intensive Care Medicine* (Vol. 19, Issue 4, pp. 202-205). Elsevier Ltd. <https://doi.org/10.1016/j.mpaic.2018.01.005>
- Risser, C., Hewener, H., Fournelle, M., Fonfara, H., Barry-hummel, S., Weber, S., Speicher, D., & Tretbar, S. (2021). Real-time volumetric ultrasound research platform with 1024 parallel transmit and receive channels. *Applied Sciences*, 11(13), Article 5795. <https://doi.org/10.3390/app11135795>
- Rodriguez-Molares, A., Torp, H., Denarie, B., & Lovstakken, L. (2015). The angular apodization in coherent plane-wave compounding. *IEEE Transactions on Ultrasonics, Ferroelectrics, and Frequency Control*, 62(11), 2018-2023. <https://doi.org/10.1109/TUFFC.2015.007183>
- Rossi, S., & Boni, E. (2021). Embedded GPU implementation for high-performance ultrasound imaging. *Electronics*, 10(8), Article 884. <https://doi.org/10.3390/electronics>
- Seng, K. P., Lee, P. J., & Ang, L. M. (2021). Embedded intelligence on FPGA: Survey, applications and challenges. *Electronics*, 10(8), Article 895. <https://doi.org/10.3390/electronics>
- Tan, M., Kang, E., An, J. S., Chang, Z. Y., Vince, P., Mateo, T., Senegond, N., & Pertijs, M. A. P. (2020). A 64-Channel transmit beamformer with  $\pm 30$ -V bipolar high-voltage pulsers for catheter-based ultrasound probes. *IEEE Journal of Solid-State Circuits*, 55(7), 1796-1806. <https://doi.org/10.1109/JSSC.2020.2987719>
- Tang, J., Zou, B., Li, C., Feng, S., & Peng, H. (2021). Plane-wave image reconstruction via generative adversarial network and attention mechanism. *IEEE Transactions on Instrumentation and Measurement*, 70, 1-15. <https://doi.org/10.1109/TIM.2021.3087819>
- Tanter, M., & Fink, M. (2014). Ultrafast imaging in biomedical ultrasound. *IEEE Transactions on Ultrasonics, Ferroelectrics, and Frequency Control*, 61(1), 102-119. <https://doi.org/10.1109/TUFFC.2014.2882>

## Sound Sensor Placement Strategy for Condition Monitoring of Induction Motor Bearing

Iradiratu Diah Prahmana Karyatanti<sup>1\*</sup>, Istiyo Winarno<sup>1</sup>, Ardik Wijayanto<sup>2</sup>, Dwisetiono<sup>3</sup>, Nuddin Harahab<sup>4</sup>, Ratno Bagus Edy Wibowo<sup>4</sup> and Agus Budiarto<sup>4</sup>

<sup>1</sup>Department of Electrical Engineering, Faculty of Engineering and Marine Science, Hang Tuah University, Jawa Timur 60111, Indonesia

<sup>2</sup>Department of Electronic Engineering, Electronic Engineering Polytechnic Institute of Surabaya, Jawa Timur 60111, Indonesia

<sup>3</sup>Department of Marine Engineering, Faculty of Engineering and Marine Science, Hang Tuah University, Jawa Timur 60111, Indonesia

<sup>4</sup>Environmental Science, Postgraduate, Brawijaya University, Malang, Jawa Timur 65145, Indonesia

### ABSTRACT

Damage to the bearing elements will affect the rotation of the rotor and lead to the cessation of motor operation. Therefore, it is imperative to monitor the condition of the bearings to provide information on timely maintenance actions, improve reliability, and prevent serious damage. One of the important keys to an effective and accurate monitoring system is the placement of sensors and proper signal processing. Sound signal issued by the motor during operation capable of describing its elements' condition. Therefore, this study aims to develop a sound sensor placement strategy appropriate for monitoring the condition of induction motor bearing components. This study was carried out on three-phase induction motors' outer-race, inner-race, and ball-bearing sections with the signal processing method

using the spectrum analysis. Furthermore, the effect of sound sensor placement on condition monitoring accuracy was determined using the One-Way Analysis of Variance (One-Way ANOVA) approach. This process tests the null hypothesis and determines whether the average of all groups is the same (H<sub>0</sub>) or different (H<sub>1</sub>). Furthermore, Tukey's test was applied to obtain effective sound sensor placement, with voice-based condition monitoring used for effective identification. The test found

#### ARTICLE INFO

##### Article history:

Received: 26 November 2022

Accepted: 12 April 2023

Published: 09 October 2023

DOI: <https://doi.org/10.47836/pjst.31.6.25>

##### E-mail addresses:

[iradiratu@hangtuah.ac.id](mailto:iradiratu@hangtuah.ac.id) (Iradiratu Diah Prahmana Karyatanti)

[istiyo.winarno@hangtuah.ac.id](mailto:istiyo.winarno@hangtuah.ac.id) (Istiyo Winarno)

[ardik@pens.ac.id](mailto:ardik@pens.ac.id) (Ardik Wijayanto)

[dwisetiono@hangtuah.ac.id](mailto:dwisetiono@hangtuah.ac.id) (Dwisetiono)

[marmunnuddin@ub.ac.id](mailto:marmunnuddin@ub.ac.id) (Nuddin Harahab)

[rbagus@ub.ac.id](mailto:rbagus@ub.ac.id) (Ratno Bagus Edy Wibowo)

[agusfpt@ub.ac.id](mailto:agusfpt@ub.ac.id) (Agus Budiarto)

\* Corresponding author

that the accuracy of monitoring the bearing condition was 92.66% by placing the sound sensor at 100 cm from the motor body.

*Keywords:* Bearing, condition monitoring, placement strategy, sound signal, spectrum analysis

---

## INTRODUCTION

An induction motor is widely used as an industrial driving machine, while 90% serve as prime movers compared to other engine types (Gundewar & Kane, 2021). Damage to its parts can occur in the stator, rotor, bearings, and other parts. Bearing is one of the induction motor elements that play a significant role in aiding the rotating rotor. From the survey carried out by Toma et al. (2020), it was discovered that over 40% of the bearing gets damaged. It is caused by a lack of lubrication, inappropriate lubricants, incorrect installation, and overload. A monitoring system is needed to avoid its negative impact on motor parts. Furthermore, condition monitoring is necessary for industrial sustainability to boost efficiency, reliability, and safety, as well as reduce maintenance costs (Lee et al., 2021). The process was conducted by analyzing the sound generated by the motor during its operation. The advantage of this technique is that the microphone or sound sensor is relatively inexpensive, and its signal is easily captured without contact with the motor elements. This technique is usually recommended because it yields accurate results (Ewert et al., 2020).

The studies that discuss and monitor the condition of sound-based machine elements have been conducted using various signal-processing methods. Meanwhile, traditional signal processing techniques are still being developed by other research using time and frequency domain analyses, as well as a combination of both procedures (Chatterjee et al., 2020) because the adoption of Fast Fourier Transform (FFT) provides information about the condition of the motor elements. The signal in the time domain is transformed to the frequency analysis using the Fourier Series, Discrete Fourier Transform (DFT), and FFT. According to Nakamura et al. (2021), the advantage of frequency domain analysis is that it can identify signal components. Furthermore, to reduce the use of computer technology with high specifications, this technique is quite reliable and serves as an alternative system for monitoring the condition of induction motor elements (Qiao et al., 2020).

The placement of different sensor locations results in changes in sensitivity because they are affected by environmental noise around the induction motor. Zhang et al. (2020) stated that sensor placement greatly affects the accuracy of the monitoring diagnosis results. Furthermore, five sensors were placed at 30 cm to obtain detailed information concerning the bearing condition of a single-phase induction motor (Glowacz et al., 2018). Wang et al. (2019) adopted an efficient sensor placement strategy, using multi-sensors with a Multidimensional Time-Series Analysis approach. The result showed that the higher the



number of sensors used, the greater the information obtained, although this requires much money. For this reason, it is necessary to employ an effective strategy to ensure that the placement of the right sensor provides accurate monitoring information concerning the condition of the motor elements (Goyal et al., 2019). It is in addition to the proposals of a sensor placement strategy with a mathematical model based on the Response Surface Methodology (RSM) (Bhogal et al., 2015). RSM is a statistical model used to analyze problems in which several independent variables positively affect the response attribute. It led to the developing of a mathematical relationship model between input variables and response parameters to determine the optimal sensor placement for monitoring gearbox conditions with an accuracy of 92.2% (Vanraj et al., 2017).

Developing an efficient placement strategy is necessary to improve sensor data quality and monitoring accuracy. It enables the captured signal characteristics to represent the actual condition of the motor part. Therefore, this study discusses the strategy for placing sound sensors to monitor the condition of three-phase induction motor bearing elements. Spectrum analysis was employed in terms of executing this investigation. The independent variable is the microphone placement as a sound sensor subjected to six different distance treatments, with the mean difference evaluated using the ANOVA test. The results showed that environmental complexity affects the monitoring condition of the motor bearing as an industrial driving machine. Therefore, the sensor placement strategy is essential and contributes significantly to the industry.

## **MATERIALS AND METHODS**

Generally, machine condition monitoring consists of three steps: collecting relevant data, processing and analyzing data, and diagnostic and prognostic decision-making (Goyal et al., 2021). An approach flowchart of the bearing condition monitoring, which focuses on sensor placement strategies, is shown in Figure 1. It captures the sound signal from the motor operation, and the placement is tested based on six varying distances measured from the motor body. The sound signal captured by the microphone is analog. Then, this signal will be converted to a digital signal by the Analog to Digital Converter (ADC). The resulting digital signal is still in the time domain, so a feature generation process step is needed to obtain a signal in the frequency domain (using the FFT algorithm). The bearing condition can be diagnosed using spectrum analysis. Spectrum analysis is a diagnostic approach employed to monitor the bearing conditions due to its frequency characteristics. The sound signal is processed with FFT to obtain a sign in the frequency domain. Meanwhile, the spectrum analysis is used to determine the condition of the outer and inner races, as well as the ball bearing in the induction motor rotor. Figure 2 shows the experimental setup of the bearing elements condition and monitoring system. The induction motor tested has specifications of 3 phases, 380 V, 3.68 A 1.5 kW, and 4 poles. Monitoring data is captured

using a sound sensor (USB microphone). The test bearing specifications are 6205 2R, with a bore diameter of 25 mm, an outer diameter of 52 mm, and a number of balls of 9 pieces. The motor load is in the form of a mechanical load. Therefore, artificial damage is carried out to prove the monitoring accuracy by providing defects in the outer race bearing, broken ball bearing, and healthy inner race. The developed monitoring system should recognize the conditions tested, as shown in Figure 3.

Spectrum analysis is a diagnostic approach employed to monitor the bearing conditions due to its frequency characteristics. The sound signal generated by a faulty motor operation conveys harmonic information. The flux density in the air gap becomes asymmetrical and affects the inductance, thereby increasing the amplitude at a certain frequency (Nirwan & Ramani, 2022). Meanwhile, the frequency of the bearing elements is determined from the geometry, kinematics, and rotational speed, where  $r$ ,  $V$ ,  $\omega$ ,  $N$ ,  $d$ ,  $D_p$ , and  $\theta$  denote distance, linear speed, angular speed, number of *ball bearings*, diameter ball bearing, diameter pitch, and contact angle, respectively (Figure 4).

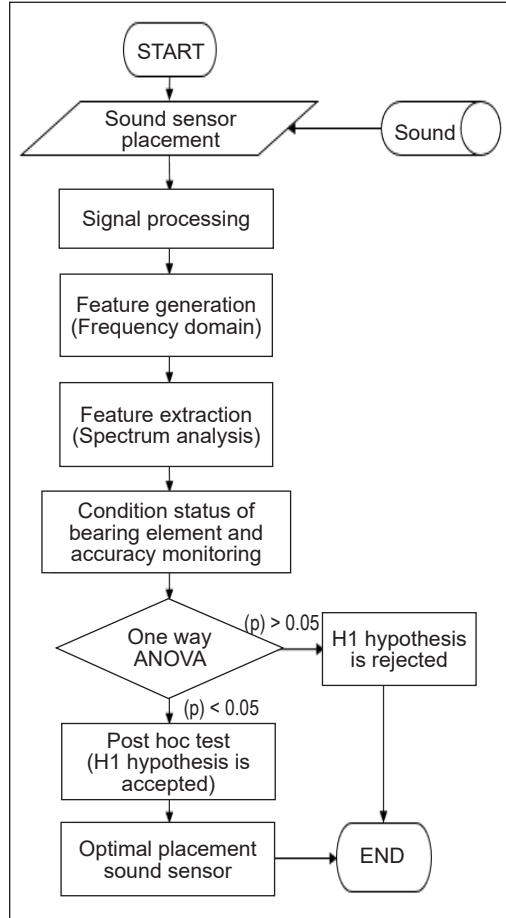


Figure 1. Flowchart of the proposed approach

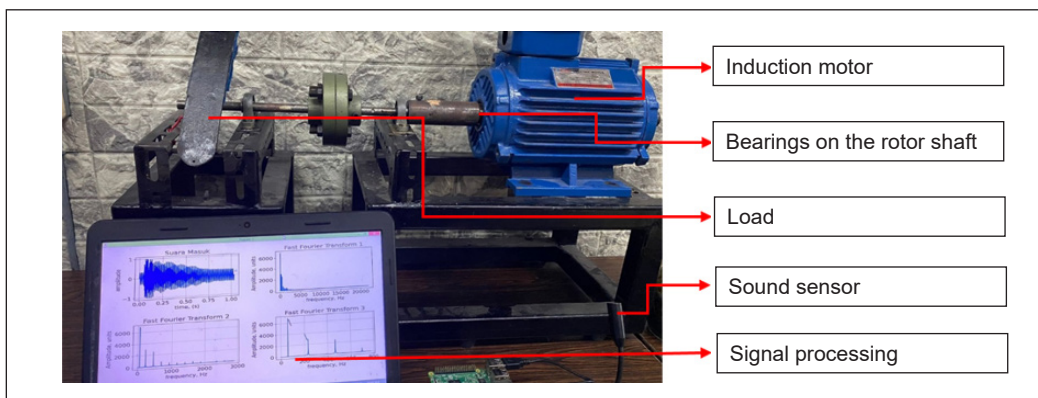


Figure 2. Experimental setup for monitoring condition-bearing

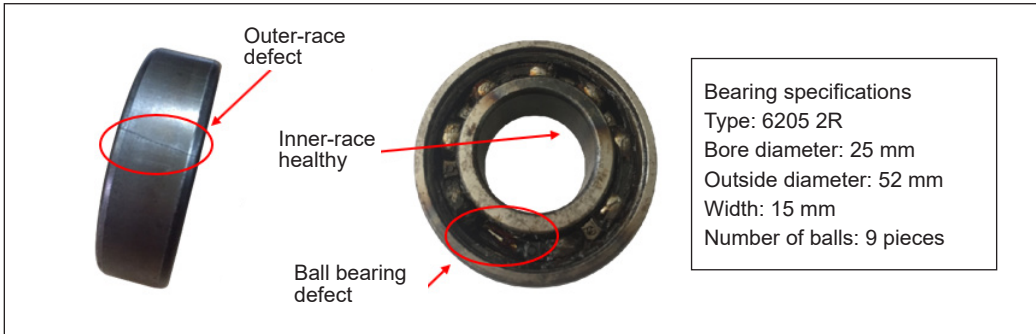


Figure 3. Bearing shaft rotor used for condition monitoring system test

When the bearing rotates, it produces a linear speed within the following range, as described in Equation 1:

$$V_c = \frac{V_i + V_o}{2} = \frac{\omega_i r_i + \omega_o r_o}{2} \quad (1)$$

where,

$$r_i = \frac{D_p}{2} - \frac{d \cos \theta}{2} \text{ and } r_o = \frac{D_p}{2} + \frac{d \cos \theta}{2}$$

$$V_c = \omega_c r_c = \omega_c \left( \frac{D_p}{2} \right) \text{ if } r_c = \frac{D_p}{2}$$

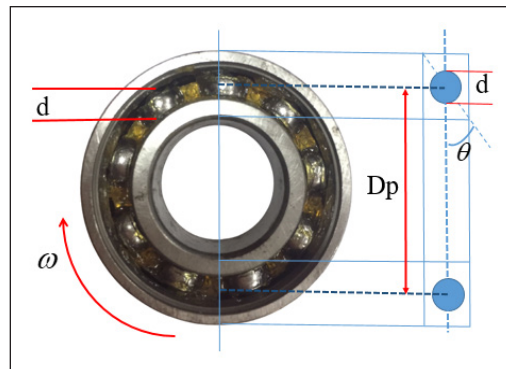


Figure 4. Bearing front view

Therefore, the angular speed of cage bearing formulated in Equation 2:

$$\omega_c = \left( \frac{2V_c}{D_p} \right) = \left( \frac{2}{D_p} \right) \cdot V_c = \left( \frac{2}{D_p} \right) \times \left( \frac{\omega_i r_i + \omega_o r_o}{2} \right) = \frac{\omega_i r_i + \omega_o r_o}{D_p} \quad (2)$$

The distance between the inner and outer races is as follows:

$$r_i = \frac{D_p}{2} - \frac{d \cos \theta}{2} \text{ and } r_o = \frac{D_p}{2} + \frac{d \cos \theta}{2}$$

Hence, the angular speed of the cage bearing is shown in Equation 3

$$\omega_c = \frac{\omega_i \left( \frac{D_p}{2} - \frac{d \cos \theta}{2} \right) + \omega_o \left( \frac{D_p}{2} + \frac{d \cos \theta}{2} \right)}{D_p} = \frac{1}{2} \left[ \omega_i \left( 1 - \frac{d \cos \theta}{D_p} \right) + \omega_o \left( 1 + \frac{d \cos \theta}{D_p} \right) \right] \quad (3)$$

Because  $\omega$  is  $2\pi f$  then the frequency of cage bearing formulated in Equation 4:

$$f_c = \frac{1}{2} \left[ f_i \left( 1 - \frac{d \cos \theta}{D_p} \right) + f_o \left( 1 + \frac{d \cos \theta}{D_p} \right) \right] \quad (4)$$

Additionally, a defect in the outer race causes a spike in amplitude at a certain frequency. Its bearing rotation frequency, namely the Ball Pass Frequency of Outer Race (BPFO), is calculated as follows:

$$f_{BPFO} = N(\omega_c - \omega_o) = \frac{N}{2}(f_i - f_o) \cdot \left(1 - \frac{d \cos \theta}{D_p}\right)$$

The outer race bearing frequency is assumed to be 0 because it is locked with the external casing, where the inner race and the motor rotor shaft frequency ( $f_i = f_s$ ) are the same (Barusu & Deivasigamani, 2020). Therefore, the outer race bearing frequency formulated in Equation 5:

$$f_{BPFO} = \frac{N}{2} f_s \left(1 - \frac{d \cos \theta}{D_p}\right) \quad (5)$$

Similarly, the Ball Pass Frequency of Inner Race (BPFi) is shown in Equation 6:

$$f_{BPFi} = N(\omega_i - \omega_c) = \frac{N}{2}(f_i - f_o) \left(1 + \frac{d \cos \theta}{D_p}\right)$$

$$f_{BPFi} = \frac{N}{2} f_s \left(1 + \frac{d \cos \theta}{D_p}\right) \quad (6)$$

The ball bearing frequency can be formulated as Ball Spin Frequency (BSF) using the following equation:

$$\omega_r = \frac{V_r}{r_r} = \frac{(\omega_i - \omega_c)r_i}{r_r} = \frac{(\omega_i - \left\{ \frac{1}{2} \left[ \omega_i \left(1 - \frac{d \cos \theta}{D_p}\right) + \omega_i \left(1 + \frac{d \cos \theta}{D_p}\right) \right] \right\})r_i}{r_r}$$

$$\omega_r = \frac{D_p}{2d} (\omega_i - \omega_o) \left[ 1 - \left( \frac{d \cos \theta}{D_p} \right)^2 \right] \text{ then } f_r = \frac{D_p}{2d} (f_i - f_o) \left[ 1 - \left( \frac{d \cos \theta}{D_p} \right)^2 \right]$$

The Ball Spin Frequency (BSF) is described in Equation 7:

$$f_{BSF} = f_r = \frac{D_p}{2d} f_s \left[ 1 - \left( \frac{d \cos \theta}{D_p} \right)^2 \right] \quad (7)$$

The characteristics of the sound signal at the  $f_{BPFO}$ ,  $f_{BPFi}$ , and  $f_{BSF}$  frequencies indicate the condition of each bearing section.

Monitoring accuracy is proven by the percentage of correctness based on the condition of the bearing elements tested. Interestingly, a one-way ANOVA approach was used to test the hypothesis. This comparative evaluation examines the difference in the mean data of two or more groups. The hypothesis (H1) states that the sound sensor placement significantly affects the accuracy of monitoring the motor bearing condition. On the other hand, the (H0) hypothesis states that sensor placement has an insignificant effect on monitoring accuracy. The one-way ANOVA hypothesis test formulation is shown in Equation 8:

$$\begin{aligned}
 H_0 : \alpha_1 = \alpha_2 = \dots = \alpha_k \\
 H_1 = \text{not all group means are equal}
 \end{aligned}
 \tag{8}$$

Where  $\alpha_k$  is the average group  $k$ , and  $k$  is the total number of groups. Assuming the one-way ANOVA test value states that  $(H_1)$  is accepted, a post hoc test is carried out to determine the optimal sensor placement. The approach proposed by Tukey (honestly significant difference) is a post hoc test that is applied if  $(H_0)$  is rejected (Shabbir et al., 2020). The Tukey test formula is shown in Equation 9:

$$|t| = \frac{|y_i - y_j|}{\sqrt{MSE \left( \frac{1}{n_i} + \frac{1}{n_j} \right)}} > \frac{1}{\sqrt{2}} q_{\alpha, k, N-k}
 \tag{9}$$

where the sample means of the group  $i$  and  $j$  are symbolized by  $y_i$  and  $y_j$ , MSE is a mean squared error,  $n_i$  and  $n_j$  are sample size group,  $q_{\alpha, k, N-k}$  is Tukey table,  $\alpha$  is the significance level,  $N$  is the total number of observations, and  $k$  is the number of groups.

## RESULTS AND DISCUSSION

The microphone captures a signal in the time domain as a sound sensor. Sound data is retrieved for 30 seconds with a sampling frequency of 44.1 kHz. The data acquired in the time domain is transformed into that of the frequency using the FFT algorithm. Then, spectrum analysis is carried out by calculating the frequency of its characteristics to determine the condition of the bearing elements. Referring to the specifications in Figure 3 and the application of Equations 5, 6, and 7, the frequency of each bearing element is:

$$\begin{aligned}
 f_{BPFO} &= \frac{9}{2} 24.96 \left( 1 - \frac{7.25 \cos 0^\circ}{38.5} \right) = 91.18 \text{ Hz} \\
 f_{BPFI} &= \frac{9}{2} 24.96 \left( 1 + \frac{7.25 \cos 0^\circ}{38.5} \right) = 133.50 \text{ Hz} \\
 f_{BSF} &= \frac{38.5}{2 \times 7.25} 24.96 \left[ 1 - \left( \frac{7.25 \cos 0^\circ}{38.5} \right)^2 \right] = 43.67 \text{ Hz}
 \end{aligned}$$

The following 91.18 Hz, 133.50 Hz, and 43.67 Hz are the fundamental frequencies of the outer and inner races, as well as the ball bearing. Each frequency of the harmonic element bearing was further observed. A sample spectrum of 800 Hz generates 6, 8, and 18 frequencies at  $f_{BSF}$ ,  $f_{BPFO}$  and  $f_{BPFI}$ . Therefore, one sample data spectrum analysis is used to observe the amplitude at 32 harmonic frequencies.

Figure 5 shows spectrum analysis at the fundamental frequency, where (a) depicts the sound spectrum with sensor placements of 50 cm, (b) 100 cm, and (c) 150 cm. The blue signal is the reference sound spectrum obtained from the operational bearing under a healthy condition, while the red is the test spectrum. If the test amplitude exceeds the

reference, the element bearing is declared to be in a damaged condition. On the other hand, assuming the reverse was the case, the element bearing is declared fit. Based on the test on the sensor placement of 50 cm from the motor body, the ball bearing was detected under a healthy condition; likewise, the outer race, while the inner one, was damaged. The monitoring results are inappropriate because the bearing elements were detected under damage conditions. In this case, the condition monitoring system is less accurate. However, this is different when reviewing the spectrum analysis results with the 100 cm sensor placement, as shown in Figure 5(b). The frequency of all bearing elements indicates the actual condition monitoring where the ball bearing and outer race are detected under faulty conditions while the inner one is in a healthy state. Figure 5(c) shows the sound spectrum with 150 cm sensor placement; the results of condition monitoring are less accurate.

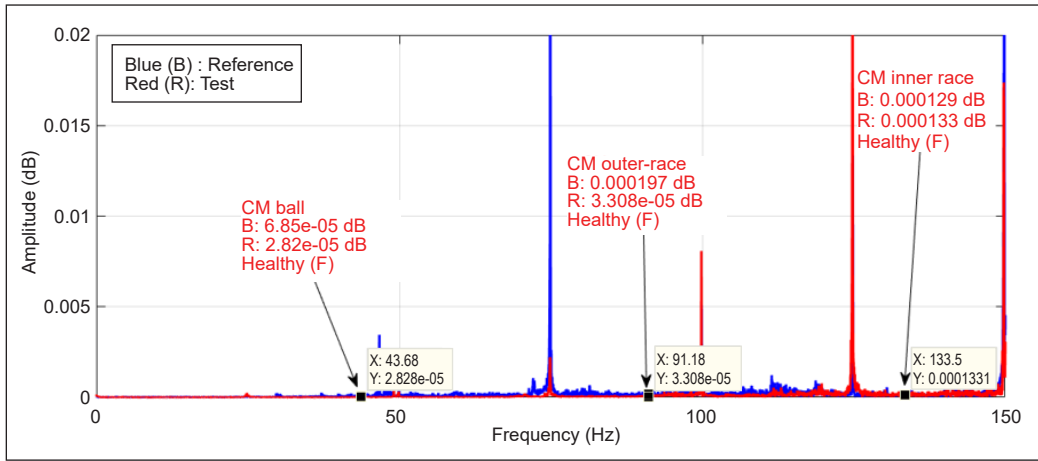
The condition monitoring results of the bearing elements up to the fourth harmonic frequency shown in Table 1 is a detailed test of the first data where accuracy is calculated based on the percentage truth for the condition monitoring results of all bearing elements. Data was retrieved on each sensor placement variation four times to get valid results.

The accuracy of the condition monitoring for all data repetitions is shown in Table 2. One-way ANOVA is performed using the data in Table 2 with respect to the hypothesis test. The requirements are that the sample data used should be normally distributed, its population must have a homogeneous variance, and the samples do not need to be related to each other. The normality test shows that the acquired information has been normally distributed with a P-value greater than 0.05, relatively 0.546. Meanwhile, the data homogeneity test was used to obtain a value of 0.275, meaning it is homogeneous.

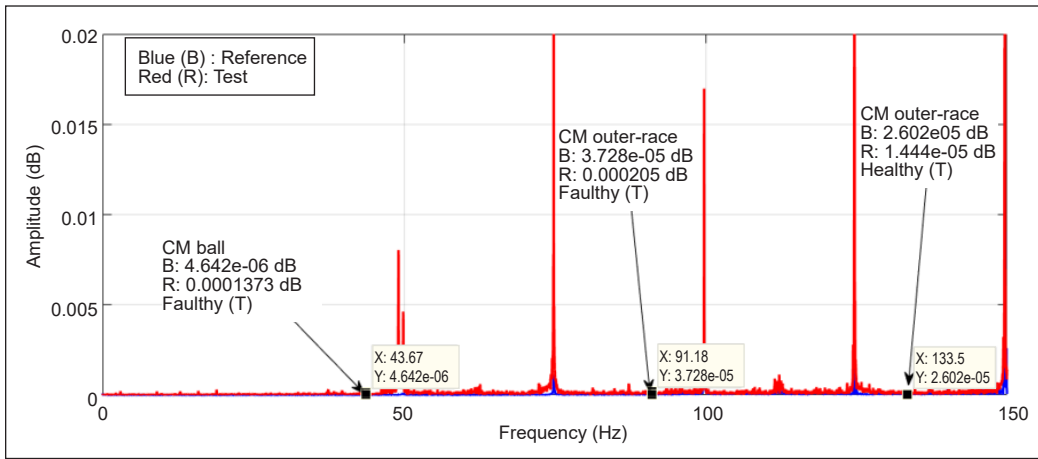
Table 3 is a one-way sensor placement ANOVA regarding accurately monitoring the bearing elements' conditions. It shows that the P-value is less than 5%. Therefore, it was concluded that (H1) is accepted, indicating that the sensor placement significantly affects the monitoring accuracy of bearing elements. The post hoc and Tukey tests were conducted to detect the best placement. Figure 6 shows the Tukey test results with a 95% confidence level. Based on the data grouping, the 100 cm sensor placement is the best location for monitoring the condition of bearing elements, with an average accuracy of 92.66%. Relatively high accuracy is achieved with the proposed approach, thereby being highly recommended as an alternative for monitoring the condition of an induction motor.

Similar studies are shown in Table 4 as a discourse on developing motor condition monitoring. It also depicts studies that discuss monitoring the condition of motor elements based on sound and vibration data, where both are strongly influenced by ambient noise. Previous analyses presented this challenge to develop a condition-monitoring system by examining the effect of noise on accuracy (AlShorman et al., 2021). Therefore, the present study examines the optimal and effective sensor placement because the sound is susceptible to ambient noise.

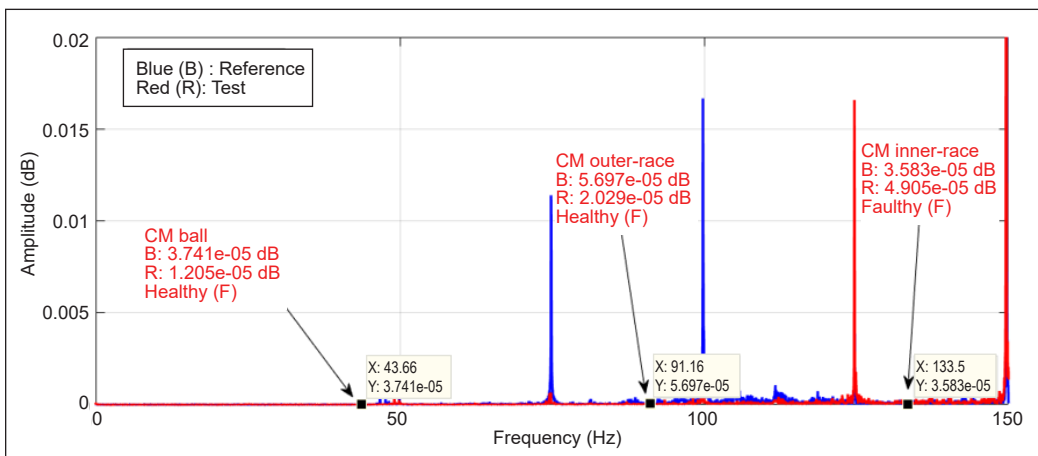
Sound Sensor Placement Strategy



(a)



(b)



(c)

Figure 5. Spectrum analysis on the different sensor placements: (a) 50 cm; (b) 100 cm; and (c) 150 cm

Table 1  
*Spectrum analysis for condition monitoring and detection accuracy*

Placement	Bearing Condition	Freq (Hz)	Amplitude (dB)		Result	Accuracy (%)
			Ref	Test		
50 cm	Ball bearing defect	$f$	0.000068	0.000028	False	49.07 %
		$f_{x2}$	0.000121	0.000038	False	
		$f_{x3}$	0.000168	0.000071	False	
		$f_{x4}$	0.003058	0.004393	True	
	Outer-race defect	$f$	0.000197	0.000033	False	
		$f_{x2}$	0.000190	0.000218	True	
		$f_{x3}$	0.000174	0.000237	True	
		$f_{x4}$	0.000138	0.000203	True	
	Inner-race healthy	$f$	0.000129	0.000133	False	
		$f_{x2}$	0.000158	0.000227	False	
		$f_{x3}$	0.000387	0.000633	False	
		$f_{x4}$	0.000157	0.000359	False	
100 cm	Ball bearing defect	$f$	0.000004	0.000137	True	94.44 %
		$f_{x2}$	0.000018	0.000288	True	
		$f_{x3}$	0.000032	0.000109	True	
		$f_{x4}$	0.006436	0.056430	True	
	Outer-race defect	$f$	0.000037	0.000205	True	
		$f_{x2}$	0.000138	0.000425	True	
		$f_{x3}$	0.000018	0.000279	True	
		$f_{x4}$	0.000191	0.000199	True	
	Inner-race healthy	$f$	0.000026	0.000014	True	
		$f_{x2}$	0.000138	0.000077	True	
		$f_{x3}$	0.000310	0.000242	True	
		$f_{x4}$	0.000228	0.000139	True	
150 cm	Ball bearing defect	$f$	0.000037	0.000012	False	60.55 %
		$f_{x2}$	0.000037	0.000073	True	
		$f_{x3}$	0.000055	0.000067	True	
		$f_{x4}$	0.008330	0.035380	True	
	Outer-race defect	$f$	0.000056	0.000020	False	
		$f_{x2}$	0.000079	0.000171	True	
		$f_{x3}$	0.000168	0.000506	True	
		$f_{x4}$	0.000204	0.000216	True	
	Inner-race healthy	$f$	0.000035	0.000049	False	
		$f_{x2}$	0.000351	0.000106	True	
		$f_{x3}$	0.000107	0.000077	True	
		$f_{x4}$	0.000298	0.000620	False	



Table 2  
Detection accuracy in all test cases

Placement (cm)	Repetition (r)				Average
	1	2	3	4	
0	13,33 %	15,18 %	20 %	24,16 %	18,17 %
50	49,07 %	60,55 %	47,87 %	56,38 %	53,47 %
100	94,44 %	87,77 %	92,12 %	96,29 %	92,66 %
150	60,55 %	56,20 %	58,70 %	54,53 %	57,49 %
200	59,90 %	44,90 %	57,59 %	50,92 %	53,33 %
250	50,18 %	41,85 %	47,87 %	52,03 %	47,98 %

Table 3  
One-way analysis of variance placement sensor

Source of Diversity	Degrees Free	Sum of squares	Middle square	F-Value	P-Value
Treatment	5	11308.4	2261.68	92.57	0.000
Galat	18	439.8	24.43		
Total	23	11748.2			

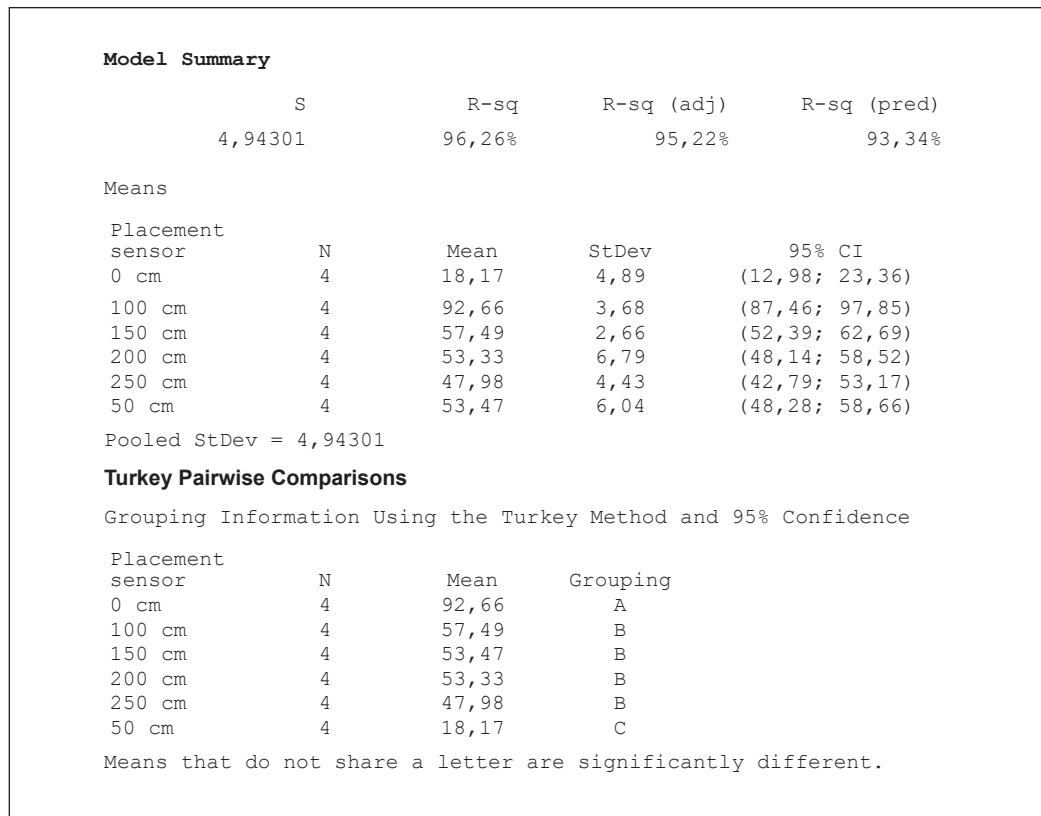


Figure 6. Tukey test

Table 4  
*Comparison of similar research with proposed research*

Reference	Feature extraction method	Sensor	Placement strategy	Highlight
Vanraj et al., 2017	No discussion	Microphone	RSM	Sensor placement strategy using RSM approach with 112.5 cm.
Glowacs et al., 2018	MSAF-20-MULTIEXPANDED	Microphone	30 cm sensor placement	The sensor placement strategy approach is not discussed.
Wang et al., 2019	MultiDTSA and ARIMA	Microphone and accelerometer	No discussion	Future studies are recommended to optimize sensor settings.
Vamsi et al., 2019	wavelet decomposition	Microphone and accelerometer	No discussion	The placement of the sound sensor is free and more accurate than that of the vibration.
Goyal et al., 2019	FFT	Accelerometer	NC-OSP strategy	RSM can be used to track the optimal non-contact sensor location.
Nirwan & Ramani, 2022	FFT	Microphone, Accelerometer	No discussion	The bearing monitoring results using sound data are better than a vibration.
Zhang et al., 2020	FFT	Accelerometer	No discussion	A sound and vibration sensor placement strategy is needed to get high accuracy.
AlShorman et al., 2021	Review all technique	Microphone	No discussion	Review, challenges, and future trends are discussed for developing the effect of noise on monitoring accuracy. This factor may be affected by providing the sensor placement treatment.
Proposed method	Spectrum analysis	Microphone	One way ANOVA	The sensor placement is the best strategy to get the accuracy of bearing elements monitoring.

## CONCLUSION

The sound characteristics are used to describe the condition of the motor elements, and their monitoring is strongly influenced by ambient noise. The right placement of the sound sensor is extremely important in determining the follow-up actions for motor maintenance. It provides an opportunity for the noise signal to overlap with that generated by the operation of the motor. Furthermore, spectrum analysis is a reliable solution for monitoring the condition of bearing elements with an overview of its conditions strongly influenced by sound sensor placement. The accuracy of bearing elements monitoring is determined using the One-way ANOVA test. Based on the Tukey test, the placement of the sensor 100 cm from the motor body gives the best accuracy of all treatments, which is 92.66%. Future studies are expected to examine the sensor placement in more

detail because the treatment applied in the present study has a difference of 50 cm. This research contributes to the right sensor placement strategy to obtain accurate monitoring results. It enables the industrial community to carry out diagnostics and prognostics of the motor as the main driver.

## ACKNOWLEDGEMENTS

The authors are grateful to the Electrical Machinery Laboratory and Energy Conversion Laboratory research team at Hang Tuah University, Indonesia, for their many contributions to this study.

## REFERENCES

- AlShorman, O., Alkhatni, F., Masadeh, M., Irfan, M., Glowacz, A., Althobiani, F., Kozik, J. & Glowacz, W. (2021). Sounds and acoustic emission-based early fault diagnosis of induction motor: A review study. *Advances in Mechanical Engineering*, 13(2), 1-19. <https://doi.org/10.1177/1687814021996915>
- Barusu, M. R., & Deivasigamani, M. (2020). Non-invasive vibration measurement for diagnosis of bearing faults in 3-phase squirrel cage induction motor using microwave sensor. *IEEE Sensors Journal*, 21(2), 1026-1039. <https://doi.org/10.1109/JSEN.2020.3004515>
- Bhogal, S. S., Sindhu, C., Dhama, S. S., & Pabla, B. S. (2015). Minimization of surface roughness and tool vibration in CNC milling operation. *Journal of Optimization*, 2015, Article 192030. <https://doi.org/10.1155/2015/192030>
- Chatterjee, S., Barman, R., Roy, S. & Dey, S. (2020, December 16-19). *Bearing fault detection in induction motors employing difference visibility graph*. [Paper presentation]. 2020 IEEE International Conference on Power Electronics, Drives and Energy Systems (PEDES), Rajasthan, India. <https://doi.org/10.1109/PEDES49360.2020.9379635>
- Ewert, P., Kowalski, C. T., & Orłowska-Kowalska, T. (2020). Low-cost monitoring and diagnosis system for rolling bearing faults of the induction motor based on neural network approach. *Electronics*, 9(9), Article 1334. <https://doi.org/10.3390/electronics9091334>
- Glowacz, A., Glowacz, W., Glowacz, Z., & Kozik, J. (2018). Early fault diagnosis of bearing and stator faults of the single-phase induction motor using acoustic signals. *Measurement*, 113, 1-9. <https://doi.org/10.1016/j.measurement.2017.08.036>
- Goyal, D., Mongia, C., & Sehgal, S. (2021). Applications of digital signal processing in monitoring machining processes and rotary components: A review. *IEEE Sensors Journal*, 21(7), 8780-8804. <https://doi.org/10.1109/JSEN.2021.3050718>
- Goyal, D., Pabla, B. S., & Dhama, S. S. (2019). Non-contact sensor placement strategy for condition monitoring of rotating machine-elements. *Engineering Science and Technology, an International Journal*, 22(2), 489-501. <https://doi.org/10.1016/j.jestch.2018.12.006>
- Gundewar, S. K., & Kane, P. V. (2021). Condition monitoring and fault diagnosis of induction motor. *Journal of Vibration Engineering & Technologies*, 9(4), 643-674. <https://doi.org/10.1007/s42417-020-00253-y>

- Lee, W. J., Xia, K., Denton, N. L., Ribeiro, B., & Sutherland, J. W. (2021). Development of a speed invariant deep learning model with application to condition monitoring of rotating machinery. *Journal of Intelligent Manufacturing*, 32(2), 393-406. <https://doi.org/10.1007/s10845-020-01578-x>
- Nakamura, H., Asano, K., Usuda, S., & Mizuno, Y. (2021). A diagnosis method of bearing and stator fault in motor using rotating sound based on deep learning. *Energies*, 14(5), Article 1319. <https://doi.org/10.3390/en14051319>
- Nirwan, N. W., & Ramani, H. B. (2022). Condition monitoring and fault detection in roller bearing used in rolling mill by acoustic emission and vibration analysis. *Proceedings of Materials Today*, 51, 344-354. <https://doi.org/10.1016/j.matpr.2021.05.447>
- Qiao, M., Yan, S., Tang, X., & Xu, C. (2020). Deep convolutional and LSTM recurrent neural networks for rolling bearing fault diagnosis under strong noises and variable loads. *IEEE Access*, 8, 66257-66269. <https://doi.org/doi:10.1109/access.2020.2985617>
- Shabbir, M. N. S. K., Liang, X., & Chakrabarti, S. (2020). An ANOVA-based fault diagnosis approach for variable frequency drive-fed induction motors. *IEEE Transactions on Energy Conversion*, 36(1), 500-512. <https://doi.org/10.1109/TEC.2020.3003838>
- Toma, R. N., Prosvirin, A. E., & Kim, J. M. (2020). Bearing fault diagnosis of induction motors using a genetic algorithm and machine learning classifiers. *Sensors*, 20(7), Article 1884. <https://doi.org/10.3390/s20071884>
- Vamsi, I., Sabareesh, G. R., & Penumakala, P. K. (2019). Comparison of condition monitoring techniques in assessing fault severity for a wind turbine gearbox under non-stationary loading. *Mechanical Systems and Signal Processing*, 124, 1-20. <https://doi.org/10.1016/j.ymssp.2019.01.038>
- Vanraj, Dhami, S. S., & Pabla, B. S. (2017). Optimization of sound sensor placement for condition monitoring of fixed-axis gearbox. *Cogent Engineering*, 4(1), Article 1345673. <https://doi.org/10.1080/23311916.2017.1345673>
- Wang, T., Lu, G., & Yan, P. (2019). Multi-sensors based condition monitoring of rotary machines: An approach of multidimensional time-series analysis. *Measurement*, 134, 326-335. <https://doi.org/10.1016/j.measurement.2018.10.089>
- Zhang, S., Wang, B., Kanemaru, M., Lin, C., Liu, D., Miyoshi, M., Teo, K. H., & Habetler, T. G. (2020). Model-based analysis and quantification of bearing faults in induction machines. *IEEE Transactions on Industry Applications*, 56(3), pp.2158-2170. <https://doi.org/10.1109/tia.2020.2979383>

## Adaptive Threshold-based Fault Detection for Systems Exposed to Model Uncertainty and Deterministic Disturbance

Masood Ahmad<sup>1,2</sup> and Rosmiwati Mohd-Mokhtar<sup>1\*</sup>

<sup>1</sup>*School of Electrical and Electronic Engineering, Universiti Sains Malaysia, Engineering Campus, 14300 Nibong Tebal, Pulau Pinang, Malaysia*

<sup>2</sup>*Department of Electrical and Computer Engineering, COMSATS University Islamabad (Lahore Campus) Lahore, Pakistan*

### ABSTRACT

The fault detection problem is investigated for discrete-time linear uncertain systems. Instead of designing a fault detection system from the viewpoint of observer design for robust residual generation, an adaptive threshold approach is proposed to attain robustness against disturbance and norm-bounded model uncertainty. The main goal of the research is to develop a threshold design method that could establish an appropriate trade-off between false alarms and missed fault detection in the presence of model uncertainty. For this purpose, the  $H_\infty$  optimization technique is adopted in the linear matrix inequality framework to compute the unknown parameters of an adaptive threshold. It is shown that the proposed fault detection system based on an adaptive threshold depends only on the system parameters and the control input of the monitored system. It is independent of robust residual generator designs in traditional observer-based fault detection systems. The effectiveness of the proposed approach is verified on two well-known benchmark systems: a direct-current motor and three tank systems. Several types of faults are successfully detected in both applications.

**Keywords:** Adaptive threshold, fault detection,  $H_\infty$  optimization, linear matrix inequality, model uncertainty

### ARTICLE INFO

*Article history:*

Received: 27 November 2022

Accepted: 04 April 2023

Published: 09 October 2023

DOI: <https://doi.org/10.47836/pjst.31.6.26>

*E-mail addresses:*

masoodjaffar@student.usm.my (Masood Ahmad)

eerosmiwati@usm.my (Rosmiwati Mohd-Mokhtar)

\* Corresponding author

### INTRODUCTION

The reliability and safety of engineering systems remain the prime focus as technology advances. In this regard, several sophisticated systems have been developed with the aid of advanced and robust control theories that ensure the desired performance

of the system. The performance is governed by the system's internal components and by the functionality of sensors and actuators (Ahmad & Mohd-Mokhtar, 2021; Rahnavard et al., 2019).

Faults in these critical parts significantly reduce the system's overall performance and, in some cases, put the system in danger if not handled immediately. Fault detection (FD) plays a vital role in such situations by promptly identifying the presence of a fault and assisting in preventing both financial and fatal losses (Na & Ahmad, 2019; Salimi et al., 2019).

In the existing literature, FD techniques are typically classified as data-driven and model-based (Chen & Patton, 2012; Ding, 2014). The data-driven approach is adopted when system dynamics cannot be quantitatively modeled due to insufficient knowledge of the system's internal behavior. In contrast to data-driven techniques, model-based FD is chosen based on knowledge of the system dynamics, and mathematical model equations are developed. These equations are used to reconstruct the system output and verify that the anticipated output is consistent with the measured output from the sensors. The output error is treated as a residual. It should ideally be zero if there is no fault and non-zero otherwise.

Model-based FD techniques are further categorized as parameter estimation techniques, observer-based techniques, and parity relation techniques. In this study, the focus is on the observer-based technique. This technique consists of residual generation and evaluation, including threshold design. The primary task of the first stage, i.e., residual generation, is to generate a residual that indicates the possible occurrence of the fault. In the second stage, the residual is evaluated using signal and system norms to distinguish the fault from disturbance and noise and then compared with the threshold (Ahmad & Mohd Mokhtar, 2022; Gertler, 2017). Finally, a fault is declared upon simple decision logic, in which if the evaluated residual exceeds the threshold, the fault is declared and vice versa.

Most practical systems encounter unknown inputs, i.e., deterministic disturbance and/or random noise and model uncertainties. The unknown inputs cause deviation in the residual from zero in fault-free cases, which ultimately reduces the FD system performance. Thus, an indispensable need is to design a robust FD system where these unknown inputs are treated very carefully. In this context, two approaches have been used to deal with these unknown inputs in a model-based framework. In the first method, the residual generator is designed to either generate a residual completely decoupled from unknown inputs or use optimization approaches to make the residual robust against unknown inputs. Robust residual generation using optimization approaches has gained much attention, and very good results have been reported for linear systems subjected to unknown disturbance and random noise in the existing literature (Blanke et al., 2015; Gertler, 2017; Isermann, 2006). It is worth mentioning that generated residuals satisfy the sensitivity and robustness criterion in terms of performance indexes such as  $H_\infty/H_\infty$ ,  $H/H_\infty$ , and  $H_2/H_\infty$ . In the second

approach, rather than designing a robust residual generator, a robust threshold is designed to handle the unknown inputs in the residual evaluation stage.

More specifically, in the former case, an observer is designed to produce an unbiased estimation of the system's outputs, irrespective of the influence of model uncertainties and unknown disturbances that make output error zero, a desired phenomenon in FD. Robust residual generation is only possible when the observer design meets the robustness and sensitivity requirements of certain performance indexes. In the latter case, robustness to model uncertainties and unknown disturbances is ensured by a robust threshold in the residual evaluation stage rather than the residual generation stage (Amirkhani et al., 2020; Raka & Combastel, 2013; Puig et al., 2013; Montes de Oca et al., 2012). A robust threshold determines the maximum tolerance limit of an unknown disturbance and model uncertainty of the residual in the fault-free case. This approach eliminates the need for a separate robust residual generator design. The separate design of robust residual generation refers to an independent design of an observer, which is not linked with the threshold design in the second stage. In this case, the observer and threshold are designed separately for successful FD (former case). In robust threshold design, the threshold is designed in such a way that it could minimize the effect of the unknown inputs. Residual generation and threshold design are integrated into a single stage.

On the other side, the main challenges in the robust threshold design are false alarms and missed detection of the faults that must be addressed for successful FD. False alarms are generated due to unknown inputs, which forces the residual to cross the threshold even in fault-free cases. In this study, a threshold is designed for linear discrete-time systems subjected to norm-bounded model uncertainty and deterministic disturbances, which is the main contribution and becomes the paper's objective that distinguishes it from the existing literature. In this paper, the residual is generated by a fault detection filter (FDF), and the  $H_\infty$  optimization technique is used in the linear matrix inequality (LMI) framework to calculate the unknown parameters of the threshold. In the proposed threshold design, the maximum influence of unknown disturbance and model uncertainty is not considered, compared to the standard threshold, which reduces the missed detection of the fault because of the lower value of the detection threshold and increases the false alarms in the system. In the end, a DC motor and three-tank system illustrate the significance of the proposed scheme via simulations. The effectiveness of the proposed threshold in detecting the fault is assessed using a variety of sensor and actuator faults.

## PROBLEM FORMULATION

A linear discrete-time dynamic system, driven by  $l_2$  norm bounded control input  $u(k) \in R^p$ , unknown input  $d(k) \in R^{k_d}$ , and affected by  $f(k) \in R^{k_f}$  and model uncertainties ( $\Delta s$ ) is represented by the following Equation 1:

$$\begin{aligned}
 x(k+1) &= (A + \Delta A)x(k) + (B + \Delta B)u(k) + E_d d(k) + E_f f(k) \\
 y(k) &= (C + \Delta C)x(k) + (D + \Delta D)u(k) + F_d d(k) + F_f f(k)
 \end{aligned}
 \tag{1}$$

where  $x(k) \in R^n$  denotes the state vector and  $y(k) \in R^m$  be the measurement vector.  $A, B, C, D, E_d, F_d, E_f,$  and  $F_f$  are known matrices with appropriate dimensions.  $\Delta A, \Delta B, \Delta C, \Delta D$  are norm-bounded model uncertainties, defined as Equation 2:

$$\begin{bmatrix} \Delta A & \Delta B \\ \Delta C & \Delta D \end{bmatrix} = \begin{bmatrix} H_1 \Sigma G_1 & H_1 \Sigma G_2 \\ H_2 \Sigma G_1 & H_2 \Sigma G_2 \end{bmatrix}
 \tag{2}$$

where  $H_1, H_2, G_1$  and  $G_2$  are known matrices with compatible dimensions, and  $\Sigma$  is an unknown scalar constant but bounded with a condition that holds  $\Sigma^T \Sigma \leq \delta$  and  $0 < \delta \leq 1$ . Furthermore, it is assumed that  $\sup_{d \neq 0} \|d(k)\|_2 \leq \delta_d$ , where  $\delta_d$  is the upper limit of energy of unknown disturbance. Note that  $\delta_d$  and  $\delta$  represent the maximum possible influence of disturbance and model uncertainty on the system dynamics.

Observer-based residual generator, so-called FDF, is described by Equation 3:

$$\begin{aligned}
 \hat{x}(k+1) &= A\hat{x}(k) + Bu(k) + \\
 r(k) &= y(k) - \hat{y}(k)
 \end{aligned}
 \tag{3}$$

where  $\hat{y}(k) = C\hat{x}(k) + Du(k)$

$\hat{x}(k)$  is a state estimation vector,  $\hat{y}(k) \in R^m$  is the estimated output vector, and  $r(k)$  is the residual signal. The new vector, i.e., state estimation error vector,  $e(k) = x(k) - \hat{x}(k)$ , illustrates the dynamics of FDF (Equation 3) and is described by Equations 4 and 5:

$$\begin{aligned}
 e(k+1) &= (A - LC)e(k) + (\Delta A - L\Delta C)x(k) + (\Delta B - L\Delta D)u(k) + \\
 & (E_d - LF_d)d(k) + (E_f - LF_f)f(k)
 \end{aligned}
 \tag{4}$$

$$Ce(k) + \Delta Cx(k) + \Delta Du(k) + F_d d(k) + F_f f(k)
 \tag{5}$$

It is evident from Equation 5 that residual is sensitive to fault as well as unknown input, control input, and system's state. For residual evaluation purposes, the  $l_2$  norm of the residual Equation 5 is used and can be expressed as Equation 6:

$$J(k) = \|r(k)\|_{2,[k,k+N]}^2 = \sum_{j=0}^N r^T(k+j)r(k+j)
 \tag{6}$$

Recall that the  $l_2$  norm of a signal evaluates the change in energy of a signal in a certain evaluation window  $(k, k+N)$ . For FD purposes, it is desired to use the energy of the residual signal as an evaluation function rather than the residual's maximum/minimum peak value.



Furthermore, the standard threshold for FD is defined as Equation 7:

$$J_{th} = \sum^T \sum \leq \delta I, \sup_{\|d(k)\|_2 \leq \delta_d, f=0} \|r(k)\|_2^2 \quad (7)$$

It is evident from Equation 7 that the threshold represents the maximum value of the residual energy under the maximum possible influence of disturbance and model uncertainty in fault-free cases, leading the false alarms to zero. On the other hand, residual signals with small faults cannot cross the threshold because the fault signal disappears in the residual, ultimately increasing the missed detection of the faults.

New variables are defined below for designing a proposed threshold.

$$\delta_{dd} \leq \delta_d \text{ and } \delta_{\Delta s} \leq \delta$$

where  $\delta_{dd}$  and  $\delta_{\Delta s}$  represent the influence of certain energy levels of disturbance and model uncertainty on the system, respectively. The following threshold is proposed (Equation 8) to decrease the missed detection of the faults:

$$J_{th} = \sum^T \sum \leq \delta_{\Delta s} I, \sup_{\|d(k)\|_2 \leq \delta_{dd}, f=0} \|r(k)\|_2^2 \quad (8)$$

The threshold in Equation 8 determines the maximum change in energy of the  $r(k)$  when  $r(k)$  is influenced by disturbance and model uncertainty of a certain energy level, i.e.,  $\delta_{dd}$  and  $\delta_{\Delta s}$ , rather than the maximum possible influence, i.e.,  $\delta_d$  and  $\delta$ . Setting the threshold according to Equation 8 decreases the missed detection of the faults. On the other hand, disturbance  $\|d(k)\|_2 > \delta_{dd}$  and model uncertainty  $\Delta A, \Delta B, \Delta C, \Delta D$  in which  $\sum^T \sum > \delta_{\Delta s} I$  force the residual  $r(k)$  to cross the  $J_{th}$  in Equation 8 in fault-free cases lead to an increase in false alarms. Thus, there is a need to develop a method of threshold design for FD in the uncertain system in Equation 1 that can establish a suitable trade-off between missed detection of faults and false alarms. Following Equation 8, the proposed threshold in a fault-free case can be written as Equations 9 and 10:

$$J_{th} = \sum^T \sum \leq \delta_{\Delta s} I, \sup_{\|d(k)\|_2 \leq \delta_{dd}, f=0} \|G_{ru}(z)u(z) + G_{rd}(z)d(z)\|_2 \quad (9)$$

$$J_{th} = \sum^T \sum \leq \delta_{\Delta s} I, \sup_{\|d(k)\|_2 \leq \delta_{dd}, f=0} (\|G_{ru}(z)u(z)\|_2 + \|G_{rd}(z)d(z)\|_2) \quad (10)$$

where  $G_{ru}$  and  $G_{rd}$  represent the transfer function matrices from  $u$  and  $d$  to  $r$

$$G_{ru} = C(zI - A + LC)^{-1}(\Delta B - L\Delta D) + \Delta$$

$$G_{rd} = C(zI - A + LC)^{-1}(E_d - LF_d) + F_d$$

**Lemma 1:** Let  $B: S_1 \rightarrow S_2$  are two systems with appropriate dimensions and  $S_1, S_2 \in (0, \infty]$  then  $\|AB\|_2 \leq \|A\|_\infty \|B\|_2$

Applying Lemma 1 on Equation 10 leads to Equations 11, 12, and 13:

$$J_{th} = \sum^T \Sigma \leq \delta_{\Delta_S} I, \|d(k)\|_2 \leq \delta_{dd}, f = 0 \left( \|G_{ru}(z)\|_\infty \|u(z)\|_2 + \|G_{rd}(z)\|_\infty \|d(z)\|_2 \right) \quad (11)$$

$$J_{th} = \sum^T \Sigma \leq \delta_{\Delta_S} I, \|d(k)\|_2 \leq \delta_{dd}, f = 0 \left( \gamma_u \|u(z)\|_2 + \gamma_d \|d(z)\|_2 \right) \quad (12)$$

$$J_{th} = \sum^T \Sigma \leq \delta_{\Delta_S} I, \|d(k)\|_2 \leq \delta_{dd}, f = 0 \left( \gamma_u \|u(z)\|_2 + \gamma_d \delta_{dd} \right) \quad (13)$$

$\delta_{dd}$  is the certain energy level of unknown disturbance, which is assumed to be known.  $\|u\|_2$  is the  $l_2$  norm of the control input, generally known in practical systems. The control input varies during the system operation, eventually changing the FD threshold. Such a threshold is an adaptive threshold, which depends on the real values of system input. Thus, the aim here is to find the unknown parameters of the threshold in Equation 8, i.e.,  $\gamma_u$  and  $\gamma_d$ .

### METHOD TO FIND THE UNKNOWN PARAMETERS

A frequency domain representation of the residual in Equation 5 is written as Equation 14:

$$r(z) = G_{rd}(z)d(z) + G_{rf}(z)f(z) + G_{r\bar{u}}(z)\bar{u}(z) \quad (14)$$

where  $G_{r\bar{u}}, G_{rd}$ , and  $G_{rf}$  represent the transfer function matrices from  $\bar{u}, d$ , and  $f$  to  $r$

$$G_{r\bar{u}} = [C(zI - A + LC)^{-1}[(\Delta A - L\Delta C) \quad (\Delta B - L\Delta D)] + [\Delta C \quad \Delta D]]$$

$$G_{rd} = C(zI - A + LC)^{-1}(E_d - LF_d) + F_d$$

$$G_{rf} = C(zI - A + LC)^{-1}(E_f - LF_f) + F_f$$

$$\text{and } \bar{u}(z) = \begin{bmatrix} x(z) \\ u(z) \end{bmatrix}$$

In Equation 14,  $G_{r\bar{u}}(z)\bar{u}(z)$  contains uncertain system matrices. Therefore, it is separately treated as written in Equations 15 and 16:

$$[\Delta A - L\Delta C \quad \Delta B - L\Delta D] \begin{bmatrix} x(z) \\ u(z) \end{bmatrix} + [\Delta C \quad \Delta D] \begin{bmatrix} x(z) \\ u(z) \end{bmatrix} \quad (15)$$

$$(H_1 - LH_2)\Sigma[G_1 \quad G_2] \begin{bmatrix} x(z) \\ u(z) \end{bmatrix} + H_2\Sigma[G_1 \quad G_2] \begin{bmatrix} x(z) \\ u(z) \end{bmatrix} \quad (16)$$

From Equation 16, defining a new variable as in Equation 17:

$$B_a = [G_1 \quad G_2] \begin{bmatrix} x(z) \\ u(z) \end{bmatrix} = G_1 x(z) + G_2 u(z) \quad (17)$$

where  $x(z) = (zI - A - \Delta A)^{-1} [B + \Delta B \quad E_d] \begin{bmatrix} u(z) \\ d(z) \end{bmatrix}$ .  $x(z)$  is the dynamic response of  $B_a$  subject to unknown disturbance  $d$  and known control input  $u$ . Hence, Equation 17 becomes Equation 18:

$$B_a = G_1 (zI - A - \Delta A)^{-1} (B + \Delta B \quad E_d) + (G_2 \quad 0) \begin{bmatrix} u(z) \\ d(z) \end{bmatrix} \quad (18)$$

By using Equation 18, Equation 16 can be written as Equation 19:

$$(H_1 - LH_2) \Sigma B_a + H_2 \Sigma B_a \quad (19)$$

By incorporating Equation 19 into Equation 14, it can be expanded to Equations 20, 21, 22, and 23:

$$r(z) = [C(zI - A + LC)^{-1} (E_d - LF_d) + F_d] d(z) + [C(zI - A + LC)^{-1} (E_f - LF_f) + F_f] f(z) + C(zI - A + LC)^{-1} [(H_1 - LH_2) + H_2] \Sigma B_a \quad (20)$$

$$r(z) = [C(zI - A + LC)^{-1} (H_1 - LH_2 \quad E_d - LF_d) + (H_2 \quad F_d)] \begin{bmatrix} \Sigma B_a \\ d(z) \end{bmatrix} + [C(zI - A + LC)^{-1} (E_f - LF_f) + F_f] f(z) \quad (21)$$

$$r(z) = [C(zI - A + LC)^{-1} (H_1 \quad E_d) - L(H_2 \quad F_d) + (H_2 \quad F_d)] \begin{bmatrix} \Sigma B_a \\ d(z) \end{bmatrix} + [C(zI - A + LC)^{-1} (E_f - LF_f) + F_f] f(z) \quad (22)$$

$$r(z) = [C(zI - A + LC)^{-1} (\bar{E}_{\bar{u}} - L\bar{F}_{\bar{u}}) + \bar{F}_{\bar{u}}] \bar{u}(z) + [C(zI - A + LC)^{-1} (E_f - LF_f) + F_f] f(z) \quad (23)$$

where

$$\bar{u}(z) = \begin{bmatrix} \Sigma B_a \\ d(z) \end{bmatrix}, \bar{E}_{\bar{u}} = (H_1 \quad E_d) \text{ and } \bar{F}_{\bar{u}} = (H_2 \quad F_d)$$

Finally, the expression for the residual signal is written as Equation 24:

$$r(z) = G_{r\bar{u}d}(z) \bar{u}(z) + G_{rf}(z) f(z) \quad (24)$$

By using the residual signal in Equation 24, the proposed threshold in Equation 8 in a fault-free case can be expressed as Equation 25:

$$J_{th} = \sup \sum^T \Sigma \leq \delta_{\Delta S} I, \|d(k)\|_2 \leq \delta_{dd}, f = 0 \|G_{r\bar{u}d}(z) \bar{u}(z)\|_2 \quad (25)$$

Applying Lemma 1, Equation 25 turns to Equations 26, 27 and 28:

$$J_{th} = \|G_{r\bar{u}\bar{d}}(z)\|_{\infty} \sup_{\Sigma^T \Sigma \leq \delta_{\Delta_S} I, \|d(k)\|_2 \leq \delta_{dd}, f=0} \|\bar{u}(z)\|_2 \quad (26)$$

$$J_{th} = \|G_{r\bar{u}\bar{d}}\|_{\infty} \sup_{\Sigma^T \Sigma \leq \delta_{\Delta_S} I, \|d(k)\|_2 \leq \delta_{dd}, f=0} \left\| \frac{\sum B_a}{d(z)} \right\|_2 \quad (27)$$

$$J_{th} = \|G_{r\bar{u}\bar{d}}\|_{\infty} \sup_{\Sigma^T \Sigma \leq \delta_{\Delta_S} I, \|d(k)\|_2 \leq \delta_{dd}, f=0} \|\Sigma\|_2 \cdot \|B_a\|_2 + \|d(z)\|_2 \quad (28)$$

Assuming the bounds on  $d, \Sigma$ , i.e.,  $\|d\|_2 \leq \delta_{dd}, \Sigma^T \Sigma \leq \delta_{\Delta_S} I$ , the threshold turns to Equation 29:

$$J_{th} = \|G_{r\bar{u}\bar{d}}\|_{\infty} (\delta_{\Delta_S}) \|B_a\|_2 + \delta_{dd} \quad (29)$$

By carefully observing Equation 18, it is clear that  $B_a$  is the output of the system driven by the inputs  $u$  and  $d$ , and it can be described as Equation 30:

$$G_{B_a} = G_1(zI - A - \Delta A)^{-1} (B + \Delta B \quad E_d) + (G_2 \quad 0) \quad (30)$$

Using Lemma 1, it is reasonable to write Equation 31:

$$\|B_a\|_2 \leq \|G_{B_a}\|_{\infty} \cdot (\delta_{dd} + \|u\|_2) \quad (31)$$

Hence, Equation 29 turns to Equation 32:

$$J_{th} = \|G_{r\bar{u}\bar{d}}\|_{\infty} (\delta_{\Delta_S}) [\|G_{B_a}\|_{\infty} (\delta_{dd} + \|u\|_2)] + \delta_{dd} \quad (32)$$

In Equation 32, all the parameters of the proposed threshold are known except the H-infinity norm of  $G_{B_a}$  and  $G_{r\bar{u}\bar{d}}$ . Theorem 1 presents a method to determine the H-infinity norm of  $G_{B_a}$ . Due to space constraints, the proof is omitted here but can be obtained by solving a bounded real lemma (Boyd et al., 1994).

**Theorem 1:** For discrete-time linear uncertain system (Equation 33):

$$\begin{aligned} x(k+1) &= \bar{A}x(k) + \bar{B}ud(k) \\ y(k) &= \bar{C}x(k) + \bar{D}ud(k) \end{aligned} \quad (33)$$

where  $\bar{A} = (A + \Delta A)$ ,  $\bar{B} = [B + \Delta B \quad E_d]$ ,  $\bar{C} = G_1$

$$\bar{D} = [G_2 \quad 0], \quad \Delta A = H_1 \Sigma G_1, \quad \Delta B = H_1 \Sigma G_2$$

$$\bar{B} = [B \quad E_d], \text{ and } \Sigma^T \Sigma \leq \delta I$$

Given  $\gamma > 0$ , if there exists a scalar  $\varepsilon > 0$  and positive definite matrix  $P > 0$  such that the following LMI in Equation 34 holds, then the system in Equation 33 is asymptotically stable, and the  $H_\infty$  norm of transfer function  $G_{yud}$  satisfies  $\|G_{yud}\|_\infty < \gamma$ .

$$\begin{bmatrix} -\varepsilon I & 0 & 0 & H_1^T & 0 & 0 \\ * & -P & 0 & A^T P & \bar{C}^T & G_1^T \varepsilon \\ * & * & -\gamma^2 I & \bar{B}^T P & \bar{D}^T & G_2^T \varepsilon \\ * & * & * & -P & 0 & 0 \\ * & * & * & * & -I & * \\ * & * & * & * & * & -\varepsilon I \end{bmatrix} < 0 \tag{34}$$

Using Theorem 1, seeking a minimum value of  $\gamma$  satisfies the following Equation 35

$$\|G_{B_a}\|_\infty < \gamma \Leftrightarrow \|G_1(zI - A - \Delta A)^{-1}(B + \Delta B \quad E_d) + (G_2 \quad 0)\|_\infty < \gamma \tag{35}$$

Hence, Equation 32 becomes Equation 36:

$$J_{th} = \|G_{r\bar{u}d}\|_\infty (\delta_{\Delta s}) [\gamma \cdot (\delta_{dd} + \|u(z)\|_2)] + \delta_{dd} \tag{36}$$

To this end, the only unknown is  $\|G_{r\bar{u}d}\|_\infty$  to compute the proposed threshold. The following lemma provides the solution of  $\|G_{r\bar{u}d}\|_\infty$ .

**Lemma 2 (Ding, 2013):** Given an LTI system,  $G_{r\bar{u}d}(z) = C(zI - A + LC)^{-1}\bar{E}_{\bar{u}} + \bar{F}_{\bar{u}}$ , and for given  $\bar{\gamma}_d > 0$  if there exists a symmetric matrix  $P$  such that the following LMI Equation 37 holds then  $\|G_{r\bar{u}d}(z)\|_\infty < \bar{\gamma}_d$

$$\begin{bmatrix} -P & P(A - LC) & P\bar{E}_{\bar{u}} & 0 \\ * & -P & 0 & C^T \\ * & * & -\bar{\gamma}_d I & \bar{F}_{\bar{u}}^T \\ * & * & * & -\bar{\gamma}_d I \end{bmatrix} < 0, \quad P > 0 \tag{37}$$

Solving LMI Equation 37 in MATLAB and minimum  $\bar{\gamma}_d$  can be found at which a feasible solution of LMI Equation 37 is obtained. Finally, we are able to write the final expression of the adaptive threshold in Equation 36 as Equation 38:

$$J_{th} = \bar{\gamma}_d \cdot (\delta_{\Delta s} \gamma (\delta_{dd} + \|u(z)\|_2) + \delta_{dd}) \tag{38}$$

Rearranging Equation 37 gives Equation 39:

$$J_{th} = \bar{\gamma}_d \delta_{\Delta s} \gamma \delta_{dd} + \bar{\gamma}_d \delta_{\Delta s} \gamma \|u(z)\|_2 + \bar{\gamma}_d \delta_{dd} \tag{39}$$

Denoting,  $\gamma_u = \bar{\gamma}_d \delta_{\Delta s} \gamma$  and  $\gamma_d = \bar{\gamma}_d (1 + \delta_{\Delta s} \gamma)$

By correlating Equations 13 and 39, unknown adaptive threshold parameters can be obtained. It is worth remembering that robust threshold design Equation 39 depends on

the system parameters and control input. Furthermore, FD is independent of the residual generator design. A fault can be successfully detected when an evaluated residual using Equation 6 crosses the threshold of Equation 39.

#### Algorithm for Computation of Adaptive Threshold

**Step 1:** Define the matrices according to Equations 16 and 24

**Step 2:** Find the minimum value of  $\gamma$  using Theorem 1 for the given value of  $\delta_{dd}$  and  $\delta_{\Delta s}$

**Step 3:** Find the minimum value of  $\bar{\gamma}_d$  using Lemma 2

**Step 4:** Compute the residual evaluation function using Equation 6

**Step 5:** Calculate the online value of  $\|u(k)\|_2$

**Step 6:** Set  $J_{th}$  according to Equation 38

**Step 7:** Compare the evaluated residual,  $J(k)$ , in Equation 6 with the threshold,  $J_{th}$ , in Equation 38 such that  $J(k) \leq J_{th}$  is fault-free and vice versa.

## SIMULATION RESULTS

The performance of the FD system based on the proposed threshold is examined through simulations. Two system models are tested: (1) A DC motor system and (2) A three-tank benchmark system. For simulation purposes, two types of faults are considered: (1) Abrupt fault and (2) Intermittent fault. Since the system's behavior changes dramatically and could potentially harm its stability, abrupt faults seem severe for the system. The sensors and actuators of the system also frequently experience intermittent faults that degrade the system's performance. These faults are introduced to show how well the proposed method can identify critical faults.

### Application to a DC Motor System

A linear discrete-time model of a DC motor with nominal system matrices is shown below:

$$A = \begin{bmatrix} 0.2592 & 0.0017 \\ -0.0033 & 0.0025 \end{bmatrix}, \quad E_f = B = \begin{bmatrix} 0.0148 \\ 0.9974 \end{bmatrix}$$

$$E_d = \begin{bmatrix} -1.6460 \\ 0.0148 \end{bmatrix}, \quad C = [1 \quad 0], \quad F_d = F_f = 1$$

$\omega_m$  and  $i_a$  are the state variables, defined as angular velocity and armature current of the DC motor, respectively. Model uncertainty is represented as:

$$H_1 = \text{diag}[0.1 \quad 0.1], \quad H_2 = [0.1 \quad 0]$$

$$G_1 = \text{diag}[0.1 \quad 0.1], \quad G_2 = [0 \quad 0.1]^T$$

For simulations, the unknown parameter ( $\Sigma = \text{diag}[0.9597, 0.9597]$ ) of the norm-bounded model, uncertainty, is chosen randomly. Load torque variation is treated

as an unknown input to the DC motor that holds the bounded condition, i.e.,  $d(k) \in [-0.01, 0.01]$ . Furthermore, matrix  $A + \Delta A$  is stable if  $\Delta A$  holds the condition in Equation 2. Sensor fault is considered in this simulation that occurs in the speed sensor of the DC motor.

Control input  $u(k)$  (Figure 1) is applied to the DC motor for simulation. As stated previously, the algorithm to find the unknown parameters of the adaptive threshold is implemented in MATLAB.

By referring to Equation 38, i.e.,  $J_{th} = \gamma_u \|u(k)\|_2 + \gamma_d \delta_{dd}$  where  $\gamma_u = \bar{\gamma}_d \delta_{\Delta s} \gamma$  and  $\gamma_d = \bar{\gamma}_d (1 + \delta_{\Delta s} \gamma)$ ,

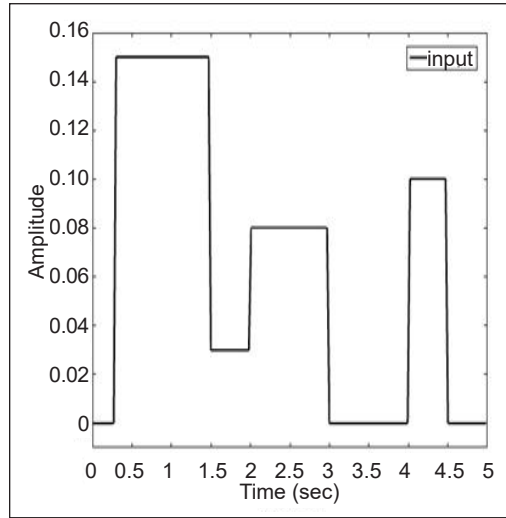


Figure 1. Control input to DC motor

$\delta_{dd} = 0.005$  and  $\delta_{\Delta s} = 0.5155$  is taken for threshold computation.  $\|u(k)\|_2$  is the  $l_2$  norm of the control input, known during the system's operation. The only unknown parameters in  $J_{th}$  are  $\gamma$  and  $\bar{\gamma}_d$ , which can be determined easily by solving Equations 34 and 36 using the MATLAB LMI toolbox. After several iterations,  $\gamma$  and  $\bar{\gamma}_d$  are reduced to 0.4029 and 1.9135, respectively. For a residual generation, observer structure Equation 3 is used, and filter gain  $L$ , using Lemma 2, is calculated as:

$$L = \begin{bmatrix} -0.2592 \\ 0.0016 \end{bmatrix}$$

Figure 2 represents the abrupt speed sensor fault detection using the proposed and standard thresholds. At  $t = 2$  seconds, the speed sensor experiences an abrupt fault. An abrupt fault of extremely small magnitude is simulated as a step function of 0.1 amplitude. It can be observed that the evaluation function is below the detection threshold in the case of a fault-free sensor with a certain amount of false alarms, but the residual evaluation function crosses the adaptive threshold at the time of fault occurrence, which shows the explicit demonstration of the FD in the sensor. The evaluated residual is also compared with the state-of-the-art threshold Equation 7, stated in the literature for the same type of speed sensor fault. It is evident from Figure 2 that if a threshold using Equation 7 is selected, there are missed detections of the faults. Missed detection of the faults causes the FD system's performance to decrease, ultimately leading to monitored system failure. The effectiveness of the proposed threshold can be observed in Figure 2. It becomes obvious that the effect of a fault is considerably increased using the proposed threshold Equation 38 with negligible false alarms, which delivers fast detection of the fault. Faults cannot be detected accurately using a standard threshold, irrespective of zero false alarms.

In Figure 3, an intermittent sensor fault, which shows the improper functioning of the sensor, is simulated for FD. Figure 3 demonstrates that the evaluated residual is above the threshold for the time of fault occurrence. Both types of sensor faults are successfully detected using the adaptive threshold technique. Thus, these findings support the efficacy

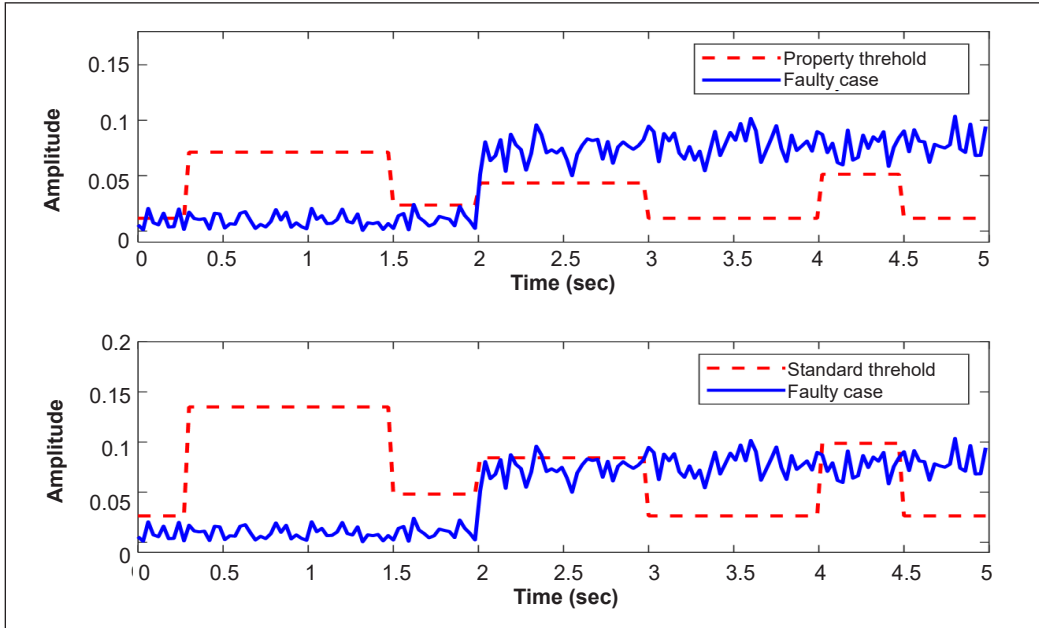


Figure 2. Abrupt sensor FD: proposed threshold (top), standard threshold (bottom)

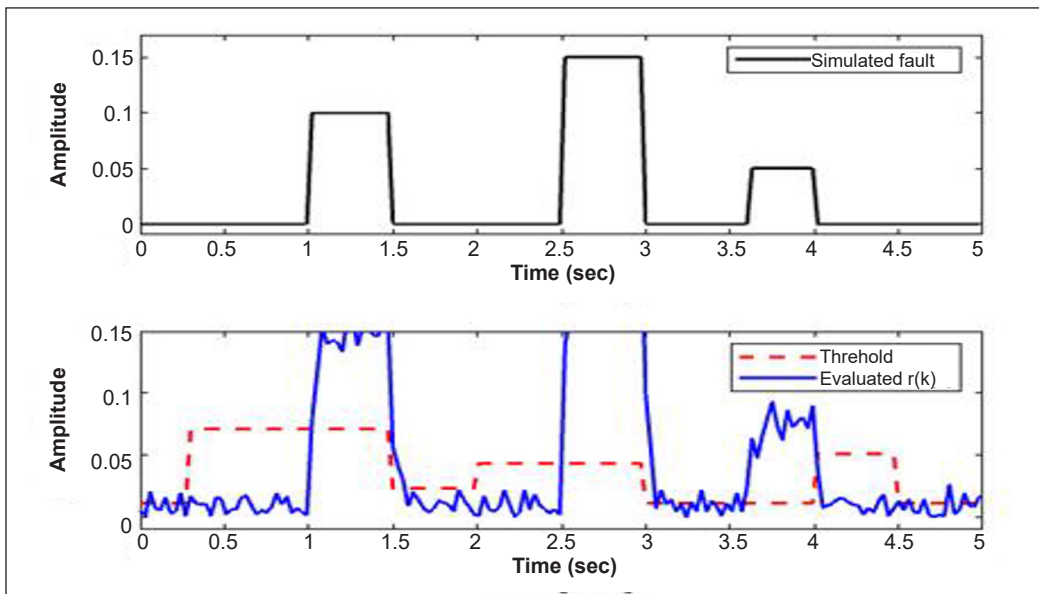


Figure 3. Simulated intermittent sensor fault (top) and fault detection (bottom)



of the proposed approach by accurately and quickly identifying the sensor fault in the DC motor regardless of unknown disturbances and model uncertainty in the system state matrix as well as in the input and measurement matrices.

### Application to a Three-tank System

As seen in Figure 4, the three-tank system is a benchmark system that has been extensively studied in chemical engineering. It is employed in real-time software and practical applications to implement various control and FD techniques. The three-tank system's dynamics are nonlinear. Linearizing the nonlinear model introduces modeling errors that are considered norm-bound model uncertainty. It makes it a useful benchmark for FD algorithm testing.

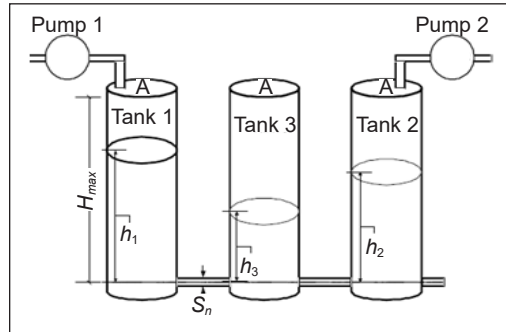


Figure 4. Three-tank system (Ding, 2013)

The following equations express the nonlinear dynamics of the three-tank system and are represented in Equation 40:

$$\begin{aligned}
 A\dot{h}_1 &= Q_1 - Q_{13} \\
 A\dot{h}_2 &= Q_2 + Q_{32} - Q_{20} \\
 A\dot{h}_3 &= Q_{13} - Q_{32}
 \end{aligned} \tag{40}$$

with

$$\begin{aligned}
 Q_{13} &= a_1 s_{13} \operatorname{sgn}(h_1 - h_3) \sqrt{2g|h_1 - h_3|} \\
 Q_{32} &= a_3 s_{23} \operatorname{sgn}(h_3 - h_2) \sqrt{2g|h_3 - h_2|} \\
 Q_{20} &= a_2 s_0 \sqrt{2gh_2}
 \end{aligned}$$

Water levels  $h_1$ ,  $h_2$  and  $h_3$  in respective tanks are the process outputs  $y(k)$ , while mass flows  $Q_1$ ,  $Q_2$  are taken as the process inputs  $u_1(k)$ ,  $u_2(k)$ . The mass flow from the  $i$ th tank to the  $j$ th tank is represented by  $Q_{ij}$ . The cross-sectional areas of the pipe linking tank 1-tank 3 and tank 2-tank 3 are represented by  $S_{13}$  and  $S_{23}$ , respectively.  $S_0$  is the cross-sectional area of the tank 2 outlet pipe. The signum function, abbreviated as  $\operatorname{sgn}$ , is described as:

$$\operatorname{sgn}(x) = \begin{cases} -1 & \text{if } x < 0 \\ 0 & \text{if } x = 0 \\ 1 & \text{if } x > 0 \end{cases}$$

$$s_{13} = s_{23} = s_0 = s_n$$

Table 1 lists the system’s coefficients and relevant parameters. The disturbance in the three-tank system is caused by the water bubbles produced as a result of the pumps’ water released into the tanks. There is also measurement noise in the sensors that determines the water levels. The system’s linear model is developed for FD by expanding Taylor’s series around the equilibrium or operating point using the linearization approach. A discrete-time linear model, expressed in the state-space form (1), is obtained by performing the linearization at the operating points  $h_1=45$  cm,  $h_2=15$  cm  $h_3$  and = 30 cm, and discretizing the linearized model at a sampling time of 1 second. Nominal matrices are defined as:

$$A = \begin{bmatrix} 0.9915 & 0 & 0.0084 \\ 0 & 0.9807 & 0.0082 \\ 0.0084 & 0.0082 & 0.9833 \end{bmatrix}, C = \text{diag}[1,1,1]$$

$$B = \begin{bmatrix} 0.0065 & 0.0008 \\ 0.0008 & 0.0065 \\ 0 & 0 \end{bmatrix}, E_d = \begin{bmatrix} 0.25 & 0 & 0 \\ 0 & 0.25 & 0 \\ 0 & 0 & 0.25 \end{bmatrix}$$

$$D = 0, E_f = B, F_d = F_f = C$$

The modeling errors brought in by the linearization process, defined below, represent the model uncertainty in the system matrices.

$$H_1 = H_2 = \begin{bmatrix} -0.01 & 0 & 0 \\ 0 & -0.01 & 0 \\ 0 & 0 & -0.01 \end{bmatrix}$$

$$G_1 = \begin{bmatrix} 0.01 & 0 & 0.015 \\ 0 & 0.01 & 0.015 \\ 0.01 & 0.01 & 0.05 \end{bmatrix}$$

The same procedure simulates the model, with a constant inflow of pumps  $Q_1 = 100$  cm<sup>3</sup>/sec,  $Q_2 = 100$  cm<sup>3</sup>/sec, uniform disturbance,  $d(k) \in [-0.01,0.01]$ .  $l_2$  norm of the

Table 1  
Parameters of the three-tank system

Parameters	Symbol	Value	Unit
Cross-section area of the tank	$A$	154	cm <sup>2</sup>
Cross-section area of the pipe	$S_n$	0.5	cm <sup>2</sup>
Maximum height of the tank	$H_{max}$	62	cm
Maximum flow rate of pump 1	$Q1_{max}$	100	cm <sup>3</sup> /sec
Maximum flow rate of pump 2	$Q2_{max}$	100	cm <sup>3</sup> /sec
Coefficient of flow for pipe 1	$a_2$	0.46	
Coefficient of flow of pipe 2	$a_2$	0.60	
Coefficient of flow for pipe 3	$a_3$	0.45	

control input is determined online.  $\delta_{dd} = 0.005$  and  $\delta_{\Delta s} = 0.5155$  are the energy levels of disturbance and model uncertainty, respectively. MATLAB LMI toolbox is used to compute the unknown parameters,  $\gamma$  and  $\bar{\gamma}_d$ , in  $J_{th}$  by solving Equations 34 and 36, respectively. After several iterations,  $\gamma$  and  $\bar{\gamma}_d$  are reduced to 0.023 and 1.006, respectively.

For a residual generation, observer gain  $L$  is calculated using Lemma 2 as:

$$L = \begin{bmatrix} 0.2461 & 0 & 0 \\ * & 0.2461 & 0 \\ * & * & 0.2461 \end{bmatrix}$$

One of the three sensors' offset faults is taken into account during the simulation. The offset value ranges from 0 to  $H_{max}$ . In this regard, at  $t = 80$  seconds, a 2 cm offset sensor fault is introduced into the sensor of tank 3.

It can be shown from Figure 5 that fault detectability using the proposed threshold is significantly improved as compared to a standard threshold. However, there are false alarms in the system that are in an acceptable range and do not affect the FD system's performance. Similar results are obtained for the sensor intermittent fault in tank 1 and abrupt actuator fault in pump 1 in Figures 6 and 7, respectively. It can be noticed from the simulation results of both benchmark systems that fault detection is quite easier using the proposed threshold. The reason is the improved fault detectability of the proposed threshold.

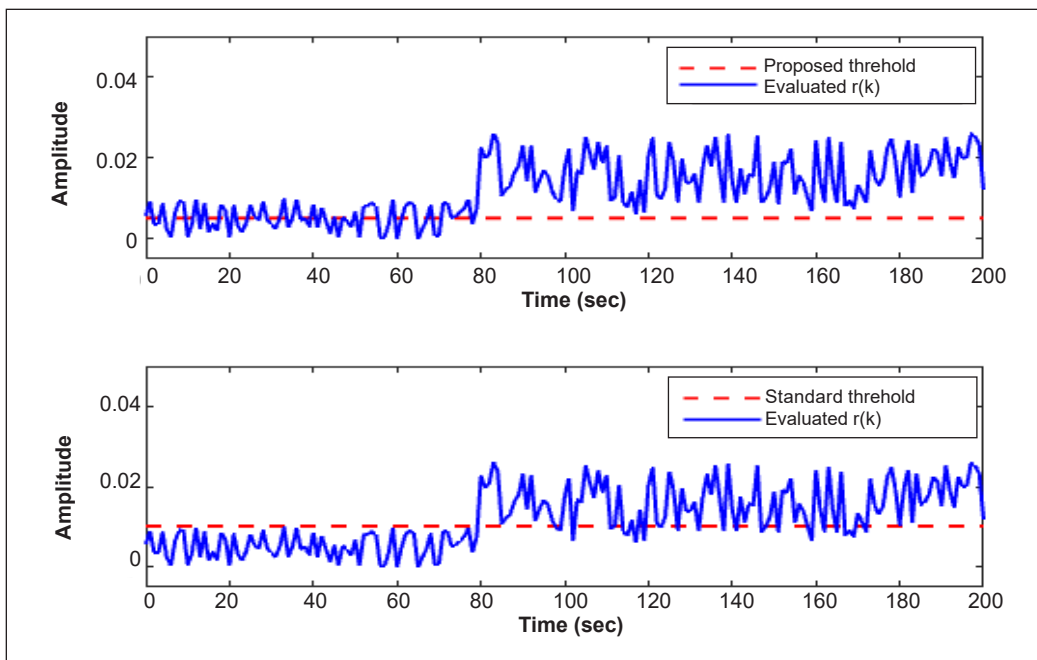


Figure 5. Abrupt sensor FD in tank 3: proposed threshold (top), standard threshold (bottom)

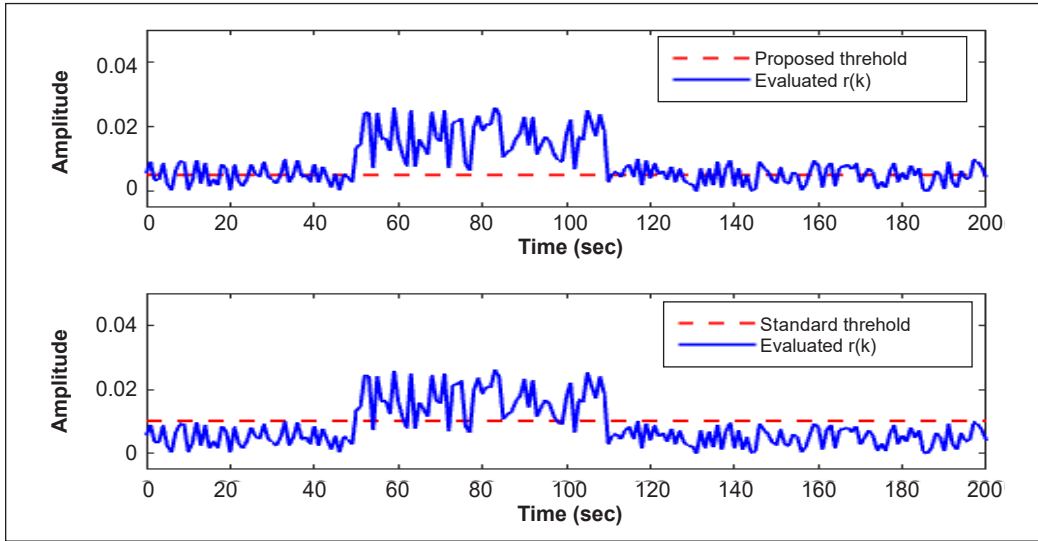


Figure 6. Intermittent sensor FD in tank 1: proposed threshold (top), standard threshold (bottom)

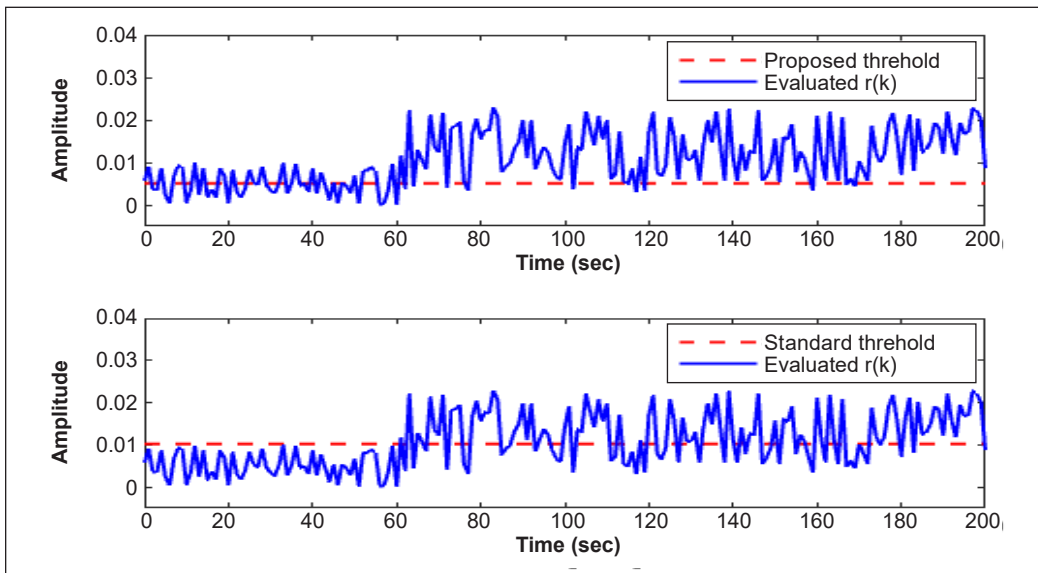


Figure 7. Abrupt actuator FD in pump 1: proposed threshold (top), standard threshold (bottom)

## CONCLUSION

An adaptive threshold-based fault detection system has been designed for linear systems subjected to norm-bounded model uncertainty and a deterministic disturbance signal. The computation of unknown threshold parameters is formulated as an  $H_\infty$  optimization. The main contribution of this paper is the design of an adaptive threshold and its integration into a fault detection system, such that fault detectability is improved. Due to the integrated

design, a separate design for the robust residual generator is not required. It is shown that the proposed threshold is a linear function of unknown disturbances and known control inputs that are available for online computation. The performance of the proposed approach is verified by simulations of two well-known applications for different kinds of faults. Results show that all faults were successfully detected.

## ACKNOWLEDGMENTS

The work is supported by the Ministry of Higher Education Malaysia for Fundamental Research Grant Scheme with Project Code: FRGS/1/2019/TK04/USM/02/12 and the HRDI-UESTPS scholarship program funded by the Higher Education Commission (HEC) of Pakistan.

## REFERENCES

- Ahmad, M., & Mohd-Mokhtar, R. (2021). Fault detection full order filter apply to discrete time-invariant linear system. *Journal of Engineering Science and Technology*, 16(5), 4221-4234.
- Ahmad, M., & Mohd-Mokhtar, R. (2022). A survey on model based fault detection techniques for linear time invariant systems with numerical analysis. *Pertanika Journal of Science & Technology*, 30(1), 53-78. <https://doi.org/10.47836/pjst.30.1.04>
- Ammiche, M., Kouadri, A., Halabi, L. M., Guichi, A., & Mekhilef, S. (2018). Fault detection in a grid-connected photovoltaic system using adaptive thresholding method. *Solar Energy*, 174, 762-769. <https://doi.org/10.1016/j.solener.2018.09.024>
- Blanke, M., Kinnaert, M., Lunze, J., & Staroswiecki, M. (2015). *Diagnosis and Fault-Tolerant Control* (3rd ed.). Springer.
- Boyd, S., El Ghaoui, L., Feron, E., & Balakrishnan, V. (1994). *Linear Matrix Inequalities in System and Control Theory*. Society for Industrial and Applied Mathematics.
- Chen, J., & Patton, R. J. (2012). *Robust Model-Based Fault Diagnosis for Dynamic Systems*. Springer Science & Business Media.
- Ding, S. X. (2013). *Model-Based Fault Diagnosis Techniques: Design Schemes, Algorithms, and Tools*. Springer Science & Business Media.
- Ding, S. X. (2014). *Data-Driven Design of Fault Diagnosis and Fault-Tolerant Control Systems*. Springer Science & Business Media.
- Gertler, J. J. (2017). *Fault Detection and Diagnosis in Engineering Systems*. CRC Press.
- Isermann, R. (2006). *Fault Diagnosis Systems*. Springer.
- Montes de Oca, S., Puig, V., & Blesa, J. (2012). Robust fault detection based on adaptive threshold generation using interval LPV observers. *International Journal of Adaptive Control and Signal Processing*, 26(3), 258-283. <https://doi.org/10.1002/acs.1263>

- Na, Y., & Ahmad, M. (2019). A fault detection scheme for switched systems with noise under asynchronous switching. In *9th International Conference on Information Science and Technology* (pp. 258-262). IEEE Publishing. <https://doi.org/10.1109/ICIST.2019.8836838>
- Rahnavard, M., Ayati, M., Yazdi, M. R. H., & Mousavi, M. (2019). Finite time estimation of actuator faults, states, and aerodynamic load of a realistic wind turbine. *Renewable Energy*, *130*, 256-267. <https://doi.org/10.1016/j.renene.2018.06.053>
- Puig, V., Montes de Oca, S., & Blesa, J. (2013). Adaptive threshold generation in robust fault detection using interval models: Time-domain and frequency-domain approaches. *International Journal of Adaptive Control and Signal Processing*, *27*(10), 873-901. <https://doi.org/10.1002/acs.2362>
- Raka, S. A., & Combastel, C. (2013). Fault detection based on robust adaptive thresholds: A dynamic interval approach. *Annual Reviews in Control*, *37*(1), 119-128. <https://doi.org/10.1016/j.arcontrol.2013.04.001>
- Salimi, A., Batmani, Y., & Bevrani, H. (2019). Model-based fault detection in DC microgrids. In *2019 Smart Grid Conference (SGC)* (pp. 1-6). IEEE Publishing. <https://doi.org/10.1109/SGC49328.2019.9056589>

## Dibenzofuran Degradation by Bacterial Community in Landfill Leachate

Farah Najwa Ahmad<sup>1,2</sup>, Noor Faizul Hadry Nordin<sup>1\*</sup>, Muhamad Shirwan Abdullah Sani<sup>1</sup> and Wan Syibrah Hanisah Wan Sulaiman<sup>1</sup>

<sup>1</sup>International Institute for Halal Research and Training (INHART), International Islamic University Malaysia, Jalan Gombak, 53100 IIUM, Kuala Lumpur, Malaysia

<sup>2</sup>Department Agrotechnology and Bio-Industry, Polytechnic Nilai Negeri Sembilan, Nilai Education Hub, 71760 Nilai, Negeri Sembilan, Malaysia

### ABSTRACT

The contamination of the environment has been a global issue, and bioremediation is proposed as an option to clean up the contamination sites with the promising utilization of bacterial community capabilities. The indigenous bacterial community in the landfill leachate is recognized to carry enzymes for the degradation of contaminants such as dioxin congeners, the dibenzofuran. Environmental factors have been known to influence the process to achieve successful biodegradation, and the optimized conditions may speed up the biodegradation process. Thus, this study was conducted to optimize the substrate availability, temperature, and pH factor for the degradation of dibenzofuran from landfill leachate by the native bacterial community in landfill leachate. This study uses the one-factor-at-time (OFAT) approach to measure dibenzofuran degradation. The landfill leachate with enrichment of dibenzofuran (15 to 45 mg L<sup>-1</sup>) was incubated at temperatures (30°C to 42°C) and pH (5 to 9) for 24 hours before being extracted and analyzed. From the first part of the study, 15 mg L<sup>-1</sup> of dibenzofuran, 30°C temperature, and pH 7 have shown

the highest dibenzofuran degradation. Later, the optimum condition of dibenzofuran removal (74.40%) was achieved when the landfill leachate was spiked with 15 ppm dibenzofuran at 30°C and pH 7 for 24 hours. This study proposes optimized conditions that give a better result for dibenzofuran degradation, which may enhance bioremediation.

**Keywords:** Bacterial community, biodegradation, dibenzofuran, landfill leachate, One-Factor-at-a-Time (OFAT)

### ARTICLE INFO

#### Article history:

Received: 09 December 2022

Accepted: 12 April 2023

Published: 12 October 2023

DOI: <https://doi.org/10.47836/pjst.31.6.27>

#### E-mail addresses:

farahnajwaahmad@gmail.com; farah.najwa@live.iium.edu.my

(Farah Najwa Ahmad)

faizul@iium.edu.my (Noor Faizul Hadry Nordin)

shirwansany@iium.edu.my (Muhamad Shirwan Abdullah Sani)

syibrahamis@iium.edu.my (Wan Syibrah Hanisah Wan Sulaiman)

\*Corresponding author

## INTRODUCTION

The aquatic ecosystem pollution from many anthropogenic activities is becoming a global concern. One of the biggest concerns is the occurrence of organic contaminants that are found to be highly persistent in the environment and have destructive biological effects on humans and animals (Baran et al., 2020; Baran et al., 2021; Eskenazi et al., 2018). Amongst the harmful organic contaminants are Chlorinated Hydrocarbons (CHs) found in the atmosphere and hydrosphere recently (Haedrich et al., 2020; Zhao et al., 2022).

The landfill site is one of the sources of organic contaminants released into the environment (Njoku et al., 2019). More than half of the related products containing CHs were estimated to enter the landfill site, which mixed with other materials to form landfill leachate. Compounds containing CHs, such as dioxin congeners, are among the hazardous pollutants in landfill leachate (Salam & Nilza, 2021). Leachate formed from chemical reactions in a landfill was one of the major potential contributors of dioxins released to the environment, especially into soil and water bodies (Ferronato & Toretta, 2019). According to Szajner et al. (2021), the adverse effects of dioxins on the health of humans and animals were found devastating and irreversible. Dibenzofuran, one of the harmless dioxin congeners, has been chosen as the model in this study.

Several conventional physical and chemical techniques are available for dioxin removal and clean-up, but most of the techniques fail to destroy the compounds completely, and often, the techniques lead to other types of situations (Earnden et al., 2022; Rashwan et al., 2022). There are photocatalytic degradation (Gaur et al., 2022) and chemical oxidation process (Eldos et al., 2022). An effective method to destroy the contaminants is an urgent concern to date. One of the techniques available to treat organic contaminants is bioremediation, a low-cost and eco-friendly method (Tarekegn et al., 2020). This technique converts harmful contaminants into less toxic ones using microorganisms such as bacteria (Ambust et al., 2021; Morris et al., 2018; Soare et al., 2019).

It was reported that indigenous microbial communities inhabiting the contaminated sites could potentially biodegrade these xenobiotic compounds (Tas et al., 2018). Studies on a microcosm of microorganisms and their ability have shown some hope for dioxins bioremediation (Terzaghi et al., 2020). These strategies were carried out by harnessing the ability of microorganisms, mainly bacteria, to utilize chlorinated hydrocarbons by breaking down the compounds using specific enzymes, including biphenyl dioxygenase and dioxin dioxygenase. Previously, no data was available about the native bacterial community of landfill leachate that degrades organic contaminants, specifically dibenzofuran. The study was intended to determine the optimal condition for dibenzofuran degradation by the native bacterial community in the landfill leachate.



## MATERIALS AND METHODS

### Sampling – Selangor, Malaysia

The leachate sample was collected from Jeram Sanitary Landfill, Selangor, at coordinates of 3°11'27.3"N 101°22'02.1"E. The landfill has the capacity of receiving 2500 tons of waste per day. A hydro lab quanta multi-probe meter is used as the sampling device to collect five liters of the landfill leachate sample. The physicochemical properties of the leachate, pH, total dissolved solids (TDS), turbidity, temperature, and dissolved oxygen (DO) were recorded. The sample was kept in a polyethylene tube and stored for further analysis.

### Biodegradation Studies

**Optimization of Dibenzofurans Biodegradation Parameters.** The study was based on a one-factor-at-a-time (OFAT) design. The parameters chosen to be optimized were dibenzofuran concentration, pH, and temperature. The parameters studied were the most crucial environmental components for bacterial growth: pH, temperature, and substrate availability. The levels of parameters were selected to represent different growth conditions for the bacteria community. The study was conducted in a 250 ml Erlenmeyer flask and carried out in triplicate. The culture was incubated at a 200-rpm shaking rate for 24 hours. Twenty-four hours is chosen as it is the most optimum time for bacterial degradation of dibenzofuran (Tajudin, 2017; Sanusi, 2017). The degradation of dibenzofuran is decreasing, and the bacteria undergo the death phase after 24 hours of incubation time. A flask containing similar content/ ingredients without bacterial inoculation was prepared as a control to determine abiotic degradation. The response determined was the amount of dibenzofuran removal at the end of the study. The biodegradation efficiency of dibenzofuran (%) is calculated through the following Equation 1:

$$\text{Biodegradation efficiency (\%)} = \frac{(C_i - C_f)}{C_i} \times 100 \quad (1)$$

Where  $C_i$  and  $C_f$  are the initial and final concentrations of dibenzofuran (ppm) in the experiment solution.

**Effect of Dibenzofuran Concentration on Dibenzofuran Degradation.** Different substrate concentrations were set to discover the best level of dibenzofuran for maximum degradation. Three different dibenzofuran concentrations (15 ppm, 30 ppm, and 45 ppm) were examined to find the dibenzofuran utilization by the bacterial community in the landfill leachate. The growth medium was incubated at 37°C, with a pH of 7.

**Effect of Temperature on Dibenzofuran Degradation.** For the temperature study, different temperatures representing different conditions for bacterial growth were chosen and set for

bacterial incubation. The different temperatures are 30°C, 37°C, and 42°C sets (Sanusi, 2017). The media will be enriched with 30 ppm dibenzofuran concentration at pH 7.

***Effect of pH on Dibenzofuran Degradation.*** pH levels of 5, 7, and 9 were used to study the effect of pH on the degradation of dibenzofuran by the bacterial community in landfill leachate. The pH chosen and set represented different pH conditions for bacterial growth. The media will be enriched with 30 ppm incubated at 37°C. The pH will be adjusted by using HCL or NaOH solution.

**Liquid-Liquid Extraction of Dibenzofuran from Landfill Leachate.** Based on the previous study, LLE has been widely used to extract organic pollutants in water (Razali et al., 2018). Hence, LLE was chosen to extract dibenzofuran from the landfill leachate. Hexane was chosen as the solvent in this study as it had shown the highest percentage of recovery of dibenzofuran from landfill leachate after the extraction process (Tajudin, 2017). Another recent study supports it by using hexane as the solvent to elute Polychlorinated Dibenzofurans (PCDFs) from an environmental sample (Baran et al., 2020).

For sample preparation, a 1000 ml sample of landfill leachate was homogenized using 500 ml of hexane. The mixture was left in a separatory funnel for separations. Leachate was discarded after 6 hours. The separated hexane was kept for further analysis. A rotary evaporator was run to remove solvents from the extracted sample gently. The sample was eluted by Nitrogen gas blow. Before performing the degradations studies, extraction of dibenzofuran from the landfill leachate was conducted to identify the initial amount of dibenzofuran in the landfill leachate sample collected.

### **Qualitative and Quantification of Dibenzofuran by Gas Chromatography-Mass Spectrophotometry (GC-MS)**

The standard curve was formed using a series of dibenzofuran concentrations ranging from 1 ppm to 120 ppm with hexane as solvents in a 1 ml volumetric flask and injected into Gas Chromatography-Mass Spectrophotometry (GC-MS). Analysis was performed to get  $R^2$  from the generated linear graph of the external standards.

Separation and quantification of dibenzofuran were conducted by an Agilent Technologies 7890 gas chromatography (GC) system equipped with an Agilent Technologies 5975 mass spectrometer (MS) system (Agilent Technologies, USA). The working standards and top hexane layer of the landfill leachate extracts were injected into an injector temperature maintained at 300°C. The compounds were separated by an HP-5MS column with an oven temperature for the column set (1) 70°C for 2 minutes and (2) 300°C and held for 15 minutes at the flow rate of 20°C/min. The dibenzofuran detection and quantification were determined in scan and selected ion monitoring (SIM) modes.

The dibenzofuran was identified by the retention time, comparison of their mass fragmentation patterns with standards from the National Institute of Standard (NIST) Mass Spectral 11 library, and confirmation with the working standards. The span of the calibration curve was established and assessed, with the correlation coefficient  $R^2 > 0.98$  showing an acceptable identification (Sani et al., 2022).

### Statistical Analysis

The data were expressed as mean and standard deviation of the triplicate of dibenzofuran degraded. One-way analysis of variance (ANOVA) was performed through XLSTAT-Pro (2019) statistical software (Addinsoft, Paris, France) to identify the significant difference between the means at a 95% confidence level ( $p < 0.05$ ) with Tukey's Test.

### Bacterial Community Identification

The bacterial community identification has been performed. The isolation of the bacterial community was performed prior to DNA extraction. Later, the Polymerase Chain Reaction was conducted using a 27F and 1492R universal primer set with an annealing temperature set at 56°C. The Polymerase Chain Reaction products were sent to the sequencing service provider. The Nucleotide Basic Local Alignment Search Tool (BLAST) was run to identify the species.

## RESULTS AND DISCUSSION

### Landfill Leachate Characteristics

Landfill leachate collected from Jeram Landfill recorded the physicochemical parameters as shown in Table 1. The parameters observed were pH, total dissolved solids, turbidity, temperature, and dissolved oxygen. pH, as one of the significant parameters representing the landfill condition, was shown at pH 8.38, which could indicate the landfill's operations age and the landfill leachate's stabilization phase (Arliyani et al., 2021). A previous study stated that when the landfill operated for more than 10 years, the pH of the leachate should be more than 7.5 as the leachate is in stabilized condition (Wdowczyk & Szymańska-Pulikowska, 2021). This finding agrees that Jeram landfill has been operated for more than 10 years, since 1 January 2007. The recorded pH characterizes the Jeram landfill as being in the methanogenic phase, where the volatile fatty acid in leachate declined, thus leading to an inclining of the pH values. For temperature, it was recorded at 32.84°C during the sample collection. The temperature of the landfill leachate is highly influenced by the weather at the landfill site, and it is known that the common daily temperature in Peninsular Malaysia is between 30°C and 40°C (Zakaria & Aziz, 2018).

Table 1  
*Physicochemical parameter of leachate from Jeram sanitary landfill*

Parameters	Value
pH	8.38 ± 0.20
Temperature (°C)	32.84 ± 0.20
Dissolved Oxygen (mg/L)	8.29 ± 0.43
Total Dissolved Solid (mg/L)	2.03 x 10 <sup>4</sup> ± 8.00
Turbidity (NTU)	222 ± 6.50

*Note.* ± represents the standard error of the mean value

Dissolved Oxygen (DO) is an important parameter in determining water pollution. The DO recorded was 8.29 mg/L, slightly higher than the WHO range of healthy water (6.0 to 8.0 mg/L) (Dávalos-Peña et al., 2021). The composition of DO is normally low due to a microbial community employing dissolved oxygen for the waste aerobic decomposition. It probably indicates the presence of an anaerobic microbial community. The Total Dissolved Solid (TDS) was recorded as 2.03 x 10<sup>4</sup> mg/L, which is also considered high compared to the previous study (Zakaria & Aziz, 2018).

This parameter characterizes the organic components of leachate and the total ions in the aqueous solution. High TDS in leachate may represent the whole number of pollutants as it reflects the degradation process of organic matter and the mineral salt in the waste (Kumari et al., 2018). The turbidity recorded for the landfill leachate was 222 NTU. It is considered a moderate level for landfill leachate (Aziz et al., 2018). Even though turbidity is not a direct indicator of the contaminated condition, high turbidity could influence leachate leakage through minimized movements of the compounds. The physicochemical parameters of the landfill leachate observed and recorded might be attributed to numerous factors, including the type of waste dumped onto the landfill (Salam & Nilza, 2021). Further observation of the landfill leachate parameters needs to be conducted to prevent leachate leakage that could cause environmental pollution.

### Optimization of Dibenzofurans Biodegradation

For the dibenzofuran concentration effect on the dibenzofuran degradation by the bacterial community, landfill leachate that has been spiked with 15 ppm dibenzofuran has shown the most degraded dibenzofuran, which is 63.35% (Figure 1). In 30 ppm and 45 ppm dibenzofuran concentrations, the bacterial community showed degradation at 39.60% and 26.04%, respectively. It has been shown in this study that the lowest dibenzofuran concentration (15 ppm) had shown the best concentration for maximum bacterial degradation of dibenzofuran in landfill leachate. Substrate availability represents the carbon sources the bacterial community uses to proliferate (Xiang et al., 2020). Lower substrate concentration might cause disability of the bacteria to proliferate, while in higher substrate concentration, accumulation of the by-products might inhibit bacterial growth to the extent that it is toxic to the bacteria cells (Maier & Pepper, 2015).

### Dibenzofuran Degradation by Bacterial Community

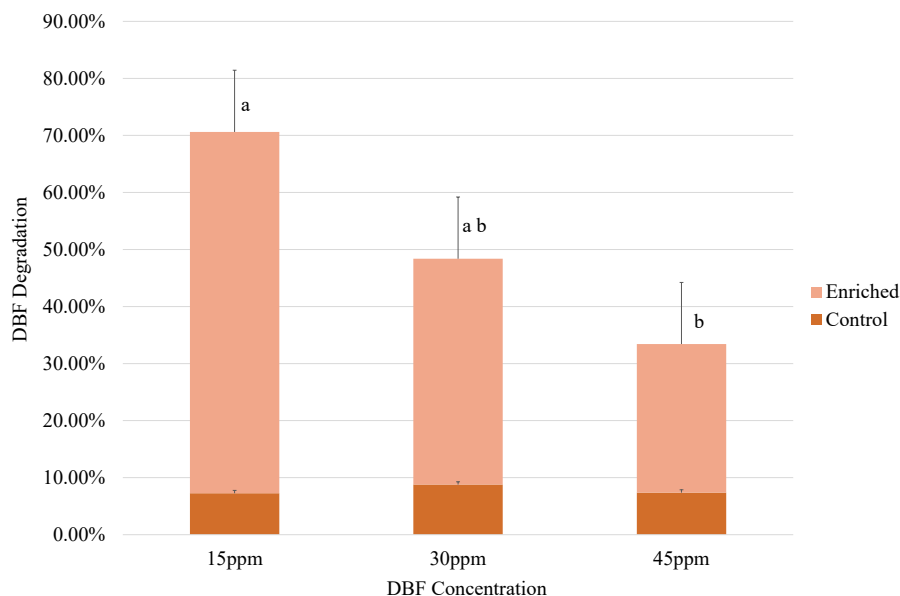


Figure 1. Percentage of dibenzofuran (DBF) degradation with different concentrations of DBF within 24 hours of incubation. Each experimental sample was performed in triplicates. Error bars represent the standard error of the mean. \*Means with the same letter are not significantly different.

Note. Enriched: Percentage of dibenzofuran degraded in landfill leachate by native bacterial community enriched with 15 ppm, 30 ppm, and 45 ppm dibenzofuran, respectively, incubated at 37°C and pH 7. Control: Percentage of dibenzofuran degraded in landfill leachate enriched with 15 ppm, 30 ppm, and 45 ppm dibenzofuran without any inoculum of bacteria.

Figure 2 shows that the best temperature for the bacterial community to degrade dibenzofuran (68.33%) is 30°C. At 37°C and 42°C environmental conditions, the degradation of dibenzofuran was recorded at 39.60% and 54.97%. These findings are supported by other studies that demonstrate the best temperature for dibenzofuran degradation by the bacteria is 30°C (Tajudin, 2017; Sanusi, 2017). Bacterial metabolism is influenced by environmental temperature since an enzyme is a protein-made substance. According to Imron et al. (2020), a lower temperature might disrupt bacterial metabolism, while a higher temperature might speed up bacterial metabolism to a certain extent. Above that extent, higher temperatures will cause the enzyme to degrade and lower the bacterial metabolism (Vidonish et al., 2016).

pH study discovered that the best pH for dibenzofuran degradation by the native bacterial community in landfill leachate is 7 (39.60%) (Figure 3). While for pH 5 and pH 9, the study found that 2.12% and 0.59% dibenzofuran degradation had happened. Most enzymes in the bacterial community can only perform and function at a certain pH value, thus making pH value one of the most crucial factors influencing compound degradation

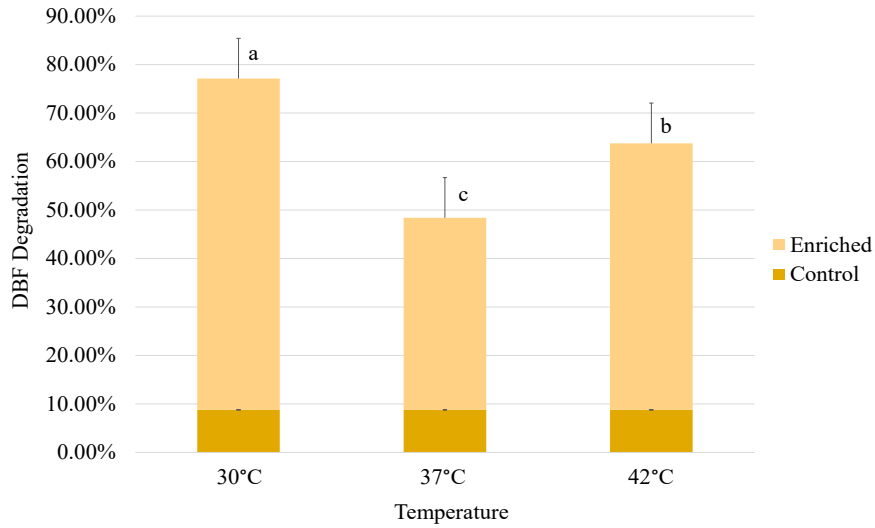


Figure 2. Percentage of dibenzofuran (DBF) degradation with different incubation temperatures within 24 hours of incubation. Each experimental sample was performed in triplicates. Error bars represent the standard error of the mean. \*Means with the same letter are not significantly different.

Note. Enriched: Percentage of dibenzofuran degraded in landfill leachate by native bacterial community enriched with 30 ppm dibenzofuran, pH 7 and incubated in 30°C, 37°C and 42°C respectively. Control: Percentage of dibenzofuran degraded in landfill leachate enriched with 30 ppm, without any inoculum of bacteria.

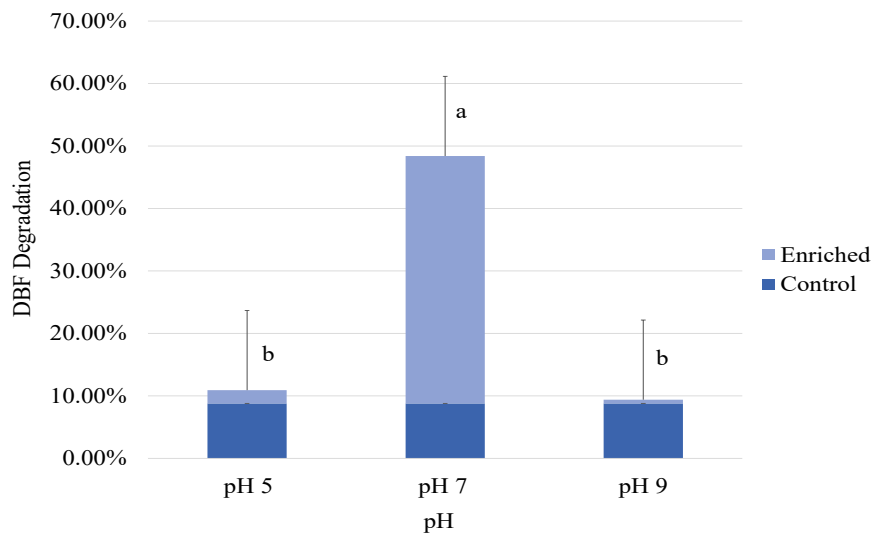
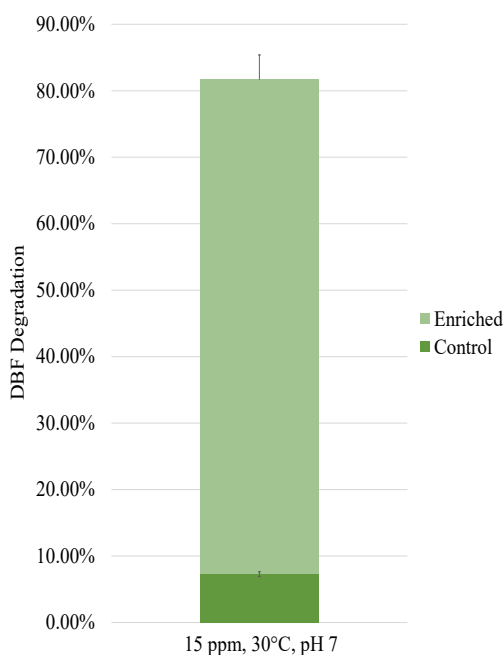


Figure 3. Percentage of dibenzofuran (DBF) degradation with different pH incubation within 24 hours of incubation. Each experimental sample was performed in triplicates. Error bars represent the standard error of the mean. \*Means with the same letter are not significantly different.

Note. Enriched: Percentage of dibenzofuran degraded in landfill leachate by native bacterial community enriched with 30 ppm dibenzofuran, incubated at 37°C with pH 5, pH 7, and pH 9, respectively. Control: Percentage of dibenzofuran degraded in landfill leachate enriched with 30 ppm, without any inoculum of bacteria.

(Imron et al., 2020). Large numbers of heterotrophic bacteria are chosen to proliferate better in a neutral to alkaline pH value (Al-Hawash et al., 2018). The previous study also recorded similar findings, in which the neutral condition is the best for dibenzofuran degradation compared to acidic and basic conditions (Tajudin, 2017; Sanusi, 2017).

The best parameters (15 ppm, 30°C, and pH 7) were executed to the bacterial community in the landfill leachate to observe the optimum degradation of dibenzofuran. It is recorded that 74.40% of dibenzofuran had been degraded within 24 hours of incubation, which is the best degradation rate recorded throughout the study (Figure 4). The optimum degradation condition is significant in bioremediation; thus, the pollutant compounds will be degraded effectively through the metabolism of the bacterial community (Zhao et al., 2021).



**Figure 4.** Percentage of dibenzofuran (DBF) degradation supplemented with 15 ppm DBF and incubated at 30°C at pH 7 within 24 hours of incubation. Each experimental sample was performed in triplicates. Error bars represent the standard error of the mean.

**Note.** Enriched: Percentage of dibenzofuran degraded in landfill leachate by native bacterial community enriched with 15 ppm dibenzofuran, pH 7 and incubated at 30°C. Control: Percentage of dibenzofuran degraded in landfill leachate enriched with 15 ppm, without any inoculum of bacteria.

### Bacterial Community and Pathway of Dibenzofuran Degradation

In this study, the bacterial community found is from Phylum Pseudomonadota. Six *Pseudomonas* species were identified as involved in the dibenzofuran degradation that is *Pseudomonas* sp., *Pseudomonas putida*, *Pseudomonas japonica*, *Pseudomonas qingdaonensis*, *Pseudomonas brassicae* and *Pseudomonas cichorii*. The role of *Pseudomonas* sp. in the bioremediation of Chlorinated Hydrocarbons is also emphasized in other studies (Ambust et al., 2021; Mahjoubi et al., 2021; Soare et al., 2019).

The main metabolic pathway of the bacterial community in degrading dibenzofuran is the biphenyl dioxygenase pathway through the presence of the biphenyl dioxygenase enzyme. According to Nhung et al. (2022), 2,3-dioxygenase could destroy the stable benzene rings in the dibenzofuran compounds through molecular oxygen catechol. Some mono and dioxygenase enzymes were also required to place oxygen in the benzene ring to make the compounds more vulnerable to degradation (Saibu et al., 2020). The large subunit of terminal

dioxygenase is included for the substrate specificity of the biphenyl dioxygenase. Hence, huge subunit genes need to be involved in the development of molecular engineering.

## CONCLUSION

Based on the result collected, it could be seen that the optimum condition for the bacterial community in landfill leachate to degrade dibenzofuran is spiked with 15 ppm dibenzofuran and environmental condition set at 30°C and pH 7. 74.40% dibenzofuran degradation has been recorded future research shall exploit larger volume of landfill leachate sample to discover more about the native bacterial community. To conclude, the degradation of dibenzofuran enriched to the landfill leachate by the native bacterial communities was assisted by the environmental conditions, including temperature and pH, proposing that a bio-stimulation technique could be applied for in-situ bioremediation for the possible dioxin-contaminated site.

## ACKNOWLEDGEMENT

The authors wish to extend full gratitude to International Islamic University Malaysia (IIUM) and the Ministry of Higher Education, Malaysia for funding this work. The study was funded by the Ministry of Higher Education Malaysia under the Fundamental Research Grant Scheme (FRGS/1/2018/WAB05/UIAM/02/2).

## REFERENCES

- Al-Hawash, A. B., Dragh, M. A., Li, S., Alhujaily, A., Abbood, H. A., Zhang, X., & Ma, F. (2018). Principles of microbial degradation of petroleum hydrocarbons in the environment. *Egyptian Journal of Aquatic Research*, 44(2), 71-76. <https://doi.org/10.1016/j.ejar.2018.06.001>
- Ambust, S., Das, A. J., & Kumar, R. (2021). Bioremediation of petroleum contaminated soil through biosurfactant and *Pseudomonas* sp. SA3 amended design treatments. *Current Research in Microbial Sciences*, 2, Article 100031. <https://doi.org/10.1016/j.crmicr.2021.100031>
- Arliyani, I., Tangahu, B. V., & Mangkoedihardjo, S. (2021). Selection of plants for constructed wetlands based on climate and area in the interest of processing pollutant parameters on leachate: A review. *IOP Conference Series: Earth and Environmental Science*, 835(1), Article 012003. <https://doi.org/10.1088/1755-1315/835/1/012003>
- Aziz, S. Q., Bashir, M. J. K., Aziz, H. A., Mojiri, A., Salem, S., Amr, A., & Maulood, Y. I. (2018). Statistical analysis of municipal solid waste landfill leachate characteristics in different countries. *Zanco Journal of Pure and Applied Sciences*, 30(6), 85-96. <https://doi.org/10.21271/zjpas.30.6.8>
- Baran, A., Mierzwa-Hersztek, M., Urbaniak, M., Gondek, K., Tarnawski, M., Szara, M., & Zieliński, M. (2020). An assessment of the concentrations of PCDDs/Fs in contaminated bottom sediments and their sources and ecological risk. *Journal of Soils and Sediments*, 20, 2588-2597. <https://doi.org/10.1007/s11368-019-02492-3>



- Baran, A., Urbaniak, M., Szara, M., & Tarnawski, M. (2021). Concentration of dioxin and screening level ecotoxicity of pore water from bottom sediments in relation to organic carbon contents. *Ecotoxicology*, *30*, 57-66. <https://doi.org/10.1007/s10646-020-02318-w>
- Dávalos-Peña, I., Fuentes-Rivas, R. M., Fonseca-Montes de Oca, R. M. G., Ramos-Leal, J. A., Morán-Ramírez, J., & Martínez Alva, G. (2021). Assessment of physicochemical groundwater quality and hydrogeochemical processes in an area near a municipal landfill site: A case study of the toluca valley. *International Journal of Environmental Research and Public Health*, *18*(21), Article 11195. <https://doi.org/10.3390/ijerph182111195>
- Earnden, L., Marangoni, A. G., Laredo, T., Stobbs, J., Marshall, T., & Pensini, E. (2022). Decontamination of water co-polluted by copper, toluene and tetrahydrofuran using lauric acid. *Scientific Reports*, *12*(1), 1-20. <https://doi.org/10.1038/s41598-022-20241-4>
- Eldos, H. I., Zouari, N., Saeed, S., & Al-Ghouthi, M. A. (2022). Recent advances in the treatment of PAHs in the environment: Application of nanomaterial-based technologies. *Arabian Journal of Chemistry*, *15*, Article 103918. <https://doi.org/10.1016/j.arabjc.2022.103918>
- Eskenazi, B., Warner, M., Brambilla, P., Signorini, S., Ames, J., & Mocarelli, P. (2018). The Seveso accident: A look at 40 years of health research and beyond. *Environment International*, *121*, 71-84. <https://doi.org/10.1016/j.envint.2018.08.051>
- Ferronato, N., & Toretta, V. (2019). Waste mismanagement in developing countries: A review of global issues. *International Journal of Environmental Research and Public Health*, *16*(1060), 1-28. <https://doi.org/10.3390/ijerph16061060>
- Gaur, N., Dutta, D., Singh, A., Dubey, R., & Kamboj, D. V. (2022). Recent advances in the elimination of persistent organic pollutants by photocatalysis. *Frontiers in Environmental Science*, *10*, Article 872514. <https://doi.org/10.3389/fenvs.2022.872514>
- Haedrich, J., Stumpf, C., & Denison, M. S. (2020). Rapid extraction of total lipids and lipophilic POPs from all EU - regulated foods of animal origin: Smedes' method revisited and enhanced. *Environmental Sciences Europe*, *32*(118), 1-33. <https://doi.org/10.1186/s12302-020-00396-5>
- Imron, M. F., Kurniawan, S. B., Ismail, N. I., & Abdullah, S. R. S. (2020). Future challenges in diesel biodegradation by bacteria isolates: A review. *Journal of Cleaner Production*, *251*, Article 119716. <https://doi.org/10.1016/j.jclepro.2019.119716>
- Kumari, P., Kaur, A., & Gupta, N. C. (2018). Extent of groundwater contamination due to leachate migration adjacent to unlined landfill site of Delhi. *Environmental Claims Journal*, *31*(2), 160-175. <https://doi.org/10.1080/10406026.2018.1543825>
- Mahjoubi, M., Aliyu, H., Neifar, M., Cappello, S., Chouchane, H., Souissi, Y., Masmoudi, A. S., Cowan, D. A., & Cherif, A. (2021). Genomic characterization of a polyvalent hydrocarbonoclastic bacterium *Pseudomonas* sp. strain BUN14. *Scientific Reports*, *11*, 1-13. <https://doi.org/10.1038/s41598-021-87487-2>
- Maier, R. M., & Pepper, I. L. (2015). Chapter 3 - Bacterial growth. In I. L. Pepper, C. P. Gerba & T. J. Gentry (Eds.), *Environmental Microbiology (Third Edition)* (pp. 37-56). Academic Press. <https://doi.org/10.1016/B978-0-12-394626-3.00003-X>
- Morris, S., Garcia-Cabellos, G., Enright, D., Ryan, D., & Enright, A. M. (2018). Bioremediation of landfill leachate using isolated bacterial strains. *International Journal of Environmental Bioremediation & Biodegradation*, *6*(1), 26-35. <https://doi.org/10.12691/ijebbb-6-1-4>

- Nhung, N. T. H., Nguyen, X. T. T., Long, V. D., Wei, Y., & Fujita, T. (2022). A Review of soil contaminated with dioxins and biodegradation technologies: Current status and future prospects. *Toxics*, 10(6), Article 278. <https://doi.org/10.3390/toxics10060278>
- Njoku, P. O., Edokpayi, J. N., & Odiyo, J. O. (2019). Health and environmental risks of residents living close to a landfill: A case study of thohoyandou landfill, Limpopo Province, South Africa. *International Journal of Environmental Research and Public Health*, 16(2125), 1-27. <https://doi.org/10.3390/ijerph16122125>
- Rashwan, T. L., Fournie, T., Green, M., Duchesne, A. L., Brown, J. K., Grant, G. P., Torero, J. L., & Gerhard, J. I. (2022). Applied smouldering for co-waste management: Benefits and trade-offs. *Fuel Processing Technology*, 240, Article 107542. <https://doi.org/10.1016/j.fuproc.2022.107542>
- Razali, Y. S., Tajarudin, H. A., & Daud, Z. (2018). Extraction of volatile fatty acids from leachate via liquid-liquid extraction and adsorption method. *International Journal of Integrated Engineering*, 10(9), 79-84. <https://doi.org/10.30880/ijie.2018.10.09.029>
- Saibu, S., Adebuseye, S. A., & Oyetibo, G. O. (2020). Aerobic bacterial transformation and biodegradation of dioxins: A review. *Bioresources and Bioprocessing*, 7(7), 1-21. <https://doi.org/10.1186/s40643-020-0294-0>
- Salam, M., & Nilza, N. (2021). Hazardous components of landfill leachates and its bioremediation. In M. L. Larramendy & S. Soloneski (Eds.), *Soil Contamination-Threats and Sustainable Solutions* (pp. 167-176). IntechOpen.
- Sani, M. S. A., Bakar, J., Azid, A., & Iqbal, M. J. (2022). Chemometrics-based evaluation on the effect of sonication, contact time and solid-to-solvent ratio on total phenolics and flavonoids, free fatty acids and antibacterial potency of *Carica papaya* seed against *S. enteritidis*, *B. cereus*, *V. vulnificus* and *P. mirabilis*. *Food Chemistry Advances*, 1, Article 100033. <https://doi.org/10.1016/j.focha.2022.100033>
- Sanusi, N. H. (2017). *Degradation Analysis of Dibenzofuran by Rhizospheric Bacteria*. Kulliyah of Science, International Islamic University Malaysia.
- Soare, M. G., Lakatos, E. S., Ene, N., Malo, N., Popa, O., & Babeanu, N. (2019). The potential applications of bacillus sp. And pseudomonas sp. strains with antimicrobial activity against phytopathogens in waste oils and the bioremediation of hydrocarbons. *Catalysts*, 9(11), Article 959. <https://doi.org/10.3390/catal9110959>
- Szajner, J., Czarby-Działak, M., Żeber-Dzikowska, I., Dziechciaż, M., Pawlas, N., & Walosik, A. (2021). Dioxin-like compounds (DLCs) in the environment and their impact on human health. *Journal of Elementology*, 26(2), 419-431. <https://doi.org/10.5601/jelem.2021.26.2.2130>
- Tajudin, M. T. F. M. (2017). *Microbial Degradation of Polychlorinated Biphenyls and Dibenzofuran by Burkholderia xenovorans LB400 Isolated from Landfill Leachate*. Kulliyah of Science, International Islamic University Malaysia.
- Tarekegn, M. M., Salilih, F. Z., & Ishetu, A. I. (2020). Microbes used as a tool for bioremediation of heavy metal from the environment. *Cogent Food and Agriculture*, 6(1), Article 1783174. <https://doi.org/10.1080/23311932.2020.1783174>
- Tas, N., Brandt, B. W., Braster, M., Van, B. M., & Wilfred, F. M. R. (2018). Subsurface landfill leachate contamination affects microbial metabolic potential and gene expression in the *Baniseveld aquifer*. *FEMS Microbiology Ecology*, 94(10), 1-12. <https://doi.org/10.1093/femsec/fiy156>
- Terzaghi, E., Vergani, L., Mapelli, F., Borin, S., Raspa, G., Zanardini, E., Morosini, C., Anelli, S., Nastasio, P., Sale, V. M., Armiraglio, S., & Di Guardo, A. (2020). New data set of polychlorinated dibenzo-p-dioxin

- and dibenzofuran half-lives: Natural attenuation and rhizoremediation using several common plant species in a weathered contaminated soil. *Environmental Science and Technology*, 54(16), 10000-10011. <https://doi.org/10.1021/acs.est.0c01857>
- Vidonish, J. E., Zygourakis, K., Masiello, C. A., Sabadell, G., & Alvarez, P. J. J. (2016). Thermal treatment of hydrocarbon-impacted soils: A review of technology innovation for sustainable remediation. *Engineering*, 2(4), 426-437. <https://doi.org/10.1016/J.ENG.2016.04.005>
- Wdowczyk, A., & Szymańska-Pulikowska, A. (2021). Comparison of landfill leachate properties by LPI and phytotoxicity - A case study. *Frontiers in Environmental Science*, 9, 1-14. <https://doi.org/10.3389/fenvs.2021.693112>
- Xiang, W., Wei, X., Tang, H., Li, L., & Huang, R. (2020). Complete genome sequence and biodegradation characteristics of benzoic acid-degrading bacterium *Pseudomonas* sp. SCB32. *BioMed Research International*, 2020, 1-12. <https://doi.org/10.1155/2020/6146104>
- Zakaria, S. N. F., & Aziz, H. A. (2018). Characteristic of leachate at Alor Pongsu landfill site, Perak, Malaysia: A comparative study. In *IOP Conference Series: Earth and Environmental Science* (Vol. 140, No. 1, p. 012013). IOP Publishing.
- Zhao, L., Zhou, M., Zhao, Y., Yang, J., Pu, Q., Yang, H., Wu, Y., Lyu, C., & Li, Y. (2022). Potential toxicity risk assessment and priority control strategy for PAHs metabolism and transformation behaviors in the environment. *International Journal of Environmental Research and Public Health*, 19(17), 1-25. <https://doi.org/10.3390/ijerph191710972>
- Zhao, R., Liu, J., Feng, J., Li, X., & Li, B. (2021). Microbial community composition and metabolic functions in landfill leachate from different landfills of China. *Science of the Total Environment*, 767, Article 144861. <https://doi.org/10.1016/j.scitotenv.2020.144861>



## Numerical Investigation on the Distribution of Pressure Coefficients of Modified Building Shapes

Siti Rohani Mohd Isdris<sup>1</sup>, Shaharudin Shah Zaini<sup>1\*</sup>, Mohammad Hafifi Hafiz Ishaik<sup>2</sup>, Mohammad Sharizal Abdul Aziz<sup>3</sup> and Noorhazlinda Abd Rahman<sup>1</sup>

<sup>1</sup>School of Civil Engineering, Universiti Sains Malaysia, 14300 USM, Nibong Tebal, Pulau Pinang, Malaysia

<sup>2</sup>School of Aerospace Engineering, Universiti Sains Malaysia, 14300 USM, Nibong Tebal, Pulau Pinang, Malaysia

<sup>3</sup>School of Mechanical Engineering, Universiti Sains Malaysia, 14300 USM, Nibong Tebal, Pulau Pinang, Malaysia

### ABSTRACT

The construction of tall buildings in urban areas has grown in number in recent years. However, architects and engineers face a variety of design challenges due to the variety of heights and shapes of new building designs. This study evaluates the impact of shape mitigation on tall buildings by applying corner modifications, such as chamfered, corner cut, plan changes with height, tapered, and setback, and combining a single modification model. The numerical simulations were carried out using Computational Fluid Dynamic (CFD) simulation with the RNG k- $\epsilon$  type of turbulence model. All single modifications reduced the maximum  $+C_p$  and  $-C_p$  better than the basic model. The corner-cut model was the most effective method for reducing the suction effect. Combining the setback, chamfering the corner, and twisting the building model at  $45^\circ$  modification was the most effective approach to reduce the maximum  $+C_p$  in the 25–42.10% range in Face 1. Modifying a square model with the combination of setback, chamfer, and  $45^\circ$  rotation reduced the

maximum  $-C_p$ , ranging from 36.9–50%. The composite 1 model and composite 2 model reduced the suction effect in the range of 15.38–33.33% in Face 3. The adoption of composite modification was insignificant in reducing the suction effect on the sidewall, where the maximum  $-C_p$  was recorded to be between 3.62–5.43%.

### ARTICLE INFO

#### Article history:

Received: 12 December 2022

Accepted: 10 May 2023

Published: 12 October 2023

DOI: <https://doi.org/10.47836/pjst.31.6.28>

#### E-mail addresses:

ceshaharudin@usm.my (Shaharudin Shah Zaini)

sitirohani90@student.usm.my (Siti Rohani Mohd Isdris)

mhafifhafiz@usm.my (Mohammad Hafifi Hafiz Ishaik)

msharizal@usm.my (Mohammad Sharizal Abdul Aziz)

celindarahman@usm.my (Noorhazlinda Abd Rahman)

\*Corresponding author

**Keywords:** Aerodynamic modification, CFD, tall building, wind pressure coefficient

## INTRODUCTION

Tall buildings are very common in urban areas all over the world. It is very important to study peak suctions on roofs and walls because it causes frequent damage by the peak suctions under strong wind conditions. Wind suctions at the extensions of exterior walls on corners of walls can be reduced by aerodynamic mitigation (Bitsuamlak et al., 2013). Modifying the shape of tall buildings has been proven to significantly affect crosswind loads and wind-induced responses (Irwin, 2008; Holmes, 2001; Elshaer et al., 2014; Elshaer et al., 2016). Research has been conducted to reduce excitations and improve the performance of tall buildings against wind loads. Sharma et al. (2017) studied the effect of setbacks on reducing the wind-induced response of tall buildings by three types of buildings with different setbacks and square shapes. The authors concluded that changing the cross section along the elevation through the setback could reduce the mean overturning moments along and crosswind directions. The effects and value of aerodynamic modifications, such as chamfered and recessed corners, on tall building responses were investigated by Tse et al. (2012) while maintaining the total usable floor area of the modified building form.

The study found recessed corners more effective than chamfered corners in reducing both along-wind and crosswind moments caused by buffeting and vortex-shedding excitations. Hansora et al. (2015) investigated the effect of height to width ratio of tapered-shaped tall buildings on the distribution of wind pressure coefficient around different surfaces of building models. The smallest and largest negative mean pressure coefficient on the leeward face of the building increases with increasing height/breadth (H/B) ratio. Sanyal and Dalui (2020) studied the comparison of aerodynamic coefficients of various types of Y-plans-shaped tall buildings with different types of helical, tapered, setback, and corner-modified models. Results showed that a setback building model with a rounded corner shape proved to be the most efficient among the studied models in terms of reducing wind load. In a wind tunnel test, Bandi et al. (2013) investigated aerodynamic modifications with corner cuts and helical shapes and discovered that helical buildings significantly influenced aerodynamic characteristics.

Meanwhile, Gu and Quan (2004) investigated 15 typical high-rise buildings with varying cross-sections and discovered that corner chamfers can reduce the peak value across wind base moment spectra. The review of previous work showed that most studies only focused on a single modification and effect on different types of basic models. As such, this study aims to determine the pressure distribution around various building surfaces based on single modification and changes for adopting a composite modification by using Computational Fluid Dynamics (CFD) analysis.

## METHODOLOGY

This discussion explains the numerical procedures applied for the numerical simulation on tall building surfaces using ANSYS Fluent 18.0.

### Shape Configuration

A total of eight building models were considered in this study. The building model was set with a height of 63 m, a base layout of 30 m x 30 m, and generated using a 1:10 scale ratio. The square model in this study is classified as a basic model with an aspect ratio H/B of 2.1 (Figure 1).

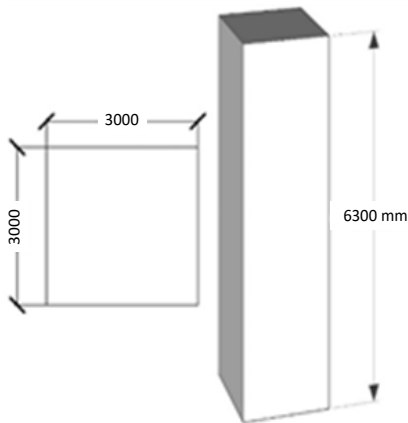


Figure 1. Basic model

The models were divided into two configurations: single modification representing a model with changes in plan area along the building height and corner modification incorporating chamfer and corner cut along four corners of the building. The chamfer and corner cut dimensions were set to be 500 mm. The detailed configuration of single modifications is shown in Figure 2.

The second type of modification includes tapering the base dimension with respect to building height, where the upper floor was reduced to 1400 mm x 1400 mm. The model with setback configuration

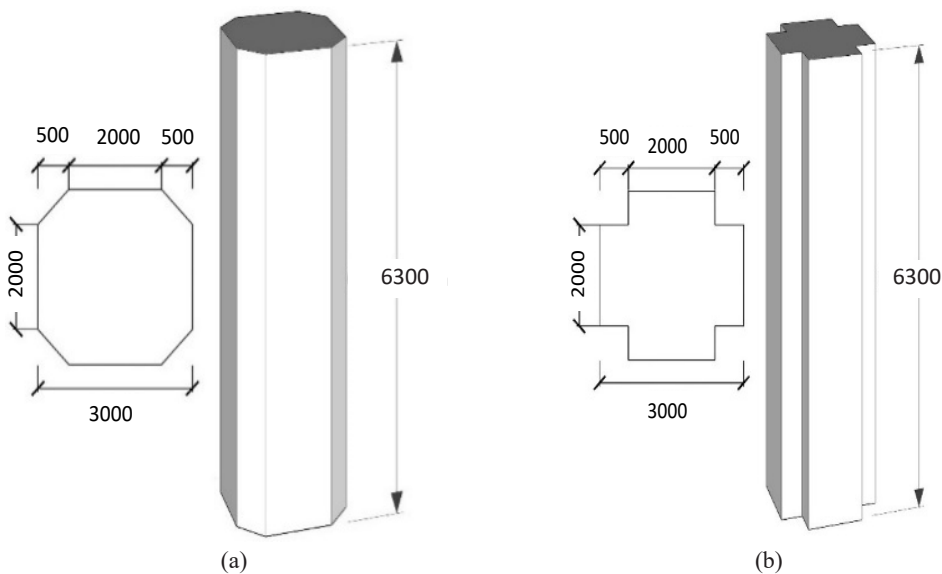


Figure 2. Single modification models (corner modification): (a) chamfered model (mm) and (b) corner cut model (mm)

was generated by reducing the plan area at every 2100 mm height. In this case, the plan dimension at 2100 mm and 4200 mm was set to be 2000 mm × 2000 mm and 1400 mm × 1400 mm (Figure 3).

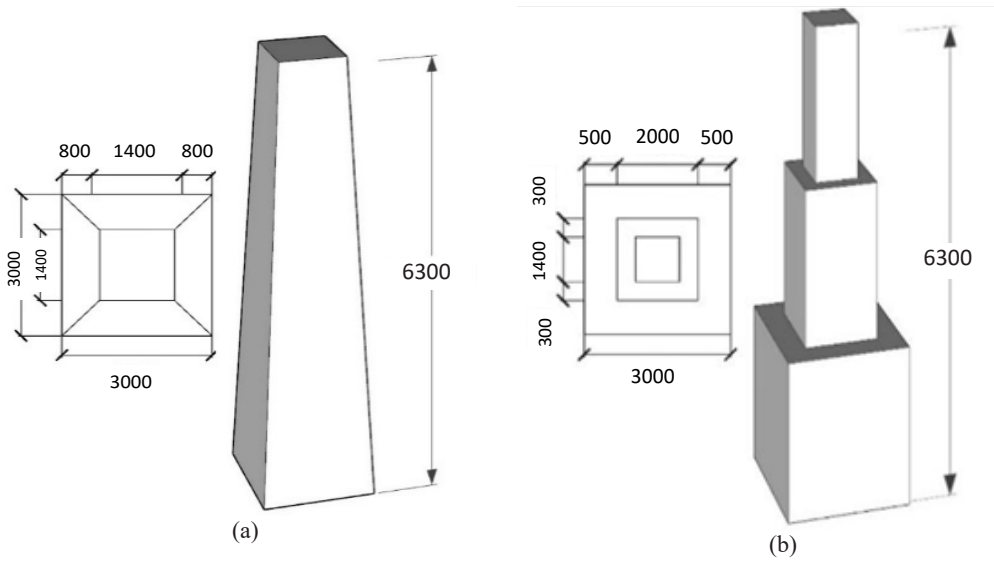
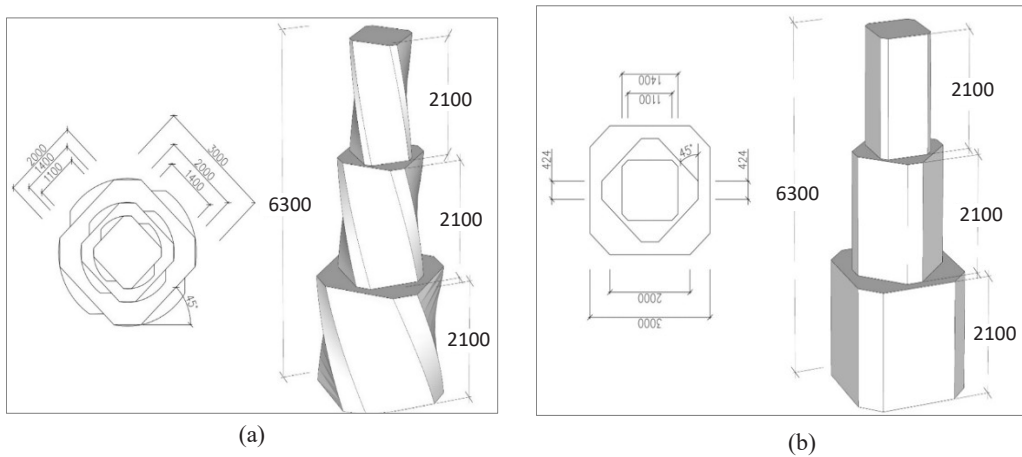


Figure 3. Single modification models (change of plan area with height): (a) tapered model (mm) and (b) corner cut model (mm)

The composite modification consists of three models with a combination of three single modifications. Figure 4 shows the details of all models under composite modification. Details of the composite models are as follows:

- Composite 1: Corner modification, setback, and rotation of 45°
- Composite 2: Corner modification, setback, and twisting of 45°
- Composite 3: Corner modification, tapered, and twisting of 45°





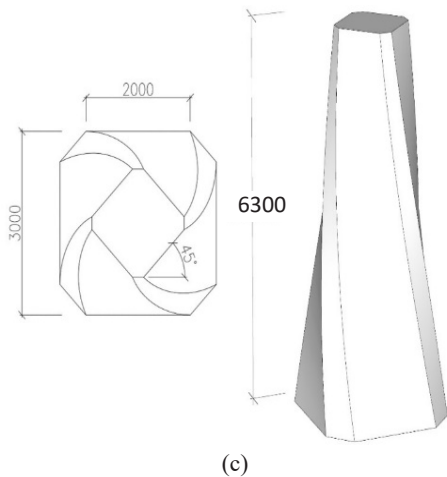


Figure 4. Composite Models (a) Composite 1 Model (mm) (b) Composite 2 Model (mm) and (c) Composite 3 Model (mm)

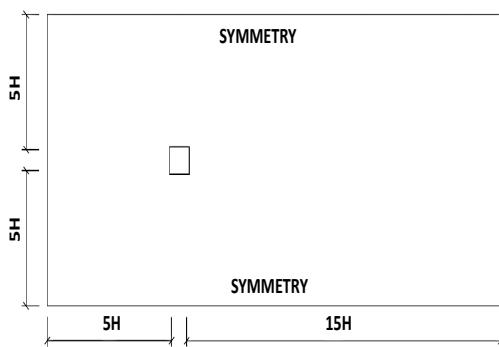


Figure 5. Plan view of the building unit in the computational domain

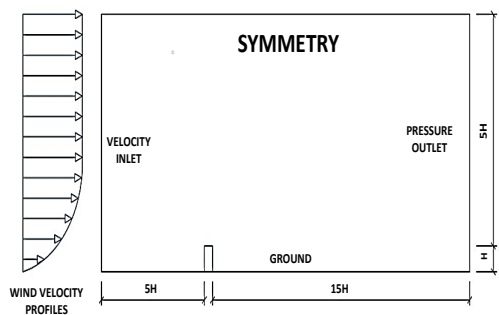


Figure 6. Side view of the building unit in the computational domain

## Domain

The computational was developed based on the recommendations proposed by Franke et al. (2004). The distances were 5H from the building model to the top and the sides of the domain and 15H for the downstream length, where H was the height of the tallest building in this study. A large space was required behind the model to allow for the formation of vortices on the leeward side and to prevent wind backflow (Hajra & Dalui, 2016). The blockage ratio in the present study is in the range of 0.38%, as Tominaga et al. (2008) recommended. Figures 5 and 6 show the plan view and side view of the computational domain, respectively.

## Numerical Simulation

There are several boundary conditions considered to complete this numerical modeling and simulation. The inlet boundary is specified as a velocity inlet condition. This condition specifies the velocity of flow entering the domain. The velocity inlet condition was applied using user-defined functions (UDF) developed by Deraman et al. (2018) and modified to suit the building height to define the wind profile at the inlet boundary. A pressure outlet condition is assigned at the outlet boundary with zero pressure. The sides and top boundaries of the domain are typically assigned as symmetry conditions. Meanwhile, the ground of the domain is specified as the ground where a no-slip wall condition is assigned. This condition specifies zero velocity at the wall and allows shear stresses to develop. A wall

function is assigned at these boundaries. The wind vertical profile was generated using the power law equation. The  $k-\epsilon$  model was used for modeling the airflow viscosity in this study. The successful use of the  $k-\epsilon$  model for analyzing the tall building model can be found in Dagneu et al. (2009), Irtaza et al. (2021), and Mou et al. (2017). Table 1 shows the overall boundary conditions used for this study.

Table 1  
*Boundary condition of the computational domain*

Location	Boundary Condition
Inlet	Fully developed ABL inlet profile
Outlet	Pressure outlet
Top and side faces	Symmetry
Ground	Wall function

Table 2  
*Overall input parameters for CFD simulation in ANSYS FLUENT 18.0*

Parameters	Inputs
Equation	Steady-RANS
Turbulence Model	RNG $k-\epsilon$
Roughness height, $k_s$	0.001 sm
Roughness constant, $C_s$	1.0
Power law exponent	0.0035
Mean wind speed, $v$	15 m/s
Pressure velocity coupling	SIMPLE algorithm
Spatial discretization for pressure and momentum	Second-order

This study used the Renormalization Group (RNG)  $k-\epsilon$  model, a Reynolds Averaged Navier Stokes (RANS) based two equations turbulence model. The inlet velocity of flow was set to be 15 m/s based on a standard tall building model tested at two research institutions, namely City University of London and National Aeronautical Establishment, to ensure that the flow over a surface will be turbulent if Reynold's Number is more than  $10^5$  (Khan & Roy, 2017). The power-law profile was scaled to 1/7 to represent flat terrain. Since scaled-down models were used, the roughness length was also scaled down to  $Z_0 = 0.035/10$ , as Khan and Roy (2017) recommended. Table 2 shows the input parameter used for this study.

### Mesh Arrangement

Mesh quality is a very important criterion for the correctness of simulation results. Structured (hexahedral) and unstructured (tetrahedrons and prisms) are two kinds of mesh that have been widely accepted in CFD simulation (Irtaza et al., 2021). Because the geometry in this study is

complex, it was impossible to have structured mesh throughout the domain. Therefore, to solve this problem, the building is placed in a rectangular prism. An unstructured mesh is generated for zones in the nesting rectangular prism, while for the zones around the nesting prism, the structured mesh is applied. Figures 7 to 9 show the mesh arrangement for the building model in this study.

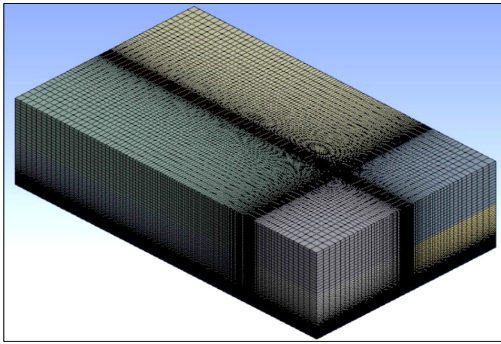


Figure 7. Isometric view showing the overall computational domain

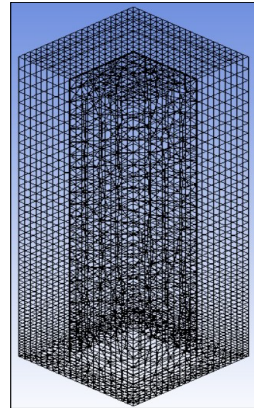


Figure 8. Zoom in, showing the model inside the domain

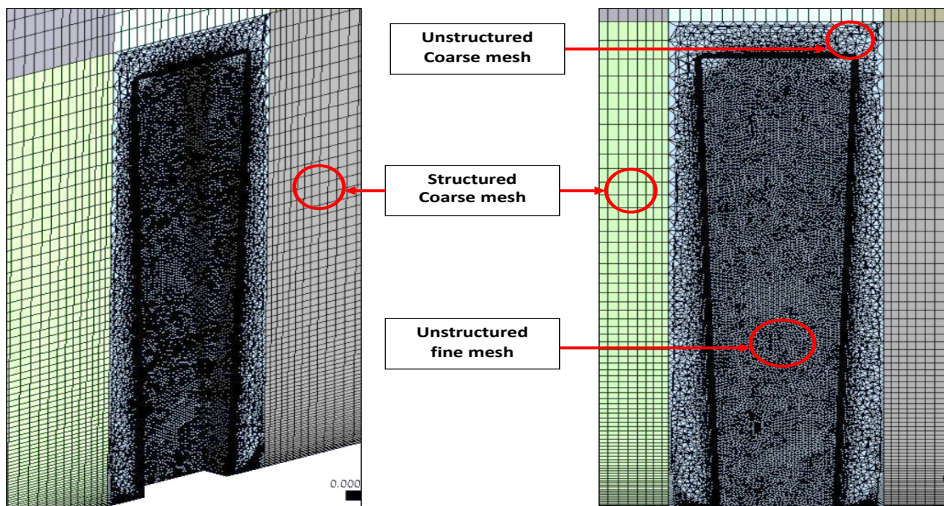


Figure 9. Cut section view

## VALIDATION AND ANALYSIS

Since numerical results are affected by a range of factors, it is essential to validate the correctness of the numerical model and the precision of numerical results.

### Grid Convergence Study

In a CFD analysis, the grid convergence study plays an important role in identifying the correct mesh pattern to significantly diminish the computational time and error (Bhattacharjee et al., 2021). Franke et al. (2004) recommend that at least three systematically refined grids be conducted to quantify the influence of the grid resolution for the solution. In this exercise, five different grid sizes, namely mesh 1 (Very Course), mesh 2 (Course),

mesh 3 (Medium), mesh 4 (Fine) and mesh 5 (Very Fine) were generated. The number of elements for these four grids is 239056, 402067, 567592, 727997, and 895985. In order to produce a constant increase in the number of elements, the difference in terms of number of elements between successive mesh regimes was set at 160,000. The difference between the very coarse and very fine grid schemes was calculated to be more than 3.2, as Franke et al. (2004) recommended. Figure 10 shows the result of the comparison of  $C_p$  profiles for grid sensitivity analysis. From the results, all models showed similar distribution, particularly true at the building's Face 1 and Face 3. In Face 1, the model with a fine grid scheme (mesh 5) showed the highest  $C_p$  (0.757), followed by mesh 4 (0.755), mesh 3 (0.751), mesh 2 (0.744), and mesh 1 (0.73). Tominaga et al. (2015) stated that the maximum  $+C_p$  on the wall should be close to 1 due to the formation of a stagnation point. As such, mesh 5 showed the most accurate results compared to other models.

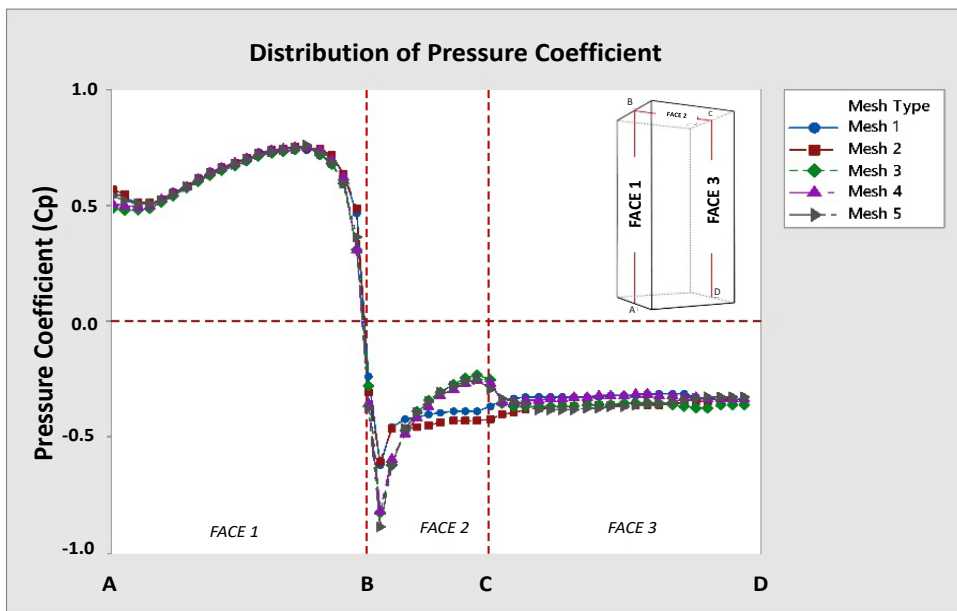


Figure 10. Comparison of  $C_p$  profiles for grid sensitivity analysis

The comparison of the overall computational time taken for every mesh model is shown in Figure 11. The results showed that Mesh 5 took approximately 10 hours to converge at 5000 iterations, followed by Mesh 4 (8 hours), Mesh 3 (6 hours), Mesh 2 (4 hours) and Mesh 1 (2 hours). Although Mesh 4 and Mesh showed relatively small differences in Face 2, the difference in terms of the computational time was calculated to be 2 hours. This difference is still manageable. By considering the importance of obtaining reliable results, model Mesh 5 was selected.

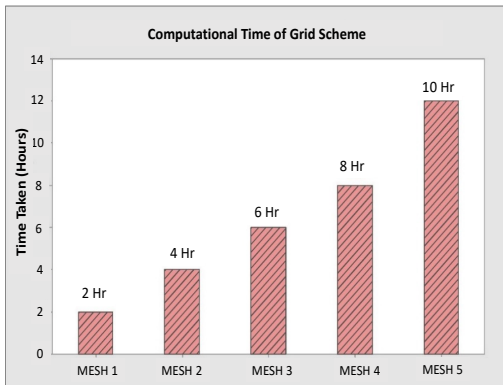


Figure 11. Comparison of time taken for every model to converge

### Validation Model

The validation exercise was performed to ensure the reliability of the input parameters in ANSYS. In this case, the Commonwealth Advisory Aeronautical Council (CAARC) standard tall building model results tested by Dagnew et al. (2009) using wind tunnel test (WTT) and CFD was used (Figure 12). The validation model's Reynolds number at  $3.8 \times 10^5$  was based on building height  $H$  and the inflow velocity  $U_H$  at  $z = H$ , as stated by Dagnew et al. (2009). Other input parameters were generated using data from

other literature (Huang et al., 2009; Meng et al., 2017; Ahsan, 2014; Liu & Niu, 2016). Parameters such as air density and solid material type were assumed to suit the condition. The density of air is affected by temperature, pressure, and dew point. This study took air density and dynamic viscosity as  $1.225 \text{ kg/m}^3$  and  $1.79 \times 10^{-5}$ , respectively. This study used the Renormalization Group (RNG)  $k-\epsilon$  Model, the Reynolds Averaged Navier Stokes (RANS) based on two equations turbulence model. The inlet velocity of flow was set to be  $12.7 \text{ m/s}$ , followed by Dagnew et al. (2009).

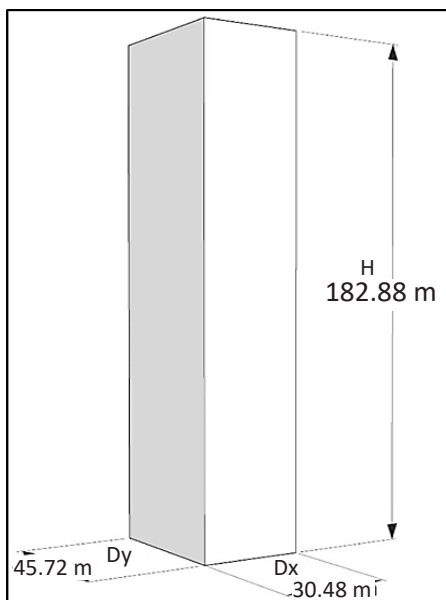


Figure 12. Isolated standard tall building

### Validation Results

Figure 13 shows the overall results from WTT and CFD by Dagnew et al. (2009) and the validation model (CFD Validation) generated using ANSYS. The wind pressure coefficient in this study was measured at  $2/3$  of the building height. It is pointed out that wind pressure coefficients at  $2H/3$  of the standard model are sufficient for model calibration (Montazeri & Blocken, 2013; Huang et al., 2009). The CFD Validation agrees with CFD Dagnew and is particularly true at Surface 1. Although both CFD results cannot capture the maximum  $+C_p$  in Surface 1, theoretically, the maximum  $+C_p$  must be 1.0 or close to 1.0 to define the location of

the stagnation point. In addition, the validation model follows the  $C_p$  distribution pattern relatively closely compared to CFD Dagnev in Surface 2, 3, and 4. In order to verify the similarity of the  $C_p$  distribution between the CFD Validation and the results from Dagnev et al. (2009), the error measures analysis was conducted, and the summary is shown in Table 3. In this case, the error measures exercise comprises Mean Absolute Error (MAE), Normalized Absolute Error, and Root Mean Square Error (RMSE). It is worth mentioning that when the similarity is high, then the discrepancy of the overall results is low (Table 3). The CFD Validation model provides the smallest error for all the error measure analyses and possesses high similarity to the WTT test and CFD work by Dagnev et al. (2009). As such, the input parameters in the CFD analysis of the validation work are reliable.

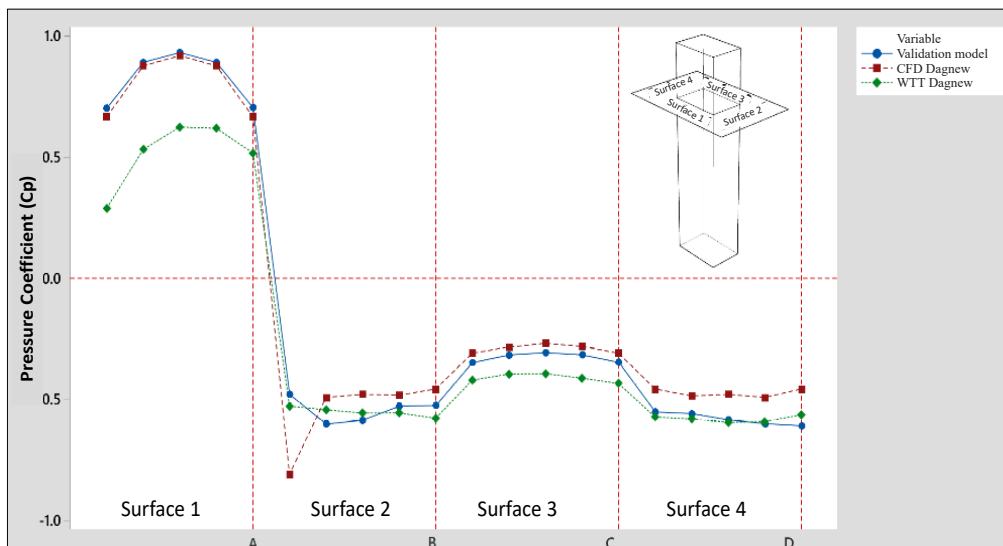


Figure 13.  $C_p$  profile between validation model, CFD Dagnev, and WTT Dagnev

Table 3  
 Summary of error measures

Error Measure	WTT Dagnev	
	CFD Dagnev	CFD Validation
MAE	0.158	0.124
NAE	0.306	0.245
RMSE	0.184	0.183

## RESULTS AND DISCUSSION

The  $C_p$  profile for the basic model with overall single-corner modification is shown in Figure 14. For the basic model, the maximum  $+C_p$  is located at approximately two-thirds of the building height for the basic model with a value of +0.76. A similar pattern was also observed in the work of Tominaga et al. (2008) and Richard et al. (2007). Meanwhile, the distribution pattern of the pressure coefficient for the Chamfered and Corner cut models is similar to the basic model. In this case, the maximum  $+C_p$  and

$-C_p$  were recorded to be +0.56 and -0.51 for chamfered and +0.6 and -0.46 for the corner cut model. By introducing chamfered corner, the reduction in terms of the overall  $C_p$  for Face 1 (windward), Face 2 (roof), and Face 3 (leeward) was calculated to be approximately 5.43% to 44.56% and 18.5% to 50.0%, respectively. The model with the chamfered corner exhibits the lowest  $+C_p$  across Face 1, and the corner-cut model generates the lowest suction along most of the surface of the roof.

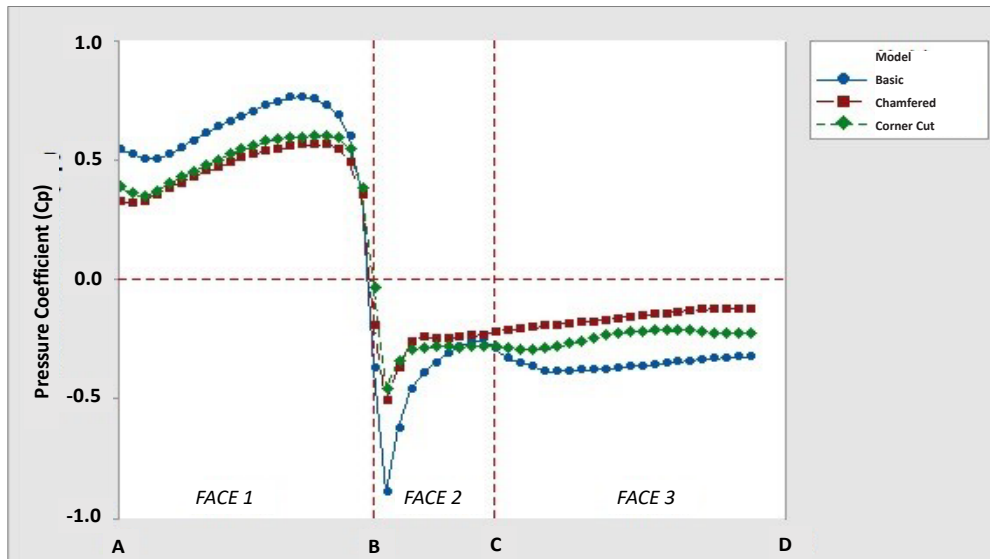


Figure 14.  $C_p$  profile for overall single modification (corner modification)

Figure 15 shows the overall comparison distribution in terms of pressure coefficient for the basic, setback, and tapered models. The pattern of the  $C_p$  distribution shows a similar trend to the basic models. However, for the setback model, a slight drop in the  $C_p$  values occurs at every setback location (refer to the red circles). The maximum  $+C_p$  was formed in Face 1, and the value was recorded to be +0.65 and +0.75 for the tapered and setback models, respectively. Moreover, the maximum  $-C_p$  for the tapered and setback models was found to be -0.49 and -0.72, respectively. The  $-C_p$  values in Face 3 are almost constant with no noticeable fluctuation for the tapered model, whereas a slight fluctuation in the pattern along Face 3 is shown for the setback model at the boundary between setbacks. As such, the modification made to the models by changing the plan area with height resulted in an efficient reduction of suction for both models.

Figure 16 shows the pressure contour on the overall surfaces of the building models. All models develop  $-C_p$  at the side wall. The reduction of  $-C_p$  at the side walls of single corner modification can be associated with sharp corners on the basic model. Sharp corners can produce stronger vortices than the models with modified corners (Holmes, 2015). In terms

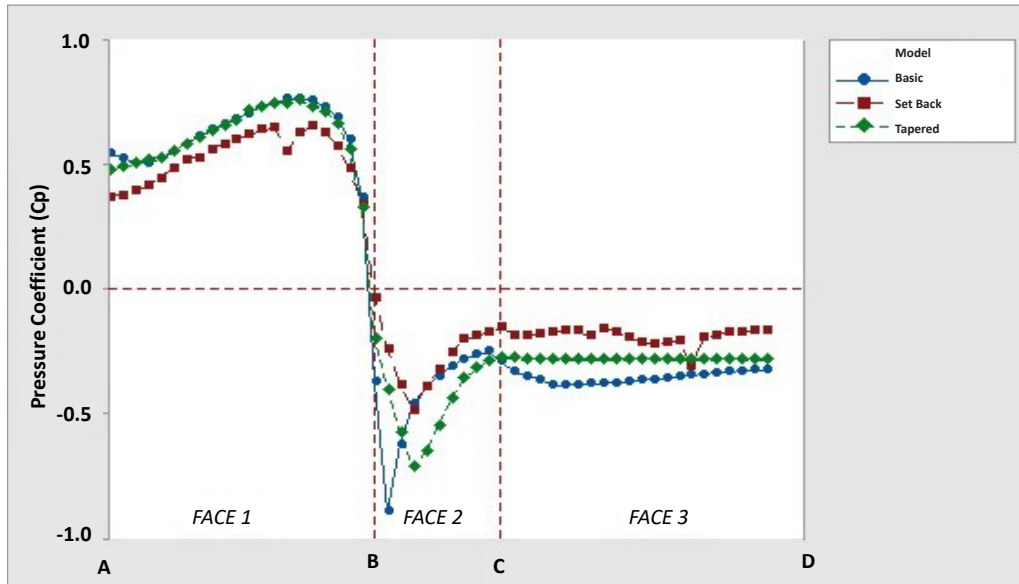


Figure 15.  $C_p$  profile for overall single modification (changes in plan area with respect to building height)

of suction, the introduction of corner cuts is more efficient than chamfering the corner. It is due to buildings with sharp corners induced strong vortices or vortex shedding. As such, to break up the vortices and lose their coherence, softening to the sharp edges must be made by introducing corner cut or chamfer, as Irwin (2008) reported. In addition, the modification of the plan area with respect to height was found to reduce the suction effect. The maximum suction for the basic model (-0.92) is reduced to -0.79 and -0.65, as shown by the tapered and setback models. Moreover, the setback model performs better than the tapered model in reducing the suction at the side wall due to the reduction of the kinetic energy in Face 1 that was prolonged to the side walls and weakened the wake region.

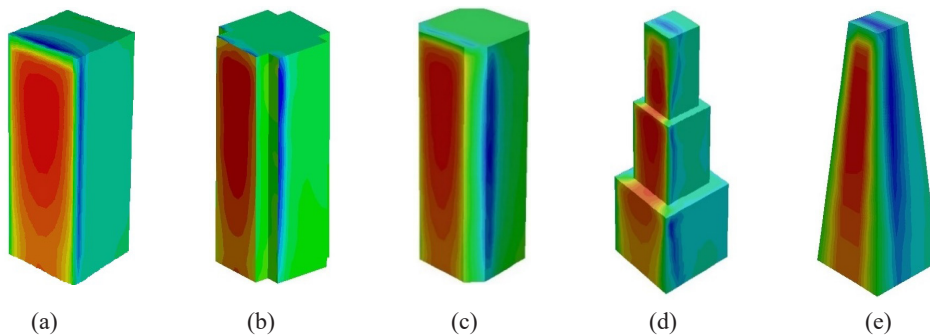


Figure 16. Pressure contour on the overall surfaces of the building models (a) Basic, (b) Corner Cut, (c) Chamfered, (d) Setback, and (e) Tapered



Figure 17 shows the overall  $C_p$  profile for composite models and basic models. The maximum  $+C_p$  recorded in Face 1 for the composite 1 model is +0.57. On the other hand, in Face 2, the maximum  $-C_p$  was found to be -0.46. The  $C_p$  distribution shows slight fluctuation in Face 3; the highest  $-C_p$  was recorded to be approximately -0.25. The distribution pattern for the composite 1 model is similar to the setback model. It is particularly true because both models show  $+C_p$  reduction at the setback locations. Meanwhile, the trend for the composite 2 model is similar to the setback model and the composite 1 model due to the relatively dominant effect of the setback feature. The maximum  $+C_p$  was recorded to be +0.44. The magnitude of the pressure drop at the upper part of the setback location is larger than the lower part of the setback. On the other hand, Face 2 develops the highest  $-C_p$ , which is recorded to be -0.58. The  $-C_p$  fluctuates and stabilizes at approximately -0.2 in Face 3. Meanwhile, unlike the composite 1 model and composite 2 model, the distribution pattern for the composite 3 model is relatively smooth without any significant drops in Face 1 and Face 3. The maximum  $+C_p$  for windward Face 1 was recorded to be +0.54, and the maximum  $-C_p$  for windward Face 2 was recorded to be -1.08. The  $-C_p$  is significantly reduced as it approaches the rear part of the roof and slightly fluctuates in Face 3. The suction effect was weakened at the lower part of Face 3, and the  $-C_p$  stabilized at approximately -0.1.

From the graph shown, it clearly can be seen that, in the case of Face 1, the results showed that all composite models showed a significant reduction in the  $+C_p$ . The composite model 1 and composite model 3 showed almost similar magnitude in terms of  $+C_p$  throughout Face 1. On the other hand, the composite model 2 was shown to produce the lowest  $+C_p$  along Face 1. This phenomenon can be associated with the effectiveness of combining chamfered, setback, and twisting to the basic model. On the other contrary, In Face 2, the composite 1 model showed the lowest  $-C_p$  (thus the suction effect) compared to other models. By studying the formation of the composite 1 model and comparing these features with the composite 2 model and composite 3 model, rotating the model at  $45^\circ$  and introducing setbacks were shown to be effective in reducing the  $-C_p$ . The kinetic energy of the airflow for the composite 2 model was reduced due to the presence of a setback where the kinetic energy was further reduced with the wind reduction drag due to the presence of twisted surfaces.

Despite significantly reducing kinetic energy (low  $+C_p$ ), the condition was not prolonged in Face 2. This phenomenon is because the separation and reattachment of airflow did not interfere with the reverse flow direction generated by the vortex in Face 3. It is evident that in the composite 1 model, although having higher kinetic energy (high  $+C_p$ ), the condition was significantly reduced when the separated flow encountered the reverse flow from the generated vortex at the upper level. Interestingly, the composite 3 model exhibited the highest  $-C_p$  in Face 2, and the value exceeded the basic model.

Although the kinetic energy in the composite 3 model was shown to be relatively similar to the composite 1 model, the suction effect in Face 2 was more dominant due to the fact that the axis of the vortex at the upper level was found to be relatively far from the suction region in Face 2. Generally, throughout Face 3, the composite models showed lower  $-C_p$  values compared to the basic model.

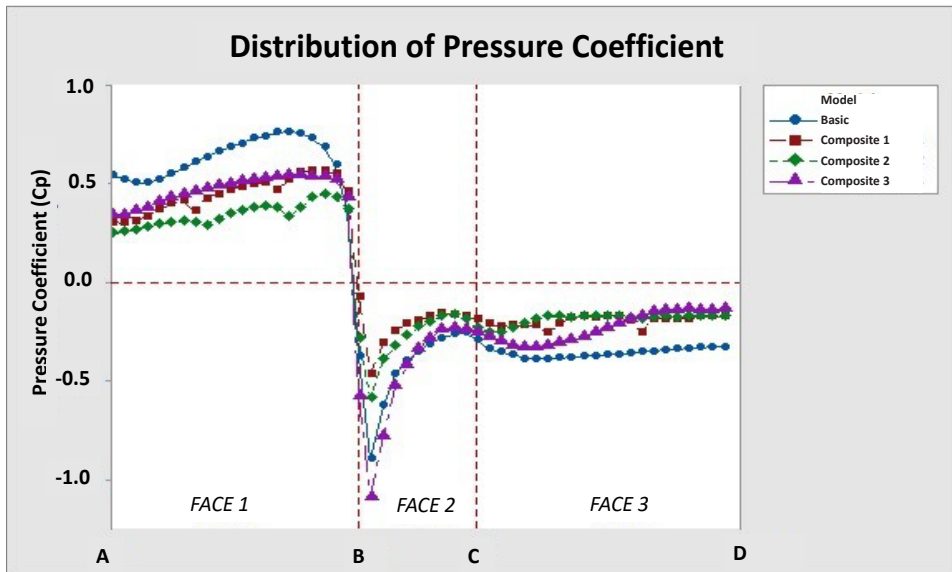


Figure 17.  $C_p$  profile for basic and overall composite modification

The pressure contour on the side of the building models is shown in Figure 18 for the composite 1 model, composite 2 model, and composite 3 model. The side surface for all models generates both  $+C_p$  and  $-C_p$ . The maximum suction exhibited from the side of the building model is shown in the composite 3 model (-1.08), followed by composite 2 model (-0.89) and composite 1 model (-0.9). In this case, only the composite 3 model exceeded the maximum suction of the basic model (-0.92). The difference was calculated to be 17.39%. In addition, the combination of setback, chamfer, and  $45^\circ$  rotation in composite model 1 can reduce the maximum  $-C_p$  approximately half of the value exhibited by the basic model. For composite modifications, the formation of the highest suction only occupies a relatively small area on the surface and close to the edge of the corner surface. Especially for the composite 2 model and composite 3 model, the area exhibiting a high suction effect was concentrated at the upper level of the building.

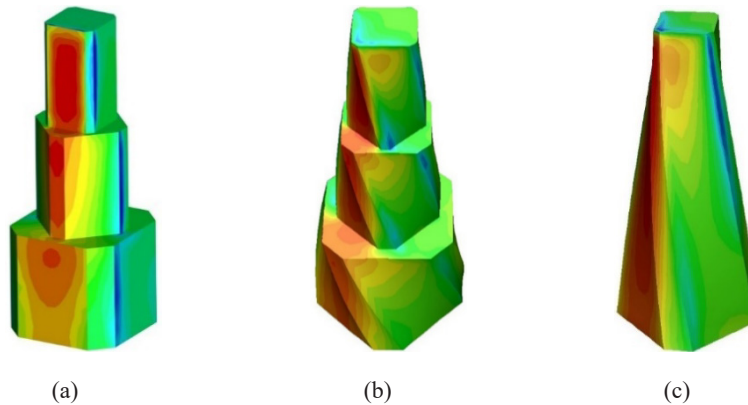


Figure 18. Pressure contour on the overall surfaces of the building models (a) composite 1, (b) composite 2, (c) composite 3

## CONCLUSION

All models subjected to single modification performed better than the basic model in reducing the maximum  $+C_p$  and  $-C_p$ . In terms of suction, a corner cut was shown to be more efficient than a chamfer. The setback model is more effective in reducing suction than the basic and tapered model. When comparing the composite 1 model with the composite 2 model in Face 1, twisting was more efficient in reducing the  $+C_p$  than rotation. For the composite 2 and the composite 3 models, a tapered configuration was more efficient than setting the building with setbacks. Meanwhile, when comparing the composite 1 model to the composite 2 model and the composite 3 model, it was discovered that rotating the model at  $45^\circ$  and introducing setbacks effectively lowered the  $-C_p$ . Choosing an efficient geometry modification for high-rise structures can help mitigate aerodynamic concerns, particularly in pressure distribution on the building surfaces. This study only focuses on the use of RNG  $k-\varepsilon$ . Other turbulence models, such as Large Eddy Simulation (LES) and Detached Eddy Simulation, can be explored with wind tunnel tests on other complex building shapes.

## ACKNOWLEDGEMENT

The authors express their gratitude and appreciation to the Universiti Sains Malaysia for providing all the required facilities.

## REFERENCES

- Ahsan, M. (2014). Numerical analysis of friction factor for a fully developed turbulent flow using  $k-\varepsilon$  turbulent model with enhanced wall treatment. *Beni-Suef University Journal of Basic and Applied Science*, 3(4), 269-277. <https://doi.org/10.1016/j.bjbas.2014.12.001>

- Bandi, E. K., Tamura, Y., Yoshida, A., Kim, Y. C., & Yang, Q. S. (2013). Experimental investigation on aerodynamic characteristics of various triangular section highrise buildings. *Journal of Wind Engineering and Industrial Aerodynamics*, 122, 60-68. <https://doi.org/10.1016/j.jweia.2013.07.002>
- Bitsuamlak, G. T., Warsido, W., Ledesma, E., & Chowdhury, A. G. (2013). Aerodynamic mitigation of roof and wall Corner suction using simple architectural elements. *Journal of Engineering Mechanics*, 139(3), 396-408. [https://doi.org/10.1061/\(ASCE\)EM.1943-7889.0000505](https://doi.org/10.1061/(ASCE)EM.1943-7889.0000505)
- Bhattacharjee, S., Banerjee, S., Majumdar, S., Saptarni, S. G., Dey, A., & Sanyal, P. (2021). Effects of irregularity on a butterfly plan-shaped tall building under wind load. *Journal of The Institution of Engineers (India): Series A*, 102, 451-467. <https://doi.org/10.1007/s40030-021-00511-6>
- Dagnew, A. K., Bitsuamalk, G. T., & Merrick, R. (2009, June 22-26). A Computational evaluation of wind pressures on tall buildings using LES. In *11th Americas Conference on Wind Engineering* (pp 1-17). San Juan, Puerto Rico. <https://doi.org/10.12989/was.2014.18.5.567>
- Deraman, S. N. C., Majid, T. A., Zaini, S. S., Yahya, W. N. W., Abdullah, J., & Ismail, M. A. (2018). Enhancement of CFD validation exercise along the roof profile of a low-rise building. In *IOP Conference Series: Earth and Environmental Science* (Vol. 140, No. 1, p. 012004). IOP Publishing. <https://doi.org/10.1088/1755-1315/140/1/012004>
- Elshaer, A., Bitsuamlak, G., & Damatty, A. E. (2014, June 1-4). Wind load reductions due to building corner modifications. In *22nd Annual conference of the CFD society of Canada* (pp. 1-5). Toronto, Canada.
- Elshaer, A., Bitsuamlak, G., & El Damatty, A. (2016, June 7-11). Aerodynamic shape optimization of tall buildings using twisting and corner modifications. In *8th International Colloquium on Bluff Body Aerodynamics and Applications Northeastern University* (pp. 1-8). Boston, MA, USA.
- Franke, J., Hirsch, C., Jensen, A. G., Krus, H. W., Schatzmann, M., Westbury, P. S., Miles, S. D., Wisse, J. A., & Wright, N. G. (2004, May 5-7). Recommendations on the use of CFD in wind engineering. In *Proceedings of the International Conference on Urban Wind Engineering and Building Aerodynamics* (pp. C.1.1-C1.11). von Karman Institute, Sint-Genesius-Rode, Belgium.
- Gu, M., & Quan, Y. (2004). Across wind loads of typical tall buildings. *Journal of Wind Engineering and Industrial Aerodynamics*, 92(13), 1147-1165. <https://doi.org/10.1016/j.jweia.2004.06.004>
- Hajra, S., & Dalui, S. K. (2016). Wind interference effect on an octagonal plan shaped tall building due to square plan shaped tall buildings. *Jordan Journal of Civil Engineering*, 10(4), 462-479. <https://doi.org/10.1007/s40091-016-0115>
- Hansora, A. G., Gehlot, K. P., & Nimodiya, P. N. (2015). Numerical analysis of wind loads on tapered shape tall buildings. *International Journal of Science Technology & Engineering*, 1(11), 92-97.
- Holmes, J. D. (2001). *Wind loading of structures: Wind Loading of Structures* (1st ed.). CRC Press. <https://doi.org/10.4324/9780203301647>
- Holmes, J. D. (2015). *Wind loading of structures* (3rd ed.). CRC Press. <https://doi.org/10.1201/b18029>
- Huang, S., Li, Q. S., & Xu, S. (2009). Numerical evaluation of wind effects on a tall steel building by CFD. *Journal of Construction Steel Research*, 63(5), 612-627 <https://doi.org/10.1016/j.jcsr.2006.06.033>

- Irwin, P. A. (2008). Bluff body aerodynamics in wind engineering. *Journal of Wind Engineering and Industrial Aerodynamics*, 96, 701-712. <https://doi.org/10.1016/j.jweia.2007.06.008>
- Irtaza H., Agarwal, A., & Shahab K. (2021). Comparison of aerodynamic loads on prismatic and twisted tall buildings using computational fluid dynamics. *Journal of The Institution of Engineers (India): Series C*, 102, 635-650. <https://doi.org/10.1007/s40032-021-00694-8>
- Khan, M. M., & Roy, A. K. (2017). CFD simulation of wind effects on industrial RCC chimney in civil engineering Conference-Innovation for sustainability. *International Journal of Civil Engineering and Technology (IJCIET)*, 8(1), 1008-1020.
- Liu, J., & Niu, J. (2016). CFD Simulation of the wind environment around an isolated high-rise building: An evaluation os SRANS, LES and DES models. *Journal of Building and Enviroment*, 96, 91-106.
- Meng, F. Q., He, B. J., Zhu, J., Zhao D. X., Darko, A., & Zhao, Z. Q., (2017). Sensitivity analysis of wind pressure coefficients on CAARC standard tall buildings in CFD Simulations. *Journal of Building Engineering*, 16, 146-158. <https://doi.org/10.1016/j.jobe.2018.01.004>
- Montazeri, H., & Blocken B. (2013). CFD simulation of wind induced pressure coefficient on buildings with and without balconies: validation and sensitivity analysis. *Journal of Building and Environment*, 60, 137-149. <https://doi.org/10.1016/j.buildenv.2012.11.012>
- Mou, B., He, B. J., Zhao, D. X., & Chau K. W., (2017). Numerical simulation of the effects of building dimensional variation on wind pressure distribution. *Engineering Applications of Computational Fluid Mechanics*, 11, 293-309. <https://doi.org/10.1080/19942060.2017.1281845>
- Richards, P. J., Hoxey, R. P., Connell, B. D., & Lander, D. P. (2007). Wind-tunnel modelling of the Silsoe Cube. *Journal of Wind Engineering and Industrial Aerodynamics*, 95, 1384-1399. <https://doi.org/10.1016/j.jweia.2007.02.005>
- Sanyal, P., & Dalui, S. K. (2020). Comparison of aerodynamic coefficients of various types of Y-plan shaped tall buildings. *Asian Journal Civil Engineering*, 21(7), 1109-1127. <https://doi.10.1007/s42107-018-0018-3>
- Sharma, A., Mittal, H., & Gairola, A. (2017, December 3-7). Investigation of aerodynamic forces on highrise buildings with setback modification. In *9th Asia-Pacific Conference, Wind Engineering* (pp. 1-4). Auckland New Zealand.
- Tse, K. T., Hitchcock, P. A., Kwok, K. C. S., Thepmongkorn, S., & Chan, C. M. (2012). Economic perspectives of aerodynamic treatments of square tall buildings. *Journal of Wind Engineering and Industrial Aerodynamics*, 97(9-10), 455-467. <https://doi:10.1016/J.JWEIA.2009.07.005>
- Tominaga, Y., Mochida, A., Yoshie, R., Kataoka, H., Nozu, T., Yoshikawa, M., & Shirasawa, T. (2008). AIJ guidelines for practical applications of CFD to pedestrian wind environment around buildings. *Journal of Wind Engineering and Industrial Aerodynamics*, 96(10-11), 1749-1761. <https://doi.org/10.1016/j.jweia.2008.02.058>
- Tominaga, Y. (2015). Air flow around isolated gable-roof buildings with different roof pitches: Wind tunnel experiments and CFD simulations. *Building and Environments*, 84, 204-213. <https://doi.org/10.1016/j.buildenv.2014.11.012>



*Review Article*

## **A Systematic Review of Ergonomics Risk Assessment Methods for Pushing and Pulling Activities at Workplace**

**Hari Krishnan Tamil Selvan\* and Mohd Nasrull Abdol Rahman**

*Department of Manufacturing and Industrial Engineering, Faculty of Mechanical and Manufacturing Engineering, Universiti Tun Hussein Onn Malaysia, 86400 UTHM, Parit Raja, Batu Pahat, Johor, Malaysia*

### **ABSTRACT**

It is vital to assess workplace pushing and pulling (PP) activities to manage musculoskeletal injuries among employees. However, there is still no clearly-suited risk assessment method. This systematic review aims to provide an overview of risk assessment methods for PP activities at the workplace. Thus, the review employed the Preferred Reporting Items for Systematic Reviews and Meta-Analyses (PRISMA). Two primary journal databases were searched, namely Scopus and Science Direct. Furthermore, to ensure the robustness of the study, the searches were expended via handpicking, snowball identification, and consultation with ergonomics experts. Atlas.ti version 8 software was used to analyse the identified articles thematically. The search resulted in nine articles eligible for the systematic analysis. From the articles, six assessment methods used force measurement as the main indicators, while three assessment methods used the weight of the load as measurement indicators. The assessment tools did not cover all the risk factors for PP activities. Besides, there was a lack of evidence showing the assessment tools or methods' reliability, validity, and usability. This systematic review highlighted the advantages and limitations of existing assessment methods, and no one method fits all. The findings showed that the assessment

methods for PP activities still needed a force measurement and did not cover all the significant risk factors associated with PP. In addition, no clarifications were presented regarding the assessment methods' reliability, validity, and applicability.

### ARTICLE INFO

*Article history:*

Received: 25 December 2022

Accepted: 10 May 2023

Published: 12 October 2023

DOI: <https://doi.org/10.47836/pjst.31.6.29>

*E-mail addresses:*

hari.krishnan.niosh@gmail.com (Hari Krishnan Tamil Selvan)

mnasrull@uthm.edu.my (Mohd Nasrull Abdol Rahman)

\*Corresponding author

*Keywords:* Ergonomics tools, manual handling, pushing and pulling, risk assessment method

## INTRODUCTION

Lifting, lowering and carrying have been major manual handling activities (Todd, 2012), which resulted in ergonomics risk (Bennet et al., 2011). Thus, pushing and pulling (PP) has been introduced to mitigate the risk of other manual handling activities (Bennet et al., 2011). The PP can be explained as a horizontally applied force. The force is led afar from the body via pushing but towards the body via pulling (Hoozemans et al., 1998; Baril-Gingras & Lortie, 1995). Furthermore, pulling requires greater force (Castro et al., 2012) and maximal voluntary grip force (Chen et al., 2015) than pushing.

While lifting creates large compression forces on the spinal disc and other spinal structures, the act of PP usually creates shear forces (Waters et al., 2011) and back muscle loading (Chen et al., 2015; Kuijjer et al., 2007; Frost et al., 2015; Hoozemans et al., 2002) reported that PP increase the risks of a shoulder injury but not necessarily lower back pain, and it is major cause for musculoskeletal injuries at the workplace (Lee, 2018).

One of the key elements for managing musculoskeletal disorders (MSDs) at the workplace is ergonomics management, which can be accessed via ergonomics risk assessment (Cohen et al., 1997; Rahman & Mohammad, 2017; Monaco et al., 2019; Gyemi et al., 2016). According to David (2005), three classes of ergonomics risk assessment include self-reporting, observation methods (basic and advanced techniques), and direct measurement.

Another important criterion of an assessment tool is the psychometric properties such as reliability, validity and usability (Jahrami et al., 2019). First, a reliable tool ensures consistent results are obtained from repeated assessments, which is necessary to identify ergonomic risk factors changes over time (Bannigan & Watson, 2009). Second, a valid tool provides accurate information about the ergonomic risk factors in a given work environment, which is necessary to develop effective interventions to reduce ergonomic risks (Cook & Beckman, 2006). Finally, a usable tool ensures that the assessment process is efficient and effective, which can increase the likelihood of the tool being adopted and used in the workplace (Occhipinti & Colombini, 2015).

Although there are many assessment tools for PP activities, such as KIM-PP (Steinberg, 2012), RAPP (Health and Safety Laboratory, 2013), PPAC (Ferreira et al., 2007) and et cetera, it is still unclear as to what is the best assessment method for PP at an industry level. Despite the different views surrounding PP assessment tools, there has been less published review in this area. Therefore, the present study addresses this research gap by reviewing the existing assessment tools for PP activities and highlights the directions for future research.



The research questions guiding this systematic review are:

- (1) What risk factors are evaluated by the PP assessment tool?
- (2) What is the assessment tool's reliability, validity and usability?

This article highlights a review of ergonomics risk assessment tools in relation to workplace PP.

## **MATERIAL AND METHODS**

### **Preferred Reporting Items for Systematic Reviews and Meta-Analyses (PRISMA)**

The review process employed the PRISMA (Moher et al., 2009). PRISMA is a published standard for performing the systematic literature review. PRISMA has been reported to guide authors to systematically evaluate and examine the quality of reviewed papers and be used for other types of research besides randomised trials (Moher et al., 2009). This methodology involves four stages, i.e., identification, screening, eligibility, and inclusion.

### **Resources**

Xiao and Watson (2019) suggested that no one database is complete, thus suggesting more than one database for the search process, and Younger (2010) mentioned that when using more than one database, it will cover each other's weaknesses. Thus, two databases have been employed for search purposes: the Scopus and Science Direct databases. One of the biggest databases of peer-reviewed literature abstracts and citations is Scopus, which has over 25,200 titles from 7000 publishers worldwide. Several academic disciplines are included in Scopus, including engineering, medicine, and health sciences. Science Direct is the second database used in the review. It has over 2,650 peer-reviewed journals with over 19 million articles and chapters.

### **The Systematic Review Process for Article Selection**

**Identification.** At the first stage of identification, relevant keywords were determined. Then, a search was done to identify similar and related keywords based on a thesaurus, a dictionary, and previous research (Table 1). The search was done on the Scopus and Science Direct databases. This search yielded insufficient material, as few journal articles included studies on ergonomics assessment tools for PP activities. As stated by Younger (2010), the researcher should perform the search process in more databases to obtain more articles related to the topic; thus, the search was expanded via handpicking, snowball identification, and consultation with ergonomics experts. This step led to identifying publications in the form of government research papers, ISO standards, and book chapters. In the end, 41 publications related to the current topic were identified.

Table 1  
*Search strings*

Database	Keyword used
Scopus	(TITLE-ABS-KEY ("manual handling") AND TITLE-ABS-KEY ("risk assessment")) AND TITLE-ABS-KEY (pushing OR pulling)
Science Direct	Title, abstract, keywords: "manual handling" AND "risk assessment"

**Screening.** In this step, duplicate publications were first removed. As a result, three articles were excluded. Next, adhering to the inclusion and exclusion criteria presented in Table 2, 37 publications were filtered. Due to the limitations of the current topic under review, the accepted literature type was widened to cover research articles, government publications, and conference proceedings. Therefore, journal publications and meta-analyses were excluded. Moreover, it should be noted that this review only covered publications in the English language. Additionally, the timeline was expanded from 1970 to 2019 to increase the possibility of retrieving related publications. Thirty-four publications were finalised for the next stage of the review.

Table 2  
*Inclusion and exclusion criteria*

Criterion	Inclusion	Exclusion
Literature type	Research articles; Government publications; Conference proceedings	Systematic literature review journals, Meta-analysis
Language	English	Non-English
Timeline	Between 1970-2019	<1970
Manual handling Type	Pushing and Pulling	Lifting, carrying, lowering
Assessment method	Self-report, observation methods (advanced and straightforward technique) and direct measurement	Biomechanical model

**Eligibility.** Thirty-four (34) publications were prepared at this stage. The publications' titles, abstracts, and content were screened thoroughly to ensure that the publications fulfilled the inclusion criteria for the current research. This step yielded 9 eligible publications. The remaining 25 publications did not match the inclusion criteria. Biomechanical models were excluded from the review due to the complexity of such assessments. Figure 1 illustrates the flow diagram for the review process.

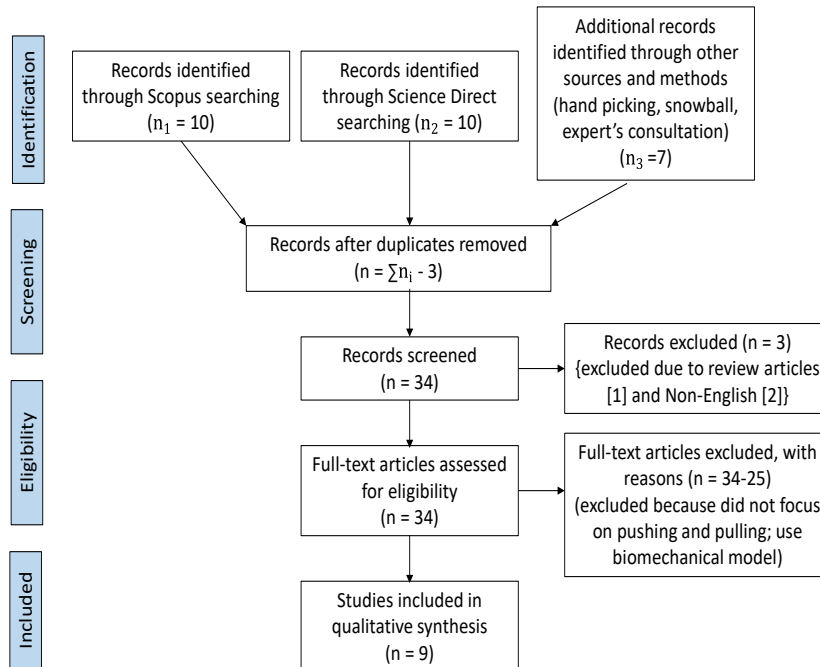


Figure 1. Flow diagram of the study (adapted from Moher et al., 2009)

## Data Extraction and Analysis

Using Atlas.ti 8 software, a thematic analysis was carried out to develop appropriate themes and subthemes according to the data compilation. Then, the authors categorised the overall themes into two: (1) the variables measured by each tool and (2) the reliability, validity, and usability of the tool.

Jung et al. (2005) pushing and pulling framework was improved by adding variables like hand grips (Ayoub & Dempsey, 1999), task duration (Rohani et al., 2018), and temperature (Snook & Ciriello, 1974). These variables were added to create variable and sub-variable categories corresponding to theme number 1 (Figure 2).

Theme number 2 was derived based on the past literature, which suggested that ergonomics risk assessment tool should be:

- Reliable when used in practical and research settings (Rohani et al., 2018; Zetterberg et al., 2019);
- Provides valid ergonomics measurement. The development stage should be emphasised (Sukadarin et al., 2015), and
- Ease of use (usability) is an important criterion that determines application among practitioners (Eliasson, 2017).

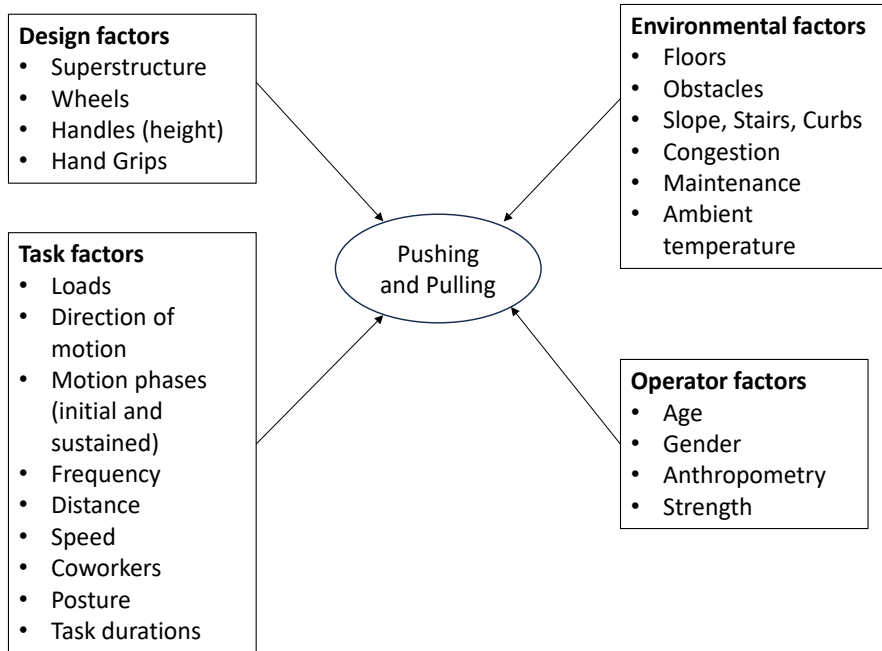


Figure 2. Factors determining pushing and pulling activities (Snook & Ciriello, 1974; Ayoub & Dempsey, 1999; Jung et al., 2005; Rohani et al., 2018)

## RESULTS

### General Study Findings and Background

The analysis identified nine risk assessment tools or methods for PP activities: four from journal articles (Snook, 1978; Snook & Ciriello, 1991; Steinberg, 2012; Lind, 2018), one from a book (Mital et al., 1997), one from ISO standards (International Organization for Standardization, 2007), two from government research reports (Ferreira et al., 2007; Health and Safety Laboratory, 2013), and one from a conference proceeding (International Organization for Standardization, 2007). Table 3 shows the included publications and the type of publication.

Table 3  
Publication related to assessment tools for pushing and pulling activities

No	Title	Publication Type	Source
1	The design of Manual Handling Table	Journal Article (Ergonomics)	Snook (1978)
2	The Design of Manual Handling Tasks: Revised Tables of Maximum Acceptable Weights and Forces	Journal Article (Ergonomics)	Snook and Ciriello (1991)
3	A Guide to Manual Material Handling	Book	Mital et al. (1997)

Table 3 (Continue)

No	Title	Publication Type	Source
4	Key Indicator Method (Pushing and Pulling) KIM-PP	Journal Article (Work)	Steinberg (2012)
5	Pushing and Pulling Operations Assessment Charts Tool (PPAC)	Government Research Report	Ferreira et al. (2007)
6	ISO 11318-2: 2907 Ergonomics–Manual handling–Part 2: Pushing and Pulling	ISO Standard	International Organization for Standardization (2007)
7	Risk assessment of pushing and pulling (RAPP) tool	Government Research Report	Health and Safety Laboratory (2013)
8	Pushing and pulling: An assessment tool for OHS practitioners	Journal Article (International Journal of Occupational Safety and Ergonomics)	Lind (2018)
9	DUTCH: A New Tool for Practitioners for Risk Assessment of Push and Pull	Conference Proceeding	Douwes et al. (2019)

### Main Findings

The description of each method and the output type/rating score are described in Table 4. Basically, the output/rating score of the assessment methods can be divided into three types: recommendation force limit (Snook, 1978; Snook & Ciriello, 1991; Mital et al., 1997; International Organization for Standardization, 2007), risk range category (Steinberg, 2012), and traffic light grading system (Lind, 2018; Ferreira et al., 2007; Health and Safety Laboratory, 2013; Douwes et al., 2019). It is important to note that the risk range category and traffic light grading system are similar in that both illustrate low to high-risk levels. Table 5 displays the variables evaluated using all the assessment methods, while Table 6 summarises the methods' reliability, validity, and usability. Six assessment methods used force measurement as one of the risk assessment components (Snook, 1978; Snook & Ciriello, 1991; Lind, 2018; Mital et al., 1997; International Organization for Standardization, 2007; Ferreira et al., 2007), which contradict the recommendations of Steinberg (2012), the Health and Safety Laboratory (2013), and Douwes et al. (2019), all of which used the weight of the load as measurement indicators.

Table 4  
Description of assessment method for pushing and pulling

Method	Description	Strength	Limiation	Rating Score
The design of Manual Handling Table (Snook, 1978)	<ul style="list-style-type: none"> <li>Based on experimental design</li> <li>A total number of 28 male industrial workers.</li> <li>Need to perform 54 tasks that varied in frequency, travelling distance, and height.</li> </ul>	Stringent experimental methodology has been used for the development	<ul style="list-style-type: none"> <li>The data is based on the US population. It may not be appropriate to be used in different population</li> <li>Need to use force gauge</li> </ul>	Force limit information/recommendation
The Design of Manual Handling Tasks: Revised Tables of Maximum Acceptable Weights and Forces (Snook and Ciriello, 1991)	<ul style="list-style-type: none"> <li>Used a much bigger sample size for PP activities (128 subjects: 68 males and 51 females) compared to the previous research (57 subjects: 42 males and 15 females).</li> <li>Similar methodology and simulation with previous research</li> <li>The maximum acceptable initial force for the pulling task was 13% lower than the pushing task, whereas it was 29% lower for the maximum acceptable sustained force.</li> <li>In the revised table, there were six distances for pulling tasks compared to only one pulling distance in the previous table, which used a similar frequency for PP for both males and females.</li> <li>Mean forces in the revised table were lower than the original tables for female workers: initial push, 2.72 kg lower; sustained push, 0.90 kg lower; initial pull, 1.76 kg lower; and sustained pull, 3.39 kg lower.</li> <li>However, the opposite trend was reported for male workers: initial push, 1.36 kg higher; sustained push, 1.27 kg higher; initial pull, 1.53 kg higher; sustained pull, 1.11 kg higher.</li> </ul>	Stringent experimental methodology has been used for the development	<ul style="list-style-type: none"> <li>The data is based on the US population. It may not be appropriate to be used in different population</li> <li>Need to use force gauge</li> </ul>	Force limit information/recommendation

Table 4 (Continue)

Method	Description	Strength	Limitation	Rating Score
The design of Manual Handling Table (Snook, 1978)	<ul style="list-style-type: none"> <li>Based on experimental design</li> <li>A total number of 28 male industrial workers.</li> <li>Need to perform 54 tasks that varied in frequency, travelling distance, and height.</li> </ul>	Stringent experimental methodology has been used for the development	<ul style="list-style-type: none"> <li>The data is based on the US population. It may not be appropriate to be used in different population</li> <li>Need to use force gauge</li> </ul>	Force limit information/recommendation
The Design of Manual Handling Tasks: Revised Tables of Maximum Acceptable Weights and Forces (Snook and Ciriello, 1991)	<ul style="list-style-type: none"> <li>Used a much bigger sample size for PP activities (128 subjects: 68 males and 51 females) compared to the previous research (57 subjects: 42 males and 15 females).</li> <li>Similar methodology and simulation with previous research</li> <li>The maximum acceptable initial force for the pulling task was 13% lower than the pushing task, whereas it was 29% lower for the maximum acceptable sustained force.</li> <li>In the revised table, there were six distances for pulling tasks compared to only one pulling distance in the previous table, which used a similar frequency for PP for both males and females.</li> <li>Mean forces in the revised table were lower than the original tables for female workers: initial push, 2.72 kg lower; sustained push, 0.90 kg lower; initial pull, 1.76 kg lower; and sustained pull, 3.39 kg lower.</li> <li>However, the opposite trend was reported for male workers: initial push, 1.36 kg higher; sustained push, 1.27 kg higher; initial pull, 1.53 kg higher; sustained pull, 1.11 kg higher.</li> </ul>	Stringent experimental methodology has been used for the development	<ul style="list-style-type: none"> <li>The data is based on the US population. It may not be appropriate to be used in different population</li> <li>Need to use force gauge</li> </ul>	Force limit information/recommendation

Table 4 (Continue)

Method	Description	Strength	Limiation	Rating Score
A Guide to Manual Material Handling (Mital et al., 1997)	<ul style="list-style-type: none"> <li>Used data from Snook and Ciriello tables and suggested maximum acceptable force limits adjusted for various biomechanical, physiological, and epidemiological criteria.</li> </ul>	<p>Based on a large body of research on ergonomics and manual material handling, it gives it a strong scientific foundation.</p>	<ul style="list-style-type: none"> <li>The data is based on the US population. It may not be appropriate to be used in different population</li> </ul>	Force limit information/recommendation
Key Indicator Method (Pushing and Pulling) KIM-PP (Steinberg, 2012)	<ul style="list-style-type: none"> <li>KIM for pushing and pulling (KIM-PP) was developed from the year 2898 until 2901 by the Federal Institute for Occupational Safety and Health (BAuA) and the Committee of the German States for Occupational Safety and Health (LASI)</li> </ul>	<ul style="list-style-type: none"> <li>Simple and easy-to-use method</li> <li>It does not require any special equipment or training</li> </ul>	<ul style="list-style-type: none"> <li>It relies on subjective ratings of the magnitude of pushing and pulling forces, which individual perceptions and biases can influence.</li> </ul>	Risk Score and Risk Range
Pushing and Pulling Operations Assessment Charts (PPAC) (Ferreira et al., 2007)	<ul style="list-style-type: none"> <li>By UK HSE</li> <li>Developed to complement Manual handling Assessment Charts (MAC), which focused on lifting, lowering, carrying, and team handling operations.</li> </ul>	<ul style="list-style-type: none"> <li>Relatively easy to use and requires minimal training</li> <li>A quantitative measure of the risk of MSDs associated with PP tasks, which can help prioritise interventions and track progress over time</li> </ul>	<ul style="list-style-type: none"> <li>Need to use force gauge</li> </ul>	Traffic light grading system



Table 4 (Continue)

Method	Description	Strength	Limitation	Rating Score
ISO 11318-2: 2007 Ergonomics– Manual handling– Part 2: Pushing and Pulling (International Organization for Standardization, 2007)	<ul style="list-style-type: none"> <li>Detailed out two methods for identifying the risk associated with PP</li> <li>Method 1: Generalised risk estimation and risk evaluation</li> <li>Examined six risk categories: the task, load characteristics, working environment, individual capability, work organisation, and other factors presented in manual handling.</li> <li>The psychophysical tables illustrated the acceptable initial and sustained forces by considering handle height, distance travelled, and frequency of push/pull tasks for both genders: males and females.</li> </ul>	Used data from Snook and Ciriello (empirical data)	Need to use force gauge	Force limit information/recommendation
<p><i>Note: Method 2 is beyond the scope of the study since it involves a biomechanical method</i></p>				
Risk assessment of pushing and pulling (RAPP) tool (Health and Safety Laboratory, 2013)	<ul style="list-style-type: none"> <li>By UK HSE</li> <li>RAPP was mainly developed to address this concern where the assessor can assess without force gauge and by the observational method</li> <li>The tool is divided into two types of assessment, which are:                             <ul style="list-style-type: none"> <li>◇ Moving loads on wheeled equipment and</li> <li>◇ Moving load without wheeled equipment.</li> </ul> </li> </ul>	<ul style="list-style-type: none"> <li>Relatively easy to use and requires minimal training</li> <li>A quantitative measure of the risk of MSDs associated with PP tasks, which can help prioritise interventions and track progress over time</li> </ul>	Did not consider task frequency and handle height in the assessment chart	Traffic light grading system

Table 4 (Continue)

Method	Description	Strength	Limiation	Rating Score
Pushing and pulling: An assessment tool for OHS practitioners (Lind, 2018)	<ul style="list-style-type: none"> <li>Used nine multiplier equations in decision-making for the risk of PP and subsequently to determine the priority level score.</li> </ul>	Based on psychophysical, biomechanical studies in combination with judgments from an expert group consisting of senior researchers and ergonomists.	Need to use force gauge	Risk Score based on traffic light system
DUTCH: A New Tool for Practitioners for Risk Assessment of Push and Pull (Douwes et al., 2019)	<ul style="list-style-type: none"> <li>DUTCH is a web-based tool for quick evaluation of push and pull activities</li> </ul>	<ul style="list-style-type: none"> <li>Web-based</li> <li>Relatively easy to use and requires minimal training</li> </ul>	Need to have an active internet connection and device for the assessment	Risk Score based on traffic light system

Table 5  
Publications and the assessed variables

Variable Category and Variable	Publication								
	1	2	3	4	5	6	7	8	9
<b>Design Factors</b>									
Superstructure				▲			▲		
Wheels					▲				
Handles height	▲	▲	▲		▲	▲		▲	▲
Handgrip							▲	▲	
<b>Task Factors</b>									
Loads				▲			▲		▲
Direction of motion	▲	▲	▲			▲			
Motion Phases (initial and sustained)						▲			
Frequency	▲	▲	▲	▲	▲	▲	▲	▲	▲
Distance	▲	▲	▲	▲		▲	▲		▲
Speed				▲					
Co-workers									
Posture				▲	▲		▲	▲	
Task Duration				▲	▲				
<b>Environment Factors</b>									
Floors				▲	▲		▲	▲	
Obstacles				▲	▲		▲		
Slope, stairs, and curbs				▲					
Congestion					▲				
Maintenance				▲	▲		▲		
Ambient temperature					▲		▲	▲	
<b>Operator Factors</b>									
Age									
Gender	▲	▲		▲		▲			▲
Anthropometry									
Strength									
<b>Others</b>	▲ <sup>a</sup>	▲ <sup>a</sup>	▲ <sup>a</sup>	▲ <sup>b</sup>	▲ <sup>a</sup>	▲ <sup>a</sup>	▲ <sup>c</sup>	▲ <sup>a,d</sup>	

Note (Table 5):

<sup>a</sup>force

<sup>b</sup>positioning accuracy

<sup>c</sup>unstable load; the load is large and obstructs view; the load is sharp and hot and could damage touch; poor lighting conditions; strong air movements; personal protective equipment obstructs the work.

<sup>d</sup>one hand pushing/pulling; pushing/pulling in a lateral direction; team pushing

Publications:

1. The design of Manual Handling Table (Snook, 1978)
2. The Design of Manual Handling Tasks: Revised Tables of Maximum Acceptable Weights and Forces (Snook & Ciriello, 1991)
3. A Guide to Manual Material Handling (Mital et al., 1997)
4. Key Indicator Method (Pushing and Pulling) KIM-PP (Steinberg, 2012)
5. Pushing and Pulling Operations Assessment Charts Tool (PPAC) (Ferreira et al., 2007)
6. ISO 11318-2: 2907 Ergonomics – Manual handling – Part 2: Pushing and Pulling (International Organization for Standardization, 2007)
7. Risk assessment of pushing and pulling (RAPP) tool (Health and Safety Laboratory, 2013)
8. Pushing and pulling: An assessment tool for OHS practitioners (Lind, 2018)
9. DUTCH: A New Tool for Practitioners for Risk Assessment of Push and Pull (Douwes et al., 2019)

Table 6  
Reliability, validity, and usability for the assessment methods

Method	Source	Reliability	Validity	Usability
The design of Manual Handling Table	Snook (1978)	-	-	-
The Design of Manual Handling Tasks: Revised Tables of Maximum Acceptable Weights and Forces	Snook and Ciriello (1991)	-	-	-
A Guide to Manual Material Handling	Mital et al. (1997)	-	-	-
Key Indicator Method (Pushing and Pulling) KIM-PP	Steinberg (2012)	IRR=81% Kappa Score=0.705 (Douwes et al., 2019)	6/10 Moderate (Douwes et al., 2019)	-
Pushing and Pulling Operations Assessment Charts Tool (PPAC)	Ferreira et al. (2007)	-	-	-

Table 6 (Continue)

Method	Source	Reliability	Validity	Usability
ISO 11318-2: 2907 Ergonomics– Manual handling–Part 2: Pushing and Pulling	International Organization for Standardization (2007)	-	-	-
Risk assessment of pushing and pulling (RAPP) tool	Health and Safety Laboratory (2013)	-	-	+ <sup>a</sup>
Pushing and pulling: An assessment tool for OHS practitioners	Lind (2018)	-	-	+ <sup>b</sup>
DUTCH: A New Tool for Practitioners for Risk Assessment of Push and Pull	Douwes et al. (2019)	-	-	+ <sup>c</sup>

Note:

+ Tests were done with the assessment methods during the development process

- Tests were not done with the assessment methods during the development process

<sup>a</sup>Tool was easy to use: 70% by duty holders and 67% by regulatory inspectors (Health and Safety Laboratory, 2013)

<sup>b</sup>Majority (2/3) of respondents claimed that it is easy or fairly easy to do an assessment (Lind, 2017)

<sup>c</sup>No detail provided (Lind, 2018)

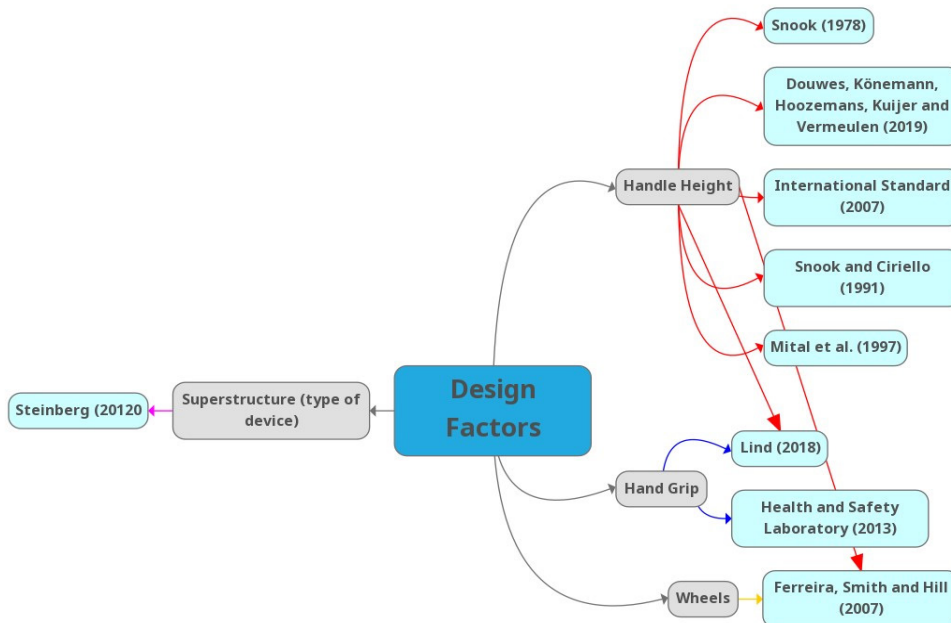


Figure 3. Schematic diagram of variables in the design factor and the associated assessment method

A schematic diagram of the variables for each factor category [design (Figure 3), task (Figure 4), environment (Figure 5) and operator (Figure 6)] and the associated assessment method are shown. The schematic diagram shows that most assessment methods emphasised the measurement of task factors, while the operator factor was given the least consideration. As for the design factor, the essential variable seemed to be handled height since all the assessment methods, except the Health and Safety Laboratory (2013) and Steinberg (2012), measured this factor.

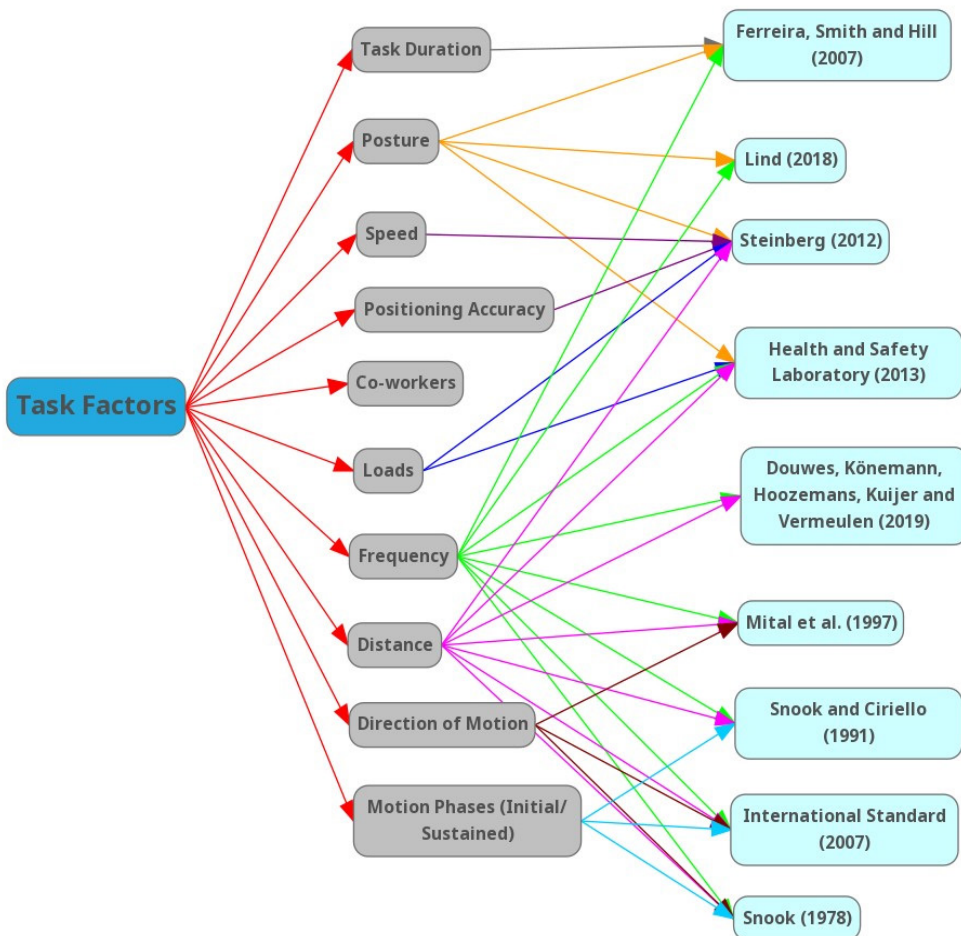


Figure 4. Schematic diagram of variables in task factor and the related assessment method

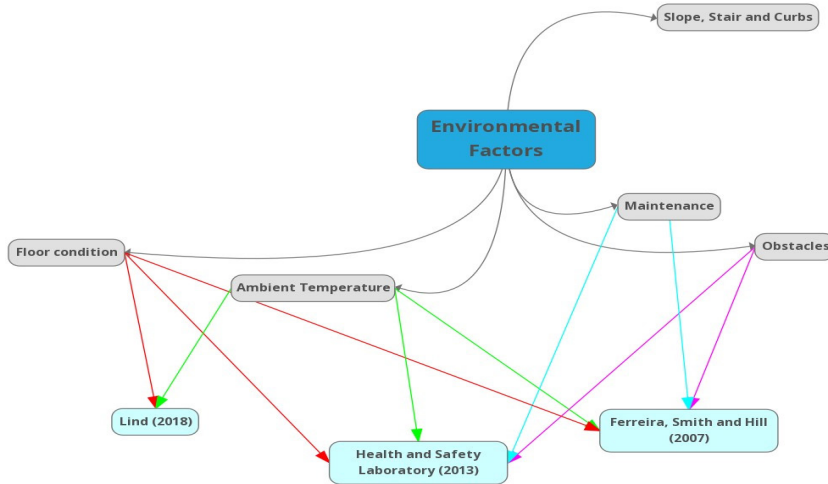


Figure 5. Schematic diagram of variables in environment factor and the related assessment method

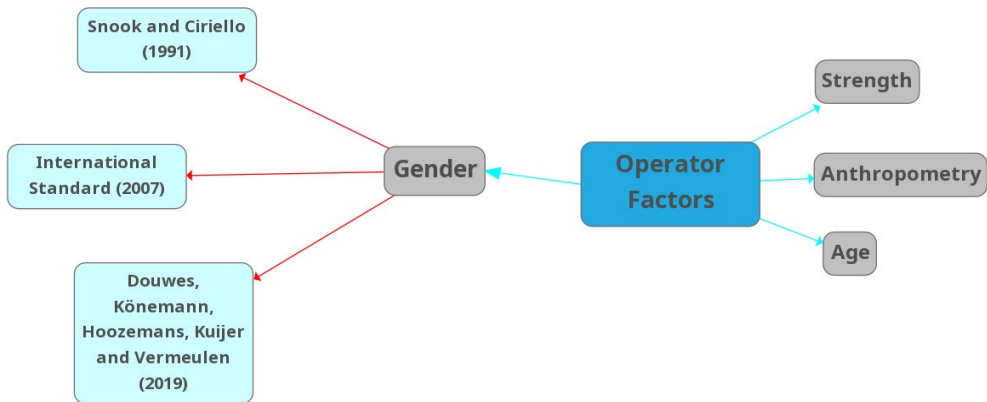


Figure 6. Schematic diagram of variables in the operator factor and the associated assessment method

## DISCUSSION

Ergonomics risk management is vital for reducing MSDs in the workplace (Cohen et al., 1997). Risk management is associated with occupational health and safety (Laws of Malaysia, 1994).

Thus, all potential main users of assessment methods will be health and safety practitioners in the workplace (Kadikon & Rahman, 2016). One of the strategies to ensure practical risk assessment at the workplace is to adopt simple, user-friendly observation methods. These methods should also reduce or eliminate the need to measure force and require minimal expert knowledge (Health and Safety Laboratory, 2013; Li & Buckle, 1999) without disrupting work activities (Kadikon & Rahman, 2016).

Based on the current review, six assessment methods (Snook, 1978; Snook & Ciriello, 1991; Lind, 2018; Mital et al., 1997; International Organization for Standardization, 2007; Ferreira et al., 2007) used a force gauge. However, as a force gauge is not readily available, assessments such as these will have limited application in the industry since organisations do not invest in the purchase of force gauges. Thus, assessing the risk of PP activities without a force gauge could present a significant challenge.

On the other hand, three methods, namely DUTCH, RAPP, and KIM-PP (Steinberg, 2012; Health and Safety Laboratory, 2013; Douwes et al., 2019), used the weight of the load as one of the variables for risk assessment. Nevertheless, for the risk assessment, RAPP and DUTCH did not take into account the handle height, disregarding the fact that previous studies showed a significant effect of handle height in PP activities on the MSDs' development (Hoozemans et al., 2004; Chaffin et al., 1983; Marras et al., 2009; Al-Eisawi et al., 1999). Furthermore, although the distance of the push and pull is considered to be a strong risk factor method (Snook, 1978; Snook and Ciriello, 1991; Cuervo et al., 2003), this variable was also not included (Lind, 2018; Ferreira et al., 2007).

There are four methods used to develop the assessment tools, namely, experimental design (Snook, 1978; Snook & Ciriello, 1991; Mital et al., 1997), literature review (Steinberg, 2012; Lind, 2018; Ferreira et al., 2007; Health and Safety Laboratory, 2013; Douwes et al., 2019), an adaptation from other assessment tools or resources (Steinberg, 2012; Lind, 2018; Mital et al., 1997; Douwes et al., 2019), and consultation with experts and expert opinions (Steinberg, 2012; Lind, 2018). However, although crucial, the testing for reliability, validity, and usability of the assessment tools in the reviewed studies during development was not clarified except for KIM-PP (Steinberg, 2012) and Douwes et al. (2019). The evidence showed that a usability test was carried out even then, only for RAPP (Health and Safety Laboratory, 2013), Pushing and Pulling: an assessment tool for OHS practitioners (Lind, 2018; Lind, 2017), and DUTCH (Lind, 2018).

This systematic review highlighted the advantages and limitations of existing assessment methods. No one method fits all. Measuring the forces associated with these activities is necessary to assess the PP activities. Also, the tools did not take into account every significant risk factor in relation to PP. There was also a lack of evidence proving the tools' reliability, validity, and usability.

## CONCLUSION

The findings showed that the assessment methods for PP activities still needed a force measurement and did not cover all the significant risk factors associated with PP, while there was a lack of psychometric data to establish acceptable reliability, validity, and usability of the tool. In summary, the ergonomics risk assessment tool for workplace PP activities must take into account all major risk factors leading to the MSDs' development.



These tools must also be subjected to a rigorous development stage of reliability, validity, and usability testing.

## **FUTURE PROSPECT**

This review recommends developing a new assessment tool for PP that includes all the main risk factors involved in the PP activities without making force measurement a requirement. The developed tool should fit the definition of a simple observation-based risk assessment guide to encourage usage among OSH practitioners. The newly developed assessment tool should be user friendly, self-explanatory and require minimal user training. During the development of the tool, selecting the critical risk factors in the assessment of PP shall consider the inputs from professional ergonomics experts and OSH practitioners, together with epidemiological evidence from the literature. It is also essential to consider the sensitivity analysis during development to determine which input variables are critical for the final risk level classification. The tool's reliability, validity, and usability testing should also be explained in detail to ensure that it can be practically applied in the industry and to dispel any doubts during the risk assessment.

## **ACKNOWLEDGEMENT**

The authors express their utmost gratitude to Dr. Hayrol Azril Bin Mohamed Shaffril for the lesson on systematic review.

## **REFERENCES**

- Al-Eisawi, K. W., Kerk, C. J., Congleton, J. J., Amendola, A. A., Jenkins, O. C., & Gaines, W. G. (1999). The effect of handle height and cart load on the initial hand forces in cart pushing and pulling. *Ergonomics*, *42*(8), 1099-1113. <https://doi.org/10.1080/001401399185162>
- Ayoub, M. M., & Dempsey, P. G. (1999). The psychophysical approach to manual materials handling task design. *Ergonomics*, *42*(1), 17-31. <https://doi.org/10.1080/001401399185775>
- Bannigan, K., & Watson, R. (2009). Reliability and validity in a nutshell. *Journal of Clinical Nursing*, *18*(23), 3237-3243. <https://doi.org/10.1111/j.1365-2702.2009.02939.x>
- Baril-Gingras, G., & Lortie M. (1995). The handling of objects other than boxes: Univariate analysis of handling techniques in a large transport company. *Ergonomics*, *38*(5), 905-925. <https://doi.org/10.1080/00140139508925159>
- Bennett, A. I., Todd, A. I., & Desai, S. D. (2011). Pushing and pulling, technique and load effects: An electromyographical study. *Work*, *38*(3), 291-299. <https://doi.org/10.3233/WOR-2011-1132>
- Castro, C., De la Vega E., Báez, G., & Carrasco, F. (2012). Maximum force levels in different positions of shoulder and elbow. *Work*, *41*, 5488-5490. <https://doi.org/10.3233/WOR-2012-0861-5488>

- Chaffin, D. B., Andres, R. O., & Garg, A. (1983). Volitional postures during maximal push/pull exertions in the sagittal plane. *Human Factors*, 25(5), 541-550. <https://doi.org/10.1177/001872088302500508>
- Chen, S. H., Lee, Y. H., & Lin, C. J. (2015). Effects of load position and force direction on back muscle loading in one-wheeled wheelbarrow tasks. *Work*, 51, 113-119. <https://doi.org/10.3233/WOR-141841>
- Cohen, A. L., Gjessing, C. C., Fine, L. J., Bernard, B. P., & McGlothlin, J. D. (1997). *Elements of ergonomics programs: A primer based on workplace evaluations of musculoskeletal disorders*. U.S. Department of Health and Human Services. <https://www.cdc.gov/niosh/docs/97-117/pdfs/97-117.pdf>
- Cook, D. A., & Beckman, T. J. (2006). Current concepts in validity and reliability for psychometric instruments: Theory and application. *American Journal of Medicine*, 119(2), 166.e7-166.e16. <https://doi.org/10.1016/j.amjmed.2005.10.036>
- Cuervo, C. A., Sarmiento, A., Quintana, L., Schulze, L. J., & Delclos, G. (2003). Determination of the maximum peak forces in the activities of pushing and pulling by experienced female workers in Colombia. *International Journal of Industrial Engineering-Theory Applications and Practice*, 10(4), 600-606.
- David, G. C. (2005). Ergonomic methods for assessing exposure to risk factors for work-related musculoskeletal disorders. *Occupational Medicine*, 55(3), 190-199. <https://doi.org/10.1093/occmed/kqi082>
- Douwes, M., Könemann, R., Hoozemans, M., Kuijjer, P., & Vermeulen, H. (2019). DUTCH: A new tool for practitioners for risk assessment of push and pull activities. *Annals of Work Exposures and Health*, 63(2), 137-144. <https://doi.org/10.1093/annweh/wxy101>
- Eliasson, K. (2017). Occupational health services in the prevention of musculoskeletal disorders: Processes, tools and organizational aspects (Doctoral dissertation). KTH Royal Institute of Technology, Sweden. <https://www.diva-portal.org/smash/record.jsf?pid=diva2%3A1069024&dsid=137>
- Ferreira, J., Smith, M., & Hill, H. (2007). *Evaluating the Feasibility of Developing Assessment Charts for High Risk Pushing and Pulling Operations*. Health and Safety Executive.
- Frost, D. M., Beach, T. A. C., Crosby, I., & McGill, S. M. (2015). Firefighter injuries are not just a fireground problem. *Work*, 52, 835-842. <https://doi.org/10.3233/wor-152111>
- Gyemi, D. L., van Wyk, P. M., Statham, M., Casey, J., & Andrews, D. M. (2016). 3D peak and cumulative low back and shoulder loads and postures during greenhouse pepper harvesting using a video-based approach. *Work*, 55, 817-829. <https://doi.org/10.3233/WOR-162442>
- Health and Safety Laboratory. (2013). *Further Work for the Development of an Inspection Tool for Risk Assessment of Pushing and Pulling Force Exertion*. London. <https://www.hse.gov.uk/research/rrhtm/rr998.htm>
- Hoozemans, M. J. M., Kuijjer, P., Kingma, I., van Dieën, J. H., de Vries, W. H. K., van der Woude, L. H. V., Veegar, D. J., van der Beek, A. J., & Frings-Dresen, M. H. W. (2004). Mechanical loading of the low back and shoulders during pushing and pulling activities. *Ergonomics*, 47(1), 1-18. <https://doi.org/10.1080/00140130310001593577>
- Hoozemans, M. J. M., van der Beek, A. J., Frings-Dresen, M. H. W., van der Woude, L. H. V., & van Dijk, F. J. H. (2002). Pushing and pulling in association with low back and shoulder complaints. *Occupational & Environmental Medicine*, 59(10), 696-702. <https://doi.org/10.1136/oem.59.10.696>
- Hoozemans, M. J. M., van der Beek, A. J., Frings-Dresen, M. H. W., van Dijk, F. J. H., & van der Woude, L. H. V. (1998). Pushing and pulling in relation to musculoskeletal disorders: A review of risk factors. *Ergonomics*, 41(6), 757-781. <https://doi.org/10.1080/001401398186621>

- International Organization for Standardization. (2007). *ISO 11228-2:2007: Ergonomics -Manual Handling-Part 2: Pushing and Pulling*. International Organization for Standardization [ISO]. Geneva. <https://www.iso.org/standard/26521.html>
- Jahrami, H., Khandakji, S., Al-Shorbaji, N., Al-Bayati, S., & Hussain, A. (2019). Assessing ergonomic risks using the Quick Exposure Check (QEC) and the Rapid Entire Body Assessment (REBA): A comparative study. *Work*, *62*(2), 291-299. <https://doi.org/10.3233/WOR-192910>
- Jung, M., Haight, J. M., & Freivalds, A. (2005). Pushing and pulling carts and two-wheeled hand trucks. *International Journal of Industrial Ergonomics*, *35*, 79-89. <https://doi.org/10.1016/j.ergon.2004.08.006>
- Kadikou, Y., & Rahman, M. N. A. (2016). Manual material handling risk assessment tool for assessing exposure to risk factors of work related musculoskeletal disorders: A review. *Journal of Engineering & Applied Sciences*, *11*(10), 2226-2232.
- Kuijjer, P. P. F. M., Hoozemans, M. J. M., & Frings-Dresen, M. H. W. (2007). A different approach for the ergonomic evaluation of pushing and pulling in practice. *International Journal of Industrial Ergonomics*, *37*(11-12), 855-862. <https://doi.org/10.1016/j.ergon.2007.07.011>
- Laws of Malaysia. (1994). *Act 514: Occupational Safety and Health Act 1994*. <http://www.dosh.gov.my/index.php/en/legislation/acts/23-02-occupational-safety-and-health-act-1994-act-514/file>
- Lee, T. H. (2018). Foot placement strategy in pushing and pulling. *Work*, *59*(2), 243-247. <https://doi.org/10.3233/wor-172671>
- Li, G., & Buckle, P. (1992). Current techniques for assessing physical exposure to work-related musculoskeletal risks, with emphasis on posture-based methods. *Ergonomics*, *42*(5), 674-695. <https://doi.org/10.1080/001401399185388>
- Lind, C. (2017). *Assessment and Design of Industrial Manual Handling to Reduce Physical Ergonomics Hazards - Use and Development of Assessment Tools* (Doctoral dissertation). KTH Royal Institute of Technology, Sweden. <https://www.diva-portal.org/smash/record.jsf?pid=diva2%3A1094542&dsid=-9633>
- Lind, C. (2018). Pushing and pulling: An assessment tool for occupational health and safety practitioners. *International Journal of Occupational Safety and Ergonomics*, *24*(1), 14-26. <http://dx.doi.org/10.1080/10803548.2016.1258811>
- Marras, W. S., Knapik, G. G., & Ferguson, S. (2009). Loading along the lumbar spine as influenced by speed, control, load magnitude, and handle height during pushing. *Clinical Biomechanics*, *24*(2), 155-163. <http://dx.doi.org/10.1016/j.clinbiomech.2008.10.007>
- Mital, A., Nicholson, A. S., & Ayoub, M. M. (1997). *A Guide to Manual Materials Handling* (2nd ed.). CRC Press.
- Moher, D., Liberati, A., Tetzlaff, J., Altman, D. G., & The PRISMA Group. (2009). Preferred reporting items for systematic reviews and meta-analyses: The PRISMA statement. *PLoS Medicine*, *6*(7), Article e1000097. <https://doi.org/10.1371/journal.pmed.1000097>
- Monaco, M. G. L., Uccello, R., Muoio, M., Greco, A., Spada, S., Coggiola, M., Pedata, P., Caputo, F., Chiodini, P., & Miraglia, N. (2019). Work-related upper limb disorders and risk assessment among automobile manufacturing workers: A retrospective cohort analysis. *Work*, *64*(4), 755-761. <https://doi.org/10.3233/WOR-193037>
- Occhipinti, E., & Colombini, D. (2015). Ergonomic risk assessment tools in occupational safety and health management: A review. *Safety and Health at Work*, *6*(1), 1-13. <https://doi.org/10.1016/j.shaw.2014.07.005>

- Rahman, M. N. A., & Mohamad, S. S. (2017). Review on pen and paper based observational methods for assessing ergonomic risk factors of computer work. *Work*, 57(1), 69-77. <https://doi.org/10.3233/WOR-172541>
- Rohani, J. M., Adeyemi, A. J., Aziz, R. A., & Rani, M. R. A. (2018). The inter-rater and intra-rater reliability analysis of workplace ergonomic risk assessment. *Jurnal Teknologi*, 80(1), 53-59.
- Snook, S. H., & Ciriello, V. M. (1991). The design of manual handling tasks: Revised tables of maximum acceptable weights and forces. *Ergonomics*, 34(9), 1197-1213. <https://doi.org/10.1080/00140139108964855>
- Snook, S. H., & Ciriello, V. M. (1974). The effects of heat stress on manual handling tasks. *American Industrial Hygiene Association Journal*, 35(11), 681-685. <https://doi.org/10.1080/0002889748507088>
- Snook, S. H. (1978). The ergonomics society the society's lecture 1978. The design of manual handling tasks. *Ergonomics*, 21(12), 963-985. <https://doi.org/10.1080/00140137808931804>
- Steinberg, U. (2012). New tools in Germany: Development and appliance of the first two KIM ("lifting, holding and carrying" and "pulling and pushing") and practical use of these methods. *Work*, 41(Supplement 1), 3990-3996. <https://doi.org/10.3233/WOR-2012-0698-3990>
- Sukadarin, E. H., Deros, B. M., Ghanib, J. A., Ismail, A. R., & Nawib, N. S. M. (2015, August 9-14). Inter-observer and intra-observer ergonomics measurement method reliability test. In *Proceedings 19th Triennial Congress of the IEA* (pp. 1-8). Melbourne, Australia.
- Todd, A. I. (2012). Impact of hand forces and start/stop frequency on physiological responses to three forms of pushing and pulling: A South African perspective. *Work*, 41(Supplement 1), 1588-1593. <https://doi.org/10.3233/WOR-2012-0357-1588>.
- Waters, T., Lloyd, J. D., Hernandez, E., & Nelson, A. (2011). AORN ergonomic tool 7: Pushing, pulling, and moving equipment on wheels. *AORN Journal*, 94(3), 254-260. <http://dx.doi.org/10.1016/j.aorn.2010.09.035>
- Xiao, Y., & Watson, M. (2019). Guidance on conducting a systematic literature review. *Journal of Planning Education and Research*, 39(1), 93-112. <https://doi.org/10.1177/0739456X17723971>
- Younger, P. (2010). Learning zone using google scholar to conduct. *Nursing Standard*, 24(45), 40-48. <https://doi.org/10.7748/ns.24.45.40.s51>
- Zetterberg, C., Heiden, M., Lindberg, P., Nylén, P., & Hemphälä, H. (2019). Reliability of a new risk assessment method for visual ergonomics. *International Journal of Industrial Ergonomics*, 72, 71-79. <https://doi.org/10.1016/j.ergon.2019.04.002>

## An Extreme Learning Machine Approach for Forecasting the Wholesale Price Index of Food Products in India

Dipankar Das\* and Satyajit Chakrabarti

University of Engineering & Management, New Town, Kolkata, 700160, India

### ABSTRACT

Precise food price forecasting is crucial for any country, and searching for appropriate approach(s) from an assortment of available strategies toward this objective is an open problem. The current Indian Wholesale Price Index (WPI) series contains sixty individual food items in the 'manufacture of food product' category. This work considered the monthly data from April 2011 to June 2022, i.e., one hundred thirty-five months' data of these sixty WPIs. The researchers extracted the linearity, curvature, and autocorrelation features for each WPI. The curvature and linearity-based grouping of these WPIs revealed that the WPIs are heterogeneous. This work proposed an extreme learning machine (ELM) approach for forecasting these WPIs. The present work employed the following twenty-two time-series forecasting techniques: six standard methods (Auto ARIMA, TSLM, SES, DES, TES, and Auto ETS), five neural networks (Auto FFNN, Auto GRNN, Auto MLP, Auto ELM, and proposed ELM), and eleven state-of-art techniques (two ARIMA-ETS based ensembles, an ARIMA-THETAF-TBATS based ensemble, one MLP, and seven LSTM-based models) to identify the best forecasting approach for these WPIs. For the majority of WPIs, the offered ELM attained suitable performance in the case of fifteen months of out-of-sample forecasting. Nearly eighty-seven percent of cases achieved high accuracy ( $MAPE \leq ten$ ) and outshined others. Upon accuracy comparison, both forecast-MAPE and forecast-RMSE,

between the proposed ELM and others, this paper observed that the proposed ELM's performance is more favorable. This paper's findings imply that the proposed ELM is a promising prospect to offer accurate forecasts of these sixty WPIs.

*Keywords:* Artificial Neural Network, extreme learning machine, feature extraction, time-series forecasting, wholesale price index

### ARTICLE INFO

#### Article history:

Received: 01 January 2023

Accepted: 04 April 2023

Published: 12 October 2023

DOI: <https://doi.org/10.47836/pjst.31.6.30>

#### E-mail addresses:

[dipankr.das@gmail.com](mailto:dipankr.das@gmail.com) (Dipankar Das)

[satyajit.chakrabarti@iemcal.com](mailto:satyajit.chakrabarti@iemcal.com) (Satyajit Chakrabarti)

\*Corresponding author

## INTRODUCTION

In the present day, manufactured food products are crucial to daily life, and the food industry delivers various food products to the human population. Price forecasting helps profit maximization (Wibowo & Yasmina, 2021; Gaspar et al., 2021) and risk minimization (Wibowo & Yasmina, 2021; Sabu & Kumar, 2020). Accurate commodity price forecasting assists in effective decision-making (Choong et al., 2021). Food price forecasting adds value to all stakeholders, e.g., policymakers, consumers, and agriculturalists, by providing reliable price projections of the food items (MacLachlan et al., 2022). Researchers applied eclectic time-series forecasting strategies to predict the prices of food items (Menculini et al., 2021; Mgale et al., 2021; Dacha et al., 2021; Sanusi et al., 2022; Mahto et al., 2021). The works of literature exhibited that the researchers utilized an assortment of techniques, e.g., Autoregressive Integrated Moving Average (ARIMA) by Adam (2022), Exponential Smoothing (ES) by Rosyid et al. (2019), 'Error, Trend, Seasonality' (ETS) by Purohit et al. (2021), Regression by Mishra et al. (2019), and Artificial Intelligence (AI) by Sanusi et al. (2022) to predict future prices of food items. Whereas an array of approaches exists for food price forecasting, and none of them is a clear winner, it is imperative that accurate food price forecasting becomes critical for all stakeholders. Therefore, searching for the most appropriate approach for price forecasting of a wide range of food items becomes an open problem.

### Food Price Forecasting Using Several Approaches

The ARIMA (p, d, q), a linear model, has a fixed structure, is more interpretable, and uses historical data to predict future values. It faces difficulty in turning point prediction and involves subjectivity in determining the p, d, and q values. The authors applied the ARIMA techniques to forecast the prices of rice (Adam, 2022; Fernando et al., 2021) and sugar (Şahinli, 2021). The researchers used this technique for forecasting chili (Septiani & Setyowati, 2021), palm oil (Yee & Humaida, 2021), and numerous other items (Zhou, 2021; Astiningrum et al., 2021; Taofik & Tihamiyu-Ibrahim, 2021) prices.

The ES technique is simple, gives a greater emphasis on recent observations, and uses the principle of the weighted sum (linear sum) of lags, where the current data has higher weights and weights reduce exponentially. It ignores the data spikes and is less effective in handling trends. Rosyid et al. (2019) used the following three ES techniques to forecast the prices of rice, chicken, beef, egg, shallot, garlic, red chili, raw chili, oil, and sugar: single exponential smoothing (SES), double exponential smoothing (DES), and triple exponential smoothing (TES). The authors (Dewi & Listiowarni, 2020; Şahinli, 2020) applied Holt-Winters (HW) to forecast various food prices. Some researchers (Lutfi et al., 2019; Fitria, 2018) utilized SES to predict food prices. Talwar and Goyal (2019) employed exponential smoothing techniques, e.g., SES, DES, and HW, to forecast coriander prices. Prakash et al. (2022) applied the HW approach to predict sweet potato prices.

The ETS - a state-space approach, uses exponential smoothing and can model the trend and seasonality components of the data. It combines the error, trend, and seasonality components and offers a family of possible models. An ETS model includes a measurement equation that explains the observations and a few state equations expressing the transition of states. The authors (Purohit et al., 2021; Koblianska et al., 2021) applied it to the potato-price forecast. Other authors utilized the ETS approach for forecasting various food item prices, e.g., onion (Purohit et al., 2021), rice (Wahyuni & Afandi, 2018), and salmon (Tharmarajah & Gjesdal, 2020).

Regression is a frequently employed quantitative technique and easily adapts to even challenging forecasting assignments. Time series regression, a statistical approach, uses autoregressive dynamics, i.e., response history and dynamics transfer from pertinent predictors to forecast. The authors applied different regression approaches to predict several food item prices, e.g., corn (Ge & Wu, 2020) and potato (Mishra et al., 2019). Asnhari et al. (2019) utilized it for red chili, onion, and garlic price prediction. Volkov et al. (2019) applied it to predict the butter, egg, and bread prices.

The Artificial Neural Network (ANN) is a prominent AI method that processes information inspired by biological-nervous systems and learns via examples. It has an innovative structure for information processing and comprises several intricately linked processing units called neurons that collaborate to address particular issues. ANN is flexible, applies universal approximators, supplies effective forecasting, and can operate on diverse time-series data, both linear and non-linear. The authors applied neural approach-based forecasting techniques to predict the future prices of various items, e.g., white beans (Sanusi et al., 2022), white maize (Sanusi et al., 2022), and soybean (Zhang et al., 2018). Some utilized ANN to forecast potato (Areef & Radha, 2020; Choudhury et al., 2019), coffee (Xu & Zhang, 2022b), and sugar (Xu & Zhang, 2022b) prices. A few employed ANN for price prediction of soybean oil (Xu & Zhang, 2022a; Xu & Zhang, 2022b), rice (Sanusi et al., 2022; Shao & Dai, 2018), and wheat (Shao & Dai, 2018).

## Motivation

To aid the stakeholders in appropriate policymaking, dependable and precise forecasting of food prices plays a vital role. The wholesale price index (WPI) is a macroeconomic indicator. It describes the wholesale pricing of commodities and records the average change in wholesale prices of products. The current WPI-series of India lists sixty individual items in the 'manufacture of food product' (food-product) category.

Das and Chakrabarti (2021) developed an MLP model to forecast the WPIs of selected food items in India, considering the data from April 2012 to March 2017, and chose thirty-six items from the food-product category that showed positive linearity and negative curvature features. This MLP [2/1/1] approach proposed by Das and Chakrabarti (2021)

exhibited promising results. They had not observed its applicability to other WPIs and have the following gap: evolvement of an efficacious forecasting strategy(s) for all the sixty individual items under the food-product category of the current WPI series of India.

The nonexistence of any work that explored various forecasting techniques on the WPI of all individual items from the food-product category of the current WPI of India and comprehending the significance of forecasting these WPIs, filling this gap thus becomes a stimulus. It motivates the present work to explore the usefulness of several standard time-series forecast approaches and some state-of-the-art techniques offered by others in forecasting all the indices of individual items from the food-product category of the WPI series of India. Further, it motivates this work to deliver a strategy that can provide effective forecasting for all these WPIs.

### **Objectives of the Study**

- To propose and construct a novel neural approach that is straightforward, easy to use, and capable of delivering effective forecasting for most indices of the individual items from the food-product category of the WPI series of India.
- To predict out-of-sample values for these WPIs using the proposed neural approach.
- To predict out-of-sample values for these WPIs employing several standard time-series forecasting approaches and some state-of-the-art forecasting techniques offered by others.
- To compare the outcomes of the offered technique with others and determine the most acceptable forecasting approach for the WPIs of the individual items from the food-product category of the WPI series of India.

## **METHODOLOGY**

### **Overview of the Research**

Figure 1 represents the overview of the present research.

The researchers collected the WPI of sixty items for one hundred thirty-five months, extracted their linearity, curvature, and auto-correlated lag features through feature engineering, obtained the proposed approach's optimized model for them, produced out-of-sample forecasts using the respective optimized models and other techniques, and evaluated the forecast performances of these approaches.

The scope of this work is limited to developing forecast models for the univariate time-series data. Thus, the authors have only considered the univariate time-series forecasting models in this work and have yet to explore the impact of various influencing factors that affect the WPI of food items in model development.



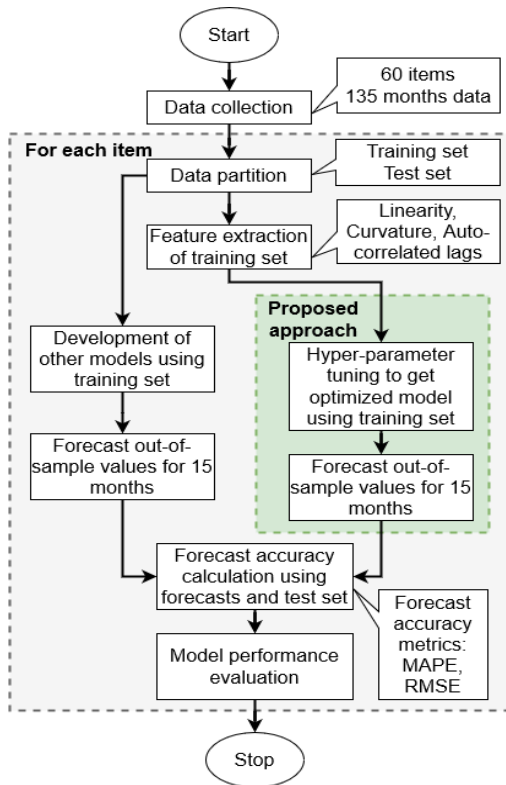


Figure 1. Research outline

Table 1  
Data partition

Start	End	Duration (months)	Description
April 2011	June 2022	135	Full dataset
April 2011	March 2021	120	Training set
April 2021	June 2022	15	Test set

The ELM uses 'Moore-Penrose generalized inverse' to set the randomly assigned weights instead of backpropagation (Erdem, 2020). Kourentzes (2019b) suggested the following for better modeling of time series with neural approaches: utilizing differences for trend removal as trend modeling is not a strong suit for them and using seasonal dummy(s) to model deterministic seasonality. The ELM is a quick learner, simple, and efficient. ELM approach exhibited promising performances when applied to diverse time-series data (Chakraborty et al., 2022; Feng et al., 2021; Talkhi et al., 2021; Niu et al., 2019).

The structure of the proposed ELM-based neural approach for forecasting the WPIS of the individual items from the food-product category of India is as follows:

### Data

This work used the monthly index of sixty individual items from the food-product category of the Indian WPI from April 2011 to June 2022, i.e., one hundred thirty-five months of data (<https://data.gov.in/resource/wholesale-price-index-base-year-2011-12-till-last-month>).

Table 1 reveals the divisions of the data set. This work applied the training set for feature extraction, tuning the model hyper-parameters, and estimating the model parameters and model building. The fifteen-month hold-out test set is used for forecast accuracy computation of the models.

### Proposed Neural Approach

An extreme learning machine (ELM) is a feed-forward neural network. It consists primarily of a single hidden layer and exhibits considerably quick convergence than conventional ones (Wang et al., 2022).

- Input  $(X) = \{x_1, x_2, \dots, x_n, ds_1, ds_2, \dots, ds_m\}$  where  $x_i$  is autocorrelated lags identified from the ACF plot of the time-series and  $ds_j$  is seasonal dummy(s) to model deterministic seasonality. The deterministic seasonality is identified using the Canova-Hansen test.
- Single hidden layer
- No. of neurons in the hidden layer  $(N) = N_1$
- Hyper-parameter tuning (Figure 2) of the ELM network to get the optimum  $N_1$  value from the search space  $(S)$  where  $S = \{100, 200, \dots, 1200\}$
- Weights of output layer estimated by lasso regression with CV
- 20 networks trained to deliver ensemble forecasts
- Used median operator to combine forecasts
- Applied first-order differencing for trend removal of the time series

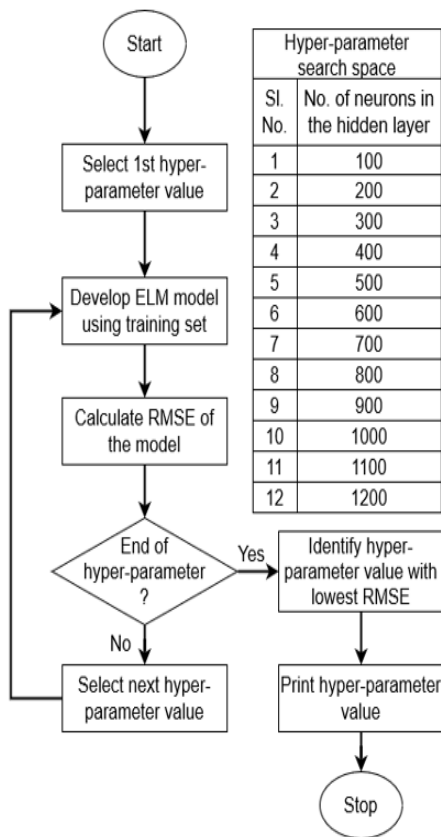


Figure 2. Hyper-parameter tuning technique

This work employed the 'nnfor' package of R (Kourentzes, 2019a) to develop the ELM. The proposed ELM, rather than using the offered automatic input selection procedure, employed a tailored strategy for input selection, selected the weight estimation type among the available estimation types (i.e., lasso, ridge, stepwise, and linear regressions), specified the combination operator from the set offered ones (i.e., mean, KDE estimation based mode, and median), selected the number of training networks, applied the number of differencing to detrend the data, designed the hyper-parameter search space to determine the number of hidden nodes for optimization, and tuned the ELM to obtain the optimized ELM from the specified search space.

Chakraborty et al. (2022) offered an ELM with many (6000) hidden nodes. Kourentzes (2019b) suggested using one hundred nodes in the hidden layer by default and adjusting it as required. This work designed the hyper-parameter search space of the proposed ELM using a heuristic

approach. It starts from the default 100 and increases in the equal interval (step length 100, i.e., equal to the default value) up to 1200. The authors developed it considering the trade-off between model performance, speed, and computational cost. Expanding the search space may deliver better performance but with much slower performance and increased computational costs.

### Other Approaches

This work applied several approaches for forecasting fifteen months of out-of-sample values of the sixty WPIs. It employed six standard time-series forecast techniques, which are as follows: linear regression (TSLM), SES, DES, TES, Auto-ARIMA, and Auto-ETS. The work further utilized four automatic neural approaches, namely, feedforward neural network (FFNN), generalized regression neural network (GRNN), Multilayer Perceptron (MLP), and ELM. This work additionally explored four state-of-the-art approaches: an MLP (Das & Chakrabarti, 2021) and three ensembles (Perone, 2022; Shaub, 2020) to evaluate the performance of the proposed ELM. Das and Chakrabarti (2021) developed an MLP to forecast the WPIs of some selected food products from India, whereas Perone (2022) applied the ARIMA-ETS-based ensembles in COVID-19 case prediction. Shaub (2020) used an ARIMA-THETAF-TBATS ensemble approach for quick and precise forecasting of time-series data. It also employed seven LSTM-based models presented by others (Brownlee, 2018; Staffini, 2022; Patel et al., 2018; Jia et al., 2019) to assess the proposed ELM.

### Accuracy Metrics

This work utilized the following forecast accuracy metrics (Saba et al., 2021; <https://www.rdocumentation.org/packages/DescTools/versions/0.99.36/topics/Measures%20of%20Accuracy>): Root-Mean-Square-Error (RMSE) and Mean-Absolute-Percentage-Error (MAPE). Several authors (Fan et al., 2010; Yadav & Nath, 2019) evaluated the model performance as follows: (a) high accuracy when  $MAPE \leq 10$ , (b) good accuracy when  $10 \leq MAPE \leq 20$ , (c) reasonable accuracy when  $20 \leq MAPE \leq 50$ , and (d) inaccurate when  $MAPE \geq 50$ .

This work computed the forecast accuracies (i.e., forecast-MAPE and forecast-RMSE) using the forecasts and test set. An in-sample prediction and training set is used to calculate in-sample RMSE.

### Experimental Setup

This paper employed the following packages of R (<https://www.r-project.org/>):

- Linear, SES, DES, TES, ETS, ARIMA, FFNN models: forecast package (Hyndman, Athanasopoulos, et al., 2022; Hyndman & Khandakar, 2008)

- MLP, ELM models: nnfor package (Kourentzes, 2019a)
- GRNN model: tsfgrnn package (Frias-Bustamante et al., 2022)
- Ensemble models: forecastHybrid package (Shaub & Ellis, 2020)
- Feature extraction: tsfeatures package (Hyndman, Kang, et al., 2022)

## RESULTS

### Features of the WPI

This work extracted the linearity, curvature, and auto-correlated lag features of each WPI. The researchers grouped the WPIs employing the extracted curvature and linearity features (Figure 3). Figure 3 reveals that the WPIs are heterogeneous based on the obtained linearity and curvature groupings.

### Optimized ELM for Each WPI

The current work developed the ELM model for each WPI using the proposed methodology for obtaining the optimized ELM, and Table 2 tabulates the optimized ELM architecture for each of them.

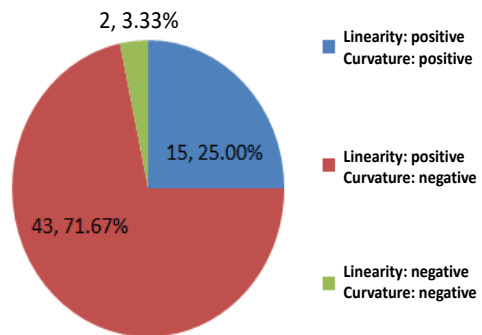


Figure 3. Grouping of the WPIs

Table 2  
Optimized ELM

Item Code	Item Name	Optimal Inputs			Optimized ELM
		Auto-correlated lags ( $x_i$ )	Seasonal dummies ( $ds_j$ )	Input (X)	
WPI1	'Buffalo meat, fresh/frozen'	21	11	32	[32-100-1] *
WPI2	'Meat of goat, fresh or chilled'	23	11	34	[34-100-1] *
WPI3	'Other meats, preserved/processed'	31	-	31	[31-100-1] <sup>s</sup>
WPI4	'Chicken/duck, dressed - fresh/frozen'	22	11	33	[33-100-1] *
WPI5	'Shrimps/Prawns - Processed/Frozen'	11	-	11	[11-100-1] <sup>s</sup>
WPI6	'Fish frozen/canned/processed'	29	11	40	[40-100-1] *
WPI7	'Fruit Juice including concentrates'	12	11	23	[23-100-1] *

Table 2 (Continue)

Item Code	Item Name	Optimal Inputs			Optimized ELM
		Auto-correlated lags ( $x_i$ )	Seasonal dummies ( $ds_j$ )	Input (X)	
WPI8	'Fruit pulp'	20	-	20	[20-100-1] <sup>s</sup>
WPI9	'Jams, jellies, marmalades and puree'	35	11	46	[46-100-1] <sup>*</sup>
WPI10	'Sauces of Vegetables (Tomato, Chilli, Soya & others)'	16	-	16	[16-100-1] <sup>s</sup>
WPI11	'Vanaspati'	29	-	29	[29-100-1] <sup>s</sup>
WPI12	'Mustard Oil'	12	11	23	[23-100-1] <sup>*</sup>
WPI13	'Soyabean Oil'	14	11	25	[25-1000-1] <sup>*</sup>
WPI14	'Sunflower Oil'	12	-	12	[12-400-1] <sup>s</sup>
WPI15	'Groundnut Oil'	11	-	11	[11-900-1] <sup>s</sup>
WPI16	'Castor Oil'	23	11	34	[34-100-1] <sup>*</sup>
WPI17	'Rice Bran Oil'	31	11	42	[42-100-1] <sup>*</sup>
WPI18	'Palm Oil'	15	-	15	[15-1000-1] <sup>s</sup>
WPI19	'Rapeseed Oil'	10	11	21	[21-100-1] <sup>*</sup>
WPI20	'Copra oil'	24	11	35	[35-700-1] <sup>*</sup>
WPI21	'Cotton seed Oil'	18	-	18	[18-1000-1] <sup>s</sup>
WPI22	'Condensed Milk'	29	11	40	[40-100-1] <sup>*</sup>
WPI23	'Ghee'	35	-	35	[35-200-1] <sup>s</sup>
WPI24	'Butter'	35	11	46	[46-100-1] <sup>*</sup>
WPI25	'Ice cream'	31	-	31	[31-100-1] <sup>s</sup>
WPI26	'Powder Milk'	13	11	24	[24-100-1] <sup>*</sup>
WPI27	'Maida'	24	11	35	[35-1200-1] <sup>*</sup>
WPI28	'Wheat flour (Atta)'	30	11	41	[41-100-1] <sup>*</sup>
WPI29	'Wheat Bran'	29	11	40	[40-700-1] <sup>*</sup>
WPI30	'Sooji (rawa)'	26	11	37	[37-100-1] <sup>*</sup>
WPI31	'Flour of cereals other than rice and wheat'	26	11	37	[37-100-1] <sup>*</sup>
WPI32	'Gram powder (besan)'	15	11	26	[26-900-1] <sup>*</sup>
WPI33	'Rice, Non-basmati'	33	11	44	[44-100-1] <sup>*</sup>
WPI34	'Basmati rice'	14	-	14	[14-100-1] <sup>s</sup>
WPI35	'Rice products'	27	11	38	[38-700-1] <sup>*</sup>
WPI36	'Vegetable starch'	12	-	12	[12-100-1] <sup>s</sup>
WPI37	'Biscuit, cookies'	30	-	30	[30-100-1] <sup>s</sup>
WPI38	'Bread, buns & croissant'	32	-	32	[32-100-1] <sup>s</sup>
WPI39	'Cakes, pastries & muffins'	29	11	40	[40-100-1] <sup>*</sup>

Table 2 (Continue)

Item Code	Item Name	Optimal Inputs			Optimized ELM
		Auto-correlated lags ( $x_i$ )	Seasonal dummies ( $ds_j$ )	Input (X)	
WPI40	'Sugar'	11	-	11	[11-100-1] <sup>§</sup>
WPI41	'Molasses'	11	11	22	[22-100-1] <sup>*</sup>
WPI42	'Bagasse'	25	-	25	[25-100-1] <sup>§</sup>
WPI43	'Gur'	15	11	26	[26-600-1] <sup>*</sup>
WPI44	'Honey'	26	-	26	[26-100-1] <sup>§</sup>
WPI45	'Chocolate & cocoa powder'	28	11	39	[39-500-1] <sup>*</sup>
WPI46	'Sugar confectionary'	36	-	36	[36-100-1] <sup>§</sup>
WPI47	'Noodles & similar extruded products'	31	-	31	[31-100-1] <sup>§</sup>
WPI48	'Processed Tea'	27	11	38	[38-1100-1] <sup>*</sup>
WPI49	'Instant Coffee'	11	11	22	[22-100-1] <sup>*</sup>
WPI50	'Coffee powder with chicory'	31	-	31	[31-100-1] <sup>§</sup>
WPI51	'Spices (including mixed spices)'	23	11	34	[34-100-1] <sup>*</sup>
WPI52	'Salt'	17	-	17	[17-100-1] <sup>§</sup>
WPI53	'Instant Food/Prepared meals based on vegetables'	31	-	31	[31-100-1] <sup>§</sup>
WPI54	'Corn Flake'	33	11	44	[44-100-1] <sup>*</sup>
WPI55	'Whey powder'	15	-	15	[15-100-1] <sup>§</sup>
WPI56	'Gola & similar Cattle Feed'	23	11	34	[34-700-1] <sup>*</sup>
WPI57	'Rice Bran Extract'	25	11	36	[36-100-1] <sup>*</sup>
WPI58	'Soya preparations excluding oil'	13	11	24	[24-100-1] <sup>*</sup>
WPI59	'Cotton seed oil cake'	25	11	36	[36-700-1] <sup>*</sup>
WPI60	'Mustard oil cake'	14	11	25	[25-100-1] <sup>*</sup>

Note. \* Input nodes of the optimized ELM are auto-correlated lags and seasonal dummies.

<sup>§</sup>Input nodes of the optimized ELM are auto-correlated lags

### Forecast Performance of the Proposed ELM

For forecasting the future values (forecast horizon of fifteen months) of each WPI, this work applied the optimized ELM obtained for each. The proposed ELM exhibited outstanding results, with nearly eighty-six-point-seven percent of cases, i.e., fifty-two out of sixty indices achieved high forecast accuracy. It attained good forecast accuracy for approximately eleven-point seven percent indices, i.e., seven out of sixty. Figure 4 exhibits the forecast performance of the proposed ELM.

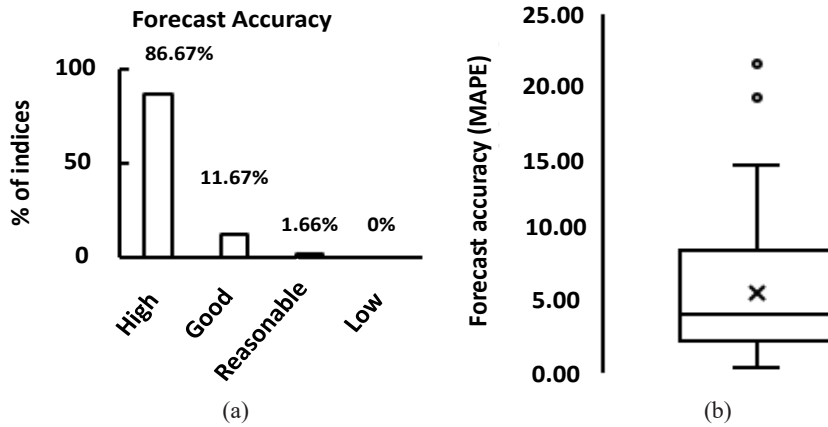


Figure 4. Forecast performance of the proposed ELM

Table 3 details the group-wise performance of the proposed ELM. The proposed ELM performed satisfactorily for group 1. It achieved high percentages of high accuracies for the WPIs with negative curvature.

Table 3  
Group-wise performance of the proposed ELM

Group No.	Group Description	WPI with MAPE $\leq$ 10
1	Linearity: positive, Curvature: positive	73.33%
2	Linearity: positive, Curvature: negative	90.70%
3	Linearity: negative, Curvature: negative	100.00%

### Forecast Accuracy Comparison of the Proposed ELM with Others

The current work applied six statistical, namely Auto-ARIMA, Auto-ETS, SES, DES, TES, and TSLM, and four neural approaches, namely Auto-FFNN, Auto-GRNN, Auto-MLP, and Auto-ELM, to make a forecast of fifteen months ahead of values for each of the sixty WPIs. This work counted the cases when each approach achieved high accuracy and compared the results. The proposed ELM topped the list with the highest count, i.e., nearly eighty-six-point seven percent high accuracy cases. Further, the work compared the proposed ELM's forecast-MAPE and forecast-RMSE with others and observed that the proposed ELM outperformed all in the maximum events. Figures 5, 6, and 7 demonstrate the determinations.

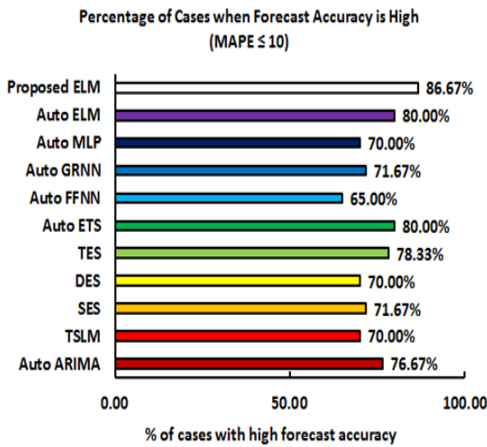


Figure 5. High accuracy: proposed ELM vs. others

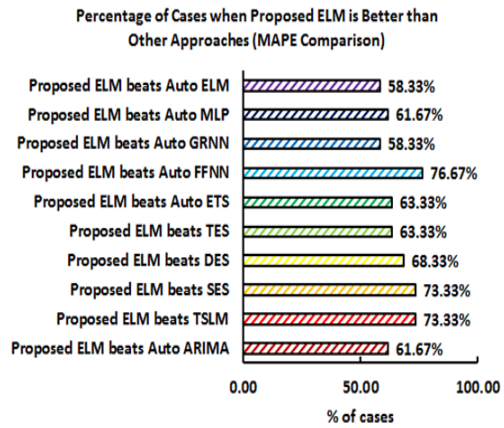


Figure 6. Forecast-MAPE comparison: proposed ELM vs. others

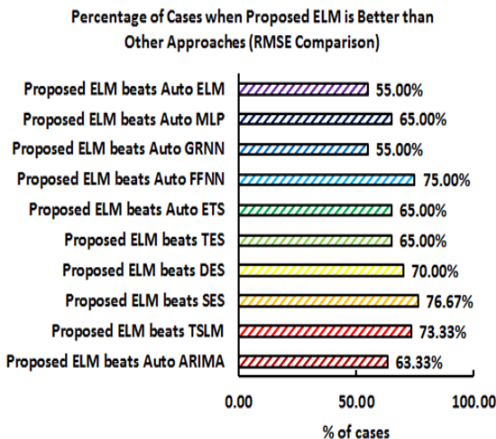


Figure 7. Forecast-RMSE comparison: proposed ELM vs. others

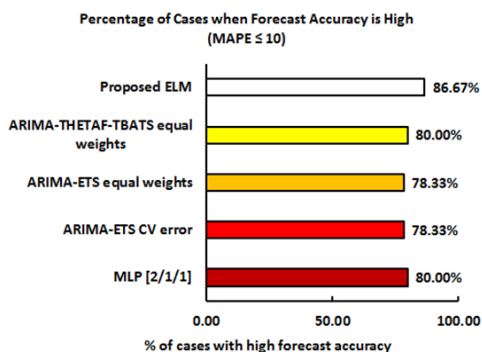


Figure 8. High forecast accuracy of proposed ELM, MLP, and ensemble approaches

The current work contrasted the proposed ELM with the following approaches and represents the findings in Figures 8 and 9:

- MLP [2/1/1] (Das & Chakrabarti, 2021)
- ARIMA-ETS equal weights (Perone, 2022)
- ARIMA-ETS CV error (Perone, 2022)
- ARIMA-THETAF-TBATS equal weights (Shaub, 2020)

The proposed ELM outperformed others as regards the counts of high accuracy and the number of cases when the proposed approach's accuracy is better.

Table 4 compares the proposed ELM with these models (i.e., an MLP and three ensemble models presented by others). The proposed ELM approach obtained lower maximum, mean, and median MAPE values than the others and surpassed them.



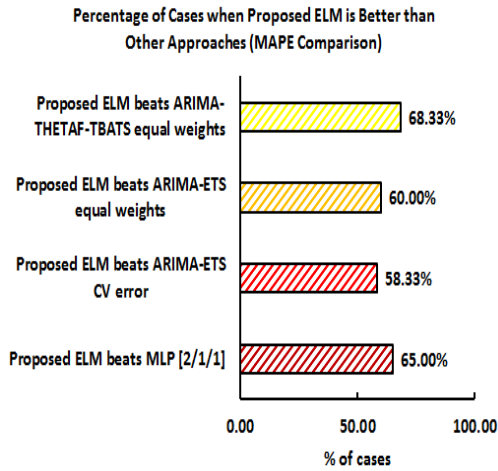


Figure 9. Forecast-MAPE comparison of proposed ELM with others

Table 4  
Comparison of the proposed ELM with others

Author	Model	Forecast horizon	Maximum MAPE	Mean MAPE	Median MAPE
Das and Chakrabarti (2021)	MLP [2/1/1]		22.26	6.51	4.36
Perone (2022)	ARIMA-ETS equal weights		26.32	6.80	4.53
Perone (2022)	ARIMA-ETS CV error	15 months	26.42	6.80	4.49
Shaub (2020)	ARIMA-THETAF-TBATS equal weights		25.12	6.75	5.06
Our work	Optimized ELM		21.46	5.63	4.12

Table 5  
Comparison of the proposed ELM with deep learning models

Author	Model	Forecast Horizon	Maximum MAPE	Mean MAPE	Median MAPE
Brownlee (2018)	LSTM	15 months	33.37	8.78	6.05

Further, to evaluate the proposed ELM's usefulness in forecasting the WPIs compared to the deep-learning approaches, this work analyzed the performance of the proposed ELM with the deep-learning models offered by other researchers (Brownlee, 2018; Staffini, 2022; Patel et al., 2018; Jia et al., 2019). This work employed the WPI data used in this paper for the purpose. Table 5 lists the findings. The proposed ELM's performance is better than others.

Table 5 (Continue)

Author	Model	Forecast Horizon	Maximum MAPE	Mean MAPE	Median MAPE
Brownlee (2018)	Stacked LSTM		34.03	9.04	6.18
	Bi-LSTM		33.89	8.63	5.96
Staffini (2022)	Stacked LSTM		33.74	8.42	6.70
Patel et al. (2018)	Stacked LSTM	15 months	34.69	8.77	6.25
Jia et al. (2019)	LSTM		27.69	8.09	5.75
	Bi-LSTM		33.97	8.24	5.91
Our work	Optimized ELM		21.46	5.63	4.12

## DISCUSSION

This research employed the monthly WPI of sixty items from the Indian WPI's food-product category for one hundred thirty-five months, from April 2011 to June 2022, and divided the data into training (one hundred twenty months) and test (out-of-sample fifteen months) sets. For each WPI, this work applied the training set for feature extraction (linearity, curvature, and auto-correlated lags), developed the forecast models using the proposed ELM and twenty-one others, performed fifteen months of out-of-sample predictions operating the developed models, and utilized the test set to compute the forecast accuracies of the models. This paper grouped the WPIs using the extracted curvature and linearity features. Three groups categorized all the indices and revealed the heterogeneity of the WPIs. The positive linearity and negative curvature group contained the majority of WPIs. The proposed ELM exhibited high accuracy for the majority (nearly eighty-seven percent of the WPIs) and outperformed others. It outperformed others as regards the maximum number of cases with high accuracy ( $MAPE \leq 10$ ). The proposed ELM also exhibited better performance regarding forecast-MAPE and forecast-RMSE comparisons.

## Novelties

The following are the novelties of the current work:

- Feature extraction (linearity, curvature, and auto-correlated lags) of the WPIs of all sixty individual items from the food-product category of the WPI-series of India for one hundred twenty months (April 2011 to June 2022)
- Grouping of the WPIs based on the extracted curvature and linearity features

- Devising a novel ELM strategy for the WPIs that is straightforward, easy to use, and capable of delivering effective forecasting
  - A simple yet effective way of selecting the inputs and specifying optimum hidden neurons by hyper-parameter adjustment from its predefined search space to obtain an ELM model for each WPI.
  - The proposed ELM approach incorporates the following to enhance the performance of the models obtained from the ELM strategy offered by Kourentzes (2019a): using a bespoke procedure for selecting the inputs rather than automated ones; noise and trend removal of data; selection of the weight estimation type and combination operator from the offered sets; set the number of training networks; hyperparameter tuning using the custom-designed search space to obtain the optimized model for each WPI. The proposed ELM outperformed the automated ELM.
- This work compared the proposed ELM with twenty-one established and state-of-the-art techniques: six automatic time-series forecasting approaches, five ANNs, three ensemble methods presented by others, and seven deep-learning models of the other researchers. For the forecast horizon of fifteen months, the proposed ELM achieved high forecast accuracies in nearly eighty-seven percent of the items and outperformed all.
- To the extent of our knowledge, it marks the initial endeavor toward ELM model development to forecast the WPIs of sixty food items using these one hundred thirty-five months of data.
- Analyzing twenty-two diverse time series forecast approaches (the proposed ELM, six automatic time-series forecasting approaches, four automated ANNs, three ensemble methods presented by others, one MLP proposed by other researchers, and seven deep-learning models of the other authors) in furnishing fifteen months of out-of-sample forecasts of the WPIs.

## LIMITATIONS

This work applied the proposed ELM to the indices of sixty individual items from the food-product category of the Indian WPI series. This work obtained the optimum ELM by applying hyper-parameter tuning using its predefined search space. It employed other preset conditions, such as the weight estimation technique, the number of training networks, and combining operators, to develop the model. This paper has not experimented with the proposed approach using different model settings and on other univariate time-series data.

## CONCLUSION AND FUTURE WORK

This research focuses on the WPIs of all sixty individual items from the food-product category of the current Indian WPI. It aimed to analyze these WPIs and present a suitable

forecasting strategy for these indices. The WPIs behaved heterogeneously per their extracted feature (i.e., curvature and linearity) based grouping. The grouping of WPIs revealed that these sixty WPIs have different trends and patterns, and their characteristics have varying natures. Therefore, this work exhibited that the design and performance of the proposed ELM approach are not confined to a particular type of univariate series but are suitable for a wide variety of time-series data. The Auto-ETS, a standard time-series forecast technique, performed best with eighty percent high accuracy cases. As per the number of high-accuracy cases, attaining the Auto-ELM, a neural approach is at par with it. Both exhibited high accuracy for a considerable quantity of WPIs. The offered ELM attained the maximum number of high-accuracy cases (nearly eighty-seven percent) among all the employed approaches. It also outshined others for the maximum number of indices concerning forecast-MAPE and forecast-RMSE comparisons. In conclusion, this research suggests that the proposed ELM is a well-suited prospect for providing effective forecasts of these sixty indices.

The future work includes attempting the proposed ELM on additional WPIs to test its pertinence. Endeavoring different combinations of model settings with an expanded hyper-parameter search space is another approach toward future research.

## ACKNOWLEDGEMENT

We thank the editorial team and *Pertanika Journal of Science & Technology* reviewers for their invaluable feedback and support. We also thank the University of Engineering & Management, Kolkata, India for providing us with the necessary resources and support throughout this research endeavor. We are thankful for this opportunity to contribute to the scientific community.

## REFERENCES

- Adam, A. I. (2022). Time series analysis of rice prices using Box-Jenkins ARIMA methodology: Case study Hargeisa-Somaliland. *Daha International University Academic Journal*, 1(1), 22-34. <https://doi.org/10.5281/zenodo.7193147>
- Areef, M., & Radha, Y. (2020). Application of GARCH and ANN models for potato price forecasting: A case study of Bangalore market, Karnataka state. *Indian Journal of Agricultural Marketing*, 34(3), 44-52.
- Asnhari, S. F., Gunawan, P. H., & Rusmawati, Y. (2019). Predicting staple food materials price using multivariable factors (regression and Fourier models with ARIMA). In *2019 7th International Conference on Information and Communication Technology (ICoICT)* (pp. 1-5). IEEE Publishing. <https://doi.org/10.1109/ICoICT.2019.8835193>
- Astiningrum, M., Wijayaningrum, V. N., & Putri, I. K. (2021). Analysis of staple food price forecasting results using various approaches. In *2021 7th International Conference on Electrical, Electronics and Information Engineering (ICEEIE)* (pp. 625-630). IEEE Publishing. <https://doi.org/10.1109/ICEEIE52663.2021.9616763>

- Brownlee, J. (2020). *How to develop LSTM models for time series forecasting*. Guiding Tech Media. <https://machinelearningmastery.com/how-to-develop-lstm-models-for-time-series-forecasting/>
- Chakraborty, A., Das, D., Mitra, S., De, D., & Pal, A. J. (2022). Forecasting adversities of COVID-19 waves in India using intelligent computing. *Innovations in Systems and Software Engineering*, 19(3), 1-17. <https://doi.org/10.1007/s11334-022-00486-y>
- Choong, K. Y., Raof, R. A. A., Sudin, S., & Ong, R. J. (2021). Time series analysis for vegetable price forecasting in e-commerce platform: A review. *Journal of Physics: Conference Series*, 1878, Article 012071. <https://doi.org/10.1088/1742-6596/1878/1/012071>
- Choudhury, K., Jha, G. K., Das, P., & Chaturvedi, K. K. (2019). Forecasting potato price using ensemble artificial neural networks. *Indian Journal of Extension Education*, 55(1), 73-77.
- Dacha, K., Cherukupalli, R., & Sinha, A. (2021). Food index forecasting. In *Applied Advanced Analytics: 6th IIMA International Conference on Advanced Data Analysis, Business Analytics and Intelligence* (pp. 125-134). Springer. [https://doi.org/10.1007/978-981-33-6656-5\\_11](https://doi.org/10.1007/978-981-33-6656-5_11)
- Das, D., & Chakrabarti, S. (2021). Forecast model development of some selected wholesale price index of India using MLP. In *Proceedings of International Conference on Computational Intelligence, Data Science and Cloud Computing* (pp. 217-230). Springer. [https://doi.org/10.1007/978-981-33-4968-1\\_18](https://doi.org/10.1007/978-981-33-4968-1_18)
- Dewi, N. P., & Listiowarni, I. (2020). Implementasi Holt-Winters exponential smoothing untuk peramalan harga bahan pangan di kabupaten pamekasan [Implementation of Holt-Winters exponential smoothing for forecasting food prices in Pamekasan Regency]. *Digital Zone: Jurnal Teknologi Informasi Dan Komunikasi*, 11(2), 219-231.
- Erdem, K. (2020). *Introduction to extreme learning machines*. Towards Data Science.
- Fan, R. Y., Ng, S. T., & Wong, J. M. (2010). Reliability of the Box–Jenkins model for forecasting construction demand covering times of economic austerity. *Construction Management and Economics*, 28(3), 241-254. <https://doi.org/10.1080/01446190903369899>
- Feng, Z. K., Niu, W. J., Tang, Z. Y., Xu, Y., & Zhang, H. R. (2021). Evolutionary artificial intelligence model via cooperation search algorithm and extreme learning machine for multiple scales nonstationary hydrological time series prediction. *Journal of Hydrology*, 595, Article 126062. <https://doi.org/10.1016/j.jhydrol.2021.126062>
- Fernando, W. H. H., Jayalath, P. M. S. C., Premarathne, R. M. S. M., & Chandrasekara, N. V. (2021, February 17). *Time series model to forecast monthly average white raw rice prices in Colombo, Sri Lanka* [Paper Presented]. Proceedings of 8th Ruhuna International Science and Technology Conference, Matara, Sri Lanka.
- Fitria, V. A. (2018). Parameter optimization of single exponential smoothing using golden section method for groceries forecasting. *Jurnal Sains, Matematika, dan Terapan*, 4(2), 89-97.
- Frias-Bustamante, M.P., Martinez-Rodriguez, A.M., Conde-Sanchez, A., & Martinez, F. (2022). *tsfgrnn: Time Series Forecasting Using GRNN* [R package version 1.0.4]. <https://cran.rstudio.com/web/packages/tsfgrnn/index.html>
- Gaspar, I., Castro, R., & Sousa, T. (2021). Optimisation and economic feasibility of battery energy storage systems in electricity markets: The Iberian market case study. *Journal of Cleaner Production*, 324, Article 129255. <https://doi.org/10.1016/j.jclepro.2021.129255>

- Ge, Y., & Wu, H. (2020). Prediction of corn price fluctuation based on multiple linear regression analysis model under big data. *Neural Computing and Applications*, 32(22), 16843-16855. <https://doi.org/10.1007/s00521-018-03970-4>
- Hyndman, R. J., & Khandakar, Y. (2008). Automatic time series forecasting: The forecast package for R. *Journal of statistical software*, 27, 1-22. <https://doi.org/10.18637/jss.v027.i03>
- Hyndman, R., Athanasopoulos, G., Bergmeir, C., Caceres, G., Chhay, L., O'Hara-Wild, M., Petropoulos, F., Razbash, S., Wang, E., & Yasmeen, F. (2022). *forecast: Forecasting functions for time series and linear models* [R package version 8.21.1]. <https://cran.r-project.org/web/packages/forecast/index.html>
- Hyndman, R., Kang, Y., Montero-Manso, P., Talagala, T., Wang, E., Yang, Y., & O'Hara-Wild, M. (2022). *tsfeatures: Time Series Feature Extraction* [R package version 1.1.1]. <https://cran.r-project.org/web/packages/tsfeatures/index.html>
- Jia, M., Huang, J., Pang, L., & Zhao, Q. (2019). Analysis and research on stock price of LSTM and bidirectional LSTM neural network. In *3rd International Conference on Computer Engineering, Information Science & Application Technology (ICCIA 2019)* (pp. 467-473). Atlantis Press.
- Koblianska, I., Kalachevska, L., Minta, S., Strochenko, N., & Lukash, S. (2021). Modelling and forecasting of potato sales prices in Ukraine. *Agricultural and Resource Economics: International Scientific E-Journal*, 7(4), 160-179. <https://doi.org/10.22004/ag.econ.316826>
- Kourentzes, N. (2019a). *nnfor: Time series forecasting with neural networks* [R package version 0.9.8]. <https://cran.r-project.org/web/packages/nnfor/index.html>
- Kourentzes, N. (2019b). *Tutorial for the nnfor R package*. <https://kourentzes.com/forecasting/2019/01/16/tutorial-for-the-nnfor-r-package/>
- Lutfi, M., Muttaqien, H., Apriliani, A., Zainuddin, H., & Yuyun, Y. (2019). Application of the Naïve bayes algorithm and simple exponential smoothing for food commodity prices forecasting. In *1st International Conference on Science and Technology, ICOST* (pp. 1-7). EAI. <http://dx.doi.org/10.4108/eai.2-5-2019.2284613>
- MacLachlan, M. J., Chelius, C. A., & Short, G. (2022). *Time-series methods for forecasting and modeling uncertainty in the food price outlook* (Technical Bulletin Number - 1957). Economic Research Service, U.S. Department of Agriculture.
- Mahto, A. K., Alam, M. A., Biswas, R., Ahmed, J., & Alam, S. I. (2021). Short-term forecasting of agriculture commodities in context of Indian market for sustainable agriculture by using the artificial neural network. *Journal of Food Quality*, 2021, Article 9939906. <https://doi.org/10.1155/2021/9939906>
- Menculini, L., Marini, A., Proietti, M., Garinei, A., Bozza, A., Moretti, C., & Marconi, M. (2021). Comparing prophet and deep learning to ARIMA in forecasting wholesale food prices. *Forecasting*, 3(3), 644-662. <https://doi.org/10.3390/forecast3030040>
- Mgale, Y. J., Yan, Y., & Timothy, S. (2021). A comparative study of ARIMA and Holt-Winters exponential smoothing models for rice price forecasting in Tanzania. *Open Access Library Journal*, 8(5), 1-9. <https://doi.org/10.4236/oalib.1107381>
- Mishra, M. K., Sisodia, B. V. S., & Rai, V. N. (2019). Forecasting technique of price of potato of Uttar Pradesh. *Journal of Pharmacognosy and Phytochemistry*, 8(3), 60-62.
- Niu, W. J., Feng, Z. K., Zeng, M., Feng, B. F., Min, Y. W., Cheng, C. T., & Zhou, J. Z. (2019). Forecasting reservoir monthly runoff via ensemble empirical mode decomposition and extreme learning machine

- optimized by an improved gravitational search algorithm. *Applied Soft Computing*, 82, Article 105589. <https://doi.org/10.1016/j.asoc.2019.105589>
- Patel, J., Patel, M., & Darji, M. (2018). Stock price prediction using RNN and LSTM. *Journal of Emerging Technologies and Innovative Research*, 5(11), 1069-1079.
- Perone, G. (2022). Comparison of ARIMA, ETS, NNAR, TBATS and hybrid models to forecast the second wave of COVID-19 hospitalizations in Italy. *The European Journal of Health Economics*, 23(6), 917-940. <https://doi.org/10.1007/s10198-021-01347-4>
- Prakash, P., Jaganathan, D., Immanuel, S., Lama, A., Sreekumar, J., & Sivakumar, P. S. (2022). Forecasting of sweet potato (*Ipomoea batatas* L.) prices in India. *Indian Journal of Extension Education*, 58(2), 15-20. <https://doi.org/10.48165/IJEE.2022.58203>
- Purohit, S. K., Panigrahi, S., Sethy, P. K., & Behera, S. K. (2021). Time series forecasting of price of agricultural products using hybrid methods. *Applied Artificial Intelligence*, 35(15), 1388-1406. <https://doi.org/10.1080/08839514.2021.1981659>
- Rosyid, H. A., Widiyaningtyas, T., & Hadinata, N. F. (2019). Implementation of the exponential smoothing method for forecasting food prices at provincial levels on java Island. In *2019 Fourth International Conference on Informatics and Computing (ICIC)* (pp. 1-5). IEEE Publishing. <https://doi.org/10.1109/ICIC47613.2019.8985872>
- Saba, T., Abunadi, I., Shahzad, M. N., & Khan, A. R. (2021). Machine learning techniques to detect and forecast the daily total COVID-19 infected and deaths cases under different lockdown types. *Microscopy Research and Technique*, 84(7), 1462-1474. <https://doi.org/10.1002/jemt.23702>
- Sabu, K. M., & Kumar, T. M. (2020). Predictive analytics in agriculture: Forecasting prices of Arecanuts in Kerala. *Procedia Computer Science*, 171, 699-708. <https://doi.org/10.1016/j.procs.2020.04.076>
- Şahinli, M. A. (2020). Potato price forecasting with Holt-Winters and ARIMA methods: A case study. *American Journal of Potato Research*, 97(4), 336-346. <https://doi.org/10.1007/s12230-020-09788-y>
- Şahinli, M. A. (2021). Predicting and analyzing of Turkish sugar price with ARCH, GARCH, EGARCH and ARIMA methods. *Scientific Papers: Management, Economic Engineering in Agriculture & Rural Development*, 21(3), 703-712.
- Sanusi, O. I., Safi, S. K., Adeeko, O., & Tabash, M. I. (2022). Forecasting agricultural commodity price using different models: a case study of widely consumed grains in Nigeria. *Agricultural and Resource Economics: International Scientific E-Journal*, 8(2), 124-140. <https://doi.org/10.22004/ag.econ.322724>
- Septiani, Y., & Setyowati, V. A. (2021). The ARIMA Box-Jenkins method has been used to predict the price of large curly red chilis. *Gorontalo Development Review*, 4(2), 89-101.
- Shao, Y. E., & Dai, J. T. (2018). Integrated feature selection of ARIMA with computational intelligence approaches for food crop price prediction. *Complexity*, 2018, Article 1910520. <https://doi.org/10.1155/2018/1910520>
- Shaub, D. (2020). Fast and accurate yearly time series forecasting with forecast combinations. *International Journal of Forecasting*, 36(1), 116-120. <https://doi.org/10.1016/j.ijforecast.2019.03.032>
- Shaub, D., & Ellis, P. (2020). *forecastHybrid: Convenient functions for ensemble time series forecasts* [R package version 5.0.19]. <https://cran.r-project.org/web/packages/forecastHybrid/index.html>

- Staffini, A. (2022). Stock price forecasting by a deep convolutional generative adversarial network. *Frontiers in Artificial Intelligence*, 5, Article 837596. <https://doi.org/10.3389/frai.2022.837596>
- Talkhi, N., Fatemi, N. A., Ataci, Z., & Nooghabi, M. J. (2021). Modeling and forecasting number of confirmed and death caused COVID-19 in IRAN: A comparison of time series forecasting methods. *Biomedical Signal Processing and Control*, 66, Article 102494. <https://doi.org/10.1016/j.bspc.2021.102494>
- Talwar, A., & Goyal, C. K. (2019). A comparative study of various exponential smoothing models for forecasting coriander price in Indian commodity market. *International Bulletin of Management and Economics*, 10, 143-155.
- Taofik, O. D., & Tihamiyu-Ibrahim, S. (2021). Autoregressive integration moving average (ARIMA) model for prices of selected grains in the South West Nigeria. *Agricultural Science Digest-A Research Journal*, 41(1), 35-41. <https://doi.org/10.18805/ag.D-239>
- Tharmarajah, T., & Gjesdal, B. (2020). *Salmon Price Forecasting: A Comparison of Univariate and Multivariate Forecasting Methods* (Master's thesis). Norwegian School of Economics, Norway. <https://openaccess.nhh.no/nhh-xmlui/bitstream/handle/11250/2737169/masterthesis.pdf?sequence=1>
- Volkov, A., Morkūnas, M., & Skvarciany, V. (2019). Is it possible to predict food retail prices? Evidence from Lithuanian market. In *Proceedings of 6th International Scientific Conference Contemporary Issues in Business, Management and Economics Engineering 2019* (pp. 181-187). VGTU Press. <https://doi.org/10.3846/cibmee.2019.018>
- Wahyuni, E. D., & Afandi, M. I. (2018). Price of rice forecasting based on pattern similarity. In *Proceedings IJCST 2017* (Vol. 1, No. 1, pp. 543-548). Public Knowledge Project.
- Wang, J., Lu, S., Wang, S. H., & Zhang, Y. D. (2022). A review on extreme learning machine. *Multimedia Tools and Applications*, 81(29), 41611-41660. <https://doi.org/10.1007/s11042-021-11007-7>
- Wibowo, A., & Yasmina, I. (2021). Food price prediction using time series linear ridge regression with the best damping factor. *Advances in Science, Technology and Engineering Systems Journal*, 6(2), 694-698. <https://doi.org/10.25046/aj060280>
- Xu, X., & Zhang, Y. (2022a). Canola and soybean oil price forecasts via neural networks. *Advances in Computational Intelligence*, 2(5), 1-12. <https://doi.org/10.1007/s43674-022-00045-9>
- Xu, X., & Zhang, Y. (2022b). Commodity price forecasting via neural networks for coffee, corn, cotton, oats, soybeans, soybean oil, sugar, and wheat. *Intelligent Systems in Accounting, Finance and Management*, 29(3), 169-181. <https://doi.org/10.1002/isaf.1519>
- Yadav, V., & Nath, S. (2019). Novel hybrid model for daily prediction of PM10 using principal component analysis and artificial neural network. *International Journal of Environmental Science and Technology*, 16(6), 2839-2848. <https://doi.org/10.1007/s13762-018-1999-x>
- Yee, K. W., & Humaida, B. S. (2021). Comparison between artificial neural network and arima model in forecasting palm oil price in Malaysia. *International Journal of Scientific Engineering and Science*, 5, 12-15.
- Zhang, D., Zang, G., Li, J., Ma, K., & Liu, H. (2018). Prediction of soybean price in China using QR-RBF neural network model. *Computers and Electronics in Agriculture*, 154, 10-17. <https://doi.org/10.1016/j.compag.2018.08.016>
- Zhou, L. (2021). Application of ARIMA model on prediction of China's corn market. *Journal of Physics: Conference Series, 1941*, Article 012064. <https://doi.org/10.1088/1742-6596/1941/1/012064>



# REFEREES FOR THE PERTANIKA JOURNAL OF SCIENCE & TECHNOLOGY

Vol. 31 (6) Oct. 2023

The Editorial Board of the Pertanika Journal of Science and Technology wishes to thank the following:

Adam Liwo  
*(University of Gdansk, Poland)*

Evangelos Baltas  
*(NTUA, Greece)*

Mohd Nizam Yusof  
*(UiTM, Malaysia)*

Adriano Gomes da Cruz  
*(IFRJ, Brazil)*

Ezrin Hani Sukadarin  
*(UMP, Malaysia)*

Mohd Shamsul Anuar  
*(UPM, Malaysia)*

Ain Nadirah Romainor  
*(Perdana University, Malaysia)*

Faiza Mohamed Nasir  
*(UniKL, Malaysia)*

Mohd Yusoff Ishak  
*(UPM, Malaysia)*

Amin Mojiri  
*(Hiroshima University, Japan)*

Farshid Keynia  
*(GUAT, Iran)*

Muhajir Ab Rahim  
*(UNIMAP, Malaysia)*

Amit Ranjan  
*(IFPGS, India)*

Hasnuri Mat Hassan  
*(USM, Malaysia)*

Nadiahnor Md Yusop  
*(UiTM, Malaysia)*

Arien Heryansyah  
*(UTM, Malaysia)*

Hazlee Azil Ilias  
*(UM, Malaysia)*

Nadiatul Adilah Ahmad Abdul  
Ghani  
*(UMP, Malaysia)*

At-Tasneem Mohd Amin  
*(UMP, Malaysia)*

Hidemi Nagao  
*(Kanazawa University, Japan)*

Nor Azuana Ramli  
*(UniKL, Malaysia)*

Azizan As'arry  
*(UPM, Malaysia)*

Jimoh Wasiu Adeyemi  
*(University of Ilorin, Nigeria)*

Nor Azura Husin  
*(UPM, Malaysia)*

Behrooz Taheri  
*(Islamic Azad University, Iran)*

Kek Sie Long  
*(UTHM, Malaysia)*

Noram Irwan Ramli  
*(UMP, Malaysia)*

Chartchai Leenawong  
*(KMITL, Thailand)*

Mahboobeh Azadi  
*(Semnan University, Iran)*

Norlaila Mohd Zanuri  
*(USM, Malaysia)*

Chua Han Bing  
*(Curtin University, Malaysia)*

Mahirah Jahari  
*(UPM, Malaysia)*

Nur Anisah Mohamed Rahman  
*(UM, Malaysia)*

Chuah Joon Huang  
*(UM, Malaysia)*

Mazlin Jumain  
*(UTM, Malaysia)*

Paulo Jorge Costa Nunes  
*(IPG, Portugal)*

Dian Darina Indah Daruis  
*(DIPNM, Malaysia)*

Mohammed Fouad El Basuini  
*(Tanta University, Egypt)*

Rafal M. Lukasik  
*(LNEG, Portugal)*

Elango Natarajan  
*(UCSI University, Malaysia)*

Mohd Aizuddin Mohd Lazaldin  
*(UTM, Malaysia)*

Raja Mohd Kamil Raja Ahmad  
*(UPM, Malaysia)*

Razi Ahmad  
(UNIMAP, Malaysia)

Saiful Effendi Syafruddin  
(UKM, Malaysia)

Tan Tse Guan  
(UMK, Malaysia)

Richard Lee Smith Jr.  
(Tohoku University, Japan)

Sarwan Kumar  
(PAU, India)

Tawfik A. Saleh  
(KFUPM, Saudi Arabia)

Robiah Ahmad  
(UTM, Malaysia)

Siti Noratikah Che Deraman  
(IIUM, Malaysia)

Vilmar Alves Pereira  
(UNIB, Brazil)

Ruben Lostado-Lorza  
(UNIRIOJA, Spain)

Stalin Balasubramaniam  
(Anna University, India)

Wong Yan Chiew  
(UTeM, Malaysia)

Sahazati Md Rozali  
(UTeM, Malaysia)

Sunil Datt Sharma  
(JUIT, India)

Wooi Chin Leong  
(UNIMAP, Malaysia)

---

GUAT	– Graduate University of Advanced Technology
IFRJ	– Federal Institute of Education, Science and Technology of Rio de Janeiro
IFPGS	– Institute of Fisheries Post Graduate Studies
IIUM	– International Islamic University Malaysia
IPG	– Polytechnic Institute of Guarda
JUIT	– Jaypee University of Information Technology
KFUPM	– King Fahd University of Petroleum & Minerals
KMITL	– King Mongkut's Institute of Technology Ladkrabang
LNEG	– Laboratório Nacional de Energia e Geologia I.P.
NTUA	– National Technical University of Athens
PAU	– Punjab Agricultural University
UNIRIOJA	– University of La Rioja
UITM	– Universiti Teknologi MARA
UKM	– Universiti Kebangsaan Malaysia
UM	– Universiti Malaya
UMK	– Universiti Malaysia Kelantan
UMP	– Universiti Malaysia Pahang
UNIB	– Universidade Internacional Iberoamericana
UniKL	– University Kuala Lumpur
UNIMAP	– Universiti Malaysia Perlis
UPM	– Universiti Putra Malaysia
UPNM	– Universiti Pertahanan Nasional Malaysia
USM	– Universiti Sains Malaysia
UTeM	– Universiti Teknikal Malaysia Melaka
UTHM	– Universiti Tun Hussein Onn Malaysia
UTM	– Universiti Teknologi Malaysia

---

While every effort has been made to include a complete list of referees for the period stated above, however if any name(s) have been omitted unintentionally or spelt incorrectly, please notify the Chief Executive Editor, *Pertanika* Journals at [executive\\_editor.pertanika@upm.edu.my](mailto:executive_editor.pertanika@upm.edu.my)

Any inclusion or exclusion of name(s) on this page does not commit the *Pertanika* Editorial Office, nor the UPM Press or the university to provide any liability for whatsoever reason.

The Design of an Efficient Low-cost FPGA-based Unit for Generation Ultrasound Beamforming <i>Soufiane Dangoury, Mouncef El marghichi, Mohamed Sadik and Abderrahim Fail</i>	3077
Sound Sensor Placement Strategy for Condition Monitoring of Induction Motor Bearing <i>Iradiratu Diah Prahmana Karyatanti, Istiyo Winarno, Ardik Wijayanto, Dwisetiono, Nuddin Harahab, Ratno Bagus Edy Wibowo and Agus Budiarto</i>	3093
Adaptive Threshold-based Fault Detection for Systems Exposed to Model Uncertainty and Deterministic Disturbance <i>Masood Ahmad and Rosmiwati Mohd-Mokhtar</i>	3107
Dibenzofuran Degradation by Bacterial Community in Landfill Leachate <i>Farah Najwa Ahmad, Noor Faizul Hadry Nordin, Muhamad Shirwan Abdullah Sani and Wan Syibrah Hanisah Wan Sulaiman</i>	3125
Numerical Investigation on the Distribution of Pressure Coefficients of Modified Building Shapes <i>Siti Rohani Mohd Isdris, Shahrudin Shah Zaini, Mohammad Hafîf Hafîz Ishaik, Mohammad Sharizal Abdul Aziz and Noorhazlinda Abd Rahman</i>	3139
<i>Review Article</i>	
A Systematic Review of Ergonomics Risk Assessment Methods for Pushing and Pulling Activities at Workplace <i>Hari Krishnan Tamil Selvan and Mohd Nasrull Abdol Rahman</i>	3157
An Extreme Learning Machine Approach for Forecasting the Wholesale Price Index of Food Products in India <i>Dipankar Das and Satyajit Chakrabarti</i>	3179

The Influence of Cavity Size and Location Within Insulation Paper on the Partial Discharge Activities <i>Muhammad Hakirin Roslan, Norhafiz Azis, Mohd Zainal Abidin Ab Kadir, Jasronita Jasni and Mohd Fairouz Mohd Yousof</i>	2915
Short-term Ageing Study on the Palm Oil and Mineral Oil in the Presence of Insulation Paper, Moisture, Low Molecular Weight Acid, and Oxygen <i>Muhammad Muzamil Mustam, Norhafiz Azis, Jasronita Jasni, Rasmina Halis, Mohd Aizam Talib, Robiah Yunus, Nurliyana Abdul Raof and Zaini Yaakub</i>	2931
Development of Sago-based Analog Rice Using Kansei and Value Engineering <i>Violetta Putri Rizky Septiani, Mirwan Ushada and Suharno</i>	2947
Utilizing Rainwater Harvesting System for Water Scarcity at a Double-story Residential House <i>Muhammad Izzuddin Rosli, Sharifah Abdullah and Nur Asmaliza Mohd Noor</i>	2961
Measuring Vulnerability Assessment Tools' Performance on the University Web Application <i>Pita Jarupunphol, Suppachochai Seatun and Wipawan Buathong</i>	2973
Nitrogen Dynamics in Soil Treated with Plant-growth Promoting Bacteria and Urea Fertilizer <i>Amaily Akter, Ali Tan Kee Zuan, Susilawati Kasim, Adibah Mohd Amin, Zakry Fitri Ab Aziz, Noor Md Rahmatullah, Buraq Musa Sadeq, Sayma Serine Chompa and Md Ekhlatur Rahman</i>	2995
Chitosan Dissolution in [BMIM]Cl Ionic Liquid: An Optimisation and Bacterial Ecotoxicity Study <i>Mok Shue Yee, Magaret Sivapragasam and Maisara Shahrom Raja Shahrom</i>	3013
Novel Pre-treatment for Lignocellulosic Biomass Delignification Using Alkaline-assisted Ohmic Heating <i>Izzah Farhana Ab Aziz, Hasfalina Che Man, Muhammad Hazwan Hamzah, Nur Syakina Jamali and Rozita Omar</i>	3039
Numerical Analysis and Validation of Characterization of Polydimethylsiloxane Using Hyper-elastic Constitutive Models <i>Sana Zulfiqar, Abdullah Aziz Saad, Zulkifli Ahmad, Feizal Yusof and Zuraihana Bachok</i>	3059

Effect of Lysine and Poultry Slaughterhouse by Product Meal on Growth Performance, Feed Efficiency, and Blood Profile of Sangkuriang Catfish ( <i>Clarias gariepinus</i> var. Sangkuriang) <i>Diana Rachmawati, Tita Elfitasari, Istiyanto Samidjan, Putut Har Riyadi and Dewi Nurhayati</i>	2751
Polynomial Regression Calibration Method of Total Dissolved Solids Sensor for Hydroponic Systems <i>Ansar Jamil, Teo Sheng Ting, Zuhairiah Zainal Abidin, Maisara Othman, Mohd Helmy Abdul Wahab, Mohammad Faiz Liew Abdullah, Mariyam Jamilah Homam, Lukman Hanif Muhammad Audah and Shaharil Mohd Shah</i>	2769
Intelligence System via Machine Learning Algorithms in Detecting the Moisture Content Removal Parameters of Seaweed Big Data <i>Olayemi Joshua Ibidoja, Fam Pei Shan, Mukhtar Eri Suheri, Jumat Sulaiman and Majid Khan Majahar Ali</i>	2783
Response Surface Methodology: A Versatile Tool for the Optimization of Particle Sizes of Cellulose Beads <i>Kimberly Wei Wei Tay, Suk Fun Chin, Mohd Effendi Wasli and Zaki Musa</i>	2805
<i>Review Article</i>	
A Review on Analysis Method of Proximal Hyperspectral Imaging for Studying Plant Traits <i>Jian Wen Lin, Mohd Shahrimie Mohd Asaari, Haidi Ibrahim, Mohamad Khairi Ishak dan Abdul Sattar Din</i>	2823
Influence of Heat Treatment on the Mechanical Properties and Precipitation Kinetic of Sugar Palm Fiber Ash Reinforced LM26 Al Matrix Composites <i>Isah Aliyu, Mohd Sapuan Salit, Edi Syams Zainudin, Mohd Zuhri Mohamed Yusoff and Ridwan Yahaya</i>	2851
Development of a Web-based Application by Employing a Convolutional Neural Network (CNN) to Identify Pests and Diseases on Pakcoy ( <i>Brassica rapa</i> subsp. <i>chinensis</i> ) <i>Achmad Zein Feroza, Nelly Oktavia Adiwijaya and Bayu Taruna Widjaja Putra</i>	2873
<i>Review Article</i>	
Renewable Energy Impact on Distance Relay Power Swing Blocking and Fault Discrimination: A Review <i>Chidiebere Okeke, Othman Mohammad Lutfi, Hizam Hashim, Mohd Zainal Abdin Ab Kadir, Noor Izzri Abdul Wahab, Osaji Emmanuel, Samuel Nwagbara and Collins Chimeleze</i>	2887

**Pertanika Journal of Science & Technology**  
**Vol. 31 (6) Oct. 2023**

**Content**

Foreword <i>Mohd Sapuan Salit</i>	i
<i>Review Article</i> Poultry Manure and its Contribution to Inflammation and Cancer Progression <i>Ana Masara Ahmad Mokhtar, Brennan Tang Yet Shen, Azam Muzafar Ahmad Mokhtar, Nor Hawani Salikin, Muaz Mohd Zaini Makhtar, Fatin Nur Izzati Mohd Fadzil, Nur Azzalia Kamaruzaman and Muggunna Balasubramaniam</i>	2645
<i>Review Article</i> Integrating Ice Protection and Noise Abatement Systems for Aircraft Application: A Review <i>Fathima Rehana Munas, Yu Kok Hwa, Norwahida Yusoff, Abdul Majeed Muzathik and Mohd Azmi Ismail</i>	2667
Magnetic Susceptibility and Hydrogen Cyanide Levels as Proxy Indicator for Gold Mining Pollution in River Sediment <i>Siti Zulaikah, Arif Juliansyah, Muhammad Fathur Rouf Hasan, Bambang Heru Iswanto, Mariyanto Mariyanto, Ardyanto Tanjung, Satria Bijaksana and Ann Marie Hirt</i>	2689
Recognition of Fruit Types from Striking and Flicking Sounds <i>Rong Phoophuangpairoj</i>	2703
Development of Artificial Neural Network Model for Medical Specialty Recommendation <i>Winda Hasuki, David Agustriawan, Arli Aditya Parikesit, Muammar Sadrawi, Moch Firmansyah, Andreas Whismu, Jacquelin Natasya, Ryan Mathew, Florensia Irena Napitupulu and Nanda Rizqia Pradana Ratnasari</i>	2723
Effect of Scaling the Electrostatic Interactions on the Free Energy of Transfer of Azurin from Water to Lipid Membrane Determined by Coarse-grained Simulations <i>Dian Fitrasari, Acep Purqon and Suprijadi</i>	2735



**Pertanika Editorial Office, Journal Division,**  
Putra Science Park,  
1st Floor, IDEA Tower II,  
UPM-MTDC Center,  
Universiti Putra Malaysia,  
43400 UPM Serdang,  
Selangor Darul Ehsan  
Malaysia

<http://www.pertanika.upm.edu.my>  
Email: [executive\\_editor@upm.edu.my](mailto:executive_editor@upm.edu.my)  
Tel. No.: +603- 9769 1622

**PENERBIT**  
**UPM**  
UNIVERSITI PUTRA MALAYSIA  
**PRESS**

<http://www.penerbit.upm.edu.my>  
Email: [penerbit@upm.edu.my](mailto:penerbit@upm.edu.my)  
Tel. No.: +603- 9769 8851

